THE UNIVERSITY
of ADELAIDE

Low Reynolds Number Two- and Three-Dimensional Cavity Flows and the Effect of a Cavity on Airfoil Tonal Noise

by

Karn Lee Schumacher

October 2020

School of Mechanical Engineering
The University of Adelaide

A Thesis submitted in fulfilment of the requirements of the Degree of Doctor of Philosophy in Mechanical Engineering.

Dedication

This thesis is dedicated to my late father, Wayne Juan Schumacher, a mechanical genius and my late mother, Anong Lee, an industrious entrepreneur.

Abstract

This thesis discusses the flow over rectangular and modified cavity geometries at low Reynolds number, as well as the role of a cavity in an airfoil surface in the production of airfoil tonal noise. Cavity flows can be found on many land, air and water vehicles where they can be a significant source of tonal or broadband noise. Modifying the cavity geometry is established as an effective passive control technique for cavity flow noise.

The flow about, and noise produced by, two-dimensional rectangular and modified cavity cutouts in an airfoil surface ('airfoil with cavity') were studied using an anechoic wind tunnel. As L/θ_0 increased, the coherence of shear layer vortices decreased, with an increase in the number of cavity oscillation modes found, each with lower intensity. Mean convection velocity ratio data were reported for an extended range compared to the literature, with cavity oscillation mode numbers also reported. The effect of sloping the front and rear cavity walls was investigated, with a significant change in shear layer roll-up modes found and cavity oscillation modes detected, compared to the rectangular cavity.

The production of airfoil tonal noise was unexpectedly found from the 'airfoil with cavity' profile. As the cavity position was varied on the airfoil surface, the airfoil tonal frequencies were found to vary. The noise was attributed to an aeroacoustic feedback loop, of a similar form to that responsible for cavity tones – the existence of this feedback loop as it pertains to airfoil tonal noise had been debated in the literature. A region of receptivity was identified near the cavity trailing edge where inflectional velocity profiles were measured. Boundary layer disturbances at the frequencies of the airfoil tones were detected downstream of this region. These disturbances were found to be amplified over a separation bubble upstream of the airfoil trailing edge. When external acoustic forcing was applied, the airfoil tonal noise frequencies were selectively reinforced – rather than the boundary layer's entire unstable frequency range responding to the external forcing in a smooth curve peaking at the most unstable Tollmien-Schlichting wave frequency. This suggested that a constructive feedback loop existed between the airfoil trailing edge and the region of receptivity near the cavity.

The flow about three-dimensional cavity cutouts in a flat plate were investigated using a recirculating water tunnel. The shear layer structure about a shallow, narrow rectangular cavity flow was characterised. At low Reynolds

number, ‘spanwise’ shear layer vortices were found to have significant curvature. The lateral growth of the cavity shear layer beyond the sides of the cavity was found to be significant, with a periodic flow pattern identified adjacent to the sides of the cavity. The pattern is explained in terms of an interaction of the streamwise-orientated portions of preceding and following shear layer vortices. This finally causes the formation of a tornado-like feature on the flat plate adjacent to the sides of the cavity. An asymmetric flow structure was found about a modified chevron-like cavity geometry, which was attributed to a shear layer twisting mode.

Thesis Declaration

I certify that this work contains no material which has been accepted for the award of any other degree or diploma in my name, in any university or other tertiary institution and, to the best of my knowledge and belief, contains no material previously published or written by another person, except where due reference has been made in the text. In addition, I certify that no part of this work will, in the future, be used in a submission in my name, for any other degree or diploma in any university or other tertiary institution without the prior approval of the University of Adelaide and where applicable, any partner institution responsible for the joint-award of this degree.

I acknowledge that copyright of published works contained within this thesis resides with the copyright holder(s) of those works.

I also give permission for the digital version of my thesis to be made available on the world wide web, via the University's digital research repository, the Library Search and also through world wide web search engines, unless permission has been granted by the University to restrict access for a period of time.

I acknowledge the support I have received for my research through the provision of an Australian Government Research Training Program Scholarship.

Karn Lee Schumacher

Date 25 / 10 / 2020

Acknowledgements

I wish to express my sincerest thanks to my supervisors, Associate Professor Richard M. Kelso and Professor Con J. Doolan, for their time, expertise and encouragement. I would also like to thank the School of Mechanical Engineering's academic staff, as well as research student colleagues, for helpful discussions on technical and conceptual matters (especially Dr. Chia Thong, Dr. Elias Arcondoulis, Dr. Yunpeng Xue, Dr. Danielle Moreau, Dr. Peter Lanspeary, and Dr. Kristy Hansen).

Nomenclature

Latin Characters

A, B	Coefficients in King's law for hot-wire calibration.
BT_t	Number of discrete segments, in spectral processing.
BT_{eff}	Effective number of discrete segments, for a Hann window. with a certain proportion of segment overlap.
c	Speed of sound
C	Airfoil chord
d_p	Particle diameter
D	Cavity depth
f	Frequency
f_n	Cavity oscillation frequency with Rossiter mode, n
f_n	Airfoil tonal noise frequency with mode, n
$f_{n\,\max}$	Airfoil tonal noise frequency with mode, n
f_s	Central frequency of broadband hump of airfoil tonal noise, also central frequency of Tollmien-Schlichting instability of laminar boundary layer.
Δf	Frequency spacing of airfoil tones
F_i	Proportion of Particle Image Velocimetry (PIV) pairs lost in the PIV imaging plane
i, j	Array indicies
k	Ratio of specific heats
K	total number of segments in window for spectral processing
L	Cavity length
L_c	Feedback length
$L_{\text{char.}}$	Characteristic length
M	Mach number, $M = U/c$
n	Mode/stage number of oscillations in cavity noise
n	Mode number in airfoil tonal noise
n	Exponent (where indicated as such)
N	Sample size
N_I	Number of particles in a PIV interrogation window
p	Pressure
P_e	Perspective error in PIV
Re	Reynolds number

Re_C	Reynolds number based on airfoil chord length, $Re_C = UC/\nu$
Re_D	Reynolds number based on cavity depth, $Re_D = UD/\nu$
Re_L	Reynolds number based on cavity length, $Re_L = UL/\nu$
Re_x	Reynolds number based on boundary layer development length, $Re_x = Ux/\nu$
δs	Displacement in PIV
St	Strouhal number, non-dimensional frequency
St_D	Strouhal number based on cavity depth, $St = fD/U$
Stk	Stokes number, ratio of the settling timescale of a particle to the timescale of a fluid.
t	Airfoil thickness, where indicated as such.
t	Time
δt	Time step
T	Period
u	Local velocity
u'	Fluctuation velocity (u'=$u_{\text{instantaneous}} - u_{\text{mean}}$)
U	Freestream velocity
U_c	Convection velocity
$U_{\text{char.}}$	Characteristic velocity of a particle in PIV.
W	Cavity span or width.
$w_{i,j}$	Weighting coefficient in PIV outlier replacement
x	Boundary layer development length from flat plate leading edge.
x, y, z	Cartesian co-ordinates

Greek Characters

α	Phase lag, in the cavity oscillation loop.
$\alpha_{\text{geom.}}$	Geometric angle of attack of airfoil, with regards to airfoil tonal noise.
δ	Boundary layer thickness
δ_0	Boundary layer thickness at the cavity leading edge.
δ_{99}	99% boundary layer thickness
δ^*	Boundary layer displacement thickness
ϵ_{tot}	Total error
$\epsilon_{U_{\text{bias}}}$	Bias error
$\epsilon_{U_{\text{rms}}}$	Root-mean-squared error
θ	Boundary layer momentum thickness
θ_0	Boundary layer momentum thickness at the cavity leading edge.
κ	Mean convection velocity ratio, $\kappa = U_c/U$, of the shear layer in the cavity.
λ	Wavelength
μ	Dynamic viscosity
ν	Kinematic viscosity
ρ	Density
ρ_p	Particle density
σ_i	Uncertainty due to item i
ψ	Cavity yaw angle
ω	Vorticity

Acronyms

2D	Two-Dimensional
3D	Three-Dimensional
AWT	Anechoic Wind Tunnel
dB	Decibel
LE	Leading edge
OASPL	Overall Sound Pressure Level
PSD	Power Spectral Density
RMS	Root-Mean-Squared
SPL	Sound Pressure Level, dB reference 20 μPa
TE	Trailing edge
TI	Turbulence Intensity, $TI = u'_{\text{rms}}/U_{\text{mean}}$
T-S	Tollmien-Schlichting
PIV	Particle Image Velocimetry
HWA	Hot-wire-anemometry

Contents

1 Introduction **1**
- 1.1 Opening statements . . . 1
- 1.2 Context . . . 1
  - 1.2.1 Cavity flow noise . . . 1
  - 1.2.2 Airframe noise . . . 3
  - 1.2.3 Airfoil noise . . . 4
  - 1.2.4 Necessity of the study . . . 4
- 1.3 Aim and Objectives . . . 4
  - 1.3.1 Aim . . . 4
  - 1.3.2 Objectives . . . 5

2 Literature Review **7**
- 2.1 Introduction . . . 7
- 2.2 Background . . . 7
- 2.3 Definitions . . . 8
  - 2.3.1 Cavity Geometry . . . 8
- 2.4 Cavity Flow Noise . . . 10
  - 2.4.1 Tonal and broadband cavity noise mechanisms . . . 10
  - 2.4.2 Aeroacoustics . . . 11
- 2.5 Cavity Oscillations . . . 14
  - 2.5.1 Feedback-driven shear layer oscillations . . . 14
  - 2.5.2 Criteria for the Occurrence of Oscillations . . . 19
  - 2.5.3 Development of flow with Reynolds number . . . 20
  - 2.5.4 Staging and Intermittency . . . 24
  - 2.5.5 Coupled Cavity Oscillations . . . 24
- 2.6 Two-dimensional cavities . . . 28
  - 2.6.1 Structure of recirculation zones . . . 28
  - 2.6.2 Oscillatory Cavities . . . 29
  - 2.6.3 Wake Mode . . . 33
- 2.7 Aeroacoustic feedback loops: airfoil tonal noise . . . 34
  - 2.7.1 Introduction . . . 34
  - 2.7.2 Visualisation of laminar boundary layer instabilities . . . 35
  - 2.7.3 Laminar boundary layer instability noise . . . 35
  - 2.7.4 The role of an aeroacoustic feedback loop . . . 39

2.7.5 Questioning the role of an acoustic feedback loop 41
2.7.6 Supporting the role of an acoustic feedback loop 43
2.7.7 Summary for airfoil tonal noise produced by smooth airfoils 44
2.7.8 Airfoil tonal noise produced by airfoils with cavities . . . 45
2.7.9 Knowledge gap 45
2.8 Three-dimensional cavities 45
2.8.1 Spanwise flow structures 47
2.8.2 Shallow, narrow cavities 48
2.8.3 Impact of cavity span on flow-field & asymmetries 51
2.8.4 Relationship of three-dimensional flow field to noise . . . 56
2.8.5 Shear Layer Three-Dimensionalities 56
2.9 Control of Cavity Flow Noise 62
2.9.1 General principles 62
2.9.2 Geometric Modifications 62
2.9.3 Non-geometric control methods 63
2.10 Modified Cavity Flow 64
2.10.1 Low Speed Studies 65
2.10.2 Moderate to high Mach number studies 68
2.10.3 Studies which considered the 3D flow-field 72
2.10.4 Summary 73
2.11 Knowledge Gap 74
2.11.1 Two-Dimensional Low Speed Cavities 74
2.11.2 Three-Dimensional Low Speed Cavities 74
2.11.3 Knowledge Gap Statement 75

3 Experimental Methodology & Design 77
3.1 Introduction 77
3.2 Airfoil with two-dimensional cavity 78
3.2.1 Anechoic Wind Tunnel 78
3.2.2 Experimental model 79
3.2.3 Microphone measurements 84
3.2.4 Error analysis of microphone measurements 85
3.2.5 Hot-Wire Anemometry (HWA) 85
3.3 Three-dimensional cavity 93
3.3.1 Water Tunnel 93
3.3.2 Experimental model 95
3.3.3 Flow visualisation 96
3.3.4 Dye visualisation 99
3.3.5 Hydrogen bubble visualisation 100
3.3.6 Particle Image Velocimetry (PIV) 101
3.4 Summary of experimental methodology 103

4 Two-Dimensional Cavities: Results and Discussion 105
4.1 Introduction . . . 105
4.2 Boundary layer characteristics . . . 105
4.3 No cavity . . . 108
4.4 Rectangular cavities . . . 111
4.4.1 $L/D = 1.17$ . . . 111
4.4.2 $L/D = 2.33$ . . . 112
4.4.3 $L/D = 3.5$ . . . 113
4.4.4 $L/D = 4.67$ . . . 113
4.4.5 Overall sound pressure level produced by the rectangular cavities . . . 119
4.5 Cavity noise mechanism . . . 120
4.6 Modified 2D cavities . . . 121
4.6.1 $L/D = 1.17$ . . . 121
4.6.2 $L/D = 3.5$ . . . 125
4.6.3 $L/D = 2.33$ . . . 127
4.6.4 Discussion regarding 2D modified cavities . . . 130
4.7 Mean convection velocity ratio . . . 133
4.8 Cavity mode number . . . 135
4.9 Summary . . . 136

5 Airfoil Noise: Results and Discussion 137
5.1 Introduction . . . 137
5.2 Example noise spectra . . . 138
5.3 General characteristics . . . 141
5.3.1 Occurrence of tones . . . 141
5.3.2 Ladder structure and frequency scaling . . . 142
5.3.3 Far-field acoustic spectral density . . . 149
5.3.4 Summary . . . 151
5.4 Wake velocity measurements . . . 153
5.4.1 Streamwise wake properties . . . 153
5.4.2 Vertical measurements through wake . . . 156
5.4.3 Boundary layer displacement thickness . . . 159
5.5 Measurements at geometric angle of attack of -1° . . . 160
5.5.1 Effect of cavity position on frequency . . . 160
5.5.2 Effect of independently shifting cavity edges . . . 162
5.5.3 Velocity spectrum in cavity shear layer . . . 164
5.6 Measurements at geometric angle of attack of -7° . . . 167
5.6.1 Variation of frequency spacing with cavity trailing edge position . . . 167
5.6.2 Boundary layer receptivity and feedback mechanism . . . 168
5.6.3 Discussion regarding boundary layer measurements . . . 180
5.7 Acoustic forcing . . . 182
5.8 The role of the cavity . . . 190

5.8.1 Inflectional velocity profiles . . . 190
5.9 Cavity flow visualisation . . . 190
5.9.1 Mechanism for the role of the cavity in the feedback loop 195
5.10 Separation bubble near airfoil TE . . . 197
5.11 Boundary layer stability analysis . . . 200
5.11.1 Introduction . . . 200
5.11.2 Methodology . . . 203
5.11.3 Boundary layer profiles . . . 203
5.11.4 Case 1 results . . . 204
5.11.5 Case 2 results . . . 209
5.11.6 Case 3 results . . . 210
5.11.7 Summary of boundary layer stability analysis . . . 214
5.12 Overall summary . . . 215

6 Three-Dimensional Cavities: Results and Discussion 217
6.1 Effect of L/D on shear layer evolution . . . 217
6.1.1 Varying L/D . . . 217
6.1.2 Comparison of noise spectra to visualisations . . . 220
6.1.3 Comparison of velocity spectra to visualisations . . . 224
6.2 Mixing layer structure over the cavity . . . 227
6.3 Mixing layer structure at the sides of the cavity . . . 238
6.4 Rear corner vortices . . . 253
6.5 Chevron-shaped cavities . . . 262
6.6 Summary . . . 275

7 Conclusion 277
7.1 Summary of main findings . . . 277
7.2 Concluding remarks . . . 284

References 287

A Additional airfoil tonal noise literature 301

A PIV methodology 307
A.1 Tracer particles . . . 308
A.2 Out-of-plane motion . . . 309
A.3 PIV Processing . . . 309
A.3.1 Initial outlier tests . . . 309
A.3.2 PIV error correction . . . 309
A.3.3 Temporal averaging and outlier replacement . . . 309
A.4 PIV error analysis . . . 310
A.5 Background subtraction . . . 316

List of Figures

1.1 Schematic drawing of a two-dimensional rectangular cavity flow 2

2.1 Definition of cavity geometry 8
2.2 Sketch of open and closed cavity flow 9
2.3 Acoustic frequency spectra with and without tones. 10
2.4 Theoretical directivity of sound from a shallow wall cavity . . . 15
2.5 Feedback cycle sketch: cavity shear layer oscillations 16
2.6 Non-dimensional cavity length range for oscillations 21
2.7 Development of cavity shear layer with Re_D or L/θ_0. 22
2.8 Rossiter mode hysteresis effect 24
2.9 Sketches of flow structure in cavities with $L/D < 2$ 29
2.10 Flow structure at $L/D = 3.5$ 30
2.11 Schematic drawing of cavity flow, Özsoy *et al.* (2005) 32
2.12 Example of wake mode behaviour showing vorticity contours. . . 33
2.13 Typical structure of airfoil tonal noise, Arcondoulis *et al.* (2009) 36
2.14 Ladder structure of airfoil tonal noise 37
2.15 Cross-correlation of velocity and noise for NACA0018 airfoil . . 38
2.16 Aeroacoustic feedback loop for airfoil tonal noise 40
2.17 Maull and East's (1963) spanwise cells 47
2.18 Time-averaged pressure data (3D cavity) 49
2.19 Sketch of surface flow visualization (Crook, 2005, p. 66). 50
2.20 Annotated PIV velocity vector field and streamlines for a 3D cavity (Crook *et al.*, 2008). 52
2.21 PIV velocity vector field near rear wall of a 3D cavity (Crook *et al.*, 2008) 53
2.22 Interpretation of the time-averaged 3D flow-field 53
2.23 Streamwise velocity: left-hand-side and right-hand-side (Crook, 2011, p. 167) 55
2.24 Conditionally-averaged asymmetric flow fields (Crook, 2011) . . 57
2.25 Sketch of primary and streamwise vorticity (Rockwell and Knisely, 1980) 58
2.26 Additional sketch of primary and streamwise vorticity (Rockwell and Knisely, 1980). 59
2.27 Development of three-dimensional instability (Lasheras and Choi, 1988, p. 69) 60

2.28 Cavity trailing edge geometries (Pereira and Sousa, 1994) 65
2.29 Cavity shear layer vortex events (Pereira and Sousa, 1994) . . . 66
2.30 Laser sheet visualisation of sloped cavity floors (Kuo and Huang, 2001) 67
2.31 Time-average streamlines for various cavity geometries (Ozalp *et al.*, 2010) 68
2.32 Trailing edge modifications (Heller and Bliss, 1975) 69
2.33 Cavity with double ramps (Franke and Carr, 1975) 70
2.34 Surface oil visualisation and conceptual sketch (Doran, 2006) . . 73
2.35 Possible conceptual sketch for cross-section stream lines (Doran, 2006) 73

3.1 Flow-chart of experimental methodology 78
3.2 'Airfoil with cavity' installed in AWT 88
3.3 Leading edge profile of 'airfoil with cavity' 89
3.4 Two-dimensional cavity specification compared to frequency and oscillation requirements 90
3.5 Sketch of the airfoil with cavity 91
3.6 Rendering of the airfoil with cavity model 91
3.7 Schematic of airfoil with cavity in AWT 92
3.8 Convection velocity ratio vs. non-dimensional cavity length . . . 92
3.9 Photograph of water tunnel facility 93
3.10 Schematic diagram of water tunnel facility. 94
3.11 Sketch of 3D cavity model 96
3.12 Coordinate system for 3D cavities 98
3.13 Photograph of 3D cavity model 99
3.14 Dye visualisation example 100
3.15 Photograph of horizontal hydrogen bubble wire 101
3.16 Hydrogen bubble tests coordinate system 101
3.17 A schematic drawing of the experimental set-up for PIV experiments 103

4.1 Co-ordinate systems for 2D cavities 106
4.2 Velocity profile at cavity leading edge at $U = 30$ m/s. 106
4.3 Turbulence intensity at cavity LE 108
4.4 Noise spectra produced by the no cavity airfoil 109
4.5 Airfoil self-noise with and without cavity cutout in surface . . . 110
4.6 Spectra for $L/D = 1.17$ 111
4.7 Spectrogram for $L/D = 1.17$ 112
4.8 Spectra for $L/D = 2.33$ 113
4.9 Spectrogram for $L/D = 2.33$ 114
4.10 Spectra for $L/D = 3.5$ 115
4.11 Spectrogram for $L/D = 3.5$ 116
4.12 Spectra for $L/D = 4.67$ 117
4.13 Spectrogram for $L/D = 4.67$ 118

4.14 OASPL of rectangular cavities 119
4.15 Velocity spectrum and coherence 120
4.16 Coherence between the velocity fluctuations near the cavity LE and TE. 121
4.17 Comparison of rectangular cavity and sloped rear wall 122
4.18 Comparison of rectangular cavity and reverse sloped rear wall . 123
4.19 Comparison of rectangular cavity and reverse sloped rear wall . 124
4.20 Far-field noise from rectangular and sloped rear wall cavities . . 125
4.21 Far-field noise from rectangular and sloped rear wall cavities . . 126
4.22 Comparison of rectangular cavity and reverse sloped rear wall . 126
4.23 Comparison of rectangular cavity and reverse sloped rear wall cavity 129
4.24 Velocity measurements of rectangular and modified $L/D = 2.33$ cavities 130
4.25 Velocity profiles along rectangular and modified $L/D = 2.33$ cavities 132
4.26 $\kappa = U_c/U$ versus non-dimensional cavity length 133
4.27 Rossiter mode number, n, vs. non-dimensional cavity length . . 135

5.1 Airfoil with cavity: cavity designations and coordinate system . 138
5.2 Far-field sound spectra for different angles of attack at cavity position 1. 139
5.3 Far-field sound spectra for positive and negative angles of attack at low velocities. 140
5.4 Occurrence of airfoil tones with geometric angle of attack 141
5.5 Ladder structure of airfoil tones for cavity position 1 143
5.6 Velocity scaling for the central frequency (airfoil noise) 144
5.7 Scaling for the discrete tones (cavity position 1) 145
5.8 Scaling for the discrete tones (cavity position 2) 146
5.9 Scaling for the discrete tones (cavity position 3) 147
5.10 Scaling for the discrete tones (cavity position 4) 148
5.11 Peak spectral density for the cavity at position 1 149
5.12 Peak spectral density for positive angles of attack. 150
5.13 Variation in far-field acoustic amplitude for rectangular cavities 151
5.14 Variation in far-field acoustic amplitude for shifted cavity trailing edge at -7 degrees angle of attack 152
5.15 Velocity measurement along wake downstream of airfoil 153
5.16 Velocity profiles and coherence through the wake for cavity pos. 1. 154
5.17 Velocity profiles and coherence through the wake for cavity pos. 4. 155
5.18 Peak spectral density in a band about the airfoil tone frequency compared to in a band of arbitrary frequency 155
5.19 Phase difference between velocity measurement and acoustic reference measurement 156
5.20 Vertical velocity profiles behind airfoil 157
5.21 Comparison of vertical velocity profiles at locations downstream 158

5.22 Properties of streamwise velocity, recorded vertically through wake at $x/C = 0.012$ . . . 159
5.23 Strouhal number against chord-based Reynolds number . . . 160
5.24 Far-field noise spectra from the smooth airfoil compared with the cavity at four positions . . . 161
5.25 Impact of shifting the cavity leading and trailing edges on airfoil tonal noise . . . 163
5.26 Tonal frequencies found for rectangular cavity with and without the cavity leading edge shifted downstream . . . 164
5.27 Tonal frequencies found for rectangular cavity with and without the cavity trailing edge shifted upstream . . . 165
5.28 Velocity spectrum in the cavity shear layer . . . 166
5.29 Normalised frequency spacing versus nominal normalised feedback length . . . 167
5.30 Far-field acoustic and boundary layer velocity spectra . . . 169
5.31 Phase difference along the boundary layer . . . 170
5.32 Phase difference along the boundary layer for cavity position 4 case . . . 171
5.33 Coherence along the boundary layer . . . 172
5.34 Properties along the boundary layer for cavity position 1 . . . 173
5.35 PSD of velocity fluctuations along the boundary layer for cavity position 4 . . . 174
5.36 Coherence at 610 Hz between microphone and hot-wire . . . 175
5.37 Spectral map of the fluctuating velocity along the boundary layer 176
5.38 Velocity spectra for the cavity position 1 case . . . 177
5.39 Velocity spectra for the cavity position 4 case . . . 178
5.40 Schematic of 'airfoil with cavity' showing proposed feedback loop. 180
5.41 Schematic diagram of acoustic forcing experiment . . . 183
5.42 Properties in the pressure side boundary layer . . . 184
5.43 Velocity properties with acoustic forcing applied with hot-wire probe at location of $x/C = -0.727$ . . . 186
5.44 Velocity spectrum for the natural, unforced, case . . . 187
5.45 Velocity properties with acoustic forcing applied, with hot-wire probe at location of $x/C = -0.685$ . . . 188
5.46 Velocity spectrum for the natural, unforced, case with hot-wire probe at location of $x/C = -0.685$ . . . 189
5.47 Partial velocity profiles measured with stationary single-wire probe . . . 191
5.48 Flow visualisation for matched Reynolds number of airfoil with cavity: vertical wire . . . 193
5.49 Flow visualisation for matched Reynolds number of airfoil with cavity: horizontal wire . . . 194
5.50 Relative stability of the boundary layer near the cavity . . . 195
5.51 Surface flow visualisation of pressure side with cavity . . . 198

5.52 Surface flow visualisation of smooth pressure side 199
5.53 Shape factor over airfoil calculated by XFOIL for case 1. 204
5.54 Falkner-Skan profiles over airfoil pressure surface, for case 1 . . . 205
5.55 Local T-S wave amplification rates, α_i, for case 1 206
5.56 Total T-S amplification, A, for case 1 207
5.57 Total phase for case 1. 208
5.58 Local T-S wave amplification rates, α_i, for case 2 209
5.59 Total T-S amplification, A, for case 2 210
5.60 Total phase and, therefore, feedback tone predictions, for case 2. 211
5.61 Experimental far-field noise spectrum for case 2 211
5.62 Local amplification for case 3 212
5.63 Total amplification for case 3 213
5.64 Far-field noise spectrum for case 3 213
5.65 Total phase and, therefore, feedback tone predictions, for case 3 214
5.66 Sketch of the updated tonal noise mechanism for the streamlined plate with cavity 216

6.1 3D cavity co-ordinate system 218
6.2 3D rectangular cavities: shear layer bubble visualisation 219
6.3 Comparison of flow visualisation and noise spectra for rectangular cavity geometries 222
6.4 Flow visualisation and velocity spectra for rectangular cavity . . 225
6.5 Flow visualisation and velocity spectra for sloped front and sloped rear wall cavity 226
6.6 Shear layer roll-up: oblique side view looking downstream 229
6.7 3D cavity: typical dye pattern formed 230
6.8 Sequence of frames showing the evolution of the overall dye pattern 231
6.9 Streamlines calculated from time-average velocity vectors over the downstream portion of the rectangular 3D cavity 232
6.10 Instantaneous vector fields about downstream portion of $L/D = 6$ cavity 233
6.11 Streamwise velocity fluctuation in the shear layer of the $L/D = 6$ rectangular cavity 234
6.12 Velocity fluctuations over and along the $L/D = 6$ rectangular cavity 235
6.13 Apparent streamwise vortices 236
6.14 Cross-section showing streamwise vortices 237
6.15 Dye visualisation of mixing region at sides of cavity 239
6.16 Tornado-like vortex formed at sides of cavity 240
6.17 Dye pattern formed at side of cavity. 240
6.18 Cut-away sketch of shear layer dye visualisation pattern 241
6.19 Interaction of sequential vortices. 243
6.20 Video frames: interaction of the shear layer vortices 244
6.21 Annotated version of figure 6.20. 245
6.22 Illustration of vortex interaction at the side of the cavity. 246

6.23 Flow visualisation at side of $L/D = 6$ cavity 247
6.24 Vortex line representation 248
6.25 Unsteady surface flow pattern found at the sides of narrow cavities 250
6.26 Possible surface flow pattern 251
6.27 Cross-sections at side of cavity 252
6.28 Velocity profiles upstream of the three-dimensional AWT cavity 256
6.29 Velocity properties across the span of the three-dimensional cavity at $x/D = 3.0$ 257
6.30 Velocity properties across the span of the three-dimensional cavity at $x/D = 6.1$ 258
6.31 Velocity properties across the span of the three-dimensional cavity at $x/D = 7.5$ 259
6.32 Plan view of velocity over three-dimensional cavity 260
6.33 Cross stream view of velocity measurements near the rear corner of the cavity 260
6.34 Rear corner vortex at $L/D = 3.33$ 261
6.35 Schematic diagram of chevron cavity configuration 262
6.36 First pattern produced by chevron-cavity 263
6.37 Second pattern produced by chevron-cavity 264
6.38 Visualisation with the vertical bubble wire for chevron-shaped cavity 266
6.39 Chevron cavity: both horizontal and vertical bubble wires . . . 267
6.40 Sketch of patterns about the chevron-shaped cavity. 267
6.41 Hydrogen bubble patterns for the chevron-shaped cavity 268
6.42 Hydrogen bubble visualisation of chevron-shaped cavity with $L/D = 5$ 269
6.43 Time-average streamlines over the chevron-shaped cavity with $L/D = 2$ 270
6.44 Mean velocity magnitude calculated from time-average velocity vectors over the chevron-shaped cavity 271
6.45 Time-average R.M.S. fluctuation velocity over the chevron-shaped cavity 272
6.46 Time-average vorticity over the chevron-shaped cavity. 273
6.47 Streamlines and velocity magnitude over individual image pairs 274

7.1 Sketch of the overall tonal noise mechanism for the airfoil with cavity 280
7.2 Cut-away sketch of instantaneous dye visualisation pattern about a three-dimensional, narrow, cavity 283
7.3 Sketch of flow patterns about the chevron-shaped cavity 285

A.1 A diagram of the basic principle of PIV. 307
A.2 PIV perspective error sketch 314
A.3 PIV mean subtraction comparison 317
A.4 Before and after subtraction of raw PIV image mean 318

List of Tables

2.1 Trends in two-dimensional open cavity flows 23
2.2 Low Re, 2D cavity flow studies 27

3.1 Specifications of two-dimensional cavity 82
3.2 Specifications of overall airfoil 82
3.3 Coordinates of the streamlined flat plate profile 83
3.4 Microphone specifications 86
3.5 Specifications of water tunnel cavity model 97
3.6 Specifications of anechoic wind tunnel three-dimensional cavity model 97
3.7 Hydrogen bubble test schedule 102

4.1 Velocity and boundary layer over 2D cavities 107
4.2 Blasius boundary layer estimate 107
4.3 Attenuation of OASPL by modified cavities at $L/D = 2.33$ . . . 127

5.1 Airfoil tonal frequencies at U=16.6 m/s and $\alpha_{\text{geom.}} = -1°$ 162
5.2 Predicted and measured airfoil tonal frequencies for cavity pos. 1 and 4 181
5.3 Non-dimensional parameters for cavity flow visualisation 191
5.4 Cases for evaluation using the boundary layer analysis code . . . 203
5.5 Feedback tones for case 1 showing a comparison of experiment and theory. 208
5.6 Comparison of central frequency 215

6.1 Comparison of flow visualisation and aeroacoustic results 221
6.2 AWT 3D cavity boundary layer properties 253

A.1 Parameters used in PIV experiments 308
A.2 Summary of uncertainties in PIV 315

Chapter 1

Introduction

1.1 Opening statements

In the context of this study, 'cavity flow' refers to flow over a rectangular cavity in a flat plate and 'cavity noise' refers to the noise from such cavity flows. A rectangular cavity flow is defined as a backward facing step flow followed by a forward facing step flow and is shown in figure 1.1. Three-dimensional cavities are defined as cavities where the cavity span is less than the cavity length, while shallow cavities are defined as those where the cavity depth is less than the cavity length (refer section 2.3.1).

Cavities are found on aircraft, motor vehicles and in other applications where flows over the cavities are often associated with high noise levels. This introduction establishes the context of the study by covering the background, some applications and the significance of the project. The aims and objectives of the project are then stated. Following chapters document a literature review, methodology, experimental results and discussion of two-dimensional cavity flows, the role of a cavity in airfoil noise production, and a study of the flow structures unique to three-dimensional cavities of finite span.

1.2 Context

1.2.1 Cavity flow noise

This study takes place in the context of the field of Aeroacoustics – the study of noise generated by fluid flow. One aim of research within this field is to understand, and therefore reduce, the noise generated by the motion of air, land, and marine vehicles. This includes: understanding the behaviour of flow structures (typically vortical eddies) that contribute to the generation of the noise, surface features that strongly radiate the noise such as sharp trailing edges, and the effect of contributory acoustic phenomena such as the aeroacoustic feedback that may further enhance and excite the vortical eddies giving rise to a 'locked-on' flow-tone.

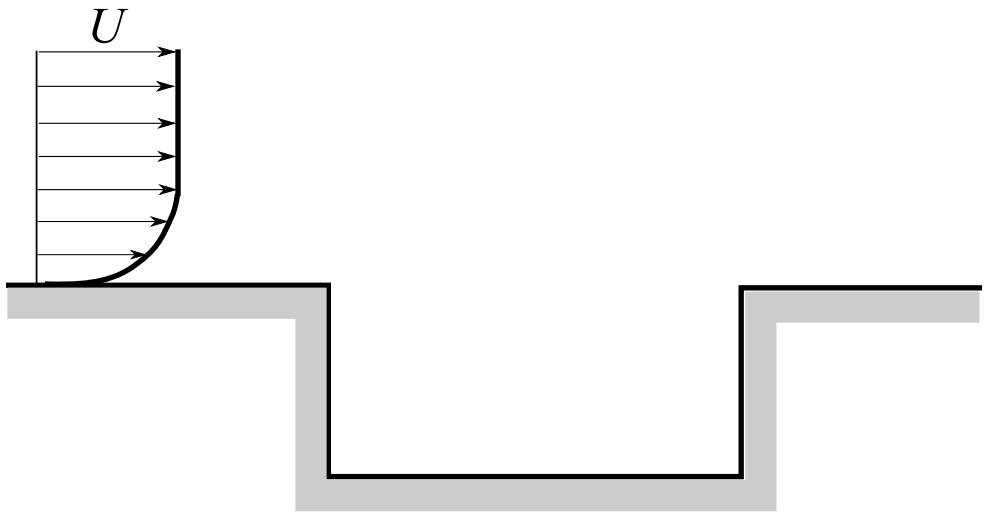

Figure 1.1: Schematic drawing of a two-dimensional rectangular cavity flow.

Cavities are found on aircraft, around automobiles and in various other applications, where they can result in significant radiated noise. On aircraft, cavities can be formed by weapons bays when the weapons bay doors are open, and wheel wells when the retractable landing gear is extended (Tam and Block, 1978). Around automobiles, cavities can be found around side mirrors (Milbank, 2004), surface joins (Crook, Hassan and Kelso, 2007), roof-racks (Harper, 2006) and open automobile sun-roofs (Zhuang, 2007, p. 1). In the former cases, the cavity can be subject to a laminar upstream boundary layer where the boundary layer development length is short. Cavities can also be found elsewhere such as the spaces between train carriages (El Hassan, Keirsbulck and Labraga, 2009a).

One focus relates to the use of weapons bay cavities as locations for stores on aircraft. Modern fighter aircraft carry stores internally in closed weapons bays to improve stealth by reducing radar signature and these weapons bays form cavities open to the flow whilst the bay doors are open during store release (Dolling, Perng and Leu, 1997). Carrying stores in closed internal cavities also provides other benefits such as reduced drag, less aerodynamic heating on the store, and improved manoeuvrability (Dolling, Perng and Leu, 1997).

When aircraft weapons bay doors are opened, high sound pressure levels and significant vibrations are produced due to flow over the cavity. MacManus and Doran (2008) found levels of over 160 dB (sound pressure level, SPL, reference 20 μPa) at 2 kHz recorded at the front wall of a cavity at M=0.9. Similarly, Shaw *et al.* (1988) recorded levels approaching 163 dB (overall sound pressure level, OASPL, reference 20 μPa) at the cavity walls in experimental tests on a 4.9% scale model of an F-111 aircraft. It is desirable to reduce these levels as large vibrations can be transmitted to structures, stores and other components causing structural fatigue (Shaw *et al.*, 1988 and Heller & Delfs,

1996) and malfunction of equipment (Smith & Shaw, 1975).

Modifications to the rectangular cavity geometry have been shown to be an effective and inexpensive method of reducing these noise levels from cavities in the literature (Lawson & Barakos, 2008, Doran, 2006, Dolling, Perng & Leu, 1997, Maull & East, 1963, and others) however the influence of modifications on three-dimensional flow structure is not well understood. For un-modified two-dimensional cavities the internal flow structures and flow physics are well understood, however limitations on the database exist for some parameter spaces. While, for three-dimensional cavities the mean internal flow structures are well understood. Existing literature has not, however, addressed the unsteady flow structures found internally and externally to three-dimensional cavity flows. Therefore a knowledge gap exists regarding the unsteady flow structures found about three-dimensional cavities, particularly at low subsonic speeds.

The expected research outcomes of this study will fill a knowledge gap regarding the unsteady flow structures found about shallow, narrow cavities at low subsonic Mach number with particular attention to the end effects created due to three-dimensional cavities having a finite span. This study will also provide further information on the effectiveness of two-dimensional and three-dimensional modified wall shapes in mitigating cavity flow noise and the mechanisms involved therein.

1.2.2 Airframe noise

Regarding practical applications, the noise and vibrations associated with cavities are an issue on aircraft weapons bays (amongst other applications) and there are several benefits of addressing these issues such as reducing fatigue or malfunction of equipment and also being able to reduce time over target by being able to have weapons bay cavity doors open at a higher flight speed (Dolling, Perng and Leu, 1997). Outcomes could include a reasonable documentation of and some understanding of certain geometric modifications that could be compatible with aircraft structural layouts. Subsequently these modifications, if they were to be practically applied, could be useful for reducing the 'important and potentially dangerous' issues associated with cavity noise and associated vibrations (Bastrzyk and Raman, 2009).

Above urban areas, a large proportion of the noise received on the ground from transport aircraft is attributed to airframe noise, that is, noise caused by fluid flow over the surfaces of the aircraft (Lilley, 2001). Transport aircraft may fly at relatively low-altitude over urban areas while they ascend or descend from airports located nearby to centres of population. It is therefore desirable to reduce airframe noise to improve amenity and comfort for the urban population. Amongst other sources (such as the landing gear itself), this airframe noise includes noise caused by the aforementioned cavity flow over the cavities formed by the landing gear wheel wells (when the landing gear is

extended), as well as airfoil self-noise caused by flow over the aircraft wings.

1.2.3 Airfoil noise

When airfoils encounter smooth flow, unsteady fluctuations are produced thereby creating airfoil noise. Airfoil noise is produced by helicopter rotors, wind turbines and airframes (Brooks, Pope and Marcolini, 1989) as well as computer cooling fans (Arcondoulis *et al.*, 2010) amongst other devices. Although there are other noise sources (such as leading edge noise and tip vortex noise), one major source of airfoil noise is the trailing edge of the airfoil, from which 'airfoil tonal noise' may be produced when there is predominantly laminar flow over at least one surface of the airfoil.

There has been a debate in the literature regarding the necessity of an aeroacoustic feedback loop in the production of airfoil tonal noise, with papers either questioning or supporting the role of an aeroacoustic feedback loop in various instances of airfoil tonal noise. To this end, further experimental or numerical avenues to investigate airfoil tonal noise would be helpful towards clarifying the mechanisms. This includes whether any acoustic feedback loop is involved, whether that applies broadly or only in certain particular instances. Subsequently, a variation in trailing edge noise tonal frequency when a circular cavity was present in a NACA 0018, compared to the same airfoil without a cavity, was identified by van Osch (2008), however no explanation for the behavior was provided by the author.

In the present work, the production of airfoil tonal noise was discovered from an 'airfoil with cavity' profile which was originally designed for the investigation of cavity noise. Thus, an investigation was conduced to determine a plausible mechanism for the production of this airfoil tonal noise, a phenomenon which had not been reported in detail previously.

1.2.4 Necessity of the study

The present study is thus necessary on a variety of grounds. Firstly, the literature (or database) on two-dimensional cavity flow physics warrants extension. Secondly, whether or not an aeroacoustic feedback loop is involved in the production of airfoil tonal noise warrants clarification. Finally, the unsteady flow structures found about cavities of finite span warrant description.

1.3 Aim and Objectives

1.3.1 Aim

The aim of this study is to investigate the flow structures caused by, and noise produced by, low Reynolds number flow over two- and three-dimensional cavities for both rectangular and modified cavity geometries. In this instance,

low Reynolds number refers to a range of Reynolds numbers of the order of 10^3 to 10^5, based on either the cavity depth or the cavity length. As an aeroacoustic feedback loop is involved in the production of cavity tonal noise, an additional aspect of this thesis is to determine the mechanism by which a two-dimensional cavity cutout on an airfoil surface results in the production of airfoil tonal noise, for chord-based Reynolds number of the airfoil within the range of 6.7 $\times 10^4$ to 3.3 $\times 10^5$.

1.3.2 Objectives

The broader objectives of this study are to:

1. Extend the literature on two-dimensional cavity flow physics.

2. Determine the role of an aeroacoustic feedback loop in the production of airfoil tonal noise, based on an 'airfoil with cavity' profile.

3. Determine the unsteady flow structures created by lateral mixing layer growth about cavities with finite span.

The specific objectives of this thesis within the framework of two-dimensional cavity flows are to:

4. Investigate the cavity tonal noise produced by rectangular or modified two-dimensional cavities with a laminar boundary layer in the range of length-to-depth ratio L/D of 1.17 to 4.67, for a depth-based Reynolds number in the range of 3.2 $\times 10^3$ to 1.6 $\times 10^5$ (sections 4.4 & 4.6).

5. Determine the noise attenuation produced by modified cavity geometries and plausible mechanisms for that attenuation (sections 4.6.3 & 4.6.4).

6. Characterise the mean convective velocity ratio for the respective non-dimensional cavity length ratios of $L/\delta_0 = 5$ – 48 (section 4.7), and the cavity oscillation mode numbers for $L/\delta_0\sqrt{Re_{\delta_0}} = 350$ – 1800 (section 4.8).

Within the framework of three-dimensional cavity flows, the specific objectives are to:

7. Investigate the structure of the mixing layer both within and immediately adjacent to predominantly shallow and narrow rectangular cavities for length-to-depth ratios, $L/D = 0.84$ – 6 and length-to-span ratios, $L/W \approx 2$ (section 6.1).

8. Study the flow-field about chevron-shaped three-dimensional cavities in the range of $L/D = 1$ – 5, with a span of $W/D = 2$, for depth-based Reynolds numbers of approximately 10^5 (section 6.5).

Within the framework of determining the role of a two-dimensional cavity cutout on an airfoil surface in the production of airfoil noise the specific objectives are:

9. To confirm that the airfoil noise is indeed produced by an airfoil tonal noise mechanism by examining the effect of angle of attack and velocity on the noise (section 5.3).

10. To investigate the effect of cavity position on the individual tones and 'broadband hump' of the airfoil noise (section 5.5).

11. To investigate the existence of boundary layer disturbances at the frequencies of the airfoil tonal noise, and whether these disturbances occur upstream, over or downstream of the cavity (section 5.6.2).

12. To investigate the effect of external acoustic forcing on the boundary layer, and therefore the airfoil tonal noise mechanism, on an airfoil with cavity (section 5.7).

13. To investigate the role of a separation bubble, if any, in the production of the noise and amplification of the tones, by conducting surface flow visualisation (section 5.9) and a stability analysis of the boundary layer over a smooth version of the airfoil profile (section 5.11).

14. To propose an overall mechanism for the role of a two-dimensional cavity cutout located on the pressure surface, in the airfoil tonal noise produced by an airfoil with cavity, including how this relates to existing mechanisms proposed for smooth airfoils in the literature (section 5.12).

Chapter 2

Literature Review

2.1 Introduction

In this literature review, there is firstly a discussion of cavity flow generally, including cavity flow as an aeroacoustic problem. Existing literature regarding two- and three-dimensional cavity flow at both low and high Reynolds numbers is reviewed. In the context of flow over an airfoil with a cavity cutout, literature is reviewed regarding the related aeroacoustic problem of airfoil tonal noise. A discussion is then made on the use of modifications of the cavity geometry as a passive control measure for cavity flow noise. Finally, multiple knowledge gaps are defined.

2.2 Background

The phenomenon of noise generated by a moving cavity was first studied by Strouhal in 1878, according to Covert (1970). A study by Wieghardt (1942) described the flow structure found about two-dimensional rectangular cavities. Amongst measurements of various bodies, Tillman (1944) published drag coefficient data for slot-shaped cavities. In 1955, Krishnamurty published findings on the strong acoustic fields radiated from cavities at transonic speeds while Roshko (1955a) published findings on velocity and pressure distributions. Maull and East (1963) produced the first study of three-dimensional features in cavity flows, while Rossiter (1964) described the fundamental aeroacoustic loop mechanism responsible for oscillations. Early numerical studies began in the late 1960s and these focused mainly on the lid-driven cavity problem, where only the flow inside a cavity, driven by a moving lid, is modelled (Yao, Cooper and Ragunathan, 2004). Research interest has been consistent and hence the overall literature on cavity flow is extensive. Cavity flow is a popular topic for Computational Fluid Dynamics (CFD) studies and control studies.

A number of reviews have been published in the literature. These include a review on experimental and theoretical analysis of cavity flow by Rockwell &

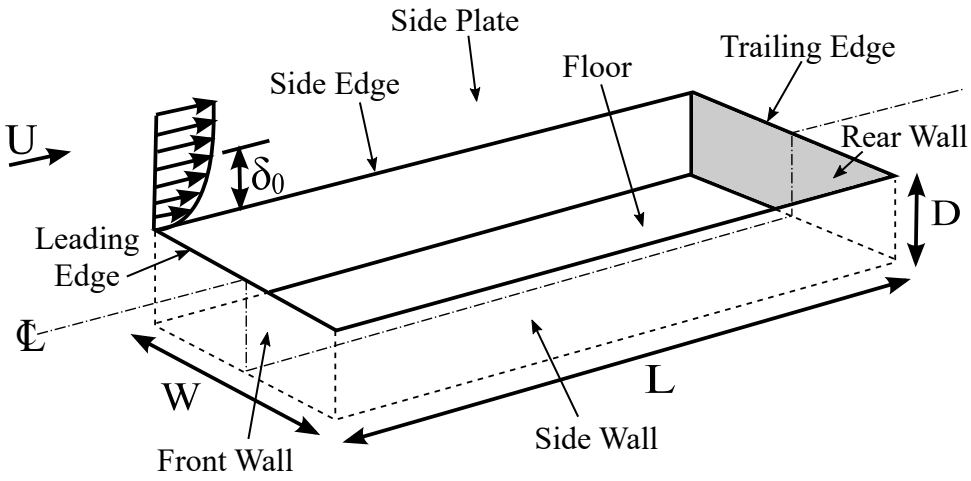

Figure 2.1: Definition of three-dimensional cavity geometry in a flat plate (the flat plate is not drawn).

Naudascher (1978), a review on control techniques for cavity flow by Rowley & Williams (2006), and a review of aspects of cavity flow research by Watmuff (2009).

2.3 Definitions

2.3.1 Cavity Geometry

The main geometrical parameters of a three-dimensional cavity are the width or span, W, length, L and depth, D. As indicated on Figure 2.1, 'leading edge' and 'trailing edge' refer to the top of the front and rear walls respectively, while 'side edge' refers to the top of the side wall. Other parameters are the free-stream flow speed, U, local velocity, u, fluctuation velocity, $u' = u_i - \bar{u}$, root-mean-square[1] (RMS) fluctuation velocity, $u' = \sqrt{\sum (u_i'^2)/n}$, turbulence intensity, u'_{RMS}/U and boundary layer characteristics just upstream: boundary layer thickness, δ_0 and momentum thickness, θ_0. Cavities are commonly characterised by their length-to-depth ratio, L/D, their length-to-momentum thickness ratio, L/θ_0, and their length-to-boundary layer thickness ratio L/δ_0 (the normalised, or non-dimensional, cavity length).

Deep and Shallow Cavities Deep cavities are considered to be those with $L/D < 1$, while shallow cavities are considered those with $L/D \geq 1$ (Sarohia, 1977).

[1]Root-mean-square (RMS) refers to a value consisting of the square root of the mean of the square of the sample values, where n is the sample size and u_i is, in this instance, the sampled velocity.

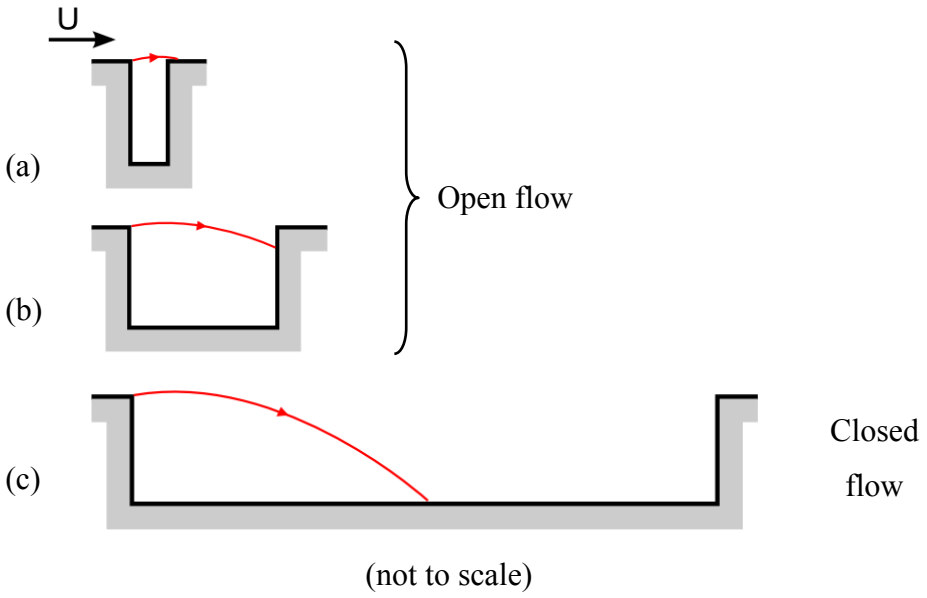

Figure 2.2: Sketch of open and closed cavity flow.

Two and Three Dimensional Cavities Ahuja and Mendoza (1995, p. 42) classified cavities with $L/W < 1$ as two-dimensional and those with $L/W > 1$ as three-dimensional based on their experimental flow visualisation observations and acoustic measurements. Using fluorescent mini-tufts, Ahuja and Mendoza (1995) found that for $L/W < 1$ the flow was two-dimensional across most of the span, whilst for $L/W > 1$ end-effects were observed to become increasingly significant. There were also significant differences in far-field acoustic spectra across the $L/W = 1$ boundary. This convention will be used here.

Open and Closed Cavity Flow In a cavity flow, a shear layer is formed by the flow over the leading edge. When this shear layer reattaches on the cavity rear wall or downstream of the cavity it is termed open flow, and when the shear layer reattaches on the cavity floor it is termed closed flow (figure 2.2). Sarohia (1977) states that the boundary between open and closed flow is $L/D \approx 7 - 8$ for low-subsonic flows. This compares to a boundary of $L/D \approx 10 - 11$ for transonic and supersonic flows (Tracy and Plentovich, 1993). This parametrical boundary between open and closed flows is also likely to be Reynolds number dependent (Milbank, 2004, p. 23).

Although both cavity types are associated with high noise levels, open flow is associated with higher noise levels than closed flow. Closed flow is more commonly associated with increased drag (Tracy and Plentovich, 1993). This project focuses on the noisier, open flow type.

Figure 2.2(a) shows the first of the two open flow cases – the case where the cavity is sufficiently short such that the shear layer skips over the cavity

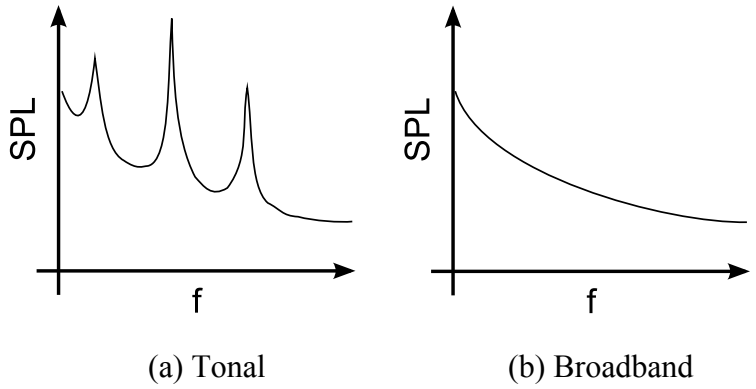

Figure 2.3: Acoustic frequency spectra with and without tones.

and reattaches downstream of the cavity. For this case, there is no association with tonal noise generation.

The second of the two open flow cases is shown in figure 2.2(b) – when the cavity is sufficiently long that the shear layer impinges on the rear wall of the cavity. This case is associated with tonal noise generation. The association is primarily with fluid-dynamic shear layer oscillations, however there are also a number of other possible tonal noise mechanisms. For example, these fluid-dynamic oscillations can be coupled with vibrations of the structure to form fluid-elastic oscillations, or coupled with standing acoustic waves to form fluid-resonant oscillations. Cavities with a large internal volume and small opening may be subject to Helmholtz resonance.

In the closed flow case, the cavity is longer still and the shear layer reattaches to the floor of the cavity (Figure 2.2(c)). In this case, broadband noise is generated due to general turbulence of a variety of scales.

2.4 Cavity Flow Noise

2.4.1 Tonal and broadband cavity noise mechanisms

Flows over rectangular cavities have been studied extensively. Such flows can produce high levels of tonal and broadband noise and researchers have sought to understand the mechanisms of these phenomena. The frequency spectra taken from recordings of cavity noise can include tonal peaks (figure 2.3(a)) while other cavities may produce broadband noise (figure 2.3(b)). In the case of tonal, or oscillatory, noise, there are many possible oscillation mechanisms. It is usually possible to determine the relevant mechanism from measurements and observations and by considering the L/D ratio and flow conditions.

The tonal noise component is primarily due to coherent feedback-driven oscillations of the shear layer over the cavity, although in some instances other

mechanisms are possible, such as acoustic depth modes or Helmholtz resonance. The noise is primarily generated as these oscillations of the shear layer interact with the cavity trailing edge. Feedback is generated by the interaction of the oscillating shear layer with the cavity trailing edge, whereby acoustic waves are generated that travel upstream to the receptive initial region of the shear layer. On the other hand, the broadband noise component is due to turbulence within the boundary layer interacting with the leading edge and also, especially, with the trailing edge. Cavities with laminar upstream boundary layers are known to produce stronger oscillations than those with turbulent upstream boundary layers, for similar free-stream conditions, due to greater receptivity to feedback and greater instability of the shear layer (Rowley, 2002).

2.4.2 Aeroacoustics

The tonal and broadband noise produced by cavity flows means that such flows are studied as an Aeroacoustic problem, where Aeroacoustics is the study of aerodynamically generated noise. The noise generated by flows is known to be produced from unsteady fluid motions (Morris, 2011), as distinct from the sound produced by flow-induced vibrations of solids (Lighthill, 1952).

Examples of canonical aeroacoustic problems include rectangular cavity flows, flows over circular or square cylinders, flows over flat plates and airfoils, junction flows (such as the junction of a cylinder and flat plate) and jet flows. These each relate to real world flows of interest, often with applications on air, land or marine vehicles, or relating to fan or turbine noise.

Lighthill (1952) developed the acoustic analogy, whereby the sound field can be directly related to a fluctuating flow field. In Lighthill's (1952) acoustic analogy, fluctuations in flows are considered to act as quadrupole noise sources with a strength given by the Lighthill stress tensor. The largest components of the Lighthill stress tensor are often the Reynolds stresses (Morris, 2011), associated with turbulent fluctuations in the flow. Hence, turbulent motions within the flow are considered to act as quadrupole noise sources. The analogy of Lighthill (1952) is below:

$$\frac{\partial^2 \rho}{\partial t^2} - c_0^2 \nabla^2 \rho = \frac{\partial^2 (\rho u_i u_j)}{\partial x_i x_j} \tag{2.1}$$

The acoustic analogy is derived by rearranging the momentum equation for a continuous medium (a form of the governing equations of fluid motion). Equation 2.1 gives Lighthill's rewritten momentum equation when Lighthill's stress tensor (the subject of the spatial derivative on the right hand side) has been simplified to contain only the Reynolds stress term, which is often the largest term (Morris, 2011). Here, u and x are the velocity and position vectors respectively with components u_i, u_j and u_k and x_i, x_j and x_k, while c_0 is the speed of sound in the uniform medium. The left hand side represents propagation of sound in a uniform medium while the right hand side repre-

sents fluctuating stresses which are the sources of sound. When the Reynolds stresses, $u_i u_j$, are zero then equation 2.1 becomes the linear wave equation (Morris, 2011).

Considering solid boundaries, Curle (1955) provided a derivation which takes into account the effects of surface pressure:

$$\nabla^2 \rho - \frac{1}{c_0^2} \frac{\partial^2 \rho}{\partial t^2} = -\frac{\partial q}{\partial t} + \frac{\partial F_i}{\partial x_i} - \frac{\partial^2 (\rho u_i u_j)}{\partial x_i x_j} \tag{2.2}$$

The right hand side contains two extra terms, so that there are now three terms - idealised monopole, dipole and quadrupole acoustic sources (Morris, 2011):

1. $\frac{\partial q}{\partial t}$ Monopole – associated with mass injection where q is mass-flow rate. For example, unsteady injection of mass at the orifice of a Helmholtz resonator. This term is also associated with unsteady heat addition.

2. $\frac{\partial F_i}{\partial x_i}$ Dipole – associated with fluctuating force as 'a dipole is equivalent to a concentrated fluctuating force' (Lighthill, 1952). F_i represent forces acting on the fluid in the direction of the i^{th} unit vector. For example, fluctuating lift forces on a circular cylinder in a crossflow.

3. $\frac{\partial^2 (\rho u_i u_j)}{\partial x_i x_j}$ Quadrupole - associated with fluctuations within the flow itself as discussed earlier.

A monopole source is stronger than a dipole, and a dipole is stronger than a quadrupole (Lighthill, 1952). So, for the same Mach number and fluid density, when unsteady fluid motion occurs near a solid boundary more noise is produced, such as flow over a flat plate or cavity, compared to unsteady fluid motion away from a boundary, such as a jet.

For cavity flows, "sound is produced by flow instability in the neighbourhood of the cavity" (Howe, 2004, p. 107). Specifically, Howe (2004) states that the noise produced by shallow cavities at low Mach number is due to a combination of two sources. Firstly, a dipole radiation source due to force fluctuations in the streamwise direction with no radiation normal to the cavity [such drag fluctuations have been shown to be associated with both Rossiter oscillations (section 2.5.1) and the 'wake' mode (section 2.6.3)]. Secondly, a monopole source due to a cavity acoustic resonance – a 'Helmholtz' mode – that radiates omni-directionally.

In addition to cavity flows, oscillating shear layers are found in many other aeroacoustic problems . Rockwell (1983) provides a detailed review on the general properties of oscillating impinging shear layers and states that there are similarities between the oscillations of externally excited non-impinging shear layers (excited by some external forcing) and self-excited impinging shear layers. Cavity flow oscillations are a type of self-excited oscillation and according to Kuo and Huang (2001) oscillations of shear layers in cavities 'tend to be

more coherent' than oscillations of free shear layers, due to the additional feedback.

For cavity flows, Howe (2004) took the total enthalpy $B = \int \mathrm{d}p/\rho + 0.5v^2$ to be the acoustic variable and rewrote Lighthill's acoustic analogy as equation 2.3.

$$\left(\frac{D}{Dt}\left(\frac{1}{c^2}\frac{D}{Dt}\right) - \frac{1}{\rho}\nabla\cdot(\rho\nabla)\right)B = \frac{1}{\rho}\mathrm{div}(\rho\omega\wedge\mathbf{v}) \tag{2.3}$$

Howe (2004) modelled the oscillating cavity shear layer as a convective vortex source which radiates noise upon interaction with the trailing edge, i.e., a dipole source, while the cavity acoustic resonance (the resonance due to the geometry and dimensions of the cavity) was modelled as a monopole source. Howe (2004, p. 109) therefore gave the acoustic Green's function as follows, with $\hat{G_0}$ representing "the uniform pressure produced by the incident wave in the neighbourhood of the cavity" and $\hat{G_M}$ and $\hat{G_D}$ representing the monopole and dipole fields near the cavity respectively.

$$\hat{G} \approx \hat{G_0} + \hat{G_M} + \hat{G_D} \tag{2.4}$$

Howe (2004, p. 112) subsequently derived the following expression for the Green's function, where $A = WL$ is the cavity planform area and $l \sim \sqrt{\pi A/4}$ is the acoustic resonance end correction for the cavity geometry. In the irrotational far-field, $B = -\delta\varphi/\delta t$ where $\varphi(\mathbf{x},t)$ is the velocity potential (Howe, 2004, p. 107). The source point $\mathbf{y}$ is within or near the cavity, while the observation point $\mathbf{x}$ is in the far-field. $\mathbf{X}(\mathbf{x}) = (X_1(\mathbf{x}), 0, X_3(\mathbf{x}))$ and $\mathbf{Y} = (Y_1, 0, Y_3)$ are Kirchoff vectors (Howe, 2004, p. 108, 109).

$$\begin{aligned} G(\mathbf{x},\mathbf{y},t-\tau) &\approx -\frac{1}{2\pi}\int_{-\infty}^{\infty}(\hat{G_0}+\hat{G_M}+\hat{G_D})(\mathbf{x},\mathbf{y},\omega)\mathrm{e}^{-i\omega(t-\tau+\mathbf{M}\cdot(\mathbf{X}-\mathbf{Y}/c_0}\mathrm{d}\omega \\ &= \frac{1}{(2\pi)^2|\mathbf{x}|}\int_{-\infty}^{\infty}\Big\{1-\left(\phi*(\mathbf{y}) - \frac{i(\omega/c_0)A}{2\pi}\right) \\ &\frac{(\omega/c_0)sin((\omega/c_0)D)}{cos\{(\omega/c_0)(D+l+i(\omega/c_0)A/(2\pi)\}} - \frac{i(\omega/c_0)\mathbf{x}\cdot\mathbf{Y}}{|\mathbf{x}|}\Big\}\mathrm{e}^{-i\omega(t-\tau-|\mathbf{x}|/c_0+\mathbf{M}\cdot(\mathbf{X}-\mathbf{Y}/c_0)}\mathrm{d}\omega \end{aligned} \tag{2.5}$$

Upon subsitution of equation 2.5 into the rearranged Lighthill's equation (equation 2.6), Howe (2004, p. 112) derived equation 2.7.

$$p \approx \frac{-\rho_0}{1+Mcos\theta}\int(\omega\wedge\mathbf{v})(\mathbf{y},\tau)\cdot\frac{\delta G}{\delta\mathbf{y}}(\mathbf{x},\mathbf{y},t-\tau)\mathrm{d}^3\mathbf{y}\mathrm{d}\tau, \quad |\mathbf{x}|\to\infty \tag{2.6}$$

$$
\begin{aligned}
p \approx & \frac{\rho_0}{(2\pi)^2(1+Mcos\theta)|\mathbf{x}|}\int(\omega\wedge\mathbf{v})(\mathbf{y},\tau)\cdot \\
& \frac{\delta}{\delta\mathbf{y}}\int_{-\infty}^{\infty}\Big\{\frac{\varphi^*(\mathbf{y})(\omega/c_0)sin((\omega/c_0)D)}{cos\{(\omega/c_0)(D+l+i(\omega/c_0)A/(2\pi)\}}+i(\omega/c_0) \\
& \left(\frac{\mathbf{x}}{|\mathbf{x}|}-\mathbf{M}\right)\cdot\mathbf{Y}\Big\}\mathrm{e}^{-i\omega\{t-\tau-(|\mathbf{x}|-\mathbf{M}\cdot\mathbf{x})/c_0\}}\mathrm{d}\omega\mathrm{d}^3\mathbf{y}\mathrm{d}\tau, \quad |\mathbf{x}|\to\infty
\end{aligned}
\tag{2.7}
$$

In further analysis, Howe (2004) finds that the 'strengths of both the monopole and dipole sources' are determined by an integral of the cavity drag force. With respect to the dipole noise source, Howe(2004, p. 115) notes that 'only the unsteady component of the drag actually contributes to the radiation' of noise from the cavity and that the mean component of drag can be excluded.

Figure 2.4 shows the directivity of overall radiated sound from a shallow wall cavity calculated from Howe's model for a cavity with $L/D = 2$ at $M = 0.05$ & $M = 0.1$ (Howe, 2004, p. 120), the analysis is based on an observer fixed relative to the cavity and therefore moving with velocity $-U$ compared to the freestream. The dipole source is due to the interaction of the oscillating cavity shear layer with the trailing edge of the cavity, and it is 'primarily the trailing edge of the cavity that is responsible for the radiated sound' (Howe, 2004, p. 113). The figure shows that at $M = 0.05$, the dipole source dominates the noise produced by the cavity. However, at $M = 0.1$, the monopole source (due to excitation of acoustic resonance of the cavity) contributes significantly and modifies the dipole.

2.5 Cavity Oscillations

2.5.1 Feedback-driven shear layer oscillations

A shear layer is formed by flow over the backwards facing step that comprises the leading edge of a cavity. The shear layer formed is both unstable and receptive to excitation. The shear layer is subject to the Kelvin-Helmholtz (K-H) instability at low subsonic Mach numbers (Unalmis, Clemens and Dolling, 2004) that causes the characteristic roll-up of the shear layer. Oscillations of shear layers in cavities 'tend to be more coherent' than oscillations of free shear layers due to this feedback (Kuo and Huang, 2001).

[2]Reprinted from *Journal of Sound and Vibration*, Vol. 273, M. S. Howe, 'Mechanism of sound generation by low Mach number flow over a wall cavity', Pages No. 103–123, Copyright (2004), with permission from Elsevier.

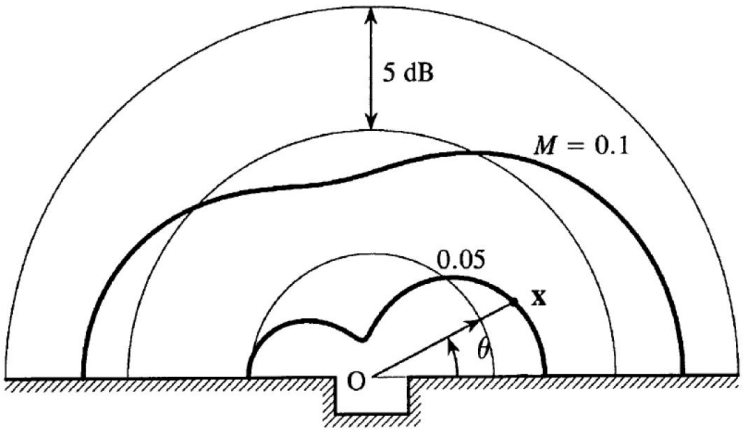

Figure 2.4: Theoretical directivity of sound from a shallow wall cavity at $M = 0.05$ & $M = 0.1$ (Howe, 2004, p. 120)[2]. [OASPL (dB) for the range $0.1 < St = fL/U < 10$.]

In a cavity flow, pressure or acoustic waves generated at the trailing edge of the cavity travel upstream and provide excitation, forming a feedback loop. Either or both can be observed depending on the flow conditions. Ashcroft and Zhang (2005) state that selective amplification causes the instability waves of the shear layer to grow, and in some cases the oscillating shear layer rolls up into discrete vortices. Although the discrete vortices are not essential to the occurrence of oscillations (Heller and Bliss, 1975), the impingement of these vortices often provides the 'discrete excitation' to maintain oscillations (Ashcroft and Zhang, 2005). Morris (2011) addresses the conjecture of whether the shear layer consists of an oscillating vortex sheet or a series of discrete vortices, citing PIV results from Ma *et al.* (2009) that suggest the shear layer oscillation may exist as a combination of the two. For a cavity with a laminar upstream boundary layer, Koschatzky *et al.* (2009) found that vorticity was concentrated into discrete vortices but with distinct braids of vorticity connecting the vortices. With a turbulent upstream boundary layer, El Hassan *et al.* (2009) identified vortical structures within the turbulent shear layer over the cavity.

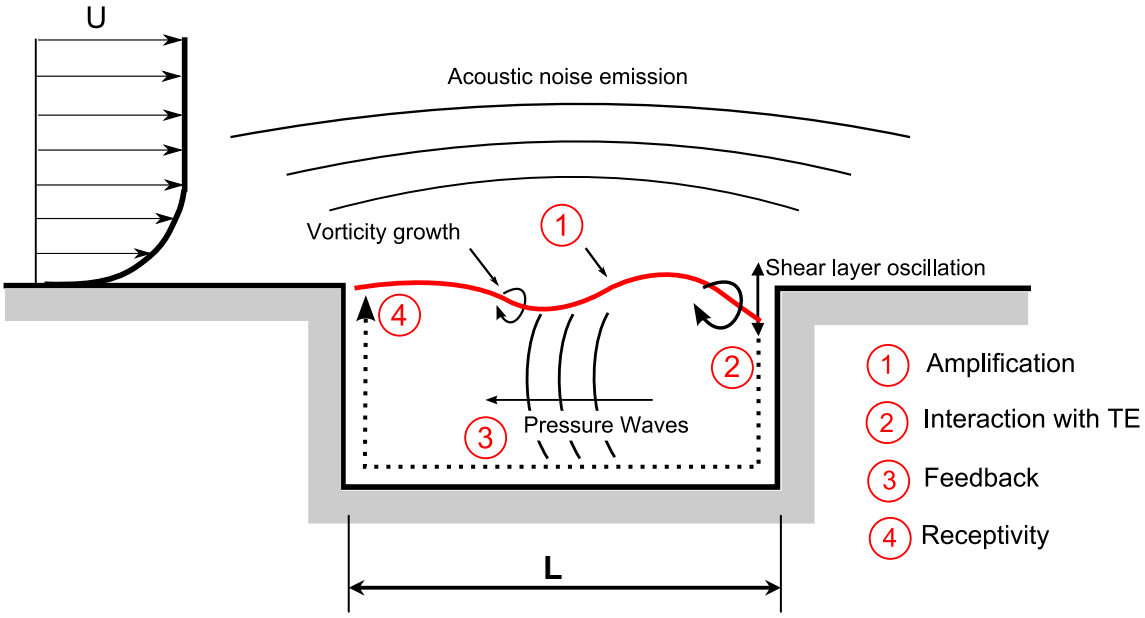

Figure 2.5: Sketch of feedback cycle involved in cavity shear layer oscillations. Adapted from Ahuja & Mendoza (1995), Czech et al. (2000) and Bastrzyk & Raman (2009).

In the feedback loop shown in figure 2.5 the following is accepted as happening (Ahuja & Mendoza, 1995, Bastrzyk & Raman, 2009 and Czech *et al.*, 2000):

1. Instability waves are amplified in the shear layer and impinge on the trailing edge of the cavity. This can be accompanied by large-scale vorticity growth.

2. When these waves reach and interact with the trailing edge of the cavity, pressure or acoustic waves are generated that travel upstream.

3. These waves reach the leading edge of the cavity and feed back to the receptive initial region of the shear layer (possibly with some phase delay), thus reinforcing certain instabilities and completing the feedback loop.

Rossiter's Equation and Rossiter Modes

Rossiter (1964) was the first to describe the aeroacoustic feedback loop mechanism in detail and to develop a formula (equations 2.8 and 2.9) to predict the discrete frequencies of oscillation. One time period of the instability is given by a downstream and upstream travelling component:

1. A vortex or crest of the oscillatory wave of the shear layer traverses the cavity downstream in the time period $T_2 = L/U_c$ where U_c is the convection velocity of the vortex.

2. A generated pressure or acoustic wave then traverses the cavity upstream in a time $T_1 = L/c$, where c is the speed of sound.

The parameter n is the 'Rossiter mode' number, or the 'stage' number, and equals the number of instability wavelengths or vortical structures in the cavity (El Hassan *et al.*, 2009a). Between event 2 and the next event 1 α is the phase delay or phase 'lag', which is the 'lag' between the upstream wave reaching the leading edge and the generation of a new downstream travelling disturbance. The unit of α is fraction of a wavelength, corresponding to the 'lag' in time (Delprat, 2006).

Equation 2.8 gives Rossiter's (1964) equation for the frequencies of tonal noise that may be produced by flow over a cavity. The equation gives possible frequencies of oscillation and does not specify which modes will necessarily occur.

$$f_n = (n - \alpha)\frac{1}{T_1 + T_2} = \frac{n - \alpha}{L/c + L/U_c} \qquad n = 1, 2, 3... \tag{2.8}$$

Equation 2.9 gives the non-dimensional Strouhal number (St) form of Rossiter's (1964) equation. The mean velocity of the vortex is non-dimensionalised as a fraction of the free-stream velocity called the mean convection velocity ratio, $\kappa = U_c/U$, while M is the Mach number, $M = U/c$. Typical values of α and κ are given below. It is possible to determine both κ and α experimentally, and for frequency prediction either typical or measured values can be used.

$$St = \frac{fL}{U} = \frac{n - \alpha}{M + 1/\kappa} \qquad n = 1, 2, 3... \tag{2.9}$$

Typical phase lag values A phase lag, α, of zero is applicable for low subsonic flows (Milbank, 2004 and El Hassan *et al.*, 2009a), while α=0.25 produces the best fit for flows with moderate[3] Mach number ($0.4 < M < 1$) (Block, 1976).

Typical convection velocity ratio values The most commonly used value of κ is 0.57. There are some limited κ data available including those published by Sarohia (1977) and El Hassan *et al.* (2009a). With suitable values of κ and α, good experimental agreement with Rossiter's equation has been achieved from low subsonic (El Hassan *et al.*, 2009a and Milbank, 2004) to hypersonic

[3]In this thesis, 'moderate' Mach number is used to refer to Mach numbers between approximately $M \sim 0.4 - 1$, which includes part of the transonic range. 'Transonic' refers to the region of operation of aircraft where the airflow around an aerodynamic body is partly subsonic and partly supersonic (approximately $M > 0.7$ to $M < 1.2$).

free-stream velocities (Unalmis, Clemens and Dolling, 2004). According to Milbank (2004), for laminar cavity flows in the range of $L/\delta_0 \approx 5$ - 10, estimating κ from the data of Sarohia (1977) considerably increases the accuracy of frequency predictions using Rossiter's equation. The following curve fit to Sarohia's (1977) data can be used:

$$\kappa = 0.223Ln(L/\delta_0) - 0.0171 \qquad 5.25 < L/\delta_0 < 10.5 \tag{2.10}$$

Cavities at yaw To correct for cavities at yaw, cavity length L in Rossiter's equation can be replaced by an effective cavity length L', equation 2.11, where ψ is yaw angle (Milbank, 2004).

$$L' = \frac{L}{cos(\psi)} \tag{2.11}$$

Modified Rossiter's Equation

A modified Rossiter's equation is often used for higher Mach number flows. Equation 2.12 was developed by Heller, Holmes and Covert (1971) and is often called the 'modified Rossiter's equation'. It corrects for high sound speed in the cavity in higher Mach number flows (Heller and Bliss, 1975). The modified Rossiter's equation is applicable for transonic to supersonic Mach number flows, with k being the ratio of specific heats.

$$\mathrm{St} = fL/U = \frac{n - \alpha}{M[1 + (k-1)\frac{M^2}{2}]^{-1/2} + \frac{1}{\kappa}} \tag{2.12}$$

For very high Mach number flows ($M = 5$), Unalmis, Clemens and Dolling (2004) showed a decoupling of the shear layer instability and acoustic feedback mode. They suggested that the correlation of Rossiter's formula at $M = 5$ was 'coincidental' due to the empirical coefficients used and that acoustic standing wave modes were able to predict the discrete tones at very high Mach number.

Fluid-dynamic and acoustic resonance

The resonance loop mechanism can take one of two forms, depending on the Mach number. Fluid-dynamic resonance occurs at low Mach number (for example, Milbank, 2004), while acoustic resonance occurs at moderate-to-high Mach numbers (for example, Rowley, 2002). In acoustic resonance, the acoustic travel time plays an important role in setting up the feedback loop, while in fluid-dynamic (or hydrodynamic) resonance the acoustic travel time does not play a significant role in setting up the feedback loop.

Fluid-dynamic resonance applies to fully-incompressible flows where the feedback is 'effectively instantaneous' (Morris, 2011). In these flows, the pressure fluctuations travel at $c >> U_c$. Thus in Rossiter's equation, the Mach

number is not a significant factor in the oscillation loop as $M << 1/\kappa$, for example, $0.1 << 2$, assuming $\kappa \sim 0.5$. Therefore, feedback from an interaction of a disturbance with the rear wall is effectively supplied back to the leading edge instantaneously.

In acoustic resonance, the feedback is provided in the form of an acoustic disturbance (Morris, 2011). In this case, $M \sim O(1/\kappa)$, and the time taken for feedback to reach the leading edge of the cavity plays an important role in the resonance loop.

Distribution of energy between modes

In a theoretical study, Rowley (2002) found that the mode number of the Rossiter mode with the greatest shear layer amplification increased with increasing non-dimensional cavity length (L/θ_0). The calculations were performed from inviscid linear stability theory using a tanh velocity profile based on the velocity profile from DNS computations at $M = 0.6$. The amplification increased to a maximum and then started to decrease with increasing L/θ_0. There were regions of overlap where two mode numbers had approximately equivalent amplification rate. Cavities with thinner boundary layers relative to the cavity depth (higher values of D/θ_0) were found to have significantly higher levels of amplification, in other words, cavities with thick relative boundary layers (lower values of D/θ_0) do not oscillate as easily. Shear layer amplification rates were found to decrease with increasing Mach number (from $M = 0.6$ to $M = 0.2$), however this was noted to be balanced by a decrease in radiation efficiency at the trailing edge.

2.5.2 Criteria for the Occurrence of Oscillations

Lower Threshold for Oscillations The most widely used lower threshold criterion for fluid-dynamic cavity oscillation is that of Sarohia (1977) and is given by equation 2.13. The criterion is empirical and based on extensive hot-wire measurements of an axi-symmetric cavity model with a laminar boundary layer at low subsonic speeds, which were plotted in Sarohia (1975, p. 84). The occurrence of oscillations depends on the non-dimensional cavity length L/δ_0, where δ_0 is the boundary layer thickness just upstream of the cavity, and Reynolds number based on δ_0, Re_{δ_0}. The criterion can also be used for turbulent upstream boundary layers according to El Hassan *et al.* (2009a).

$$\frac{L}{\delta_0}\sqrt{Re_{\delta_0}} > 290 \quad \text{(for oscillations)} \tag{2.13}$$

Regarding the influence of cavity depth on fluid-dynamic oscillations, Sarohia (1977) made two notes:

- the minimum cavity length criterion is applicable for cavities with $D/\delta_0 > 2$, with the value 290 increasing significantly for shallower cavities, so that

occurrence of fluid-dynamic oscillation is more unlikely in very shallow cavities, and

- for cavities with $D/\delta_0 > 6$, cavity depth does not affect fluid-dynamic oscillation frequency.

Regarding the underlying physics, the Sarohia (1977) criterion is the product of two factors. Firstly, the non-dimensional cavity length L/δ_0 – whereby when the cavity length is insufficient relative to upstream boundary layer thickness, the shear layer reattaches downstream of the trailing edge of the cavity rather than impinging on the cavity rear wall and therefore no cavity oscillations are produced. Secondly, the square root of the Reynolds number based on upstream boundary layer thickness, $\sqrt{Re_{\delta_0}}$ – i.e., the cavity shear layer will not oscillate when the Reynolds number is insufficient. Assuming a fixed ratio of Blasis solutions ($\theta_0 \approx 0.664/5 \times \delta_0$), the lower threshold for oscillations therefore takes the form $L/\theta_0 \propto 1/\sqrt{Re_{\delta_0}}$ which is plotted in figure 2.6.

Approximate Upper Limit for Oscillations There is an approximate upper limit (equation 2.14) for cavity oscillations identified by Sarohia (1977), where θ_0 is the momentum thickness just upstream of the cavity:

$$L < 100\theta_0 \quad \text{(for oscillations)} \tag{2.14}$$

As the cavity length is increased, cavities have been found to stop oscillating between $L = 100\theta_0$ and $L = 200\theta_0$ (Sarohia, 1977, Rockwell, 1983, and Gharib & Roshko, 1987). Therefore, unless this criterion is met oscillations cannot be expected with certainty, however longer cavities may still oscillate. Also, oscillations would not generally be expected for cavities much exceeding a length of $L = 200\theta_0$.

Combined Criteria for Oscillations Figure 2.6 shows the region where cavity flow oscillations may be expected to be found, based on the aforementioned findings.

2.5.3 Development of flow with Reynolds number

Figure 2.7 shows an illustration of the development of the shear layer in a two-dimensional, open cavity flow. This development involves parameters including the Reynolds number (Re_{δ_0} and Re_D), cavity length, relative boundary layer thickness, and relative momentum thickness[4]. Thus one main descriptor is

[4]The cavity length can be non-dimensionalised in terms of length-to-momentum thickness ratio, L/θ_0, in addition to length-to-boundary layer thickness ratio, L/θ_0. Accounting for this, partially accounts for the boundary layer type. The direct effect of boundary layer displacement thickness, δ^*, and thus boundary layer shape factor, $H = \delta^*/\theta_0$, remains underreported in the literature and thus is not included in this discussion or illustration.

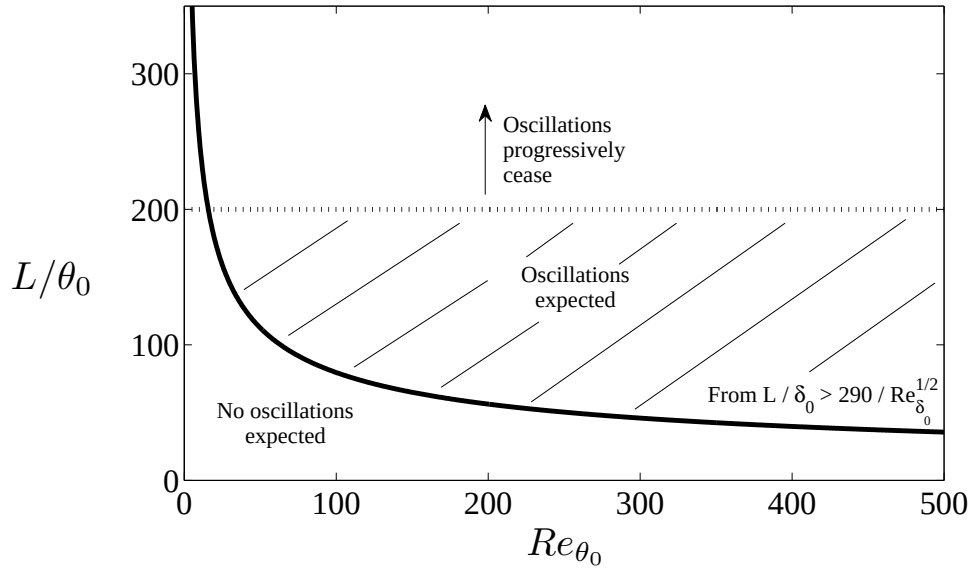

Figure 2.6: Range where oscillations are expected based on non-dimensional cavity length, L/θ_0 and momentum-thickness-based Reynolds number, Re_{θ_0}. Assumes laminar boundary layer, with ratio of Blasius solutions ($\theta_0 \approx 0.664/5 \times \delta_0$) used to convert boundary layer thickness to momentum thickness. Line given by $L/\theta_0 \approx 200$, an approximate upper value of non-dimensional cavity length. Curve given by the criterion of Sarohia (1977) and holds for $D/\delta_0 > 2$.

the aforementioned Sarohia (1977) criterion parameter, $(L/\delta_0)\sqrt{Re_{\delta_0}}$, which includes many of these properties.

Although the development of cavity flows in terms of a combination of all of the relevant parameters has not been fully reported in the literature, trends for the changes in the cavity flow with the variation of individual parameters have been reported. Table 2.1 summarises trends in cavity flows based on individual parametrical descriptors. However a complete description of the parameter space corresponding to each shear layer structure has not been clearly reported in the literature.

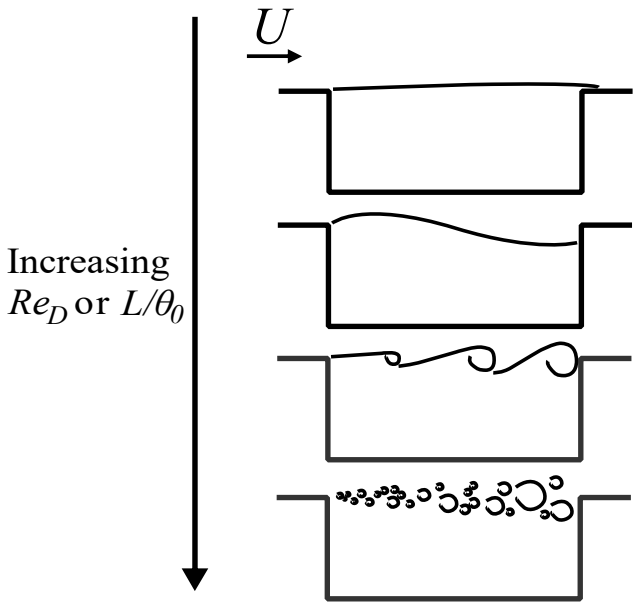

Figure 2.7: Illustration of the development of the shear layer in two-dimensional open cavity flow as Re_D or L/θ_0 is increased.

Table 2.1: Trends in two-dimensional open cavity flows

L/D		L/θ_0		D/δ_0	
Upper end of open cavity flows, $L/D \sim 7-8$	Additional recirculation zones may appear. Shear layer impinges further down the rear wall with increasing L/D and the main recirculation zone can become larger[1].	High, $L/\theta_0 > 200-300$	Vortices break down, oscillations become increasingly less coherent, oscillations cease above certain value[2].	High $D/\delta_0 > 6$	Thin relative boundary layer, greater shear layer amplification rate[3], for $D/\delta_0 > 6$ depth has little role in the oscillations[4].
Lower end of open cavity flows, $L/D \sim 1$	Initially characterised by a single recirculation zone.	Low, $L/\theta_0 < 80$	No oscillations below certain value of L/θ_0. As L/θ_0 increases, oscillations begin and may become quite strong and coherent[5].	Low $D/\delta_0 \sim 1$	Thick relative boundary layer, lower shear layer amplification rate, less likely to oscillate.

[1] Özsoy *et al.* (2005) state that energy for the recirculation is provided by the impinging shear layer.
[2] Literature varies, depends on the cavity and the specific flow conditions.
[3] Rowley (2002).
[4] Sarohia (1977).
[5] Additionally, specific criterion of Sarohia (1977), $L/\delta_0\sqrt{Re_{\delta_0}} > 290$ (for oscillations).

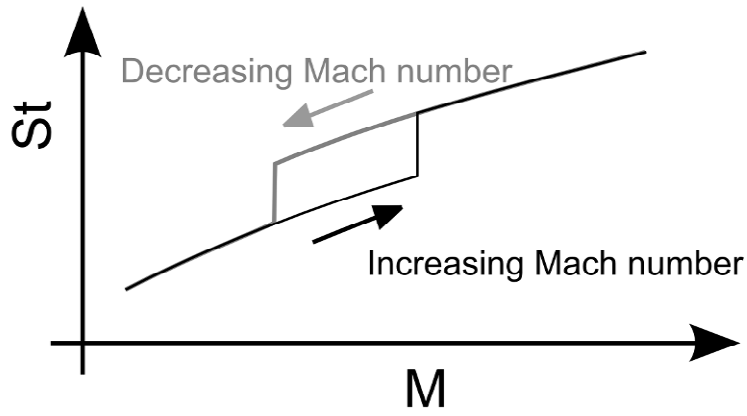

Figure 2.8: Rossiter mode number, or 'staging', hysteresis effect.

2.5.4 Staging and Intermittency

Staging

Figure 2.8 shows a sketch of a Rossiter mode hysteresis effect found by Milbank (2004) which was termed 'staging'. Staging refers to a switch of dominant oscillatory Rossiter mode, also called a 'stage'. The following behaviour was found: when the Mach number was increased the oscillation would tend to hold-on to a lower Strouhal (St) number before making the 'stage jump' up to the higher frequency (or St number). However when the Mach number was decreased, the oscillation would tend to hold-on to the higher Strouhal number for longer, with the 'stage jump' occurring at a lower Mach number. This gave, in the vicinity of 'stage jumps', a dependence of the oscillatory behaviour on whether the Mach number was being increased or decreased.

Intermittency

Intermittency refers to situations when oscillations fail to 'lock-on' properly, with oscillations of certain frequencies intermittently occurring and ceasing. Intermittent oscillations can occur when the oscillations are fairly weak, i.e., when the parameters of the cavity are near the boundaries indicated in figure 2.6 (the oscillations are starting to occur, or ceasing). Intermittent oscillations can also occur when a stage jump is imminent, and fluctuations in the external flow or internal flow of the cavity can cause intermittent switching between the different stages (Milbank, 2004, p. 40).

2.5.5 Coupled Cavity Oscillations

Fluid-dynamic oscillations can be coupled with other mechanisms to form fluid-resonant oscillations, fluid-elastic oscillations or Helmholtz resonance. These

can occur if the frequencies of fluid-dynamic oscillations are close to the frequencies of other oscillation mechanisms.

Helmholtz Resonance Coupling

Helmholtz resonance can occur when a cavity has a small opening and a large volume, forming a Helmholtz resonator. In Helmholtz resonance the air at the cavity mouth, or orifice, undergoes large oscillations with the air inside the volume of the cavity acting as a spring (Panton, 1988). Fluid-dynamic shear layer oscillations at the cavity mouth can excite the resonator (Loh, 2004) so that coupling can occur if shear layer instability frequencies are sufficiently close to the natural frequency of the resonator (Ma, Slaboch and Morris, 2009). The natural frequency of a Helmholtz-resonator is given by Equation 2.15 (Ma, Slaboch and Morris, 2009):

$$f_{\text{Helmholtz Resonance}} = \frac{c}{2\pi}\sqrt{\frac{\text{Orifice Area}}{\text{Cavity volume} \times L}} \tag{2.15}$$

Fluid-Resonant Coupling

Fluid-resonant oscillations involve 'shear flow oscillations coupled with standing [acoustic] waves' (Doran, 2006, p. 22) with either two-closed ends (lengthwise or span-wise) or one closed and one open end (depth-wise). Coupling can occur when the shear layer oscillations are sufficiently high in frequency, such that the acoustic wavelength is the same size or smaller than dimensions of the cavity (Rockwell and Naudascher, 1978). Standing acoustic waves are reinforced by constructive or destructive inference and are formed by acoustic waves reflected back and forth between two solid surfaces or one solid surface and one open end. The frequencies of standing waves are related to the dimensions of the space in which the standing wave forms (and the speed of sound in the particular medium).

Depth modes are the most common fluid-resonant mode in low speed cavity flows over deep cavities and are described by East's (1966, p. 284) formula in equation 2.16. The formula is based on equating the Strouhal number for the cavity oscillation mode from Rossiter's equation to best fit of the Strouhal number for the cavity depth mode. The former data were obtained from East's (1966) experiment, while the latter were calculated by computer using a semi-empirical model from Plumbee, Gibson and Lassiter (1962). The latter data showed good agreement with the former. The single frequency given by equation 2.16 effectively represents a mean of the major depth-mode-coupled Rossiter mode cavity oscillation frequencies present in the cavity.

$$St = \frac{fL}{U} = \left(\frac{1}{M}\right)\left(\frac{L}{D}\right)\left(\frac{0.25}{1 + 0.65(L/D)^{0.75}}\right) \tag{2.16}$$

El Hassan, Keirsbulck and Labraga (2009a) described how coupling between resonant and fluid-dynamic modes is often found at low subsonic velocity in deep cavities ($L/D < 1$) and can occur when the criteria for neither type of oscillation are met individually. They found that coupled oscillations occurred in a deep cavity at a cavity length that was much smaller than the values required for uncoupled oscillations.

Milbank (2004) derived equations 2.17, 2.18 and 2.19 for the most likely acoustic resonance modes that would apply to a cavity at low Mach number with oblique modes being considered unlikely:

$$f_{n\ \text{Length Mode}} = \frac{c}{2}\frac{n}{L} \qquad n = 1, 2, 3... \tag{2.17}$$

$$f_{n\ \text{Span Mode}} = \frac{c}{2}\frac{n}{W} \qquad n = 1, 2, 3... \tag{2.18}$$

$$f_{n\ \text{Depth Mode}} = \frac{c(2n-1)}{4D_{\text{eff}}} \qquad n = 1, 2, 3... \tag{2.19}$$

In equation 2.19, D_{eff} is the effective depth with $D_{\text{eff}} \sim 1.2D$.

Fluid-Elastic Coupling

Fluid-elastic oscillations are those that involve vibration modes of the structure, and can occur for flexible structures (Lin and Rockwell, 2000). Coupled fluid-elastic oscillations can occur when the walls have a displacement that is large enough to exert 'feedback control' on the shear layer and the combination of the inertia and other properties of the wall in conjunction with the flow is a complex one (Rockwell and Naudascher, 1978).

Table 2.2: List of low-Reynolds-number two-dimensional cavity flow studies

Authors	Re_D	Re_{θ_0}	L/D	B. L. Type	Modifications
Sarohia (1977)	Up to 82000	Up to 200	Up to 50	Laminar	
Yamamoto *et al.* (1979)	$2600 - 50000$	-	$1 - 25$	Both	
Rockwell and Knisely (1980)	-	106	1.17	Laminar	
Sinha *et al.* (1982)	$662 - 2648$	211	$0.4 - 28.6$	Laminar	
Gharib and Roshko (1987)	13100	94	$0.57 - 1.9$	Laminar	
Pereira and Sousa (1994)	3360	-	2	Laminar	Rounded trailing edges
Lin and Rockwell (2001)	24300	1320	Up to 4	Turbulent	
Kuo and Huang (2001)	5580	194	2	Laminar	Sloped floor & fences on cav. floor
Milbank (2004)	$12500 - 38400$	$240 - 420$	1	Laminar	
Grace *et al.* (2004)	$13000 - 25000$	$380 - 1260$	4	Both	
Özsoy *et al.* (2005)	$4000 - 13000$	$160 - 366$	4	Laminar	
Manovski *et al.*(2005)	$90 - 730$	$40 - 110$	$3 - 5$	Laminar	
Manovski *et al.* (2007)	$1000 - 5740$	$81 - 194$	5	Laminar	
Faure *et al.* (2007)	$2300 - 5330$	$78 - 118$	$0.5 - 2$	Laminar	
Kang *et al.* (2008)	11650	830	$1 - 2$	Turbulent	
Kang and Sung (2009)	$4700 - 24000$	$830 - 1810$	$1 - 4$	Turbulent	
Koschatzky *et al.* (2009)	$10000 - 15000$	$317 - 266$	2	Both	
Ozalp *et al.* (2010)	$5400 - 9800$	$1230 - 1700$	2	Laminar	Semi-circular and triangular cavity
Zhang and Naguib (2011)	$4070 - 16300$	$1830 - 4390$	$2.6 - 4.1$	Turbulent	

2.6 Two-dimensional cavities

The flow structures around two-dimensional rectangular cavities at low depth-based Reynolds number are relatively well understood. Open two-dimensional cavity flows with moderate L/D ratios (L/D = 0.5 - 6) have been studied extensively at low subsonic velocities. This section reviews these studies and describes the steady and unsteady flow structures have been found in these cavity flows.

Table 2.2 gives a list of low-Reynolds-number cavity flow investigations between depth-based Reynolds of Re_L = 90 - 82,000, most of which are discussed in the following text. Furthermore, reviews are given by Watmuff (2009), Rowley & Williams (2006), and Rockwell & Naudascher (1978) which pertain to two- and three-dimensional cavity flows at a range of Reynolds numbers.

2.6.1 Structure of recirculation zones

The two-dimensional sketches of Faure *et al.* (2007) shown in figure 2.9 identify common features in cavities with L/D up to 2 with a laminar upstream boundary layer. Faure *et al.* (2007) used laser illuminated smoke visualisation in a wind tunnel, with $U = 0.69 - 1.6$ m/s and a cavity depth of $D = 0.30$ m, giving cavity-depth-based Reynolds numbers of $Re_D = 2300 - 5330$. The span and depth were fixed and the length of the cavity was varied. At $Re_D = 2300$, for $L/D = 0.5$ there are upper and lower vortices in the cavity, for $L/D = 1$ the cavity is dominated by one large vortex, and for $L/D = 2$ the cavity is dominated by two vortices, a larger one in the rear of the cavity and another in the forward part of the cavity. The flow structure sketches are similar to those by ESDU (2005), with (a) and (c) similar to those of Wieghardt, as cited and reproduced in Tillman (1944), Yamamoto *et al.* (1979) and Sinha *et al.* (1982) also produced similar sketches. As L/D is further increased, the secondary (upstream) recirculation at L/D=4 is associated with much lower levels of velocity than the primary recirculation (Özsoy *et al.*, 2005).

Neary and Stephanoff (1987) studied the flow over a 'shallow rectangular cavity' at low subsonic speeds. The range of cavity-length-based Reynolds numbers investigated was Re_L = 31,900–39,600. Until the parameters reached the cavity oscillation threshold, the authors found that the cavity was filled by a large single primary vortex centred slightly downstream. As the Reynolds number increased, a secondary vortex was found to form on the floor by separation of the back-flow along the cavity floor and a tertiary vortex forms in the cavity slightly upstream from the primary vortex (figure 2.10).

[5] *Experiments in Fluids*, vol. 42, 2007, pages 180, 179, & 175, Faure, T M, Adrianos, P, Lusseyran, F, and Pastur, L, © Springer-Verlag 2006. With permission of Springer. Original captions: a) 'Sketch of the cavity flow dynamics for $R = 0.5$... for $U_e = 1.21$ m/s (Re = 2,020) and $U_e = 1.60$ m/s (Re = 2,670)', b) 'Sketch of the cavity flow dynamics for R = 1', and c) 'Sketch of the cavity flow dynamics for $R = 2$'.

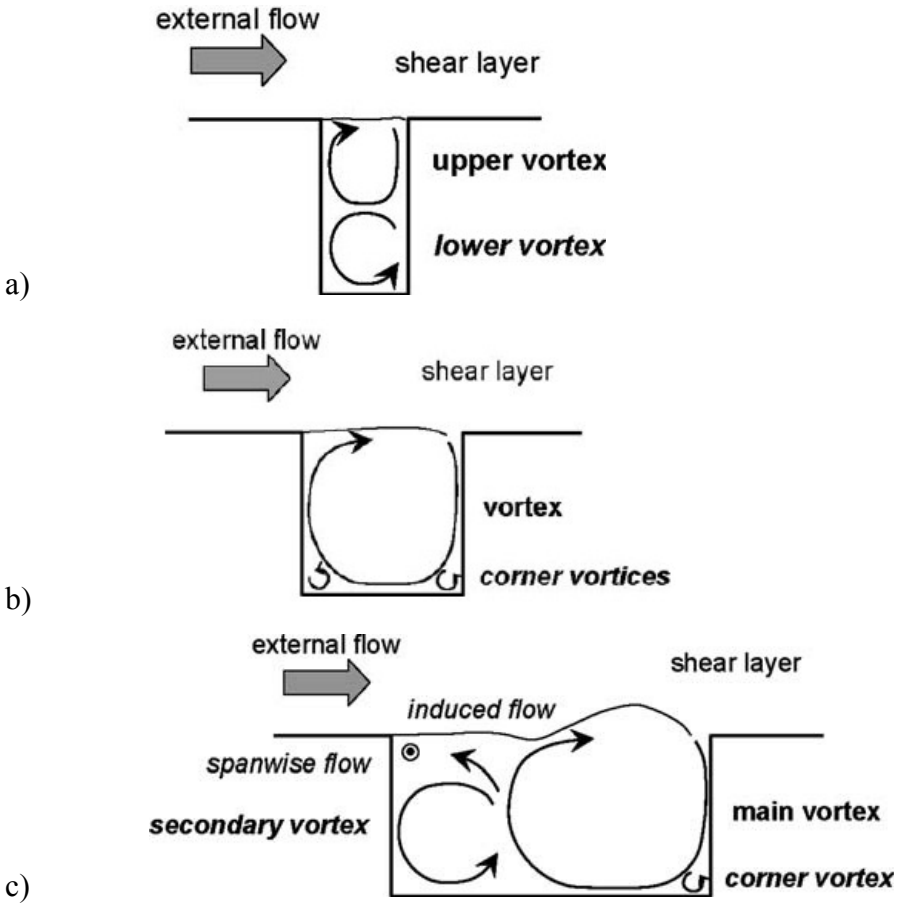

Figure 2.9: Sketches of flow structure in cavites with $L/D < 2$ for $Re_D = 2300$. a) $L/D = 0.5$, b) $L/D = 1$, c) $L/D = 2$ (Faure *et al.*, 2007)[5].

2.6.2 Oscillatory Cavities

The shear layer oscillation and the main vortex within the cavity are coupled. For instance, the flow visualisation images of Manovski *et al.* (2005) show the main recirculation vortex fluctuating as the shear layer oscillates. On the down-stroke of the shear layer, the energised impinging fluid is 'drawn into' (Neary and Stephanoff, 1987) and drives the main recirculation vortex (Özsoy *et al.*, 2005, Manovski *et al.*, 2005 and Manovski *et al.*, 2007). Typically, shear layer vortices are clipped at the trailing edge with part shed downstream and part entering the main recirculation vortex (Manovski *et al.*, 2007 and Neary & Stephanoff, 1987). Clockwise vorticity (assuming left to right flow over the cavity) from the shear layer is thus dispersed throughout the rear of the cavity and downstream of the cavity (Özsoy *et al.*, 2005). On the other hand, anti-clockwise vorticity within the cavity (again assuming left to right flow) is generated by the flow adjacent to and down the cavity rear wall, and also the flow adjacent to and upstream along the cavity floor (Özsoy *et al.*, 2005 and

Lin & Rockwell, 2001). Neary and Stephanoff (1987) observed that large shear layer fluctuations near the trailing edge are caused by both the growth of shear layer disturbances and the deflection of the shear layer by the fluctuating main recirculation vortex.

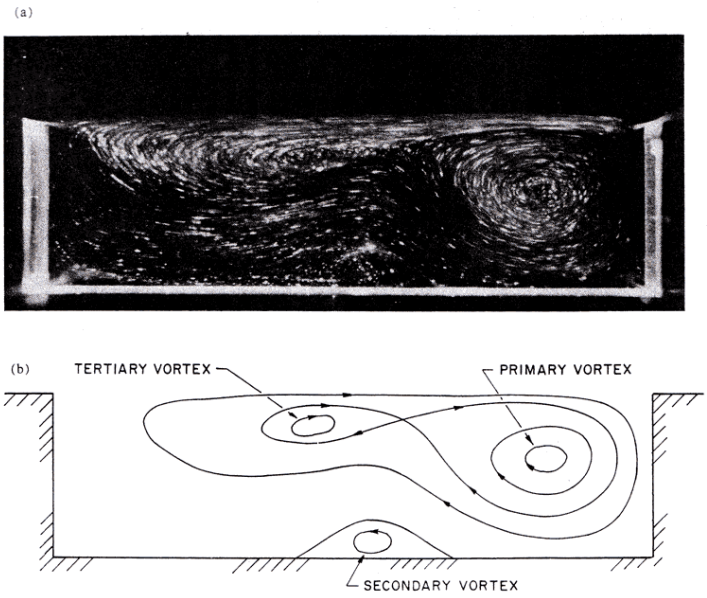

Figure 2.10: Flow structure in shallow, open cavity with $L/D = 3.5$, at a condition where oscillations just begin, $Re_L = 39,600$ and $Re_D = 11,300$ (Neary and Stephanoff, 1987)[6].

Manovski, Giacobello and Soria (2007) performed an investigation on a two-dimensional open cavity flow in a water tunnel. The cavity had a length-to-depth ratio of $L/D = 5$ with a laminar upstream boundary layer having a displacement-thickness-based Reynolds number of $Re_{\theta_0} = 81 - 194$. The cavity had a length of 100 mm and a depth of 20 mm, and was tested at $U =$ 50.1, 97.2, 190.8 and 288.2 mm/s, giving cavity-depth-based Reynolds numbers of $Re_D = 1000 - 5740$. They used laser illuminated dye visualisation and particle image velocimetry (PIV), and identified three main oscillatory regimes. The first regime (at $Re_D = 1000$) was characterised by very small amplitude disturbance waves along the shear layer and the streamline pattern for this regime was quite similar to that of Neary and Stephanoff (1987) in figure 2.10. The second regime (at $Re_D = 1930$ and $Re_D = 3800$) was characterised by disturbance waves that periodically rolled up and were usually partially clipped at the trailing edge. The third regime (at $Re_D = 5740$) was characterised by irregular oscillations – a mixture of the 'flapping' shear layer and vortex

[6]Reprinted from *Physics of Fluids*, Vol. 30 No. 10, M. D. Neary and K. D. Stephanoff, 'Shear-layer driven transition in a rectangular cavity', Pages No. 2936–2946, Copyright (1987), with the permission of AIP Publishing.

shedding with varying amplitude resulting in a mixture of complete escape and complete clipping events when vortices reached the cavity trailing edge.

Ashcroft and Zhang (2005) carried out an investigation of two-dimensional open cavities with a turbulent upstream boundary layer, finding large-scale vortical structures. The cavity aspect ratio was $L/D = 2$ – 4 ($L = 100$ – 200 mm, $D = 50$ mm and $W = 900$ mm) with PIV and other methods used in a wind tunnel at $U = 32$, 37 and 42 m/s, giving cavity-length-based Reynolds numbers of $Re_L = 220{,}000$ – 577,000. The plate was positioned at a small nose-down pitch angle of -2.5° in order to negate a small adverse pressure gradient that was found over the model. Oil-flow visualisation confirmed that the cavity was essentially two-dimensional. The time-averaged internal flow structures were characterised by recirculating vortices whose sizes and positions varied with geometry and flow conditions. Regarding the shear layer, they found an essentially linear growth of vorticity thickness along the cavities (with vorticity thickness being a measure of shear layer thickness) and the rate of growth was found to be independent of geometry. The unsteady large-scale vortical structures found in the shear layer were also found to grow linearly with distance, although these stopped growing as they neared the trailing edge.

Özsoy *et al.* (2005) investigated low Reynolds number, laminar, two -dimensional cavity flow in a low speed wind tunnel using PIV)at three velocities. The Reynolds numbers were Re_D =4000, 9000 & 13000, Re_L = 16000, 36000 & 52000 and $Re_{\theta_0} = 160 - 366$. The cavity had fixed dimensions giving $L/D = 4$ (and $L/W = 0.27$ - two-dimensional). The non-dimensional cavity lengths and depths were: $L/\theta_0 = 114 - 160$, $D/\theta_0 = 28.5 - 40$ and $D/\delta_0 = 3.5 - 4.8$ - all moderate values in the 'zone' for oscillations, neither especially small nor large. In this study, the rear recirculation vortex initially formed in the rear half of the cavity ($Re_D = 4000$) and then was found to become larger and move upstream with increasing Reynolds number ($Re_D = 13000$). In a complementary way, the forward recirculation vortex (associated with much lower velocity magnitude) became smaller with increasing Re_D. The authors' attributed the growth in the downstream recirculation to the increasingly energising effect of the shear layer with increasing Reynolds number, as the shear layer impinged further down the cavity rear wall with increasing Re_D, supplying higher momentum fluid into the cavity.

With increasing Reynolds number, Özsoy *et al.* (2005) observed a decrease in vertical fluctuation velocity and an increase in horizontal fluctuation velocity. This was attributed to the 'K-H [Kelvin-Helmholtz] instability having stronger periodic oscillations when the flow outside the cavity is laminar at low Reynolds number' (Özsoy *et al.*, 2005).

The location of maximum Reynolds stress ($u'v'$) in the shear layer was found by the authors to move upstream with increasing Re_D. Considering this study, and the study of Manovski, Honnery and Soria (2005), it appears that the flapping shear layer, location of recirculation vortex and location of maximum fluctuation are interrelated.

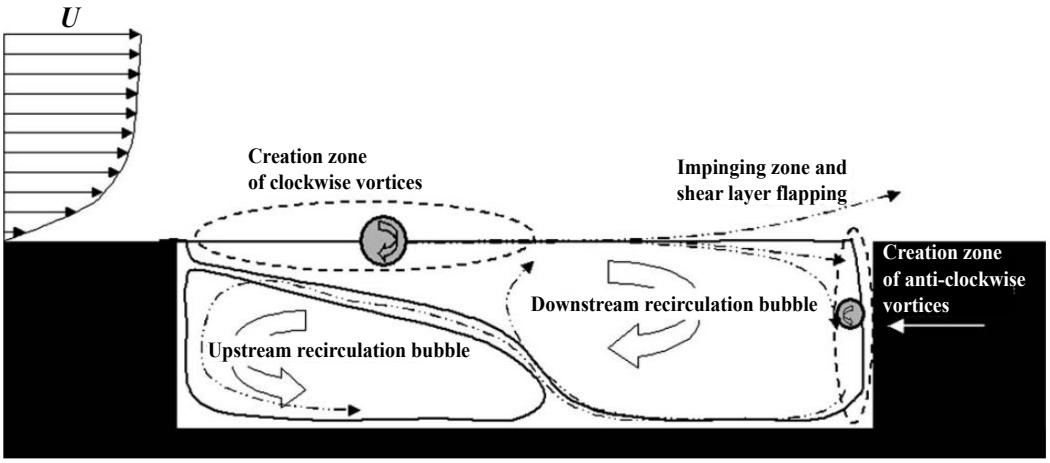

Figure 2.11: Schematic drawing of the flow paths and zones of vortex generation in an open cavity flow. $L/D = 4$ and $Re_D = 13000$, Özsoy *et al.* (2005, p. 141)[7].

Figure 2.11 shows a schematic drawing of the flow field showing the flow paths and zones of vortex generation. As noted, the vertical fluctuation (or flapping) of the shear layer was greatest at the lowest Reynolds number. Clockwise vortices are created in the separated shear layer while anti-clockwise vorticity is created by flow that impinges and travels down the rear wall with anti-clockwise vortices identified by the authors as created in this region. Since the shear layer flaps, fluid either exits over the rear of the cavity or is swept down into the cavity. Inside the cavity there are the two recirculation zones, or 'bubbles'. (As an aside, in a three-dimensionsal sense there must be some balancing method to balance the fluid that is swept into the cavity.)

Milbank (2004) investigated cavities on car wing mirrors, including the impact of yaw angle. The overall study focused on characterising these cavities and their behaviour in detail, including how the noise would be perceived by the vehicle occupant. Milbank's experimental investigations included investigations on a cavity in a flat plate at $L/D = 1$, $Re_D = 27,500$, $\delta_0 = 0.06 - 0.11$, and $Re_{\theta_0} = 191 - 315$. In this context there was a laminar boundary layer since the impingement point of the flow on the car mirror was close to the cavity. It was determined that any relevant atmospheric turbulence could be approximated by yaw and pitch. Milbank (2004) found a cellular flow structure (section 2.8.1), as well as staging and intermittency effects in the oscillatory behaviour (section 2.5.4).

[7] *Experiments in Fluids*, vol. 38, 2005, page 141, "Ozsoy, E, Rambaud, P, Stitou, A, and Riethmuller, M L, © Springer-Verlag 2005. With permission of Springer. Original caption: 'Schematic drawing of the cavity flow'.

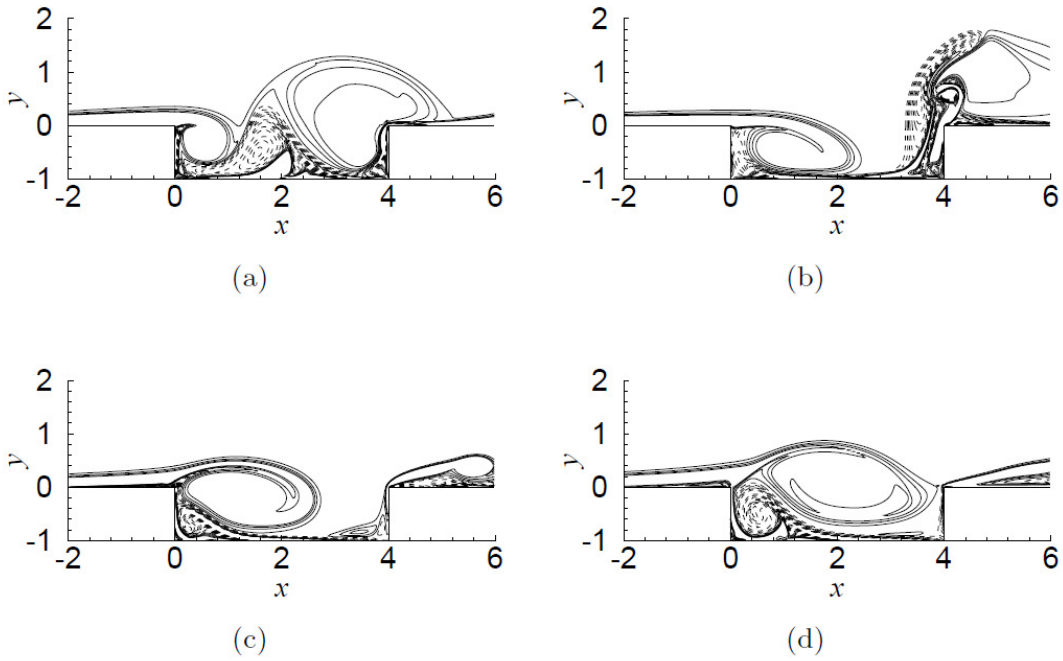

Figure 2.12: Example of wake mode behaviour showing vorticity contours (Rowley, 2002 p. 38)[8], (a) to (d) show increasing time. Dashed lines indicate counter-clockwise vorticity.

2.6.3 Wake Mode

Regarding shear layer behaviour, Gharib and Roshko (1987) described (in addition to the non-oscillating and shear layer oscillation modes) another mode of cavity flow which they called the 'wake' mode. The 'wake' mode involves the periodic downstream ejection of a vortex from the cavity, thereby resembling the shedding of vortices in the wake of a bluff body in a crossflow (Gharib and Roshko, 1987). The frequency of the cycle is considered to be independent of the flow velocity, suggesting that acoustic feedback is not involved in the mode (Rowley, 2002). Rowley (2002, p. 23) numerically found that the wake mode occurs upwards of $Re_L = 6,000$ for a cavity with $L/D = 4$ at $M = 0.6$. Figure 2.12 depicts vorticity contours showing the wake mode for $L/D = 4$ from one of Rowley's simulations. Gharib and Roshko (1987) experimentally found the 'wake' mode to occur from upwards of $Re_L = 14,000$ in a cavity with $L/D = 1.4$ in a water tunnel. The wake mode is associated with a dramatic increase in drag, compared to shear layer oscillations (Gharib and Roshko, 1987). Cavities transition from the shear layer mode to the wake mode as the

[8]Rowley, C, Colonius, T and Basu, A, 'On self-sustained oscillations in two-dimensional rectangular flow over cavities', *Journal of Fluid Mechanics*, vol. 455 pp. 315-346, Cambridge University Press, 2002, reproduced with permission.

length of the cavity or Mach number is increased (Rowley, 2002).

2.7 Aeroacoustic feedback loops: airfoil tonal noise

2.7.1 Introduction

Analogous to the tonal noise that may be produced by some cavity flows (section 2.5.1), tonal noise may also produced by flows over airfoils. This airfoil tonal noise has been attributed to an aeroacoustic feedback loop (Arbey and Bataille, 1983), similar to that present in cavity flows (Rossiter, 1964). Therefore, the related aeroacoustic problem of airfoil tonal noise is considered in this section of the literature review with a view to the subsequent study on the effect of a cavity in the surface of an airfoil, on the airfoil tonal noise produced by that airfoil (Chapter 5).

Airfoil noise is produced by helicopter rotors, wind turbines and airframes (Brooks, Pope and Marcolini, 1989) as well as computer cooling fans (Arcondoulis *et al.*, 2010) amongst other sources. When airfoils encounter smooth flow, unsteady fluctuations can be created thereby resulting in the production of airfoil noise. Although there are other sources of airfoil noise, such as leading edge noise and tip vortex noise, one major source of airfoil noise is the trailing edge of the airfoil. In trailing edge noise, an efficient source is created due to the diffraction of hydrodynamic instabilities at the sharp airfoil trailing edge (McAlpine, Nash and Lowson, 1999), leading to a source that is dipolar in nature (Desquesnes, Terracol, and Sagaut, 2007). A review of airfoil trailing edge noise is given by Arcondoulis *et al.* (2010).

In this section of the literature review, an overview of airfoil laminar boundary layer instability noise is first given. This is followed by a discussion of the airfoil tonal noise aeroacoustic feedback loop mechanism detailed in the literature. A debate in the literature regarding the necessity of an aeroacoustic feedback loop of that form in the production of airfoil tonal noise is then discussed, with some authors questioning the role aeroacoustic feedback loop in the production of various instances of airfoil tonal noise, while other authors support the role of the feedback loop in the production of the tones. Next, a brief discussion of passive control of airfoil tonal noise is given, as this gives an insight into the relative two-dimensionality of the mechanism, and the parallels can be drawn to the passive control of cavity noise. Finally, an observation in the literature about an underexplored phenomenon of airfoil tonal noise produced by an airfoil with a cavity is noted before a knowledge gap, an aim and objectives are stated.

2.7.2 Visualisation of laminar boundary layer instabilities

The 1958 study of Bergh and Berg described the flow visualisation of Tollmien-Schlichting (T-S) waves on a NACA0012 airfoil (Bergh and Berg, 1958). The waves were excited acoustically using a loudspeaker. The chord-based Reynolds numbers were in the range of Re_C = 80,000 – 120,000. Smoke was released from a finite-width slit in the airfoil, illuminated stroboscopically and photographed. Compared to the natural case, instability waves were apparent much further upstream in the boundary layer when the acoustic excitation was applied. When the airfoil was positioned at an angle of attack with the visualised side subject to an unfavourable pressure gradient, the wave pattern was found to transform into three-dimensional horseshoe-like loops (hairpin vortices). The authors noted that these loops were possibly related to the finite width disturbance introduced by the smoke slit. All experimental points studied (in terms of frequency and Reynolds number) were found to lie within the TS wave instability region, confirming that they were laminar boundary layer instabilities.

2.7.3 Laminar boundary layer instability noise

'Airfoil tonal noise' is a subset of trailing edge noise and refers to the discrete tones produced by some airfoils and streamlined flat plates (Brooks, Pope and Marcolini, 1989). It is associated with laminar flow over most or almost all of the airfoil – on at least one side, usually the pressure side – and is thus referred to as 'laminar boundary layer instability noise' (Paterson *et al.*, 1973).

Airfoil tonal noise is a form of airfoil self-noise and may dominate for low to moderate chord-based Reynolds numbers of up to approximately 600,000 (Arbey and Bataille, 1983, Arcondoulis *et al.*, 2010). Airfoil tonal noise has been attributed to a periodic vortex structure in the boundary layer over the pressure side of the airfoil (Nakano, Fujisawa and Lee, 2006). The instabilities in the transitional boundary layer over the airfoil are diffracted by the sharp trailing edge whereby they form a strong noise source (Arbey and Bataille, 1983). The spectral characteristics of the noise consist, firstly, of a broadband hump, having a central frequency, f_s. This frequency has been associated with the most amplified boundary layer Tollmien-Schlichting (T-S) wave over the airfoil (Kingan and Pearse, 2009). Secondly, around this broadband hump many individual discrete tones, f_n, may be found, each having approximately equal frequency spacing, Δf (Arbey and Bataille, 1983; Kingan and Pearse, 2009). Figure 2.13 shows a typical noise spectrum of airfoil tonal noise from Arcondoulis *et al.* (2009).

A number of different mechanisms have been proposed to explain various instances of the noise, for different geometries, Reynolds numbers, angles of attack, and even different flow facilities. In the first comprehensive study on the topic, Paterson *et al.* (1973) attributed the noise produced by NACA 0012

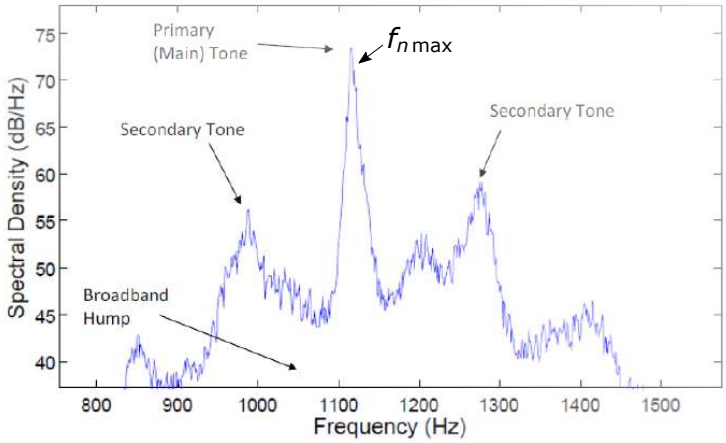

Figure 2.13: Typical structure of airfoil tonal noise from Arcondoulis *et al.* (2009). Shows far-field sound pressure spectrum from NACA0012 at zero angle of attack and $Re_C = 75{,}000$. Measurement taken in the same anechoic wind tunnnel (AWT) facility as the present study.

and NACA 0018 airfoils to vortex shedding.

Paterson *et al.* (1973) provided empirical U^a scaling relations for the mean behaviour of the airfoil tones produced by a NACA 0012. The behaviour and ladder structure of the airfoil tones are shown in figure 2.14. The equation for the scaling relation is given by equation 2.20 where f is the frequency, U is the freestream velocity, C is the chord of the airfoil, and ν is the kinematic viscosity. For the central frequency, f_s of the tones produced by flow over a NACA 0012, the value of the constant K was found to be $K = 0.011$ while the exponent a took the value $a = 1.5$. Arbey and Bataille (1983) later showed this to be equivalent to a scaling relation for the central frequency, f_s, of a NACA 0012 based on an approximately constant boundary layer displacement-thickness-based Strouhal number of 0.048. For the individual tones, f_n, Paterson *et al.* (1973) found that an exponent value of $a = 0.8$ applied.

$$f = \frac{KU^a}{(C\nu)^{1/2}} \tag{2.20}$$

For a NACA 0018 airfoil with chord-based Reynolds numbers of $Re_C = 6.9-27\times10^4$ at 8° angle of attack, Kingan and Pearse (2009) calculated that f_s varied with $U^{1.35}$ while f_n were found to scale with exponents between $a = 0.79$ and $a = 0.84$. For a sharp trailing edge flat plate with thickness/chord=0.025 (approximately one-fifth of a NACA 0012) and chord-based Reynolds numbers of $Re_C = 7.0 - 20 \times 10^4$ at zero angle of attack, Moreau *et al.* (2011) found that the individual tones, f_n, scaled with $U^{1.25}$.

Nakano, Fujisawa and Lee (2006) performed an experimental study on the unsteady flow structure around a NACA0018 airfoil, which showed that tonal noise was produced by periodic vortex structure near the trailing edge, predom-

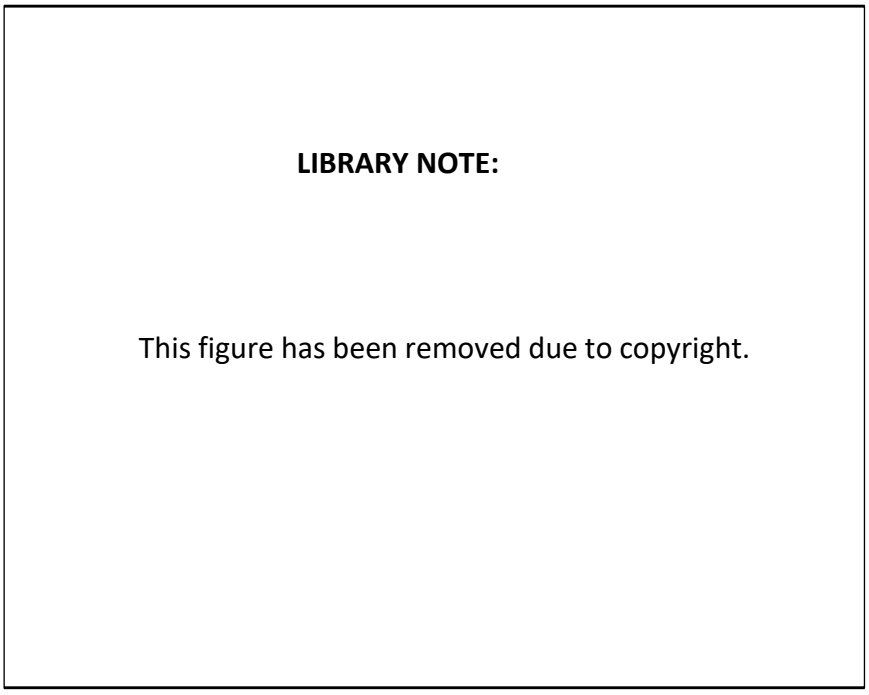

Figure 2.14: Ladder structure of airfoil tonal noise (p. 34, Arbey and Bataille, 1983, from Paterson *et al.*, 1973).

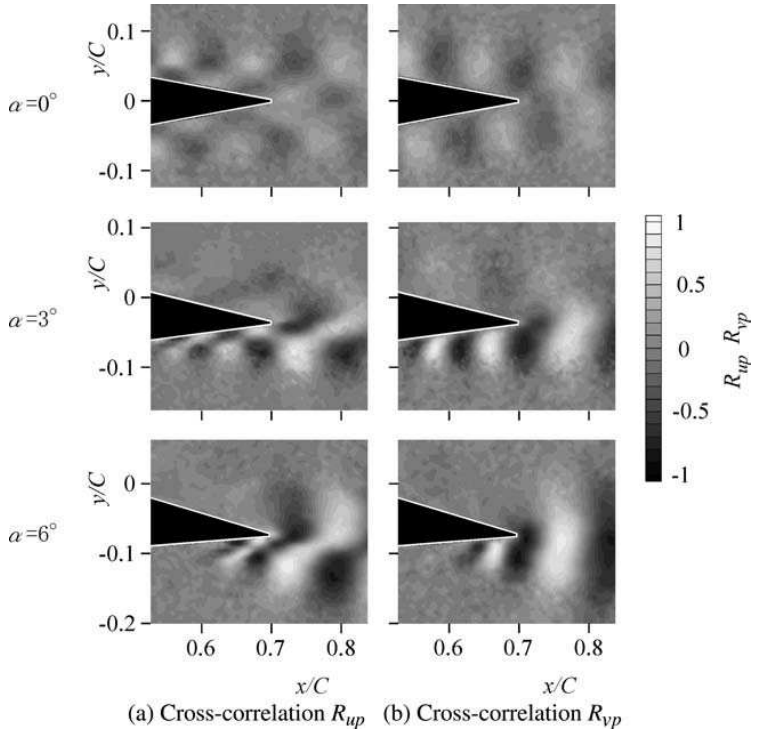

Figure 2.15: Cross-correlation of velocity fluctuation and microphone noise signal from Nakano *et al.* (2006)[9] for a NACA0018 airfoil at various angles of attack. The chord-based Reynolds number was 160,000. (a) Cross-correlation with horizontal velocity fluctuation. (b) Cross-correlation with vertical velocity fluctuation.

inantly on the high-pressure side of the airfoil. The chord Reynolds number was 1.6×10^5. Particle image velocimetry was utilized with smoke particles in air. The ceiling and floor of the wind tunnel duct were lined with acoustic-absorbing material (glass-wool). The goal of the study was to investigate the relation between the velocity and vorticity field near the trailing edge and the noise radiated by the airfoil. Figure 2.15 shows the cross-correlation found between the vertical and horizontal velocity fluctuations and a propagation-distance-corrected microphone pressure signal. The figure shows that at zero angle of attack, weakly correlated structures were found adjacent to both surfaces of the NACA0018 airfoil, consistent with the weak tones found in the noise spectrum. However, at non-zero angles of attack, an asymmetric distribution was found with highly correlated periodic structure found adjacent to the high-pressure surface of the NACA0018 airfoil at nose-up angles of attack of 3° and 6°, consistent with strong tones found in the noise spectrum. Also, a region of flow separation on the high-pressure surface was found using surface flow visualisation, and this region was found to move rearwards with increasing angle of attack.

2.7.4 The role of an aeroacoustic feedback loop

It has been considered in the literature that an aeroacoustic feedback loop is involved in the production of airfoil tonal noise, similar to the feedback loop involved in the production of cavity tonal noise. Although the phenomenon has been studied extensively, differing views have been put forth on the role (or absence) of a feedback loop in the production of the discrete tones.

Paterson *et al.* (1973) were the first to identify the discrete tones and attributed them to vortex shedding in the wake of NACA 0012 and 0018 airfoils. Paterson *et al.* (1973) found that, 'this phenomenon only occured when the boundary layer developing on the airfoil were laminar, at least on the (high-)pressure side, and the trailing edge played a crucial role in the sound generation process' (Arbey and Bataille, 1983, p. 33). The involvement of a feedback loop, however, was first proposed by Tam (1974), with feedback loop models later developed and refined by other authors such as Longhouse (1977) and Arbey & Bataille (1983).

In vortex shedding from bluff bodies, the vortex shedding instability is unrelated to instabilities found in the boundary layer over the object (Roshko, 1955b). Subsequently, Tam (1974) disagreed with the suggestion of the airfoil tones being due to vortex shedding and was the first to identify that the previously-observed tonal frequencies were within the region of unstable frequencies of the laminar boundary layer, proposing the existence of an aeroacoustic feedback loop which would better describe the 'ladder structure' that had been observed. Tam (1974) proposed a feedback loop between the airfoil trailing edge and a point in the wake, and this better described the ladder structure found by Paterson *et al.* (1973). For instance, the presence of more than one tone indicated that more than one mode was excited (1974). Note that the receptivity of laminar-transitional boundary layers around airfoils to acoustic waves was well known (Bergh and Berg, 1958).

The feedback loop model, which was furthered by numerous authors including Archibald (1975), Longhouse (1977), and Arbey & Bataille (1983), described the series of discrete tones found at a given set of flow conditions. The model contains three components (Arbey & Bataille, 1983, Longhouse, 1977):

(1) the initiation of laminar boundary layer instability waves (T-S waves) at a neutral-stability point on the airfoil surface;

(2) the convection of these waves past the trailing edge where strong acoustic waves are radiated due to diffraction of the sources in the boundary layer by the sharp trailing edge; and,

[9] *Experiments in Fluids*, vol. 40, 2006, page 487, Nakano, T, Fujisawa, N, and Lee, S, © Springer-Verlag 2006. With permission of Springer. Original caption: ' Cross-correlation contour of velocity fluctuation and noise signal: a) Cross- correlation R_{up}, b) Cross- correlation R_{vp}'.

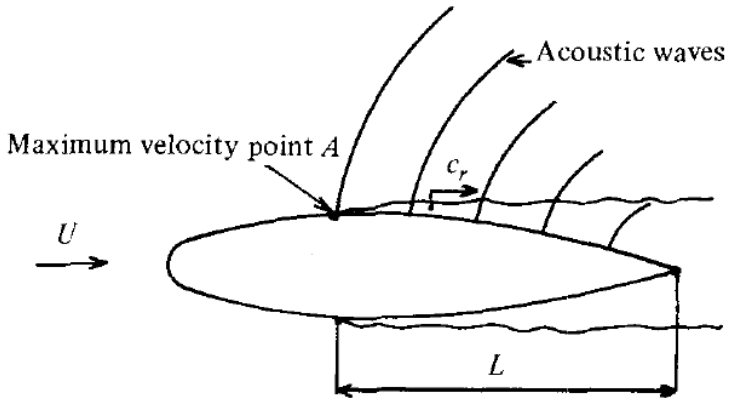

Figure 2.16: Aeroacoustic feedback loop for airfoil tonal noise proposed by Arbey and Bataille (1983, p. 44)[10], for airfoil at zero angle of attack.

(3) propagation of these acoustic waves upstream to the neutral-stability point where they cause the initiation of further instability waves in the boundary layer such that reinforcement occurs at certain frequencies.

Arbey and Bataille (1983) stated that the feedback loop occurred between the trailing edge of the airfoil and the point where hydrodynamic boundary layer instabilities (Tollmien-Schlichting waves) are created upstream on the surface of the airfoil, the 'receptivity point' or neutral-stability point, which for an airfoil at zero angle of attack they considered to be at the maximum velocity point of the airfoil . This is illustrated in figure 2.16. Arbey and Bataille (1983) found excellent agreement with experiment using this location to predict the tones produced by NACA 0012 airfoils at zero angle of attack.

Underlying Tam's (1974) feedback loop was a phase condition; this condition was modified by Arbey and Bataille (1983) for their updated version of the feedback loop model. From the phase condition, the possible frequencies of the discrete tones (f_n) were derived by Arbey and Bataille (1983). The tones needed to have a fixed total phase around the loop of $2\pi n$. Here, L is the characteristic length of the feedback loop, U_c is the convection velocity of disturbances, c is the speed of sound, U is the free-stream velocity and n is the mode number. For reinforcement 'nothing should change by going around the loop once' (Tam, 1974) and thus the condition was derived by requiring a total phase change around the feedback loop of $2\pi(n + 1/2)$, where the addition of $1/2$ accounted for a 180° phase shift at the trailing edge (Arbey and Bataille, 1983). The loop consists of a downstream component L/U_c and an upstream component $L/(c - U)$, such that the total phase change must be equal to

[10]Arbey H, and Bataille J, 'Noise generated by airfoil profiles placed in a uniform laminar flow', *Journal of Fluid Mechanics*, vol. 134 pp. 33–47, Cambridge University Press, 1983, reproduced with permission.

$\omega_n(L/U_c + L/(c-U))$ (Arbey and Bataille, 1983, Tam, 1974). Substituting $f_n = \omega_n/(2\pi)$ gives equation 2.21 (Arbey and Bataille, 1983):

$$\frac{f_n L}{U_c}(1 + \frac{U_c}{c-U}) = n + \frac{1}{2} \tag{2.21}$$

2.7.5 Questioning the role of an acoustic feedback loop

In more recent works, additional mechanisms have been identified for the production of the airfoil tonal noise. The importance of a feedback loop, where boundary layer disturbances are excited by acoustic waves, is being debated. Indeed, some recent studies have questioned the necessity or form of this feedback loop in the production of the airfoil tonal noise in some instances.

McAlpine, Nash and Lowson (1999) identified the importance of a region of separated flow (laminar separation bubble) close to the trailing edge. A NACA 0012 and a FX79 W151 airfoil were tested at chord-based Reynolds numbers of 450,000 - 870,000. The authors used a closed-section wind tunnel rather than the open-jet facilities used by previous researchers. Using Laser Doppler Anemometry measurements, together with stability analysis, they identified that amplification of the airfoil tonal frequency was controlled by a laminar separation bubble found near the trailing edge due to the presence of inflectional velocity profiles. It was found that most of the amplification occurs near the trailing edge. They considered that instability frequencies (T-S waves) were determined by the dynamics close to the point of flow separation where linear stability theory is valid. High levels of amplification then occurred over the separation bubble (McAlpine *et al.*, 1999, Kingan and Pearse, 2009). Subsequently in the wake, the vortex-shedding frequency (which is not usually related to boundary layer disturbances for bluff bodies) was determined by the 'amplification of a "selected" boundary-layer instability wave' (McAlpine, Nash and Lowson, 1999). More recently, Kingan and Pearse (2009) have demonstrated that the central frequency, f_s, can be predicted by the frequency of maximum T-S wave amplification.

McAlpine, Nash and Lowson (1999) also found that for higher Reynods numbers, no separation bubble was detected, however the inflectional profile of the boundary layer was found to be sufficient to produce the tone. On the other hand, for lower Reynolds numbers there was found to be no tone even though the separation bubble was detected – it was considered that the growth rate of instabilities was insufficient (to cause the tone). It was also found that if transition to fully-developed turbulence occurred before the trailing edge then there was no tone, even if an upstream boundary layer instability frequency was present.

Furthermore, McAlpine *et al.* (1999) did not find a 'ladder structure', and they stated that a feedback loop about a separation bubble (rather than further upstream on the boundary layer) was sufficient for the production of airfoil self-noise. They stated that there would be a feedback mechanism about the

separation bubble to create the narrowband characteristic of the tone, i.e., the reinforcement occurred near the point of flow separation rather than at an initial instability point and the single frequencies observed were not selected due to fitting the phase requirements of a feedback loop. Nash, Lowson and McAlpine (1999) eliminated the ladder structure of the tones by fitting acoustic lining to the ceiling and floor of the working section of the same wind tunnel and claimed that previous researchers may have been 'misled' by spurious feedback loops peculiar to the experimental rigs used.

Moreau, Brooks and Doolan (2011) showed that tones produced were related to vortex shedding frequencies and T-S waves were unlikely to be present at these frequencies for a flat plate with a thickness-to-chord ratio of 0.025 and a 12° wedge-shaped sharp trailing edge (flat on the pressure surface). The airfoil was a slender flat plate profile with an asymmetric wedge-shaped trailing edge. The measurement was conducted in an open-jet anechoic wind tunnel at a chord-based Reynolds number of 200,000. The tonal noise produced by this airfoil was found to be due to vortex shedding over a separation bubble detected near the trailing edge, with no boundary layer instability waves involved. Although tones with approximately equal frequency spacing were found, boundary layer instability waves at these frequencies were not detected and the frequencies were outside the instability envelope of the boundary layer according to linear stability theory. The tones were attributed to vortex shedding frequencies being sufficiently amplified by the unstable boundary layer (as evidenced by inflectional velocity profiles). In subsequent work, Doolan *et al.* (2012) performed an incompressible numerical simulation of the same plate at the same Reynolds number and found that the tonal noise could be explained by vortex shedding processes only.

Although some authors (Bergh and Berg, 1958, Archibald, 1975) have identified a single boundary layer instability determining the wake frequency of airfoils, little evidence has been previously found to describe the variety of discrete tones. Hence, the idea of vortex shedding processes determining the frequencies of airfoil tonal noise, in some instances, is being put forward (Moreau *et al.*, 2010). The essential feature of vortex shedding mechanisms determining the frequencies is that they are not related to instabilities present in the boundary layer over the object (Moreau, *et al.*2010). Roshko (1955b) states that the main feature of flow past a bluff body is 'separation from the body surface ... and the formation of a large wake' with a Karman vortex street forming downstream of the bluff body. Roshko (1955b) cites Fage and Johansen (1928) who state that the shedding frequency is inversely proportional to the width of the wake. The interaction of the two sides of the wake is important, and Roshko (1955b) demonstrates that the addition of a splitter plate downstream of a circular cylinder can suppress or modify the vortex shedding behaviour, depending on plate length and position. This phenomenon has also been investigated by Ali *et al.* (2010, 2011) for the case of a square cylinder.

For airfoil tonal noise from NACA0012 and NACA0018 airfoils, Paterson

et al. (1973) found that the broad trend of the tones followed the relation $St = f(2\delta)/U \approx 0.11$. The wake width 2δ was based on twice the boundary layer thickness from the laminar, flat plate, zero pressure gradient boundary layer equation – however the plates were positioned at angles of attack up to 10°. Paterson *et al.* (1973) noted that this is slightly lower than the St number of approximately 0.2 associated with bluff body vortex shedding.

Tam and Ju (2012) attributed the basic tone generation mechanism to the near-wake Kelvin-Helmholtz (K-H) instability at zero angle of attack. The authors elaborated, however, that other mechanisms could become possible or even dominant at non-zero angles of attack. They numerically investigated a NACA 0012 airfoil with varying trailing edge radius (from 0.5 % to 10 % truncation) in the moderate chord-based Reynolds number range of 200,000 to 500,000. The airfoil was simulated at zero angle of attack so as to deliberately avoid the presence of separation bubbles or large-scale open separations that could be possible feedback sites. They found a single tone for a given flow configuration. These tones agreed with equation 2.20 for the nearly sharp edge, whilst for more blunt edges lower frequencies forming a series of parallel curves to this equation were found. The authors performed a instability analysis which showed that the tone frequency corresponded to the most amplified K-H instability wave at the thinnest, and therefore most unstable, point of the wake. They believed that the instability initiated at this part of the wake 'is ultimately responsible for the generation of the aerofoil tones' (Tam and Ju, 2012, p. 559). For airfoils with some bluntness the wake forms smoothly at the trailing edge (with vortices appearing some distance downstream) and the authors claim that this finding 'eliminates vortex shedding as a tone generation mechanism' for such airfoils (Tam and Ju, 2012, p. 543), in the sense of discrete vortices forming over the airfoil or at the trailing edge. Like Nash *et al.* (1999), the authors believe that feedback tones are facility related and that they 'are not genuine tones' of a truly isolated airfoil (Tam and Ju, 2012, p. 567).

2.7.6 Supporting the role of an acoustic feedback loop

In contrast to the above discussion, some other recent studies have suggested that an acoustic feedback mechanism plays a role in the production of the noise. Takagi and Konishi (2010) investigated the role of artificial feedback on the noise produced by a NACA 0012 at a chord-based Reynolds number of 450,000. The addition of a splitter plate disturbed the formation of a discrete frequency vortex street, so that only a broadband T-S contribution remained, supposedly due to lack of feedback to select a discrete frequency. Artificial feedback from external acoustic forcing was found to excite a discrete frequency, from amongst the T-S broadband frequencies, and this frequency demonstrated a ladder-like structure. The authors claimed that this demonstrated the role of an acoustic feedback loop in the frequency selection of trailing edge noise. At a chord-based Reynolds number of 10,000, Ikeda, Atobe, and Takagi (2012)

numerically found that a NACA 0012 at zero angle of attack was governed by the wake instability only, yet for non-zero angle of attack instability waves were present in the suction side boundary layer which were attributed to an acoustic feedback mechanism.

Jones, Sandberg and Sandham (2010) performed a numerical simulation of the flow around a NACA 0012 at the chord-based Reynolds number of 50,000 and showed the existence of an acoustic feedback loop. The airfoil was set at a geometric angle of attack of 5° and a Mach number of 0.4 was specified. Specifically, a single, initial and finite perturbation ('wavepacket') was applied to the flowfield, and this was found to be sufficient to setup a self-sustaining oscillation. Virtual pressure probes located both within and outside the boundary layer, showed the propagation of a hydrodynamic disturbance downstream followed by the propagation of acoustic waves upstream, then followed by the creation of a new hydrodynamic wavepacket and so forth. The behavior was attributed to an acoustic feedback loop with reception said to occur near the leading edge. The authors stated that,

> *'...it appears that the downstream-travelling wavepacket induced by the initial perturbation generates upstream-travelling acoustic waves when it convects over the trailing edge. These upstream-travelling acoustic waves then reach some location of receptivity, probably the aerofoil leading edge, and generate another downstream-travelling wavepacket. The process repeats with all x-locations and hence represents an instability of the flow, via a combination of convective instability of hydrodynamic disturbances and an acoustic-feedback loop.'*
>
> *(Jones et al., 2010, p. 276–277)*[11]

2.7.7 Summary for airfoil tonal noise produced by smooth airfoils

In summary, a number of different findings have been made as to, firstly, the flow structure around airfoils that generate tonal noise, and secondly, the mechanisms involved in the generation of the noise. Some authors have questioned the role of an acoustic feedback loop in the production of the tonal noise, while other authors have supported the involvement of an acoustic feedback loop in the production of the tonal noise. Subsequently, further experimental or numerical avenues to investigate airfoil tonal noise would be helpful towards clarifying the mechanisms, including whether any acoustic feedback

[11] Jones, L E, Sandberg, R D and Sandham, N D, 'Stability and receptivity characteristics of a laminar separation bubble on an aerofoil', *Journal of Fluid Mechanics*, vol. 648, pp. 257–296, reproduced with permission.

loop is involved, whether that be broadly or in certain particular instances.[12]

2.7.8 Airfoil tonal noise produced by airfoils with cavities

To the aforementioned end of further experimental avenues to investigate airfoil tonal noise, a variation in trailing edge noise tonal frequency when a circular cavity was present in a NACA 0018 was compared to the noise from the same airfoil without a cavity by van Osch (2008). However no explanation for the observed behaviour was provided by the author. Other existing studies on airfoils with cavities primarily pertain to the aerodynamic performance of the airfoils, or to the cavity oscillation modes generated over them (for example, Lasagna *et al.*, 2011, Olsman and Colonius, 2011, and Olsman *et al.*, 2011). Note that a laminar boundary layer will re-form downstream of a cavity in the surface of an airfoil given a sufficiently low Reynolds number. For these profiles, it should be expected that the tone generation mechanisms will be similar to closed profile airfoils provided that the profile is streamlined overall, is operating in the relevant Reynolds range, and that it has a laminar boundary layer over it.

2.7.9 Knowledge gap

To best of the author's knowledge the occurence of airfoil tonal noise from a plate with an nominally non-oscillating cavity has not been described previously, and the mechanism of such noise is a valid knowledge gap.

2.8 Three-dimensional cavities

The flow fields about narrow cavities, $L/W > 1$, are known to have significant three-dimensional effects. Crook (2005, p. 65) notes from experimental observations that the flow about narrow cavities can be highly three-dimensional and two-dimensional descriptions are insufficient to fully describe the flow field. For example, in-flow and out-flow processes have been identified at the front and rear corners of cavities respectively (Ahuja & Mendoza, 1995 and Crook, Kelso & Drobik, 2007). Rossiter (1964) notes that although similar patterns to 2-D cases may found at the centre-line of even quite narrow cavities, near

[12] Since the present investigation of airfoil tonal noise was principally completed in January 2013 (with results submitted for publication and described in Chapter 5: Airfoil Tonal Noise Results and Discussion), a number of relevant studies regarding airfoil tonal noise production from NACA series airfoils have been published in the literature. These studies and their relation to the present findings are described in Appendix A. They are not discussed here, as their inclusion *a posterori* would not accurately represent the literature at the time the research was conducted.

the side walls and down-stream (due to the out-flow processes) the flow field may be quite different.

The 3D flow-field around rectangular cavities has been extensively studied at a variety of speeds. At low subsonic speeds the flow structure has been studied by authors including Crook *et al.* (Crook, Hassan & Kelso, 2008, and Crook, Kelso & Drobik, 2007), Crook (2005, 2011), Faure *et al.* (2007), Rockwell & Knisely (1980) and Maull & East (1963). At transonic speeds it has been studied by authors including Doran (2007) and Kaufman & Clark (1980). At high supersonic speeds it has been studied by authors including Dolling, Perng and Leu (1997) and it was also reported in ESDU (2005).

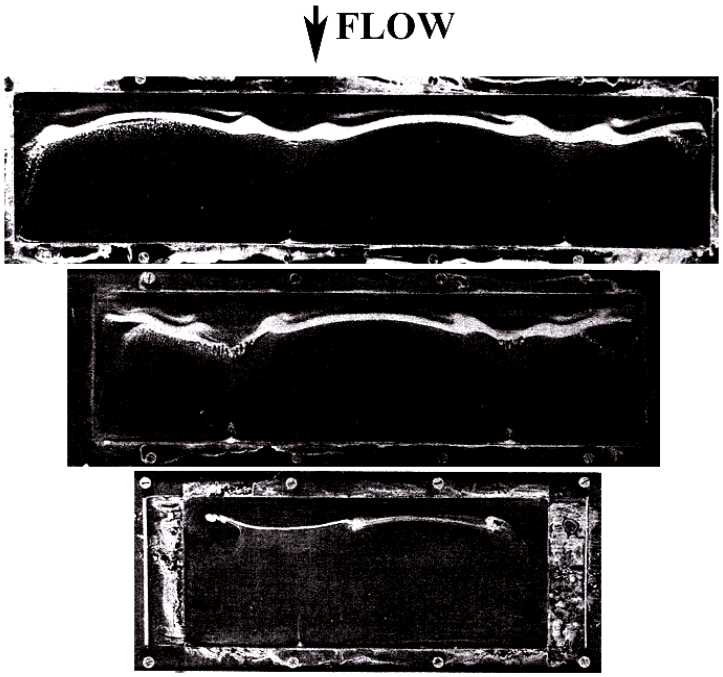

Figure 2.17: Flow visualisation of spanwise cells by Maull and East (1963)[13]. Overhead view of oil visualisation on the cavity floor. Top to bottom: $L/W = 0.21$, 0.27 and 0.4.

2.8.1 Spanwise flow structures

Maull and East (1963) were the first to identify time-averaged spanwise flow structures in nominally two-dimensional cavity flows ($L/W < 1$). In recent works, these time-averaged cellular flow structures have been associated with an unsteady centrifugal instability of the recirculating flow within the cavity (Brès and Colonius, 2008). Furthermore, where such instabilities exist, they will also impact on the unsteady flow structures of the cavity (for example, Crook, 2011).

Maull and East (1963) reported three-dimensional effects inside a nominally two-dimensional cavity for low speed wind tunnel flows. Their study consisted of two components. First, oil visualisation was carried out at $Re_D = 95,300$ and $L/D = 2$. The aspect ratios of the cavities were $L/W = 0.21$, 0.27 and 0.40. This visualisation was conducted to ensure the two-dimensionality of the flow, however it was 'immediately apparent' that the flow actually had a three-dimensional nature. The cross-sectional flow pattern for this cavity was considered by Maull and East (1963) to consist of a large main recirculation vortex and a much smaller front corner vortex. Thus the light areas of figure 2.17 show pooled oil on the floor of the cavity corresponding to the separation

[13]Maull, D and East, L, 'Three-dimensional flow in cavities', *Journal of Fluid Mechanics*, vol. 16 pp. 620-632, Cambridge University Press, 1963, reproduced with permission.

line between the two recirculation vortices. The change in the shape of the separation line is shown with increasing L/W ratio. The pooled oil was found by the authors to be subject to significant spanwise modulation with an integer number of 'cells' forming that varied with the width of the cavity. These spanwise cells were found to be steady when they occurred, however they did not occur under all conditions. The cells could also be identified from spanwise pressure distributions on the cavity floor (Maull and East, 1963). Some of the visualisations suggested that the pattern corresponds to:

> *'the presence of a row of vortices, ... having their axes normal to the bottom of the cavity and terminating on it.'*
>
> *(Maull and East, 1963, p. 623)*

Milbank (2004) also identified spanwise cells. Milbank conducted three-dimensional smoke visualisation on a relatively deep and wide cavity with open flow, which was subjected to yaw at low subsonic speeds. Span-wise cells were noted which 'appeared to break up and become less clear' as the yaw angle was increased (Milbank, 2004, p. 130). Flow visualisations by Faure *et al.* (2007) showed similar patterns to those found by Milbank (2004). Where Milbank (2004) focused on the effects of yaw at a limited range of geometries, Faure *et al.* (2007) investigated a large range of cavity aspect ratios.

Brès and Colonius (2008) investigated three-dimensionalities in cavity flows using linear stability analysis and direct numerical simulations. The authors argued 'that the [three-dimensional] instability mechanism is a generic centrifugal instability in the recirculating vortical flow near the downstream cavity wall' (Brès and Colonius, 2008, p. 318).

2.8.2 Shallow, narrow cavities

Crook and colleagues (Crook, 2005, Crook, Kelso & Drobik, 2007, Crook, Hassan & Kelso, 2008, and Crook, 2011) comprehensively studied the flow structure around relatively narrow, shallow cavities at low subsonic velocities, at the University of Adelaide finding a 'highly three-dimensional' flow field. Crook (2005) suggested that two-dimensional descriptions found in the literature were insufficient to describe three-dimensional cavities, where for example, an out-flow process was suggested at the two rear corners of the cavity (Crook *et al.*, 2008).

A cavity with $L/D = 6$ and $L/W = 3$ was the main three-dimensional geometry considered. This geometry classified the cavity flow as nominally an open, three-dimensional cavity flow. The cavity was tested at freestream velocities of 20-25 m/s in air and 108 mm/s in water, giving length-based Reynolds numbers of $Re_L = 740,000$ in air and $Re_L = 80,000$ in water. The cavity had dimensions of $L = 450$mm, $D = 75$mm and $W = 150$mm.

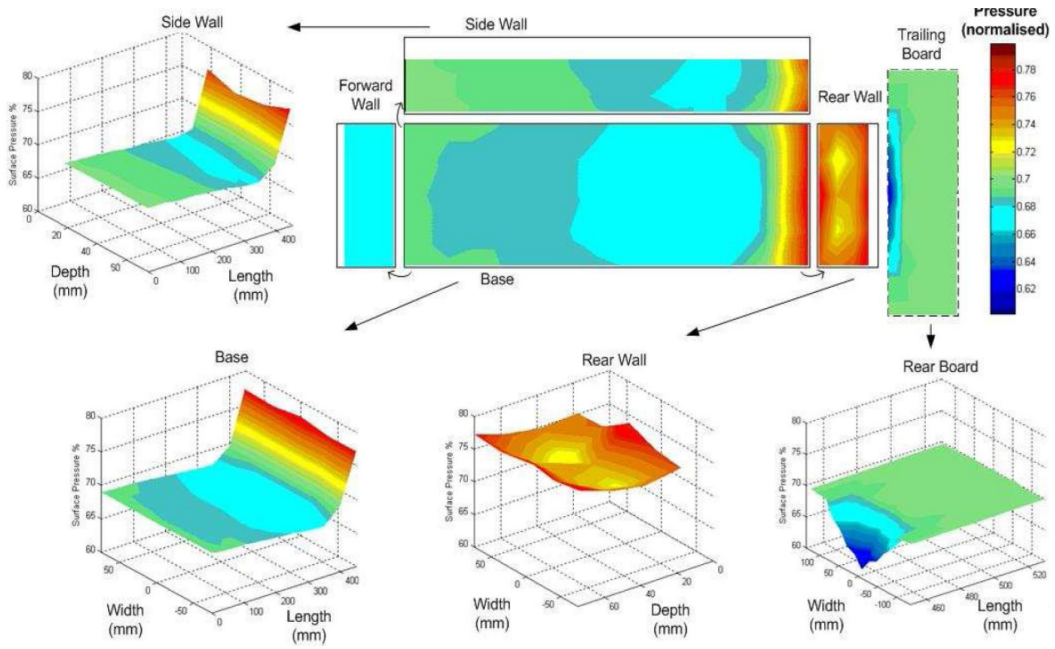

Figure 2.18: Time-averaged normalised wall pressure data obtained from pressure tappings (Crook *et al.*, 2007, p. 434). $L/D = 6$, $W/D = 2$, $Re_D = 100{,}000$, $Re_\delta = 13{,}000$ and $D/\delta_0 = 7.7$ (turbulent boundary layer type).

The time-averaged surface pressure data obtained by Crook, Kelso & Drobik (2007) from pressure tappings in the wind tunnel testing are shown in figure 2.18. Notable features are:

- The 'sharp' rise in pressure near the rear of the cavity, indicative of an open-type cavity.
- The two lower pressure regions on the rear wall suggesting two impingement points.
- The lower pressure region on the flat plate beyond the trailing edge, suggesting the region of separation.
- The low pressure in the middle of the cavity floor, associated with the main recirculation.
- Comparatively much lower normalised pressure on the front wall than the rear wall, associated with the back-flow and general recirculation inside the cavity.

Crook (2005) conducted surface flow visualisation in air using a paste consisting of a mixture of corn flour and water. Figure 2.19 shows Crook's (2005) interpretation of this surface pattern.

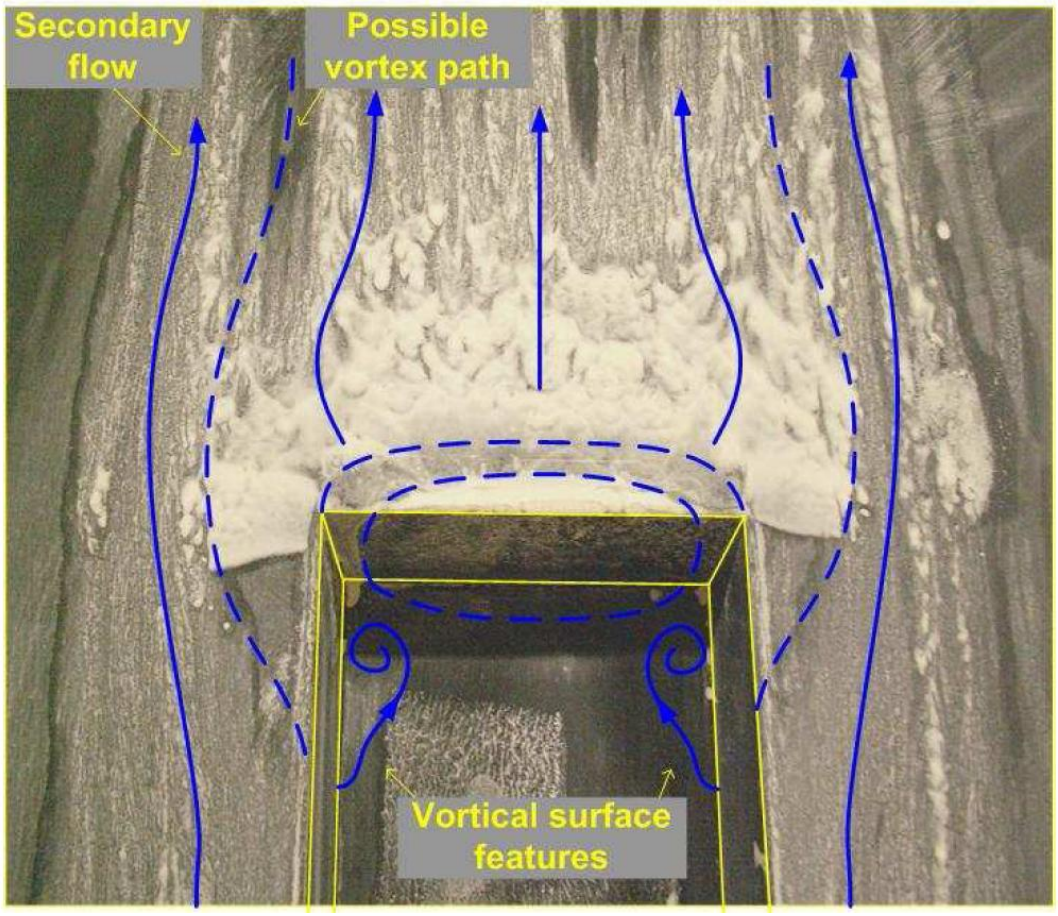

Figure 2.19: Sketch of surface flow visualization (Crook, 2005, p. 66).

Crook (2005, p. 65) 'hypothesised that the recirculation in the lower rear of the cavity may be the origin of vortices which are swept out of the cavity and continue downstream', and that these vortices may be 'responsible for transporting fluid outward from the walls' at the rear of the cavity. Atvars *et al.* (2009) experimentally found a co-recirculation in the rear of the cavity. Also, the experiments of Atvars *et al.* (2009) were supplemented with validated simulation results which appeared to show trailing vortices emerging from this co-recirculation region and exiting the cavity downstream. This may be consistent with Crook's (2005, p. 65) hypothesis.

Crook *et al.* (2008) recorded PIV data at $Re_D = 6,700$ ($Re_L = 40,000$), with a laminar boundary layer upstream ($\delta_0/D = 0.15$ and $\theta_0/D = 1.6 \times 10^{-2}$), for $L/D = 6$ and $L/W = 3$. Velocity vectors and streamlines obtained for three longitudinal measurements planes are shown in figure 2.20, these were located at $z/D = 0$, $z/D = 0.5$ and $z/D = 0.98$ (note that (1) $W = 2D$ and (2) the origin of the z-axis is located at the centreline). Crook has annotated the main features consisting of a front and rear vortex, recirculation zone and bifurcation point indicating the position of impingement of the shear layer on

the rear wall. In this instance, the rear vortex was found to be a region of co-recirculation with the same direction as the main recirculation.

Figure 2.21 shows time-averaged PIV velocity data and streamlines measured in a lateral plane near the rear wall. Crook (2011) identified a pattern with a 'number of source and sink points and bifurcation lines' and noted that the distribution was 'generally symmetric'.

Near the top of the wall, Crook (2011) identified three saddles separating two source star nodes. The bifurcation line between these features represents the time-average impingement line of the shear layer on the rear wall, above which flow exits over the top of the rear of the cavity and below which flow is swept into the recirculation within the cavity. Flow swept down into the recirculation appears to be swept towards either the centreline or side walls of the cavity.

At the lower part of the wall Crook (2011) has identified stable foci at the two lower side corners next to saddles with a sink node at the centre. Below the bifurcation line formed by these features there may be a region of separation associated with a lower rear corner vortex. The overall distribution of features on the rear wall may not be altogether that different from that found in transonic cases. For example, Knowles, Lawson and Ritchie (2007) were also able to identify vortical features in the lower rear corners on the rear wall of a 3D cavity in surface streamlines obtained from simulations, although these features were not clear in experimental surface flow visualisation.

To produce the overall flow pattern shown in figure 2.22, Knowles, Lawson & Ritchie (2007) combined the experimental findings and their numerical findings. The three marked planes are each consistent with the PIV findings. Other features, such as the tornado-like vortices, were determined from their simulation. The following list describes the features shown in figure 2.22:

- The main recirculation in the cavity.
- The tornado-like vortices near the front of the cavity.
- The corner vortex at the front of the cavity.
- The co-recirculation vortex at the rear of the cavity.
- The region of separation above the trailing edge.
- The trailing vortices emerging from the rear of the cavity.
- 'End' vortices, associated with end effects and in/out flow.

2.8.3 Impact of cavity span on flow-field & asymmetries

Secondary flow patterns

Three-dimensional effects are caused by the presence of the cavity side wall, causing the formation of secondary flow patterns (Zhang and Naguib, 2008).

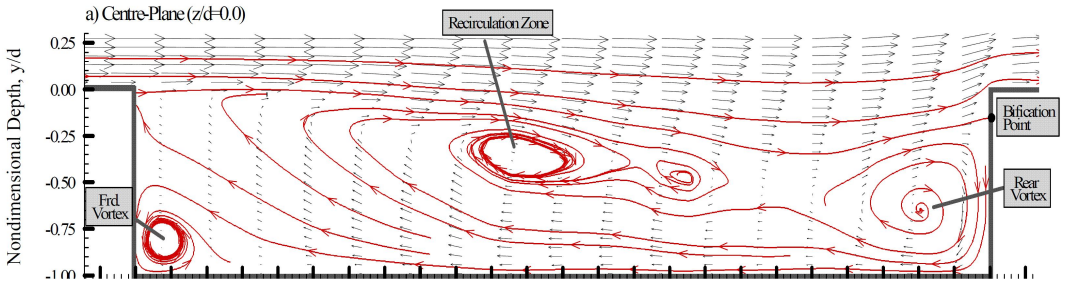

(a) Centre-plane ($z/D = 0.0$).

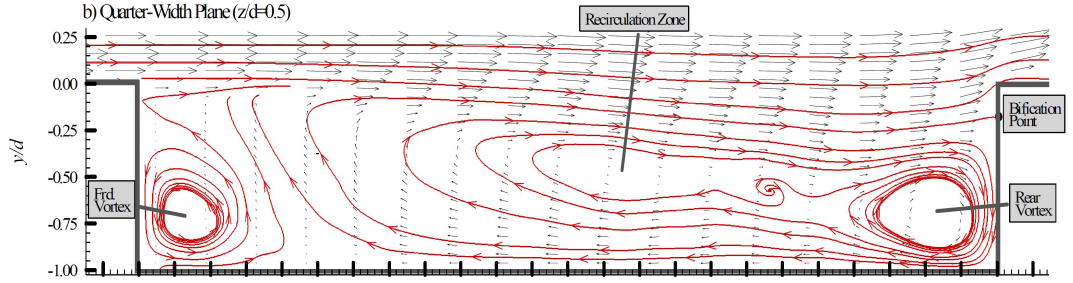

(b) Quarter-plane ($z/D = 0.5$).

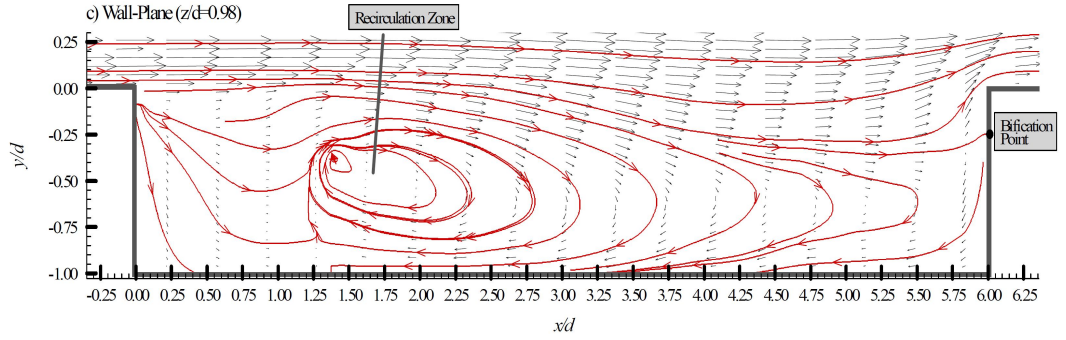

(c) Wall-plane ($z/D = 0.98$).

Figure 2.20: Annotated PIV time-average velocity vector field and streamlines along three longitudinal planes. For a three-dimensional cavity at $Re_D = 6,700$, with a laminar boundary layer ($D/\delta_0 = 6.7$), for $L/D = 6$ and $L/W = 3$ (Crook *et al.*, 2008).

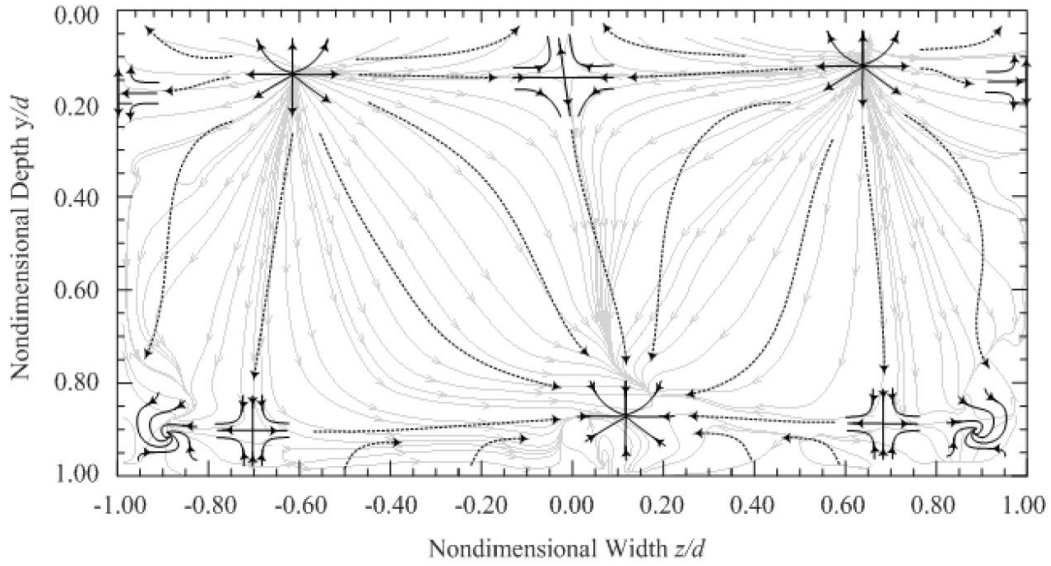

Figure 2.21: PIV velocity vector field and streamlines near the rear wall of a three-dimensional cavity at $Re_L = 40,000$ (Crook *et al.*, 2008).

Figure 2.22: Interpretation of the time-averaged three-dimensional flow-field within a cavity with $L/D = 5$ and $L/W = 2$ at $M = 0.85$ from Knowles, Lawson & Ritchie (2007).

The recirculation vortex observed by the researchers had a distorted shape near the cavity side walls, such that shear layer vortices near the centre-line impinged more 'strongly' on the cavity rear wall. Subsequently, in more recent work Crook (2011) established the presence of a cavity asymmetry due to a shear layer twisting mode in a shallow, narrow cavity, which will be discussed shortly.

The studies were conducted on low Mach number and low Reynolds number three-dimensional cavity flows (Zhang and Naguib, 2008, 2011). An axisymmetric cavity model was used to establish, as best as possible, a two-dimensional reference condition without influence of finite span (in this instance, finite azimuthal angle). Sleeves were then used to create cavities of finite span. Measurement techniques included wall-pressure measurements, hot wire velocity measurements and Laser Doppler Anemometry. The boundary layer at the leading edge of the cavity was fully turbulent. The cavity aspect ratios were L/D=2.6 – 4.1 and W/D=2.4 – 7.1. The depth-based Reynolds numbers were 4,070 – 16,300.

Zhang and Naguib (2008) initially identified a surprising low-Mach-number cavity phenomenon: the pressure oscillation intensity at the centre-line of the cavity floor was found to decrease for increasing cavity span. Later, the authors identified that, in fact, peak pressure intensity was found *off* the cavity centreline as the cavity span was increased (Zhang and Naguib, 2011). The oscillations were quite low in frequency and did not correspond to Rossiter modes; instead they were more consistent with Strouhal numbers for wake mode behaviour (Zhang and Naguib, 2011).

Zhang and Naguib (2011) found at least two pressure intensity peaks, with the first peak away from each side wall located approximately one cavity depth laterally into the cavity. For the narrowest cavity the separate peaks had 'merged' into the one peak located at the centre-line. The authors found that the behaviour was because of a secondary flow pattern caused by the presence of the side wall. There was a distortion of the main recirculation zone near the side wall such that the circulation zone did not stretch as far upstream as it did near the centreline. Also a large streamwise recirculation was identified in the lateral plane near the middle of the cavity length. This circulation had a clockwise orientation (with respect to the side wall being located on the left, whilst looking downstream). This pattern was found to cause 'deeper penetration of the shear-layer vortices into the cavity' (Zhang and Naguib, 2011, p. 1228) corresponding to the peak in pressure intensity.

Shear layer twisting mode

A shear layer twisting mode has been discovered in certain shallow, narrow cavity flows. Crook (2011, p. 147) identified extreme left- and right-orientation flow patterns in the low-Reynolds-number flow over a shallow, narrow cavity by using conditional averaging. Here, the span of the cavity was twice the cavity depth, while the cavity length was six times the cavity depth. The phase

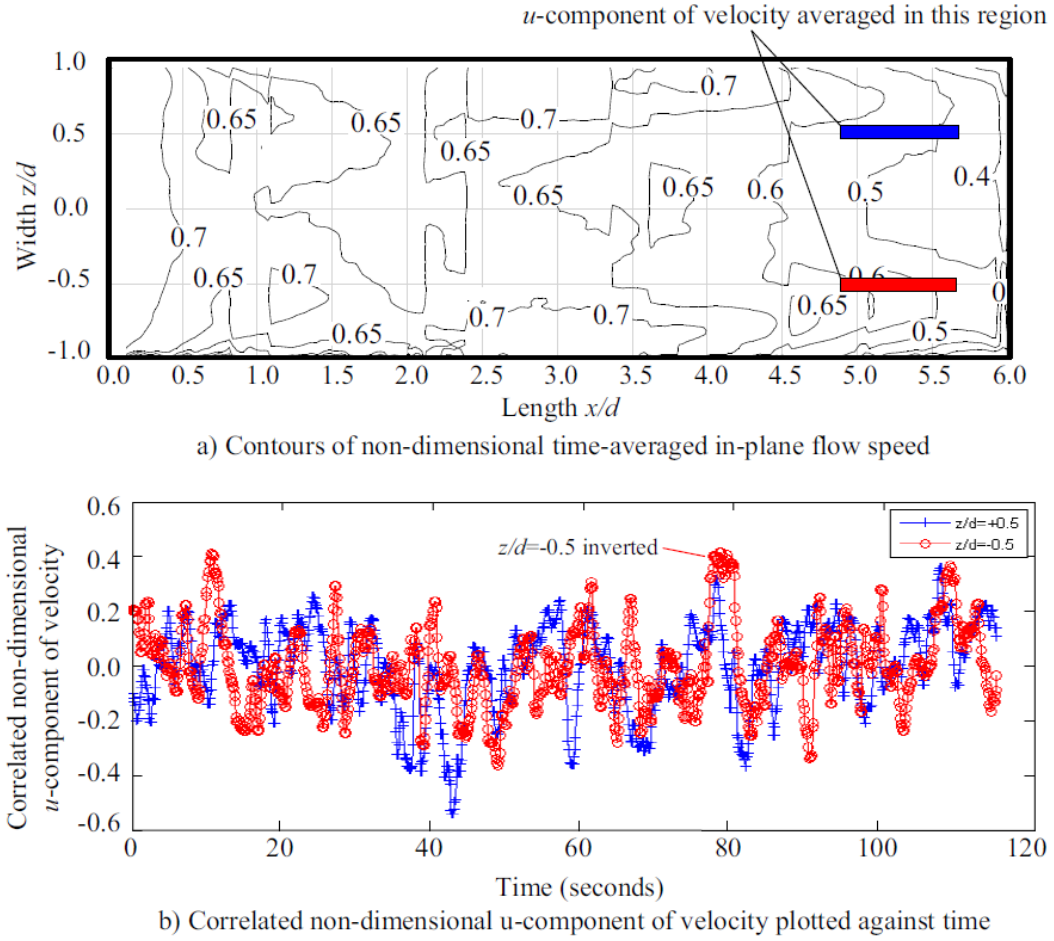

a) Contours of non-dimensional time-averaged in-plane flow speed

b) Correlated non-dimensional u-component of velocity plotted against time

Figure 2.23: Comparison of streamwise velocity at the left-hand and right-hand sides of a shallow, narrow cavity (Crook, 2011, p. 167). The depth-based Reynolds number is 7000 with a laminar boundary layer ($\delta_0/D = 0.15$ and $\theta_0/D = 1.6 \times 10^{-2}$).

averaging revealed clockwise and counter-clockwise orientations of the tornado-like vortex on the cavity floor associated with preferential impingement of the shear layer on the left- or right-hand-side of the cavity rear wall. These flow features were eliminated (or 'smeared') in conventional time-averaging. The period of the asymmetry (in terms of switching from one 'bulk' flow structure to the other, i.e., from one sign [or direction] of rotation of the tornado-like floor vortex to the other) could not be determined, but was much larger than the sampling times of the experiment which were of the order of minutes (Crook, Lau and Kelso, 2013).

Figure 2.23 gave a comparison of streamwise velocity at the left-hand and right-hand sides of the cavity. The signals in figure 2.23(b) are a time-series, averaged spatially over each of the boxes in figure 2.23(a) respectively. A correlation coefficient of -0.37 was found between the two signals, i.e., the

signals are inversely correlated, thereby supporting the notion of a shear layer twisting mode. Also notable is the lack of regular periodicity of the signals – the time period and amplitude of the signals appear to vary noticeably.

The individual streamline patterns for the positive and negative asymmetries clearly show the opposing orientation of the tornado-like vortex on the cavity floor (figure 2.24). Parts (c) and (e) show contours of the velocity magnitude. It is notable that the velocity distribution for the negative asymmetry resembles a mirrorred version of the velocity distribution for the positive asymmetry, demonstrating the truly 'inverse' nature of the two flow configurations.

2.8.4 Relationship of three-dimensional flow field to noise

Faure *et al.* (2007) state that although 3D features do not cause the frequency modes of interest in cavity flow oscillations, 3D flow features could condition the amount of in-flow and out-flow between the cavity and free-stream, subsequently impacting on the generation of noise. This suggests that by changing the three-dimensional flow structure, there could be impacts on the noise generated by the cavity. Further, Doran (2004), Bastrzyk and Raman (2009), and Kuo and Huang (2001) relate differences in flow structure to differences in cavity noise.

2.8.5 Shear Layer Three-Dimensionalities

In planar free shear layers, organised streamwise vortices have 'long been observed' (Lasheras and Choi, 1988) in addition to the spanwise rollers due to the K-H instability. Streamwise vortices create significant three-dimensionalities and cause distortion of the spanwise rollers.

Rockwell and Knisely (1980) investigated three-dimensionalities in planar free shear layers using hydrogen bubble visualization, opting to consider the case of a cavity flow due to the 'clearly defined vortex rollup' and well-defined spectral peaks. They conducted the investigation by placing a spanwise hydrogen bubble wire at different non-dimensional heights, thereby forming bubble sheets in different parts of the shear layer. There was a fixed Reynolds number ($Re_\delta = 106$) and cavity length ($L/\theta = 142$), and the upstream boundary layer was laminar.

The cavity was 'two-dimensional' in both configurations as it had straight up-and-down side walls, rather than 'steps' at its sides, and also in terms of it's L/W ratio. The cavity had $L = 8.9$ cm, $D = 7.6$ cm and $W = 25$ cm, giving $L/D = 1.17$ and $L/W = 0.36$. Even though the cavity width was greater than the cavity length (classing it as a 'two-dimensional' cavity), end wall effects were found to be significant and are discussed shortly.

[14]Reprinted from *Physics of Fluids*, Vol. 23 No. 3, D. Rockwell and C. Knisely, 'Observations of the three-dimensional nature of unstable flow past a cavity', Pages No. 425–431, Copyright (1980), with the permission of AIP Publishing.

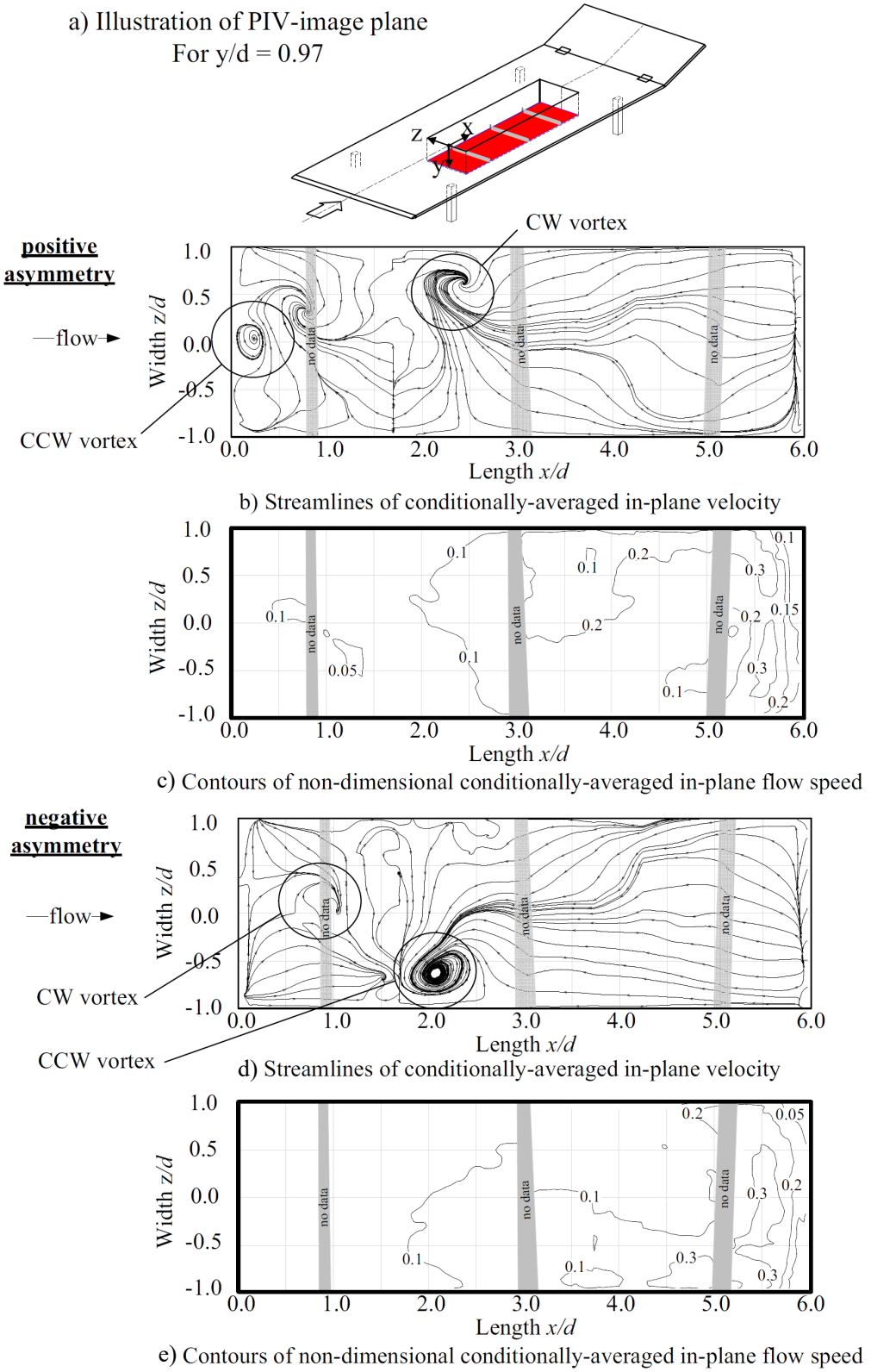

Figure 2.24: Conditionally-averaged asymmetric flow fields found by Crook (2011, p. 162). Imaging plane is shown in part (a). The depth-based Reynolds number is 7000 with a laminar boundary layer ($\delta_0/D = 0.15$ and $\theta_0/D = 1.6 \times 10^{-2}$).

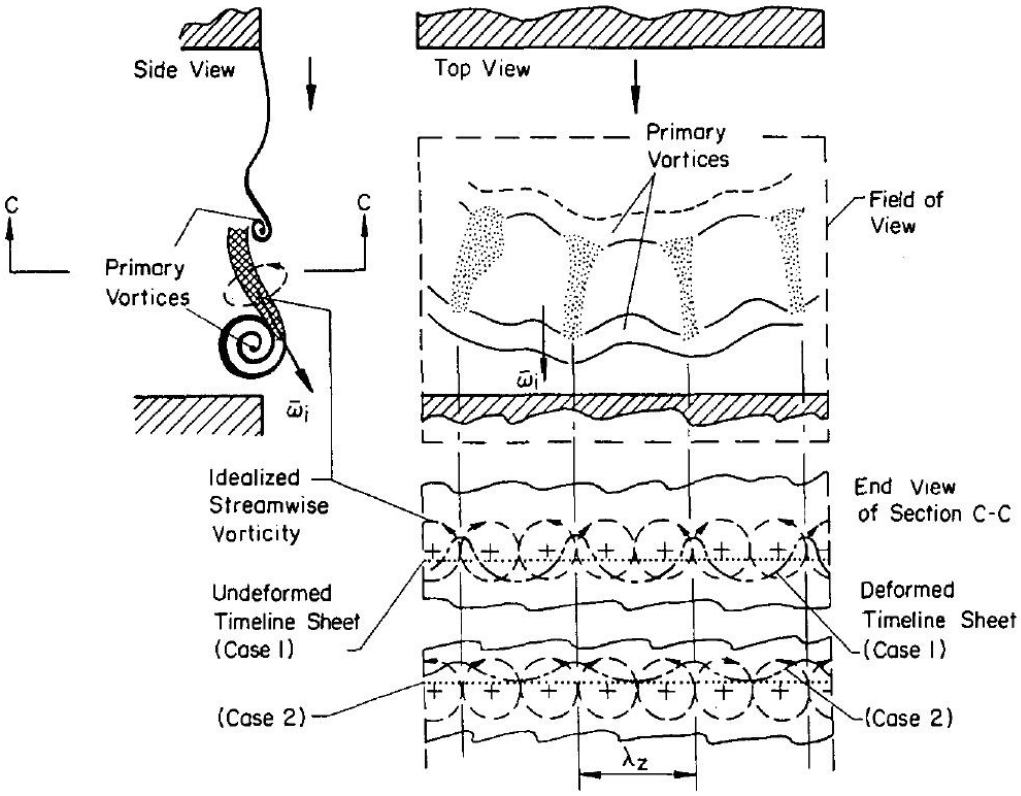

Figure 2.25: Sketch of primary, and streamwise, vorticity in the shear layer over a cavity, visualised by a hydrogen-bubble sheet (Rockwell and Knisely, 1980, p. 427)[14].

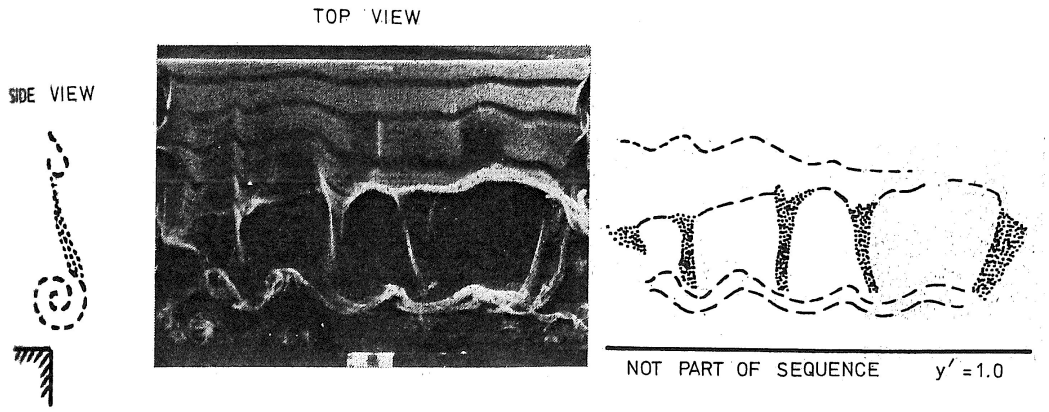

Figure 2.26: Additional sketch of primary and streamwise vorticity in the shear layer over a cavity, visualised by a hydrogen-bubble sheet (Rockwell and Knisely, 1980, p. 429)[15].

In addition to the primary spanwise vortices from the shear layer rollup, vortices whose circulation vectors were orientated in the streamwise direction were found, which they referred to as 'streamwise vortices'. Depicted in figure 2.25 is the mechanism of action between this streamwise vorticity and the bubble sheet. The result of the streamwise vortices was ultimately to distort the primary vortices. In the figure, the streamwise vortices are nominally depicted as having an idealised circular cross-section. The lower part of figure 2.25 depicts the action of these vortices depending on whether the hydrogen bubble sheet is located above or below the centres of these vortices. In either case an observable series of crests and valleys was formed in the plan view of the hydrogen bubble pattern. Longer wavelength streamwise vortices appeared both further upstream and at a lower hydrogen-bubble wire location than those with shorter wavelengths.

Rockwell and Knisely (1980) found warping, or curvature, of the primary vortex due to end wall effects, with stretching of the primary vortex by end wall effects producing the curvature in the axis of the primary vortex. This was found to be an issue even with wide spanwise aspect ratios. The region near the side walls (or end walls) of the cavity was not depicted as the authors noted that near the end walls the 'bubble pattern was not sufficiently organised to provide any insight into flow behaviour'. This overall warping of the primary vortices was thought to be evident in every photograph taken in this study, and the extent of the end wall effects was considered to be 'far greater' than the end wall boundary layer region alone.

At the lowest position of the hydrogen bubble wire (shown in figure 2.26), the appearance of three-dimensionality in the bubble sheet occurred furthest

[15]Reprinted from *Physics of Fluids*, Vol. 23 No. 3, D. Rockwell and C. Knisely, 'Observations of the three-dimensional nature of unstable flow past a cavity', Pages No. 425–431, Copyright (1980), with the permission of AIP Publishing.

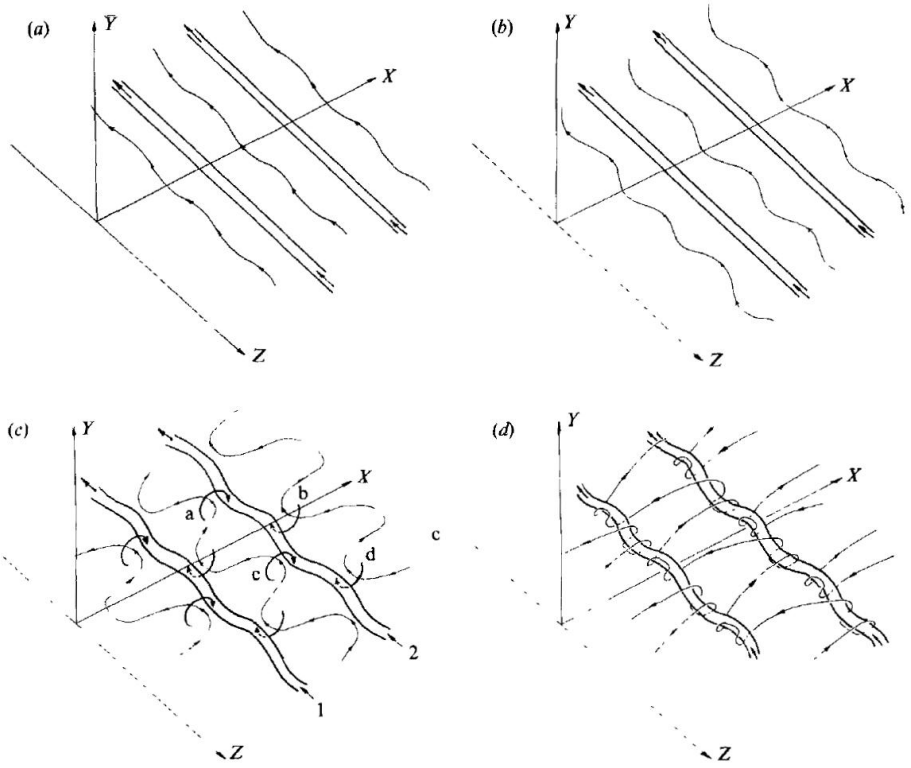

Figure 2.27: Development of three-dimensional instability in planar shear layer (Lasheras and Choi, 1988, p. 69)[16]. Flow in 'X' direction.

upstream. Observed to form initially were 'shallow pockets', followed by what were called 'discrete cells'. The authors noted that there was 'an ordered relation between the location of the maxima and minima of the primary vortex distortion and the location of each longitudinal bubble patch' (Rockwell and Knisely, 1980). This is clarified in the work of Lasheras and Choi (1988).

Lasheras and Choi (1988) experimentally investigated deliberately perturbed streamwise instabilities in a plane shear layer formed between two water streams of differing velocity. They subjected the shear layer to both horizontal and/or vertical sinusoidal perturbations to create streamwise vortices that were more strongly ordered than in the 'natural' case. In the perturbed cases, care was taken to minimise other upstream disturbances. Strongly ordered streamwise vorticity was found, and a mechanism was described for the formation of these vortices by Lasheras & Choi (1988). In the 'natural' case with 'uncontrolled small random disturbances', a similar, although less regular, flow structure was observed and the formation of the streamwise vortices was attributed to a similar mechanism.

The authors state that first spanwise rollers develop due to the primary Kelvin-Helmholtz instability. These spanwise rollers act to concentrate the vorticity sheet into strong and weak regions. In the case of the horizontal perturbation, the authors stated that the streamwise (or secondary) instabilities were found to grow from the weak vorticity in the 'braid' region in-between the spanwise rollers, where there is a strong strain field. This strong strain field causes the perturbation component of vorticity to be stretched axially. A schematic is shown in figure 2.27. These instabilities were found to grow in the direction of principle strain and later wrap around the spanwise rollers, furthermore causing the cores of the spanwise rollers to become wavy. The phase of the horizontal waviness of the spanwise roller cores was opposite to that of the streamwise instability, as seen in figure 2.27(c).

The case with only vertical perturbations was found to produce a similar structure to the case of horizontal perturbations, with the vertical peaks (on the fast stream side) being aligned with the same phase as the instabilities in the 'braid' region. In the case with a vertical *and* horizontal perturbation, when the two perturbations were out of phase, it was found that the vertical perturbation could cancel or reverse the effect of the horizontal perturbation. The horizontal perturbation (magnitude 8mm) was almost cancelled at a vertical perturbation magnitude of 3mm (creating an almost two-dimensional flow) and the phase was reversed at vertical perturbation magnitude of 4mm, suggesting that a smaller vertical perturbation gives the same effect as a larger horizontal perturbation. Note that these amplitudes compare to the initial boundary layer thicknesses, which were 6mm in the upper stream and 9mm in the lower stream ($\delta_1 = 6\,\text{mm}$ and $\delta_2 = 9\,\text{mm}$). Furthermore, $Re_{\theta_0} = 45$ at the origin of the shear layer, with momentum thicknesses, $\theta_1 = 0.8\,\text{mm}$ and $\theta_2 = 1.2\,\text{mm}$ respectively for the faster and slower streams.]

Lasheras and Choi (1988) also studied a case with a non-uniform spanwise velocity profile in each stream, in order to generate a 'bend' in the spanwise rollers. Therefore the direction of maximum strain between the rollers was not in the streamwise direction. The 'streamwise' vortices were found to form in the direction of maximum strain which was now at an angle to the streamwise direction, the authors therefore noted that 'strain-orientated vortex tubes' would be more exact terminology to describe these flow structures.

[16]Lasheras, J C and Choi, H, 'Three-dimensional instability of a plane free shear layer: an experimental study of the formation and evolution of steamwise vortices', *Journal of Fluid Mechanics*, vol. 189, pp. 53-86, Cambridge University Press, 1988, reproduced with permission.

2.9 Control of Cavity Flow Noise

2.9.1 General principles

There are a number of passive means to reduce cavity flow noise. One way is to reduce shear layer amplification by, for example, thickening the shear layer. Another is to eliminate the oscillations completely, for example by reducing the length of the cavity sufficiently (equivalently, thickening the boundary layer sufficiently) or increasing the cavity length sufficiently, such that the cavity is outside the range of occurrence of oscillations (Crook, 2011). This section focuses on geometric modifications to the cavity geometry as a passive means to reduce cavity flow noise.

2.9.2 Geometric Modifications

Various geometric modifications to otherwise rectangular cavity geometries have been shown to be valid means of reducing cavity flow noise, having been found to be simple and often effective. First, several types of geometric modifications are described. Secondly, the general literature on this topic is reviewed. Finally, the most similar studies are reviewed.

Types of Geometric Modifications:

Bulk Geometric Modifications These 'bulk' geometric modifications refer to bulk modifications to the front or rear walls of a cavity, for example, slanted or chevron-shaped front or rear cavity walls. Ways that 'bulk' geometric modifications can reduce cavity noise include:

- By moving the impingement point of the shear layer further downstream by sloping the cavity rear wall, thereby reducing high levels of pressure and amplitude fluctuations that may otherwise be found at the cavity rear wall (Stallings & Wilcox, 1987; Zhang & Edwards, 1992).
- Similarly, by deflecting the shear layer by other means so it impinges less on the cavity rear wall (Milbank, 2004; Doran, 2006).
- By changing the shear layer instability characteristics, for example, stabilising the shear layer by thickening it (Milbank, 2004; Franke and Carr, 1975) or stabilising the shear layer by changing the trajectory/impingement angle (Heller and Bliss, 1975).
- By altering the rate of in-flow or out-flow that occurs near the trailing edge of a cavity (Heller and Bliss, 1975).
- By affecting the shear layer deflection, and hence oscillation, by modifying the position and shape of the recirculating vortex within the cavity by utilising different cavity shapes (Ozalp, Pinarbasi and Sahin, 2010).

Minor Geometric Modifications 'Minor' geometric modifications refer to modifications such as rods across the flow ahead of the cavity or spoilers (for example, Heller and Bliss, 1975). Ways that 'minor' geometric modifications can reduce cavity noise include:

- By reducing spanwise coherence (Heller and Bliss, 1975), for example by using vortex generators ahead of the cavity leading edge.
- By periodic forcing at the receptive initial region of shear layer (Gharib, 1983, p. 48), for example high frequency forcing (Gharib, 1983) using a shedding rod in order to break up large scale structures, known as a large-eddy break-up (LEBU) device.

2.9.3 Non-geometric control methods

This section briefly summarises the various non-geometric control methods that have been attempted and some of the intended functions of these methods. These methods include non-geometric passive techniques and active flow control techniques.

Non-geometric passive techniques

Non-geometric passive techniques that have been trialled include porous cavity walls (Lai and Luo, 2008) and upstream surface waviness which was intended to thicken the shear layer and disrupt the feedback mechanism at the leading edge (Hughes, Mamo and Dala, 2009).

Active flow control

Active flow control techniques are categorised under open-loop and closed-loop methods. A review of active flow control of cavity flow was published by Cattafesta *et al.* (2008). These methods have often been shown to be very effective. Active flow control techniques trialled include zero-net-mass forcing (Debiasi *et al.*, 2004), pulsed mass injection (Stanek *et al.*, 2007), supersonic microjets (Zhuang *et al.*, 2003) and blowing/suction devices (Heller and Delfs, 1996).

Closed-loop approaches generally require significantly less actuator energy than open-loop approaches (Rowley and Williams, 2006). For example, Cattafesta *et al.* (1997) found that when using a closed-loop method the energy requirement was 5-20% of that of an open-loop method, with both methods providing an effective and significant reduction in sound pressure levels. Due to the lower energy requirements, closed-loop approaches could be more suitable for aircraft than open-loop approaches (Rowley and Williams, 2006).

While most authors have used adaptive controllers where a precise model of the system is not required (Rowley & Williams, 2006), some authors have attempted to create model-based closed loop control systems (including models

of the flow and other components of the system) based on techniques such as neural networks (Efe *et al.*, 2005), delay-based models and Proper Orthogonal Decomposition (POD) (Samimy *et al.*, 2007). Generally the level of difficulty is high, and practical implementation is only partially achieved.

Compared to geometric modifications, active methods have an advantage in that they can be tuned to operate across a wider range of conditions than geometric modifications, however disadvantages include that they require auxiliary power (Bastrzyk and Raman, 2009) and are substantially more complex to design and implement.

2.10 Modified Cavity Flow

Modified cavity flows have been experimentally studied in low subsonic flows as well as in moderate and high Mach number flows. It will be shown in this section that:

- Geometric modifications have been found to be effective in reducing cavity noise and oscillations for open cavities across a wide range of velocities.
- There is evidence that changing the geometry around cavities can lead to significant changes in the flow structure.

To the author's knowledge, the majority of studies on modified cavity flows have not considered the flow structure implications of the geometric modifications or they have only looked at the flow structure in two-dimensions. The few studies that have considered the impact of geometric modifications on the three-dimensional flow structure are discussed in the later part of the section, and these studies largely relate to moderate and high Mach number flows.

Use of Three-Dimensional Wall Shapes The role of modifications in terms of varying the three-dimensional flow structure has not been extensively discussed to the author's knowledge. While most geometry changes trialled have been two-dimensional (i.e., with a uniform cross-section in the spanwise direction), three-dimensional-shaped walls could be effective for changing the three-dimensional flow structure. An example of a two-dimensional geometric modification to a cavity is a ramped rear wall, while an example of a three-dimensional modification is a chevron-shaped or tapered cavity – in the latter, the cross-section of the cavity is not uniform in the spanwise direction.

Dolling, Perng and Leu (1997) suggest that it is 'logical' to use a three-dimensional wall shape in response to the three-dimensional flow pattern. This was supported by their findings: their most effective modification was a three-dimensional rear cavity wall, which they found to be slightly more effective than a similar but simpler two-dimensional rear wall. Only a handful of three-dimensional wall shapes have been trialled and other possibilities for this potentially effective geometric modification have not yet been investigated.

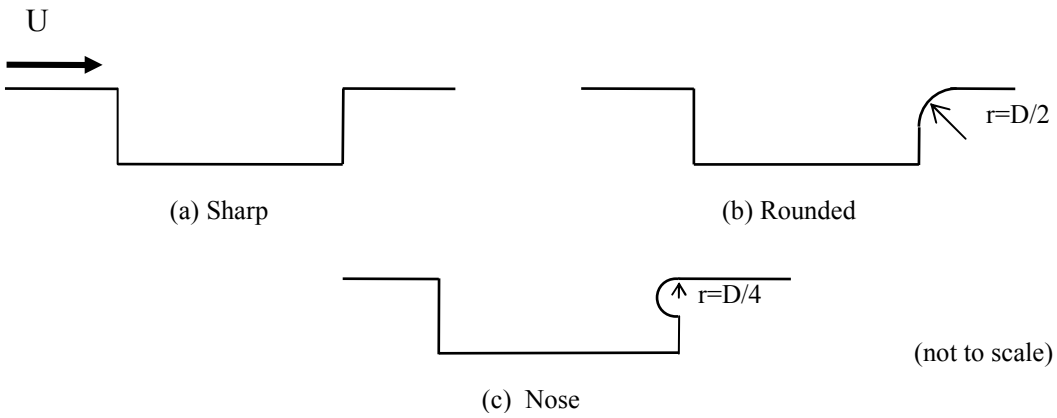

Figure 2.28: Sketch of cavity trailing edge geometries trialled by Pereira and Sousa (1994).

Limitations of geometric modifications There are limitations to the geometric modifications that can be achieved in practical cavities. For aircraft applications, Dix & Butler (1990) note that modifications such as a slanted rear wall are not structurally favourable as they increase the length of the cavity, with subsequent undesirable implications for the arrangement of aircraft structural members. However certain geometric modifications, such as swept cavities that could fit with the leading edge angle of a swept wing, could be reasonably practical.

2.10.1 Low Speed Studies

Pereira and Sousa (1994) investigated 'sharp', 'rounded' and 'nose-shaped' trailing edges, shown in figure 2.28, on a cavity with $L/D = 2$ and $L/W = 0.24$ at a cavity-depth-based Reynolds number, Re_D, of 3,360 and length-based Reynolds number of Re_L = 6,720. Figure 2.29 depicts smoke visualisation which shows the different events to which large shear layer vortices are subjected: (a) & (b) partial escape, (c) complete escape and (d) complete clipping. Complete clipping is rare for the rectangular cavity but common for the rounded trailing edge (shown in (e) & (f)) while complete escape was found to be common for the nose-shaped trailing edge (shown in (g) & (h)) where there was a subsequent reduction in oscillation amplitude. Pereira and Sousa (1994) cite Ethembabaoglu who in 1973 found a reduction in oscillation amplitude using a 1:5 ellipse-shaped edge, while Maull and East (1963) demonstrated a 75% reduction of oscillation amplitude using a semi-circular rounded edge.

Kuo and Huang (2001) investigated the impact of sloped cavity floors on a cavity with $L/D = 2$ in a water tunnel at $Re_D = 620$ with $Re_{\theta_0} = 194$. They used two-dimensional laser sheet visualisation, shown in figure 2.30. Significant changes in internal cavity flow structure were found that contributed to the

Figure 2.29: Different events that can happen to a vortex in the cavity shear layer (Pereira and Sousa, 1994).

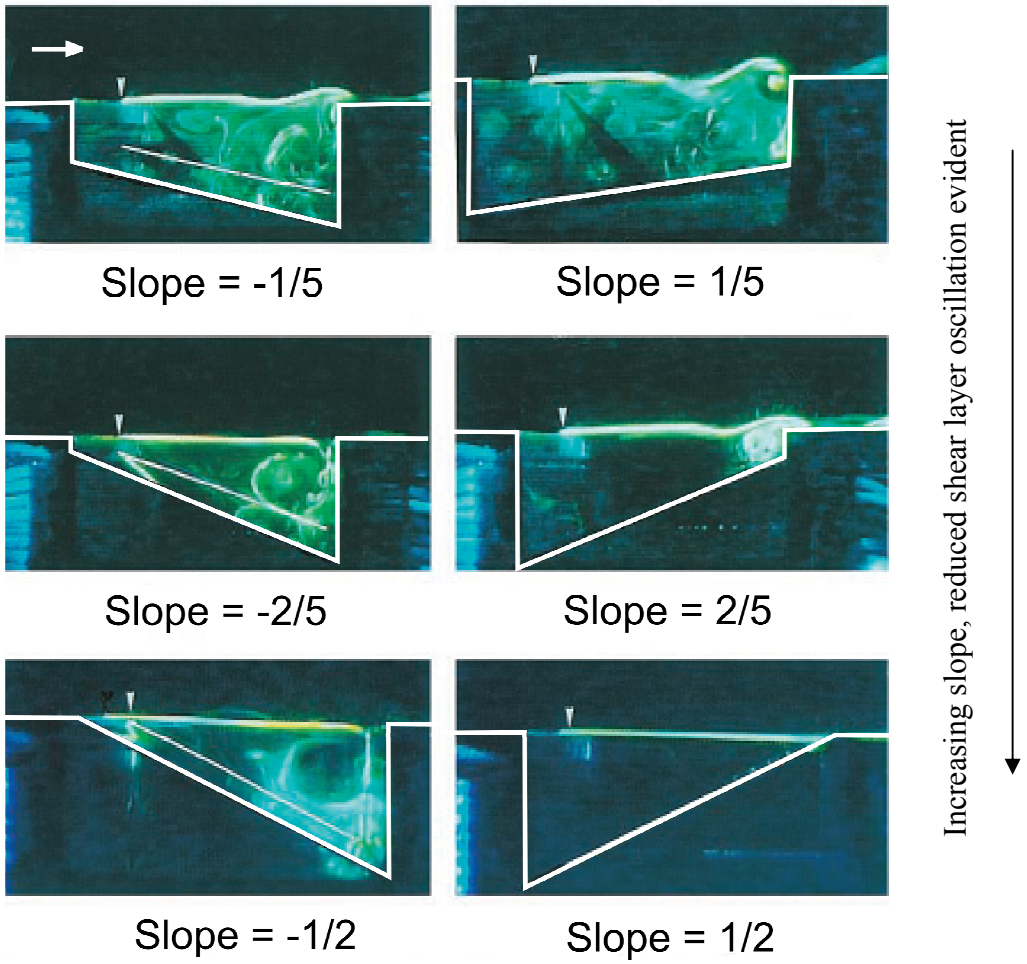

Figure 2.30: Laser sheet visualisation of sloped cavity floors (Kuo and Huang, 2001). $Re_D = 620$ and $Re_{\theta_0} = 194$. Note: laminar boundary layer with shape factor $H = 2.52$.

oscillations being completely suppressed at the most extreme slope ratio. In the most extreme cases, the volume of the cavity was reduced by as much as 50 %.

Ozalp *et al.* (2010) investigated rectangular and modified triangular and semi-circular two-dimensional cavities with $L/D = 2$ using PIV in a water-tunnel. The cavities had $L = 100$ mm and were tested at $U = 120$, 170 and 220 m/s giving $Re_L = 10{,}700$ – $19{,}600$ and $Re_D = 5{,}350$ – $9{,}800$. There was a turbulent boundary layer upstream of the cavities with $Re_{\theta_0} = 1230$ – 1700, and the cavities were non-oscillatory. The time-average streamlines they found at $Re_D = 9{,}800$ are shown in figure 2.31. Compared to the rectangular cavity, the main vortex was found higher up in the triangular cavity and very rearward in the semi-circular cavity. They measured velocity spectra in the shear layer near the leading and trailing edges of the cavities. Although the

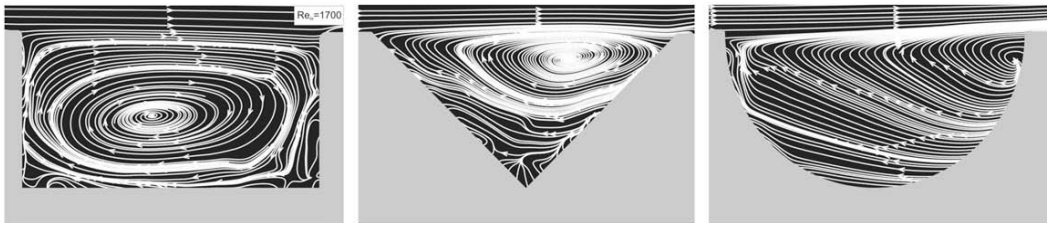

Figure 2.31: Time-average streamlines from PIV for rectangular, triangular and semi-circular cavities at $Re_D = 9800$ and $Re_{\theta_0} = 1700$, with turbulent boundary layer type (Ozalp *et al.*, 2010)[17].

cavities were non-oscillatory, they found lower levels of broadband noise in the velocity spectra for the modified cavities.

2.10.2 Moderate to high Mach number studies

Heller and Bliss (1975) studied the impact of ramped walls, including in combination with spoilers, and airfoils positioned at the trailing edge, which they called a 'cowl'. The stated purpose of Heller and Bliss' (1975) sloped rear wall was to stabilise the shear layer. The reasoning given was that a curved shear layer is unstable, and that without the proper impingement angle, the impingement point would be unsteady. Thus the ramped rear wall provides the stabilising effect as it enables the shear layer to have the proper impingement angle while also being un-curved.

Heller and Bliss (1975) took one-third octave bands of the pressure recorded at the leading-edge of a cavity with $L/D = 2.3$ at $M = 0.8$. Considering figure 2.32(a), the slanted wall was effective in reducing frequency peaks with a reduction of the main tone by 20 dB and a reduction of broadband levels by approximately 9 dB from 30 to 600 Hz.

Figure 2.32(b) shows Heller and Bliss' (1975) trailing edge cowl which had the stated purpose to 'prevent' the mass inflow and outflow at the trailing edge. The authors described the cowl as achieving this by creating lower pressure between the cowl and slanted wall (so that fluid was sucked out of the cavity) when the shear layer deflects downwards, thereby cancelling the mass addition that usually happens at that part of the cycle. Considering figure 2.32(b), the cowl/slant combination was effective in reducing fluctuations, with the configuration with the cowl trailing edge raised 2" vertically into the free-stream having similar effectiveness to the slant and spoiler combination, while the un-raised cowl was not as effective in reducing the main frequency peak. The slant-only modification was a little more effective at reducing broadband

[17]Reprinted from *Experimental Thermal and Fluid Science*, Vol. 34, C. Ozalp, A. Pinarbasi & B. Sahin, 'Experimental measurement of flow past cavities of different shapes', Pages No. 505–515, Copyright (2010), with permission from Elsevier.

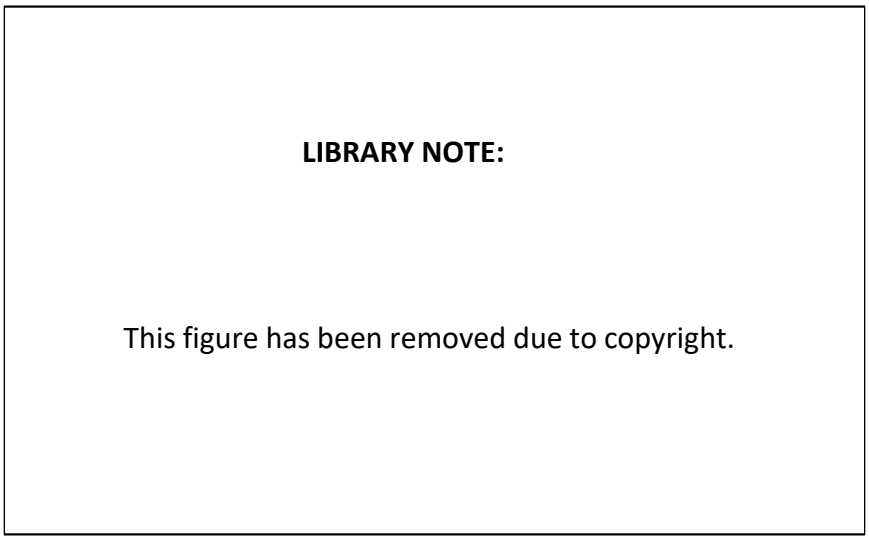

Figure 2.32: Third-octave bands of pressure recorded at leading edge, for trailing edge modifications trialled by Heller and Bliss (1975).

levels at low frequencies.

Franke and Carr (1975) conducted a study on the 'effects of geometry on open cavity flow' trialling a number of configurations of slanted walls, tandem cavities, airfoils positioned at the leading and/or trailing edges and baffles. Some of their shapes were based on those of Heller and Bliss (1975).

In Franke and Carr's (1975) study, the configurations were first trialled in a water tunnel. The cavities typically had L/D=2. Several configurations and those with ramps at the front and rear (which they called 'double ramps') were found to 'significantly' reduce oscillations. For double ramps, the shear layer was found to follow the ramps and there was 'almost no' shear layer oscillation evident. Aircraft store (weapons) models which touched the cavity shear layer were found to reduce shear layer oscillations. The airfoil, or 'cowl', was found to generally be effective, and when it was placed with negative angle of attack at the trailing edge it managed to prevent the shear layer from entering the cavity and thus the shear layer did not impinge on the rear wall. The cowl was not effective however when used in combination with double ramps.

Franke and Carr (1975) then trialled selected configurations in a wind tunnel at $M = 1.6$. Their wind tunnel apparatus consisted of a jet that discharged through a nozzle into a chamber that was quite narrow in the spanwise direction. Franke and Carr (1975) found some interesting results regarding the ramps and airfoils, or 'cowls'. The double ramp cavity was effective in substantially reducing the main oscillation - reducing the main peak by 25 dB at $M = 1.6$ (figure 2.33). The reasoning given for this behaviour was that the thickening of the shear layer – the rectangular cavity had a thin shear layer which was observed to become 'wavy' whilst the cavity with double ramps had a shear layer which appeared 'thicker and less disturbed'. In isolation, the

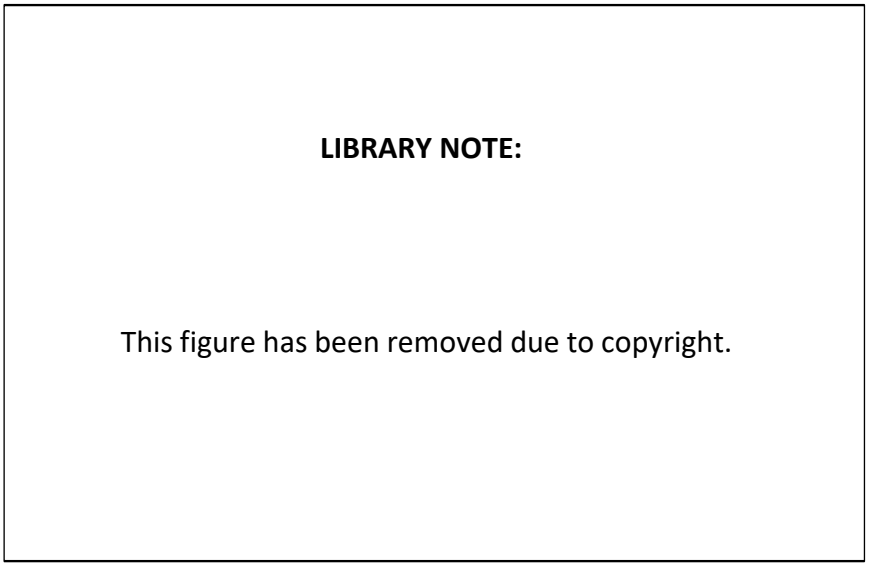

Figure 2.33: Cavity with double ramps (Franke and Carr, 1975).

trailing edge ramp was more effective than the leading edge ramp. Regarding their wind tunnel results, Franke and Carr (1975) caution however that since the boundary layer was just on the verge of transition to turbulence at the leading edge in the rectangular cavity case, then there may have been a transition to turbulence on the leading edge ramp which the authors suggest would increase suppression levels.

Marquardt (1975) studied the influence of various sloped walls, in a study where tandem cavities and aircraft store positions were also considered. At $M = 0.5 - 1.5$, cavities with $L/D = 2$ and $L/D = 4.25$ (with varying length for the same depth) were studied. A leading edge ramp of 15° was effective for the shorter cavity but worsened oscillations in the longer one. Sloping of the rear wall (away from the up-right position) was also found to be increasingly effective.

Vikramaditya and Kurian (2009) investigated the impact of ramped and sloped rear walls on a cavity at $M = 1.86$. 'Ramped' refers to the angled part of the rear wall stopping at half of the cavity depth, while 'sloped' refers to the angled part continuing to the cavity floor. The cavity geometry was $L/D = 3$ ($L = 60$ mm, $D = 10$ mm, & $W = 574$ mm, i.e., the cavity was effectively two-dimensional), with a turbulent boundary layer upstream with thickness $\delta_0 = 6$ mm, such that $\delta_0/D = 0.6$ (i.e., the boundary layer was thick relative to the cavity depth). The 'ramped' rear walls were the focus of the paper, and consist of a rear wall that is angled to half the cavity depth. For the progressively smaller angles the 'effective cavity length' (or cavity mouth length) was increased.

First, the cavities were visualised with the shadowgraph technique. The authors identified a flapping shear layer with the presence of large vortices, and noted a reduction in flapping motion with increased ramp angle. For ramp angles of 90°, 75° and 60°, four waves were identified:

1. Compression or expansion wave associated with upwards or downwards flapping of shear layer respectively.

2. Waves associated with convection of vortices in the shear layer.

3. Bow shock at the cavity trailing wall.

4. The 'imprint' in the freestream flow of the upstream acoustic wave within the cavity.

However for the smaller ramp angles of 45°, 30° and 15°only the first type of wave was found to be present. Hence, the phenomena associated with the motion of vortices and thus Rossiter (shear layer oscillation) modes, were much weaker. The authors also observed that the shear layer in these cavities was 'less wavy' – suggesting a 'more stable' shear layer.

Unsteady pressure measurements were taken using pressure transducers located on the front wall, floor and rear wall of the cavity. The authors noted that the highest amplitude of the tonal and broadband noise levels occurred at the rear of the cavity. In comparison, at the front wall of the cavity, the tonal noise levels were noticeably *above* the broadband levels. The authors attributed the higher broadband noise level at the rear of the cavity to 'the turbulent structures that grow in size towards the rear of the cavity', and therefore are absent at the front of the cavity. Considering the transducers on the cavity floor, the broadband noise levels were higher towards the rear of the cavity, which the authors attributed to the turbulent structures swept down into the rear of the cavity, at the downward stroke of the shear layer (Vikramaditya and Kurian, 2009).

The dominant Rossiter mode was found to change with the different ramp angles, suggesting that 'the ramp angle influences mode switching among the different modes' (Vikramaditya & Kurian, 2009). For the rectangular baseline cavity, the first Rossiter mode is dominant. Yet, for a ramp angle of 75° the second and third Rossiter modes have a stronger relative amplitude, and the authors note that 'the acoustic energy is rather more distributed over the three modes', showing that in general 'the ramp angle has a profound effect on acoustic energy distribution'.

In coherence measurements between pressure transducers located on the rear wall and front wall, the shear layer oscillation frequencies were found to be highly coherent between these walls (Vikramaditya & Kurian, 2009). On the other hand, the range of other frequencies comprising the broadband noise was found to have very low levels of coherence between the front and rear walls. The authors state that this supports the view that the distinct Rossiter

modes are due to 'global instability' of the flow field – i.e., instability found at both the front and rear of the cavity – while the broadband noise is due to turbulent nature of the flow.

Considering the overall sound pressure level (OASPL) for the various ramp angles and locations, Vikramaditya & Kurian (2009) found lower levels with ramp angles closer to horizontal. For these ramp angles, the levels were higher at the rear of the cavity than at the front, which the authors attributed to the 'direct impingement of the shear layer', while the lower levels at the front of the cavity with ramp angles closer to horizontal were attributed by the authors to weaker upstream traveling acoustic waves being generated at the rear of the cavity.

A quite different behavior was found when comparing the aforementioned 'ramped' rear walls (the angled part of the rear wall stopping at half of the cavity depth) to 'sloped' rear walls (the angled part continuing to the cavity floor) of the same angle and forming the same effective cavity length. Experiments on the latter are only briefly described in the paper with only sound pressure spectra results given. Vikramaditya & Kurian (2009) found a *much* greater reduction in tonal noise levels with the 'sloped' rear walls than with 'ramped' rear walls of the same angle. This would suggest that the internal cavity flow field plays a very significant role in the oscillations.

2.10.3 Studies which considered the 3D flow-field

A number of studies have considered the effect of modified geometry on the three-dimensional flow field about shallow cavities. Typically, significant effects from the modified geometry have been found.

Doran (2006) performed a study on passive transonic cavity flow control which focused on leading edge geometry modifications. The cavity, with $L/D = 5$ and $L/W = 4$, was tested in a wind tunnel at $M = 0.7 - 0.9$. The cavity dimensions were $L = 100$ mm, $D = 20$ mm and $W = 25$ mm. A number of chevron-shaped, swept and sloped walls were trialled as well as various 'step-down' configurations. The most effective step, which stepped down 30% of the cavity depth, produced an overall sound pressure level (OASPL) attenuation of 7.5 dB at the cavity walls. The leading-edge sloped wall and chevron shapes were found to be relatively ineffective, with OASPL attenuation of less than 3 dB. There was also a small attenuation of oscillation amplitude with a swept front wall. Doran (2006) observed the changes to the three-dimensional flow structure for the case of the most effective step. Surface oil flow visualisation was used, revealing backflow on the step face and on the adjacent side walls. In relating the reduction in the noise to the flow structure, Doran (2006, p. 107) theorised that the back flow acts to 'blow' the shear layer outwards, thereby moving the impingement point downstream beyond the cavity trailing edge. Conceptual sketches are shown in figure 2.34 and figure 2.35.

[18]Reproduced with the permission of the Cranfield University Library.

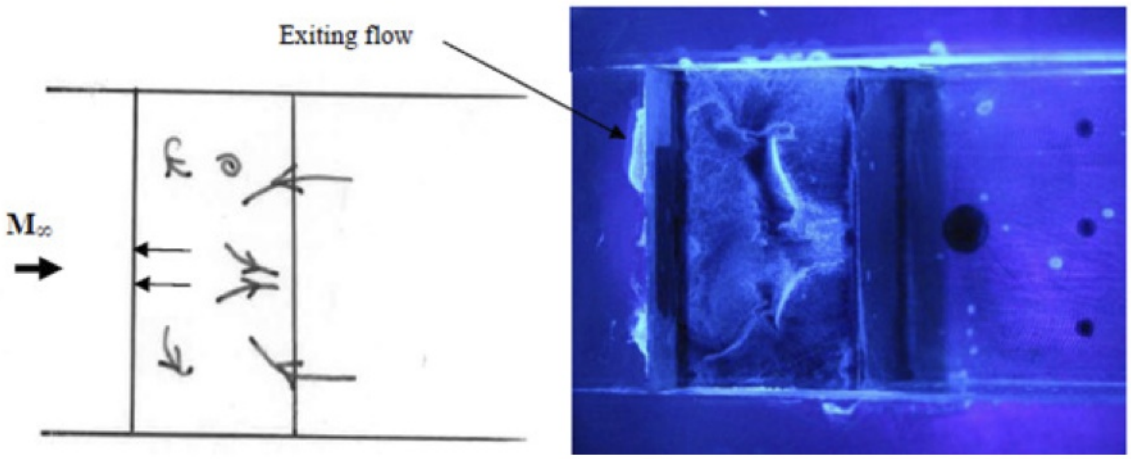

Figure 2.34: Surface oil visualisation and conceptual sketch for back-flow on the step face (plan view). (Doran, 2006, p. 101)[18]

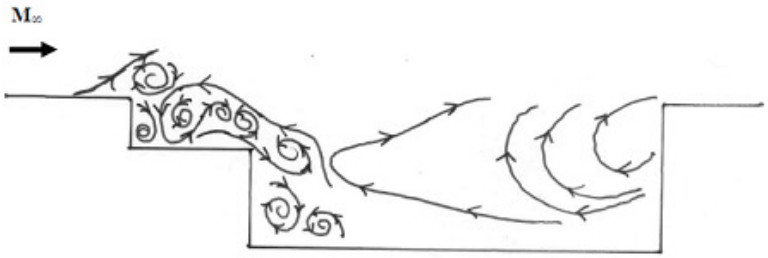

Figure 2.35: Possible conceptual sketch for cross-section stream lines based on flow visualisation (side view). (Doran, 2006, p. 108)[19]

2.10.4 Summary

In this section it has been established that modified cavity flows may produce lower noise levels than 'equivalent' rectangular cavity flows. Modified cavity flows can produce significant differences in 2D and 3D flow structure compared to rectangular cavity flows, although little information is available regarding the latter. In regards to the modifications themselves, Dolling, Perng and Leu (1997) suggest that it is 'logical' to use 3D wall shapes in response to the 3D flow and thus a 3D modification could be effective.

[19]Reproduced with the permission of the Cranfield University Library.

2.11 Knowledge Gap

2.11.1 Two-Dimensional Low Speed Cavities

Many studies have considered two-dimensional, shallow ($L/D \geq 1$), open cavities at low speed. Milbank (2004) investigated spectra and flow around two-dimensional cavities at low speed, however mainly rectangular cavities, including the impact of yaw, were considered. Planar PIV investigations of the flow structure about open, shallow cavity flows have focused on rectangular cavities, for example Ashcroft & Zhang (2005) and several other studies.

Other investigations have looked at the flow structure of deep ($L/D < 1$) cavities at low subsonic speed (for example, Faure *et al.*, 2007) and have also only considered rectangular cavities. Although studies have been carried out in industry (Milbank, 2004, p. 64) and consulting to alleviate cavity noise from these sorts of small low speed 2D cavities (for example, in an automotive context) using geometric modifications of some sort, to best of the author's knowledge, there is little in the published literature directly regarding bulk geometric modifications on 2D low speed cavities at very low Mach number.

Kuo & Huang (2001) and Periera & Sousa (1994) appear to provide the only studies on the flow structure of modified 2D cavities at low speeds. However, they did not consider the impact of cavity length, and have only considered a few selected modifications. Acoustic and velocity spectra were not used for comparison in the Periera and Sousa (1994) study. Other studies that have looked at many different geometric modifications on two-dimensional cavities, including spectra, such as Heller & Bliss (1975) and Franke & Carr (1975), have only considered moderate subsonic to supersonic Mach numbers. Although Harper (2006) looked at geom etric modifications and sp ectra on two-dimensional cavities at low speed, the base shape of the cavity was very different. Therefore, it appears that there is little information on two-dimensional cavities at low subsonic speed with 'bulk' modifications, and in particular, there have been very few studies that consider the acoustic and velocity spectra.

2.11.2 Three-Dimensional Low Speed Cavities

The impact of geometric modifications on three-dimensional flow structure appears to have only been considered for a few cases at moderate subsonic to supersonic speeds, while at low subsonic speeds the impact of geometric changes on shallow, narrow, open cavities has not been investigated. Subsequently, the impacts of geometric changes on noise and three-dimensional flow structure around shallow and relatively narrow cavities at low subsonic velocities are unaddressed. Also, only a handful of three-dimensional wall shapes appear to have been investigated at any speed.

2.11.3 Knowledge Gap Statement

The flow structure around rectangular open cavities is well understood, however:

1. A complete description of the parameter space corresponding to each cavity shear layer structure in two- and three-dimensional cavities has not been clearly reported in the literature, thus partial characterisation of this development forms a knowledge gap in this study.

2. The flow structure and noise generated by two- and three-dimensional cavities with modified geometries compared with rectangular geometries remains under-explored at low Reynolds numbers (of the order of 10^4 to 10^5). This includes the noise attenuation achieved by the modified geometries, and the flow mechanisms responsible for this noise attenuation.

3. The unsteady flow structures caused by the finite span of narrow ($L/W > 1$) three-dimensional cavities are unexplored, especially in the region adjacent to the sides of the cavity, where the mixing layer grows in the spanwise direction beyond the span of the cavity.

Furthermore, as stated in section 2.7.9:

4. To best of the author's knowledge the occurence of airfoil tonal noise from a plate with an nominally non-oscillating cavity has not been described previously, and the mechanism of such noise is a valid knowledge gap.

Chapter 3

Experimental Methodology & Design

3.1 Introduction

An experimental approach was used in this study. Figure 3.1 shows an outline of the experimental methodology of the study. Two experimental facilities were used in the present study: an anechoic wind tunnel and a recirculating water tunnel. Cavity flow noise is primarily investigated using a two-dimensional cavity in the former facility, while cavity flow structures are primarily investigated using a thee-dimensional cavity in the latter water tunnel.

The two main experimental models are discussed in this methodology chapter: the airfoil with a two-dimensional cavity ('airfoil with cavity'), for the anechoic wind tunnel, and the flat plate with a three-dimensional cavity, for the recirculating water tunnel. Under each section, the experimental facility, experimental model and experimental techniques are discussed. Additionally a ~ 40 % scale version of the flat plate with three-dimensional cavity, for the anechoic wind tunnel, is also used.

Firstly, the 'airfoil with cavity' is discussed. Microphone measurements and hot-wire anemometry were used. This model was primarily tested in an anechoic wind tunnel facility. This facility allows the noise produced by aeroacoustic sources to be measured in an environment that approximates a free-field.

Secondly, the flat plate with a three-dimensional cavity is discussed. This model was primarily tested in a water tunnel facility. Water tunnels are particularly suited for flow visualisation using ordinary video cameras as, relative to air, higher Reynolds numbers can be produced with slower-moving flows. Additionally, it is possible to conduct Particle Image Velocimetry (PIV) with a higher relative temporal resolution compared to air, for PIV systems with equivalent repetition rates.

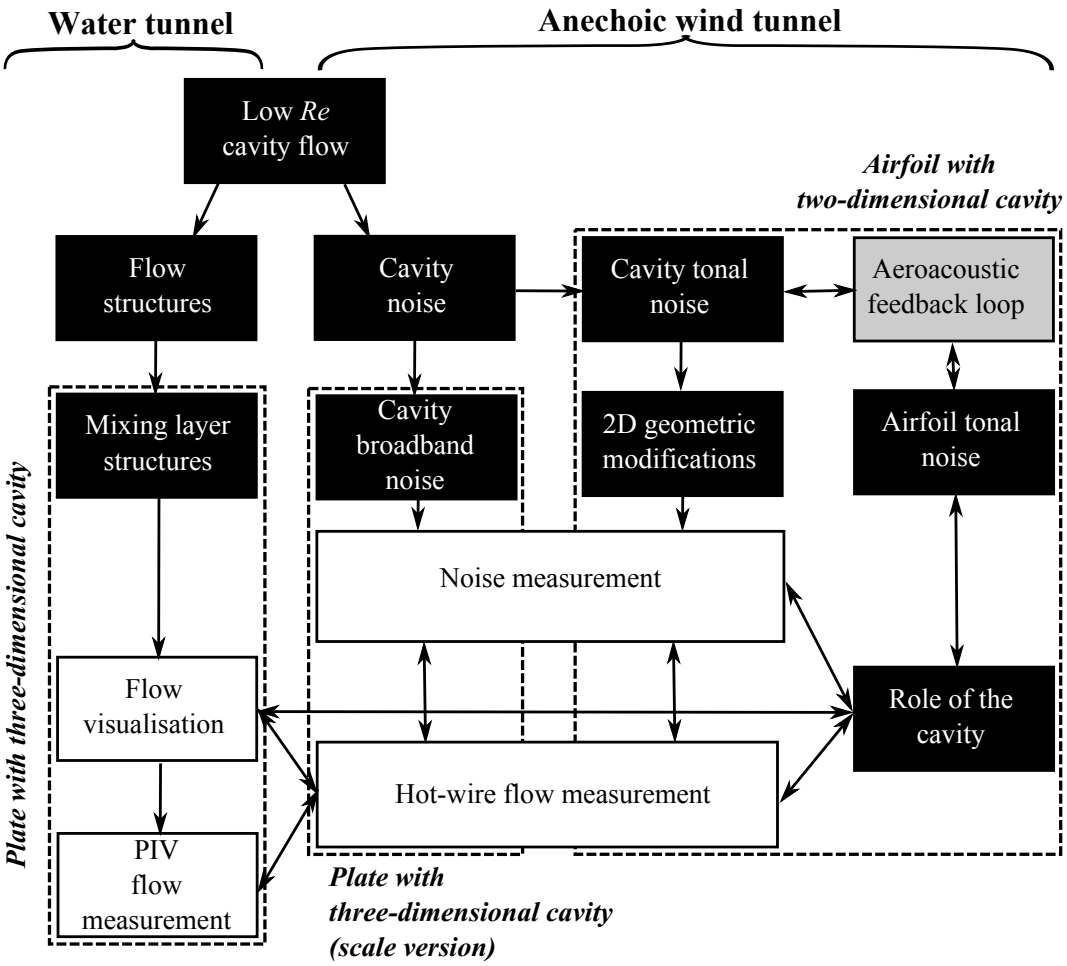

Figure 3.1: Flow-chart of experimental methodology. Experimental facilities are listed at the top. Black- or grey-filled boxes represent the topic, or a sub-topic. The white boxes indicate an experimental technique. The dashed border indicates the experimental model used for that section of the study.

3.2 Airfoil with two-dimensional cavity

3.2.1 Anechoic Wind Tunnel

Anechoic wind tunnel facilities enable the measurement of noise from aeroacoustic sources in an environment that approximates free-field conditions (Reichl, 2007). The University of Adelaide Anechoic Wind Tunnel (AWT) was used in the present study.

In the AWT facility, the flow leaves the contraction in an open jet with outlet dimensions of 275 mm $\times$ 75 mm. The maximum velocity of the wind tunnel is approximately 40 m/s. The anechoic chamber enclosure measures $2 \times 2 \times 2$ m in internal dimensions and is positioned above the building floor on vibration isolators. The enclosure is anechoic at frequencies above 200 Hz.

Reichl (2007) verified that the tunnel had background sound pressure levels below 50 dB(A) across the entire range of velocities, and that the AWT had turbulence intensity in the potential core of the outlet jet less than the design criterion of 1%. The AWT has low background noise levels, apart from below 200 Hz. Below 200 Hz, large, slow-moving circulations create low-frequency noise within the chamber, which is poorly attenuated by the acoustic enclosure (Reichl, 2007, p. 36).

Figure 3.2 shows photographs of the 'airfoil with cavity' model (section 3.2.2) positioned in the Anechoic Wind Tunnel jet outlet. The acoustic foam wedges used to line the chamber are visible, as are the side plates used to hold the airfoil. The techniques used within the AWT included far-field acoustic microphone measurements (section 3.2.3), hot-wire anemometry (section 3.2.5), and surface flow visualisation.

3.2.2 Experimental model

The purpose of the 'airfoil with cavity' was to investigate oscillatory cavity noise in the depth-based Reynolds number range of approximately 6,000–16,000 and the length-based Reynolds number range of 10,000–74,000. Specifically, the features of cavity flow and noise to be investigated were:

- the noise spectra produced by cavities between $L/D = 1.17$ to 4.67 across the available range of velocities of the facility,
- the mean convection velocity ratio, $\kappa = U_c/U$, for cavity flows between $L/\delta_0 = 10$ to $L/\delta_0 = 48$,
- the Rossiter mode numbers of cavity oscillations produced between $L/\delta_0\sqrt{\mathrm{Re}_{\delta_0}} = 350$ and $L/\delta_0\sqrt{\mathrm{Re}_{\delta_0}} = 1800$,
- the effect of sloping the front and rear cavity walls on the cavity shear layer and on the noise produced by the cavity, and
- cavity noise spectra & shear layer velocity spectra at $\mathrm{Re}_D = 11{,}900$ which could be compared to shear layer flow visualisation in water, for rectangular cavities between $L/D = 1.17$ to 4.67 and a cavity with sloped front and rear walls at $L/D = 2.33$.

The 'airfoil with cavity' was designed to meet the following criteria:

- provide a thin laminar boundary layer at the leading edge of the cavity,
- allow for a range of rectangular cavity L/D ratios – in the range where oscillatory cavity noise should be produced,
- allow the investigation of modified two-dimensional cavity geometries,

- be sufficiently compact to fit within the existing airfoil-holder attachment for the AWT, and
- produce a sufficient level of oscillatory cavity noise.

For the cavity itself, a two-dimensional configuration was chosen. For a small flat-plate boundary layer development length, the cavity length would need to be quite small so as to be in the range for oscillations. A three-dimensional 'narrow' cavity would be quite small in span, and would have limited radiating power. Conversely, for a larger three-dimensional cavity, the boundary length development length required (to place the cavity in the range of oscillations) would be impractically large. Therefore it was decided to use a two-dimensional cavity positioned within an airfoil-like flat plate, and such a model would fit entirely within the potential core of the AWT open jet. For this 'airfoil with cavity', a super-elliptic leading edge (Narashima and Prasad, 1994) and tapered trailing edge were used to encourage attached flow over the plate and laminar flow at the cavity leading edge. Only the middle section of the airfoil, containing the cavity, was indeed flat. To attempt to ensure oscillations, the estimated boundary layer characteristics and cavity length were selected so that they satisfied the criteria for oscillatory cavity flow, while the large span of the 2D cavity should allow for sufficient radiating power so that the oscillations are readily detectable.

The 2D cavity model follows many ideas of Milbank (2004) who used a flat plate with a cavity placed near the outlet of a jet 283 mm $\times$ 71 mm in size, with far-field microphone measurements taken inside a semi-anechoic enclosure. The flat plate had a super-elliptic leading edge. The 'airfoil with cavity' used in the present work is broadly similar but much shorter in chord length. The airfoil has a super-elliptic leading edge which ensures laminar flow at the cavity, while the tail is linearly tapered (with a spline curve to smooth the transition from parallel section to tail).

Leading edge A super-elliptic leading edge is selected in order to attempt to avoid flow separation at the nose of the model. Such leading edges are regularly used in studies involving flat plates. Equation 3.1 gives the shape of the super-elliptic profile, with nose length, a, and half-thickness, b (Narasimha and Prasad, 1994):

$$\left(\frac{(a-x)}{a}\right)^n + \left(\frac{y}{b}\right)^n = 1, \qquad 0 \leq x \leq a \qquad n > 2 \tag{3.1}$$

The recommendations of Narasimha and Prasad (1994) regarding leading edge geometry were followed. Narasimha and Prasad (1994) computationally investigated different nose-to-thickness configurations, finding that the ratio of $a/(2b) = 3$, with an exponent $n = 3.15$, gave the shortest nose length where separation was not likely. The selected profile, following these recommendations, is shown in figure 3.3.

Boundary layer development length The distance, x, from the airfoil leading edge to the cavity determines the estimated laminar boundary layer thickness, δ, at the leading edge of the cavity. This parameter relates to the required cavity length and required cavity depth for oscillations to occur.

$$\delta = \frac{5x}{Re_x^{1/2}} \text{ (Blasius solution – Laminar)} \tag{3.2}$$

A critical Reynolds number of $Re_{x,cr} = 300,000$ was used for estimating whether the flow at the cavity leading edge would be laminar, based on equation 3.2 above, which gave a maximum value of x. Subsequently, the selected leading edge length ($x = 0.033$ m) should allow for a laminar boundary layer as $Re_x = 21000 - 84000$ for the entire range of expected velocities, 10-40 m/s.

Cavity length Cavity lengths of 7 – 28 mm were selected. From the literature (section 2.6, table 2.2) there are numerous studies with $Re_L = 1,000$ to 100,000, and the cavity-length-based Reynolds number of this model range from 2,410 to 77,000.

It is desirable that the expected oscillation frequencies be well above 200 Hz, as the AWT facility has good anechoic performance only above 200 Hz. Oscillations should be well above this 200 Hz criterion for a cavity 7 mm in length (figure 3.4(a)).

The minimum and maximum cavity length curves (from section 2.5.2, on cavity oscillation criteria), indicated by the dashed lines in figure figure 3.4(b), are based on estimated characteristics of a laminar boundary layer for the given lead-in length. From upwards of 20 m/s, a cavity length of 7 mm meets the minimum cavity length criterion of Sarohia (1977). A longer cavity length of 28 mm does not meet the more conservative $L < 100\theta_0$ (for oscillations) upper criterion, however it does meet a more liberal $L < 200\theta_0$ upper bound for oscillations (section 2.5.2), and with a positive pressure gradient applied across the model, the longer cavities from 14 mm to 28 mm in length may also oscillate.

Tail section Trailing edges of flat plates, or airfoils, can be significant sources of aeroacoustic noise (Marsden *et al.*2007). Thus the flat plate should be reasonably long to place the trailing edge position reasonably far downstream from the cavity. The plate was therefore made as long as possible within the constraint of fitting within the existing airfoil-holder attachment for the AWT. A taper angle of 6° was selected, and, together with the nose and flat plate sections, this specifies the geometry of the 'airfoil with cavity'.

Overall specifications

Figure 3.5 shows the 'airfoil with cavity' model, which consists of three main components: the super-elliptic nose, a flat-plate section containing the cavity

Table 3.1: Specifications of two-dimensional cavity

Cavity length extremes, L, mm	7		28	
L/D	1.17		4.67	
Velocity extremes, U, m/s	10	40	10	40
Re_L	2410	19240	19240	77000
Predicted first Rossiter mode, f_1, Hz	800	3054	200	763
Cavity width, W, mm	275			
Cavity depth, D, mm	6			

Table 3.2: Specifications of overall airfoil

Boundary layer development length, x, mm	33
Re_x	21,000 - 84,000
Estimated δ_0, mm	1.1 - 0.57
Estimated θ_0, mm	0.15 - 0.076
Overall chord, C, mm	130
Chord-based Reynolds numbers, Re_C	6.7 $\times 10^4$ to 3.3 $\times 10^5$
Overall thickness, t, mm	11

cut-outs, and a tail section. The nose section is 33 mm in chordwise length. The flat plate section of the model contains the 28 mm long section for the cavity cut-outs. The tail section is linearly tapered at 6° and is approximately 69 mm in length, including a section which smoothly transitions from parallel surfaces to tapered via an arbitrary spline curve.

Tables 3.1 and 3.2 give the specifications of the cavity and of the overall airfoil profile respectively. The 'airfoil with cavity' model was machined from aluminium alloy using a computer-numerical-controlled machine. Table 3.3 tabulates the coordinates of the profile in normalised units for reference purposes, note that the origin is fixed to the plate's trailing edge and the plate is at zero angle of attack.

Positioning The model is positioned within the potential core region of the AWT jet, within the existing airfoil-holder attachment and near the centreline of the jet. Figure 3.7 shows a schematic diagram of the placement of the airfoil in the open jet. Upon conducting experiments with a similar apparatus, Milbank (2004) found a modulation of the oscillatory cavity noise, due to the

Table 3.3: Coordinates of the flat plate profile for zero angle of attack. Italics indicate the location of the 28 mm long slot. Note that the origin of the coordinate system is at the airfoil trailing edge, with positive x being in the downstream direction and positive y being in the stream-normal direction.

x/C	-1	-0.974	-0.949	-0.923	-0.885
y/C	0	0.0284	0.0341	0.0374	0.0402
x/C	-0.846	-0.788	*-0.746*	*-0.531*	-0.473
y/C	0.0416	0.0423	*0.0423*	*0.0423*	0.0423
x/C	-0.423	-0.354	-0.277	-0.154	0
y/C	0.0407	0.0364	0.0291	0.0162	0

proximity of the cavity to the free shear layer of the jet. This was fixed by moving the cavity further away from the free shear layer. In an attempt to avoid this issue, the present model was offset 12 mm below the centreline of the jet – so that the adjacent free shear layer is further away from the cavity-side of the profile.

To install the airfoil in the Anechoic Wind Tunnel, the airfoil was mounted using pins into two rigid PVC side plates which fitted within the existing support frame, as depicted in figure 3.6. The baseline position was at a nose-down geometric angle of $-1°$. This was done in order to attempt to impart a small positive pressure gradient, which helped ensure the occurrence of attached flow and therefore oscillatory cavity flow.

There were 5 holes in the PVC sides for securing the trailing edge of the 'airfoil with cavity' in order to produce different angles of attack. These are shown in figure 3.6, and produced $\alpha_{\text{geom.}} = 11°, 5°, -1°, -7°$ & $-13°$, where a negative angle of attack refers to nose-down. Additionally, there was sufficient friction from an 'interference fit' that the airfoil could also be held in place at $\alpha_{\text{geom.}} = 0°$ (without the use of the trailing edge retaining pins), as in section 5.2.

Other considerations

Acoustic compactness According to Milbank (2004), a cavity is acoustically compact if the acoustic wavelength, λ, is 'much greater' than the cavity length, L, following equation 3.3 below. 'Much greater' represents a factor of at least 5. Acoustic compactness means that feedback takes the form of hydro-dynamic pressure waves, and also that the leading edge is in the acoustic near-field of the trailing edge. Subsequently the phase lag (or delay), α, is taken to be zero. Considering the extremes of the cavity length, the acoustic

wavelength of the first mode is approximately 110 mm for the 7 mm cavity and approximately 450 mm for the 28 mm cavity. Therefore, all cavity configurations are acoustically compact.

$$\lambda = \frac{c}{f} >> L \tag{3.3}$$

Mean convection velocity ratio for L/δ=5-10 Although the convection velocity ratio, κ, is often taken to be an empirical constant, it can also be measured. Data published by Sarohia (1977) are shown in figure 3.8, where κ is plotted against non-dimensional cavity length, L/δ. The data are limited to cavity lengths from approximately five to ten times the boundary layer thickness.

From these data, Milbank (2004) determined an empirical relation for κ based on L/δ. Milbank (2004) found when using values of κ based on this empirical relation, that the predicted non-dimensional frequencies agreed well with experimental results.

Modified geometries – sloped inserts Two 45° sloped wall insert blocks were manufactured, which can also be installed upside down to form reverse-sloped walls. These geometric modifications are applied such that the cavity volume remains constant.

Corrected angle of attack The true angle of attack is less than the geometric angle of attack due to the deflection of the open jet. This is especially significant when the airfoil chord is large compared to the height of the jet (Brooks, Pope and Marcolini, 1989, p. 5), which is the case here. The geometric angle of attack, $\alpha_{\text{geom.}}$, is defined in figure 3.7.

A correction factor has been provided in the literature by Brooks, Marcolini & Pope (1986) and Brooks *et al.* (1989). It is assumed that the jet height does not expand significantly between the contraction outlet and the airfoil. The correction factor for this airfoil is 0.13 . The corrected angles of attack are thus $-0.13°$, $-0.90°$, and $-1.7°$ respectively for geometric angles of attack of $-1.0°$, $-7.0°$, and $-13°$ respectively. The geometric angle of attack will be quoted in the rest of this paper. Unless stated otherwise, measurements were taken at the baseline angle of attack ($\alpha_{\text{geom.}} = -1.0°$).

3.2.3 Microphone measurements

In order to experimentally characterise the noise produced by aeroacoustic sources, far-field noise measurements were taken using a Brüel & Kjær half-inch condenser microphone, model number 4190. Table 3.4 shows the microphone measurement and spectral processing specifications.

In Chapter 4 (2D Cavity Flow: Results & Discussion), the microphone was located 600 mm from the 'airfoil with cavity', positioned directly perpendicular to the mean flow direction and adjacent to the centre of the cut-out for the cavities (i.e., 600 mm from $x/C = -0.638$ where $x/C = 0$ is located at the airfoil trailing edge and negative x is upstream). Data were sampled at 50 kHz for a duration of 10 seconds and they were processed using MATLAB® numerical analysis software. To improve the clarity of the plots, the frequency resolution of the spectra plotted in Chapter 4 is typically 10Hz. Due to the nature of the experiment, the spectrograms were calculated differently. Within the spectrograms, each constituent spectrum is based on a sample of 0.1 seconds duration at 50 kHz sampling frequency, giving a bandwidth of 20 Hz. The A-weighted Overall Sound Pressure Level (OASPL) was calculated by integrating the noise spectrum after applying A-weighting.

In Chapter 5 (Airfoil Noise: Results & Discussion) the microphone was located directly perpendicular to the trailing edge of the airfoil at a distance of 600 mm for section 5.3 to 5.5 and a distance of 585 mm for sections 5.6 onwards. Data were sampled at 50 kHz for a duration of 20 seconds, and processed using MATLAB® software. The frequency resolution of the spectra was generally 1 Hz, although for plotting purposes the frequency resolution was reduced to 10 Hz for clarity.

3.2.4 Error analysis of microphone measurements

According to Milbank (2004, p. C-9) the spectral precision (random) error of a spectral estimate is given by equation 3.4. In this equation, BT_t represents the number of discrete segments, however it can be replaced by $BT_t = K(BT_{\text{eff}})$ where K is the total number of segments, and a Hann window with a 50% overlap has a coefficient $BT_{\text{eff}} = 0.947$.

$$\epsilon = \frac{1}{2\sqrt{BT_t}} \tag{3.4}$$

From equation 3.4, with 95% confidence the margin of error due to the spectral estimate calculation can be found to be ± 0.60 dB for a sample length of 10 seconds, and ± 0.43 dB for a sample length of 20 seconds, in both instances with a segment length of 0.1 seconds.

3.2.5 Hot-Wire Anemometry (HWA)

Hot-wire anemometry (HWA) is a method for measuring velocity using a highly sensitive heated wire whose rate of cooling depends on flow speed. The technique allows for velocity measurements with a very high frequency response.

Two methods of HWA are possible: constant-temperature anemometry and constant-current anemometry. In this thesis, constant-temperature anemometry was used. A Wheatstone bridge circuit is used to maintain the probe at

Table 3.4: Microphone measurement & spectral processing specifications

Microphone	Brüel & Kjær half-inch condenser, model 4190
Sampling frequency, Hz	50,000
Sample duration, seconds	10 or 20
Spectral bandwidth, Hz	1 or 10
Window function	von Hann
Overlap	50%

a constant temperature and the fluctuating bridge voltage is measured to find the velocity.

In the present study the frequency response was more than sufficient to resolve the oscillations of interest. Single-wire probes with a tungsten wire of diameter of $\sim$5 μm were used. Such probes give the magnitude of velocity perpendicular to the wire. A hot-wire probe consists of a very thin wire soldered between two inert prongs, in turn connected to a cylindrical support.

A single-wire TSI 1260A-T1.5 probe (for sections up to 5.5) or a single-wire TSI 1210-T1.5 probe (section 5.6 onwards) were used together with a TSI IFA300 anemometer. The hot-wire probes were calibrated using a TSI plenum-type calibrator (model number 1127) connected to a MKS Baratron differential pressure transducer. The probe was positioned using a DANTEC three-dimensional automatic traversing system which is fixed to the anechoic chamber floor. The positional accuracy of the traverse was $\pm$.003 mm in the X and Y directions. Data were sampled at 50 kHz for a duration of 10 seconds (Chapter 4) or 20 seconds (Chapter 5) and they were processed using MATLAB® numerical analysis software. The frequency resolution of the spectra was generally 1 Hz, although for plotting purposes, in most instances, the frequency resolution was reduced to 10 Hz for clarity.

Hot-wire calibration

Perry (1982) states that it is best to directly calibrate velocity to bridge voltage, rather than using more fundamental models that consider heat transfer.

$$U^2 = A + BU^n \tag{3.5}$$

After acquiring the data, various methods can be used to find the relationship. These include King's Law (or the Cooling Law) which involves finding a linear relationship between the square of voltage and the square root of velocity, to give a fourth order polynomial. Equation 3.5 becomes King's Law if the exponent, n, is equal to 0.5. The exponent may be varied between 0.45 and 0.55, depending on the value which gives the optimal fit. Rather than using

the above equation, a computer is often used to generate a higher order polynomial curve fit. In this study, a fifth-order polynomial curve fit was generated by computer.

Error analysis of HWA measurements

According to Bruun (1999), typical velocity measurement accuracy of hot-wire anemometry is approximately 1%. The error of a hot-wire anemometry measurement consists (apart from drift) of two main components: a random error (which can be estimated statistically) and a bias error (arising from errors in calibration).

The uncertainty of the calculated velocity from the hot-wire measurement is equal to the uncertainty of the flow velocity used to construct the calibration. (While the hot-wire calibration is constructed from the relationship between voltage and flow velocity, the voltages used to construct the calibration curve however consist of the mean of a large number of samples and is a negligible source of error.) This flow velocity at the calibrator is determined from equation 3.6 by measuring the dynamic pressure. Dynamic pressure was found using differential pressure across the exit nozzle, measured by an MKS Baratron.

$$U = \sqrt{\frac{\Delta p}{0.5\rho}} \tag{3.6}$$

The ambient pressure and ambient temperature are used to determine the air density in equation 3.6, by the ideal gas law. These are estimated from a thermometer and high-precision barometer in the laboratory. These quantities are negligible sources of uncertainty in the flow velocity. Also, the uncertainty in the dynamic pressure – from the precision uncertainty of the MKS Baratron of ± 0.07 Pa – is another negligible source of error contributing uncertainty in the computed velocity of less than approximately ± 0.06 m/s at slower experimental velocities tested, and less uncertainty at higher velocities. Furthermore, the statistical margin of error of the mean velocities used to construct the calibration, with 95% confidence, was also found to be negligible[1] – indeed, the calibrator apparatus produced a highly stable and consistent flow.

The margin of error of the spectral estimate used to find velocity spectra from HWA measurement was found (in the same manner as section 3.2.4) to be $\pm 16\%$ for $\Delta f = 1$ Hz and $\pm 5.1\%$ for $\Delta f = 10$ Hz. As the velocity spectra typically span orders of magnitude difference, this margin of error therefore does not have a significant impact on the discussions and findings following from the spectra.

[1]With 95% confidence, the statistical margin of error is given by $\pm\ 1.96 \times s/\sqrt{N}$ with s being an estimate of the standard deviation given by the sample standard deviation of $s = \sqrt{1/(N-1)\sum(x_i - \bar{x})^2}$, where x_i are the sample values, $\bar{x}$ is the sample mean and N is the sample size.

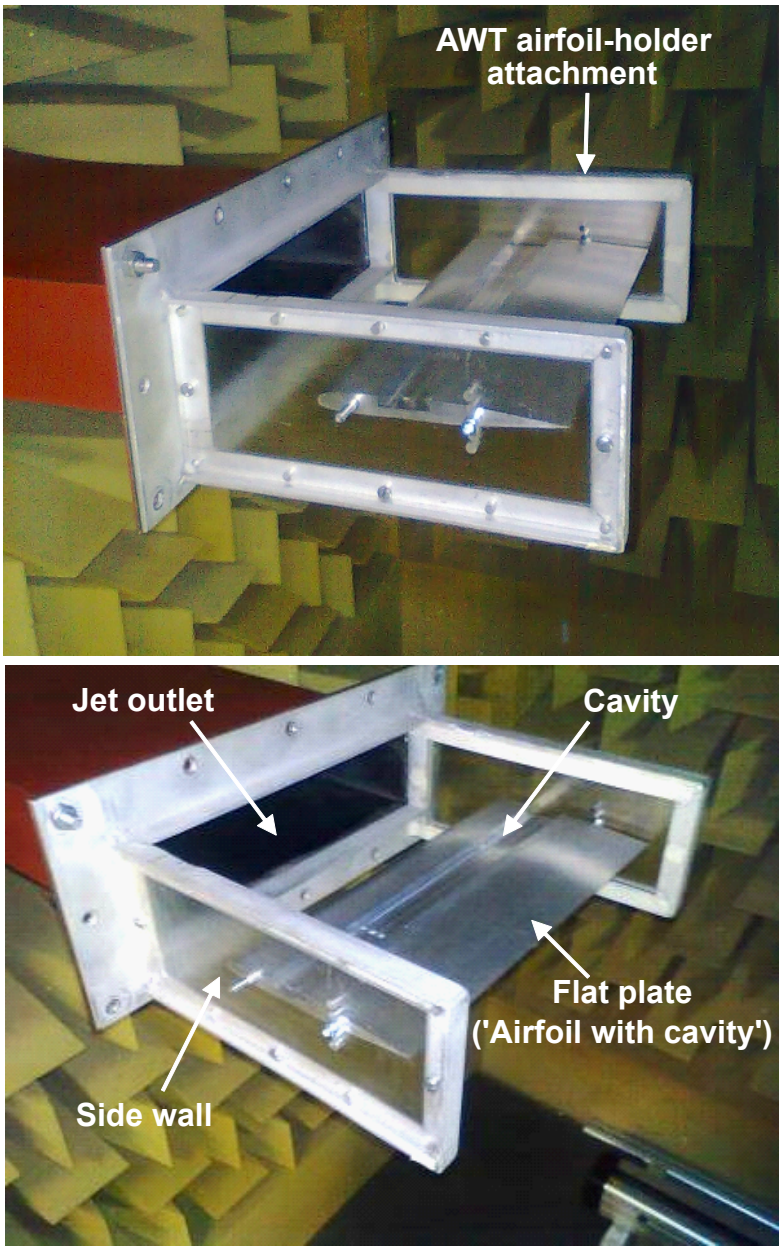

Figure 3.2: Photographs of 'airfoil with cavity' model positioned in Anechoic Wind Tunnel.

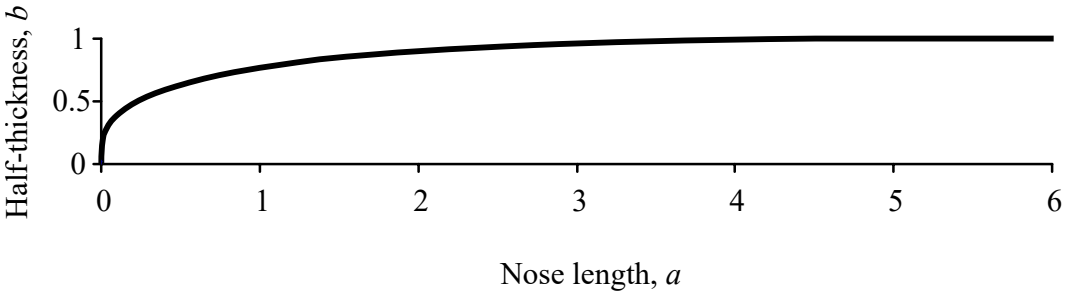

Figure 3.3: The super-elliptic leading edge profile of the 'airfoil with cavity' model.

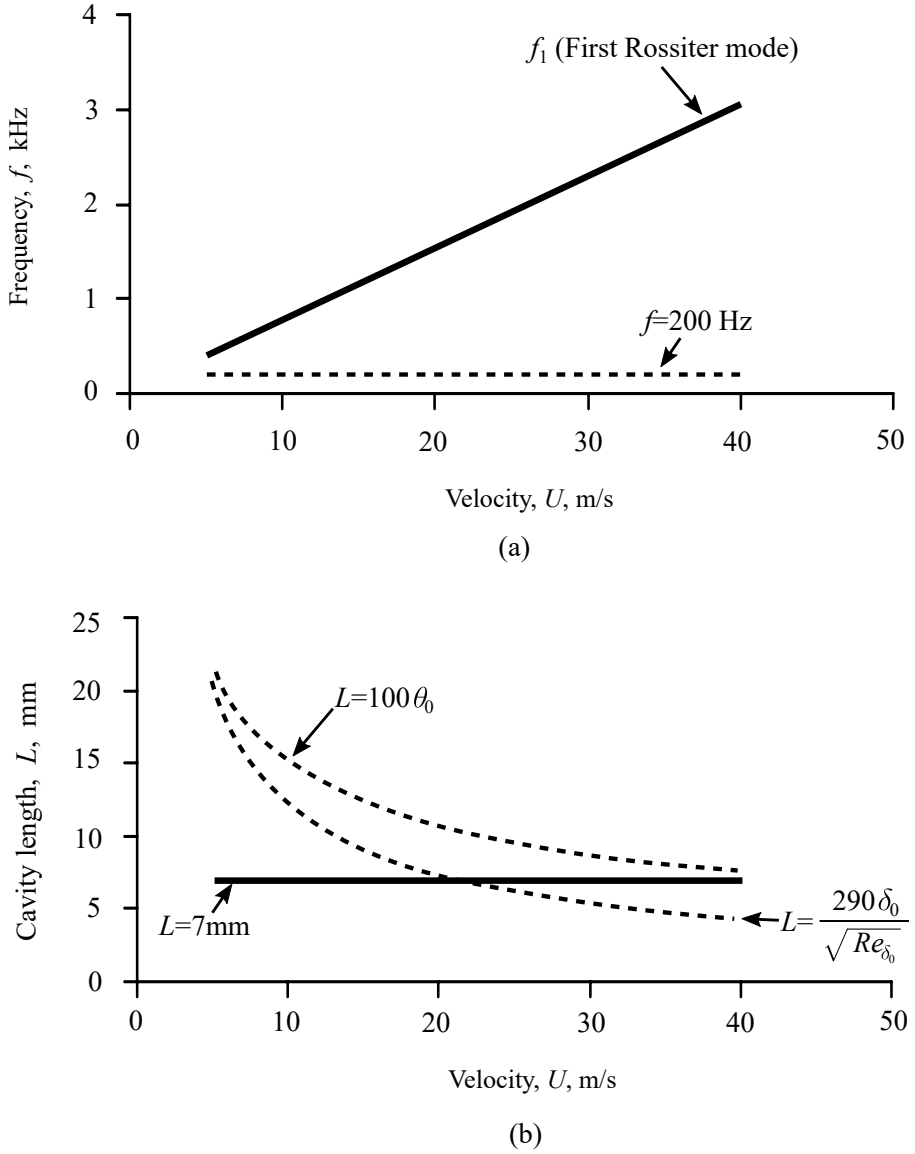

Figure 3.4: Two-dimensional cavity specification compared to frequency and oscillation requirements. (a) Estimated frequency of first mode of Rossiter oscillations (solid line) for the shortest cavity, $L = 7$ mm, compared to the minimum threshold for the anechoic wind tunnel of 200 Hz. Higher modes would have a higher oscillation frequency. (b) Minimum and nominal maximum cavity lengths for occurrence of cavity oscillations based on boundary layer development length of x=33 mm, across the range of velocities achievable by the Anechoic Wind Tunnel. The solid horizontal line indicates the $L = 7$ mm cavity. The lower dashed line gives the minimum cavity length for oscillations, from Sarohia's (1977) criterion: $L = 290\delta_0/\sqrt{Re_{\delta_0}}$ (section 2.5.2). The upper dashed line is an approximate upper limit on cavity length for oscillations, given by $L = 100\theta_0$ (Sarohia, 1977, Rockwell, 1983 and Gharib & Roshko, 1987; section 2.5.2).

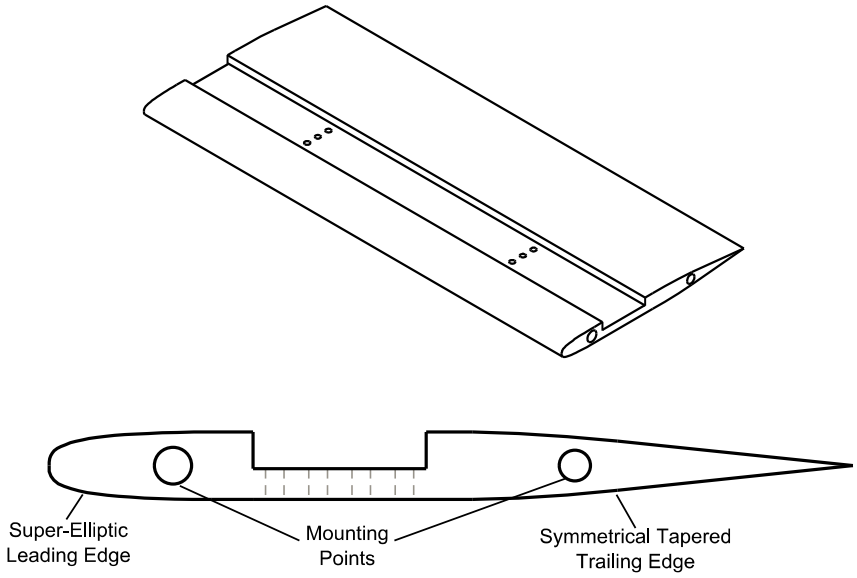

Figure 3.5: Sketch of the airfoil with cavity, which contains a cavity cut-out where various inserts can be fitted to form a range of cavity geometries.

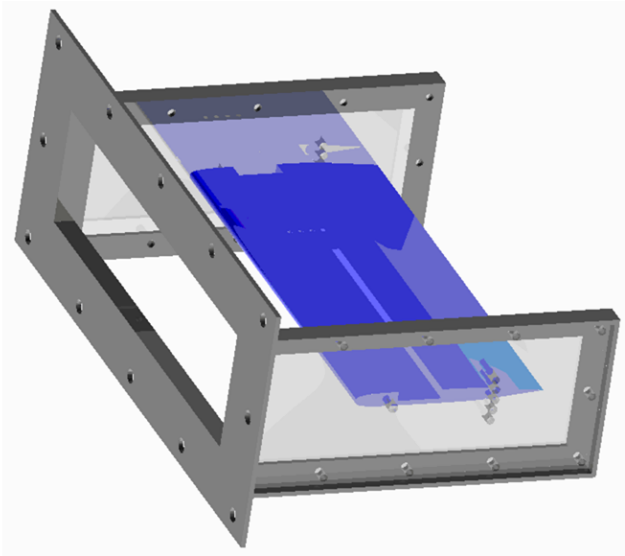

Figure 3.6: Rendering of the airfoil with cavity model. Shown here attached to the existing airfoil-holder attachment, which attaches to a flange on the outlet of the open jet.

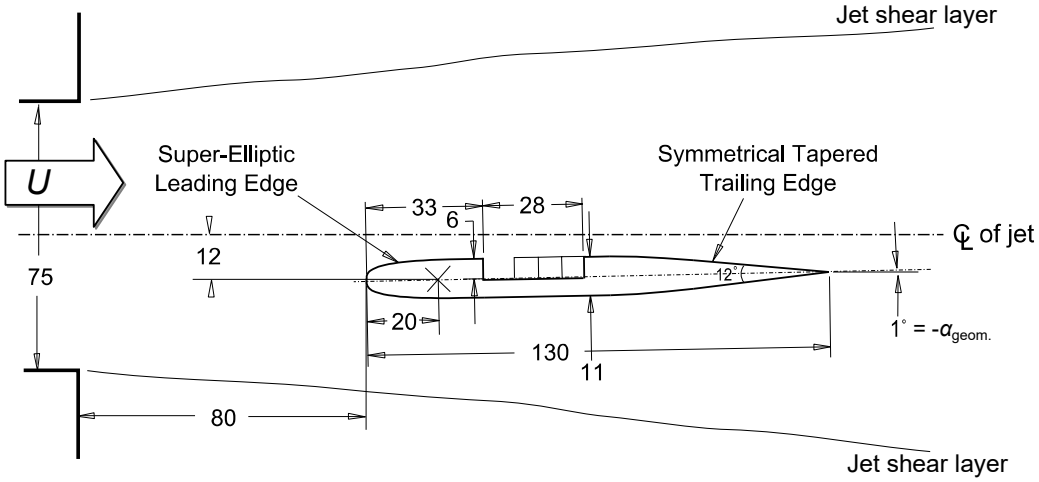

Figure 3.7: Schematic diagram of the placement of the 'airfoil with cavity' model within the jet of the Anechoic Wind Tunnel. Note that $\alpha_{\text{geom.}}$ is defined as being positive in the clockwise direction (when the airfoil is nose-up), therefore the baseline angle of attack of 1° nose-down equates to $\alpha_{\text{geom.}} = -1°$.

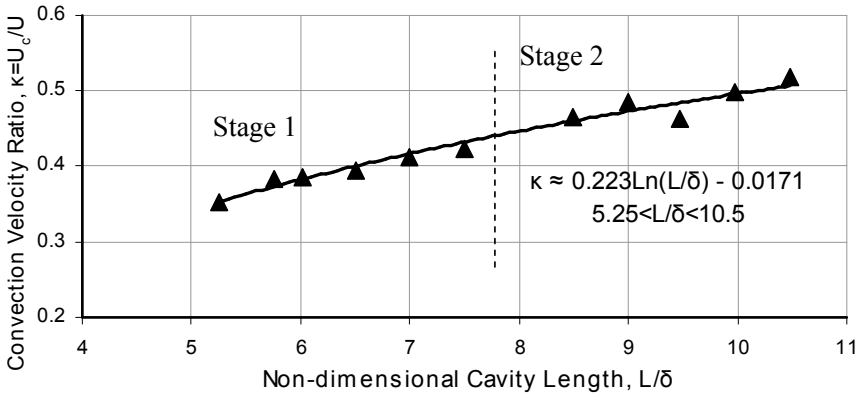

Figure 3.8: Convection velocity ratio versus non-dimensional cavity length for a laminar boundary layer. Transposed from Sarohia (1977).

3.3 Three-dimensional cavity

3.3.1 Water Tunnel

Water tunnels have been used extensively in cavity flow research for the observation of flow features (e.g., Maull and East 1963, Kuo and Huang 2001 and others). The recirculating water tunnel used in this study had a working section cross-sectional area of 0.5×0.5 m^2 and a maximum velocity of approximately 400 mm/s. Figure 3.9 shows a photograph of the facility, while figure 3.10 shows a schematic diagram.

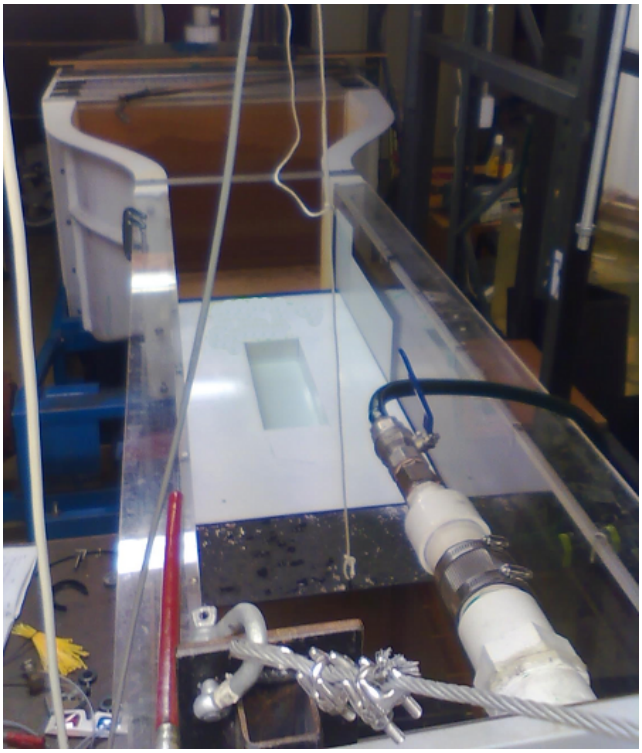

Figure 3.9: Photograph of water tunnel facility. Flow from top to bottom. The three-dimensional cavity in a flat plate can be seen in the working section.

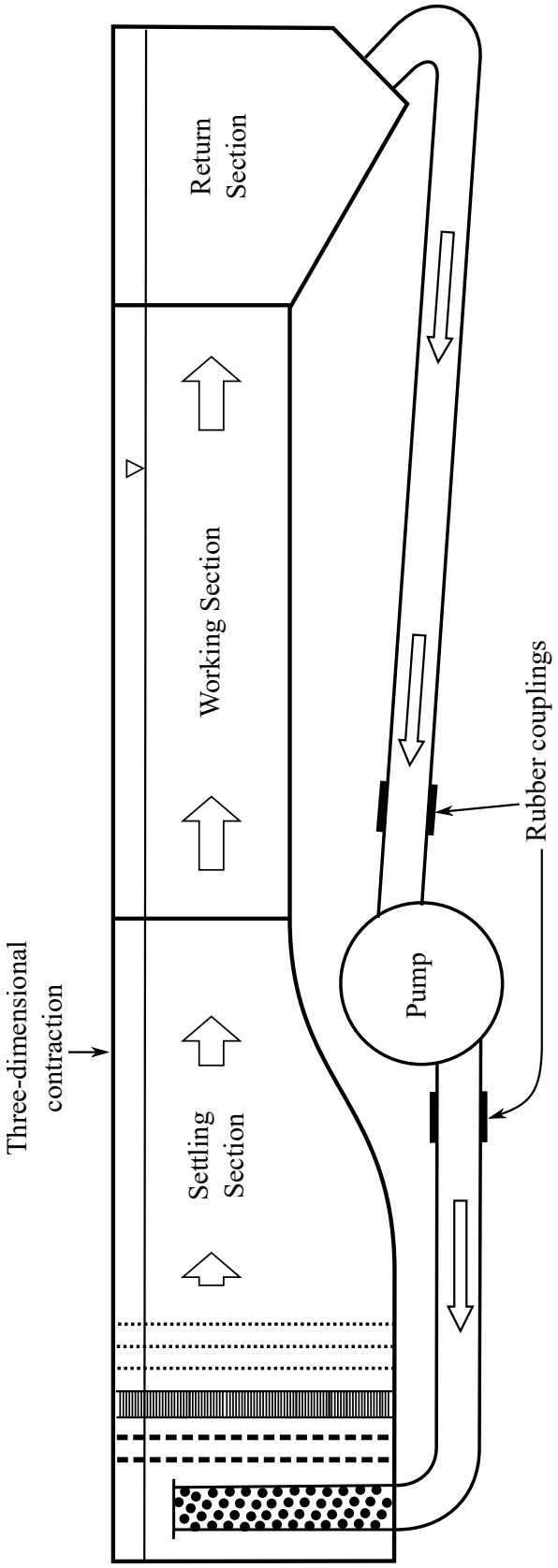

Figure 3.10: Schematic diagram of water tunnel facility.

There were a number of advantages to investigating the flow at low Reynolds number in a water tunnel. In a low-Reynolds-number cavity flow, unsteady flow features can be easily observed. Observation of these unsteady flow structures helps to fill knowledge gaps, as much of the existing literature concerns time-averaged flows. Finally, available conventional video cameras and low-frequency PIV systems can be used to both observe and measure the flow respectively, whereas high-frequency measuring systems would be required to resolve the unsteady flow at high-Reynolds-number, especially in a wind tunnel flow. On the other hand, flow physics dealing with acoustic effects could differ.

3.3.2 Experimental model

A three-dimensional cavity experimental model was used in water to investigate the unsteady flow structures associated with the cavity tonal noise and velocity spectra obtained in Chapter 4 (Two-Dimensional Cavities: Results and Discussion). Where the 'airfoil with cavity' in air allowed the investigation of two-dimensional cavity shear layer phenomena, the three-dimensional cavity model will allow the investigation of three-dimensional shear layer effects such as end effects due to finite span.

The three-dimensional cavity experimental model used in this study was designed and built previously by Crook (2011). It consists of a free-standing flat plate with a rectangular cavity cut-out which is placed within the working section of the recirculating water tunnel. The depth-based Reynolds numbers were in the range of approximately 3,000 to 14,000. The length-to-depth ratio (L/D) of the cavity varied from 0.84 to 6, while the span-to-depth ratio (W/D) was fixed at 2, with length-to-span ratio (L/W) varying in the range 0.42 to 3.

Figures 3.11 and 3.13 shows a sketch and photograph of the model respectively. It is constructed with an acrylic semi-elliptic leading edge, painted steel sheet forming the flat plate and the cavity itself formed by clear rigid PVC sides, with one side unpainted for optical access. The plate has a downstream circulation control flap fitted, the angle of which can be set to ensure development of a zero-pressure gradient laminar boundary layer on the flat plate. The model was repainted before each set of experiments, however deterioration of the paint with use is visible in some flow visualisation photographs.

Table 3.5 lists the physical dimensions and geometric non-dimensional parameters of the model. The relatively large physical dimensions enabled good access for flow visualisation. A number of perspex cavity inserts were designed and manufactured for use in the water tunnel model, to allow the cavity's rectangular geometry to be modified in various ways. This reduced the volume of the cavity slightly. The modifications chosen had provided some noise attenuation when trialled in an anechoic wind tunnel on a separate model.

Figure 3.12 shows a sketch of the co-ordinate system used in the three-

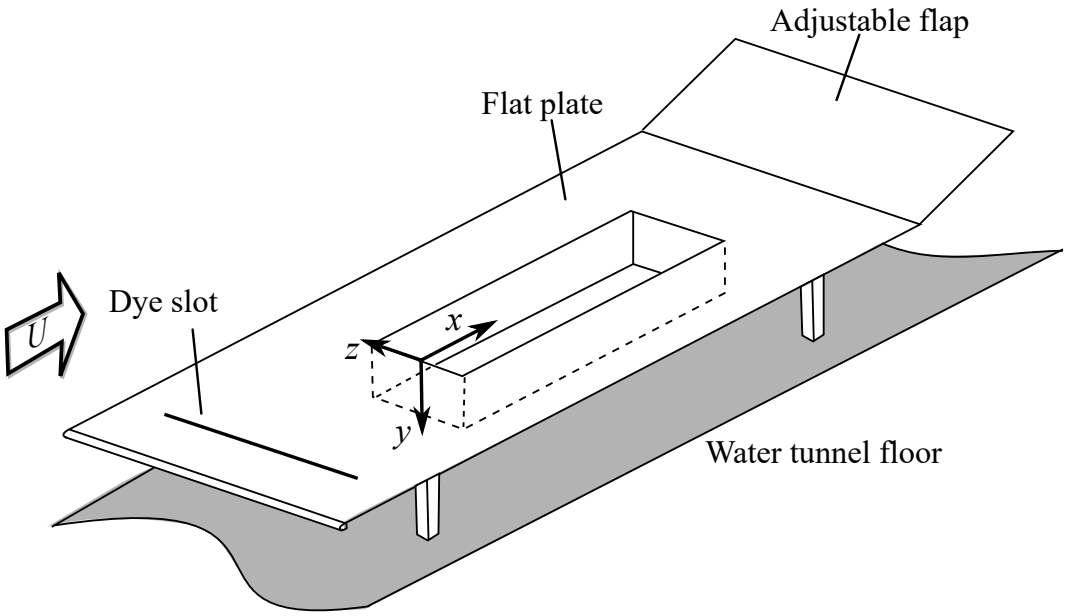

Figure 3.11: Sketch of water tunnel three-dimensional cavity model.

dimensional cavity section. Note that the Y axis has been orientated downwards in order to give the desired orientation of the Z axis.

Scale version of 3D cavity (air)

A scale version of the three-dimensional cavity model was constructed for use in air. This consisted of a flat plate with a three-dimensional shallow, narrow, cavity cutout at 43% scale of the water tunnel model. There were upright sides to control the expansion of the open jet, however there was no ceiling above the cavity in order to enable far-field acoustic measurement. The specifications of the three-dimensional cavity is given in table 3.6.

The flat-plate was fitted with a semi-circular nose profile, thus giving a boundary layer with $D/\delta_0 \approx 4.0$, having a shape factor $H = 2.0$. Note that flat-plate was raised slightly relative to the contraction surface, such that the developed contraction boundary layer was directed under the nose and beneath the flat plate.

3.3.3 Flow visualisation

Flow visualisation involves techniques to mark, and therefore visualise, otherwise transparent fluid flow. The intention is for the flow visualisation medium, such as a tracer, to accurately mark the flow for some distance, whilst not interfering with the flow. In water flows, these tracers can take the form of dye or ink to mark the flow or small particles such as bubbles of hydrogen gas or small solid particles.

Table 3.5: Specifications of water tunnel cavity model

Cavity length, L, m	0.063 – 0.45	
Cavity depth, D, m	0.075	
Cavity width, W, m	0.15	
L/D	0.84 – 6	
W/D	2	
Re_D (dye visualisation)	2,700	
Re_D (hydrogen-bubble visualisation)	8,000 – 14,000	
Re_D (PIV)	6,000 – 10,700	
B. L. development length, x, m	0.336	
B. L. type	laminar	
U, mm/s	40	144
Re_x	13,400	48,000
B. L. thickness[1] δ_0, mm	14.5	7.7
B. L. momentum thickness[1] θ_0, mm	1.9	1.0
D/δ_0	5.2	9.8
D/θ_0	39	74
L/θ_0	33	443
Re_{θ_0}	77	146

[1] Values estimated from Blasius boundary layer theory.

Table 3.6: Specifications of anechoic wind tunnel three-dimensional cavity model

Boundary layer thickness at cavity leading edge, δ_0, mm	8.0
Normalised boundary layer thickness, δ_0/D	0.25
Boundary layer shape factor, H	2.0
Boundary layer momentum thickness, θ_0	1.0 mm
Normalised momentum thickness, θ_0/D	3.1×10^{-2}
Cavity length, L, mm	194
Cavity span, W, mm	68
Cavity depth, D, mm	32
Velocity, U, m/s	3
Depth-based Reynolds number, Re_D	6,400

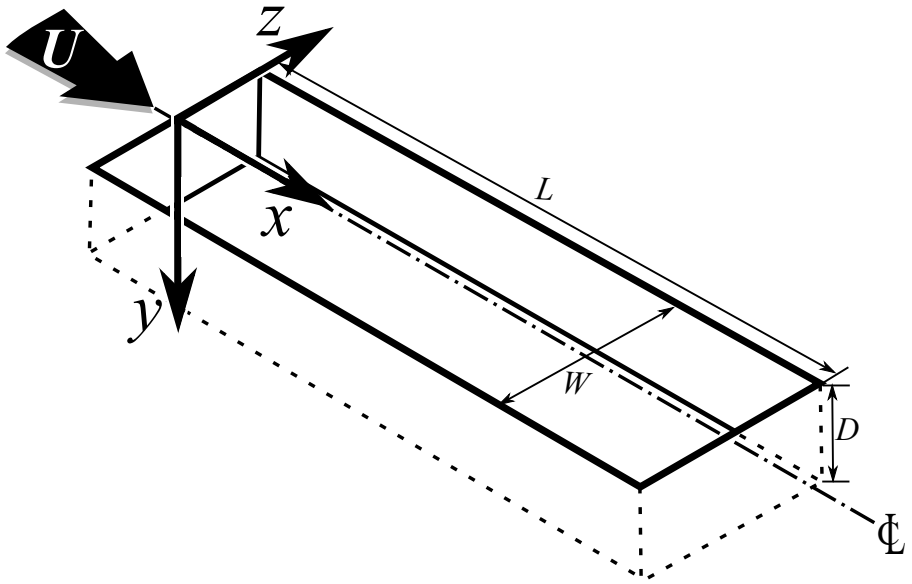

Figure 3.12: A sketch of the coordinate system used for three-dimensional cavities, including for the PIV experiments.

The objective of the water tunnel flow visualisation experiment was to use this technique to investigate the flow structure around a three-dimensional, open cavity, with either rectangular or modified geometry. Two flow visualisation methods were used: dye visualisation and hydrogen bubble visualisation. In the former, dye was injected from a dye slot, ports or probes upstream of the cavity, or near the region of interest. In the latter, a hydrogen bubble wire was positioned upstream of, or within, the cavity.

The streaklines visualised by the aforementioned flow visualisation techniques are not equivalent to streamlines in unsteady flows. Tracers used in flow visualisation produce streaklines which show an integration of all the proceeding parts of the flow that the tracer has travelled through. Thus this difference between streaklines and streamlines can, potentially, be misleading when interpreting the flow visualisation (Gursul, Lusseyran and Rockwell 1990).

Gursul, Lusseyran and Rockwell (1990) state that this difference between streaklines and streamlines is most significant in cases where the tracer is released in an 'arbitrary' location. For example, if the tracer is injected downstream from the generation of instabilities then a misleading interpretation could be drawn because streaklines do not immediately reveal features such as vortices (Gursul, Lusseyran and Rockwell 1990). Not until further downstream would the roll-up of the tracer be evident. Gursul, Lusseyran and Rockwell (1990) state that in shear layer flows this effect could be minimised by releasing the dye at the 'origin of the unsteady shear layer', for example, the stagnation point on a bluff body.

Figure 3.13: Photograph of the water tunnel three-dimensional cavity model.

Downstream, the streaklines show the integrated result of the upstream flow. For example, the fluid, and streaklines, may 'roll-up' in the presence of a vortical feature. Although the vortical feature itself may decay as the fluid flows downstream, the 'rolled-up' tracer on the other hand may convect downstream and could give the mistaken impression that an active vortical feature remains. An example is provided by Cimbala, Nagib and Roshko (1988, p. 271). In the example, a different flow pattern is produced depending on where a smoke wire is positioned relative to a cylinder in a crossflow.

3.3.4 Dye visualisation

In the dye visualisation, a dye solution was introduced to the flow in order to visualise the region of interest. The dye solution was fed under gravity through either: a small dye probe (small diameter tubing orientated downstream), a small dye port on the experimental rig, or a small dye slot on the experimental rig. Thereby, a dye filament or dye sheet was formed. Figure 3.14 gives an example of dye visualisation, in this instance the dye is being used to mark vorticity in the shear layer over a cavity.

The density of the dye must be close to that of the working fluid, as otherwise buoyancy effects will be significant. Therefore ordinary food colouring dye was mixed with tunnel working fluid shortly before use, to ensure the dye solution was at a similar temperature to the tunnel water; while the density

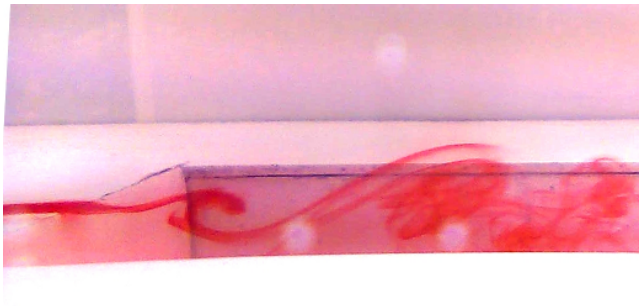

Figure 3.14: Dye visualisation example, with the dye enabling visualisation of shear layer roll-up over a cavity. Flow from left to right.

of the dye solution was adjusted by adding ethanol if required. An advantage of food colouring dyes is that they can be illuminated with ordinary lighting sources, unlike fluorescent dyes.

Another consideration is the diffusivity of the tracer. This is characterised by the Schmidt number – the ratio of momentum diffusivity to the molecular diffusivity. Compared to smoke in air (Schmidt number, $\sim$ 100–1,000), dye in water has a higher Schmidt number ($\sim$ 2,000). Therefore the dye in water diffuses more slowly compared to smoke in air, thereby showing the vorticity distribution less accurately compared to smoke in air.

3.3.5 Hydrogen bubble visualisation

The hydrogen bubble flow visualisation technique was used to visualise flow structures about the three-dimensional cavities of various geometries. In this method, fine hydrogen bubbles are created by electrolysis in order to visualise the flow. Tungsten wires were used as the negative electrode, while an arbitrary (ferrous) metal object was used as the positive electrode.

Disadvantages of the hydrogen bubble technique include the buoyancy of the bubbles, and the need to achieve suitable lighting so that the bubbles can be observed clearly. Unfortunately, this has necessitated the use of an oblique camera angle in most cases, which can make it hard to distinguish between different planes of motion, particularly with regards to three-dimensional structures.

Both horizontal and vertical orientations of the wire were used. The vertical wire was fixed to a movable support with the vertical wire held between two short horizontal prongs fixed to rigid vertical tube. The horizontal wire, on the other hand, was fixed just above the surface of the plate as shown in figure 3.15. The horizontal wire was located at a height of 4mm above the flat plate surface (y/D=0.125), and positioned 31mm upstream of the cavity leading edge (x/D=-0.42). The wire height of 4 mm compares to an estimated $\delta_{99\%}$ boundary layer thickness of 8.1 mm and boundary layer momentum thickness of 1.1 mm, from Blasius theory, for the primary free-stream testing velocity of

144 mm/s, corresponding to depth-based Reynolds number of 10,700. Thus at this depth-based Reynolds number, the non-dimensional boundary layer thickness based on the cavity depth was $\delta_{99\%}/D = 0.11$, while the non-dimensional momentum thickness based on the cavity depth was $\theta_0/D = 1.5 \times 10^{-2}$.

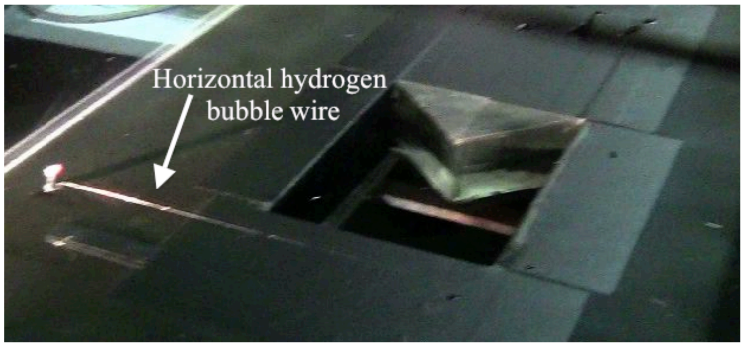

Figure 3.15: Photograph of plate showing the horizontal hydrogen bubble wire.

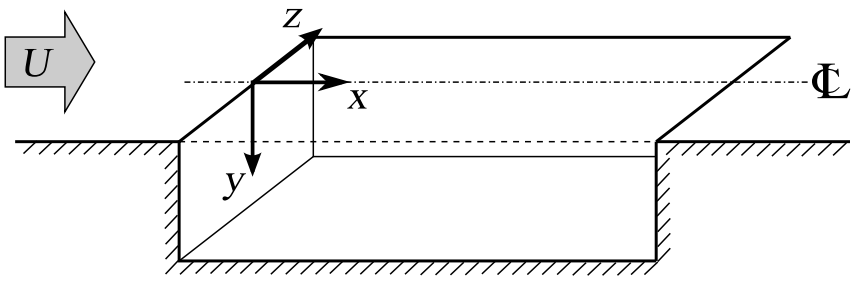

Figure 3.16: Coordinate system for hydrogen bubble visualisation of three-dimensional cavity.

Rectangular and modified cavity configurations with varying L/D ratio were tested. The testing schedule is outlined in table 3.7 while the coordinate system used in these tests is defined in figure 3.16.

3.3.6 Particle Image Velocimetry (PIV)

Particle Image Velocimetry (PIV) was used to measure the flowfield about rectangular and modified cavities. In the PIV technique, the flow is seeded by tracer particles which are illuminated by a laser sheet. A camera is then used to record the flow, whose images are then analysed using interrogation windows. The average displacement of particles in each window between frames is determined mathematically to give the velocity field. This method can provide extremely detailed information about the flow. Figure 3.17 shows a sketch of the experimental setup for PIV experiments. The methodology used for PIV is discussed in detail in Appendix A).

Table 3.7: Hydrogen bubble test schedule

(a) Velocities and Reynolds numbers

Flow velocities, mm/s	Depth-based Reynolds number
111	8,250
144	10,700[a]
186	13,800

[a] Note: primary testing Reynods number.

(b) Cavity configurations

Cavity configuration	L/D	U (mm/s)
Rectangular	0.84, 2, 3, 3.84, 4.84, 6	144
Chevron-shaped cavity	1, 2, 3.84, 5	111, 144
Other modified cavities[b]	3	144
Airfoil with cavity test (rectangular)	0.87	103

[b] Note: other modified cavities include sloped rear wall, sloped front wall & sloped rear wall, beak rear wall, chevron rear wall, chevron front wall, chevron front wall & double-swept rear wall, double-swept front wall, double-swept rear wall, double-swept front & double-swept rear wall, swept front & rear walls, swept front wall, and swept rear wall.

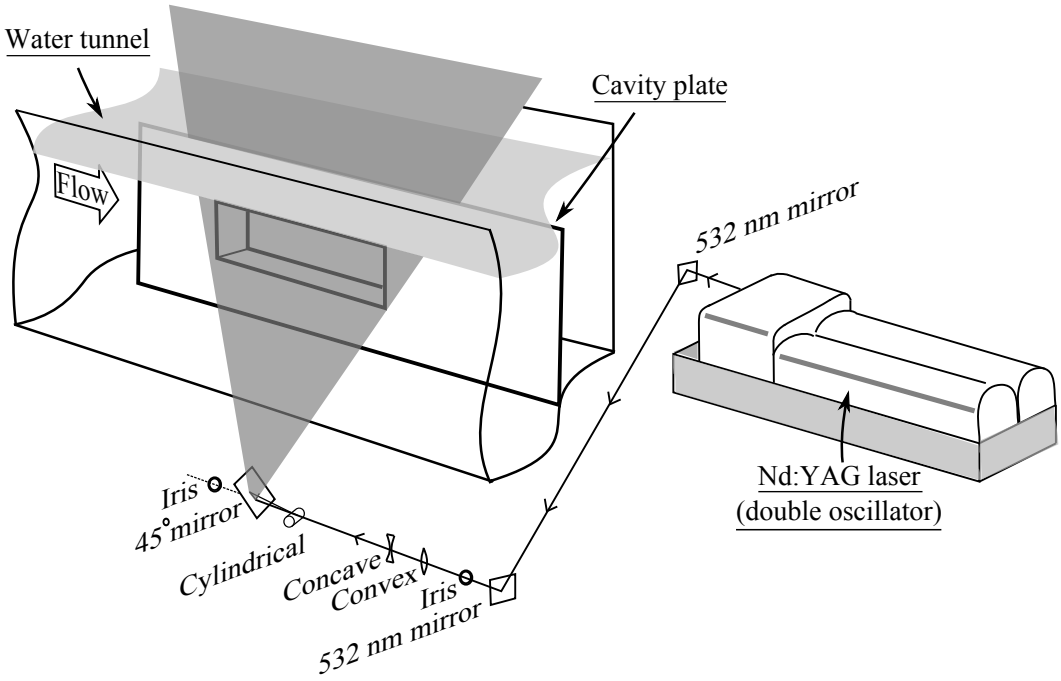

Figure 3.17: A sketch of the experimental set-up for PIV experiments.

3.4 Summary of experimental methodology

In summary, the experimental methodology consists of three main sections. Firstly, two-dimensional cavities (both rectangular and modified) are studied using an 'airfoil with cavity' model. As airfoil tonal noise was also found from this model (particularly when there was a cavity cutout present in the surface, but the flow was outside the paramater space for cavity oscillations), this was investigated to determine the aeroacoustic mechanism involved. Finally, the flow structures about and noise produced by narrow, three-dimensional cavities (both rectangular and modified) were investigated using flat-plate models containing cavity cut-outs.

Chapter 4

Two-Dimensional Cavities: Results and Discussion

4.1 Introduction

In this chapter, acoustic and velocity measurements of the two-dimensional cavity model ('airfoil with cavity') placed in the Anechoic Wind Tunnel are discussed. This model was described in section 3.2.2 of Chapter 3: Experimental Methodology & Design.

Rectangular cavities are initially investigated. The cavity depth, D, is fixed while the cavity length, L, is varied giving length-to-depth ratios of L/D = 1.17, 2.33, 3.5 and 4.67. The Reynolds numbers based on cavity depth are in the range Re_D = 3,800–15,300 while the Reynolds numbers based on the estimated momentum thicknesses are in the range $Re_{\theta_0} = 100 - 190$.

The co-ordinate systems used in this chapter of the thesis are given in figure 4.1. The 'cavity mouth length' or 'the mouth of the cavity' refers to the open portion of the cavity located along $y/D = 1$ in figure 4.1b, i.e., directly between the cavity LE and the cavity TE.

4.2 Boundary layer characteristics

Regarding the boundary layer characteristics at the leading edge of the cavity, for design purposes estimated values of δ_0 and θ_0 were used. These were based on the assumptions of a plate length equal to the horizontal distance from the nose of the model to the cavity, and a laminar boundary layer. The freestream velocity ranges from U = 10 – 40 m/s. All results listed in this chapter are recorded with the plate at a nose-down angle of attack of $\alpha_{\text{geom.}} = -1^\circ$, to ensure a slightly favourable pressure gradient over the flat plate, and thus attached flow.

To find the actual boundary layer characteristics, cavity leading edge velocity profiles were measured at nominal free-stream velocities of U = 20, 30 and 40 m/s. The velocity profile just behind the leading edge of the cavity was

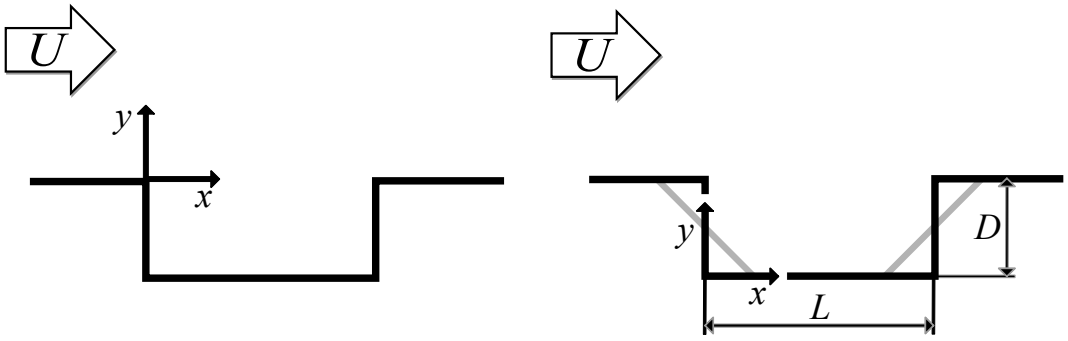

(a) Co-ordinate system for boundary layer characterisation.

(b) Co-ordinate system for rectangular and modified cavity geometries at L/D=2.33.

Figure 4.1: Co-ordinate systems used in this chapter of the thesis.

recorded using a single-wire hot wire velocity probe, which was attached to a traverse. The probe was positioned within the cavity, as close as practicable to the leading edge of the cavity. Despite the -1° angle of attack of the plate, the profile is similar in shape to the Blasius solution for flow on a flat plate at zero pressure gradient – figure 4.2 shows the case for $U = 30$m/s. This confirms that the cavity is subject to a laminar upstream boundary layer. The experimental results diverge from the Blasius solution close to the wall since the profile is taken just inside the cavity.

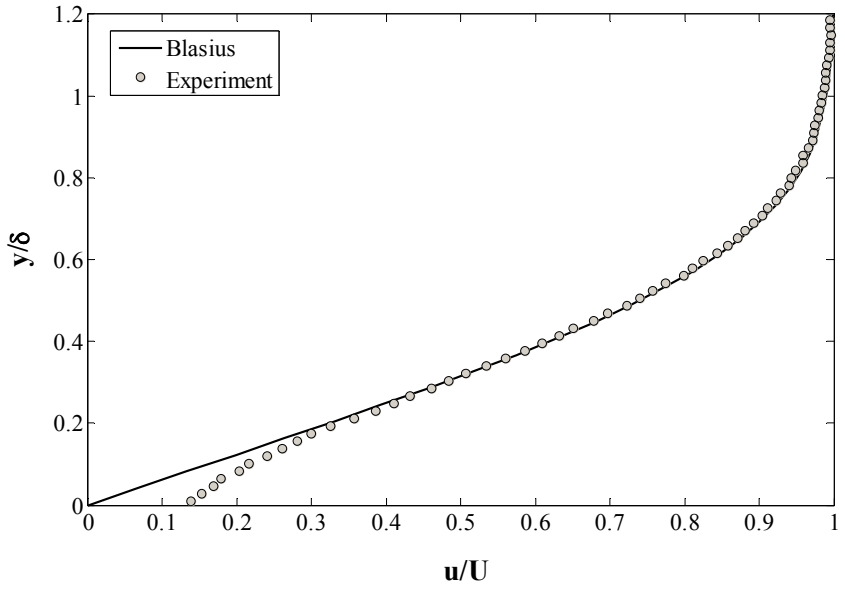

Figure 4.2: Velocity profile at cavity leading edge at $U = 30$ m/s.

Compared with the nominal free-stream velocity, the flow is accelerated slightly around the plate and over the cavity, with the highest velocity just

Table 4.1: Velocity over cavity, and boundary layer properties, estimated from measurement.

Nominal U, m/s	Velocity over cavity, m/s	Estimate for δ_0, mm	Estimate for θ_0, mm
20	23.3	0.77	0.092
30	32.5	0.68	0.083
40	43.2	0.63	0.070

Table 4.2: Blasius boundary layer estimate.

Nominal U, m/s	Velocity over cavity, m/s	Blasius δ_0, mm	Blasius θ_0, mm
20	23.3	0.73	0.097
30	32.5	0.64	0.082
40	43.2	0.54	0.071

at the top of the boundary layer. The measured velocities over the top of the cavity and boundary layer thicknesses, δ_0, estimated from these measured velocity profiles are listed in table 4.1. The values listed in the table are intended only as a guide, as the flow was already moving into the cavity, to a small extent, at the location of measurement. The velocity profiles were also extrapolated to zero and integrated to give an estimate of the momentum thickness, θ_0. The boundary layer and momentum thicknesses estimated from the measured velocity profiles were within 5–10 % of predictions from Blasius laminar flat-plate theory (table 4.2).

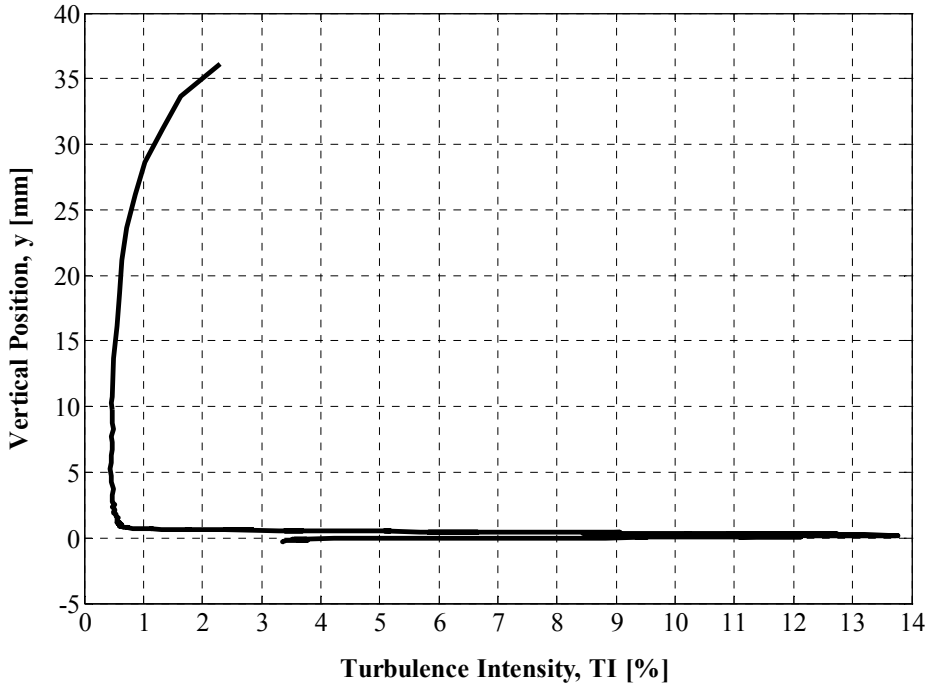

Figure 4.3: Turbulence Intensity at and above the leading edge of the cavity for $U = 30$ m/s.

Figure 4.3 shows turbulence intensity plotted against vertical position, located just downstream of the leading edge of the cavity. The turbulence intensity is based on $U_{mean}(y)$ at that height, with $TI = u'_{\text{r.m.s.}}/U_{mean}(y)$. With increasing vertical position there are firstly high values of turbulence intensity in the shear layer. The next region is the core flow of the jet with a turbulence intensity of approximately 0.4%, and then there is increasing turbulence intensity through the outside jet shear layer of the AWT facility.

As the velocity was slightly higher at the top of the cavity compared to the nominal free-stream velocity, please note that in sections 4.3 and 4.4 the nominal velocity values are listed on the plots of acoustic spectra. Furthermore, estimated values of θ_0 were considered to be sufficiently accurate for comparing the maximum cavity length criterion to the experiment.

4.3 No cavity

Figure 4.4 shows the far-field noise spectra recorded for flow over the 'No Cavity' airfoil, i.e., the airfoil with the cavity filled-in. As expected, no cavity tones are found. However, a broad 'hump' is found with a central frequency of the order of 10^3 Hz. The frequency of this hump changes with velocity. It is proposed that this 'hump' can be attributed to self-noise of the airfoil profile, specifically airfoil tonal trailing edge noise.

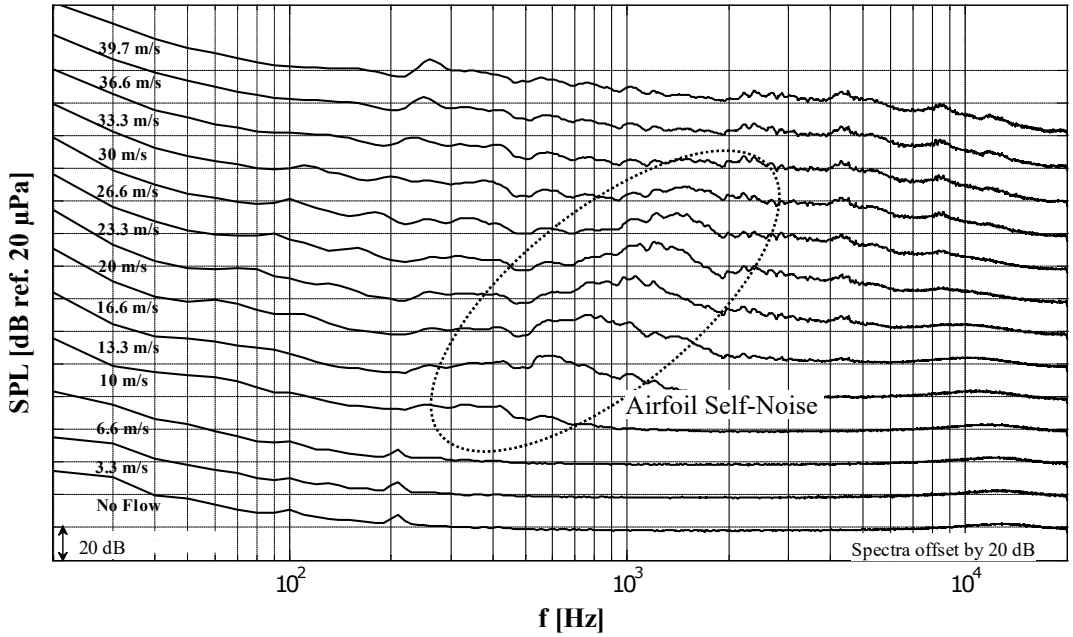

Figure 4.4: Far-field noise spectra from the smooth 'No Cavity' airfoil, i.e., the airfoil with the cavity filled-in.

Figure 4.5 compares the noise spectrum of three cases at $\mathrm{Re}_C = 10.4 \times 10^5$. Firstly, the thick grey line gives the noise spectrum for the 'No Cavity' case of the smooth airfoil, where a broad 'hump' centred at approximately 800 Hz is present. Secondly, the thin black line shows the spectrum, when there *is* a cavity present, for $L = 21$ mm ($L/D = 3.5$). For $L = 21$ mm, the broad 'hump' is not present however discrete cavity tones are present.

Finally, the thick black line gives the noise spectrum when a cavity with $L = 7$ mm ($L/D = 1.17$) is present. Interestingly, for this case not only is the broad 'hump' at 800 Hz present, but a series of discrete peaks are present about the 'hump'.

Note that for this $L = 7$ mm cavity, the cavity length is below the minimum required for the onset of cavity oscillations at this velocity. Potentially, the presence of the cavity appears to have enhanced the intensity of the airfoil self-noise. The involvement of the cavity in an airfoil tonal noise mechanism is a new finding, and is investigated separately in detail in Chapter 5.

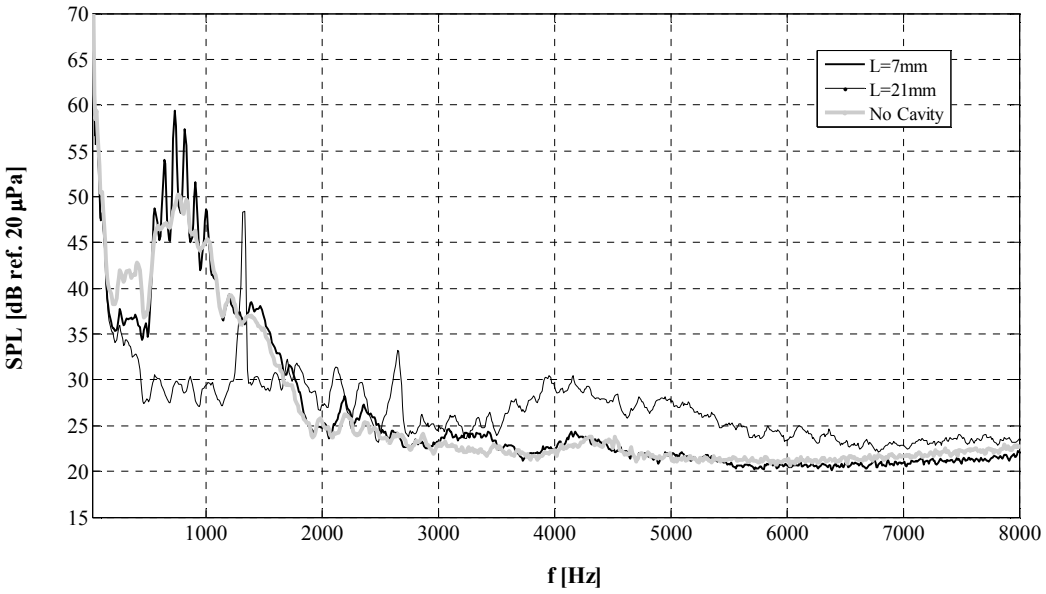

Figure 4.5: Airfoil self-noise produced by the airfoil profile, with and without cavity cutouts in the airfoil's surface. The cavity lengths were $L = 7$ mm ($L/D = 1.13$) and $L = 21$ mm ($L/D = 3.5$). The nominal velocity was $U = 16.6$ m/s, giving a chord-based Reynolds number of 1.4×10^5.

4.4 Rectangular cavities

In this section, the acoustic spectra for each of the different flow velocities for the rectangular two-dimensional cavities are presented.

4.4.1 $L/D = 1.17$

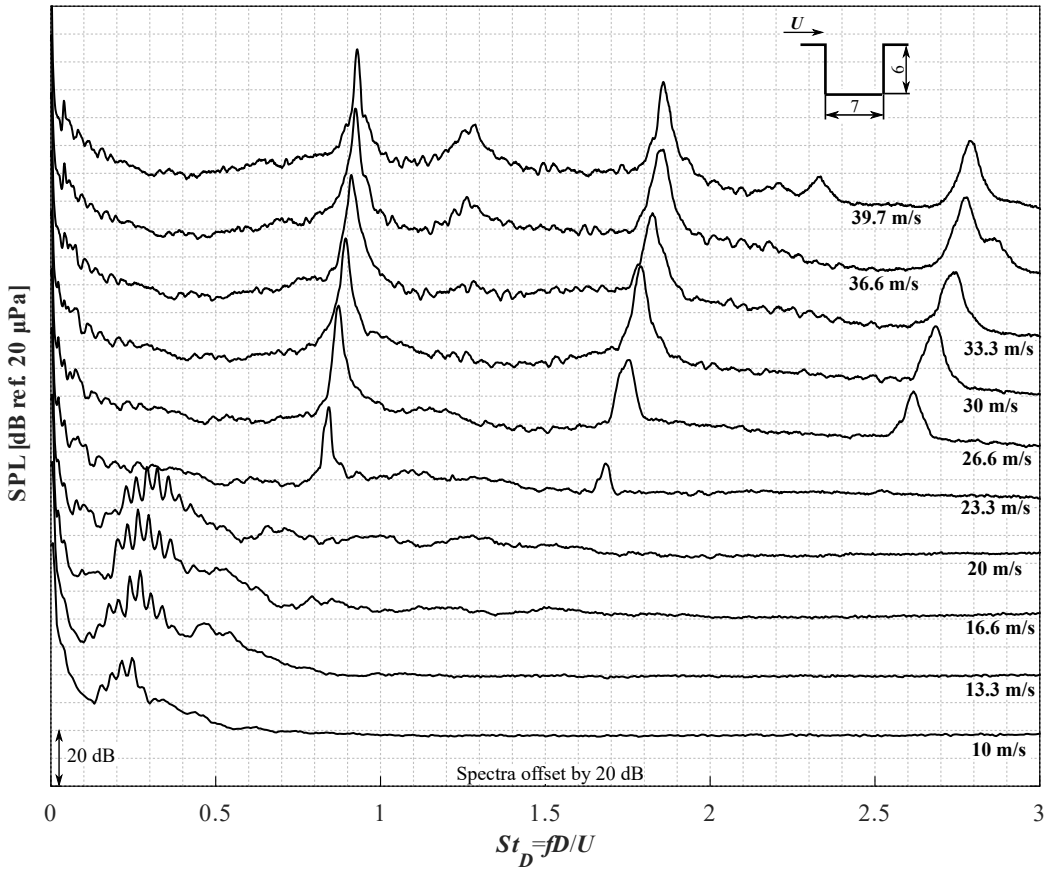

Figure 4.6: Far-field acoustic spectra for L/D =1.17. The spectra are offset by 20 dB for clarity.

Figure 4.6 shows spectra of the far-field noise recorded from the airfoil with the $L/D = 1.17$ cavity ($L = 7$ mm), across the range of flow speeds. There is a series of closely-spaced tones about a broadband hump from U =10 - 20 m/s (in the St_D range of 0.3), which is related to airfoil self-noise as stated earlier. Clear and prominent cavity tones are found for velocities upwards of $U = 23.3$ m/s, and above this velocity the airfoil self-noise is no longer evident.

In this instance, Sarohia's (1977) criterion provides an accurate indication for the occurence of cavity tones. The criterion predicts oscillations to begin from 21 m/s, and indeed cavity oscillations begin between $U = 20$ m/s and U = 23.3 m/s.

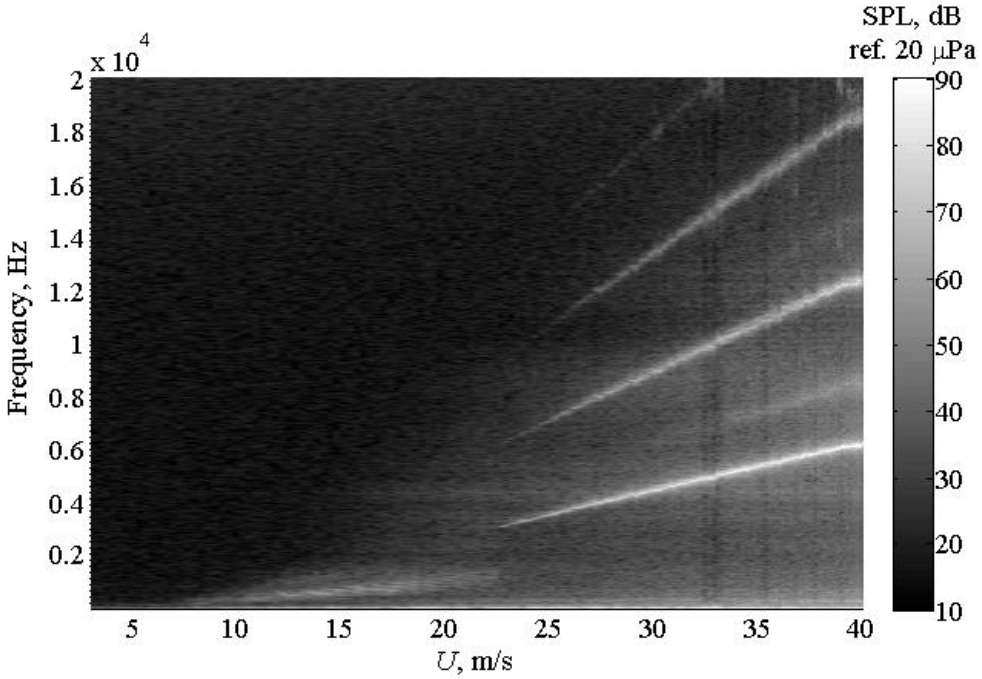

Figure 4.7: Spectrogram of far-field acoustic spectra versus velocity, for $L/D = 1.17$.

Figure 4.7 shows a velocity spectrogram of the cavity noise produced by the $L/D = 1.17$ cavity. Below approximately $U = 23\,\mathrm{m/s}$, no cavity oscillations are found (only the region of airfoil self-noise near 1 kHz). Above $U = 23\,\mathrm{m/s}$, a series of cavity tones are found. When comparing these tones to Rossiter's equation (equation 2.8), and using the mean convection velocity ratio calculated by equation 2.10 [from the data of Sarohia (1977)], it was determined that these tones are the 2nd, 4th, 6th and 8th Rossiter modes. Furthermore, the 3rd Rossiter mode is apparent above 33 m/s.

4.4.2 $L/D = 2.33$

Figure 4.8 shows noise spectra for $L/D = 2.33$ ($L = 14$ mm) across the range of velocities. It is notable that the nominal, conservative, upper cavity length criterion (above which oscillations are not necessarily expected) of $L_{\max} \approx 100\theta$ is exceeded after 10 m/s, however the oscillations continue until the highest flow speed of $U = 40$ m/s, which corresponds to $L = 200\theta$.

Figure 4.9 shows a velocity spectrogram for $L/D = 2.33$. A stage jump is present near U=17 m/s where the tones switch from one set of modes (and/or harmonics) to another. This corresponds to $L/\delta \approx 17$, while for comparison Sarohia (1977) found stage jumps at $L/\delta = 8$ and $L/\delta = 13$.

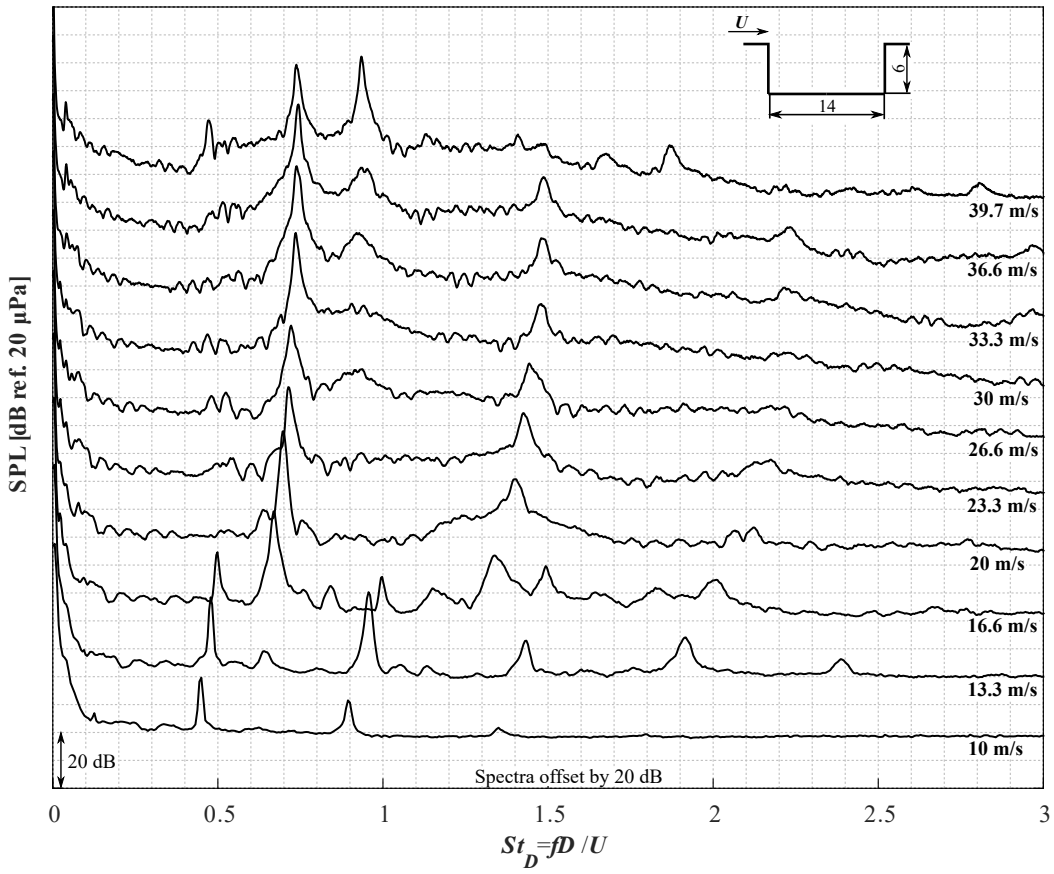

Figure 4.8: Far-field acoustic spectra for $L/D = 2.33$. The spectra are offset by 20 dB for clarity.

4.4.3 $L/D = 3.5$

Figure 4.10 shows noise spectra for the cavity with $L = 14$ mm (L/D =2.33) across the range of velocities. Upwards of $U = 30$ m/s, the tones appear to decay somewhat and they may be losing spanwise coherence. The upper criterion for cavity oscillations of $L_{\max(\text{upper})} = 200\theta$ is exceeded from upwards of 20 m/s, however the oscillations continue well in excess of this conservative criterion.

Figure 4.11 shows a velocity spectrogram for the $L/D = 3.5$ cavity. Due to the increase in cavity length dimension, the tones occur at lower frequencies compared to the shorter cavities. Also there are more modes present which can be attributed to a sharing of energy between a greater number of modes.

4.4.4 $L/D = 4.67$

For $L/D = 4.67$, the upper nominal maximum cavity length for oscillations of $L_{\max} = 200\theta$ is exceeded from upwards of 13 m/s. Figure 4.12 shows oscilla-

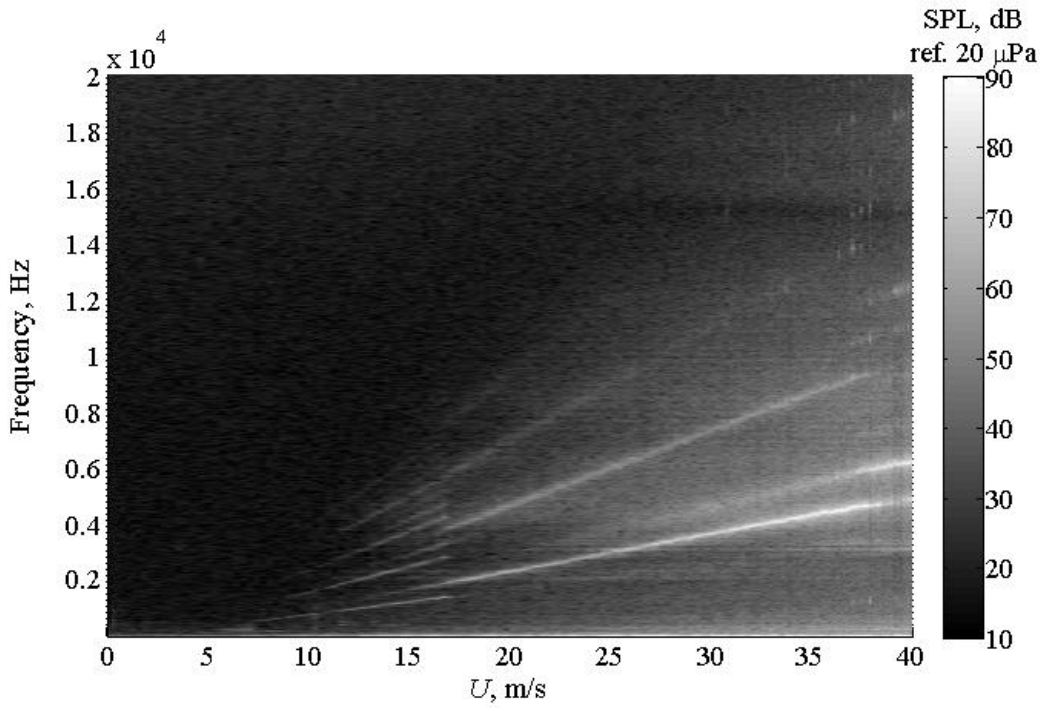

Figure 4.9: Spectrogram of far-field acoustic spectra versus velocity, for $L/D = 2.33$.

tions continue well beyond that, with cavity tones present at $U = 39.7$ m/s corresponding to $L = 370\theta$, however the tones appear to decay in amplitude as the highest velocity is approached. This would suggest that increasing flow velocity, or the cavity length, much further may result in no tonal noise.

Figure 4.13 shows a velocity spectrogram for the $L/D = 4.67$ cavity. Again, the tones occur at lower frequencies compared to the shorter-length cavities due to the additional cavity length. Furthermore, the energy in the shear layer appears to be distributed between a greater number of modes compared to the shorter cavities.

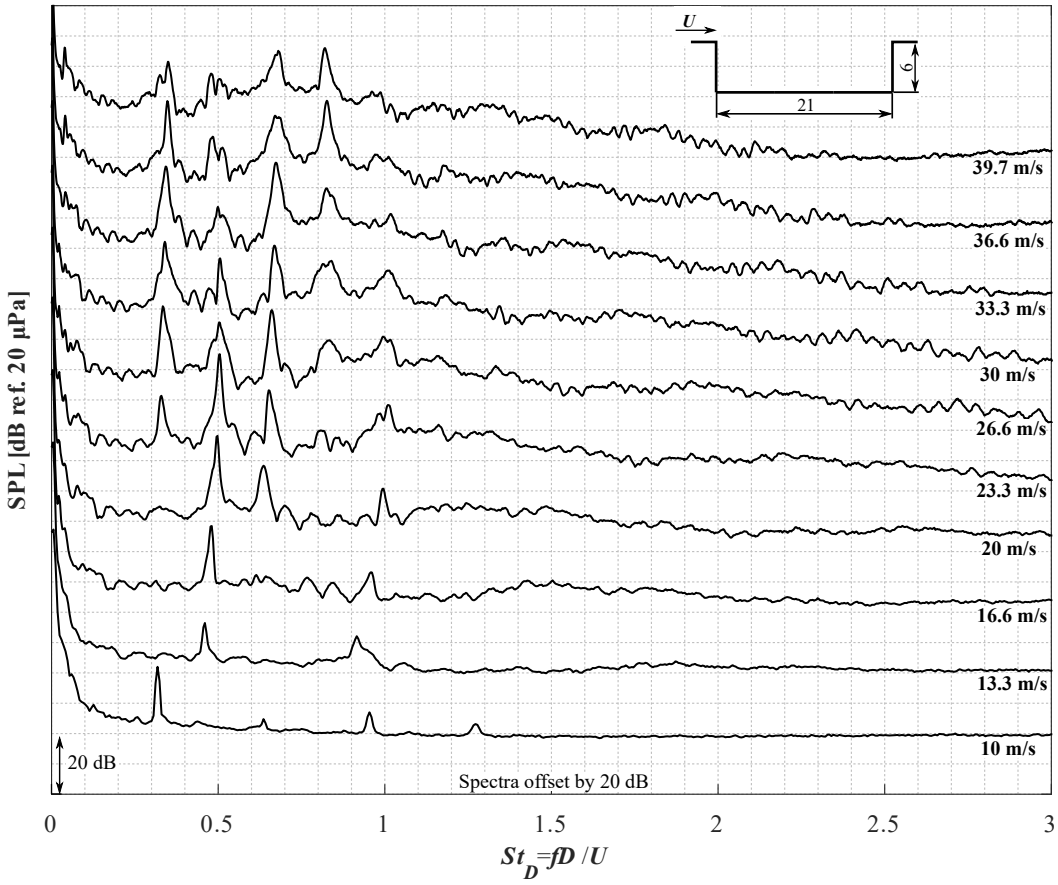

Figure 4.10: Far-field acoustic spectra for L/D =3.5. The spectra are offset by 20 dB for clarity.

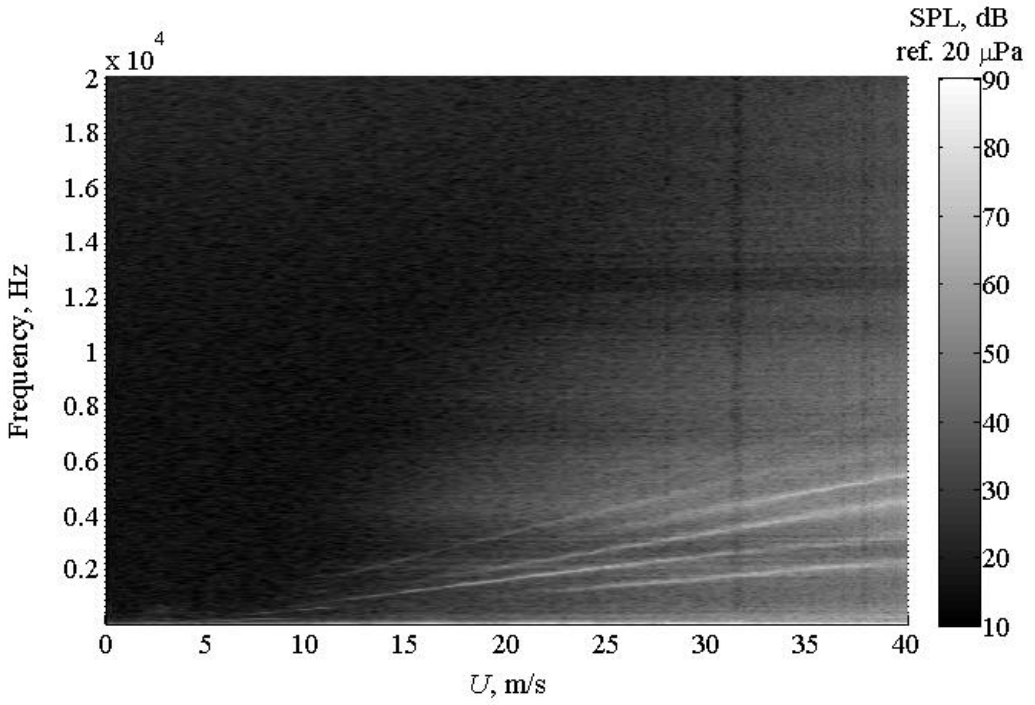

Figure 4.11: Spectrogram of far-field acoustic spectra versus velocity, for $L/D = 3.5$.

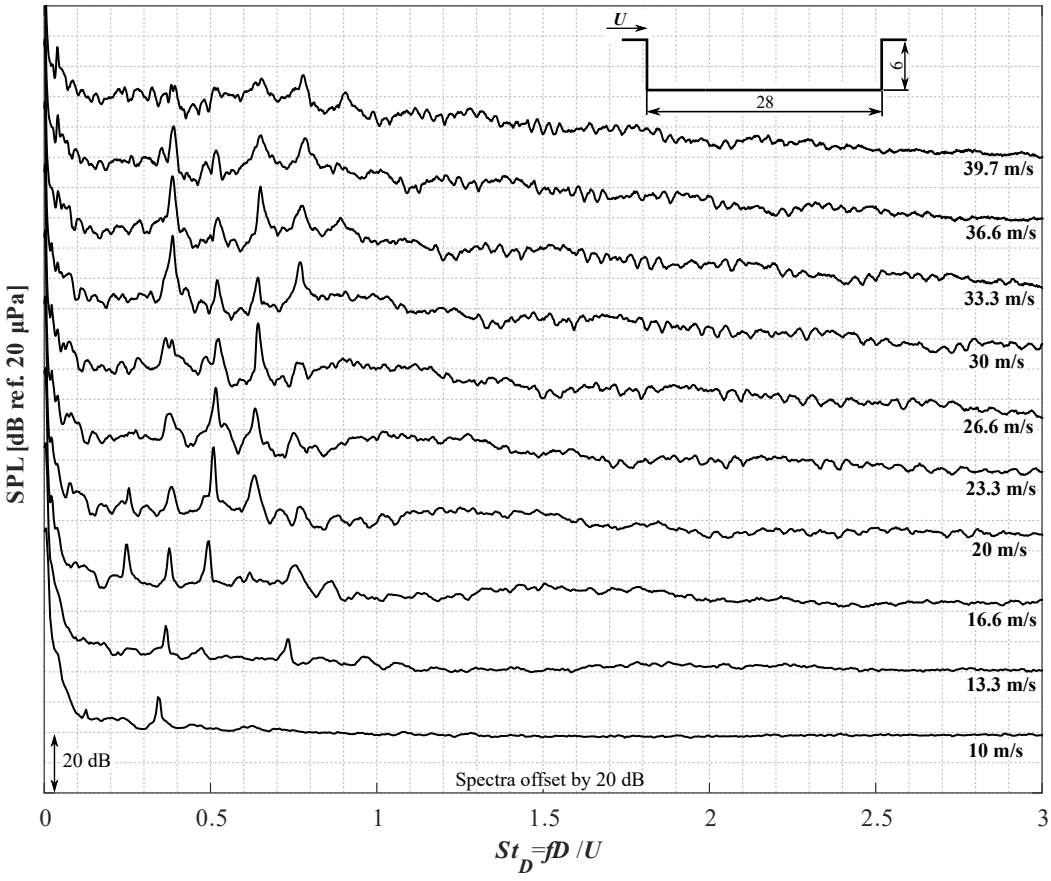

Figure 4.12: Far-field acoustic spectra for L/D =4.67. The spectra are offset by 20 dB for clarity.

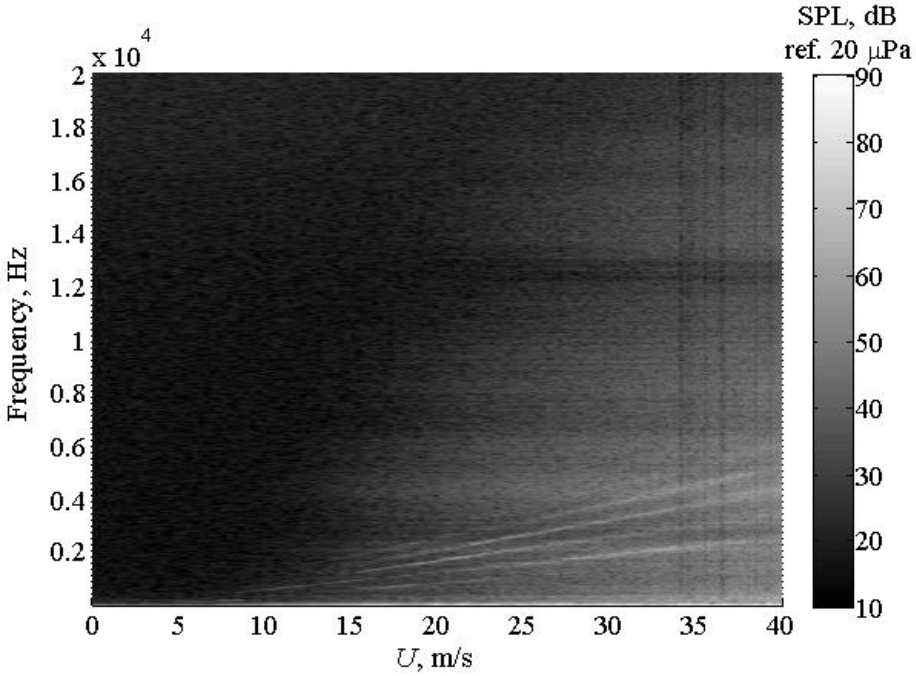

Figure 4.13: Spectrogram of far-field acoustic spectra versus velocity, for $L/D = 4.67$.

4.4.5 Overall sound pressure level produced by the rectangular cavities

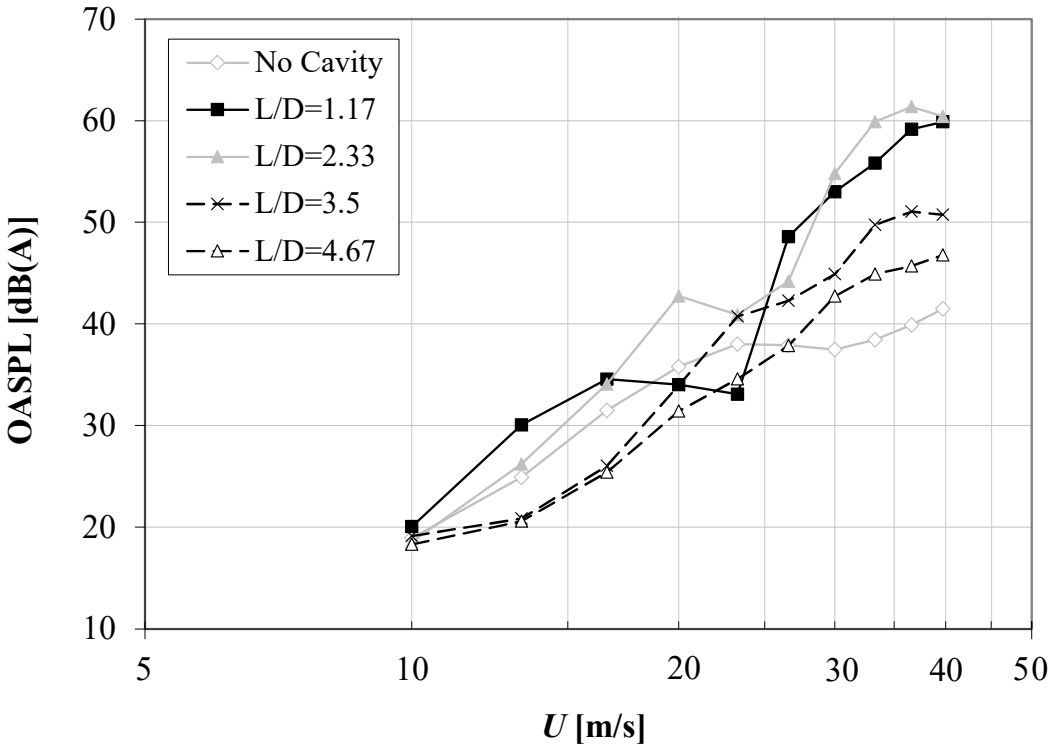

Figure 4.14: Overall sound pressure level (OASPL) in dB(A) for the rectangular cavities.

Figure 4.14 shows the overall sound pressure level (OASPL) for the rectangular cavities plotted against the freestream velocity. Upon reviewing the individual curves, a number of observations can be made.

Compared to the two higher L/D cavities, the smooth plate (with no cavity) is louder below 20 m/s due to the presence of an airfoil self-noise mechanism. This is indicated by the initial hump (between 10 and 26 m/s) before the noise levels taper off once the airfoil self-noise mechanism ceases at higher velocities. Similarly, there is a hump below 23 m/s for $L/D = 1.17$, apparently due to this cavity *enhancing* the airfoil self-noise mechanism (see Chapter 5).

The highest A-weighted sound pressure levels are produced by the two shortest cavities ($L/D = 1.17$ and $L/D = 2.33$). When the cavity noise mechanism is active, these higher noise levels can be attributed to high energy tones.

For $L/D = 2.33$, there is a dip in the OASPL either side of $U = 25$ m/s. This dip can be attributed to the presence of a stage jump. Either side of the stage jump a greater number of modes exist near the transition – hence the

OASPL is less due to the peak SPL of the tones being lower, since energy is distributed across a greater number of modes.

The longest cavity, $L/D = 4.67$, is quieter than the next longest one, $L/D = 3.5$. This can be attributed to weaker shear layer oscillations, spread between more modes.

4.5 Cavity noise mechanism

Figure 4.15(a) shows the velocity spectrum at $x/L = 0.5$ and $y/D = 1$ for $L/D = 2.33$ for a jet velocity of $U = 30$ m/s, recorded using a single-wire hot wire probe. This spectrum shows that the cavity shear layer is fluctuating at distinct cavity oscillation frequencies. The coherence between the far-field microphone signal perpendicular to the cavity and the hot-wire signal, shown in figure 4.15(b), was estimated and demonstrates that there is good coherence at the cavity oscillation frequencies of 3700 and 7400 Hz. On the other hand, the broadband noise at other frequencies is essentially uncorrelated with the velocity signal.

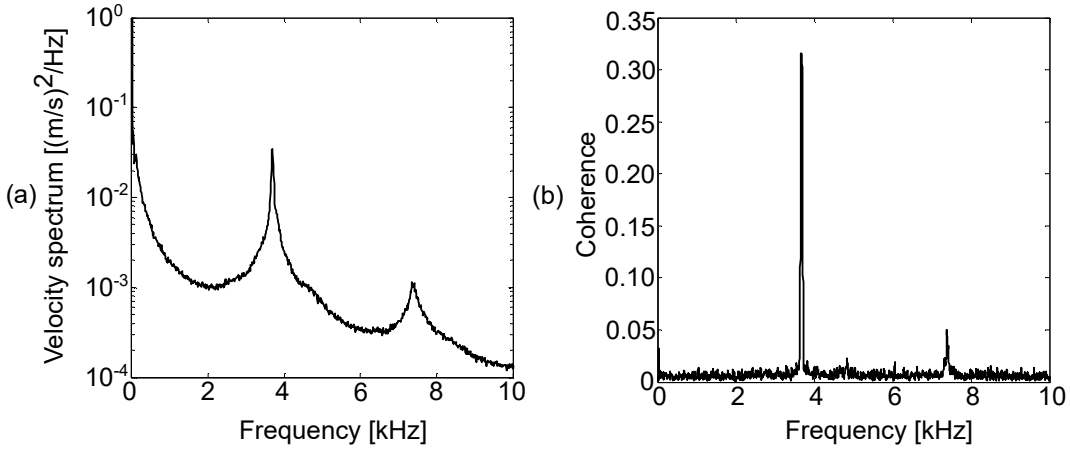

Figure 4.15: Velocity measurement at $y/D = 1$, $x/L = 0.5$, with $Re_D = 11,900$ ($U = 30$ m/s), and $L/D = 2.33$. (a) Velocity spectrum. (b) Coherence between hot-wire signal and far-field microphone signal perpendicular to the cavity.

To estimate the coherence of shear layer structures along the cavity (i.e., from the cavity LE to the cavity TE), the coherence was found between hot-wire probes located near the leading and trailing edges of the cavity (figure 4.16). The length of the spacing between the probes was at least 75% of the length of the cavity. The probes were offset laterally slightly, to avoid the wake of the first probe interfering with the measurement of the second probe.

The coherence (at the cavity tonal frequencies) was found to be greatest at $L/D = 1.17$ (figure 4.16a) and decrease significantly with increasing L/D, with much lower coherence found at $L/D = 4.67$ (figure 4.16d). This is consistent

with a greater 'break down' of shear layer structures, along the length of the cavity, as L/D increases. I.e., the large, organised, periodic shear layer vortical structures break down into smaller, and less regularly timed, vortical structures as cavity length is increased (with other parameters held constant).

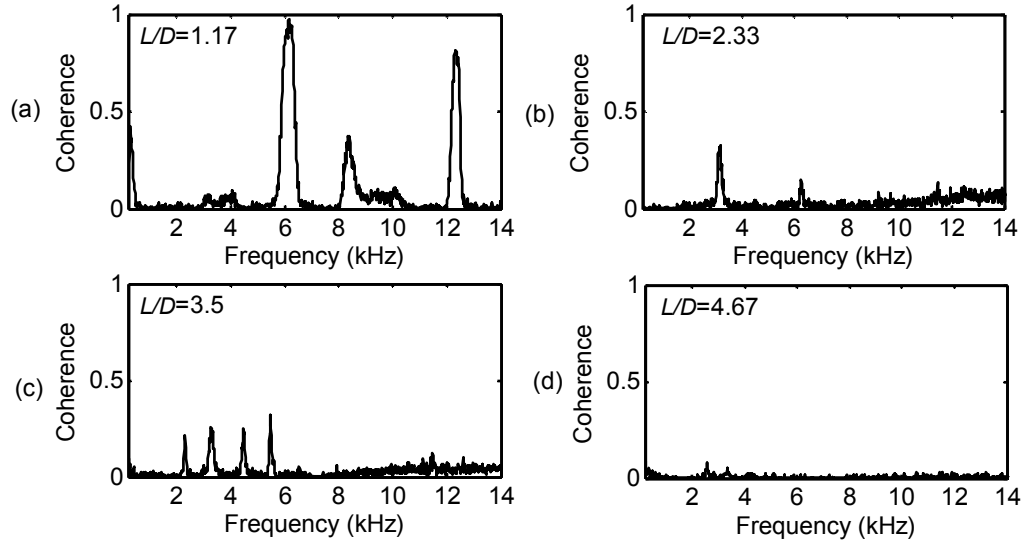

Figure 4.16: Coherence between two hot-wire probes located within the shear layer near to the leading and trailing edges of the cavity respectively, at a depth-based Reynolds number of $Re_D = 18,500$ ($U = 40$ m/s).

4.6 Modified 2D cavities

In this section, far-field noise and velocity spectra are presented to illustrate the effect of sloped wall geometric modifications on two-dimensional cavities. In each instance, the cavity volume was held constant. Results are primarily presented at the depth-based Reynolds number of 11,900, corresponding to $U = 30$ m/s. The far-field microphone was located perpendicular to the airfoil at a distance of 0.6 m.

4.6.1 $L/D = 1.17$

The sloped rear wall at $L/D = 1.17$ gave a 5 dB ref. 20μPa reduction in sound pressure level of the main tone and more significant reductions of over 10 dB ref. 20μPa for the next two tones (figure 4.17). There was a reduction of about 6 dB ref. 20μPa of the amplitude of the fourth tone. Interestingly, the tones appear to be shifted to a slightly higher frequency in the modified cavity, which is unexplained since owing to the cavity mouth length being longer, lower frequency tones would be expected. One explanation could be that the

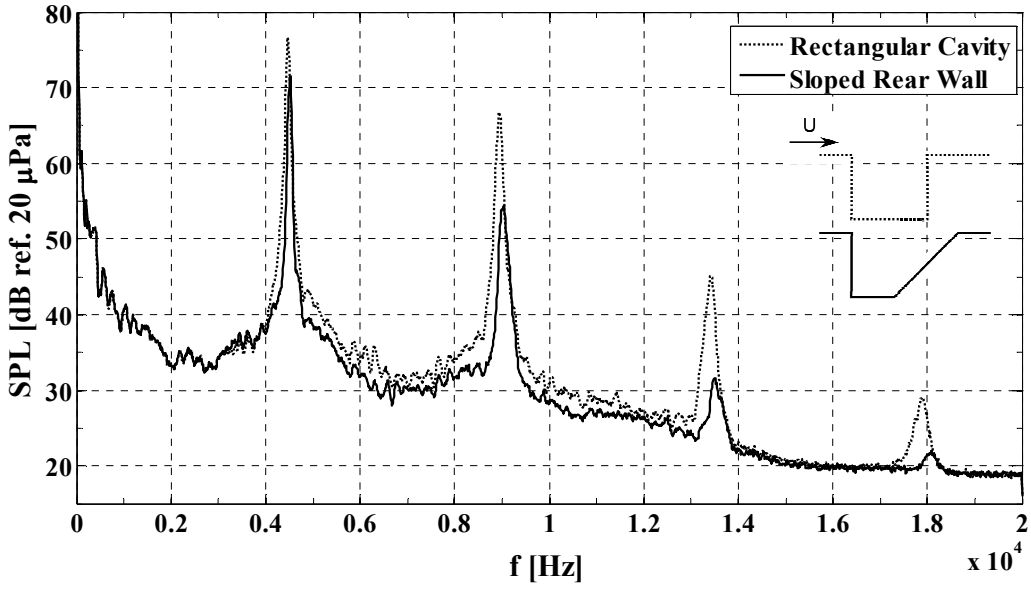

Figure 4.17: Comparison of far-field acoustic spectra produced by rectangular cavity and cavity with sloped rear wall at $L/D = 1.17$, for $Re_D = 11,900$ ($U = 30$ m/s).

sloped rear wall cavity presents a lower resistance to the flow, therefore the flow velocity over the cavity is higher, and thus oscillation frequencies are higher.

For $L/D = 1.17$, the reverse sloped rear wall eliminated the tones completely (figure 4.18). As the cavity volume was maintained constant, therefore the 'mouth' of the cavity was reduced in length. The large reduction is due to the cavity being too short for oscillations to occur. When this cavity does indeed start to oscillate, at higher flow velocity, it is louder than the rectangular cavity. This might be expected due to the presence of the sharper trailing edge on which the shear layer impinges.

Figure 4.19 shows the overall sound pressure level (OASPL) for the rectangular and modified cavities at $L/D = 1.17$. The figure shows that the sloped rear wall cavity typically produces a lower OASPL than the rectangular cavity.

Note that below 23 m/s, none of the cavities produce cavity tones. Below 23 m/s, the cavity with the reverse sloped rear wall exceeds the OASPL of the other two.

Between 23 m/s and 36 m/s, the rectangular and sloped rear wall cavities are producing tonal noise with the sloped rear wall cavity contributing to an attenuation of the OASPL. In this range, the reverse sloped rear wall cavity is yet to produce cavity tones, due to its effectively shorter, and thus insufficient, cavity mouth length.

Above 36 m/s, the reverse sloped real wall produces the highest OASPL. This can be attributed to shear layer vortices (turbulence) striking a sharp edge, thus enhancing feedback resulting in strong radiation. The sloped rear

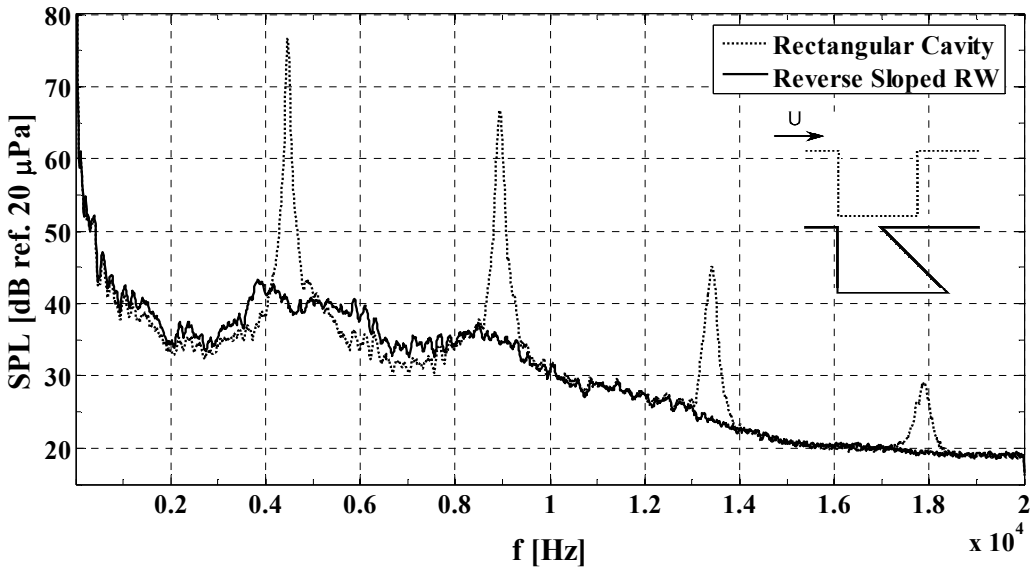

Figure 4.18: Comparison of far-field acoustic spectra produced by rectangular cavity and cavity with reverse sloped rear wall at $L/D = 1.17$, for $Re_D = 11,900$ ($U = 30$ m/s).

wall continues to provide an attenuation of OASPL, compared to the rectangular cavity.

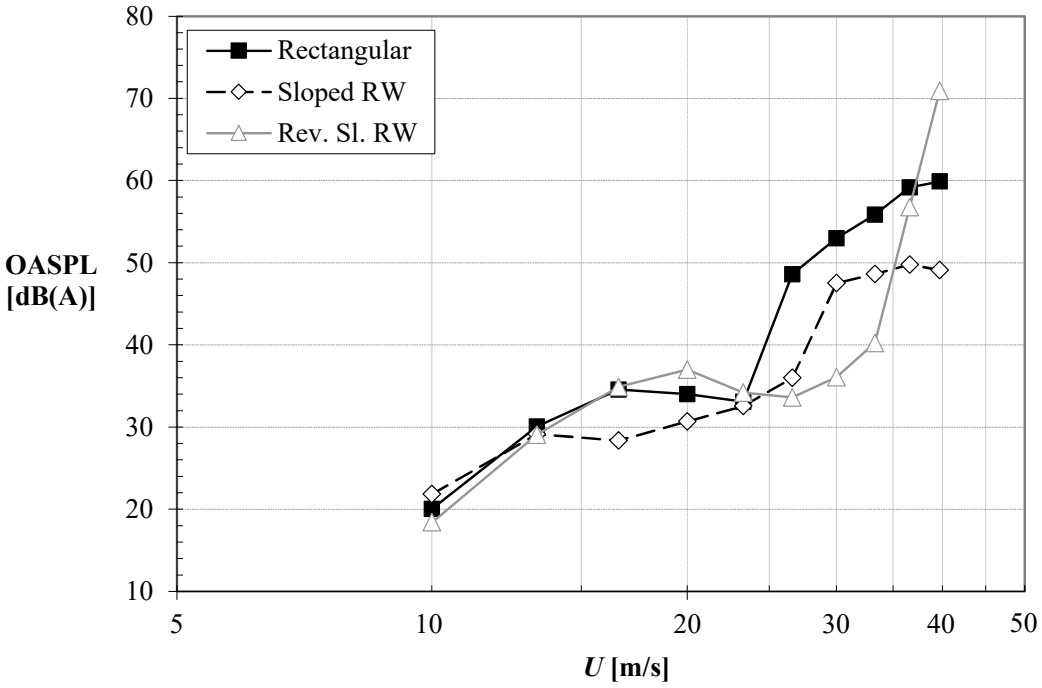

Figure 4.19: Overall sound pressure level recorded for the rectangular and modified cavities at $L/D = 1.17$.

4.6.2 $L/D = 3.5$

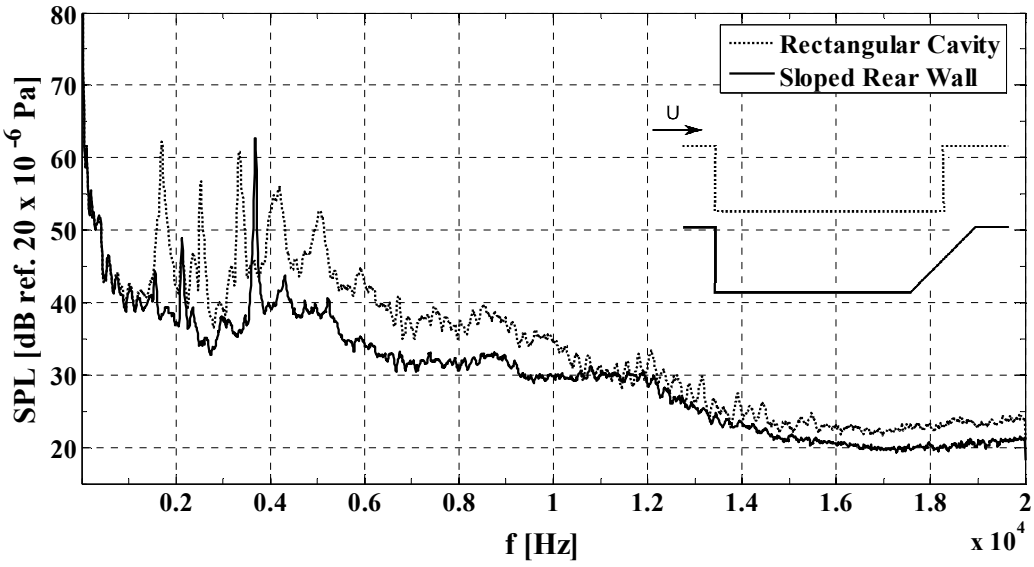

Figure 4.20: Comparison of far-field noise spectra from rectangular and sloped rear wall cavities for $L/D = 3.5$ at $Re_D = 11,900$ ($U = 30$ m/s).

Figure 4.20 shows the far-field noise spectra for the $L/D = 3.5$ cavity with the sloped rear wall. There is a reduction in broadband noise levels across the majority of the frequency range, especially between 6 and 10 kHz. Although there is no reduction in the peak tonal amplitude, there is a reduction in the number of major tones present in the far-field noise spectra from five to two. There is also a shift in tonal frequencies

Figure 4.21 shows the far-field noise spectra for the $L/D = 3.5$ cavity, with the reverse sloped rear wall. The figure shows that with the reverse sloped rear wall tonal amplitudes are up to 20 dB higher compared to the rectangular cavity and there are multiple major tones present. There is also a significant increase in broadband noise across a wide range of frequencies. The broadband noise level is increased by approximately 10 dB ref. 20 μPa between 4 and 10 kHz. This can be attributed to a stronger radiation of broadband noise as turbulence impinges on the sharp trailing edge of the cavity.

The OASPL produced by the rectangular and modified cavities with $L/D = 3.5$ are plotted in figure 4.22. The reverse sloped rear wall produces an increase in OASPL compared to the rectangular cavity, while the sloped rear wall produces an attenuation of OASPL compared to the rectangular cavity. Respectively, this can be attributed to the sharper impingement edge of the reverse sloped rear wall, and possibly the partial deflection of the shear layer and acoustic feedback out of the cavity by the sloped rear wall.

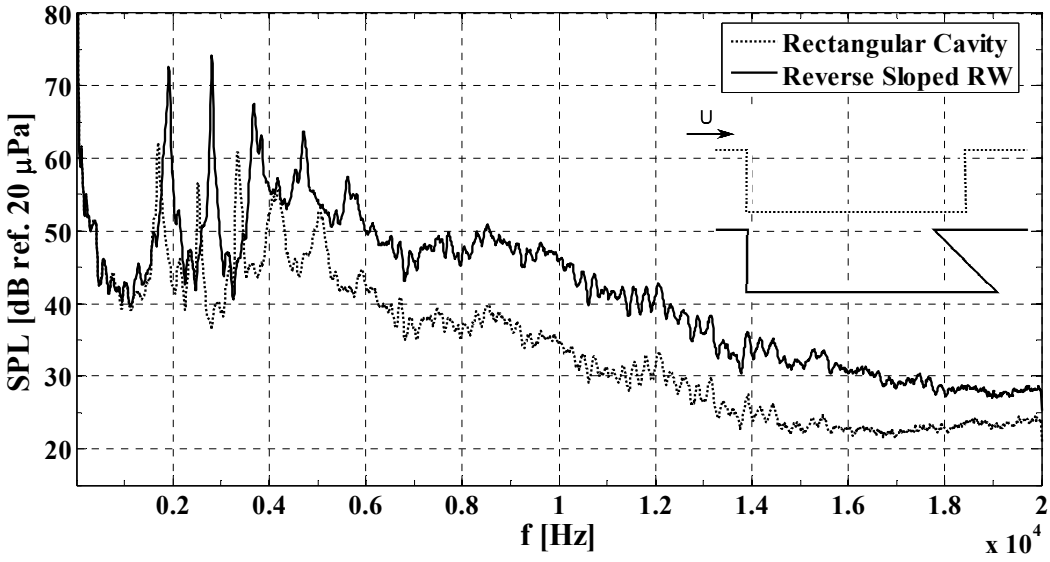

Figure 4.21: Comparison of far-field noise spectra from rectangular and reverse sloped rear wall cavities for $L/D = 3.5$ at $Re_D = 11,900$ ($U = 30$ m/s).

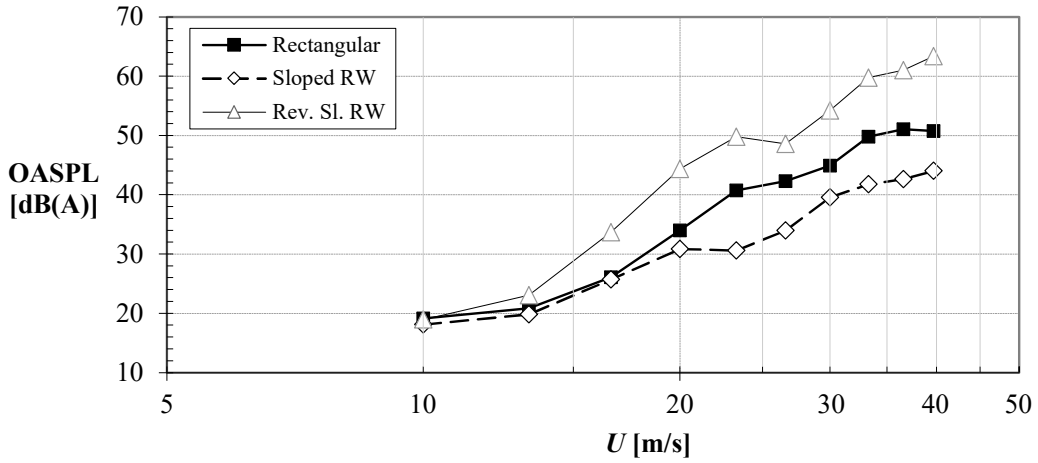

Figure 4.22: Overall sound pressure level recorded for the rectangular and modified cavities at $L/D = 3.5$.

Table 4.3: Attenuation of overall sound pressure level (OASPL) of modified cavities, compared to rectangular cavity, at $L/D = 2.33$.

Jet velocity (m/s)	Attenuation compared to rectangular cavity (dB)		
	Sloped Front Wall	Sloped Rear Wall	Sloped FW & Sloped RW
20	0.4	7.3	7.6
25	3.0	3.4	12.1
30	8.7	10.8	17.5
35	5.5	11.1	18.0

4.6.3 $L/D = 2.33$

The most extensive investigation of modified cavities was conducted for $L/D = 2.33$. The rectangular cavity was compared to cavities with a sloped rear wall, sloped front wall and a combination of sloped front and rear walls. The volume of the cavity was kept constant in each case, with the front and rear cavity walls being sloped at 45° about a midpoint at the rectangular cavity wall position (figure 4.1b). The cavity mouth length was 6 mm longer with the sloped front and rear wall combination, and 3 mm longer with sloped front or rear wall individually. Thus the 'geometric' L/D ratios, if L was taken to be the cavity mouth length, were 3.33 and 2.83 respectively – however this was not reflected in the volume of the cavities which remained constant. Note that velocity measurements were only recorded for the rectangular and combination-sloped front and rear wall cases at $L/D = 2.33$.

The attenuation of unweighted overall sound pressure level (which was taken from 200 Hz to 20 kHz, as below 200 Hz the noise spectrum was dominated by extraneous facility noise) is given in table 4.3. The greatest attenuation was found for the combination of sloped front and rear walls. It was found that the combination of sloped front and rear walls was more effective as a passive control measure than either modification individually.

A notable observation from table 4.3 is the very large reduction in OASPL for the cavity with the combination of sloped front and real walls. This geometry combines multiple methods that disrupt the cavity noise and feedback loop mechanisms. Although the cavity feedback loop is not completely absent, it is substantially decreased in intensity.

Figure 4.23 shows a comparison of far-field acoustic and velocity spectra for the rectangular and modified (combination of sloped front and rear wall) cavities with $L/D = 2.33$ at $Re_D = 11,900$. Noise and velocity spectra are presented for one velocity, as this was representative of the behaviour at other velocities. Regarding the peak tonal sound pressure levels, both the sloped front wall cavity and the sloped rear wall cavity produced an attenuation of the peak far-field SPL of 13 dB. A significantly larger attenuation was produced by the combination of sloped front and rear walls, where the peak tonal SPL was reduced by 21 dB.

The sloped rear wall modification is assoicated with reduced broadband noise compared to the rectangular cavity [figure 4.23(b)]. As cavity broadband noise is primarily generated by the interaction of shear layer turbulence with the sharp trailing edge, the sloped rear wall appears to alleviate some of this interaction, thus reducing the production of broadband noise across a range of frequencies. With the sloped front wall only, where the sharp trailing edge is still present, there is no reduction in broadband noise level [figure 4.23(a)].

A comparison of velocity spectra between the rectangular and combination-sloped front and rear wall cavity is shown in figure 4.23(d). The location of the velocity measurement is towards the rear of the cavity just above the cavity mouth line. As there are many tones in the spectrum of the modified cavity, the tones have been labelled for reference. Frequencies (a), (c) and (d) correspond to those found in the far-field noise spectrum [figure 4.23(c)].

Frequency (b), despite having a strong magnitude in the velocity spectrum, does not appear to be involved in far-field noise production or is involved at a much lower level. Indeed, considering the evolution of the velocity spectra at four locations along the cavity [$x/L = 0.14$–0.74, figure 4.24(b)] shows that frequency (b) is present all along the cavity. This suggests frequency (b) may be due to an extraneous source, which is suspected to be an electrical signal from the wind tunnel's fan controller. By comparison, the other tonal frequencies increase in intensity towards the rear of the cavity.

Frequencies (e)-(i) are either not involved in far-field noise production, or are involved below background levels. Additionally, there is a possible peak in the acoustic spectrum at approximately 4.5 kHz [figure 4.23(c)], which may be just below the broadband levels in the velocity spectrum [figure 4.23(d)].

There are a number of possible explanations for the differences in tone locations between the rectangular cavity and the cavities with either sloped front or rear walls. These could perhaps be attributed to the 3 mm longer cavity mouth length, such that differences in impingement location or a stage shift might be causing the differences in frequency between these cases. To clarify, for the sloped front and rear walls together (at a cavity volume equivalent to $L/D = 2.33$, figure 4.23(c)), some of the tones align quite closely with those for $L/D = 3.5$ cavity (figure 4.10) which has a 1mm longer effective cavity mouth length. The tones are found at 1690, 3470, 4060 Hz for the sloped front and rear walls together compared to 1700, 2520, 3350 and 4180 Hz for

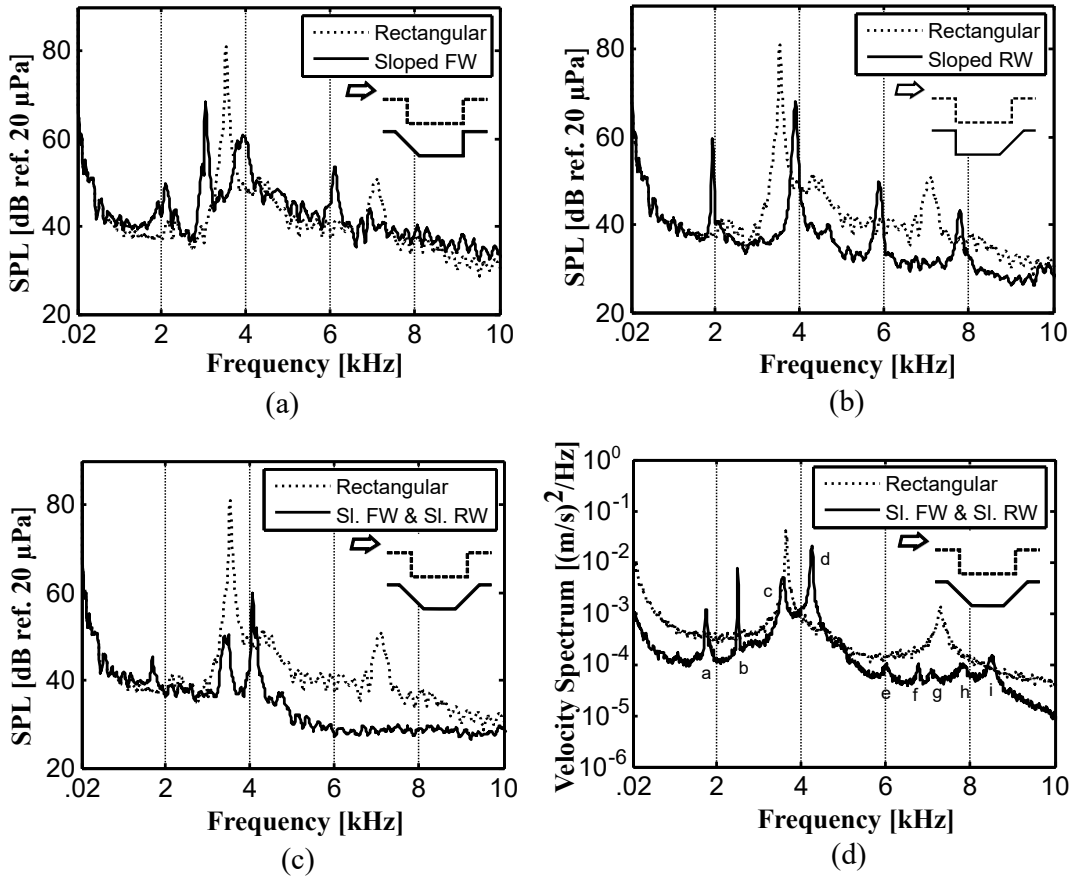

Figure 4.23: Spectra comparison for rectangular and modified cavities at $L/D = 2.33$, where $Re_D = 11,900$ ($U = 30$ m/s). (a) Far-field acoustic spectra of sloped front wall cavity. (b) Far-field acoustic spectra of sloped rear wall cavity. (c) Far-field acoustic spectra of combination sloped front and rear wall cavity. (d) Velocity spectra at $x/L = 0.79$ and $y/D = 1.16$ for sloped front and sloped rear wall cavity.

the $L/D = 3.5$ cavity. It appears that fewer modes are being amplified in the modified cavity which could be related to the reduced feedback. It could also be related to the different internal flow structure of the modified cavity and the role this may play a role in contributing to the deflection of the shear layer.

Figure 4.24 shows further velocity measurements of the rectangular and modified cavities. The development of the shear layer along the cavity is shown in figure 4.24(a) & (b). The development of tonal oscillations with increasing x/L can be seen (putting aside frequency 'b', mentioned in figure 4.23 earlier, which is probably an extraneous disturbance).

Figure 4.24(a) shows velocity spectra for the rectangular cavity case at $y/D = 1.04$, while figure 4.24(b) shows similar spectra at equivalent positions for the modified cavity. In the upstream part of the cavity, in both cases, a broad hump at approximately 4050 Hz is initially excited close to the leading

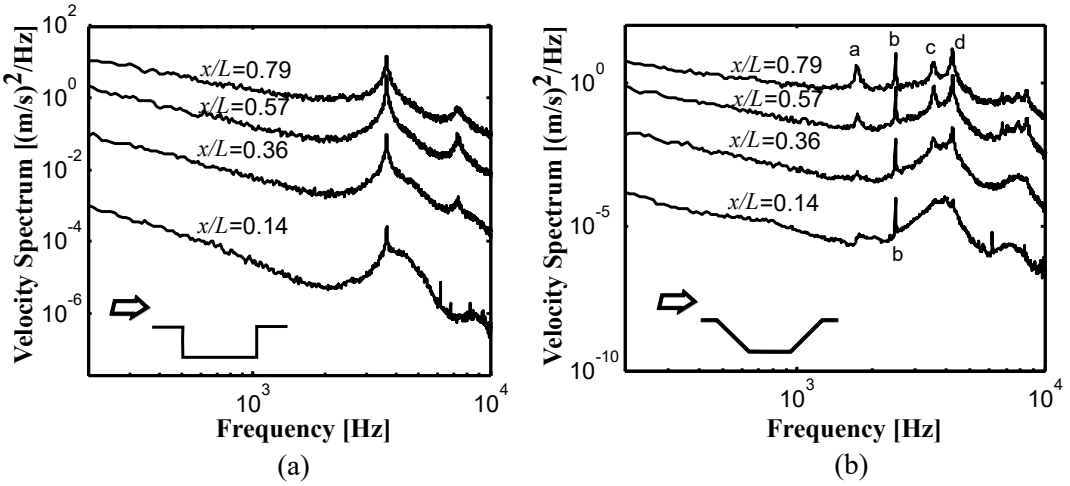

Figure 4.24: Velocity spectra along the shear layer of rectangular and combination sloped front & rear wall cavities. $L/D = 2.33$, $Re_D = 11,900$, and nominal jet velocity, $U = 30$ m/s. Velocity spectra are offset by an order of magnitude for clarity. (a) Velocity spectra at various streamwise positions for rectangular cavity case at the height y/D=1.04. (b) Velocity spectra at various streawise positions for sloped front wall and sloped rear wall cavity case at the height y/D=1.04.

edge of the cavity. For the modified cavity, there is initially a second broad hump at approximately 7600 Hz. Further along the cavity, a number of tones are selectively amplified. Two tonal oscillation frequencies are excited in the case of the rectangular cavity, while more than four are excited in the case of combined sloped front and rear walls. However, in the modified cavity, the energy appears to be spread between a larger number of modes, each having a lower intensity of oscillation.

Figures 4.25(a) and 4.25(b) show velocity profiles along the cavity, for both cases. Figure 4.25(a) supports the expectation that the shear layer has deflected into the cavity more for the modified case, owing to the sloped front wall configuration and a more upstream separation point compared to the sharp leading edge. On the other hand, figure 4.25(b) shows that the fluctuation velocity magnitude is slightly less for the modified cavity compared to the rectangular one.

4.6.4 Discussion regarding 2D modified cavities

The effect of two-dimensional sloped front and/or rear walls at various L/D ratios has been investigated. The lower noise levels of the modified cavities are attributable to a variety of actions, as discussed in the following paragraphs.

Sloped front wall Sloping the front wall produces a reduction in tonal levels but no reduction in broadband levels. By delaying separation (i.e., the flow is attached around the corner before separating, unlike the immediate separation caused by the sharp leading edge), the sloped front wall may promote a thicker, more stable, shear layer – therefore subject to less amplification of coherent disturbances and lower tonal amplitudes. The sloped front wall, on its own, does not provide a reduction in broadband noise levels. This is because shear layer turbulence still impinges on the sharp cavity trailing edge, contributing to the radiation of broadband noise.

Sloped rear wall The sloped rear wall is responsible for a reduced broadband noise component of cavity noise. This can be attributed to the absence of a sharp trailing edge for shear layer turbulence to impinge upon. Since the broadband noise is primarily generated by the interaction of turbulence with the cavity TE, when this interaction is alleviated by the sloped rear wall there is a reduction in broadband noise generated by the cavity.

A reduction in tonal noise levels is also found with the sloped rear wall. This can be attributed to a reduction in the impingement of coherent disturbances on the rear of the cavity, thus reducing feedback and subsequently amplification. That is, weaker acoustic waves are created, thereby reducing the feedback supplied to the initial region of the shear layer. Similarly, the angled nature of the wall may direct the acoustic waves out of the cavity, rather than towards the leading edge, also reducing feedback.

Combination of sloped front and rear walls When the front and rear sloped walls are used together, the attributes of both modifications are combined. The combined effects of the sloped front wall in stabilising the shear layer (by delaying separation) and the sloped rear wall in reducing feedback, contribute to the largest attenuation of tonal noise levels compared to the rectangular cavity. Meanwhile, the sloped rear wall produces an attenutation of broadband noise levels across a wide range of frequencies.

Reducing cavity length Reducing the effective cavity length, i.e., the length of the cavity seen by the flow, to below the minimum required for the onset of oscillations will eliminate the cavity tones completely (even though the volume of the cavity is maintained constant). Where possible, this is a very effective means to reduce overall cavity noise levels (which typically are dominated by the strong cavity tones, if they are present).

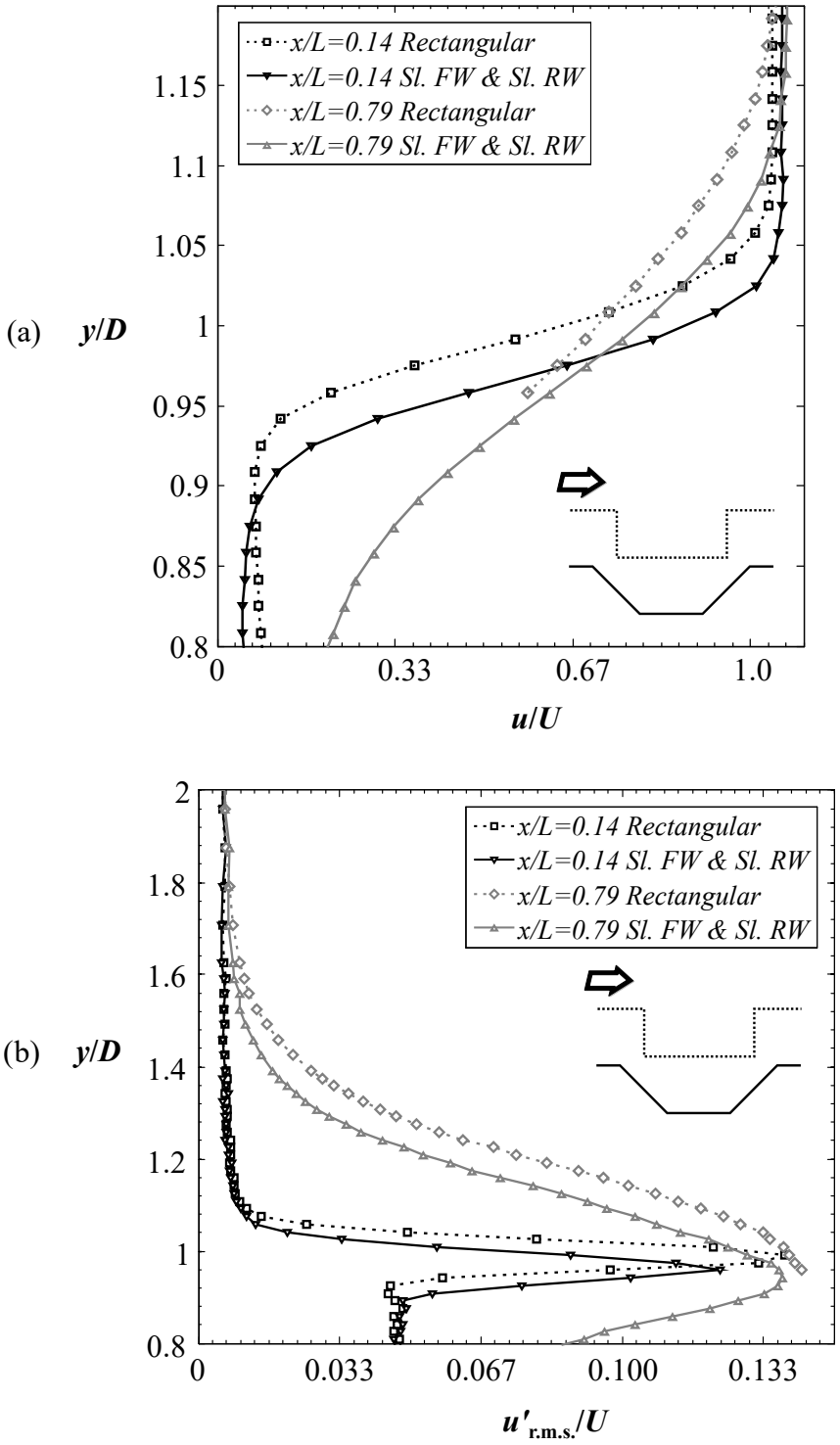

Figure 4.25: Streamwise velocity profiles normal to rectangular and combination sloped front & rear wall cavities. $L/D = 2.33$, $Re_D = 11,900$, and nominal jet velocity, $U = 30$ m/s. (a) Normalised velocity. (b) Normalised root-mean-square fluctuation velocity.

4.7 Mean convection velocity ratio

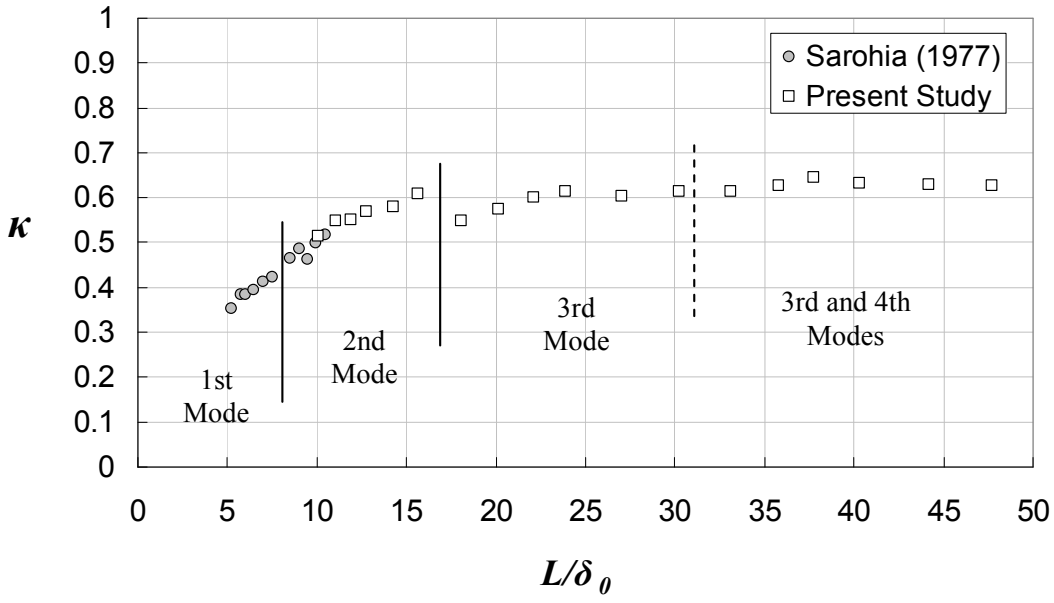

Figure 4.26: Mean convection velocity ratio, $\kappa = U_c/U$, versus non-dimensional cavity length, L/δ_0. The dominant mode number, for each region, is indicated.

The mean convection velocity ratios, $\kappa = U_c/U$, across the cavity were estimated empirically based on the recorded far-field cavity tone frequencies and Rossiter's equation, equation 2.8 [with the knowledge that α, the phase lag, is typically zero, (Milbank 2004)]. These are plotted in figure 4.26. A range of L/δ_0 ratios were achievable by varying the L/D ratio and by varying the boundary layer thickness, δ_0 (by varying the freestream velocity). Estimated boundary layer properties based on the Blasius relation for a laminar boundary layer have been used. In the literature, Sarohia (1977) measured the convection velocity ratio directly using the cross-correlation between two hot-wire probes. Sarohia's (1977) data are also plotted in the figure and the present data appear to be consistent with these.

In figure 4.26, the solid vertical lines represent stage jumps. The dominant cavity modes in each region are listed. Sarohia identified a stage jump between the first and second modes at approximately $L/\delta_0 = 8$. Milbank (2004, p. 158) identified a stage jump between the second and third modes at approximately $L/\delta_0 = 14.6$ with the third mode first appearing at $L/\delta_0 = 13.0$. In the present study, the third mode was first noticeable above background noise levels at $L/\delta_0 = 15.7$. Between $L/\delta_0 = 15.7$ to 17.1, the third mode progressively increased in magnitude relative to the second mode. At approximately $L/\delta_0 = 17.1$, the second mode either ceased or went below background noise levels, while the third mode remained as the dominant mode. It is notable that

in the present work the velocity was only increased, however Milbank (2004) identified a hysteresis effect where the cavity would hold on to a higher mode number when the velocity (and therefore L/δ_0) was being decreased, whereas the mode number would stay at the lower value when the velocity (and L/δ_0) was being increased from zero.

From beyond the dashed line in figure 4.26 (at approximately $L/\delta_0 \approx 31$) both the 3rd and 4th modes were found to typically have similar far-field acoustic magnitudes. For the purposes of design, from $5 < L/\delta_0 < 17$, using both the present data and those of Sarohia (1977), the following curve fit gives a reasonable prediction of κ. The coefficient of determination (R^2) is 0.98.

$$\kappa \approx 0.239\mathrm{Ln}(\mathrm{L}/\delta_0) - 0.047 \qquad 5 < \mathrm{L}/\delta_0 < 17 \tag{4.1}$$

Between $18 < L/\delta_0 < 24$, κ can be approximated as:

$$\kappa \approx 0.238\mathrm{Ln}(\mathrm{L}/\delta_0) - 0.140 \qquad 18 < \mathrm{L}/\delta_0 < 24 \tag{4.2}$$

Above $L/\delta_0 > 25$, the convection velocity ratio appears to flatten out. For the purposes of design, it could be approximated as $\kappa \approx 0.62$ for $L/\delta_0 > 25$ (up to $L/\delta_0 = 48$).

4.8 Cavity mode number

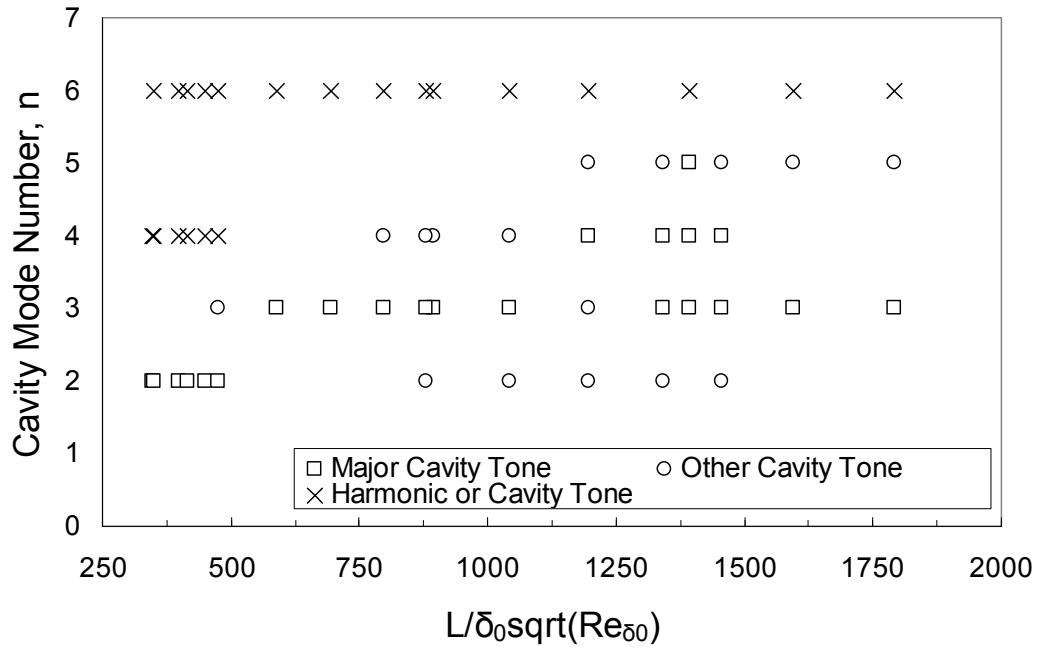

Figure 4.27: The corresponding Rossiter mode number, n, of the tones found in the far-field noise spectra plotted against Sarohia's (1977) non-dimensional cavity length parameter.

In figure 4.27, the corresponding Rossiter mode number, n, of the tones found in the far-field noise spectra are plotted against Sarohia's (1977) non-dimensional cavity length parameter. Sarohia's (1977) parameter is used as it incorporates the flow velocity in addition to the cavity length and boundary layer thickness. The second cavity mode dominates from $L/\delta_0\sqrt{\mathrm{Re}_{\delta_0}} = 350$ to 475. The third cavity mode dominates from $L/\delta_0\sqrt{\mathrm{Re}_{\delta_0}} = 590$ to 800. From $L/\delta_0\sqrt{\mathrm{Re}_{\delta_0}} = 875$ to 1400 there are multiple cavity modes present, from the second through to fifth modes. Indeed, at $L/\delta_0\sqrt{\mathrm{Re}_{\delta_0}} = 1400$ there were three major cavity modes, each of which had similar far-field acoustic amplitude. For $L/\delta_0\sqrt{\mathrm{Re}_{\delta_0}} > 1600$, the third mode again becomes the major mode (to the limit of the range of the data at $L/\delta_0\sqrt{\mathrm{Re}_{\delta_0}} = 1800$).

Since the phase lag, α, is zero the frequencies of harmonics are equivalent to the frequencies of higher mode Rossiter tones. Thus either higher order cavity modes appear to be present (in the acoustic spectra), or these may be harmonics of the lower order cavity modes. For $L/\delta_0\sqrt{\mathrm{Re}_{\delta_0}} = 350$ to 475, the second and third harmonics may be present. Above $L/\delta_0\sqrt{\mathrm{Re}_{\delta_0}} = 475$, the second harmonic may be present.

4.9 Summary

An investigation has been conducted into a two-dimensional cavity contained within an airfoil placed within an anechoic wind tunnel. Noise spectra were reported for rectangular cavities between $L/D = 1.17$ to 4.67, across the range of velocities of the facility. The relation of mean convection velocity ratio ($\kappa = U_c/U$) and non-dimensional cavity length (L/δ_0) were estimated in the range $L/\delta_0 = 5$ to 48 – extending the range for which data are available compared to the literature. The cavity modes found for the Sarohia (1977) parameter ($L/\delta_0\sqrt{\mathrm{Re}_{\delta_0}}$) in the range 350 to 1800 were reported.

As cavity length was increased while all other parameters were held constant, lower coherence was found between shear layer fluctuations measured simultaneously near the leading and trailing edges of the cavity. It was found that the number of cavity oscillation modes detected increases with increasing L/D while the intensity of each mode tends to decrease; this may be explained by a reduction in the coherence of vortical structures across the cavity span as L/D increases (for fixed D and Re_D).

Flows over two-dimensional modified cavity geometries were investigated to examine the effects of sloping the front or rear cavity walls at various L/D ratios. It was found that a sloped cavity rear wall is responsible for a reduced broadband noise component of cavity noise, while sloping the cavity front wall produces a reduction in tonal levels but no reduction in broadband levels. Reducing the effective cavity length, i.e., the length of the cavity mouth seen by the flow, to below the minimum required for the onset of oscillations will eliminate the cavity tones completely, even if the volume of the cavity is maintained constant. Sloping the front and rear walls in combination was found to be most effective at attenuating cavity noise, for a given cavity volume.

It is believed that the sloped front wall causes delayed separation (i.e., the flow is attached around the corner before separating), and a thicker, more stable, shear layer. Meanwhile, the sloped rear wall reduces the level of impingement and therefore feedback to the shear layer, while also reducing the broadband component of noise that is otherwise generated by the impingement of shear layer turbulence on a sharp cavity trailing edge. Combining the two modifications gives the best overall noise attenuation.

The 'airfoil with cavity' was found to produce airfoil tonal noise; this may involve an aeroacoustic feedback loop similar to that for cavity tonal noise. This is investigated in chapter 5.

Chapter 5

Airfoil Noise: Results and Discussion

5.1 Introduction

This chapter discusses results relating to the airfoil tonal noise produced by the 'airfoil with cavity' profile. The investigation was motivated by the discovery of the production of airfoil tonal noise from the airfoil profile with cavity, as discussed in section 4.3. The objective was to identify the mechanism responsible for the noise.

Initially, some example spectra are shown, in order to illustrate the phenomenon. The next item investigates whether the noise is genuinely due to airfoil tonal noise. This is done by discussing the general characteristics of the noise and showing that these characteristics, indeed, are consistent with those for airfoil tonal noise. Following that, velocity measurements are presented. These show the existence of disturbances in the boundary layer at the airfoil tonal frequencies. The disturbances are found only downstream of the cavity. This supports the notion of the existence of a feedback loop between the airfoil trailing edge and the cavity trailing edge. Subsequently, the effect of acoustic forcing is investigated and it is found the airfoil responds more strongly at the tonal frequencies than other frequencies, which is believed to be to due to reinforcement of the naturally-occuring feedback loop – the feedback loop was not 'saturated' before the application of additional acoustic forcing. After this, surface flow visualisation results are presented which support the existence of a region of separated flow along the tapered tail section of the airfoil. A stability analysis of the flow over the smooth airfoil, using a code supplied by Dr. Michael J. Kingan (Kingan and Pearse, 2009), shows that high levels of amplification occur over this region of separation, which is consistent with the boundary layer velocity measurements. Finally, an overall mechanism for the noise is presented, combining the insights gained from the aforementioned measurements and analysis.

To assist with the description of the experiments, some extra terminology is

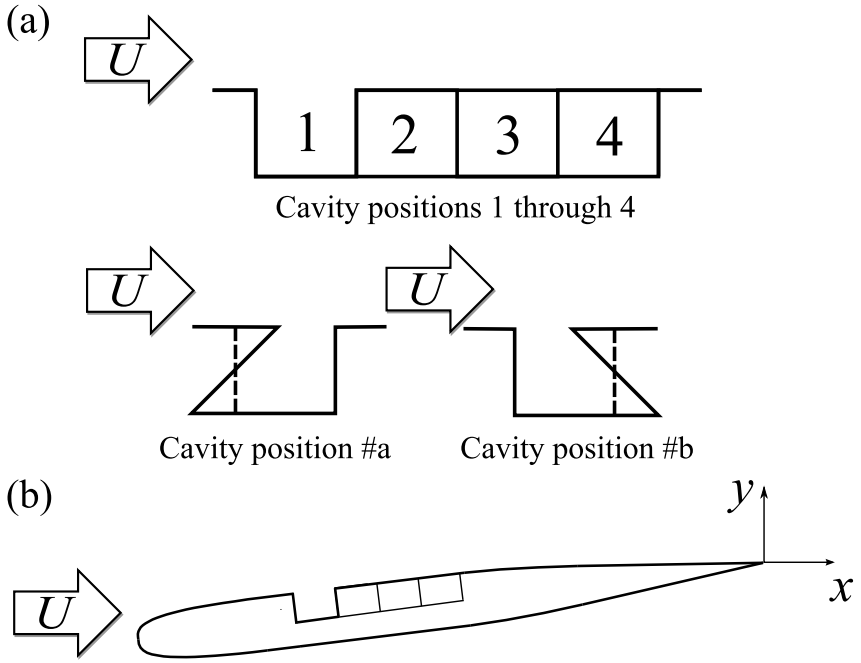

Figure 5.1: (a) Cavity designations, with regards to airfoil tonal noise. (b) Co-ordinate system. Origin is always fixed at airfoil trailing edge, however x and y axes remain in horizontal and vertical directions, rather than chord-wise and chord-normal, regardless of airfoil angle of attack.

introduced. Figure 5.1(a) defines the co-ordinate system, which has its origin fixed at the airfoil trailing edge, such that the x and y axes remain in the horizontal or vertical directions regardless of the angle of attack (rather than being aligned with the chord-wise and chord-normal directions). Figure 5.1(b) shows the naming system for the cavity positions; positions 1 through 4 are from upstream to downstream (with each cavity being of a rectangular shape and 7 mm in length), whilst cavity position '#a' refers to that cavity with the cavity leading edge shifted downstream and cavity position '#b' refers to that cavity with the cavity trailing edge shifted upstream (in the manner depicted in figure 5.1). Note that the geometric angle of attack of the 'airfoil with cavity', $\alpha_{\text{geom.}}$, is defined in figure 3.7.

5.2 Example noise spectra

This section contains some example noise spectra; the purpose being to illustrate the character of the noise and its distinction from the cavity tones. It will be shown that in some instances airfoil tones and cavity tones occurred concurrently but generally the two phenomena did not interfere with each other.

Comparison of different angles of attack Figure 5.2 shows an example comparison of different angles of attack, for a fixed velocity of $U = 16.6$ m/s. When the cavity was on the pressure side[1] of the plate, cavity oscillations were found to occur at lower jet velocities for increasingly negative angles of attack. It was found that airfoil and cavity tones could both be present well above background noise levels at some angles of attack and Reynolds numbers. Figure 5.2 shows that at 16.6 m/s, for zero angle of attack, weak airfoil tones are present. When the angle is changed to $-7°$ the airfoil tones are much stronger *and* two strong cavity tones are present. As the angle of attack increases to $-13°$, multiple stronger cavity tones appear but no airfoil tones are discernible.

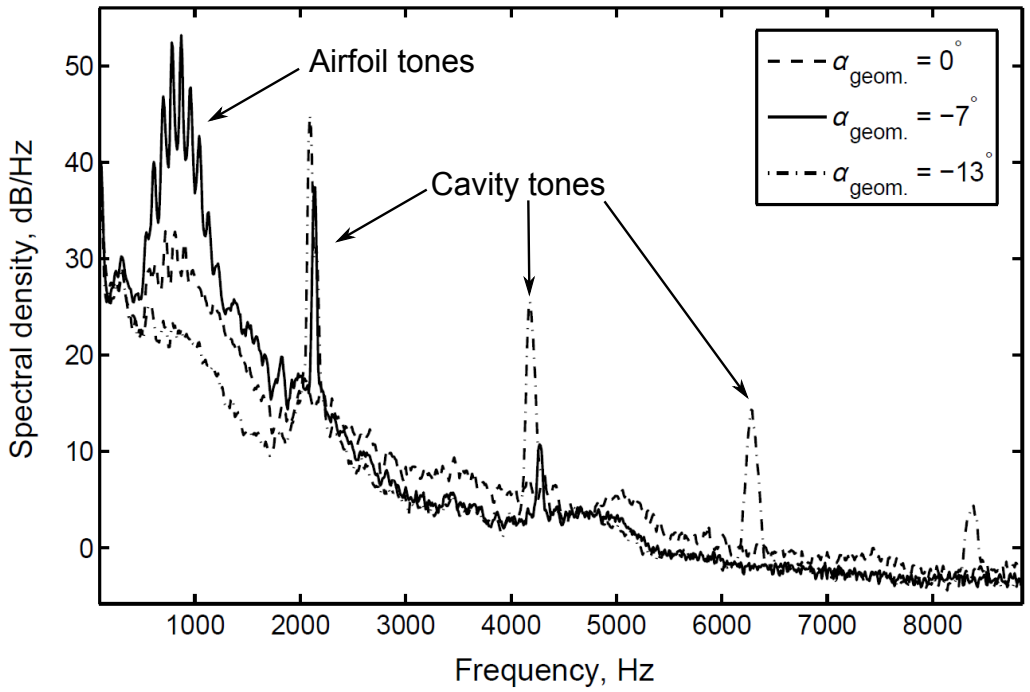

Figure 5.2: Far-field sound spectra with 7mm long cavity at position 1 for different angles of attack, at a jet velocity of 16.6 m/s.

Comparison of positive and negative angles of attack Comparing geometric angles of attack of $-7°$ and $7°$, it is clear from figure 5.3 that *when* the cavity is present that strong airfoil tones occur at a lower velocity. Figure 5.3(c) and (d) show that as the velocity is increased, that the airfoil tones begin to have higher amplitudes when the high-pressure surface is smooth (i.e., $\alpha_{\text{geom.}} = 7°$) than when the cavity is present ($\alpha_{\text{geom.}} = -7°$) .

[1]Note that from herein, 'pressure side' or 'pressure surface' refers to the high-pressure surface of the airfoil, or plate, while 'suction side' or 'suction surface' refers to the low-pressure surface of the airfoil, or plate.

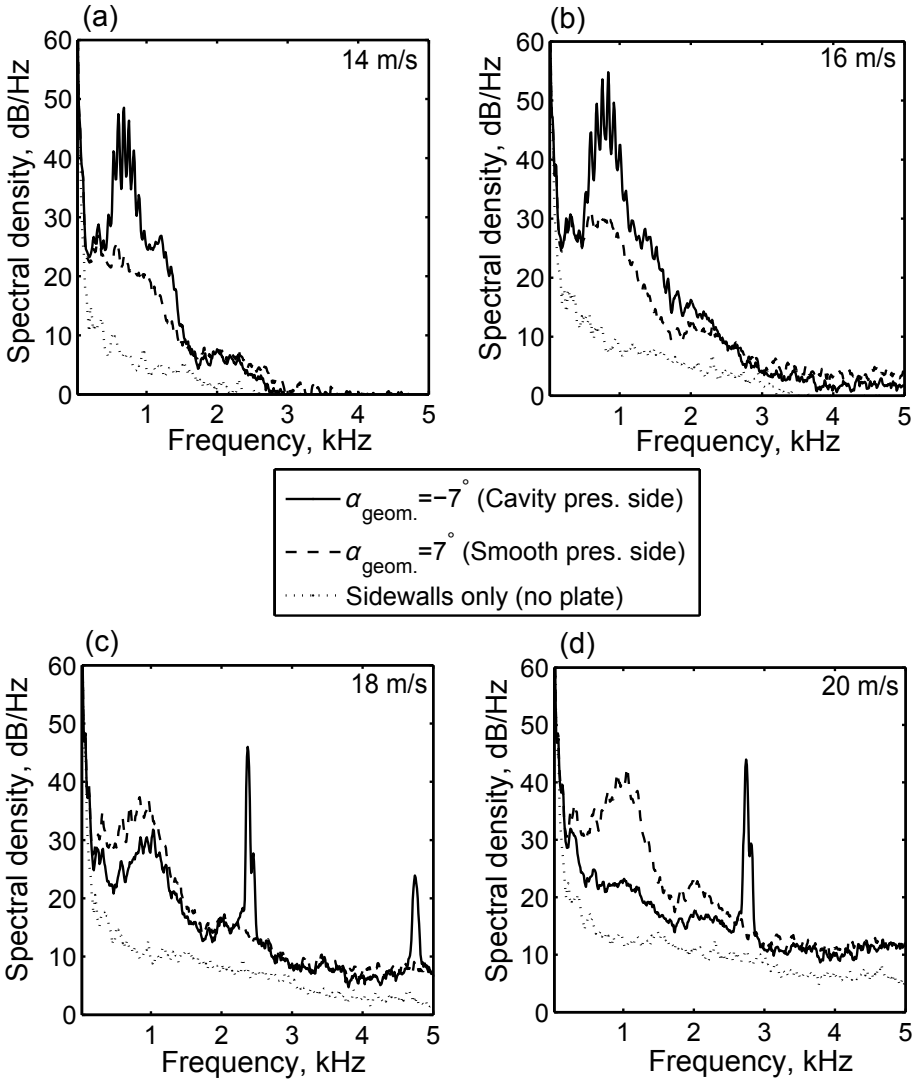

Figure 5.3: Far-field sound spectra at $\alpha_{\text{geom.}} = -7°$ and 7°, for (a) 14 m/s, (b) 16 m/s, (c) 18 m/s and (d) 20 m/s. Part (c) shows the presence of *both* cavity and airfoil tones.

5.3 General characteristics

5.3.1 Occurrence of tones

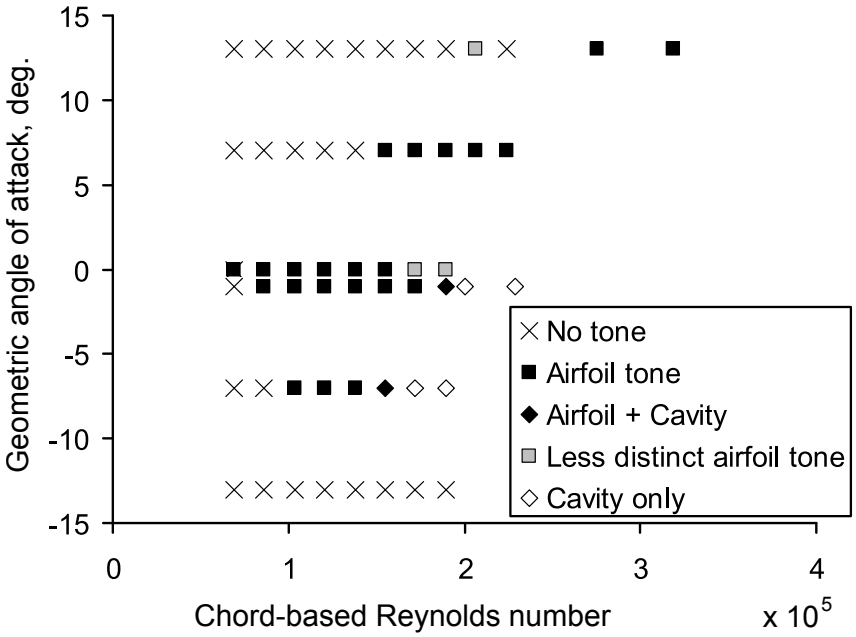

Figure 5.4: Occurrence of airfoil tones with geometric angle of attack and Reynolds number. Cavity located at cavity position 1. Negative angles of attack correspond to the cavity on the pressure side. Positive angles of attack correspond to the smooth pressure side. The specific angles of attack were $-13°$, $-7°$, $-1°$, $0°$, $7°$, and $13°$. Note that positive angles of attack were achieved by remounting the plate upside down, such that the cavity cutout at position 1 was then on the suction surface.

To begin with, the general characteristics of the airfoil tonal noise were investigated. Figure 5.4 shows the occurrence of airfoil tones against geometric angle of attack and Reynolds number. The occurrence of tones was identified from far-field sound pressure spectra. Negative angles of attack correspond to the cavity being located on the pressure side of the plate. The two positive angles of attack correspond to the smooth pressure side and were achieved by remounting the plate upside down, i.e., geometric angles of $7°$ and $-7°$ are equivalent aside from the mounting of the plate and the microphone being always adjacent to the pressure side of the plate.

The effect of the cavity is to make the airfoil tones occur at a lower Reynolds number compared to the smooth side, but also to make the tones cease at a lower Reynolds number. Once the fluctuations over the cavity become too great, presumably the coherent instability waves downstream of the cavity are not supported. However, if the fluctuations are not too substantial, at some

Reynolds numbers it was found that both the airfoil tones and cavity tones can co-exist, as discussed earlier. The frequencies of the cavity tones were well distinct from the airfoil tones, and were readily distinguished by the much larger spacing between the tones and generally far higher frequencies.

The cavity causes the strong airfoil tones to occur at a lower Reynolds number than those at which they would otherwise occur. This behaviour may be analogous in an inverse sense to the leading edge protuberances tested by Hansen, Kelso and Doolan (2010) which caused a reduction in the trailing edge noise tone strength via the introduction of three-dimensionalities into the flow in the form of streamwise vortices which reduced spanwise coherence. In the present case the cavity, on the other hand, forms a two-dimensional geometric feature across the span of the airfoil which could perhaps support the generation of strongly spanwise-coherent structures. Of course, this is a strongly Reynolds-number-dependent phenomenon, and the Reynolds number needs to be sufficiently low for the cavity to act in this way because when the Reynolds number is too high the strong cavity (Rossiter) fluctuations may act to remove the coherent fluctuations in the boundary layer downstream of the cavity. This is evidenced by the presence of strong cavity oscillations yet an absence of downstream boundary layer fluctuations to create the airfoil tones in figure 5.3(d) when viewing the 'cavity pressure side' curve, whilst the 'smooth pressure side' curve shows that without the cavity at that Reynolds number then airfoil tones could otherwise be supported.

5.3.2 Ladder structure and frequency scaling

Ladder structure

The results showed behaviour typical of airfoil trailing edge noise as described in a proportion of the literature (e.g., Arbey and Bataille, 1983, Kingan and Pearse, 2009). For most cases, multiple tones were found which had approximately equal frequency spacing and these tones exhibited a ladder-like structure. Figure 5.5 shows the distinguishable tones for the plate with the cavity at position 1 on the pressure side and demonstrates the presence of this structure. The major tones were the peak tone in the spectra as well as other tones with a sound pressure level within 2 dB re 20 μPa of the peak tone. The minor tones were the remainder of the tones that could be distinguished in the sound pressure spectra. For the overall trend, the major tones were found to approximately follow a $f \propto U^{1.35}$ proportionality relationship. This is close to the $f \propto U^{1.5}$ scaling found by Paterson *et al.* (1973). The individual 'rungs' of the ladder show an approximate proportionality relationship of $f \propto U^{0.80-0.97}$.

Scaling relations

To describe the frequencies of the tones, two empirical relations are provided by Arbey and Bataille (1983). The first is the Paterson *et al.* (1973) relation

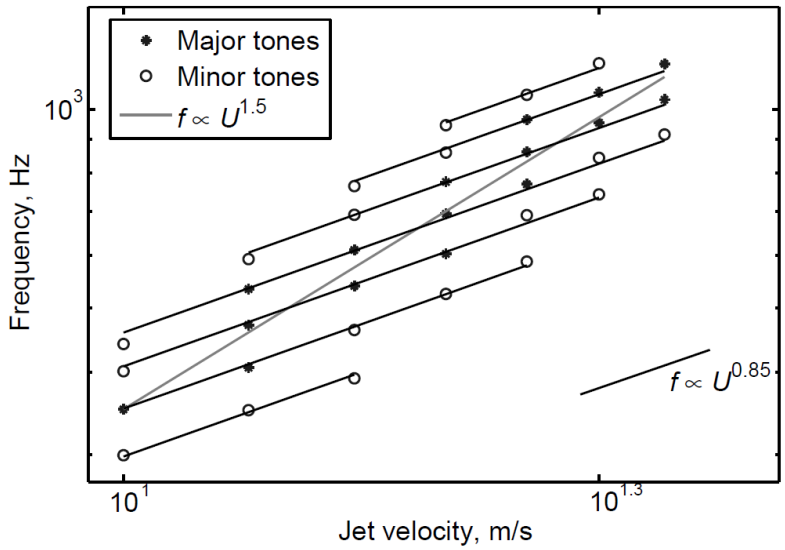

Figure 5.5: Tonal frequency versus velocity for the plate with the cavity at position 1 on the pressure side and a geometric angle of attack of $-1°$.

for the central frequency, given by equation 5.1. The second is a relation for the discrete tones, given by equation 5.2. The two different empirical coefficients have been denoted K_1 and K_2 respectively here for clarity.

$$\frac{f_s}{U^{1.5}} = K_1(C\nu)^{-1/2} \tag{5.1}$$

$$\frac{f_n}{U^{0.85}} = (n + 1/2)\frac{K_2}{L} \tag{5.2}$$

Central frequency scaling Figure 5.6 shows the overall behaviour of the noise. Following equation 5.1, the frequency spectra are scaled by $U^{1.5}$ and show good collapse with the central frequency of the broadband 'hump', $f_s/U^{1.5}$, approximately collapsing to a constant equal to $K_1(Cv)^{-1/2}$. For the current plate the empirical coefficient $K_1 = 0.011$, determined by Paterson *et al.* (1973) for the NACA 0012 & NACA 0018 sections, under-predicts the central frequency. $K_1 = 0.0135$ describes the behaviour better for the current plate.

Discrete frequencies scaling Figures 5.7, 5.8, 5.9, and 5.10, for cavity positions 1 through 4 respectively, indicate that the discrete tones show good collapse when the frequency spectra are scaled by $U^{0.85}$, following equation 5.2. This suggests that the tonal noise mechanism behaves similarly to that reported for smooth aerofoils. The discrete values given by equation 5.1 are plotted as dashed vertical lines. *A posteriori* the feedback length, L, was taken to be the distance from the cavity trailing edge to the aerofoil trailing edge. It can be seen that the frequencies are spaced further apart for cavity position 4

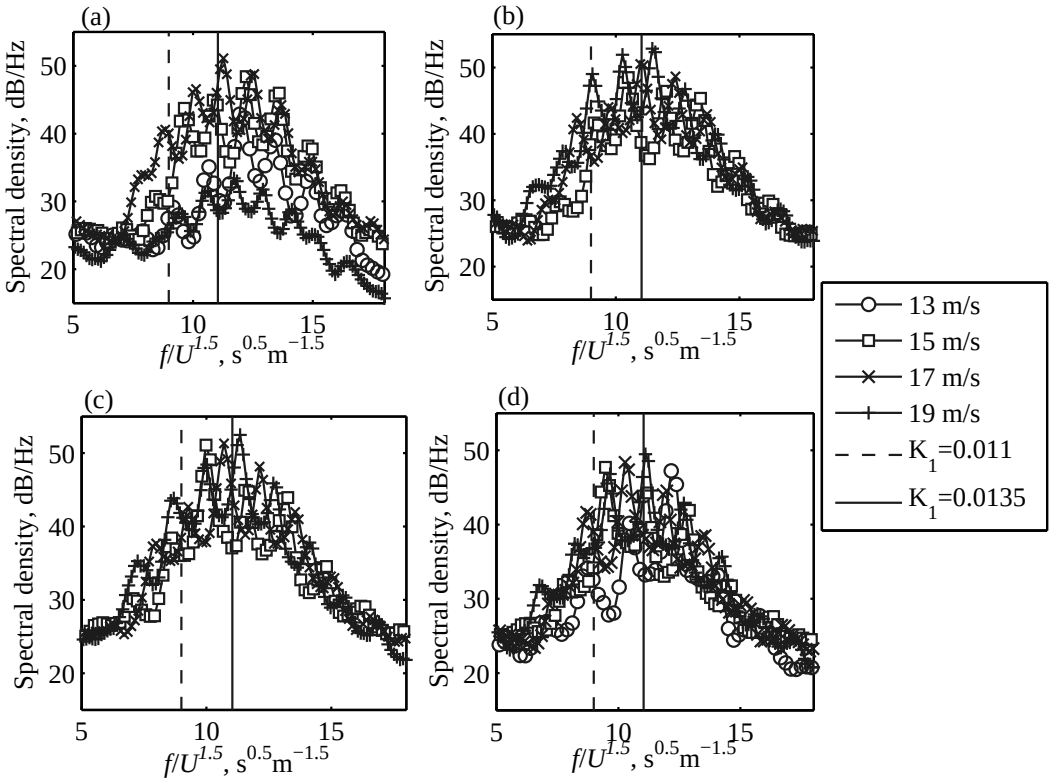

Figure 5.6: Velocity scaling for the central frequency of the broadband contribution. (a) Cavity position 1, (b) cavity position 2, (c) cavity position 3, and (d) cavity position 4. The geometric angle of attack was -7 degrees.

than cavity position 1. This is consistent with the requirement of the feedback loop that Δf increases for a shorter feedback length. Empirical coefficients of $K_2 = 0.675$ for cavity position 1, $K_2 = 0.680$ for cavity position 2, $K_2 = 0.685$ for cavity position 3, and $K_2 = 0.695$ for cavity position 4, describe the data well. These are lower than the value of $K_2 = 0.85$ for the NACA 0012 airfoil (Arbey and Bataille, 1983).

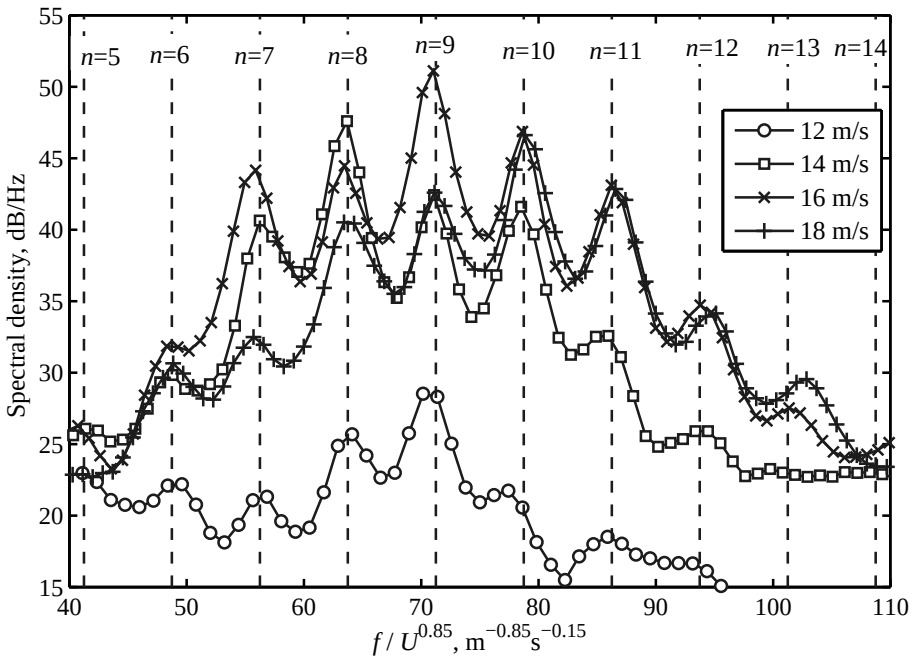

Figure 5.7: Velocity scaling for the discrete tonal frequencies for cavity position 1. At a geometric angle of attack of -7 degrees. For equation 5.2, $K_2 = 0.675$ provides a good fit to the experiment. Equation 5.2 is denoted by the dashed vertical lines.

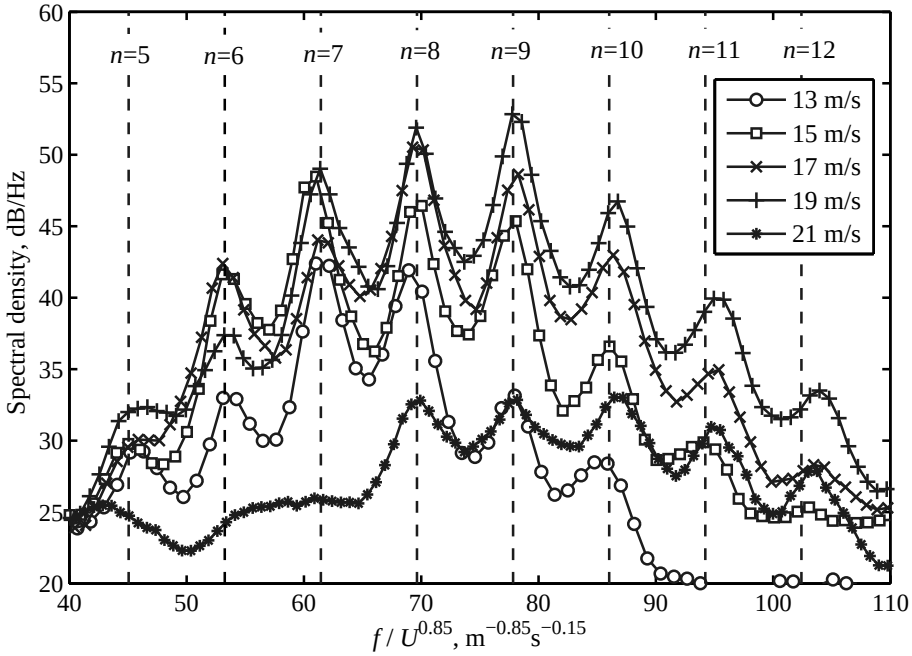

Figure 5.8: Velocity scaling for the discrete tonal frequencies for cavity position 2. At a geometric angle of attack of -7 degrees. For equation 5.2, $K_2 = 0.680$ provides a good fit to the experiment. Equation 5.2 is denoted by the dashed vertical lines.

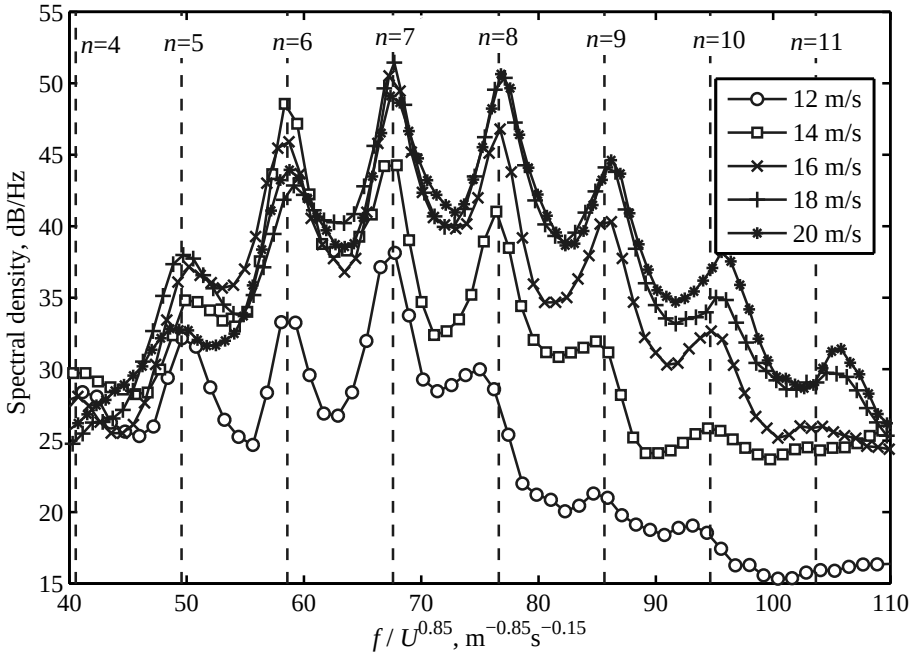

Figure 5.9: Velocity scaling for the discrete tonal frequencies for cavity position 3. At a geometric angle of attack of -7 degrees. For equation 5.2, $K_2 = 0.685$ provides a good fit to the experiment. Equation 5.2 is denoted by the dashed vertical lines.

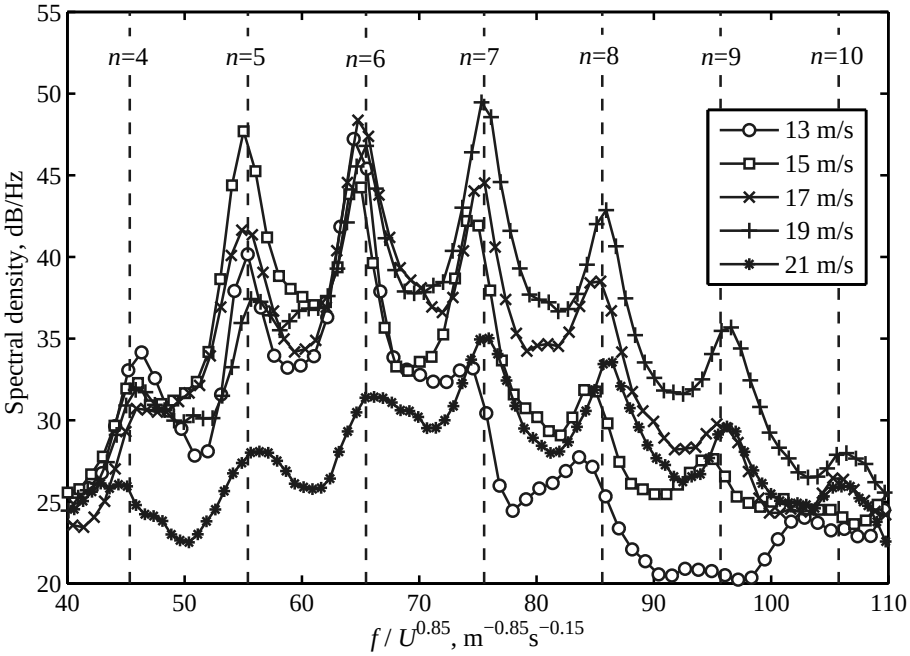

Figure 5.10: Velocity scaling for the discrete tonal frequencies for cavity position 4. At a geometric angle of attack of -7 degrees. For equation 5.2, $K_2 = 0.695$ provides a good fit to the experiment. Equation 5.2 is denoted by the dashed vertical lines.

5.3.3 Far-field acoustic spectral density

In this section some results for the far-field acoustic spectral density are discussed. The noise produced by the airfoil was recorded for different angles of attack, cavity position and flow velocity. The peak spectral density is generally dominated by the level of the strongest tone.

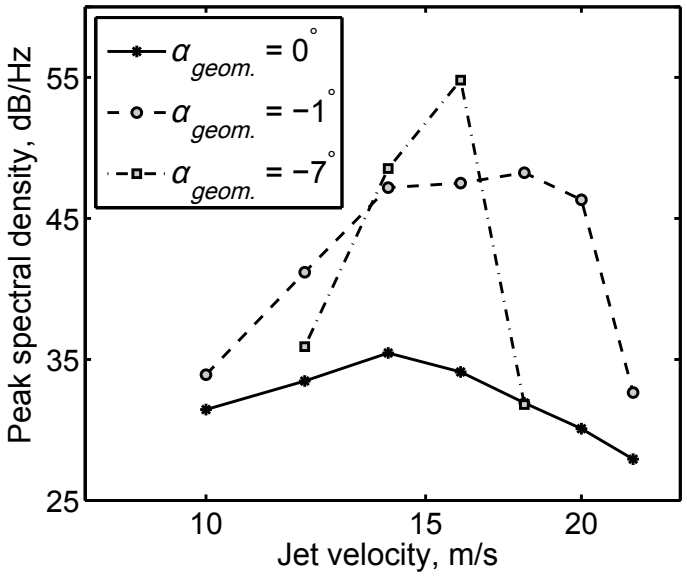

Figure 5.11: Peak spectral density of far-field noise versus geometric angle of attack for negative angles of attack. The cavity is on the pressure side of the plate at position 1. No airfoil tones were found for higher jet velocities, up to the facility's maximum jet velocity of approximately 40 m/s.

Peak spectral density for varying angle of attack With the cavity on the pressure side of the airfoil at position 1, the peak spectral density of the trailing edge noise, at varying angle of attack, was found to show the typical trends expected of airfoil trailing edge noise. The peak spectral density is plotted in figure 5.11. The trend of a rise, plateau and drop that is typical of airfoil tonal noise (Paterson *et al.*, 1973) was found and the highest amplitude level is found for the largest angle of attack, where the tones were found to occur over a smaller range of velocities.

Different behaviour is found for a smooth pressure side, that is, positive angles of attack (figure 5.12). The case at zero angle of attack remains the same as before. At $-7°$, the peak spectral density of the loudest airfoil tone continues to climb until 26 m/s (data for this configuration weren't recorded for higher velocities). At $-7°$, the peak spectral density continues to climb

until 37 m/s (the maximum speed of the wind tunnel). Presumably the levels would plateau or drop if more data could be acquired.

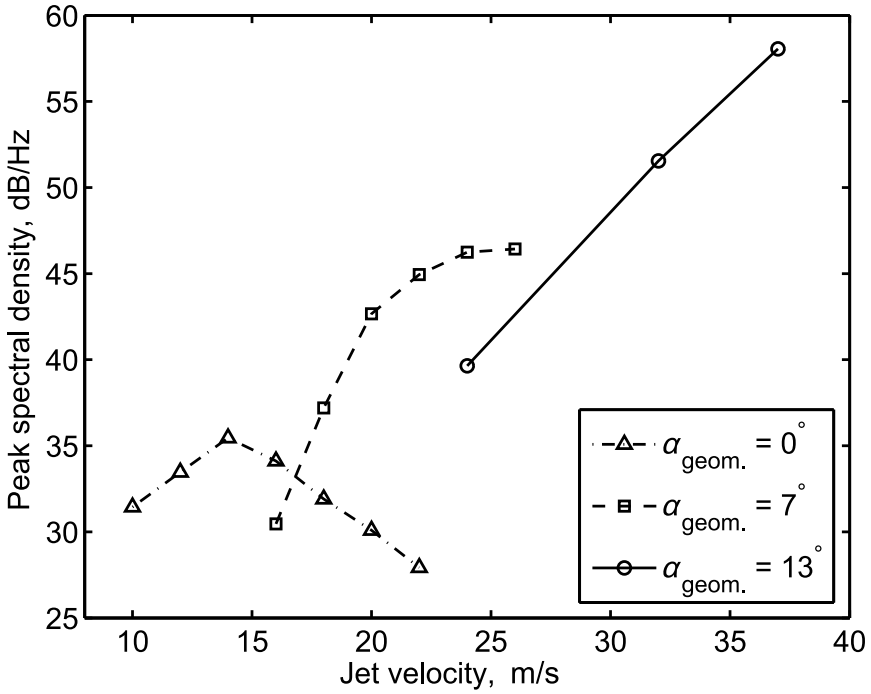

Figure 5.12: Peak spectral density versus geometric angle of attack for positive angles of attack (smooth side of plate mounted on pressure side). Cavity located at cavity position 1 on suction side of plate.

Peak spectral density for varying cavity position For the full assortment of cavity positions, the typical behaviour – being a plateau of the peak spectral amplitude – was found. This would suggest that even with the cavity in place (and regardless of the position of the cavity), the tonal noise mechanism is similar to that for smooth airfoils.

Figures 5.13 and 5.14 show the variation in peak far-field acoustic amplitude of airfoil tones at -7 degrees angle of attack, the former for the rectangular cavities and the latter for the cavities with the shifted trailing edges. It can be seen that the cavity appears to have some complex effect on the peak spectral density, for an otherwise equivalent overall airfoil profile. For instance, the peak spectral density occurs over a narrower range of velocities for cavity position 1 than cavity position 3 or 4 (figure 5.13). As another example, figure 5.14 shows that the greatest peak spectral density occurs at a lower velocity for cavity position 2b than 1b or 3b.

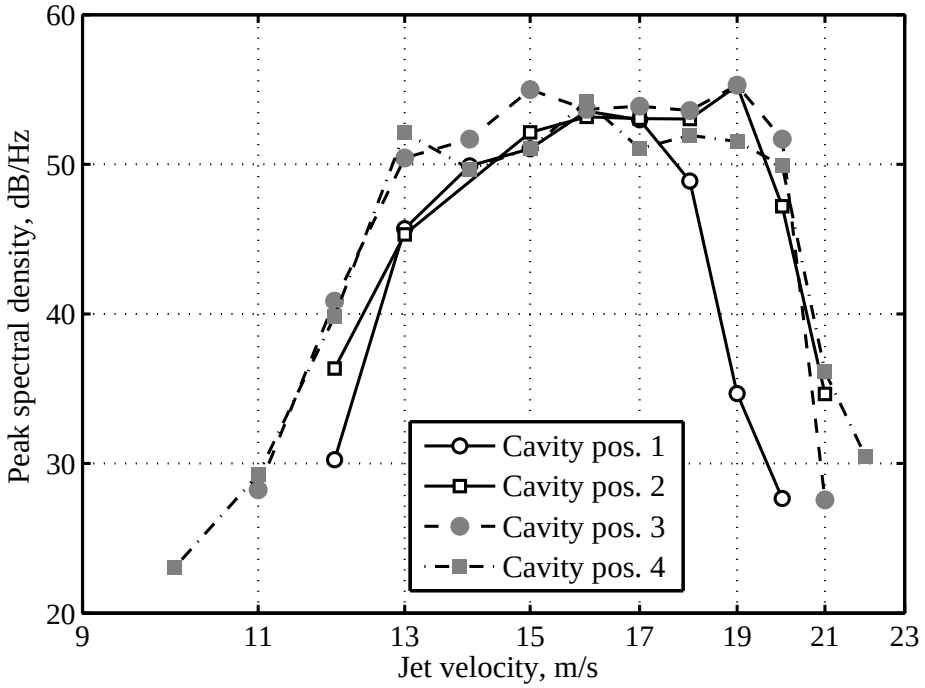

Figure 5.13: Variation in peak far-field acoustic amplitude of airfoil tones for rectangular cavities at -7 degrees angle of attack.

5.3.4 Summary

In summary, the consistency of these results with prior literature suggests that the underlying mechanism of airfoil tonal noise here is the same as reported on previously. Some key differences are found however. The effect of the cavity appears to be to make the airfoil tones occur at a lower Reynolds number than they would otherwise. Conversely, at higher Reynolds number when strong tones are produced by a smooth plate, the additional presence of a cavity, appears to disrupt the mechanism.

To illustrate the effect of the cavity on airfoil tones in more detail, various wake measurements will be discussed next, followed by microphone and hot-wire measurements for geometric angles of attack of $-1°$ and $-7°$. This will be followed by an investigation of the effect of external acoustic forcing.

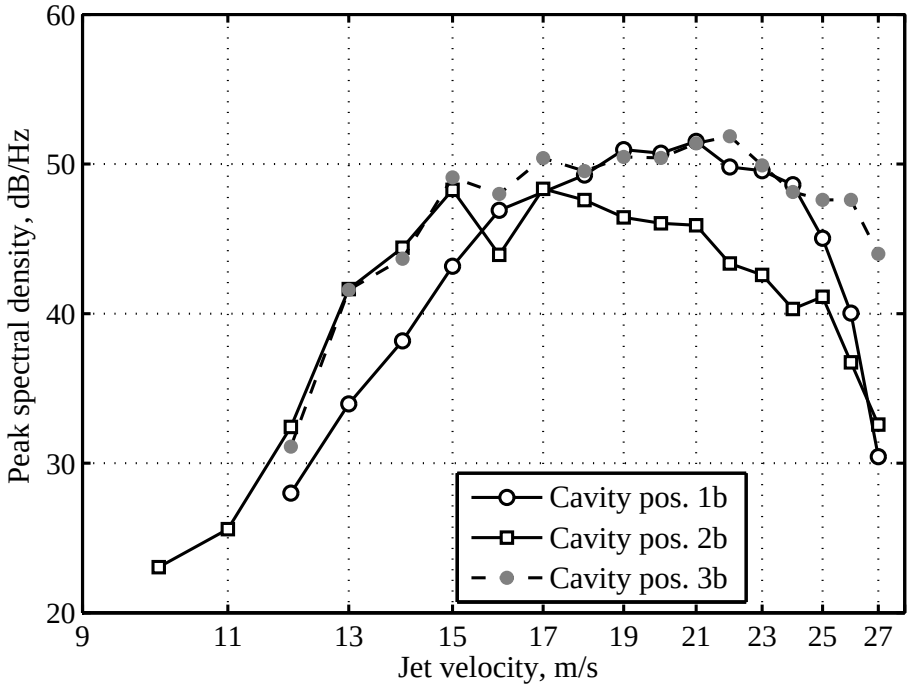

Figure 5.14: Variation in peak far-field acoustic amplitude of airfoil tones for cavities with shifted cavity trailing edge at -7 degrees angle of attack.

5.4 Wake velocity measurements

Further to the acoustic measurements discussed so far, velocity measurements were also acquired. Initially, these consisted of measurements of the wake region downstream of the airfoil and these results are discussed here. Please recall that the origin of the co-ordinate system is at the airfoil trailing edge, as described in figure 5.1. More extensive velocity measurements, along the airfoil boundary layer and within the cavity, are discussed in subsequent sections.

5.4.1 Streamwise wake properties

This portion of the report describes some streamwise properties of the wake. Figure 5.15 shows the streamwise velocity profiles recorded horizontally along the wake, downstream of the pressure surface of the airfoil for cavity position 1 at a nominal jet velocity of 16.6 m/s and with the plate at a geometric angle of attack of $-1°$. A velocity maximum in the wake was found at $x/C \approx 0.3$, however it appears that the distance of measurement does not extend far enough to capture the maximum r.m.s. fluctuation velocity in the wake.

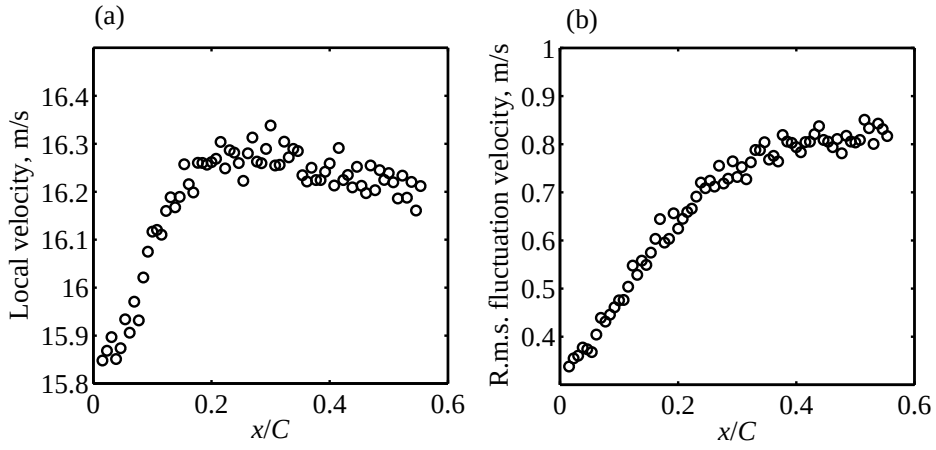

Figure 5.15: Velocity measurement horizontally (downstream) through the wake at $y/C = 0$. For cavity at position 1, U=16.6 m/s, and geometric angle of attack of $-1°$. (a) Local streamwise velocity, u. (b) R.m.s. fluctation velocity, $u'_{\text{r.m.s.}}$.

Figures 5.16 and 5.17, for cavity position 1 and cavity position 4 respectively, show spectrograms of (a) power spectral density of velocity and (b) coherence between velocity and far-field microphone signals. Comparing figures 5.16 and 5.17, it can be seen that the airfoil tones appear to extend more strongly through the flow and are more coherent for cavity position 1, than for cavity position 4. This is consistent with the higher amplitudes of airfoil tonal noise found for the cavity position 1 case than the cavity position 4 case, at this angle of attack.

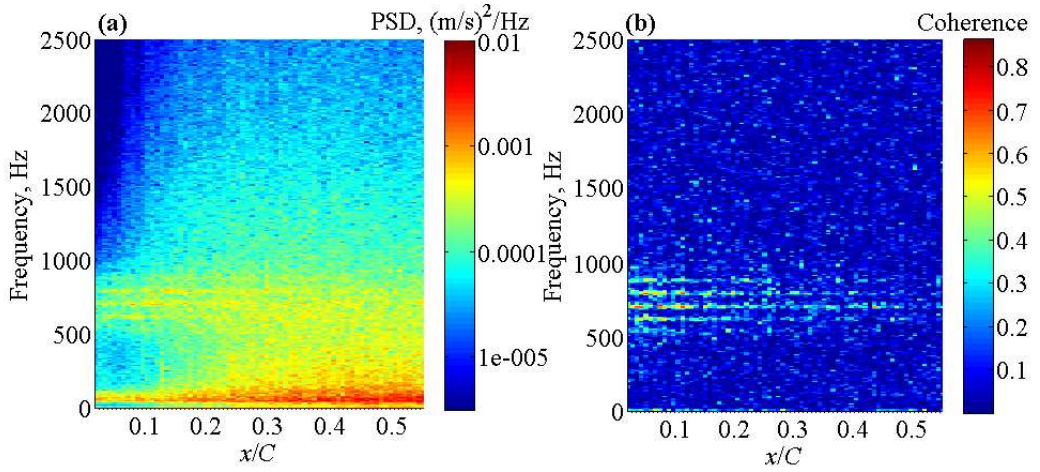

Figure 5.16: Velocity profiles through the wake along horizontal line at $y/C = 0$ for cavity at position 1. (a) Power spectral density of velocity, and (b) coherence between velocity signal and far-field microphone signal. U=16.6 m/s, and geometric angle of attack of $-1°$.

Figure 5.18 shows the peak spectral density of the velocity fluctuations in a band of frequencies 30 Hz either side of the airfoil tone at 710 Hz and an arbitrary comparison frequency of 350 Hz, for the cavity position 1 case, recorded horizontally through the wake. It can be seen that the level at 710 Hz is approximately steady while that at 350 Hz starts at a lower value at the airfoil trailing edge and, with downstream distance, increases noticeably before reaching a similar value. This shows there is a strong disturbance at the airfoil tone frequency, in the upstream part of the wake, and most presumably emanating from strong fluctuations in the boundary layer over the object. That is, while the broadband turbulence develops downstream, on the other hand, the fluctuation at the airfoil tone is already there at the earlier part of the wake.

Similarly, the phase suggests there is an ordered fluctuation at 710 Hz but not 350 Hz. Figure 5.19 shows the relative phase throughout the wake for (a) 710 Hz, the airfoil tone, and (b) 350 Hz, which is an arbitrary non-tonal comparison. The phase difference is taken between the velocity measurement, at varying positions, and a fixed reference phase given by the microphone of fixed location. The steadily-increasing phase for the 710 Hz band shows that there is a periodic fluctuation present, while the essentially random variation in phase for the 350 Hz band suggests no periodic fluctuation is present at that frequency. This supports the notion that there is an organised disturbance at the airfoil tone frequency through the wake.

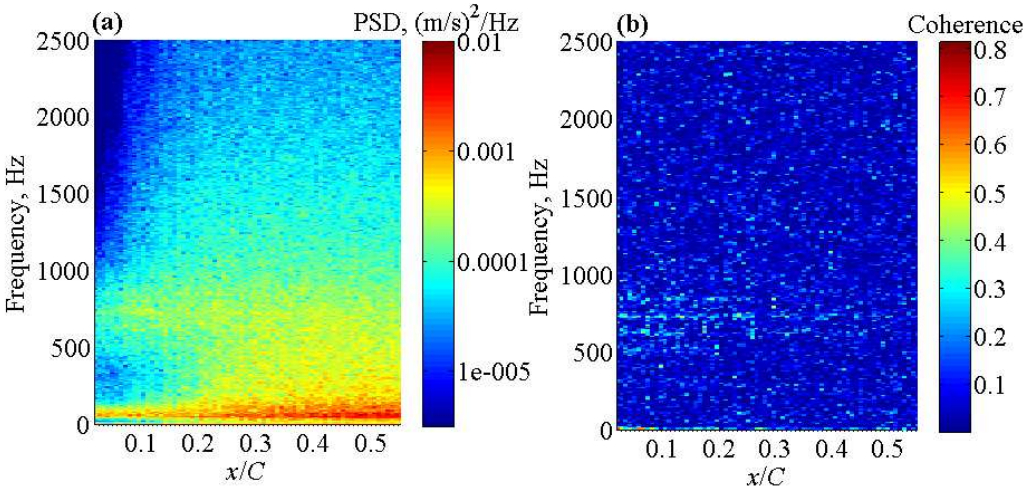

Figure 5.17: Velocity profiles through the wake along horizontal line at $y/C = 0$ for cavity at position 4. (a) Power spectral density of velocity, and (b) coherence between velocity and far-field microphone signals. U=16.6 m/s, and geometric angle of attack of $-1°$.

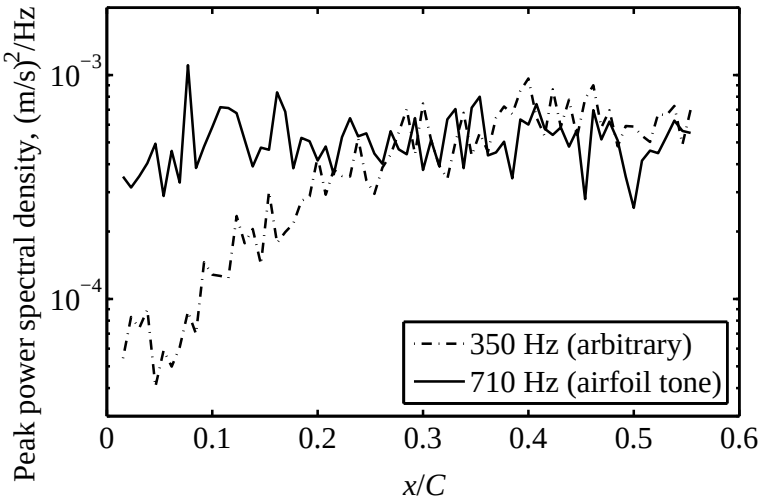

Figure 5.18: Peak spectral density in a band of frequencies 30 Hz either side of the airfoil tone at 710 Hz and, also, either side of an arbitrary comparison frequency of 350 Hz, for cavity position 1 along a horizontal line through the wake at $y/C = 0$. U=16.6 m/s, and geometric angle of attack of $-1°$.

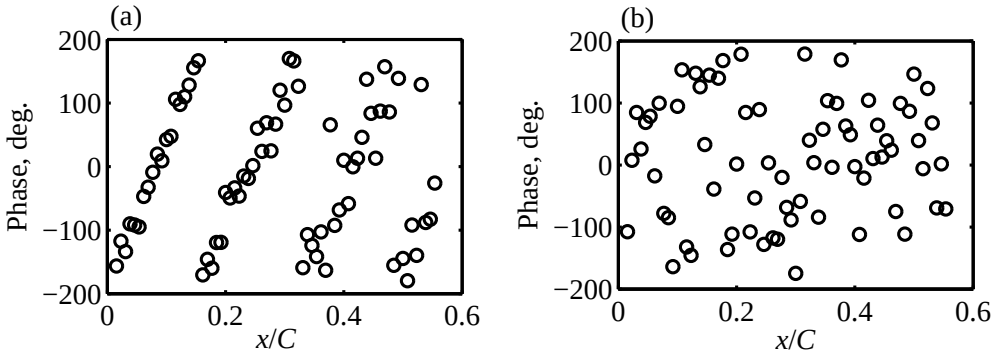

Figure 5.19: Phase difference between velocity measurement and (fixed) acoustic reference measurement, through the wake along the horizontal line at $y/C = 0$. (a) At a frequency of 710 Hz, an airfoil tone. (b) At 350 Hz, an arbitrary non-tonal comparison frequency. Cavity at position 1, U=16.6 m/s, and geometric angle of attack of $-1°$.

5.4.2 Vertical measurements through wake

Figure 5.20(a) shows profiles of streamwise velocity recorded through a vertical line downstream of the plate, for the cavity position 1 case. Since the angle of attack of the plate is negative, the wake of the pressure side (containing the cavity cutout) is on the top half of the plot ($y > 0$).

Figure 5.20(b) shows the root-mean-square (r.m.s.) fluctuation velocity downstream of the airfoil, for the cavity position 1 case. It can be seen that there are higher levels of r.m.s. fluctuation velocity downstream of the pressure side of the airfoil. The levels downstream of the suction side are comparatively lower.

Streamwise velocity recorded at a variety of distances downstream from the plate are shown in figure 5.21. The wake develops in a typical manner, whereby the velocity deficit near the centre-line becomes engerised with increasing distance downstream. In a similar way, the concentration of eddies in the wake becomes distributed over a broader transverse distance (figure 5.21(b)).

Figure 5.22 shows properties of streamwise velocity, recorded vertically through wake at $x/C = 0.012$. Part (a) of the figure shows a spectrogram of the spectral density of the fluctuating velocity while part (b) shows the coherence between the hot-wire velocity measurement and the far-field acoustic measurement. The strong structured fluctuations at the airfoil tonal frequencies are only found downstream of the (top) pressure side. This is shown both by the spectral density and by the coherence to the far-field noise. The coherence result (i.e., strong coherence at the airfoil tone frequencies) suggests that the noise results from these disturbances over the pressure surface. This is consistent with the literature (section 2.7.3), which suggests that airfoil tonal

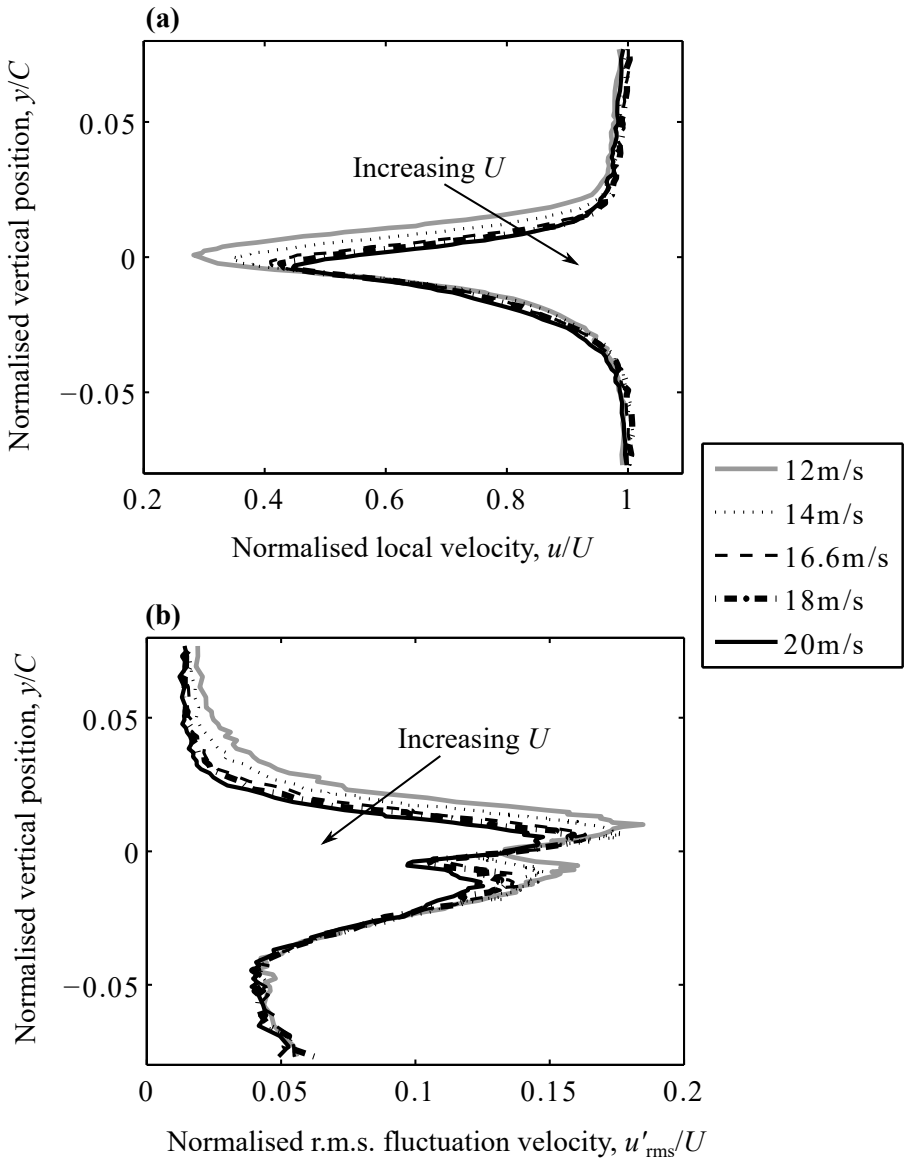

Figure 5.20: Velocity profiles recorded behind the airfoil trailing edge at $x/C = 0.02$ for a variety of free stream flow velocities. The cavity was at position 1 and the plate was at $\alpha_{\text{geom.}} = -1°$. (a) Normalised local velocity. (b) Normalised r.m.s. fluctuation velocity.

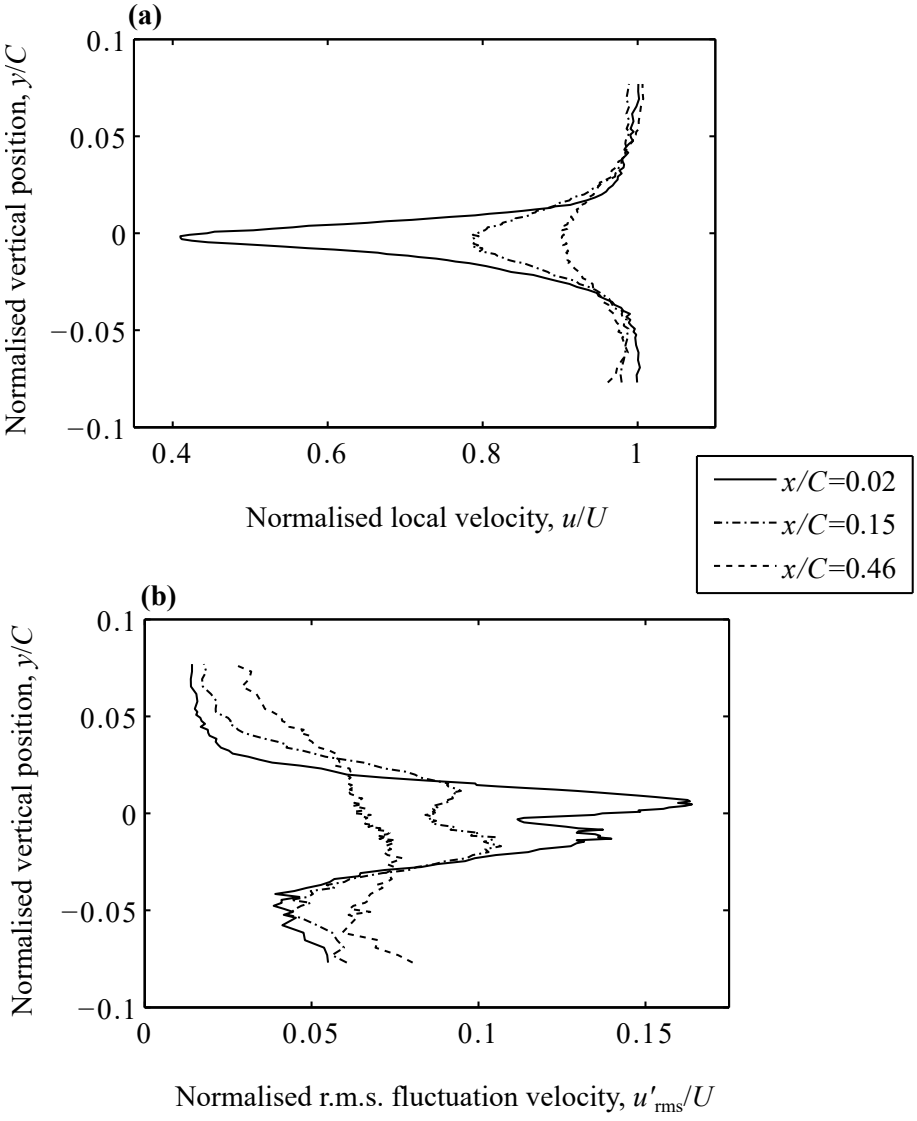

Figure 5.21: Comparison of velocity profiles at various positions downstream in the wake ($x/C = 0.02, 0.15$ & 0.46). The cavity was at position 1 and the plate was at $\alpha_{\text{geom.}} = -1°$. (a) Normalised local velocity. (b) Normalised r.m.s. fluctuation velocity.

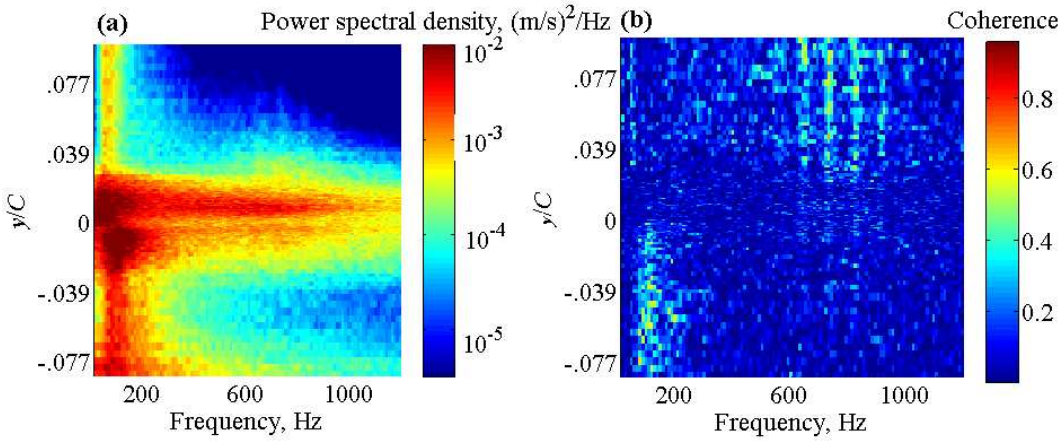

Figure 5.22: Properties of streamwise velocity, recorded vertically through wake at $x/C = 0.012$, $U = 16.6$ m/s and geometric angle of attack of -1°. (a) Spectrogram of power spectral density. (b) Coherence between velocity measurement and noise measurement.

noise is primarily a result of velocity disturbances over the pressure side of an airfoil (for example, Nakano, Fujisawa and Lee, 2006).

An alternate explanation is possible, whereby the airfoil tonal noise is controlled by low frequency vortex shedding from the (bottom) suction surface. Figure 5.22 shows that adjacent to the suction surface ($y/C < 0$), a region of high velocity power spectral density and high coherence is found at approximately 100 Hz. This is close to the frequency of Δf, and the low frequency vortex shedding from the suction surface may modulate the higher frequency fluctuations (between 600 and 1000Hz) found adjacent to the pressure suface, thereby creating the distinctive airfoil tonal peaks. However, this alternate explanation is not fully consistent with the results of section 5.5 where Δf is found to vary as the location of the cavity cutout located on the pressure surface of the airfoil is changed, with section 5.5.2 showing that even very small changes in cavity trailing edge position produce a change in Δf.

5.4.3 Boundary layer displacement thickness

The cavity position does not have a major effect on the pressure side boundary layer displacement thickness based Strouhal number, $St^* = \delta^* f_s / U$, which is shown in fig. 5.23. The pressure side boundary layer displacement thickness, δ^*, was estimated from hot-wire velocity profiles just downstream of the airfoil trailing edge at $x/C = 0.016$ (with the Y-direction spatial resolution of the velocity measurement being 0.1 mm), while the central frequency, f_s, was estimated as the centre frequency of the broadband contribution (or 'broadband hump') found from the frequency spectra of far-field microphone measurements. The plot shows that there are no significant differences in St^*

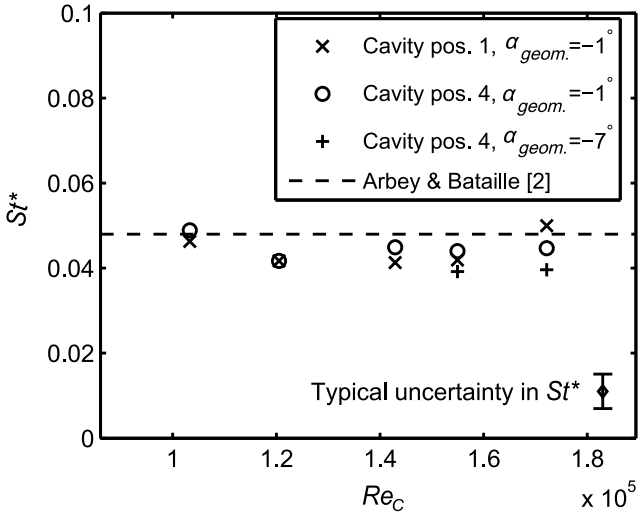

Figure 5.23: Plot of Strouhal number, $St^* = \delta^* f_s/U$, against chord-based Reynolds number. The dashed line gives the mean behavior found by Arbey and Bataille (1983). The typical uncertainty in St^* was obtained via an error analysis of the constituent variables.

between when the cavity is at position 1 compared with position 4, which means that the variation in airfoil tonal frequency is *not* explained by a variation in boundary layer profile caused by a variation in the cavity position. The data are broadly consistent with the mean Strouhal number of St^*=0.048 found by Arbey and Bataille (1983). Note that this mean Strouhal number is also equivalent to the Paterson formula (Arbey and Bataille, 1983), so the present results show agreement with equation 5.1.

5.5 Measurements at geometric angle of attack of -1°

5.5.1 Effect of cavity position on frequency

The affect of the position of the cavity on the frequencies of the tonal noise was found to be significant. The overall airfoil profile, angle of attack and freestream velocity were otherwise equivalent between the cases. Figure 5.24 shows a comparison of far-field noise spectra from the 'smooth' plate and the cavity at four different positions at U=16.6 m/s. It shows that the broadband airfoil noise contribution is present at an approximately constant position for all five cases, however the frequencies and amplitudes of the individual tones vary between the cases. At cavity positions 1 and 2, six distinct individual tones are present. When the cavity is moved downstream to positions 3 and 4,

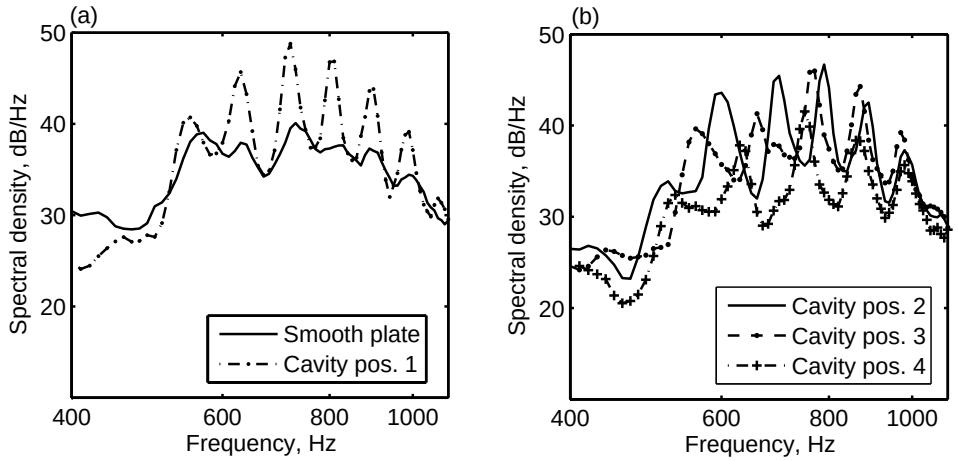

Figure 5.24: Comparison of far-field noise spectra from the plate only and the plate with the cavity at four different positions, at U=16.6 m/s. The plate was at a geometric angle of attack of −1°.

only five distinct tones are present and the spacing between them is larger. The peak far-field acoustic amplitude decreases as the cavity is moved downstream.

At a velocity of U = 16.6 m/s, the tones are much less distinct for the smooth plate than when the cavity is present. The modes are apparently more strongly amplified when the cavity is present. If an acoustic feedback loop is involved, as described in the literature, then the cavity geometry could be involved in certain tones being reinforced more strongly than in the smooth-plate case.

It is worth noting here that the "smooth" airfoil is the one where the cavity is entirely filled-in on the pressure side in this measurement. There is a slight roughness at the leading edge of the filled-in cavity, which may be a point of receptivity as discussed later in Section 3.3.2 regarding Figure 5.33. This is consistent with Δf being smaller for the "smooth" airfoil (a larger feedback length, L). However it could also be a coincidence, as what is found in that section is an increased detection of the acoustic wave (the acoustic component of velocity) rather than a point of receptivity, such that the natural point of receptivity for the smooth airfoil may be somewhere further upstream than cavity position 1 but without being sure of its location.

Table 5.1 lists the positions of the tonal frequencies, f_n, for the five cases at 16.6 m/s. The frequencies with the maximum amplitude, $f_{n\ \max}$, are listed in italics and are all between 700 and 800 Hz. According to Arbey and Bataille (1983) the maximum amplitude feedback frequency is one which is close to the central frequency, f_s. The spacing of the tones was found to be approximately constant for each cavity position, although it does vary slightly. As per Kingan and Pearse (2009), the spacing of the tones, Δf, was taken to be the average spacing between the tones either side of $f_{n\ \max}$. As the position of the cavity

Table 5.1: Tonal frequencies at U=16.6 m/s and $\alpha_{\text{geom.}} = -1°$. The tone with peak far-field acoustic spectral density, $f_{n\ \max}$, is listed in italics.

	f_n				
Cavity Position	1	2	3	4	Smooth plate
	551	601	565	534	563
	633	701	662	636	639
	714	*788*	*766*	*748*	*729*
	804	888	864	859	803
	898	974	976	975	885
	990				996
Δf	86	94	101	112	82

is moved towards the rear of the plate, the frequency spacing increases. This is consistent with a reduction of the characteristic length of a feedback loop between the airfoil trailing edge and the cavity.

5.5.2 Effect of independently shifting cavity edges

The effect of independently shifting cavity edges was investigated. The specific tonal frequencies appear to vary with the cavity trailing edge position rather than the cavity leading edge position. When the cavity trailing edge was moved independently of the cavity leading edge, there was found to be a significant shift in the airfoil tone frequencies. On the other hand, on moving the cavity leading edge independently of the cavity trailing edge, the airfoil tone frequencies showed very little change. There were also differences in the amplitudes of the tones as the length of the cavity and cavity edge positions were varied.

Figure 5.25 shows far-field noise spectra that demonstrate the impact of shifting the cavity leading and trailing edges on airfoil tonal noise frequencies at a jet velocity of 16.6 m/s. The cavity length is shorter for the modified cavities. The 7 mm long (where length refers to the chordwise dimension of the cavity) rectangular cavity was in cavity position 2, as per figure 5.1. As the flow is not impinging on the rear cavity wall (evidenced by the lack of cavity tonal noise), the use of a non-rectangular geometry is unlikely to make a significant difference to the basic trend. The plot shows that, at 10 Hz frequency resolution, the tones for the rectangular cavity are 600, 700, 790, 890, and 980 Hz. The tones with the cavity leading edge shifted are also 600, 700, 790, 890, and 980 Hz. The tones with the cavity trailing edge shifted, on the other hand, are found at 580, 670, 760, 860, and 950 Hz. The tonal noise frequencies thus appear to vary principally with the cavity trailing edge position.

More extensive results are shown in Figures 5.26 and 5.27. A comparison

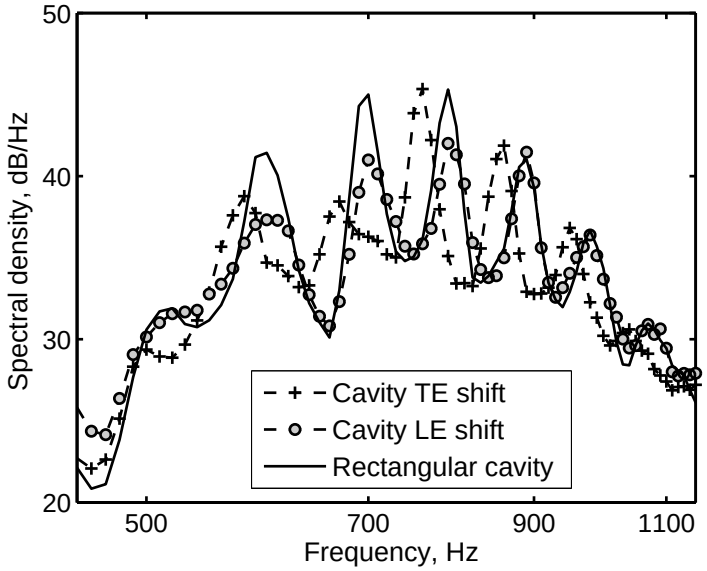

Figure 5.25: Far-field noise spectra showing the impact on airfoil tonal noise of shifting the cavity leading- and trailing edges independently, denoted 'LE' and 'TE' respectively. Measurements taken at jet velocity of 16.6 m/s for cavity position 2, cavity position 2a (cavity leading edge shifted downstream by 3 mm) and cavity position 2b (cavity trailing edge shifted upstream by 3 mm). Geometries are as per fig. 5.1.

between the figures shows that when the cavity trailing edge position is fixed but the cavity leading edge is shifted, the frequencies are generally very similar to those of the rectangular cavity. Minor variations might be attributable to experimental error and to the unknown influence on the airfoil noise of using non-rectangular cavity geometries – as it is known that non-rectangular geometries will have an impact on the internal cavity flow structure and this may subsequently have some influence on the cavity shear layer (Ozalp *et al.*, 2010). On the other hand, figure 5.27 shows that the frequencies are generally significantly different when the cavity trailing edge is shifted and the cavity leading edge is held fixed. Note that the difference in tonal frequencies is more evident at higher velocities, owing to the frequency spacing increasing as velocity increases. Even though the cavity leading edge is a very unstable and notionally receptive point on the airfoil due to the geometry-enforced separation (Dovgal *et al.*, 1994), these results would tend to suggest that a feedback loop may exist between the airfoil trailing edge and a point at, near or controlled by the cavity trailing edge position.

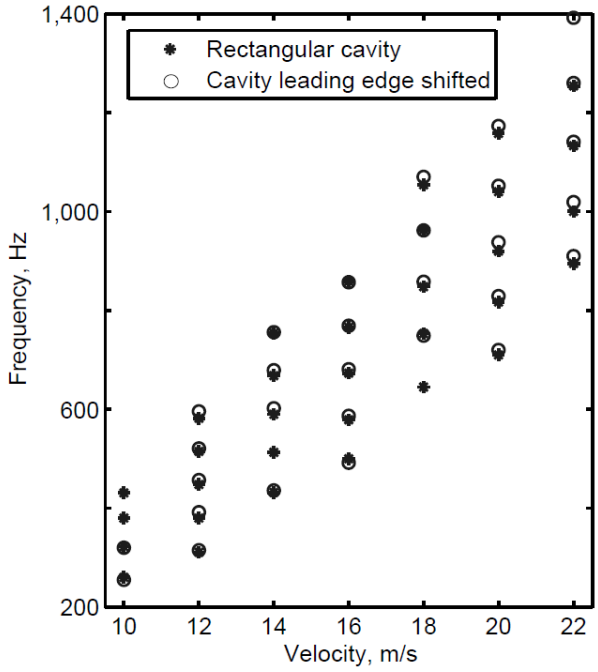

Figure 5.26: Tonal frequencies found for rectangular cavity at position 2 compared to cavity at position 2 with cavity leading edge shifted downstream (cavity position '2a' following figure 5.1). Airfoil at geometric angle of attack of $-1°$.

5.5.3 Velocity spectrum in cavity shear layer

Initial hot-wire measurements were taken at various locations around the airfoil and wake. It was found that in the wake downstream of the pressure side, velocity fluctuations at the airfoil tone frequencies were present. To investigate the role of the cavity, velocity measurements were taken in the cavity shear layer.

In the shear layer over the cavity, velocity fluctuations at backward-facing-step vortex shedding frequencies were found to be present for a typical trailing edge noise case. Figure 5.28 shows a velocity spectrum recorded in the cavity shear layer. The flow configuration was $U = 16.6$ m/s, $\alpha_{\text{geom.}} = -1°$ and the cavity was at position 1. The hot-wire probe was positioned upstream of the cavity trailing edge and below the cavity mouth line. Three broad spectral peaks were found to be present in the shear layer over the cavity. These fluctuations were different from Rossiter (1964) cavity oscillation frequencies. The Strouhal numbers of these observed fluctuations were $St_h = 0.50, 0.66,$ & 0.79, where h is the step-height (in this case, the cavity depth), which are consistent with values for backward-facing-step flows (Lai, Yue and Platzer, 2002). These 'unforced' backward-facing-step frequencies occur rather than cavity frequencies due to a lack of feedback from the cavity trailing edge to the

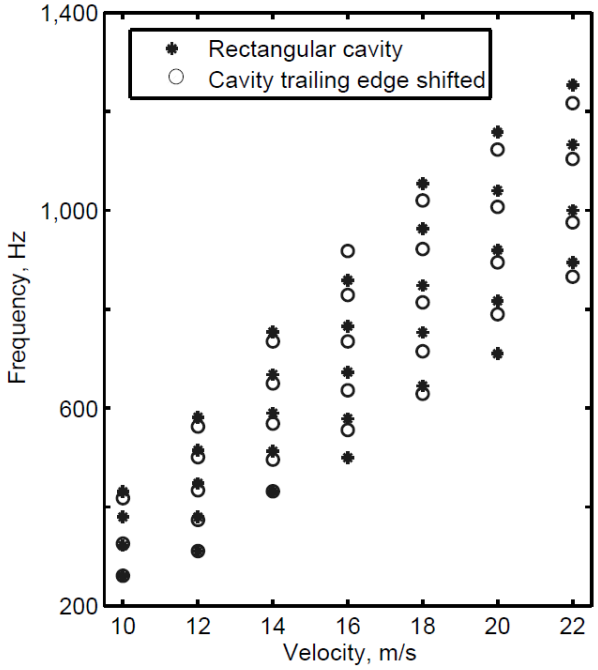

Figure 5.27: Tonal frequencies found for rectangular cavity at position 2 compared to cavity at position 2 with cavity trailing edge shifted upstream (cavity position '2b' following figure 5.1). Airfoil at geometric angle of attack of −1°.

cavity leading edge. The airfoil tones are clearly different to these backward-facing-step vortex shedding frequencies.

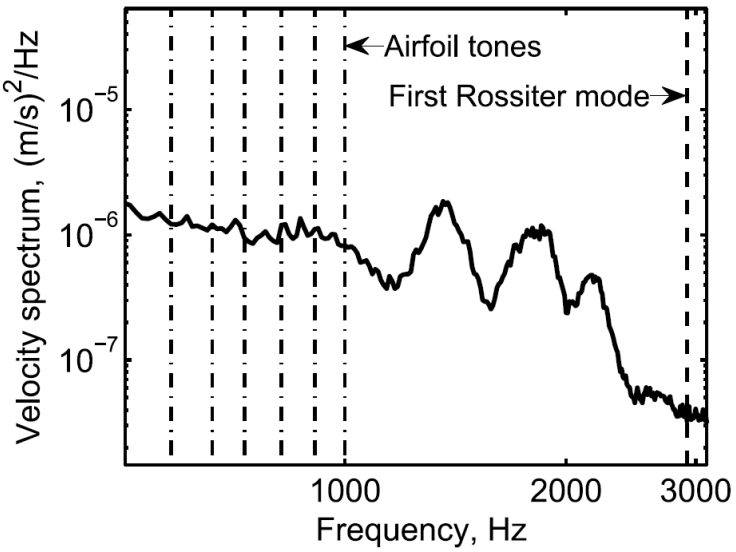

Figure 5.28: Velocity spectrum in the cavity shear layer. U=16.6m/s, $\alpha_{\text{geom.}} = -1^\circ$ and the cavity was at position 1. Probe located at a position of $x/C = -0.70$ and $y/C = 8.5 \times 10^{-3}$, which is upstream of the cavity TE and below the cavity mouth line.

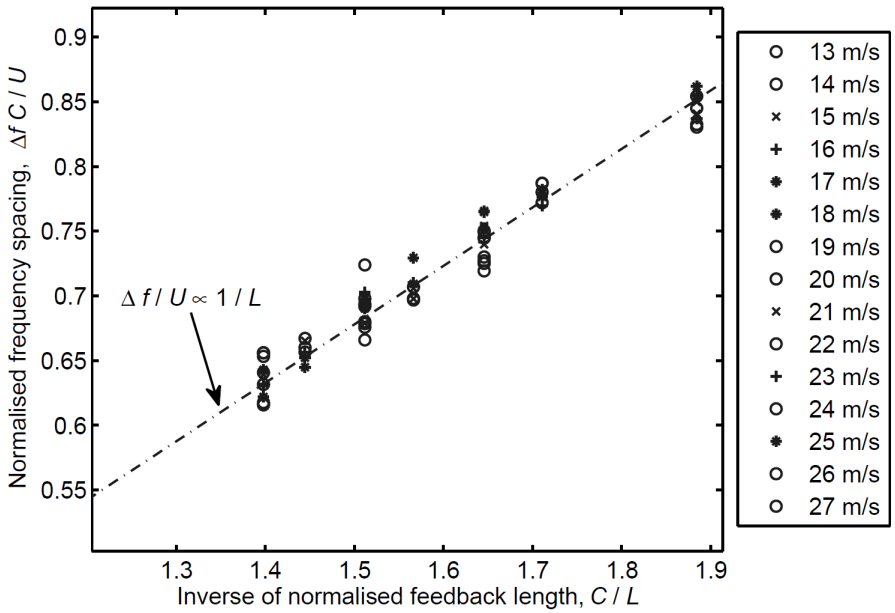

Figure 5.29: Normalised frequency spacing versus nominal normalised feedback length, for seven different cavity trailing edge positions. Data are for cavity positions 1, 1b, 2, 2b, 3, 3b and 4, with plate at a geometric angle of attack of $-7°$.

5.6 Measurements at geometric angle of attack of $-7°$

To attempt to investigate the more fundamental role of the cavity in the production of the airfoil tones, further measurements were taken. Far-field noise and hot-wire measurements were taken at a geometric angle of attack of $-7°$. Firstly, the variation of frequency spacing with cavity trailing edge position was investigated. Secondly, some basic properties of the velocity fluctuations along the boundary layer were investigated. Finally, the effect of acoustic forcing was tested, for a sweep of frequencies, at locations along the boundary layer and in the cavity shear layer. From this, a mechanism for the role of the cavity in the feedback loop is discussed.

5.6.1 Variation of frequency spacing with cavity trailing edge position

The variation in frequency spacing with cavity trailing edge position was investigated. Based on the finding of section 5.5.2, the nominal feedback length was taken to be the distance from the cavity trailing edge to the airfoil trailing edge.

Figure 5.29 shows the normalized frequency spacing ($\Delta C/U$) versus the inverse of the nominal normalized feedback length (C/L, where L is the feedback length), for the seven different cavity trailing edge positions. The cavity geometries were as per Figure 5.1, consisting of positions 1, 1b, 2, 2b, 3, 3b and 4. A linear relation was found (i.e., $\Delta f/U \propto 1/L$) which shows that the frequency spacing is inversely proportional to this distance, across the range of velocities. That is, the frequency spacing varies in line with the geometric ratio of points on the airfoil. If the feedback loop did not originate from the airfoil and was facility related (as suggested by Nash *et al.*, 1999, and Tam & Ju, 2012) then it is unlikely that this would be the case. (Note that, here, frequency spacing was calculated slightly differently to earlier sections: it is the average spacing of all the tones that were reasonably far above the background noise level.)

To the authors' knowledge this is the first time that the inverse proportionality of the frequency spacing – relative to the distance from the airfoil trailing edge to a position on the airfoil – has been experimentally demonstrated, for otherwise equivalent velocity and the same overall airfoil profile, . In the present case, this position is the location of a cavity geometric feature, where there is an enforced separation. Such proportionality is a fundamental feature of the feedback loop model, but it has not been experimentally demonstrated in this way previously.

5.6.2 Boundary layer receptivity and feedback mechanism

Further hot-wire measurements were taken to attempt to clarify the mechanism responsible for the variation in frequency spacing. Measurements were taken along the chord in the boundary layer for U=14 m/s and a geometric angle of attack of $-7°$, for the cases of cavity positions 1 and 4. These cases were chosen to give the largest difference in location, as well as having the most different airfoil tonal frequencies. The probe was automatically lowered to a height corresponding to a local velocity of $u/U = 0.5 \pm 0.05$ for incremental locations along the chord. It was found that discrete velocity fluctuations in the boundary layer were able to be detected at this height.

Figure 5.30(a) and (b) show that multiple discrete tones were present in the noise radiated by the airfoil and that the tones were approximately equally spaced. As for other cases, variation in the trailing edge noise tonal frequencies was found when the cavity position was varied. For cavity position 1, the major tonal frequencies in the far-field noise are at 528, 595, 667, and 742 Hz. The peak tone is 595 Hz. For cavity position 4, the major tonal frequencies in the far-field noise are at 435, 522, 613, and 706 Hz. The peak tone is 613 Hz. The frequency spacing, Δf, was taken to be the average spacing either side of the peak tone following Kingan and Pearse (2009), and was significantly different between the cases. For cavity position 1, Δf=70 Hz,

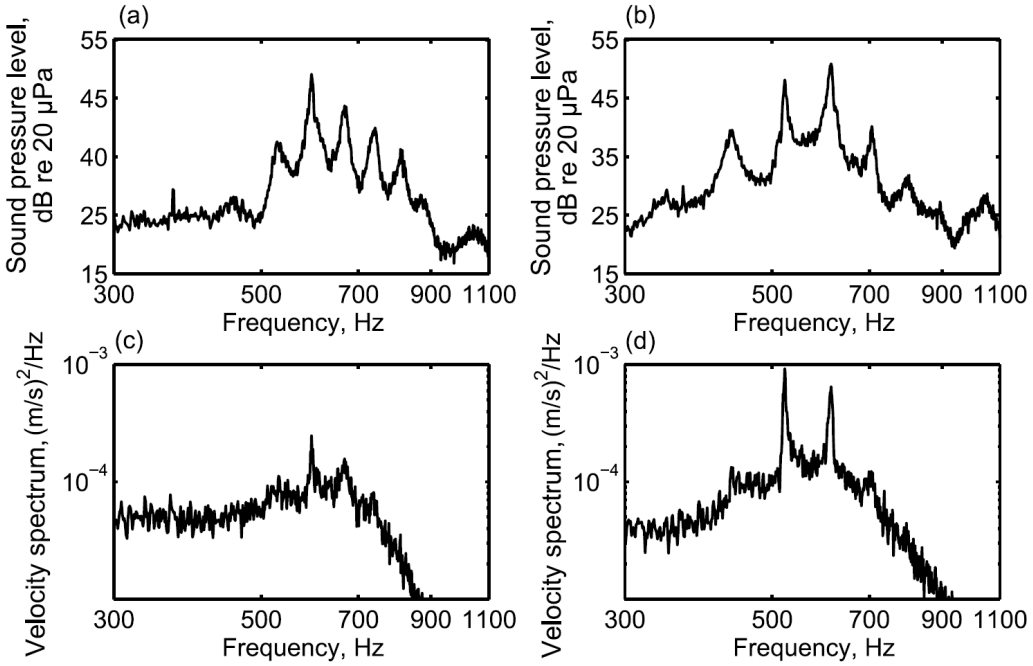

Figure 5.30: Comparison of acoustic (upper) and velocity (lower) spectrum for $U = 14$ m/s and $\alpha_{\text{geom.}} = -7°$. The bandwidth is 1 Hz. Far-field acoustic spectrum for (a) cavity position 1 and (b) cavity position 4. Spectral density of fluctuating velocity in the pressure side boundary layer, measured at $x/C = -0.06$ and height corresponding to $u/U = 0.5 \pm 0.05$, for (c) cavity position 1 and (d) cavity position 4.

but when the cavity moves downstream to position 4, Δf increases to 92 Hz. Velocity spectra taken upstream of the airfoil trailing edge at $x/C = -0.06$ show that velocity fluctuations are present in the boundary layer at essentially the same frequencies as those found in the far-field noise. For cavity position 1 (fig. 5.30(c)), velocity fluctuations were found at 531, 595, 667, and 738 Hz, with the peak at 595 Hz. For cavity position 4 (fig. 5.30(d)), velocity fluctuations were found at 435, 522, 613 and 705 Hz, with the peak at 522 Hz.

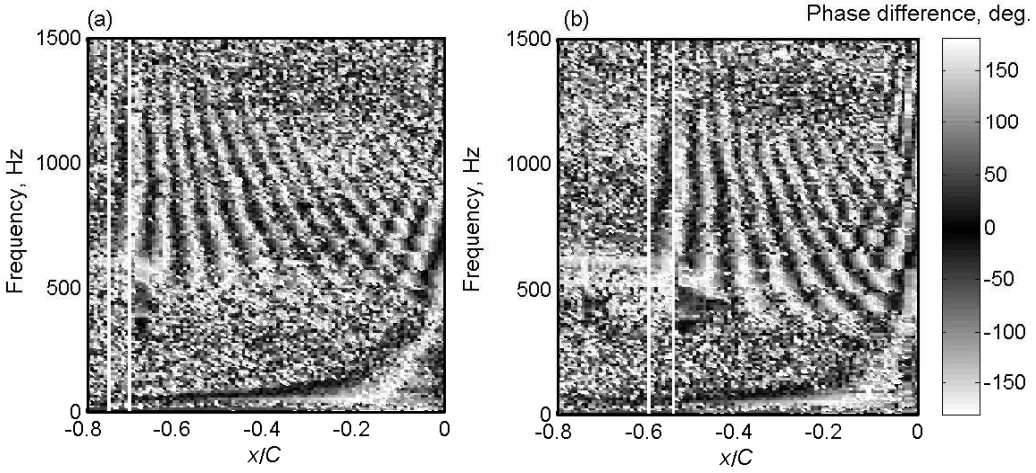

Figure 5.31: Spectral map of phase difference between velocity measurement in the boundary layer, at height corresponding to $u/U = 0.5 \pm 0.05$, and far-field acoustic measurement for (a) cavity position 1 and (b) cavity position 4. The pair of vertical white lines indicate the position of the cavity, with the cavity trailing edge on the right. $U = 14$ m/s and $\alpha_{\text{geom.}} = -7°$.

Figure 5.31 shows spectral maps of the phase difference between the velocity measurement in the boundary layer and the fixed reference given by the far-field acoustic measurement. These plots show that convective boundary layer disturbances at the trailing edge noise frequencies are only detecte downstream of the cavities in each case. These convective disturbances are indicated by the black and white bands which show the relative phase of the disturbances cycling through 2π with each wavelength.

For clarity, figure 5.32 shows the phase difference (represented continuously, starting from an arbitrary value of zero) specifically at one of the airfoil tones, at 610 Hz, for the cavity position 4 case. The author believes that the existence of these waves from, and only from, downstream of some particular location (for which Δf has inverse proportionality relative to distance) has never been experimentally verified previously.

The broadband component of these disturbances covers a range of frequencies from approximately 500 to 1000 Hz. At the presumptive region of formation of these disturbances, nearby to the cavity, similar phase is found for the

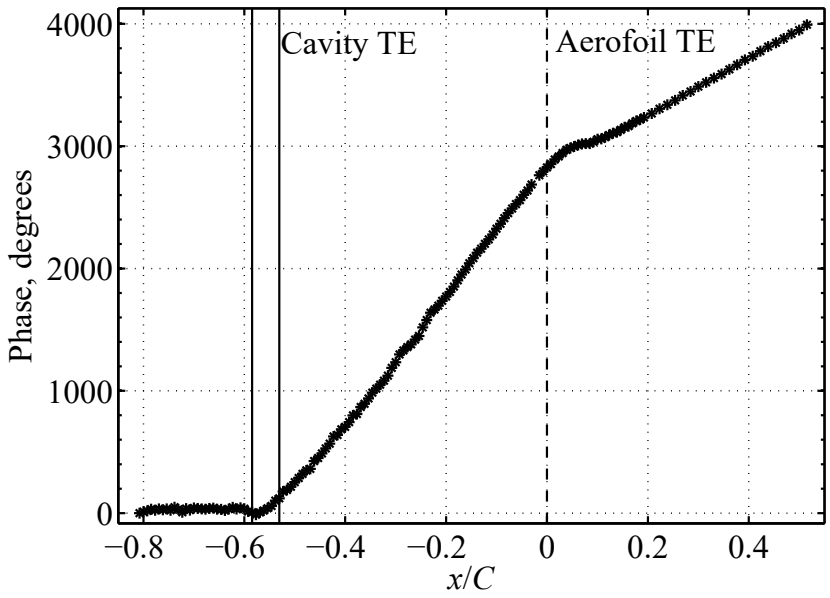

Figure 5.32: Phase difference at 610 Hz, an airfoil tonal noise frequency, between the velocity measurement and far-field reference microphone for cavity at position 4, U=14 m/s and geometric angle of attack of −7°. Velocity measurement heights are as per figure 5.31. The solid vertical lines indicate the position of the cavity.

different frequencies. Having different wavelengths, they deviate downstream. Speckled areas on the plots in figure 5.31 indicate regions where no structured fluctuation is detected, as the relation between phase and position is random.

From figure 5.31, at the peak tone of 600 Hz for cavity position 1, approximately 9.5 convective wavelengths are found between the cavity trailing edge and the airfoil trailing edge. Likewise at 610 Hz for cavity position 4, approximately 7.5 convective wavelengths are found between the cavity trailing edge and the airfoil trailing edge. Knowing the length, the convective velocity over the airfoil can thus be estimated to be $U_c \approx 0.4U$ for both cavity positions. Figure 5.32 demonstrates more clearly how this can be determined by using the slope of the phase plot. Note that downstream in the wake ($x/C > 0.08$) the convective velocity is found to be approximately $U_c = 0.90U$ (based on the nominal, higher, free stream velocity upstream at the jet outlet).

Figure 5.33 shows the coherence between velocity measurements and noise measurements along the boundary layer. Reasonably strong coherence was found between the velocity fluctuations and far-field noise at the tonal noise frequencies. This is indicated by the dark horizontal bands of higher coherence. The white areas, covering most of the plot, indicate frequencies where low coherence was found. Also note that the frequencies are spaced further apart for the cavity at position 4, compared to the more upstream cavity position 1.

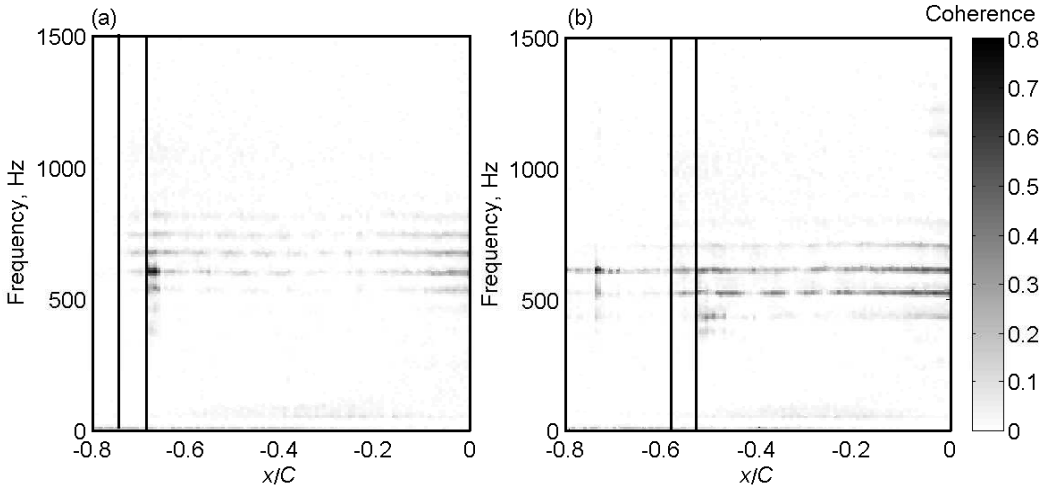

Figure 5.33: Spectral map of coherence between velocity measurement in the boundary layer, at height corresponding to $u/U = 0.5 \pm 0.05$, and far-field acoustic measurement for (a) cavity position 1 and (b) cavity position 4. The pair of vertical lines indicate the position of the cavity. $U = 14$ m/s and $\alpha_{\text{geom.}} = -7°$.

Although high coherence at the tones is found upstream of the cavity in fig. 5.33(b), this is due to the acoustic component of the velocity fluctuation being detected. This is shown to be the acoustic component of velocity by the phase measurement in figure 5.31(b), where upstream of the cavity there are white horizontal bands of nearly constant phase (at the airfoil tones) which are due to the comparatively large acoustic wavelength. It is also shown by the nearly constant phase upstream of the cavity in figure 5.32.

In figure 5.33(b), at $x/C = -0.75$, it appears that the slight roughness present at the very beginning of the first insert (i.e., at the leading edge location of the filled-in cavity position 1) has increased the detection of the acoustic component of velocity in the boundary layer, and hence a stronger coherence has been found. This may be due to the roughness exerting a slightly destabilising effect on the boundary layer, or providing a scattering surface.

Figure 5.34(a) shows the spectral density of the fluctuating velocity along the boundary layer, at the peak tone of 595 Hz for cavity position 1. A local maximum is present just downstream of the cavity trailing edge. This is consistent with a reattachment point of the flow being located there (Diwan and Ramesh, 2009). Downstream, the spectral density steadily increases towards the airfoil trailing edge, starting from just before the final 20% of the chord. Figure 5.34(b) shows the coherence between velocity measurement and far-field noise measurement at 600 Hz. Here it can be seen more clearly that a maximum coherence of 0.74 is found just downstream of the cavity trailing edge. The wave-like pattern in figure 5.34(b) between x/C =-0.6 and x/C =-

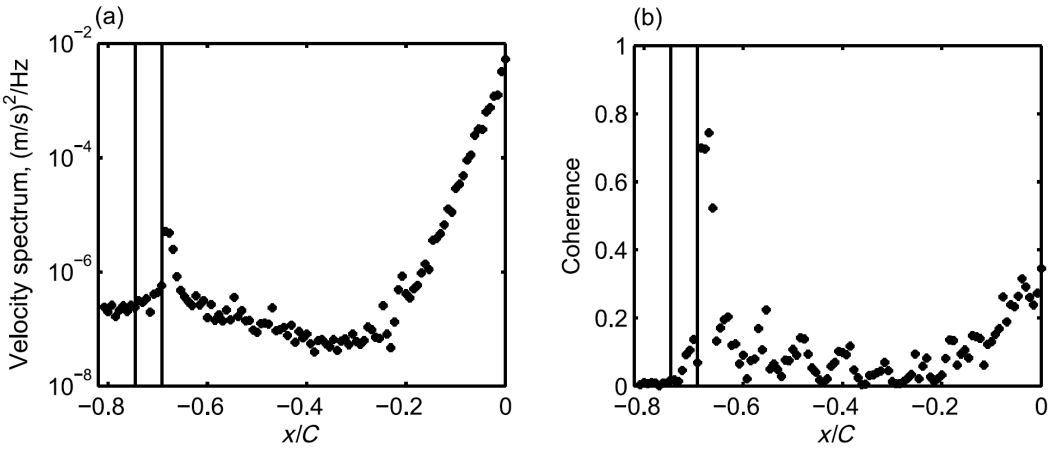

Figure 5.34: Properties along the boundary layer for cavity position 1 at height corresponding to $u/U = 0.5 \pm 0.05$. (a) Spectral density of fluctuating velocity measurement in the boundary layer at 595 Hz. (b) Coherence between velocity measurements and far-field noise at 600 Hz. Note that coherence was calculated with a frequency resolution of 10 Hz, hence the slightly different frequency being plotted. The pair of vertical lines indicate the location of cavity position 1. $U = 14$ m/s and $\alpha_{\text{geom.}} = -7°$.

0.2 is possibly due to an interference pattern between the acoustic velocity and the fluctuating component of the convective velocity; when cancellation occurs the boundary layer fluctuation is difficult to detect, so low coherence is found. The coherence begins to steadily increase from approximately the final 20% of the chord.

Figure 5.35 shows a similar plot (to the cavity position 1 case) for the tone at 610 Hz for the cavity position 4 case. In this instance, local maxima are present at $x/C = -0.52$ (at the cavity trailing edge) and $x/C = 0.02$ (just downstream of the airfoil trailing edge). The local maximum at $x/C = -0.75$ is believed to be due to slight roughness as discussed earlier.

It was considered that scattering at the cavity TE could be the primary acoustic contribution. However, this idea was discounted. A high level of coherence is actually located downstream of the airfoil trailing edge. Coherence measurements for cavity position 4 are included here in figure 5.36. It can be seen that a high level of coherence between the velocity measurement and far-field noise is found downstream of the airfoil TE. In this case, the airfoil TE is known as an efficient noise source. It is known that Rossiter tones, due to impingement of vortices on the cavity TE, are not being produced in this case. Therefore tonal noise is not being produced by impingement on the cavity TE, as if it were it would be locked onto the Rossiter tones. While if there was vortex shedding from a laminar separation bubble located *just downstream* of the cavity TE, i.e., located over the flat plate, then these vortices would

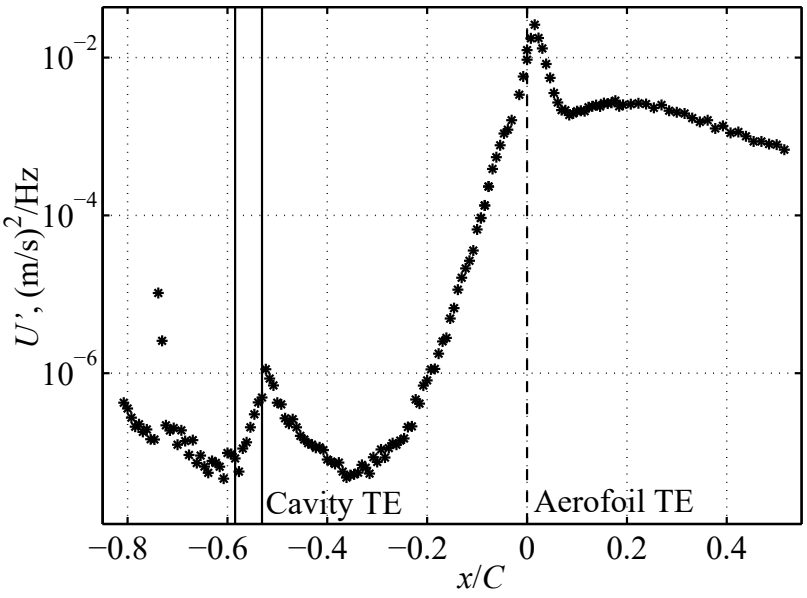

Figure 5.35: Power spectral density amplitude of the fluctuating velocity signal at 610 Hz (corresponding to the main aerofoil tone) for cavity position 4, U=14 m/s, and $\alpha_{\text{geom.}} = -7°$. The solid vertical lines indicate the position of the cavity. Velocity measurement heights correspond to $u/U = 0.5 \pm 0.05$. Measurement through the *wake* taken as a horizontal line downstream from the most downstream boundary layer measurement point.

be a much weaker noise source as compared to the disturbances passing the sharp airfoil TE. Therefore it is discounted that the cavity TE could be the major noise source for this particular type of tone, with the noise likely to be produced near the sharp airfoil TE.

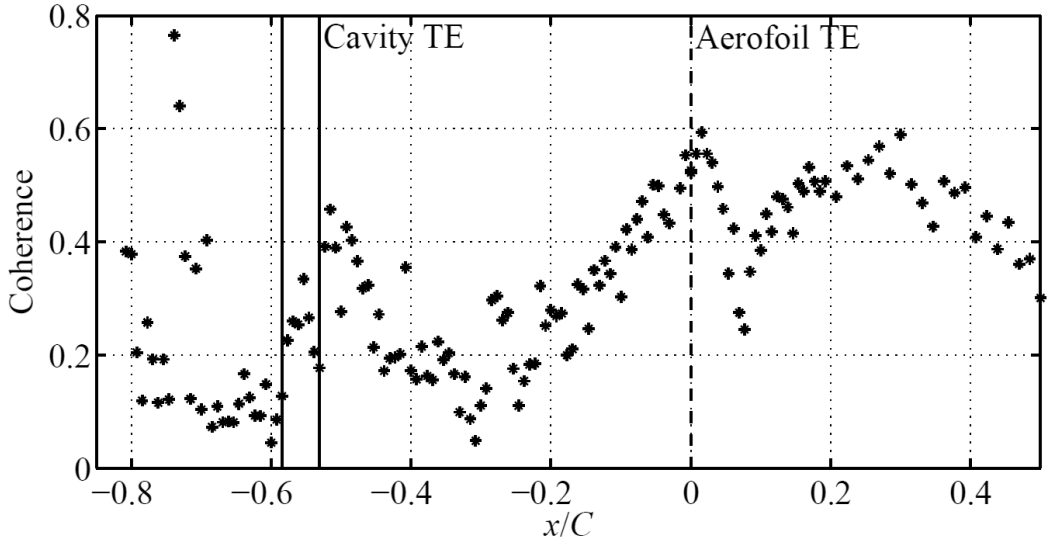

Figure 5.36: Coherence at 610 Hz between the velocity measurement and far-field microphone measurement. $U = 14$ m/s, $\alpha_{\text{geom.}} = -7°$, and cavity at position 4. Measurement height in the boundary layer corresponds to local velocity $u/U = 0.5 \pm 0.05$. Measurement through the *wake* taken as a horizontal line downstream from the most downstream boundary layer measurement point. The solid vertical lines indicate the position of the cavity.

Figure 5.37 shows a spectral map of the fluctuating velocity along the boundary layer. It shows that there is some higher frequency broadband content located around the rear of the cavity, up to approximately 1800 Hz for cavity position 1 and up to approximately 1600 Hz for cavity position 4. This is believed to be related to (broad) backward-facing-step vortex shedding modes over the cavity. Approaching the airfoil trailing edge there is the usual increase in energy content across a range of higher frequencies.

Figure 5.37 also shows that there is at least one strong peak present just downstream of the cavity trailing edge in both cases. It is found at 530 Hz for cavity position 1 and 520 Hz for cavity position 4. There is also another reasonably strong peak at 600 Hz for cavity position 1. These peaks correspond to the airfoil tones in each case.

Velocity spectra that more clearly illustrate the aforementioned peaks are shown in figure 5.38 for the cavity position 1 case. Note that, as the signal level was very low at higher frequencies, some extraneous noise was detected in the form of some very low-intensity narrowband peaks found above 1000 Hz. However this does not impact upon the fundamental conclusions drawn

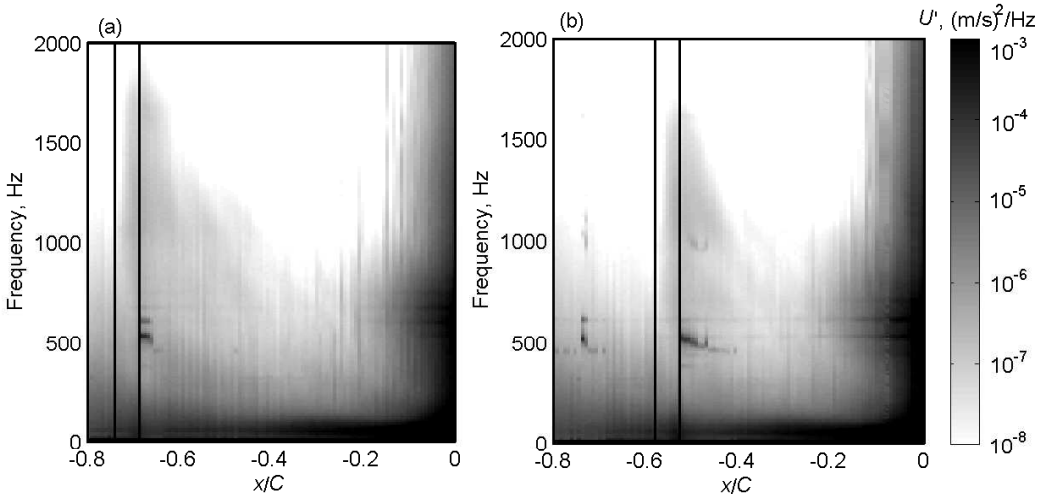

Figure 5.37: Spectral map of the fluctuating velocity along the boundary layer at a height corresponding to $u/U = 0.5 \pm 0.05$, for $U = 14$ m/s and $\alpha_{\text{geom.}} = -7°$. The pair of black vertical lines indicates the locations of the cavities. (a) Cavity position 1. (b) Cavity position 4.

from the results. It can be seen that the boundary layer upstream of the cavity ($x/C = -0.75$) does not contain any major peaks. Within the cavity ($x/C = -0.73$) some peaks start to emerge at approximately 1060 Hz and 1700 Hz which are believed to be possible backward-facing-step vortex-shedding modes. A broad 'hump' forms around these frequencies. This vortex shedding 'hump' loses it's distinction over and above the background noise shortly downstream of the cavity and does not regain it as the airfoil trailing edge is approached. Just downstream of the cavity trailing edge at $x/C = -0.68$, the previously-mentioned major peak is found at 530 Hz, with the other strong peak at 600 Hz, as well another peak at 670 Hz. All of these peaks correspond to the airfoil tones.

As seen in figure 5.34(a), figure 5.38 shows that midway between the cavity and airfoil trailing edge, the fluctuations are relatively weaker and subsequently there are no major peaks evident in the spectra. This can be explained by the boundary layer stabilising once it reattaches. As the airfoil trailing edge is approached ($x/C \geq -0.31$) the broadband 'hump' containing the narrowband airfoil tones emerges clearly in the spectra. This hump and these tones steadily increase in intensity approaching the airfoil trailing edge. This can be explained by the disturbances starting to grow again once the boundary layer separates – the presence of a separation bubble is discussed later in section 5.10.

Figure 5.39 shows that for the cavity position 4 case, the behaviour is very similar to that observed for the cavity position 1 case. The boundary layer upstream of the cavity does not contain any major peaks, aside from one at 310 Hz, the origin of which is unknown. Just downstream of cavity position

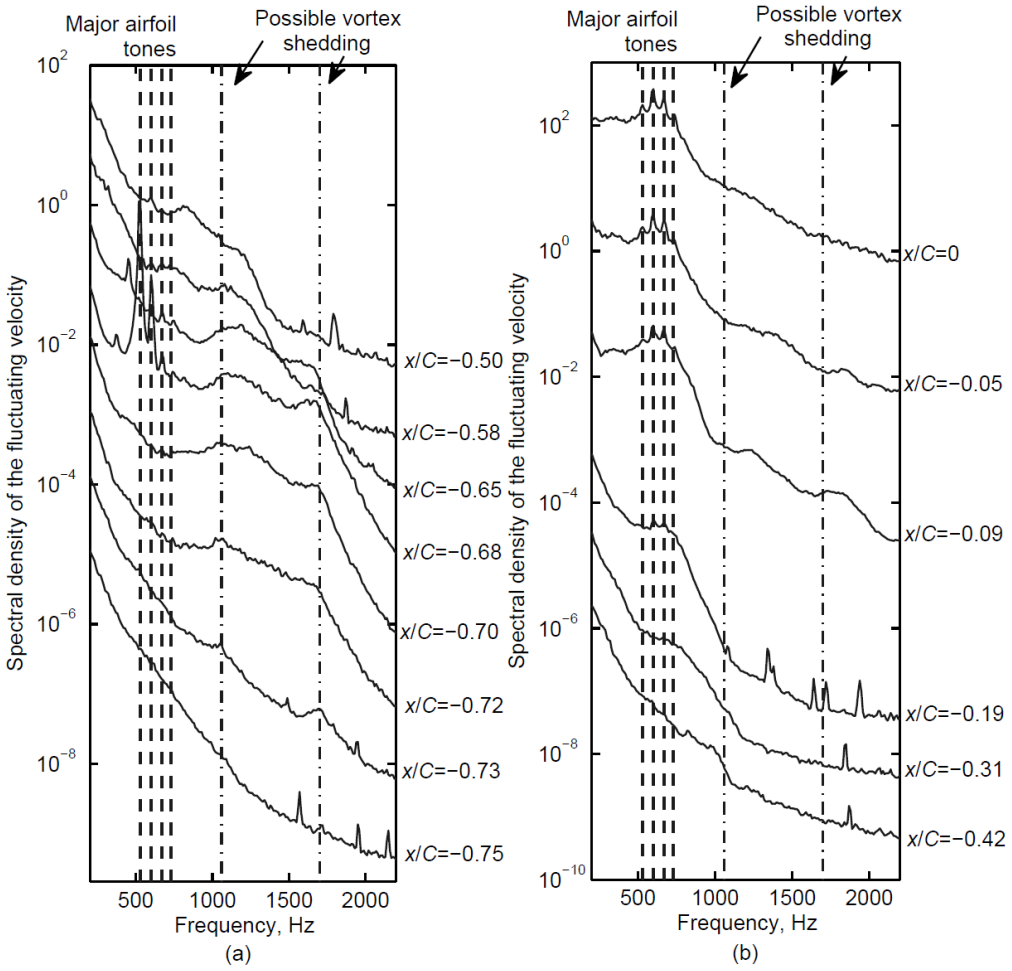

Figure 5.38: Velocity spectra for the cavity position 1 case for (a) locations near the cavity and (b) locations approaching the airfoil trailing edge. Measured at a height corresponding to $u/U = 0.5 \pm 0.05$ in the boundary layer. The spectra are offset by one order of magnitude for clarity. Note that the small narrowband peaks above 1000 Hz are due to extraneous noise, as the signal level was very low. $U = 14$ m/s and $\alpha_{\text{geom.}} = -7°$.

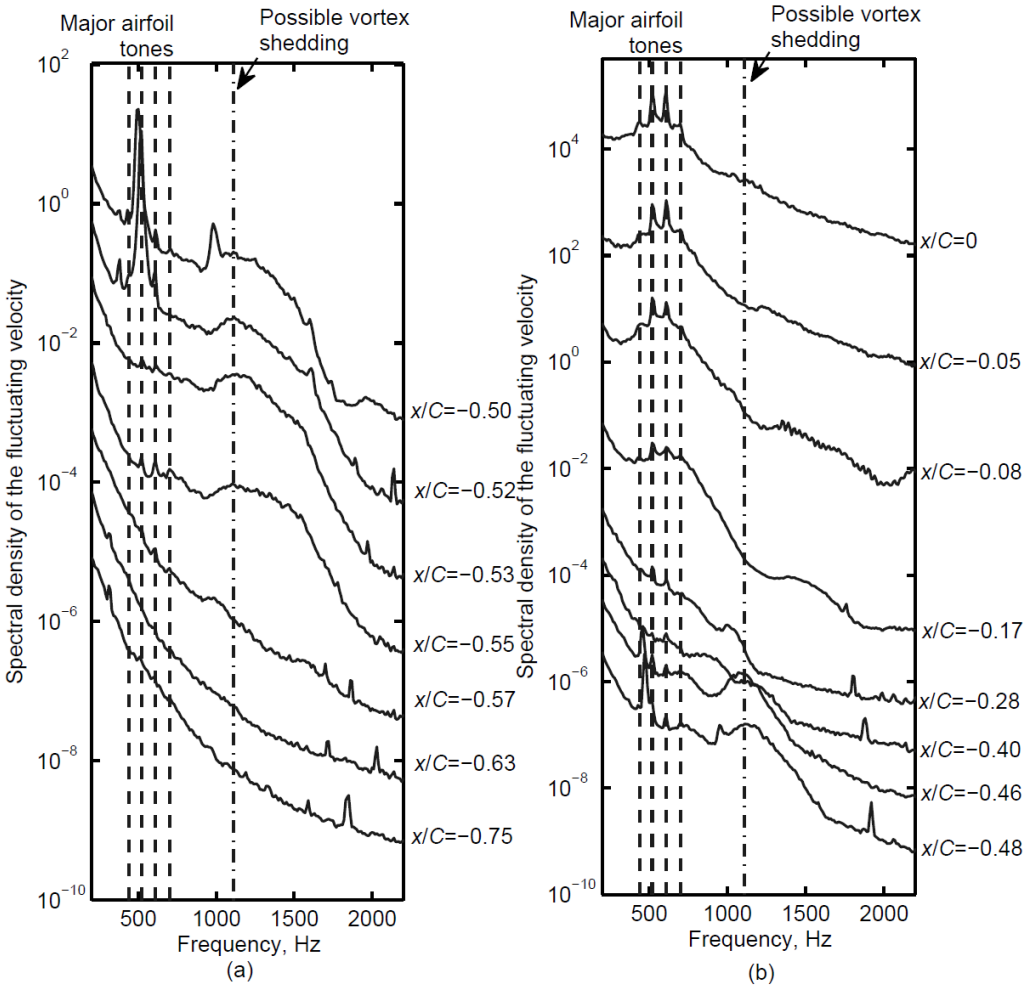

Figure 5.39: Velocity spectra for the cavity position 4 case for (a) locations near the cavity and (b) locations approaching the airfoil trailing edge. Measured at a height corresponding to $u/U = 0.5 \pm 0.05$ in the boundary layer. The spectra are offset by one order of magnitude for clarity. Note that the small narrowband peaks above 1000 Hz are due to extraneous noise, as the signal level was very low. $U = 14$ m/s and $\alpha_{\text{geom.}} = -7°$.

4, at $x/C = -0.52$, a major peak appears at 520 Hz, which corresponds to one of the airfoil tones. The peak found to the left of the 'possible vortex shedding' line for $x/C = -0.50$ and $x/C = -0.48$ is the second harmonic of this major peak. Traveling downstream from the cavity, from $x/C = -0.52$ to $x/C = -0.46$, this major peak appears to shift to lower frequencies and likewise for it's harmonic; although another peak appears at the 520 Hz tone frequency and similarly for the other tone at 610 Hz. As with the cavity position 1 case, as the trailing edge is approached the broadband hump with narrowband airfoil tones emerges clearly in the spectra.

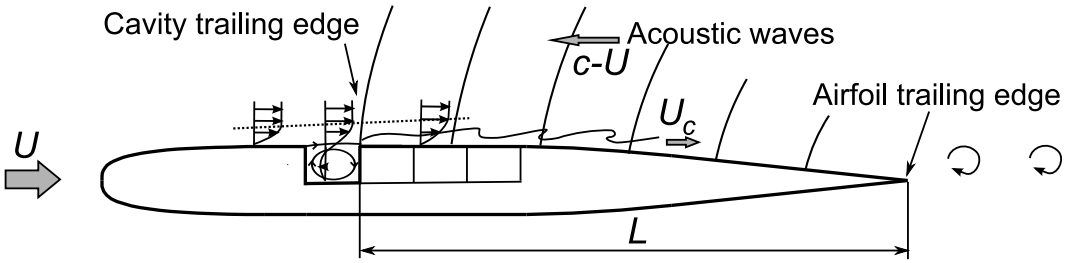

Figure 5.40: Schematic of 'airfoil with cavity' showing proposed feedback loop.

5.6.3 Discussion regarding boundary layer measurements

This section provides a discussion of the proposed airfoil tonal noise mechanism based on the results up to this point. This discussion will be expanded and elaborated upon in later sections (section 5.8 regarding the role of the cavity shear layer and the boundary layer just downstream of the cavity, and sections 5.9 & 5.11 regarding a speration bubble near the airfoil trailing edge).

The cavity cutout in the 'airfoil with cavity' profile is located along the maximum thickness of the airfoil and creates a region of separation. On closed profile airfoils, separation bubbles occur due to the change in pressure gradient near the mid-chord (Dovgal, Kozlov & Michalke 1994). For this plate, a separation point is strongly fixed at the cavity leading edge. Cavity oscillation frequencies are not found for the flow configuration considered in the previous section as the non-dimensional cavity length is below the minimum threshold of 290 (Sarohia, 1977) being approximately 220. Hence the flow separates at the leading edge and reattaches downstream of the cavity trailing edge on the airfoil surface and not on the cavity rear wall.

It is possible to describe the observed behavior as a feedback loop of a form similar to that proposed by Arbey and Bataille (1983). They stated that an acoustic feedback loop occurred between the airfoil trailing edge and the maximum velocity point. As discussed earlier, for this airfoil when varying the cavity leading edge and trailing edge independently, the frequencies were found to change with the cavity trailing edge position. Hence it appears that if an acoustic feedback loop occurs it may occur between the airfoil trailing edge and a point at, near or controlled by the cavity trailing edge position. This is sketched in figure 5.40. Arbey and Bataille's (1983) equation for predicting the feedback tones (equation 2.21) is repeated below as equation 5.3.

$$\frac{f_n L}{U_c}(1 + \frac{U_c}{c - U}) = n + \frac{1}{2} \tag{5.3}$$

For these two flow cases (cavity positions 1 and 4, $U = 14$ m/s and $-7°$ geometric angle of attack), comparisons of experimental frequencies with those given by equation 5.3 were made, taking L to be the distance from the cavity trailing edge to the airfoil trailing edge and using the experimentally found

Table 5.2: Predicted and measured frequencies for cavity positions 1 and 4, $U = 14$ m/s and $-7°$ geometric angle of attack. 'Pred.' refers to predicted frequency from feedback loop model. 'Vel.' refers to tone frequency found from velocity measurement. 'Acous.' refers to tone frequency found from acoustic measurement.

Cavity position 1				Cavity position 4			
Mode	Pred.	Vel.	Acous.	Mode	Pred.	Vel.	Acous.
8	528	531	528	5	439	435	435
9	590	595	595	6	520	522	522
10	652	667	667	7	599	613	613
11	714	738	742	8	679	705	706

value of $U_c \approx 0.4U$ (from section 5.6.2). The nominal feedback length is $L = 90$ mm for cavity position 1 and $L = 69$ mm for cavity position 4. For cavity position 1 the tonal frequencies predicted by equation 2.21 are 528, 590, 652, & 714 Hz for modes $n = 8$ to 11. For cavity position 4 the predicted tonal frequencies are 439, 520, 599, & 679 Hz for modes $n = 5$ to 8. These values show agreement within 5% of the experimental values (either the acoustic or velocity results). For easy comparison, the values are tabulated in table 5.2. The predicted frequency spacing from equation 5.3 (taking $\Delta f = f_{n+1} - f_n$) gives Δf=62 Hz and Δf=80 Hz for cavity positions 1 and 4 respectively. These are under predictions by approximately 13% for both cases compared to experiment, although the trend of frequency spacing being inversely proportional to L is consistent with experiment.

If a feedback loop exists, coupling between acoustic disturbances and convective boundary layer disturbances is happening near the cavity trailing edge where, according to the literature, the acoustic and velocity disturbances would need to be in phase for the acoustic forcing to occur. Strong coherence and strong velocity fluctuations are found there. Just under $n + 1/2$ convective wavelengths were found to occur between the cavity trailing edge and the airfoil trailing edge. This is consistent with the convective disturbance being (nearly) out of phase at the airfoil trailing edge (compared to at the cavity trailing edge) so that an upstream-traveling acoustic disturbance is generated with the correct phase to provide reinforcement at the upstream point, due to the 180° phase shift of the generated acoustic wave (Arbey and Bataille, 1983). The remaining small fraction of a wavelength would be taken up by the acoustic wave, which would close the acoustic feedback loop.

The overall mechanism (as discussed by Arbey and Bataille (1983)) would involve, firstly, there being a broad band of frequencies where instabilities occur in the boundary layer. These frequencies would relate to the neutral stability curves at stations along the airfoil, varying slightly along the airfoil. In this instance, figures 5.31(a) & 5.31(b) show that this band ranges from

approximately 500 Hz to just over 1000 Hz. Upon reaching the trailing edge, the broadband disturbances cause noise due to diffraction. Secondly, coupling occurs upstream. At certain frequencies, corresponding to the feedback loop, acoustic energy serves to reinforce disturbances due to the phasing relation. In this way, discrete tones are selected from the broadband range of frequencies where the boundary layer is unstable. This discussion is believed to report the first evidence of a cavity playing a role in such a feedback loop.

5.7 Acoustic forcing

To investigate the effect of acoustic excitation on the airfoil boundary layer, an attempt was made to drive the boundary layer disturbances using external acoustic forcing. The purpose of these experiments was to observe if, when subject to acoustic forcing at a level above that of the naturally-occuring trailing edge noise, the airfoil boundary layer responded by smoothly peaking at the most unstable Tollmein-Schlichting frequency of the boundary layer, or if discrete frequencies were selectively reinforced indicating the presence of an aeroacoustic feedback loop.

Figure 5.41 shows a schematic diagram of the experimental setup. Sinusoidal waves, for a sweep of frequencies at 10 Hz increments, were generated using a function generator and played through a loudspeaker. The speaker was located downstream of the airfoil, centered at $x/C \approx 2.9$ and $y/C \approx -0.77$. The speaker was facing upstream at an angle of 45° to the horizontal. The airfoil was positioned at a geometric angle of attack of $-7°$. At this angle of attack the airfoil causes deflection of the open jet away from the speaker, so there was minimal effect of the loudspeaker on the flow. The amplitude of the acoustic forcing was maintained constant: assuming an ideal anechoic room, the sound power at the speaker was estimated to be approximately 7 $\times 10^{-4}$ Watts, or a sound power level of 88 dB re: 10^{-12} W.

The first set of measurements were taken for cavity position 1 at $U =$ 13.2 m/s with $\alpha_{\text{geom.}} = -7°$. A hot-wire was positioned in the pressure side boundary layer just upstream of the airfoil trailing edge. It was positioned at a height corresponding to $u/U = 0.5$ and it was located at $x/C = -0.06$.

For this set of measurements, the speaker was able to excite hydrodynamic waves in the boundary layer. Figure 5.42(a) shows the phase difference between the far-field microphone and the hot-wire. The variation in phase at the hot-wire due purely to the variation in acoustic wavelength from the speaker would be expected to be only approximately 700° or $\sim 4\pi$ radians (between 300 Hz and 700 Hz driving frequency). Clearly the actual variation in phase found is far greater than this, which shows that convective instabilities are present.

Figure 5.42(c) plots the spectral density of the velocity fluctuation at the driving frequency and shows that some frequencies appear to be strongly preferred compared to others. This was the case even though the acoustic forcing amplitude was maintained constant and was far greater in level than that pro-

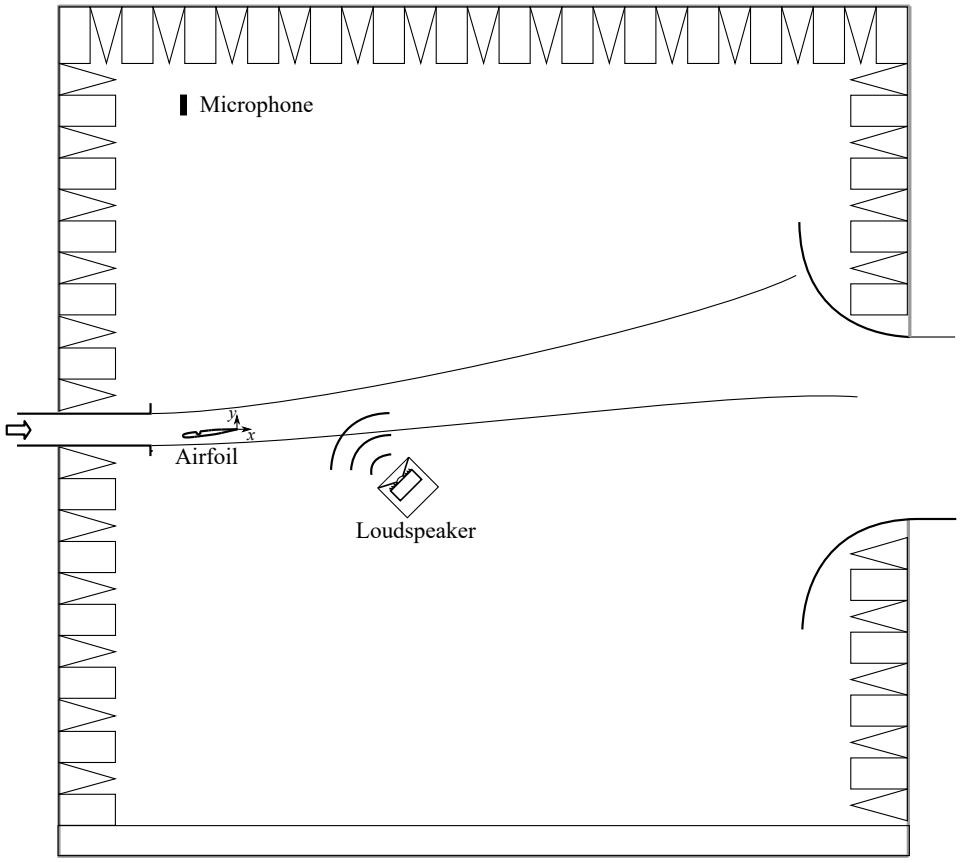

Figure 5.41: Schematic diagram of acoustic forcing experiment.

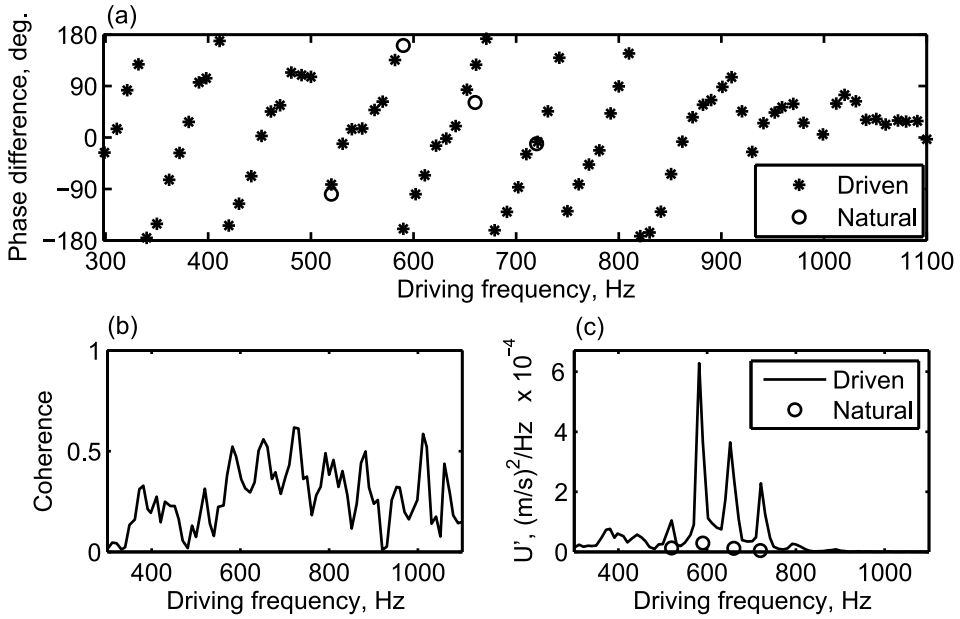

Figure 5.42: Properties in the pressure side boundary layer with acoustic forcing, at $x/C = -0.06$ and height corresponding to $u/U = 0.5$. Cavity at position 1, $U = 13.2$ m/s, and $\alpha_{\text{geom.}} = -7°$. (a) Phase difference (at the driving frequency) between the hot-wire and the far-field microphone. (b) Coherence (at the driving frequency) between the hot-wire and the far-field microphone. (c) Spectral density of the fluctuating velocity (at the driving frequency).

duced naturally by the plate. The preferred frequencies are approximately spaced at 70 Hz, as with the naturally occurring tones, and also they correspond to the naturally occurring frequencies, being located at approximately 520, 590, 660 and 720 Hz. Figure 5.42(b) shows that higher coherence between the microphone and hot-wire is also found at these and other certain frequencies, also spaced at approximately 70 Hz.

It is proposed that although the speaker forces the vortices to have a certain phase, by the definition of the feedback loop at the supported frequencies, the flow-generated acoustic waves will also match in phase upstream at the coupling point. This occurs since the right number of convective wavelengths are present in order that the acoustic waves generated at the airfoil trailing edge have the required phase to provide reinforcement at these particular frequencies. Therefore the feedback loop still reinforces certain frequencies; the system organizes itself so that the relative phase is the same as it would be naturally, as seen in figure 5.42(a). This apparent preference for some frequencies is consistent with the existence of some form of acoustic feedback loop. The initial level of the convective disturbance is greater due to the forcing; therefore the flow-generated noise at the trailing edge is greater due to the stronger disturbance, and then this flow-generated noise feeds back constructively adding to the external forcing, and so on.

The spectral density of the velocity fluctuation at the peak of 582 Hz is approximately 20 times greater in the forced case than in the natural case. Presumably in the natural case, insufficient acoustic feedback is produced to saturate the mechanism. Figure 5.11 confirms that this particular flow configuration ($U = 13.2$ m/s, $\alpha_{\text{geom.}} = -7°$ & cavity position 1) is below the 'plateau' in amplitude which is supposed to be indicative of a saturated feedback loop (Tam, 1974). Hence there is 'room' for the boundary layer disturbances to be stronger when supplied with more acoustic energy. However, the response is stronger at certain nearly-discrete frequencies. If there was no acoustic feedback loop, then the fluctuation strength should be purely due to the level of acoustic forcing, which was fixed, and the growth rate for the boundary layer disturbance at that frequency would be expected to vary in a smooth manner (for example, the growth rate curves given by Kingan and Pearse (2009)). That is, with no feedback loop, a smooth curve peaking at the most amplified Tollmien-Schlichting (T-S) boundary layer instability frequency would be expected, which is not the case observed here.

To investigate the response of the airfoil to acoustic forcing further, measurements were taken in the cavity shear layer and also immediately downstream of the cavity. In the cavity shear layer, only acoustic disturbances appeared to be detected at the airfoil tone frequencies. Figure 5.43 shows velocity properties in the cavity shear layer with acoustic forcing applied. The hot-wire probe was located downstream of and near to the cavity leading edge. At this position, figure 5.43(a) shows that the variation in phase found across the driving frequencies is of the order of $\sim 4\pi$ suggesting that the velocity

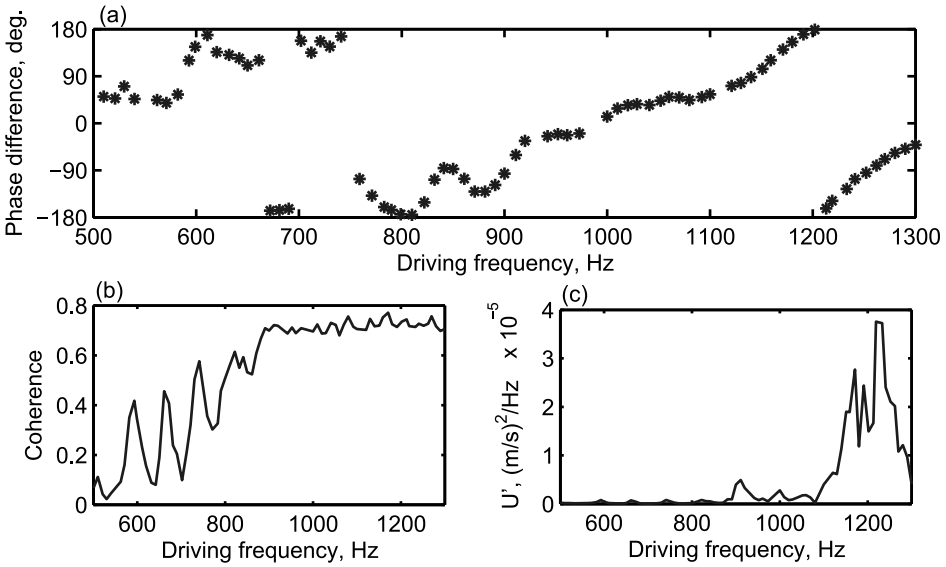

Figure 5.43: Velocity properties in the cavity shear layer with acoustic forcing applied, with hot-wire probe at location of $x/C = -0.727$ and at height corresponding to $u/U = 0.5$ ($y/C = -0.131$). This location is in the cavity shear layer downstream of the cavity leading edge. Measurement taken at U=17.5 m/s, with cavity at position 1 and plate at -7° geometric angle of attack. (a) Phase difference (at the driving frequency) between the hot-wire and the speaker signal. (b) Coherence (at the driving frequency) between the hot-wire signal and the far-field microphone signal. (c) Spectral density of the fluctuating velocity (at the driving frequency).

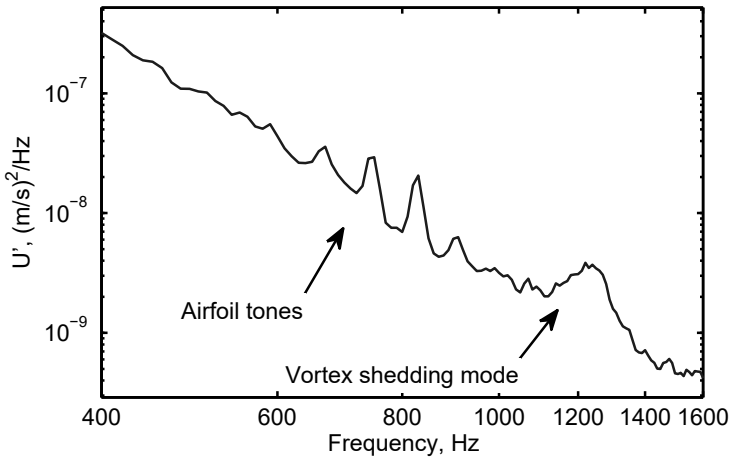

Figure 5.44: Velocity spectrum for the natural, unforced, case with hot-wire probe at location of $x/C = -0.727$ and at height corresponding to $u/U = 0.5$ ($y/C = -0.131$, note origin is fixed to airfoil trailing edge but y-direction is in the geometric Aww). This location is in the cavity shear layer downstream of the cavity leading edge. Measurement taken at U=17.5 m/s, with cavity at position 1 and plate at $-7°$ geometric angle of attack.

fluctuations detected at the airfoil tone frequencies are acoustic in nature. Figure 5.43(c) shows that the shear layer responds to the acoustic forcing at a range of frequencies centered around 1220 Hz. The velocity fluctuation level at this frequency with the acoustic forcing applied is three orders of magnitude greater than the natural level. Figure 5.44 is the natural, unforced, velocity spectrum at the same location in the cavity shear layer and this shows that for the unforced case there is a broad hump present which is centred around 1230 Hz. This is likely to be a backward-facing-step vortex-shedding mode. The airfoil tones present in this velocity spectrum are believed to be due to detection of the acoustic component of velocity only. Therefore, with forcing, the cavity shear layer appears to be responding to the acoustic forcing at the vortex shedding mode but not at the airfoil tones. This would tend to suggest that the cavity shear layer is, expectedly, unstable (both naturally and to acoustic forcing) but only for higher frequencies than those of the airfoil tones.

Figure 5.45 shows the velocity properties in the boundary layer, with acoustic forcing applied, at a location slightly downstream of the cavity trailing edge. The phase difference here shows that convective disturbances *are* detected at the lower end of the driven frequency range, up to approximately 750 Hz. The spectral density of the fluctuating velocity (figure 5.45(c)) shows that the response here is strong at 560 Hz. There is a separate peak at 670 Hz. The 670 Hz peak corresponds to an airfoil tone and the 560 Hz peak is near to the frequencies of the airfoil tones. The spectral density of the fluctuating

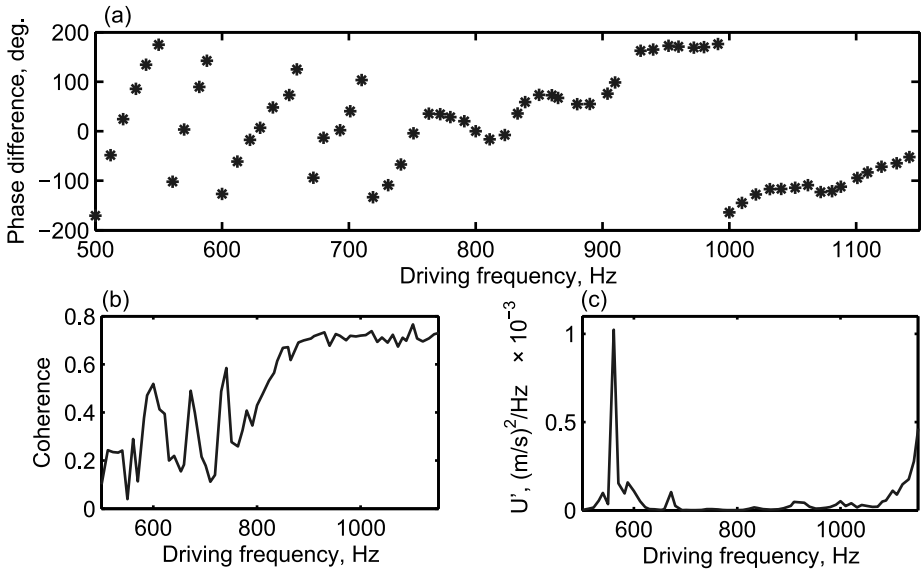

Figure 5.45: Velocity properties with acoustic forcing applied, with hot-wire probe at location of $x/C = -0.685$ and at height corresponding to $u/U = 0.5$ ($y/C = -0.129$). This location is in the boundary layer just downstream of the cavity trailing edge on the pressure surface of the plate. Measurement taken at U=17.5 m/s, with cavity at position 1 and plate at -7° geometric angle of attack. (a) Phase difference (at the driving frequency) between the hot-wire and the speaker signal. (b) Coherence (at the driving frequency) between the hot-wire signal and the far-field microphone signal. (c) Spectral density of the fluctuating velocity (at the driving frequency).

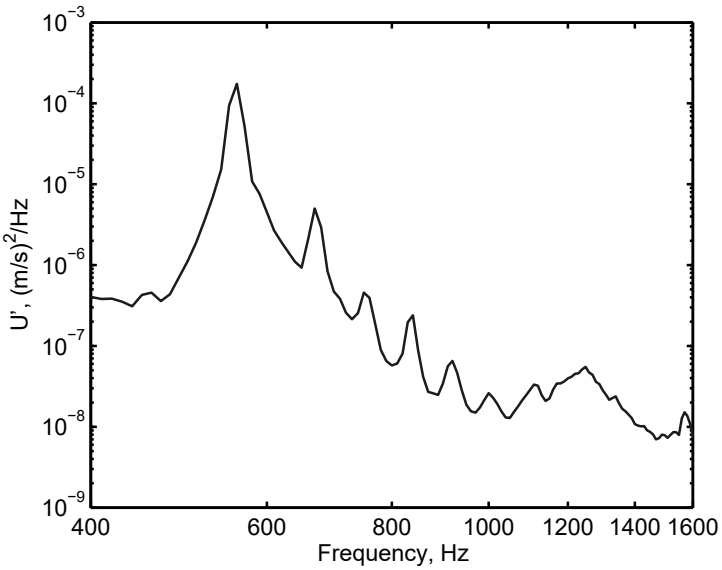

Figure 5.46: Velocity spectrum for the natural, unforced, case with hot-wire probe at location of $x/C = -0.685$ and at height corresponding to $u/U = 0.5$ ($y/C = -0.129$). This location is in the boundary layer, slightly downstream of the cavity trailing edge. Measurement taken at U=17.5 m/s, with cavity at position 1 and plate at $-7°$ geometric angle of attack.

velocity starts to increase at the upper end of the frequency range (near the backward-facing-step frequencies) which is believed to be due to the response of the upstream cavity shear layer.

Figure 5.46 shows the velocity spectrum for the natural unforced case, at the same location slightly downstream of the cavity trailing edge, as for figure 5.45. Here, the strong peak present at 560 Hz can be seen. The intensity of this peak, when the acoustic forcing was applied, was an order of magnitude larger compared to the level found in the natural case. A second peak at 670 Hz is present. This peak was three orders of magnitude larger when acoustic forcing was applied, compared to this unforced case. There are further peaks at 750 Hz and 840 Hz. The three higher frequency peaks corresponded to the airfoil tones, which at the far-field microphone (at 1 Hz frequency resolution) were identified at 669 Hz, 753 Hz and 835 Hz. The preceding airfoil tone is at 596 Hz rather than 560 Hz however. As the measurement position is not at the cavity trailing edge, but rather it is slightly downstream from it, the strong peak has presumably drifted away from the airfoil tone frequency slightly by this location as seen in, and discussed for, figure 5.39.

5.8 The role of the cavity

5.8.1 Inflectional velocity profiles

For the flow configuration discussed in section 5.6.2, inflectional velocity profiles due to separation may be present for at least 10 mm downstream of the cavity trailing edge at position 4. The stationary single-wire hot-wire probe used to measure velocity is incapable of discerning reversed flow. According to Watmuff (1999), the region affected by rectification errors may extend, from the wall, well beyond any region of reversed flow due to the 'greater amplitude of the velocity fluctuations approaching reattachment' (Watmuff, 1999, p. 143). The velocity profiles shown in fig. 5.47 (upstream, $x/C < -0.546$, and downstream of the cavity trailing edge, $x/C > -0.523$) are not reliable, nevertheless they serve as an indication of the existence of reversed flow and inflectional profiles downstream of the cavity trailing edge, in the region where the boundary layer reattaches. Such velocity profiles are likely to be more unstable than non-inflectional profiles (Nash *et al.*, 1999).

5.9 Cavity flow visualisation

A water tunnel hydrogen bubble flow visualisation was conducted with cavity parameters representative of the 'airfoil with cavity' flow configuration. The freestream velocity was set to 103 mm/s, giving a length-based Reynolds number of 6,700 ($L = 65$ mm & $D = 75$ mm). This is close to the 'airfoil with cavity' in air where the length-based Reynolds number of the cavity was 6,500

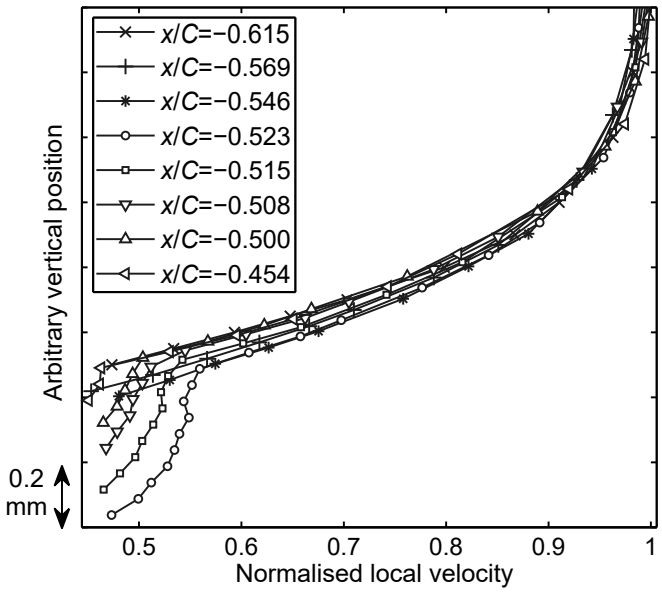

Figure 5.47: Partial velocity profiles measured with stationary single-wire probe. Measurement taken at U=14 m/s, with cavity at position 4 and plate at $-7°$ geometric angle of attack. The horizontal locations with normalised values greater (or less negative) than $x/C = -0.523$ are downstream of the cavity trailing edge.

(L = 7 mm & D = 6 mm) for a freestream velocity of 14 m/s. Table 5.3 compares the non-dimensional flow parameters between the 'airfoil with cavity' in the AWT and the cavity model in the water tunnel, and shows that the parameters for the visualisation in water were very close to the experiment in air. Both models had a laminar boundary layer type. Boundary layer parameters were estimated based on Blasius boundary layer theory and the boundary layer characteristics of the 'airfoil with cavity' were confirmed in section 4.2. The final column of table 5.3 shows the Sarohia (1977) parameter, with both cavity flows being below the threshold of 290 indicated for cavity oscillations.

Figure 5.48 shows that although vortices roll up over the cavity, the vortices

Table 5.3: Non-dimensional boundary layer parameters for cavity flow visualisation.

	L/D	Re_L	Re_{δ_0}	Re_{θ_0}	D/δ_0	D/θ_0	L/δ_0	L/θ_0	$L/\delta_0\sqrt{Re_{\delta_0}}$
Air	1.17	6500	874	116	8.3	48	7.4	56	220
Water	0.087	6700	929	123	6.4	62	7.2	54	219

do not impinge on the rear wall of the cavity, and are found to mostly escape from the cavity. Therefore an intermittent region of separation forms, just downstream of the trailing edge of the cavity. This region of separation is consistent with the inflectional velocity profiles measured in air in section 5.8.1.

It was found that the shear layer over the cavity, and especially the boundary layer downstream, had 'smooth' flow as expected. This is depicted in figure 5.49. This is consistent with the notion that the reattached boundary layer downstream of the cavity (on the airfoil surface) is essentially not significantly disturbed by flowing over the cavity, for these Reynolds numbers. This is an important part of the noise airfoil tonal noise mechanism. If the vortex shedding over the cavity was excessive, then the downstream boundary layer instability waves responsible for the airfoil tonal noise would perhaps not be supported. Note that in figure 5.49, the third frame is essentially the same as the first frame, indicating a highly periodic flow.

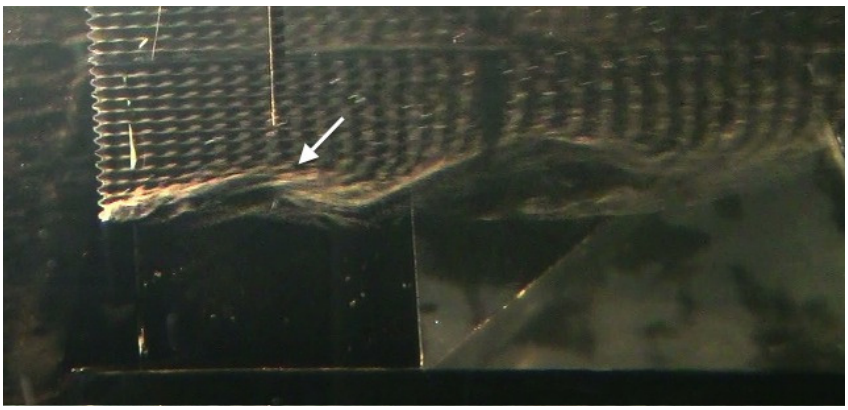

(a) $t = 0$ s

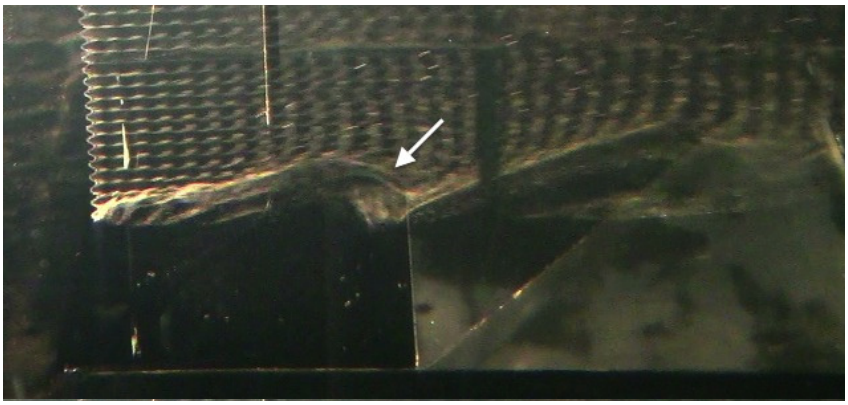

(b) $t = 0.3$ s

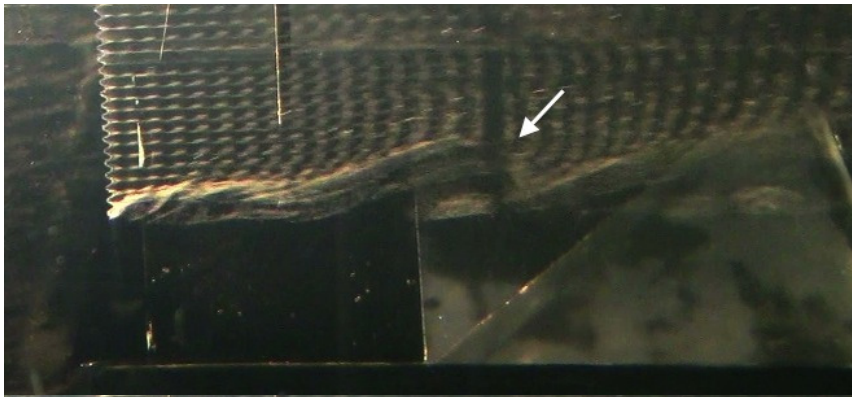

(c) $t = 0.6$ s

Figure 5.48: Flow pattern produced by the vertical hydrogen bubble wire. Wire position at $z/D = 0$. Length-to-depth ratio is 0.87. Length-based Reynolds number is 6700. Flow is from left to right.

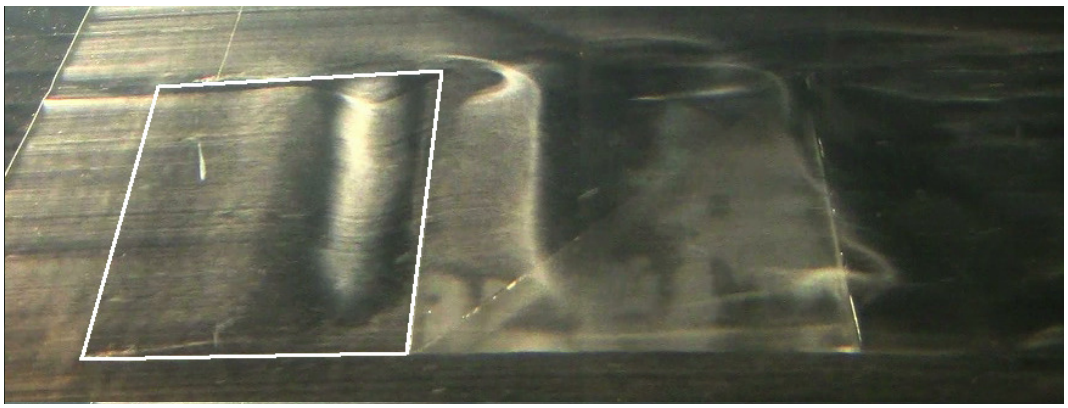

(a) $t = 0$ s

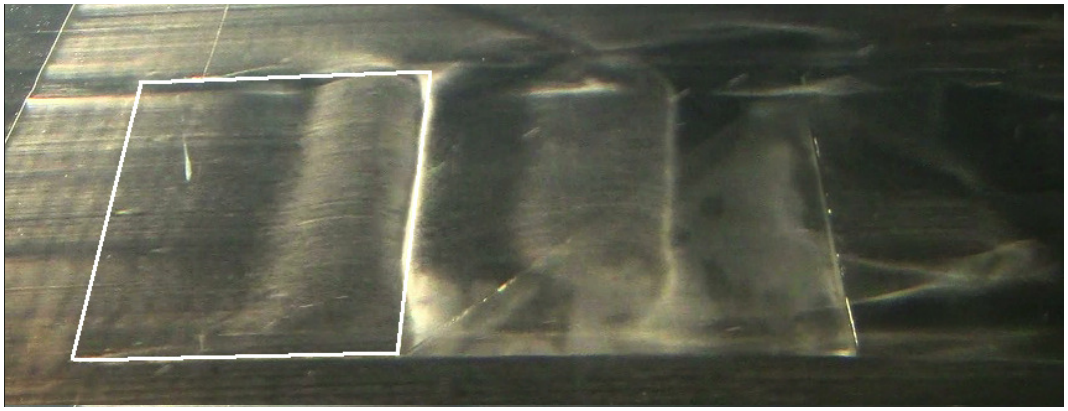

(b) $t = 0.4$ s

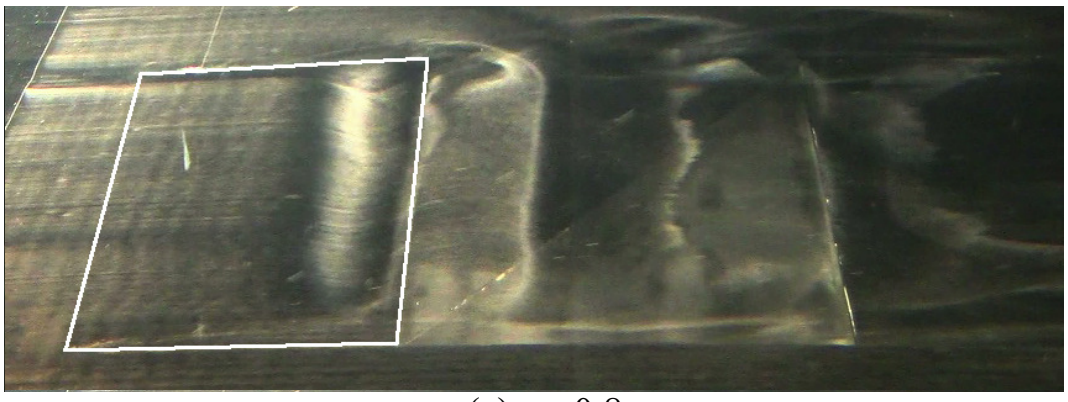

(c) $t = 0.8$ s

Figure 5.49: Hydrogen bubble flow visualisation of rectangular cavity with $L/D = 0.87$, with horizontal wire. Length-based Reynolds number is 6,700 (U =103 mm/s, and the depth-based Reynolds number is 7,700). Flow from left to right. The camera view is oblique, and the top edges of the cavity have been indicated using a white quadrilateral.

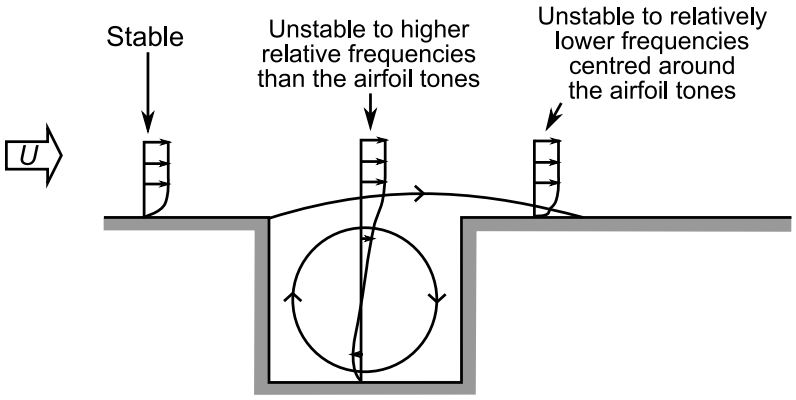

Figure 5.50: Sketch of the likely relative stability of the boundary layer around the cavity, in the production of airfoil tonal noise from the 'airfoil with cavity'.

5.9.1 Mechanism for the role of the cavity in the feedback loop

Figure 5.50 summarises the preceding discussion in a sketch. The role of the cavity in the feedback loop can be related to a qualitatively simple mechanism, which is: the cavity is not responsive to acoustic forcing at the airfoil tone frequencies (section 5.7), while the boundary layer downstream of it is. Following figure 5.50:

1. For this airfoil profile, the boundary layer upstream of the cavity appears to be stable. It is generally subject to a favorable pressure gradient, until the cavity leading edge is reached.

2. The cavity leading edge is a very unstable point in the flow over the airfoil due to the geometry-enforced separation. However, the cavity shear layer is unstable (both naturally and to acoustic forcing) at higher frequencies than the airfoil tones. Specifically, fluctuations at backward-facing-step vortex shedding modes were present [identified in both velocity measurement (section 5.6.2 & section 5.7) and flow visualisation (section 5.9)], which were at higher frequencies than the airfoil tones.

3. The boundary layer downstream of the cavity is unstable to lower frequencies than the cavity shear layer. It has an inflectional velocity profile [identified in velocity measurement (section 5.8.1)]. It is unstable to acoustic forcing at these frequencies. This range of lower unstable frequencies is centred around the airfoil tones. Due to the low Reynolds number and short cavity length, the boundary layer does not become turbulent downstream of the cavity but rather it is laminar-transitional; thus it supports the boundary layer waves that are ultimately involved in the production of the trailing edge noise. This trailing edge noise pro-

vides the acoustic forcing back to the cavity trailing edge, which closes the feedback loop.

5.10 Separation bubble near airfoil TE

In order to identify regions of flow separation, the flow on the surface of the plate was visualised. A mixture of methylated spirits, water, talcum powder and food colouring was applied. This was allowed to dry under the influence of the flow.

Figure 5.51 shows the pattern for the cavity on the pressure side, and figure 5.52 shows the pattern for the smooth surface on the pressure side. In both cases, the airfoil was at a geometric angle of attack of $-7°$. The region where there is an influence of the exposed screwheads on the smooth pressure side is not thought to be too significant, and can be ignored.

Both patterns suggest that there may be an elongated region of separated reversed flow located along the tapered tail section of the airfoil. It can be seen that the pattern upstream of this tail section is uniform and smooth.

The smooth version of the profile was also simulated using XFOIL (Drela, 1989), a panel-method code coupled with the integral boundary layer method. Results from this code were consistent with the flow visualisation, in that they suggested that a region of mildly separated flow may exist along the tail section of the profile on the pressure side.

Regarding the location of separation, the flow visualisation for the cavity pressure side suggests separation may occur at approximately 64% to 72% chord. Similarly, the flow visualisation for the smooth pressure side suggests separation may occur at approximately 64% to 74% chord. Additionally, XFOIL skin friction results are consistent with this as they suggest separation occurring at approximately 70% chord, for the chord-based Reynolds range of 100,000 to 200,000.

Referring to the spectral density plot for the cavity position 1, $U = 14$ m/s case, shown in figure 5.34(a), it can be seen that steady amplification of disturbances occurs downstream of $x/C = -0.3$ – i.e., 70% chord, consistent with the location of the TE separation bubble found via flow visualisation. The role of a trailing edge separation bubble in amplifying boundary layer disturbances was discussed by Nash *et al.* (1999). In this case, the increase in spectral density downstream of $x/C = -0.3$ is consistent with the TE separation bubble amplifying the disturbances. (On the other hand, upstream of $x/C = -0.3$ there is little growth in disturbance amplitude (figure 5.34(a)). Indeed, between $x/C = -0.6$ and $x/C = -0.3$, there is a decrease in spectral density with increasing downstream distance.)

To summarise, previous studies have found amplification of disturbances approaching the airfoil TE as discussed in section 5.6.2, while in this section an apparent region of separation near the TE has been identified. These observations are consistent with major aspects of the airfoil noise model proposed by Nash *et al.* (1999). Although Nash *et al.* (1999) described that separation played an important role in amplifying the disturbances, they proposed that feedback occurred about this bubble rather than an Arbey and Bataille (1983)

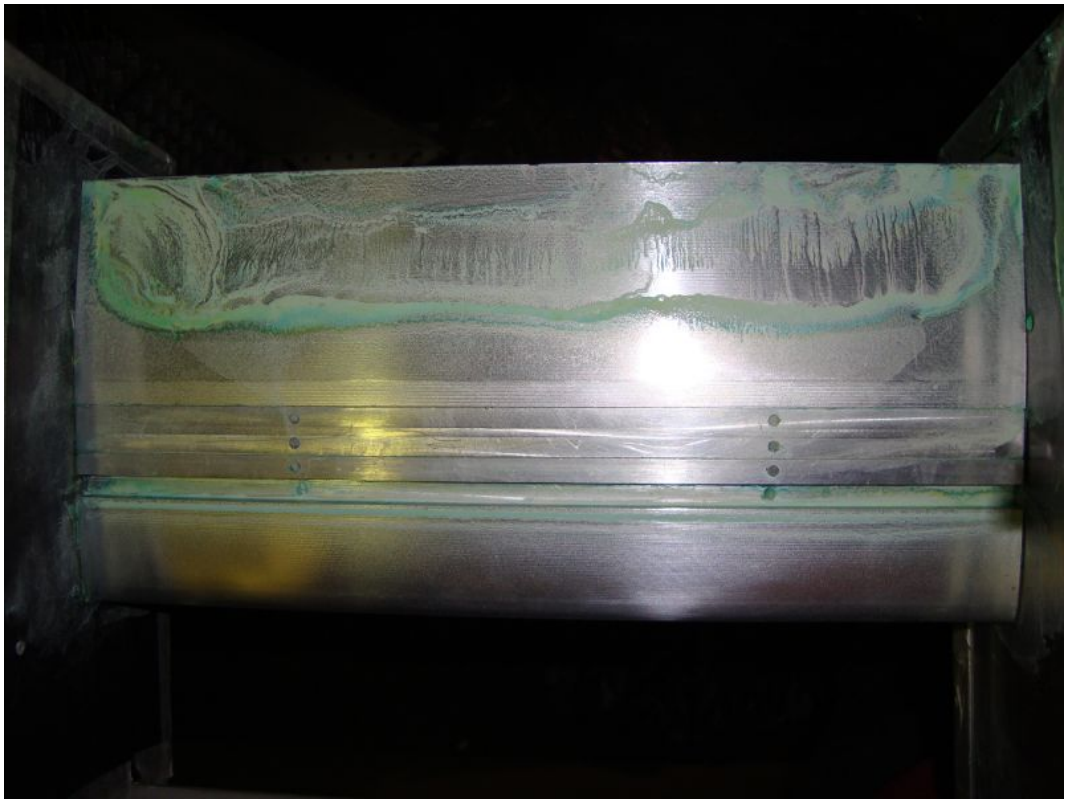

Figure 5.51: Surface flow visualisation of airfoil pressure side with cavity, flow from bottom to top.

type feedback loop with a point of receptivity further upstream. Here, on the other hand, clear behaviour consistent with the Arbey and Bataille (1983) type feedback loop has additionally been shown. Although the TE separation bubble exists and presumably plays a role in amplifying the disturbances here, it seems to, in this case, exist in the context of an overall mechanism where the feedback loop is *also* important.

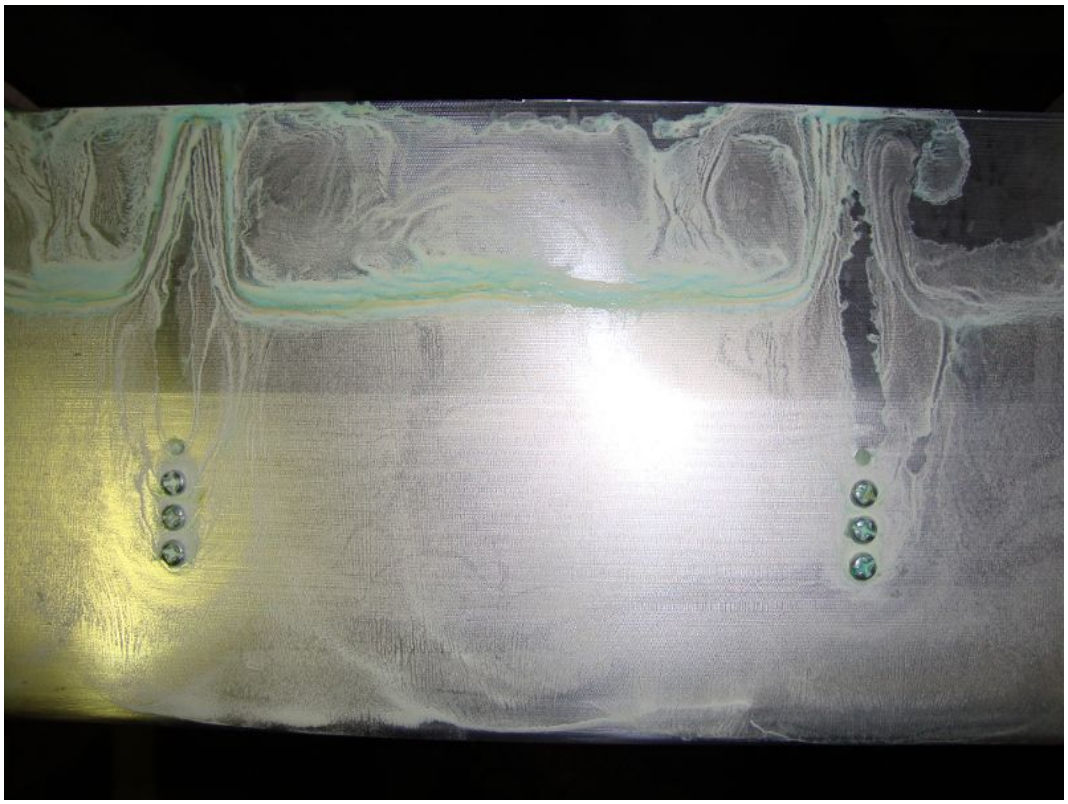

Figure 5.52: Surface flow visualisation of smooth airfoil pressure side, flow from bottom to top.

5.11 Boundary layer stability analysis

5.11.1 Introduction

An airfoil boundary layer stability analysis code written by Dr. Michael J. Kingan and associates was very kindly provided for the use of the flow and noise research group at the University of Adelaide. This code was applied to the present flat plate profile (without the cavity cutout), and the results are presented and discussed in this section. The code was the core part of a theoretical model for airfoil tonal noise developed by Kingan and Pearse (2009), and it was an extension of the theoretical model developed by McAlpine, Nash and Lowson (1999).

While the McAlpine *et al.* (1999) model requires the use of experimental boundary layer profiles acquired at a limited number of stations (with a least-squares polynomial fitted to the results in-between the stations), the Kingan model is fully automated and enables the calculation of local amplification rates at finely spaced stations along an arbitrary airfoil, without any requirements for experimental data. The total amplification is calculated by integrating the local amplification rates over the airfoil. Finally, the feedback frequencies are estimated based on the calculated phase of the disturbances over the airfoil and assuming a feedback loop of the form proposed by Arbey and Bataille (1983).

The advantage of the model is that, unlike empirical models specific to particular airfoils and flow conditions, the model developed by Kingan and Pearse is 'purely theoretical and could be used to predict the frequency of laminar instability boundary layer noise produced by an arbitrary aerofoil' (Kingan and Pearse, 2009, p. 808). Therefore the model is well suited to be applied to the arbitrary 'airfoil with cavity' profile considered in the present study, whereas other models, developed specifically for NACA-series airfoils, are not suitable for the present profile.

Details of the boundary layer stability analysis method are given in the paper by Kingan and Pearse (2009). The structure of the method is:

1. The mean flow over an arbitrary airfoil is computed at 2% chord intervals using XFOIL (Drela, 1989; described in section 5.10) which quickly determines the flow over any airfoil even with mildly separated flow. XFOIL assumes a Falkner-Skan boundary layer formulation.

2. The pressure side boundary layer properties computed by XFOIL (displacement thickness, shape factor) are replaced by Falkner-Skan velocity profiles with identical shape factor. The Falkner-Skan profiles are determined using a parallel shooting technique.

3. At the positions along the chord, the Orr-Sommerfeld equation is solved for a sweep of fixed frequencies to give the complex wavenumber (of the least stable mode) at each frequency.

4. From the complex wavenumber, the most amplified frequency over the airfoil (i.e., central frequency, f_s) is determined. Also, the feedback tones are determined.

Stability analysis Kingan and Pearse's (2009) stability analysis method consists of solving the Orr-Sommerfeld equation (equation 5.4) in an automated manner, which requires no initial guess. The Orr-Sommerfeld equation (equation 5.4) represents the perturbations which will be amplified in a boundary layer and is derived from the two-dimensional Navier-Stokes equations.

The stream function, ψ, of the Tollmien-Schlichting (T-S) wave is given by equation 5.5. In the formulation of the problem, $\hat{\eta}$ is the stream-normal coordinate, $\hat{\xi}$ is the stream-wise coordinate and t is time, ϕ is the perturbation amplitude, and α is the complex wavenumber. The frequency of the disturbance is given by $\hat{\omega}$. In equation 5.4, the prime represents differentiation with respect to the dimensionless stream-normal co-ordinate $\eta = \hat{\eta}/L_1$, where $L_1 = \delta^*/\gamma$ is a stream-normal boundary layer length-scale based on $\gamma = \int_0^\infty (1 - f')\mathrm{d}\eta$. Here, f' is the dimensionless Falkner-Skan boundary layer velocity profile, and δ^* is the boundary layer displacement thickness. Other non-dimensional properties in the formulation are the Reynolds number $R = U_\infty L_1/\nu$, dimensionless complex wavenumber $\alpha = \hat{\alpha}L_1$, dimensionless velocity $U = \hat{U}/U_\infty$ where U_∞ is the free-stream velocity, and dimensionless frequency $\omega = \hat{\omega}L_1/U_\infty$. Note that the complex wavenumber is non-dimensionalised in the form $\hat{\alpha} = \alpha/L_1$. For the wavenumber, the imaginary part, $\hat{\alpha_i}$, relates to amplification while the real part, $\hat{\alpha_r}$, relates to the phase.

$$(U\alpha - \omega)(\phi'' - \alpha^2\phi) - U''\alpha\phi + \frac{i}{R}(\phi'''' - 2\alpha^2\phi'' + \alpha^4\phi) = 0 \tag{5.4}$$

$$\psi(\hat{\xi}, \hat{\eta}, t) = \phi(\hat{\eta})\mathrm{e}^{\mathrm{i}\left(\int \hat{\alpha}(\hat{\xi})\mathrm{d}\hat{\xi} - \hat{\omega}\mathrm{t}\right)} \tag{5.5}$$

The following boundary conditions at the wall and far-field are applied, requiring zero perturbation amplitude *and* a zero stream-normal spatial derivative of the perturbation amplitude, at the wall and far field. Note that in the solution method employed by Kingan and Pearse (2009) the domain is truncated at $\eta = l$ and therefore the second boundary condition is applied there rather than at infinity.

$$\eta = 0, \qquad \phi = 0, \qquad \phi' = 0 \tag{5.6}$$

$$\lim_{\eta\to\infty}, \qquad \phi = 0, \qquad \phi' = 0 \tag{5.7}$$

Numerical solution method The details of the numerical solution method are given by Kingan and Pearse (2009). Briefly, the eigenvalues (wave numbers, α) are first calculated. The Chebyshev matrix technique is used, so

that the problem is formulated as a 'complex generalised eigenvalue problem'. The problem is then solved using the QZ algorithm. Then, the eigenvalues are sorted, with those irrelevant to T-S modes excluded, and the least stable eigenvalue is identified. This least stable eigenvalue $\hat{\alpha}$, with imaginary part $\hat{\alpha_i}$ and real part $\hat{\alpha_r}$ is then stored. These relate to the local amplification rate and phase, respectively. After that, this process is then repeated for the range of frequencies, and for all the stations along the chord (at 2 % chord intervals).

Total amplification The total amplification is given by the exponential of the integral of the local amplification rate, $\hat{\alpha_i}$ (or imaginary part of the complex wavenumber), over the airfoil. S represents the airfoil surface. $\hat{\alpha_i}$ was calculated at stations at 2% chord intervals and the total amplification, A, was evaluated using the trapezoidal rule from streamwise co-ordinate $\xi = a$ to $\xi = b$ (where a and b are the stations nearest the leading and trailing edges respectively):

$$A = \exp\left(-\int_{\mathrm{a}}^{\mathrm{b}} \hat{\alpha_{\mathrm{i}}}(\hat{\xi})\mathrm{dS}(\hat{\xi})\right) \tag{5.8}$$

Tone selection mechanism (feedback) Kingan and Pearse (2009) proposed a tone selection mechanism based on a modification of the Arbey and Bataille (1983) model. The total phase change around the loop was considered by Kingan and Pearse (2009) to consist of three components:

1. The phase change within the boundary layer is given by the integral of the real component of the complex wavenumber $\hat{\alpha}$. The point of first instability ($\hat{\xi} = a$) is considered to be where the local amplification rate α_i first becomes negative along the chord. Subsequently this phase change is $\int_a^b \hat{\alpha_r}(\hat{\xi})dS(\hat{\xi})$, where $\hat{\xi} = a$ is the point of first instability and $\hat{\xi} = b$ is the trailing edge. To estimate the effect of the cavity, for some of the cases $\hat{\xi} = a$ will be taken to be position of the cavity trailing edge instead.

2. The phase change of the upstream propagating sound wave given is by $\frac{2\pi f L}{c_0 - U_\infty}$. Here L represents the distance between $\hat{\xi} = b$ and $\hat{\xi} = a$. While c_0 is the speed of sound and U_∞ is the free-stream velocity – Kingan and Pearse (2009) took the average free-stream velocity between points a and b, however the nominal value will be used in this section.

3. The third component is the phase change due to a 180° phase shift at the trailing edge, accounted for by the addition of π to the total phase around the loop.

Table 5.4: Cases for evaluation using the boundary layer analysis code

Case	Geometric angle of attack	Jet velocity
1	-7°	14 m/s
2	-1°	16.6 m/s
3	-13°	37 m/s

Therefore the total phase change was considered by Kingan and Pearse (2009) to be:

$$\int_a^b \hat{\alpha_r}(\hat{\xi}) dS(\hat{\xi}) + \pi + \frac{2\pi f L}{c_0 - U_\infty} \tag{5.9}$$

For the feedback loop to provide reinforcement, equation 5.9 was equated to a multiple of 2π. Note that Kingan and Pearse (2009) fitted a least squares parabola to the function given by equation 5.9 (and then found those frequencies whose phase matched a multiple of 2π), however here the feedback tones will be found directly from the phase function, aside from case 3 where values found from the phase function and from a least-squares parabola are compared.

5.11.2 Methodology

Three cases were considered for evaluation using the boundary layer analysis code. They are summarized in table 5.4 [the corrected angle of attack (section 3.2.2) was used in the analysis]. Firstly, the local and total amplification rates are discussed and compared to the experimental results. Secondly, the airfoil (feedback) tones predicted using the method of Kingan and Pearse (2009) are discussed and compared to the experimental airfoil tones found.

5.11.3 Boundary layer profiles

In the Kingan method, XFOIL is used to predict the boundary layer profiles, and it predicts the existence of a region of separated flow along the tail section of the airfoil. The results presented here are for case 1 which is the same case as the hot-wire measurements in the boundary layer discussed earlier (U=14 m/s and geometric angle of angle of 7 degrees nose-down). The results are for a smooth plate.

Figure 5.53 shows the shape factor over the airfoil calculated by XFOIL. The shape factor decreases slightly along the parallel section of the airfoil, before increasing rapidly along the tapered tail section of the airfoil.

Figure 5.54 shows the Falkner-Skan profiles over the airfoil pressure surface calculated by the Kingan code, at locations along the chord. The profiles downstream of 70% chord, represent the reversed flow region predicted by XFOIL.

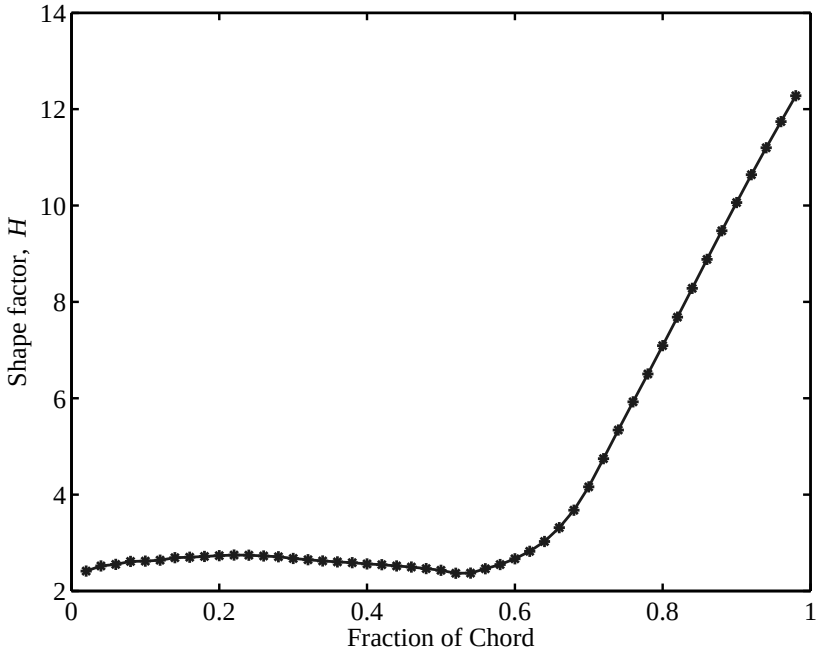

Figure 5.53: Shape factor over airfoil calculated by XFOIL for case 1.

As stated in section 5.10, XFOIL is found to be consistent with the flow visualisation results. The flow visualisation results showed that the existence of a separation bubble near the airfoil trailing edge which appeared to be quite similar regardless of the presence of the cavity.

5.11.4 Case 1 results

Local amplification rates

Figure 5.55 shows the local T-S wave amplification rates, α_i, for case 1 at various stations along the chord. The maximum local amplification is calculated at $x/C = 0.80$, and is at a frequency of 565 Hz. For comparison, in the specification of the profile of the plate, the transition between the parallel section of the plate and the (linearly tapered, symmetrical) trailing edge apex begins at $x/C = 0.53$ and is fully blended into the tail at $x/C = 0.71$. Downstream of $x/C = 0.80$, the maximum amplification rate moves to lower frequencies. At $x/C = 0.90$, the maximum local amplification is found at 410 Hz.

Total amplification over airfoil

Figure 5.56 plots the total amplification over the airfoil for case 1. The theory predicts maximum total amplification at 475 Hz (i.e., $f_s = 475$ Hz). This shows fair agreement with experiment where f_s was found to be approximately 595

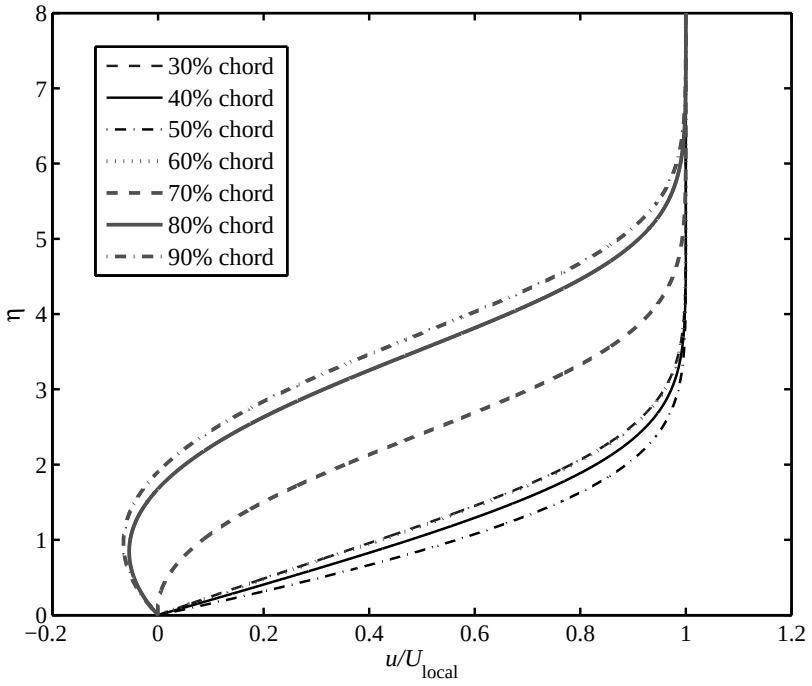

Figure 5.54: Falkner-Skan profiles over airfoil pressure surface, for case 1. Note that the curve for 60 % chord is obscured by the curve for 50 % chord, due to being very similar.

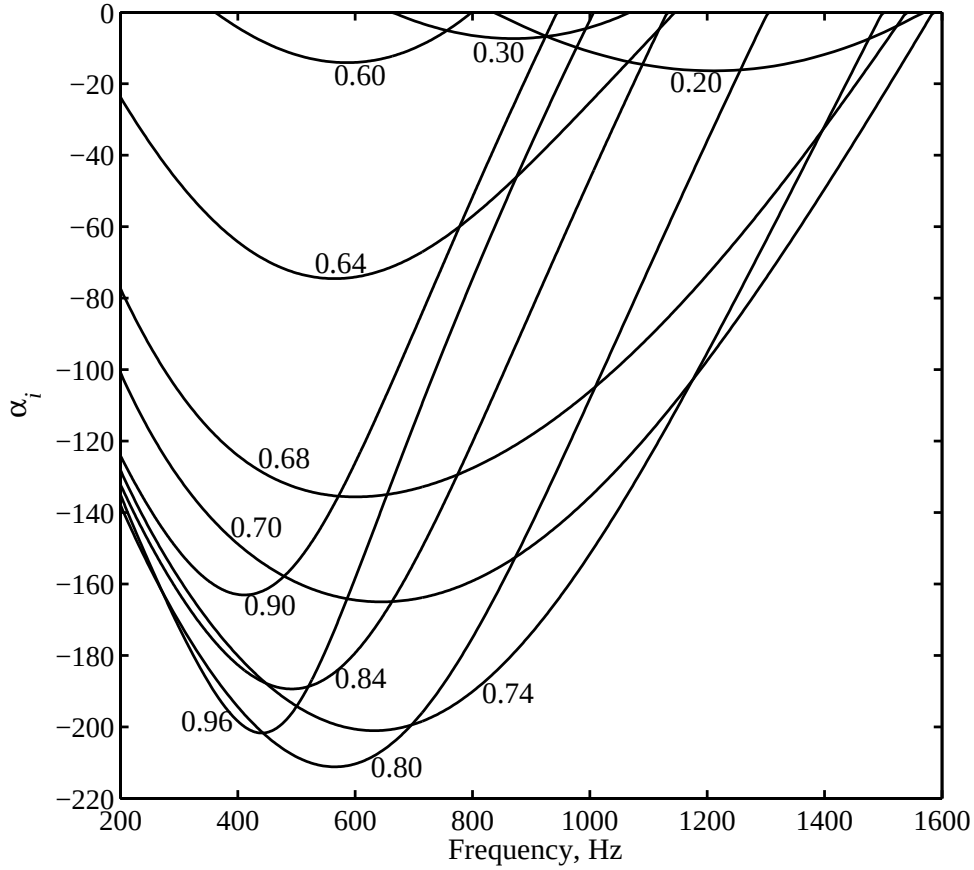

Figure 5.55: Local T-S wave amplification rates, α_i, for case 1. The station, as a fraction of the chord, is listed next to each curve.

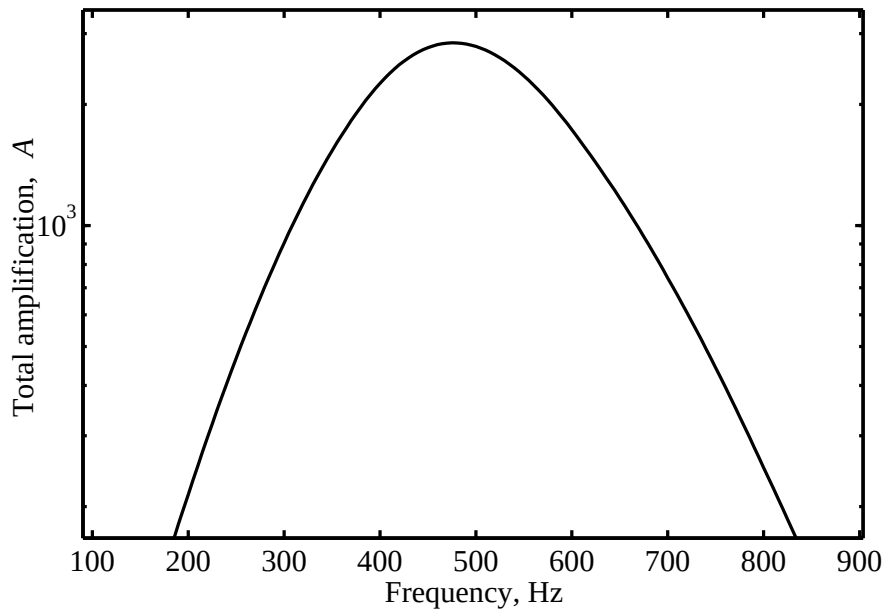

Figure 5.56: Total T-S amplification, A, for case 1.

Hz for cavity position 1 and 522 Hz for cavity position 4 (from hot-wire velocity measurements). Note that f_s could not be determined experimentally for the smooth airfoil at $U = 14$ m/s, as the onset of the airfoil tones is delayed to a higher Reynolds number for the smooth pressure side (see figure 5.12).

Feedback tone prediction

Figure 5.57 shows the total phase predicted by the Kingan theory (from equation 5.9) for case 1. The upper and lower bounding frequencies were taken to be 200 Hz and 815 Hz, as between these values the total amplification was more than 200 which was considered to be a reasonable threshold for this case. The total phase was integrated from downstream of 20% chord which was the point of first instability (where $\alpha_i < 0$) according to the theory.

Taking the frequencies where the total phase is equal to a multiple of 2π, gave the predicted feedback tones. These are tabulated in table 5.5, where experimental hot-wire values are also given for comparison purposes. Note that in the table, Δf is taken to be the average spacing between *all* the tones in each row. The theoretical feedback tones show mild agreement with experimental values, considering the differences in feedback length assumptions therein. (The boundary layer for the cavity position 1 is considered to have its receptivity point at approximately 31 % chord, while for cavity position 4 it is 47 % chord.)

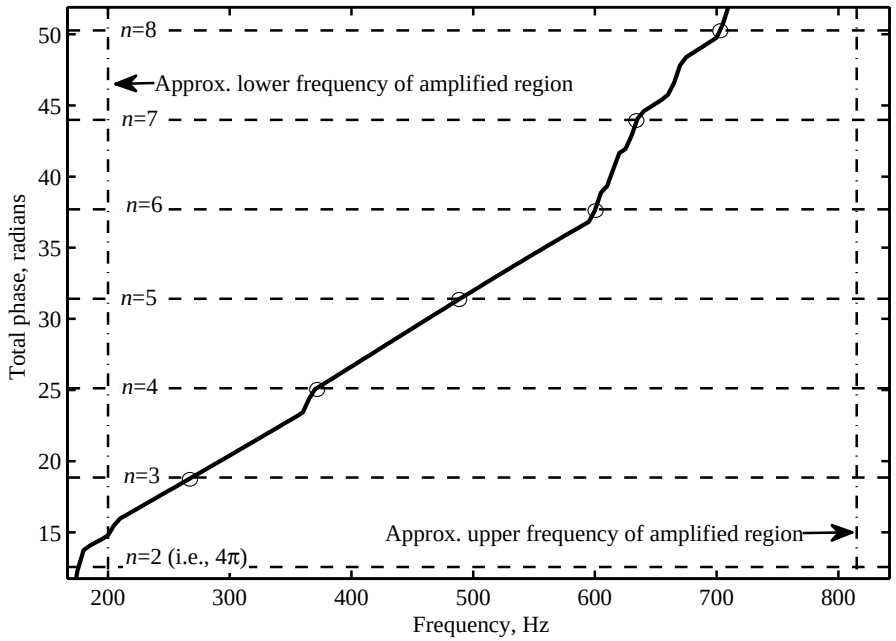

Figure 5.57: Total phase for case 1.

Table 5.5: Feedback tones for case 1 showing a comparison of experiment and theory.

Configuration	Tones (Hz)						f_s (Hz)	Δf (Hz)
Smooth plate	270	370	490	600	635	705	475	87
(Kingan theory)	$n=3$	$n=4$	$n=5$	$n=6$	$n=7$	$n=8$		
Cav. pos. 1			531	595	667	738	595	69
(Exp.: hot-wire)			$n=8$	$n=9$	$n=10$	$n=11$		
Cav. pos. 4			435	522	613	705	522	90
(Exp.: hot-wire)			$n=5$	$n=6$	$n=7$	$n=8$		

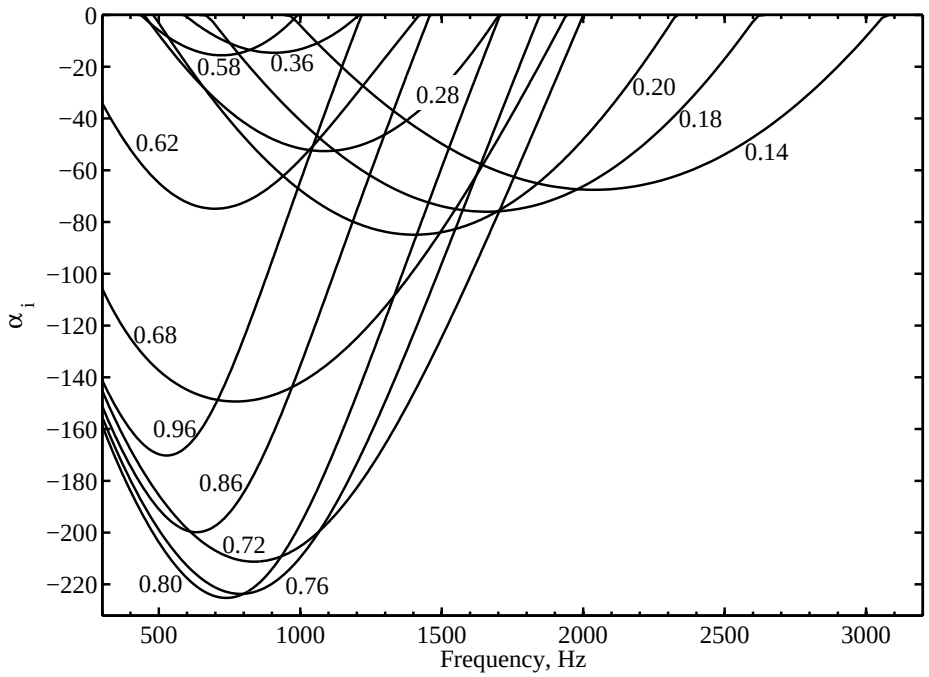

Figure 5.58: Local T-S wave amplification rates, α_i, for case 2. The station, as a fraction of the chord, is listed next to each curve.

5.11.5 Case 2 results

For case 2, results from the theory will be compared to experimental microphone data for flow over the smooth plate.

Local amplification rates

Figure 5.58 shows the local T-S wave amplification rates for case 2. The highest local amplification is predicted at a frequency of around 740 Hz, at the location of 80% chord.

Total amplification

Figure 5.59 shows the total amplification calculated for case 2. According to the theory, the highest total amplification is predicted at 740 Hz. This agrees well with experiment where, from microphone data, f_s was found to be approximately 780 Hz for this case.

Case 2 feedback tones

For this case 2, a total amplification threshold of greater than 3×10^3 was considered to be appropriate for selecting the frequency bounds for the predicted

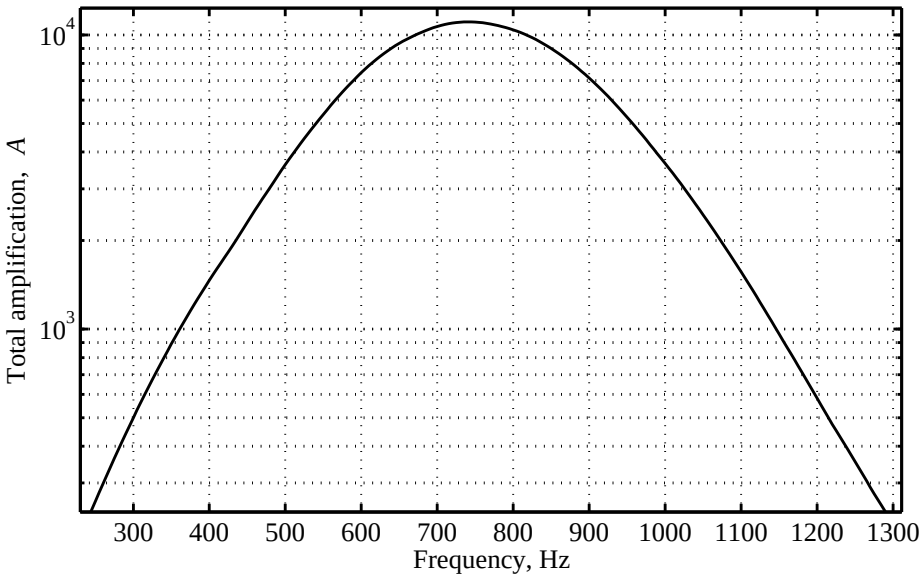

Figure 5.59: Total T-S amplification, A, for case 2.

feedback tones. Figure 5.60 shows a plot of the total phase around the loop for case 2. For this case, the local amplification, α_i, first becomes negative at 14% chord which was taken to be the point of first instability.

For the purposes of comparison, a plot of the far-field noise spectrum for this case is given in figure 5.61. The experimental peaks are found at approximately 570, 630, 730, 830, and 890 Hz. On average, the frequency spacing is Δf=80 Hz. From figure 5.60 the feedback tones predicted from theory are 515, 570, 645, 690, 770, 855, and 950 Hz. On average, the frequency spacing is Δf=73 Hz. This shows reasonable agreement on some tones, and also moderate agreement on the frequency spacing.

5.11.6 Case 3 results

As with case 2, for case 3 results are compared to experiments conducted with a smooth pressure side. This case differs in that the Reynolds number is much higher than for case 2, being 2.9×10^5 for case 3 versus 1.3×10^5 for case 2.

Local amplification rates

Local amplification rates for case 3 are given in figure 5.62. Peak local amplification is predicted at 2716 Hz at 82 % chord. As with the other cases, there is a region of moderate local amplification located upstream (from approximately 12 % to 32 % chord) at higher frequencies. This is 'followed' by a central chord-wise region of minimal local amplification, before the region of greater local amplification (which occurs at lower frequencies) begins from

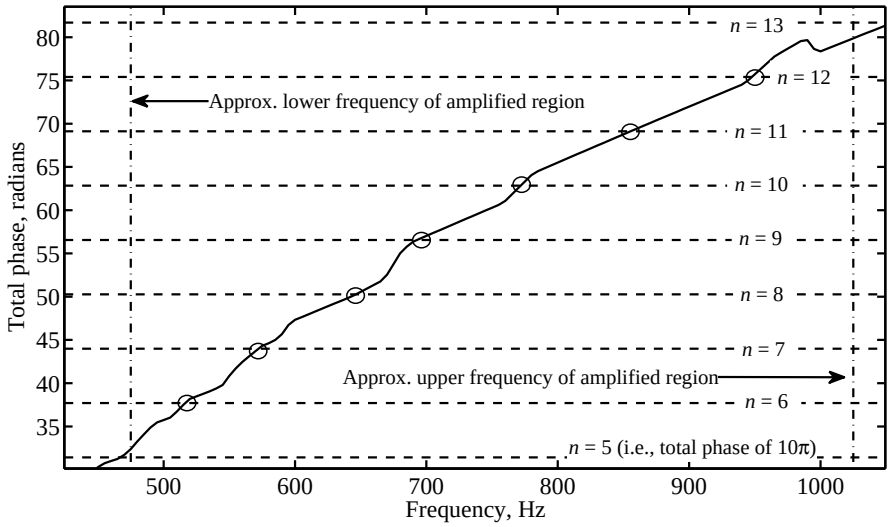

Figure 5.60: Total phase and, therefore, feedback tone predictions, for case 2.

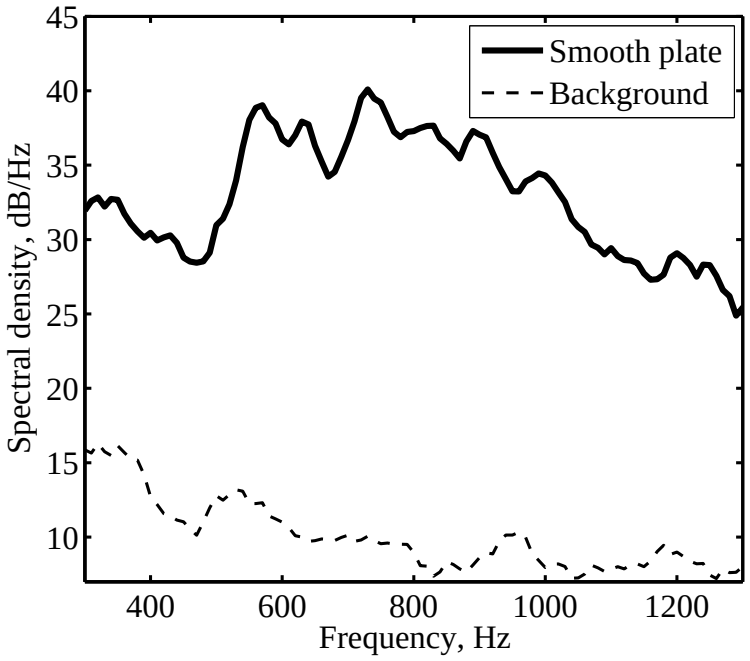

Figure 5.61: Experimental far-field noise spectrum for case 2 (smooth plate at U=16.6 m/s with a geometric angle of attack of -1°).

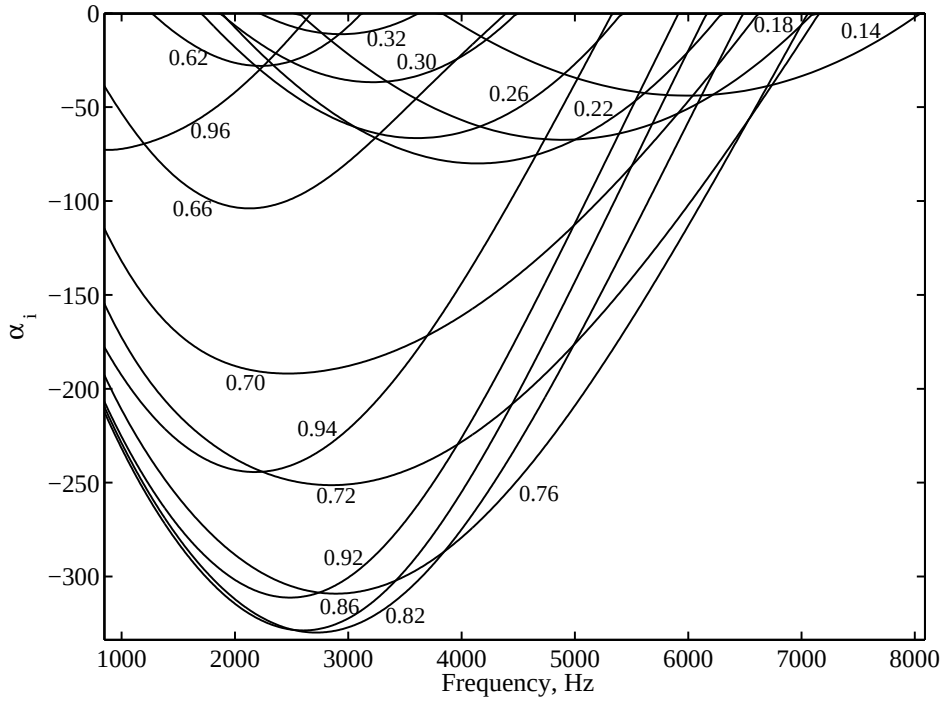

Figure 5.62: Local T-S wave amplification rates, α_i, for case 3. The station, as a fraction of the chord, is listed next to each curve.

approximately 62 % chord, continuing on downstream to the trailing edge. It is this final region of amplification that dominates.

Total amplification

The total amplification calculated for case 3 is shown in figure 5.63. Total amplification peaks at 2780 Hz, giving the central frequency prediction. With regards to comparison to experiment, figure 5.64 shows the experimentally measured far-field noise spectrum for case 3. The central frequency, f_s is estimated from the noise spectrum to be 2285 Hz.

Case 3 feedback tone predictions

In the Kingan method, a least-squares parabola is fitted to the phase function and the feedback tones are then calculated from this parabola. For this case, the calculated total phase function was particularly jagged and coarse. Therefore for this case, a parabola was fitted and the feedback tone results from both from the direct phase function, and the parabola will be given.

Figure 5.64 shows that the feedback tones are found experimentally at 1800, 1970, 2220, 2480, 2730 and 2990 Hz, while figure 5.65 shows the predicted

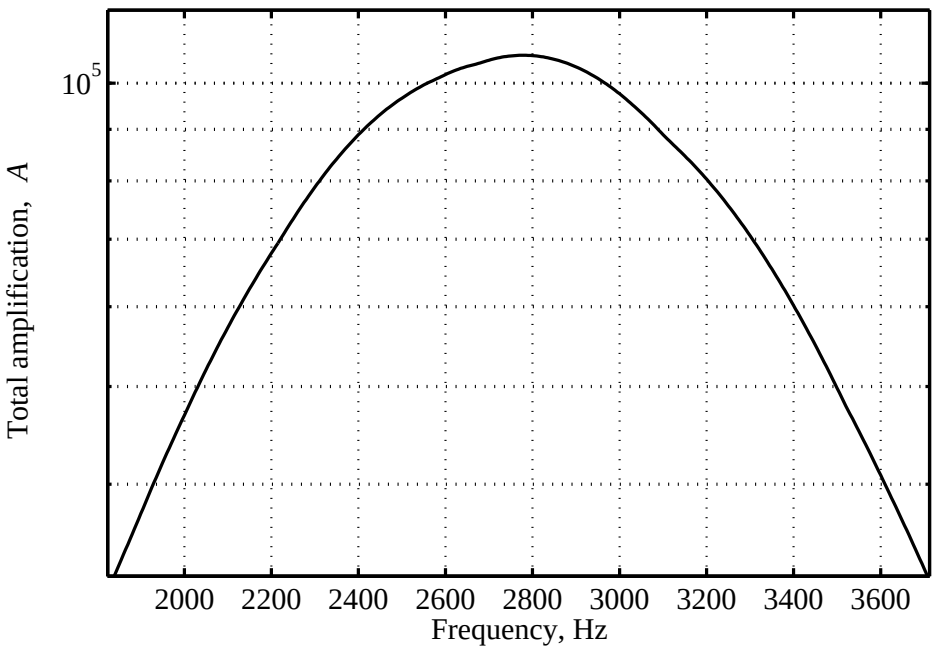

Figure 5.63: Total T-S amplification, A, for case 3.

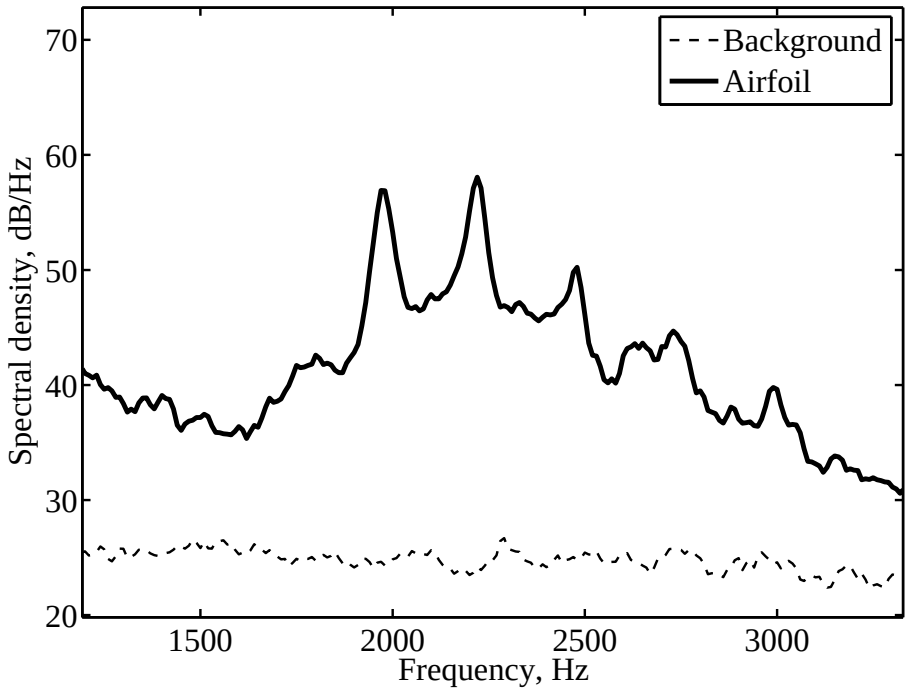

Figure 5.64: Far-field noise spectrum for case 3.

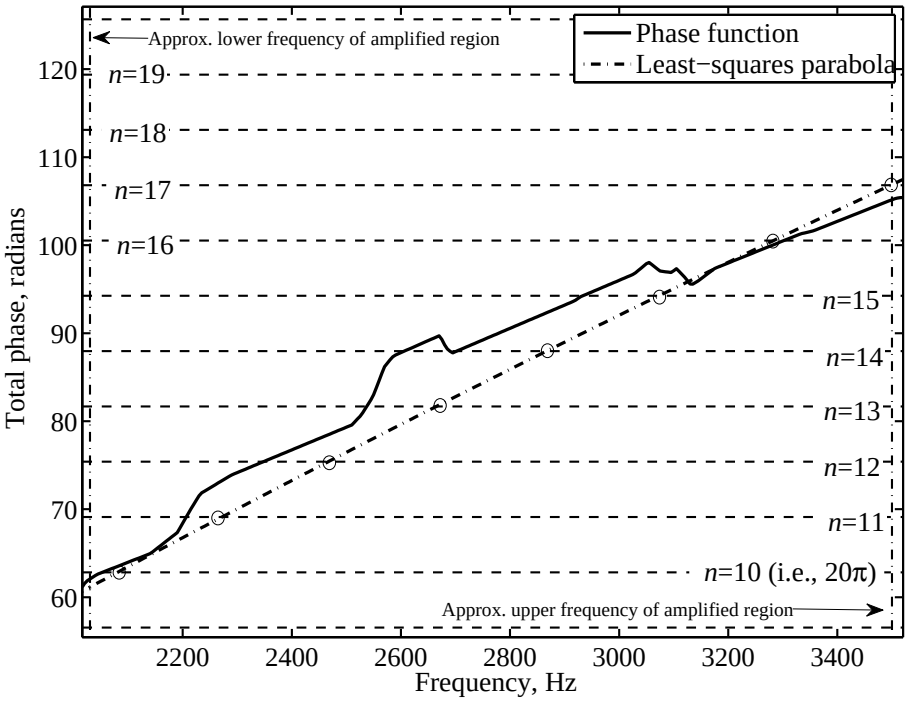

Figure 5.65: Total phase and, therefore, feedback tone predictions, for case 3.

feedback tones from theory for case 3. The location of first instability ($\alpha_i < 0$) was taken to be 12 % of chord. For this case, an amplification threshold of 4×10^4 was considered to be a suitable level. The feedback tones predicted from the least-squares parabola are 2080 Hz ($n = 10$), 2270 Hz ($n = 11$), 2465 Hz ($n = 12$), 2665 Hz ($n = 13$), 2865 Hz ($n = 14$), 3075 Hz ($n = 15$), 3285 Hz ($n = 16$) and 3500 Hz ($n = 17$). The feedback tones predicted directly from the phase function are at 2055 Hz ($n = 10$), 2205 Hz ($n = 11$), 2350 Hz ($n = 12$), 2535 Hz ($n = 13$), 2605 Hz & 2700 Hz ($n = 14$), 2935 Hz ($n = 15$), and 3305 Hz ($n = 16$). Many, but not all, of these tones are reasonably close to their experimental values.

5.11.7 Summary of boundary layer stability analysis

Local amplification appears to occur in two distinct regions, an upstream region and then a downstream region approaching the trailing edge. In the former, local amplification is predicted at a relatively lower level and at higher frequency. In the latter, which relates to the separation bubble approaching the trailing edge, local amplification is predicted at a much higher level and this amplification dominates the calculation of total amplification.

Table 5.6 shows a comparison of central frequency from theory and from

Table 5.6: Comparison of central frequency, f_s, from theory and from experiment.

Case	f_s (Theory)	f_s (Experiment)
1	475 Hz	595 Hz
2	740 Hz	780 Hz
3	2780 Hz	2285 Hz

experiment. There is at least moderate agreement for all cases. The theory does a good job of capturing the behavior of the central frequency, and it can be confidently inferred that the noise is indeed due to the laminar boundary layer instabilities which are modelled by the theory.

5.12 Overall summary

In summary, figure 5.66 is an updated version of figure 5.40 and shows the proposed airfoil tonal noise mechanism. It is believed that the boundary layer upstream of the cavity is essentially stable owing to the favourable pressure gradient. Moving downstream, the shear layer over the cavity is unstable at backward-facing-step vortex shedding frequencies, but stable to the lower frequencies of the airfoil tonal noise. The most unstable point of the boundary layer is located near the cavity trailing edge, where inflectional boundary layer profiles are present. Here, the boundary layer is receptive to the feedback from the airfoil tonal noise. Approaching the trailing edge of the airfoil, a region of separated flow is present, over which the boundary layer instabilities are highly amplified. Finally, the airfoil tonal noise is generated as these instabilities pass the trailing edge, thereby closing the feedback loop. These vortices then convect downstream of the trailing edge of the airfoil, through the wake.

Since the present investigation of airfoil tonal noise was principally completed in January 2013, a number of relevant studies regarding airfoil tonal noise production from NACA series airfoils have been published in the literature. These studies are described and discussed in Appendix A.

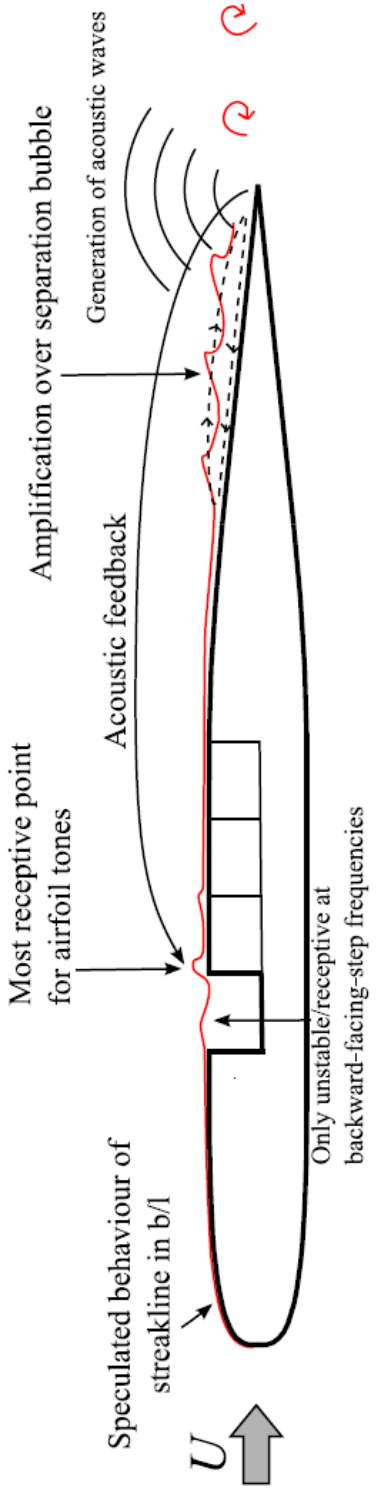

Figure 5.66: Sketch of the updated proposed tonal noise mechanism for the streamlined plate with cavity. Note that 'speculated behaviour of streakline in b/l' refers to the behaviour of a streakline released into the boundary layer very near to the stagnation point.

Chapter 6

Three-Dimensional Cavities: Results and Discussion

Unlike the earlier chapter regarding two-dimensional cavities (Chapter 4) and the cavity oscillations found therein, this chapter begins with a discussion of the shear layer vortical structures which correspond to those shear layer oscillations and then goes on to focus on the three-dimensional effects specific to narrow cavities, and the involvement of shear layer and mixing layer vortical structures in those three-dimensional effects. While Crook (2011) has detailed the flow structure around shallow and narrow cavities at low Reynolds number, the structure of the mixing layer both within and immediately beyond shallow and narrow cavities at low Reynolds number is still poorly documented. The present work thus aims to contribute to the understanding of this area using flow visualisation, hot-wire and PIV techniques. Additionally, the broadband noise produced by rectangular and three-dimensional cavities is investigated, as well as the flow structure about selected modified three-dimensional cavity geometries. Figure 6.1 shows the co-ordinate system used in this chapter, while the experimental parameters specific to each technique are discussed in section 3.3 of Chapter 3: Experimental Methodology & Design.

6.1 Effect of L/D on shear layer evolution

6.1.1 Varying L/D

The evolution of flow structures over the rectangular cavity for a *range* of length-to-depth ratios was observed at a depth-based Reynolds number of 10,700 in the water channel cavity model (model details in section 3.3.2). A number of oblique, overhead flow patterns were recorded with a horizontal hydrogen bubble wire. Note that the wire location was at a height $y/D = -0.125$ (above the flat plate), and located upstream of the cavity at $x/D = -0.42$.

The length-to-depth ratio of the rectangular cavity was varied in the range $L/D = 0.84$ – 6. Figure 6.2(a) shows the flow pattern for $L/D = 0.84$. It can

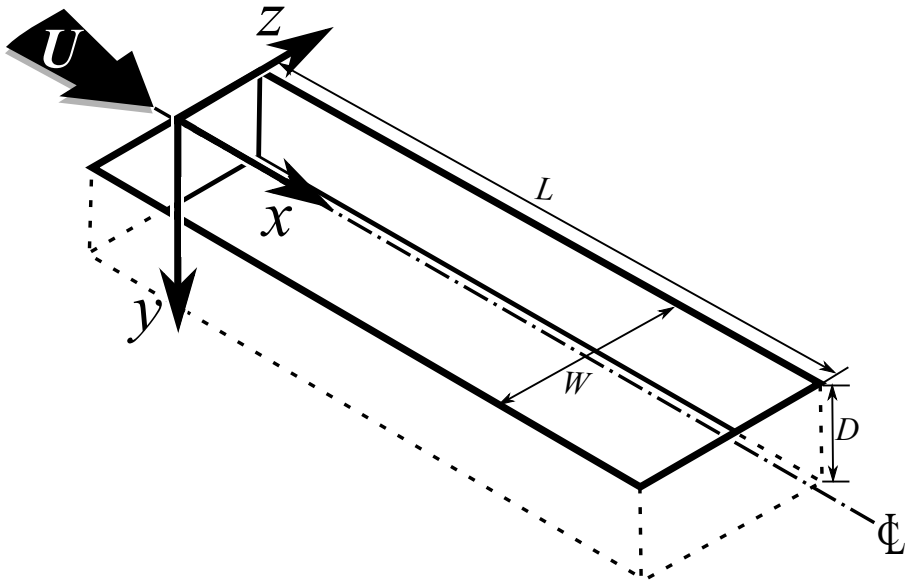

Figure 6.1: A sketch of the co-ordinate system used in this chapter.

be observed that the shear layer structures are highly uniform across the span. For $L/D = 0.84$, the shear layer vortices typically escape over the trailing edge of the cavity. Care is required in the interpretation of the structures, as fluid that has 'already rolled-up' will maintain that appearance. Bearing this in mind, the structures appear to persist in the streamwise direction for around 2 cavity-depths downstream before they diffuse.

Figure 6.2(b) shows the flow pattern for $L/D = 2$. Compared to $L/D = 0.84$, it can be seen that the shear layer structures have a lower level of spanwise uniformity. Although the structures start out fairly uniform across the span, by the downstream part of the cavity the structures are no longer uniform. In figure 6.2(b), periodic structures at the sides of the cavity can be seen, these will be discussed in detail later.

Figure 6.2(c)-(f) shows the flow patterns for $L/D = 3$ through to $L/D = 6$. The hydrogen bubbles tend to diffuse in the downstream part of the cavities with higher L/D. The structures in the upstream part of the cavity appear relatively similar for each of these aspect ratios. Periodic structures at the sides of the cavity can also be seen in each case. These will be discussed in section 6.3.

(a) L/D=0.84

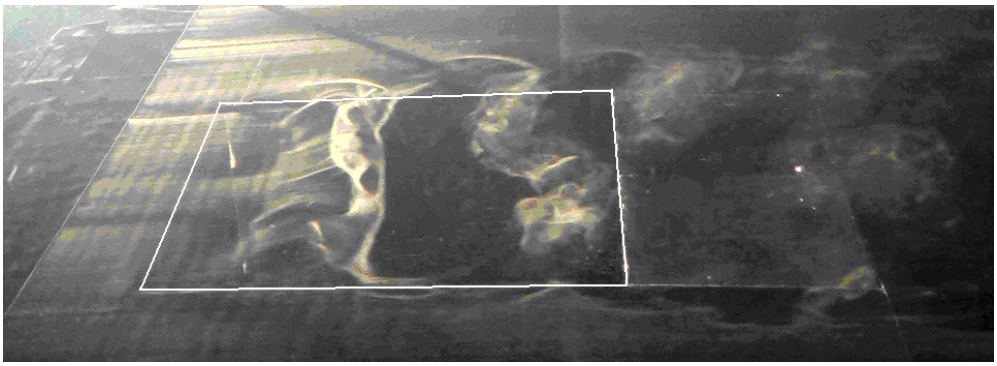

(b) L/D=2

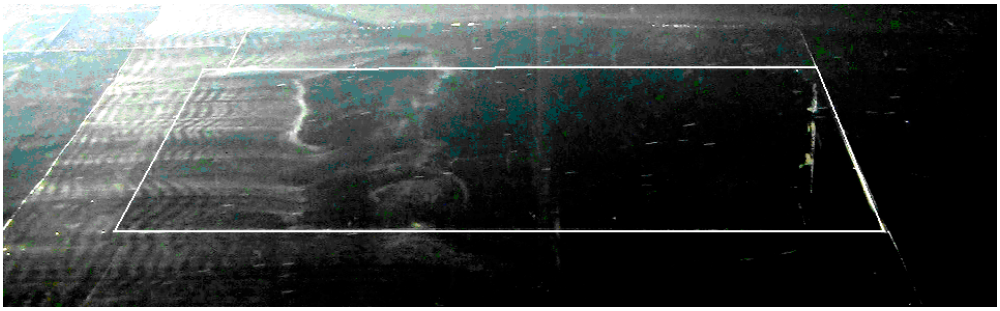

(c) L/D=3

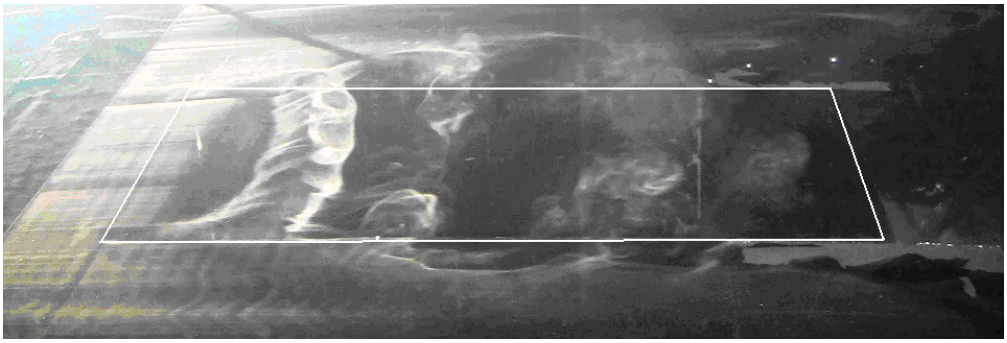

(d) L/D=3.84

Figure 6.2: Flow pattern produced by the horizontal hydrogen bubble wire located upstream of the rectangular cavities at a depth-based Reynolds number of 10,700. The flow is from left to right. Oblique view: note that the angle of the camera is different in each of the photographs. For clarity, the top four edges of the cavity have been indicated with white lines.

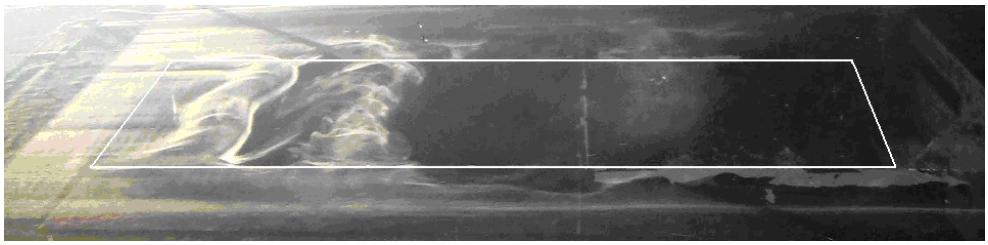

(e) L/D=4.84

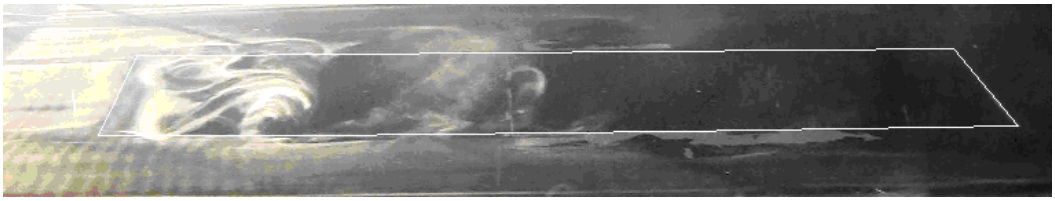

(f) L/D=6

Figure 6.2 – Continued.

6.1.2 Comparison of noise spectra to visualisations

Table 6.1 demonstrates that the Reynolds number, and also the relative non-dimensional boundary layer momentum thicknesses, were similar between the air measurements (of two-dimensional cavities) and water visualisations. These aeroacoustic results were presented in detail in section 4.4. Therefore, a summary of only certain results will be used here for comparison purposes.

Figure 6.3 shows a comparison of the noise spectra and flow visualisation for rectangular cavity geometries, for varying L/D. In the velocity spectra, it can be observed that (as would be expected) the stronger tones (in terms of sound pressure level) were found for the two smaller L/D ratios, with the tones decreasing in intensity for the larger L/D ratios. In the noise spectra, the following tones were found: $St_D = 0.90$, 1.8, 2.7, 3.6 (for $L/D = 1.17$), $St_D = 0.74$, 1.5 (for $L/D = 2.33$), $St_D = 0.34$, 0.51, 0.67, 0.84, 1.0 (for $L/D = 3.5$), and $St_D = 0.39$, 0.52, 0.64, 0.77 (for $L/D = 4.67$).

Viewing the acoustic spectra for $L/D = 3.5$ and 4.67, the energy appears to be spread between multiple frequencies of the shear layer oscillation. This is consistent with the reduced spanwise coherence observed in the flow visualisation.

Table 6.1: Experiments used for comparison of flow visualisation and aeroacoustic results with upstream laminar boundary layers. Note that boundary layer values are estimated from Blasius theory for laminar flow of water over a flat plate. Estimates taken from measurement are used for boundary layer values in air. The 'effective' L/D is given based on the modified cavity 2D (X-Y plane) cross-sectional area normalised to that of a rectangular cavity.

(a) Aeroacoustic test cases (air)

Geometry	L/D	Re_D	Re_{θ_0}	D/θ_0	D/δ_0	U, m/s
Rectangular	1.17	11,900	165	72	8.8	30
Rectangular	2.33	11,900	165	72	8.8	30
Rectangular	3.5	11,900	165	72	8.8	30
Rectangular	4.67	11,900	165	72	8.8	30
Sl. F.W. & Sl. R.W.	2.33 (eff.)	11,900	165	72	8.8	30

(b) Flow visualisation test cases (water)

Geometry	L/D	Re_D	Re_{θ_0}	D/θ_0	D/δ_0	U, mm/s
Rectangular	2	10,700	146	74	9.8	144
Rectangular	3	10,700	146	74	9.8	144
Rectangular	3.84	10,700	146	74	9.8	144
Rectangular	4.84	10,700	146	74	9.8	144
Sl. F.W. & Sl. R.W.	2.0 (eff.)	10,700	146	74	9.8	144

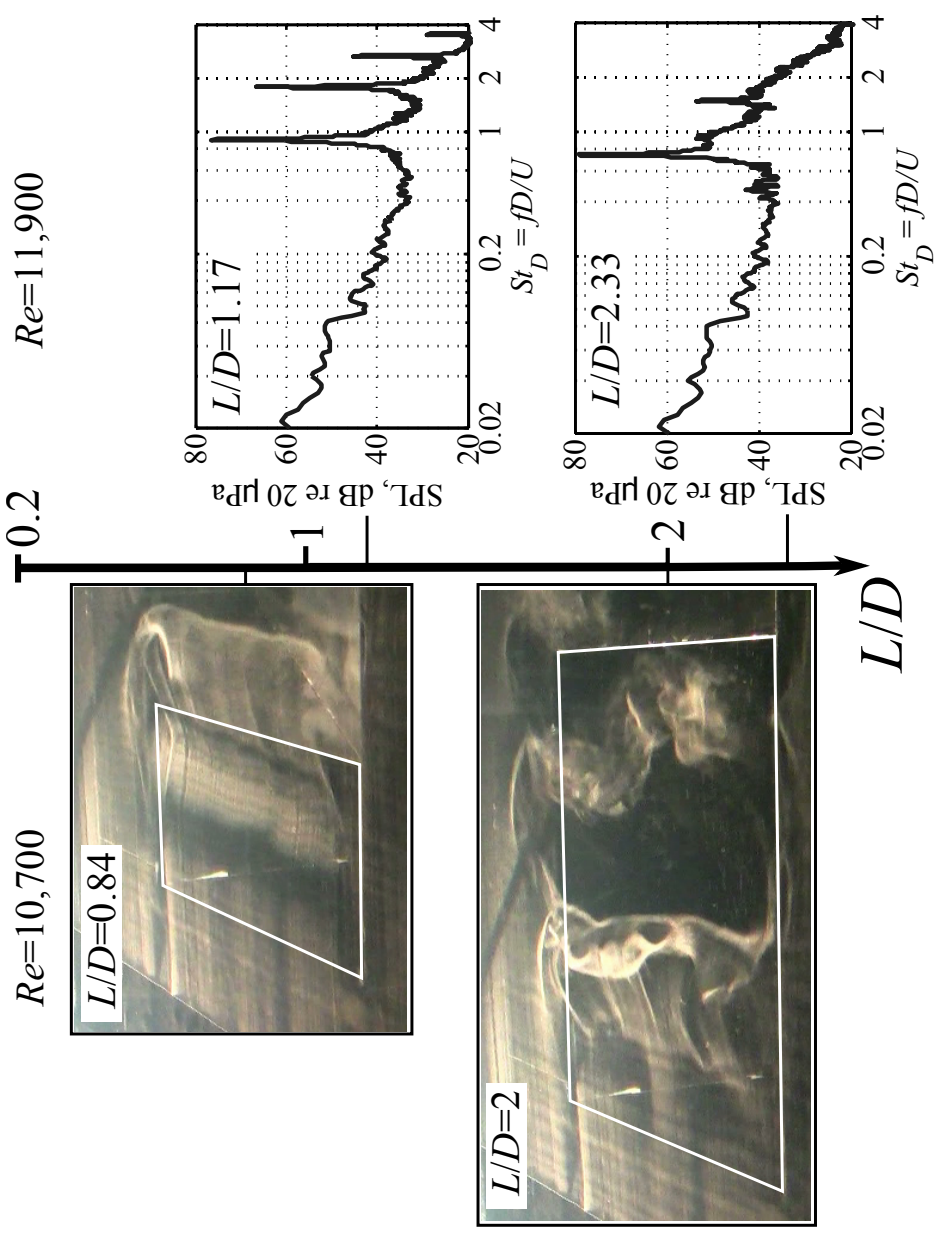

Figure 6.3: Comparison of flow visualisation and noise spectra for rectangular cavity geometries. Boundary layer properties are given in table 6.1.

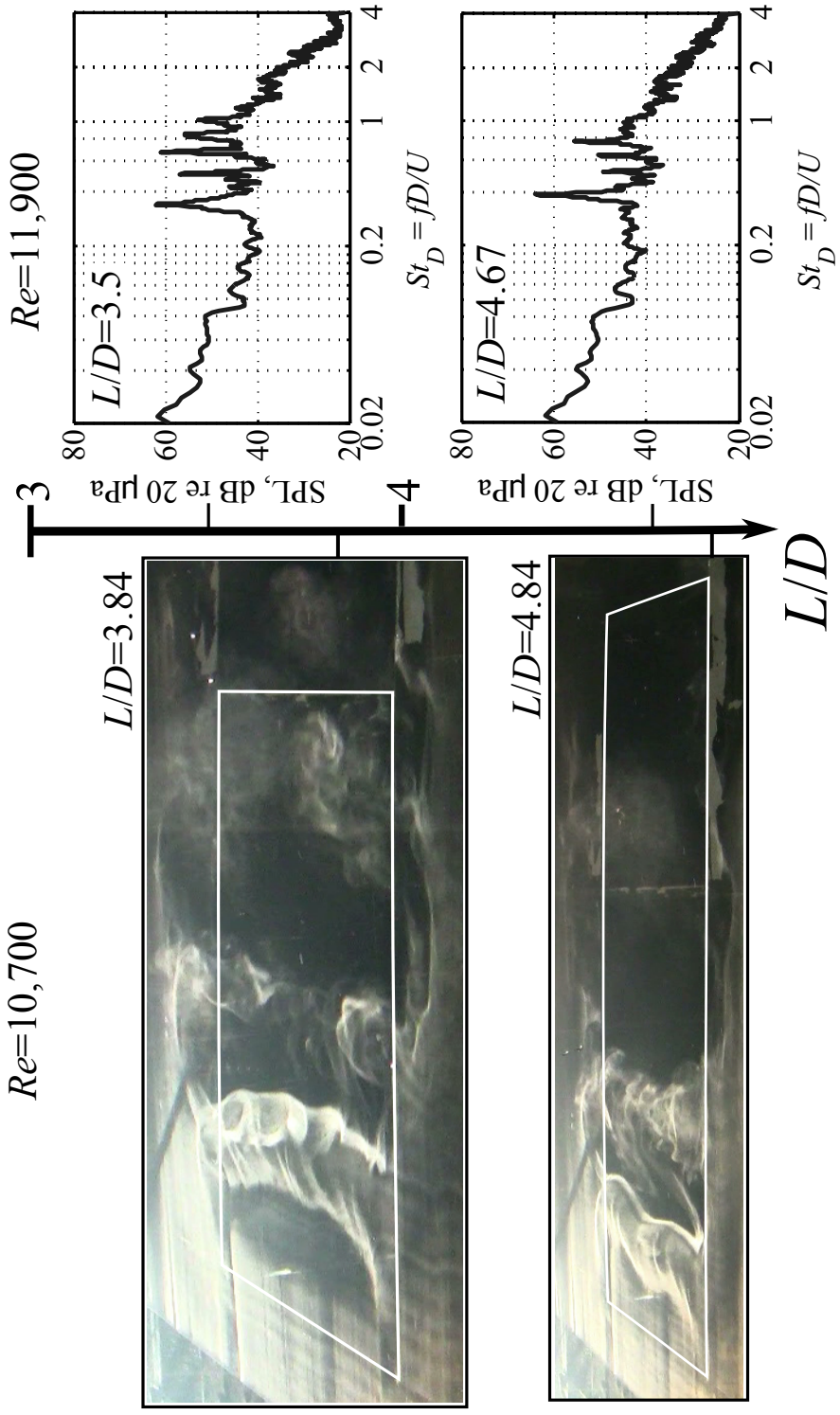

Figure 6.3 – continued.

6.1.3 Comparison of velocity spectra to visualisations

Figure 6.4 shows a comparison of velocity spectra to the flow visualisation for the rectangular cavity, while figure 6.5 shows the same for the cavity with sloped front and rear walls.

For the rectangular cavity, figure 6.4(b) shows that vortex shedding is measured in air at $St_D = fD/U = 0.73$ and $St_D = 1.46$ (possibly the first harmonic of the aforementioned tone). This is similar to the Strouhal number of $St_D = 0.67$ found in water. Possibly this can be explained by a different L/D, or a different convective velocity ratio due to a different L/δ_0 and therefore different oscillation mode (see section 4.7). Note that $L/\delta_0 = 21.5$ in air, while $L/\delta_0 = 29.3$ in water. Thus figure 4.26 (which shows the mean convection velocity ratio versus non-dimensional cavity length, in section 4.7) suggests that both cavities should be oscillating primarily in the third mode. The convective velocity ratio ($\kappa = U_c/U$) is approximately 0.6 in air, while careful observation of the video suggests a value of approximately 0.7 in water.

For the sloped front wall & sloped rear wall cavity, figure 6.5 shows a similar comparison. Several peaks were found in the velocity spectrum measured in air: $St_D = 0.34$, $St_D = 0.71$ & 0.85, and $St_D = 1.7$ (figure 6.5(b)). These peaks included two close oscillation frequencies, at $St_D = 0.71$ and 0.85. Note that the spectral peak at $St_D \approx 0.5$ found in the velocity spectra at all measurement locations is likely due to extraneous electrical noise.

Careful observation of the water flow visualisation video recording showed that there were two distinct wavelengths of vortex shedding, which are produced intermittently by the shear layer (a longer wavelength and a distinctly shorter wavelength). The first wavelength corresponds to $St_D = 0.68$ ($f = 1.31$ Hz) and the second wavelength to $St_D = 0.87$ ($f = 1.67$ Hz) . These Strouhal numbers are very similar to those of the two close oscillatory frequencies found in air (figure 6.5(b)).

The two close tonal frequencies seen in figure 6.5(b) therefore appear to be caused by two modes of oscillation occurring intermittently. Referring again to figure 4.26 [mean convection velocity ratio versus non-dimensional cavity length, in section 4.7], in this instance the shear layer appears to be operating in the parametric region where both the 3rd and 4th modes occur.

L/δ_0 in water was 29.3 for both the rectangular cavity and the cavity with sloped front & rear walls. In the rectangular case the cavity shear layer oscillated in the third mode, as predicted by figure 4.26. However, the modified cavity appeared to oscillate in the combined 3rd & 4th modes which would only be expected for $L/\delta_0 >\sim 31 - 33$ for a rectangular cavity (figure 4.26). Therefore this change in the characteristic of the shear layer may be potentially due to effects of the different cavity geometry, and subsequent differences in the internal cavity flow structure, with a subsequent influence on the cavity shear layer.

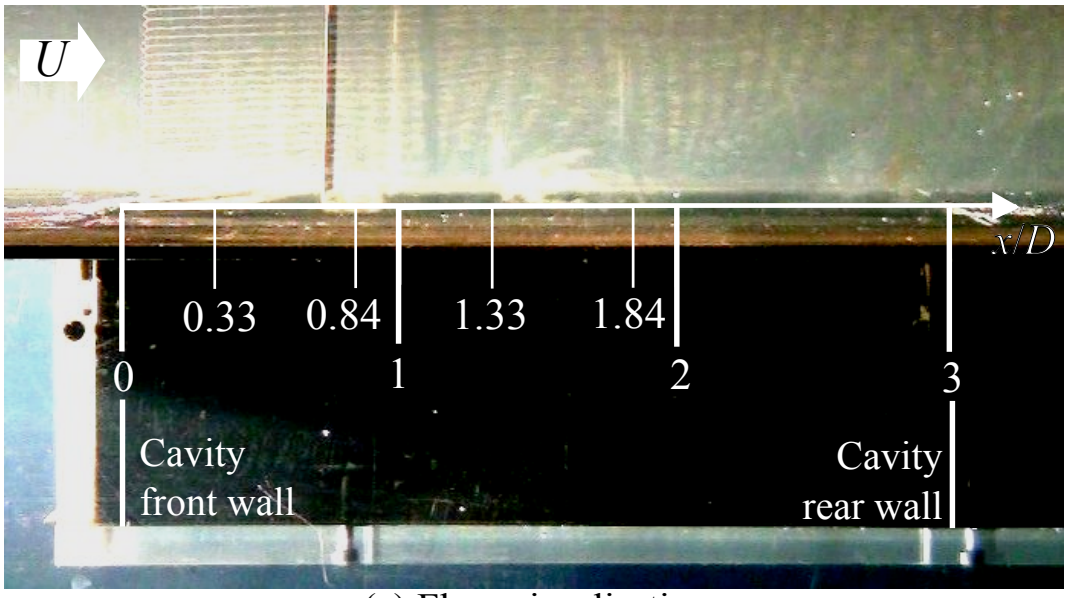

(a) Flow visualisation

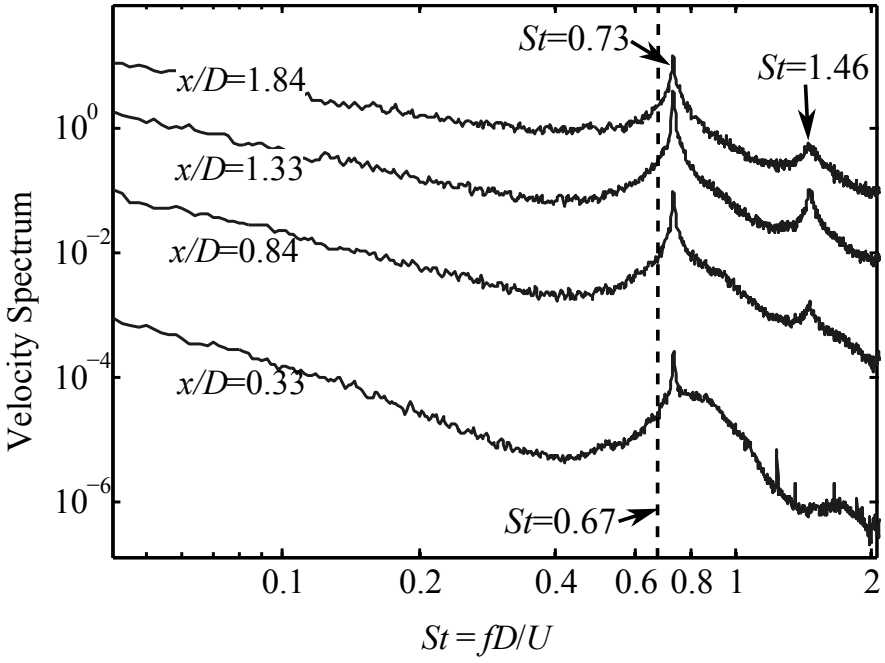

(b) Velocity spectra

Figure 6.4: Flow visualisation and velocity spectra for rectangular cavity. (a) Flow visualisation at $Re_D = 10,700$ for L/D=3. The location of the cavity front & rear walls, once corrected for perspective, are indicated. (b) Velocity spectra at $Re_D = 11,900$ for $L/D = 2.33$. Note the spectra are offset by an order of magnitude for clarity, and therefore the units of the y-axis are arbitrary. The dashed-line represents the Strouhal number found from the flow visualisation in water.

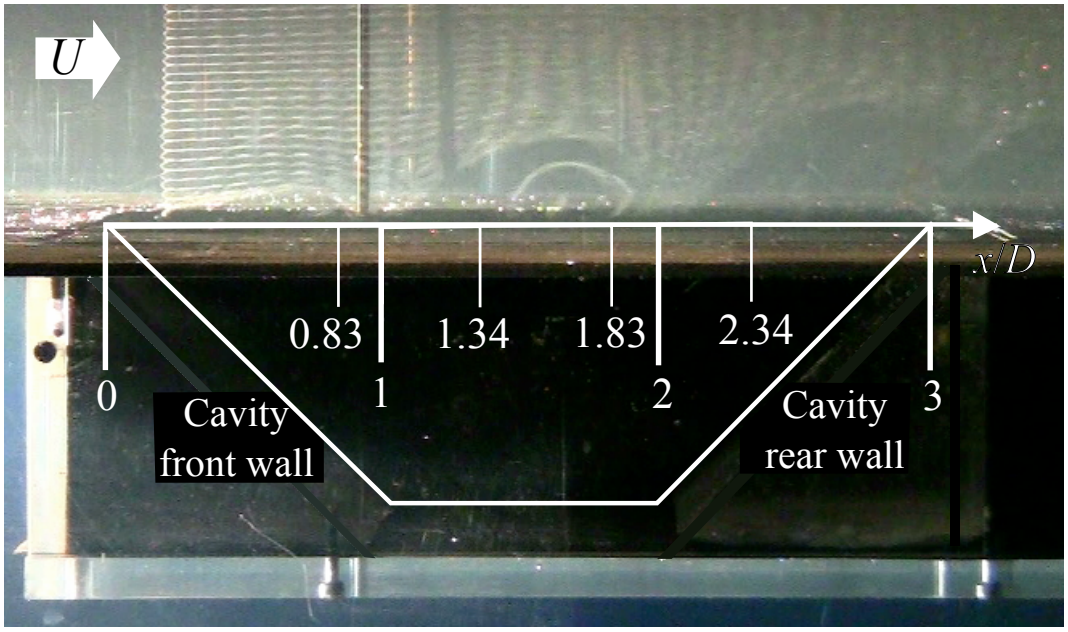

(a) Flow visualisation

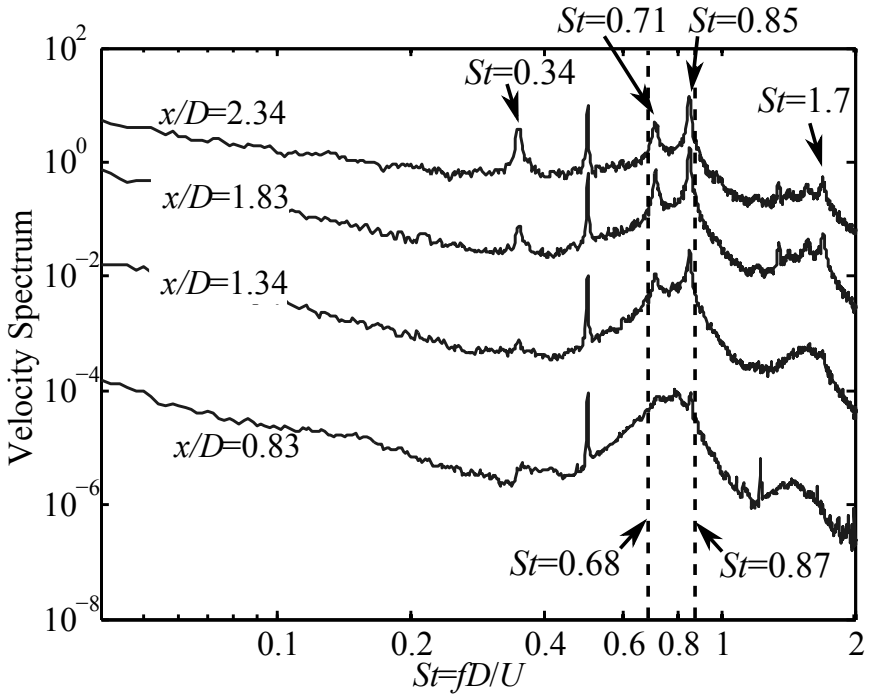

(b) Velocity spectra

Figure 6.5: Flow visualisation and velocity spectra for sloped front and sloped rear wall cavity. (a) Flow visualisation at $Re_D = 10,700$ for an effective L/D=2.5 (once normalised for cavity volume). The location of the cavity front & rear walls, once corrected for perspective, are indicated. (b) Velocity spectra at $Re_D = 11,900$ for $L/D = 2.33$. Note the spectra are offset by an order of magnitude for clarity, and therefore the units of the y-axis are arbitrary. The dashed-lines represent the Strouhal numbers found from the flow visualisation in water.

6.2 Mixing layer structure over the cavity

This section describes the mixing layer structure over the cavity for a rectangular cavity with $L/D = 6$. Figure 6.6 shows the process of roll-up of the shear layer of the cavity for $L/D = 6$ at a depth-based Reynolds number of 2,700 ($U = 40$ mm/s). A spanwise dye slot was utilised, positioned upstream of the cavity. The upstream boundary layer was of the laminar type with $D/\delta_0 \approx 5.2$ and $D/\theta_0 \approx 39$. Structures are seen to begin the breakdown into many smaller structures downstream of approximately half the length of the cavity.

Figure 6.7 shows the typical dye pattern formed as dye is released from the upstream slot. The flow field was found to be dominated by the Kelvin-Helmholtz shear layer vortices, as expected. The structures in the shear layer are periodic and highly three-dimensional. Two shear layer vortices can be seen orientated across the span of the cavity. The flow appears to be largely symmetrical for this Reynolds number.

Although it will take a certain time for the streaklines to reveal the presence of a vortical feature (Gursul, Lusseyran and Rockwell 1990), it appears that, at this Reynolds number, there is significant curvature to what is usually referred to as the 'spanwise roller' shear layer vortex. Indeed the vortex does not appear to attach to the side walls of the cavity until approximately one-half of the cavity length in this case. This curvature is thought to be due to end effects whose influence extends far beyond the side wall boundary layer (Rockwell and Knisely 1980).

Figure 6.8 gives a series of frames showing the evolution of the overall dye pattern. From observing the cavity, for this cavity and flow configuration, the instability frequency was estimated to be $f = 0.24$ Hz, giving a length-based Strouhal number $St_L = fL/U = 2.7$ or a depth-based Strouhal number $St_D = fD/U = 0.45$ (note that the Reynolds number is lower compared to the spectral results discussed earlier). The time between frames is approximately one-quarter of a roll-up cycle. The first wavefront is indicated by the solid circle, while the later wavefront is indicated by the open circle. At approximately frame (d), the first wavefront can be seen to begin to break down to turbulence.

PIV was conducted over the downstream portion of the $L/D = 6$ rectangular cavity at a depth-based Reynolds number of 6,700. The measurement plane was parallel to the flat plate, at a height $y/D \approx -0.13$ (i.e., above the flat plate).

Figure 6.9 shows streamlines calculated from time-average velocity vectors. Within the streamlines, a small amount of 'waisting' [i.e., inflow (Crook, 2011)] is evident. Crook (2011, p. 122) identified similar waisting at the slightly higher depth-based Reynolds number of 8,000 over the same $L/D = 6$ cavity. This means there is a lateral exchange of fluid, over the side edges of the cavity.

Figure 6.10 shows instantaneous vector fields over the downstream part of the cavity. The regions of low velocity magnitude are related to the passage

of shear layer vortices over the cavity. The low-velocity region at the lower right of part (a) is probably a vortical structure. This vortical structure can be seen to convect downstream out of the region of imaging in parts (b) and (c). Another 'c'-shaped, or 'half-ring', vortical structure is evident at the left of part (a). As this structure convects downstream, it appears to increase in lateral & longitudinal size. Unlike other flow visualisation techniques (where apparent convecting structures may contain no actual vorticity), PIV allows confidence that these are genuine vortical structures which are persisting and convecting (as it is measuring the displacement between each pair).

Figure 6.11 shows a time series of streamwise velocity fluctuation, at the downstream portion of the $L/D = 6$ cavity. The velocity is averaged over the box shown in figure 6.11(a) for each PIV sample (image pair). It will be shown later that a sample taken here is highly representative of a sample taken upstream, due to the highly convective nature of the structures that travel along the cavity. It is notable in figure 6.11 that the velocity fluctuation is somewhat irregular, as the Reynolds number is relatively high in this instance.

Figure 6.12 shows the streamwise velocity, along streamwise and spanwise slices, for the duration of the PIV sample. The bands in figure 6.12(d) represent the convection of structures from the upstream part of the imaging region (from small to large x/D) to the downstream part of the imaging region. For the example, a low velocity structure can be seen crossing the spanwise sampling line at approximately $t = 15$ seconds, in figure 6.12(c). The same structure can be seen convecting along the length of the cavity, along the streamwise sampling line, at a similar time in figure 6.12(d).

The convection velocity (U_c) of disturbances can be estimated from figure 6.12(d). Although there is a large variability, U_c/U is of the order of $\sim 0.5-0.6$, which is comparable to the results obtained in air.

Secondary, streamwise, vortices

Refering back to figure 6.7, the figure also shows streamwise (Rockwell & Knisely 1983) (or 'strain-orientated' (Lasheras and Choi 1988)) vortices in the cavity shear layer near the upstream shear layer vortex. These form in-between the 'spanwise rollers' in the region of high strain (Lasheras and Choi 1988).

For this cavity, the formation of one or two wavelengths of secondary (streamwise) vortices has been observed. Such undulations were dubbed cells by Rockwell and Knisely (1980). Figure 6.13(a) and (b) show the appearance of one and two cells of streamwise vortices respectively. This produces an 'undulating' appearance to the dye sheet, as found by Rockwell and Knisely (1980). The locations of the streamwise vortices are shown in figure 6.14. These 'cells' are distinct from the internal cells within the cavity, as identified by Maull and East (1963).

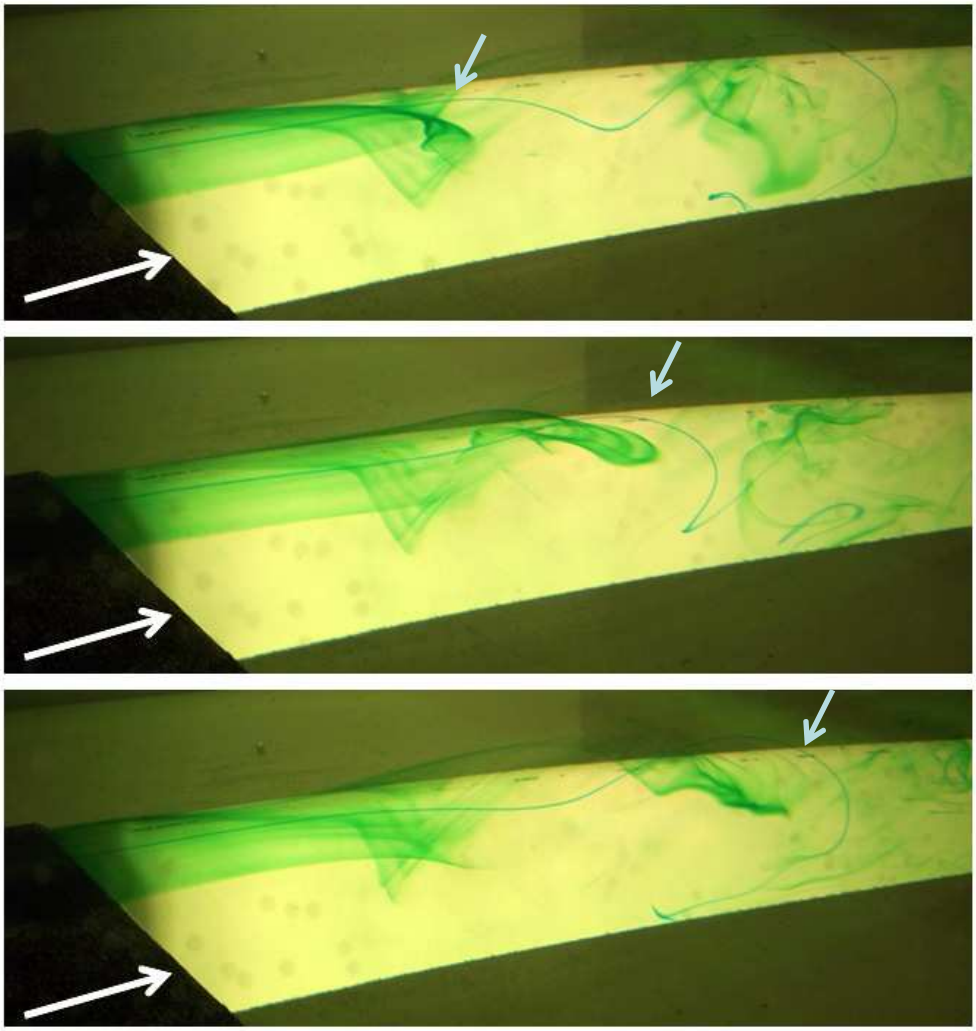

Figure 6.6: Shear layer roll-up: oblique side view looking downstream. The lower arrow in each frame denotes the direction of flow which is from left to right, with increasing time from top to bottom. The upper arrow in each frame denotes the location of a shear layer vortex as it convects along the cavity. $L/D = 6$ and $W/D = 2$. Freestream velocity is $U = 40$ mm/s, giving $Re_D = 2,700$. Green dye was released from the spanwise dye slot, upstream of the cavity. The (faint) blue streakline (near the upper arrow) was released at $z = 0$, at a height $y/D = -0.08$ (above the flat plate).

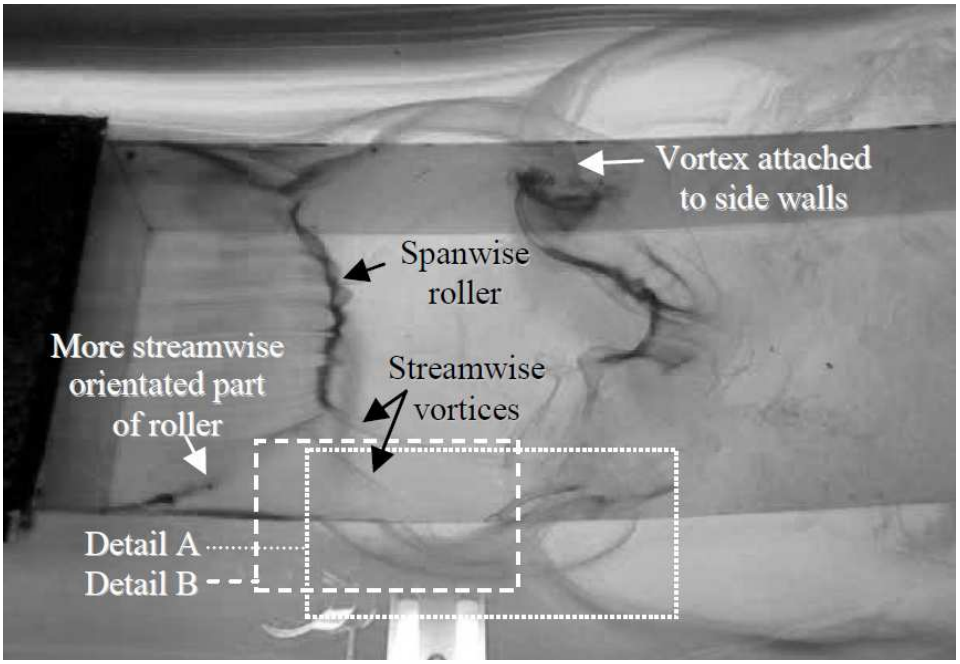

Figure 6.7: Typical dye pattern formed when dye is introduced from a slot upstream of the cavity. Flow is from left to right. View: $0 \leq x/L \leq 0.8$. The depth-based Reynolds number was $Re_D = 2{,}700$, $L/D = 6$ and $W/D = 2$. 'Detail A' and 'detail B' denote fields of view which are referred to in later figures 6.17 and 6.19.

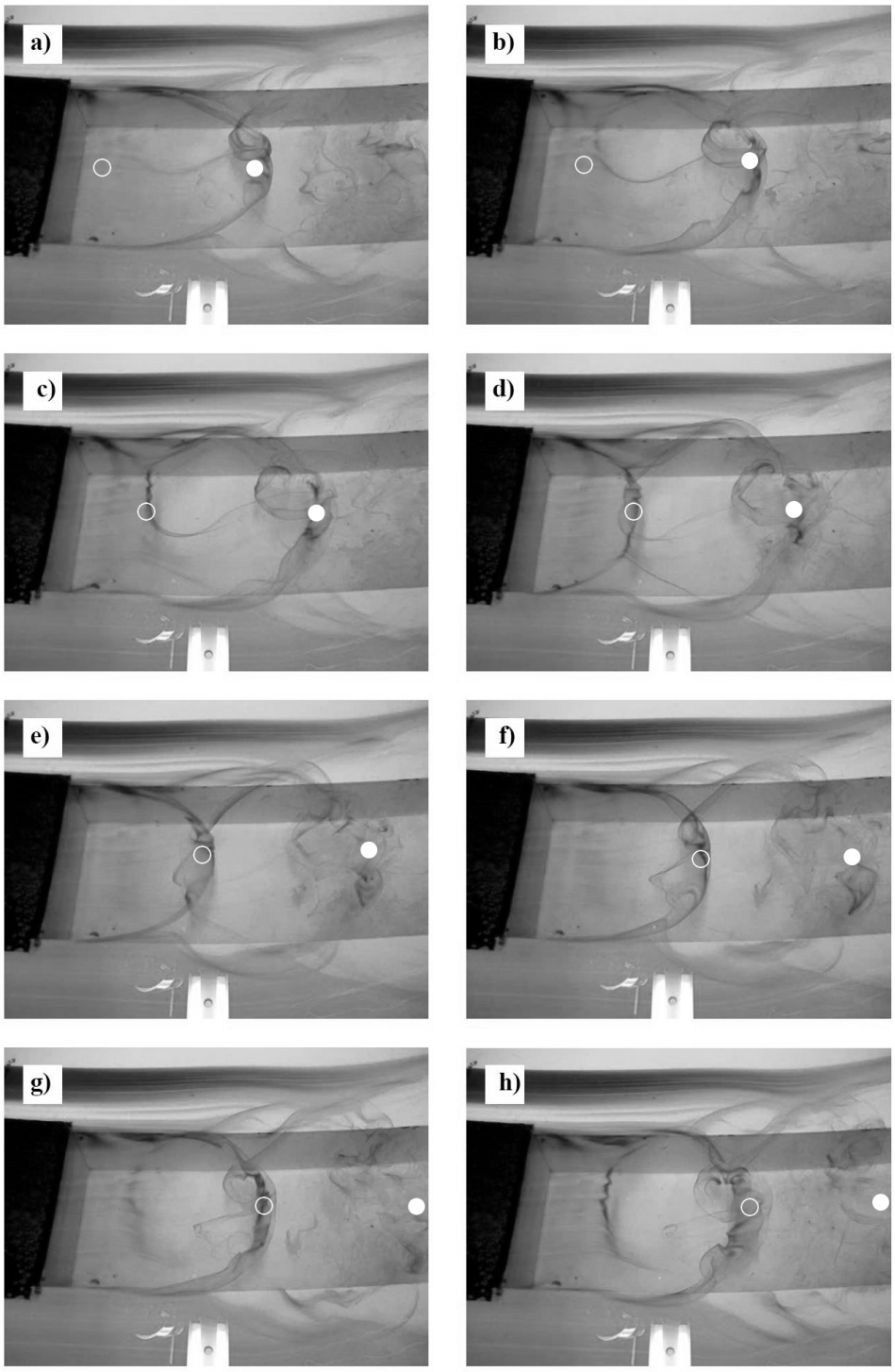

Figure 6.8: Sequence of frames showing the evolution of the overall dye pattern. Temporal spacing between frames is 1 second, approximately $\frac{1}{4}$ of a roll-up cycle. Flow is from left to right. Increasing time from left to right and from top to bottom. The first wavefront is indicated by the solid circle, while the subsequent wavefront is indicated by the open circle.

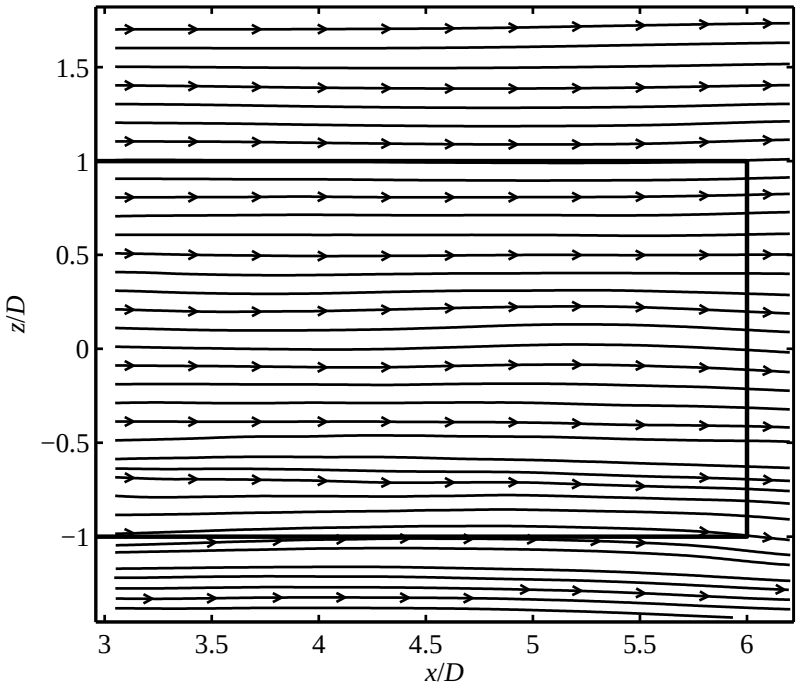

Figure 6.9: Streamlines calculated from time-average velocity vectors over the downstream portion of the rectangular cavity. L/D=6 and depth-based Reynolds number was $Re_D = 6,700$ ($U = 90$ mm/s). The imaging plane is approximately parallel to the flat plate at a height of approximately $y/D \approx 0.13$.

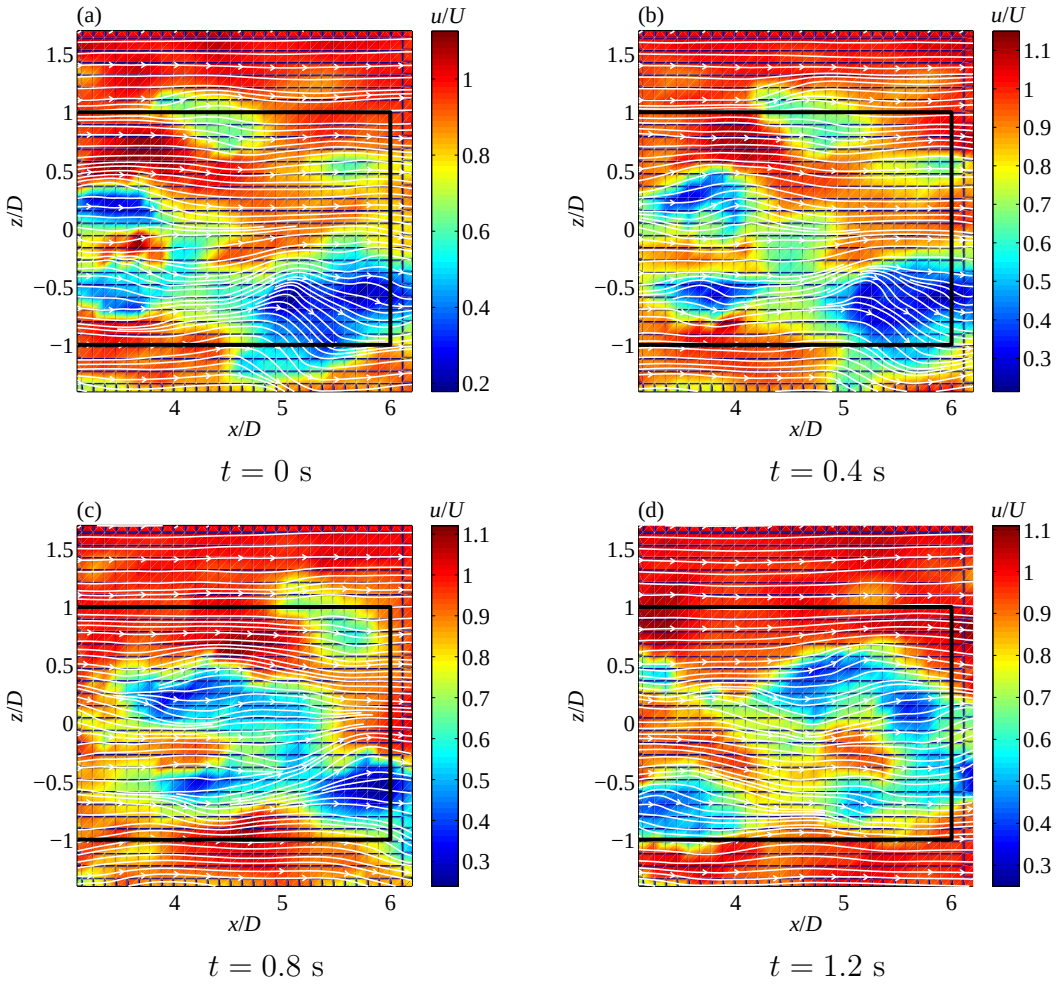

Figure 6.10: Instantaneous vector fields about downstream portion of $L/D = 6$ cavity. The colour contours give the magnitude of the velocity. The depth-based Reynolds number was $Re_D = 6,700$ ($U = 90$ mm/s). The imaging plane is approximately parallel to the flat plate at a height of approximately $y/D \approx 0.13$. (a) $t = 0$ s, (b) $t = 0.4$ s, (c) $t = 0.8$ s, and (d) $t = 1.2$.

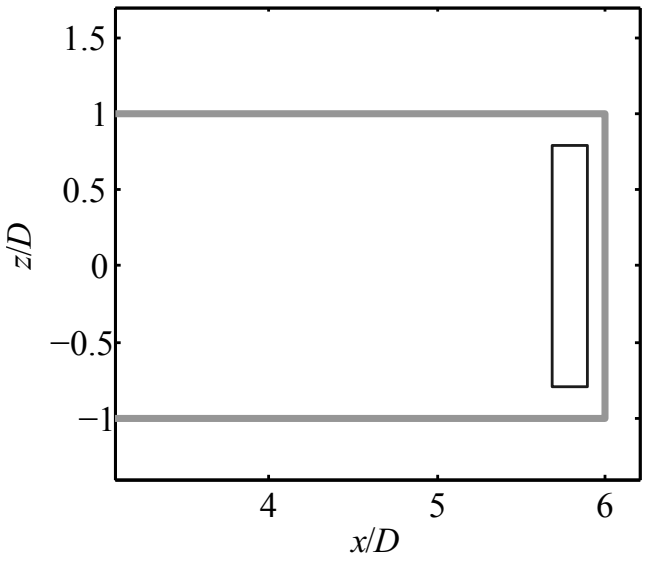

(a) Location of velocity sample, flow from left to right.

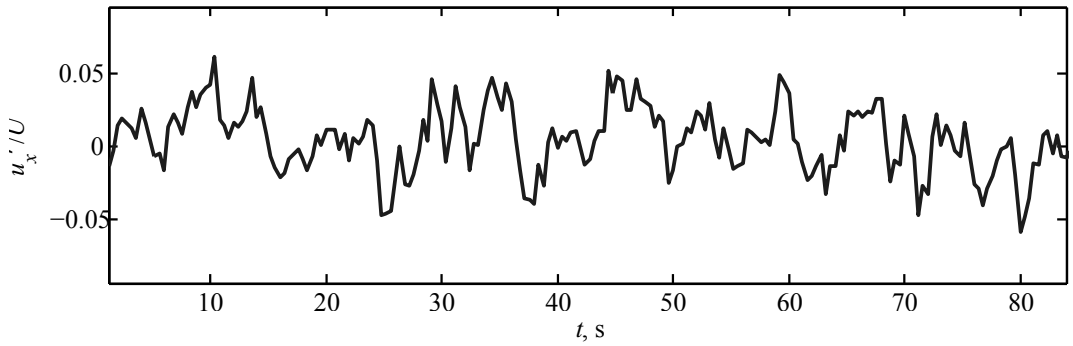

(b) Time series of streamwise velocity fluctuation

Figure 6.11: Streamwise velocity fluctuation in the shear layer over the $L/D = 6$ rectangular cavity. The depth-based Reynolds number was $Re_D = 6,700$ ($U = 90$ mm/s). The imaging plane is approximately parallel to the flat plate at a height of approximately $y/D \approx 0.13$.

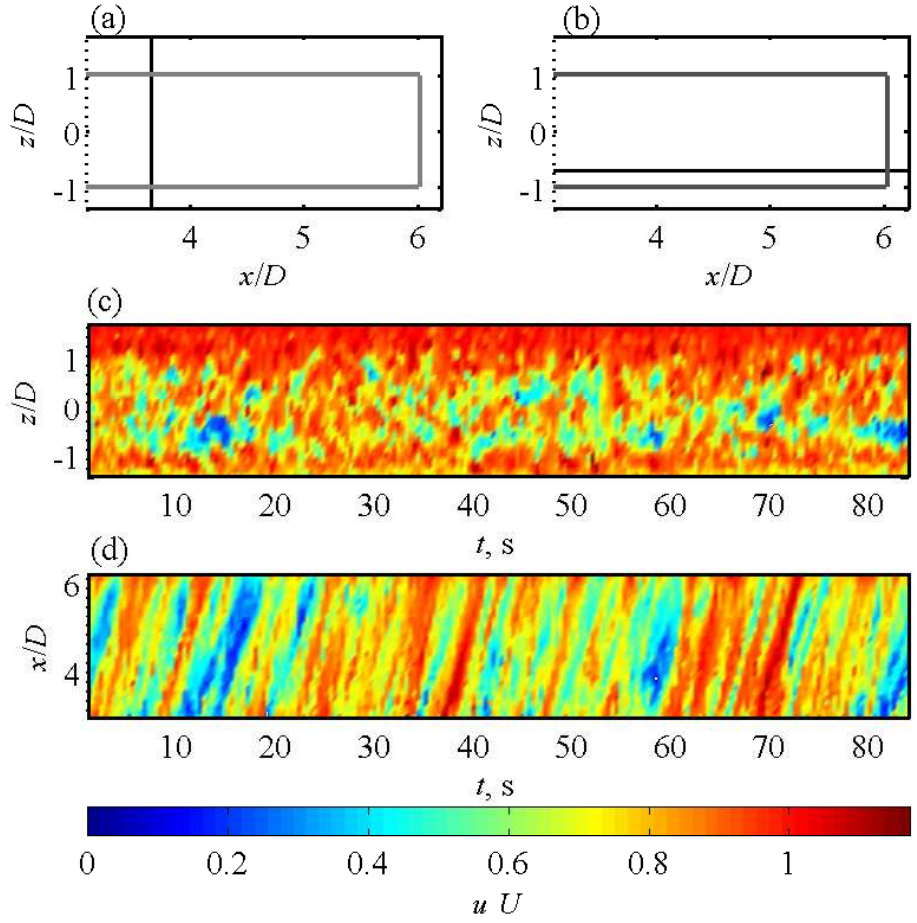

Figure 6.12: Velocity fluctuations over and along the rectangular cavity with $L/D = 6$. (a) Location of the streamwise sample. (b) Location of the spanwise sample. (c) Streamwise velocity for the duration of the PIV data, showing the convection of structures *over* the cavity at the location indicated in part (a). (d) Streamwise velocity for the duration of the PIV data, showing the convection of structures *along* the cavity at the location indicated in part (b). L/D=6 and depth-based Reynolds number of $Re_D = 6,700$ ($U = 90$ mm/s). The imaging plane is approximately parallel to the flat plate at a height of approximately $y/D \approx 0.13$.

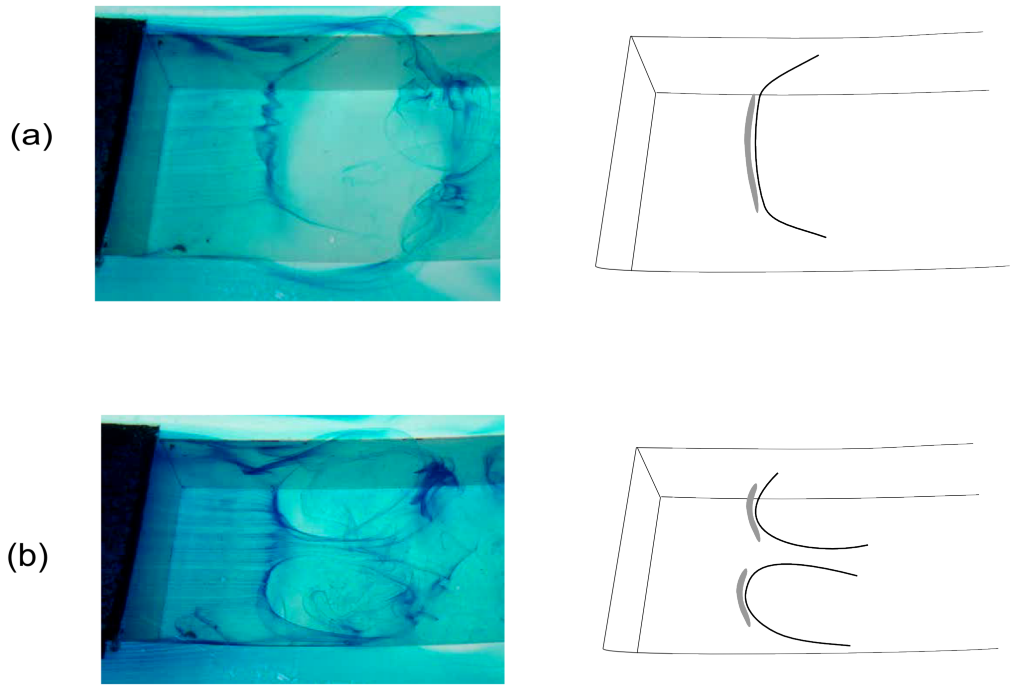

Figure 6.13: Apparent streamwise vortices at $Re_D = 2700$ ($U = 40$ mm/s) for $L/D = 6$ and $W/D = 2$. (a) 1 'cell.' (b) 2 'cells.' Flow from left to right.

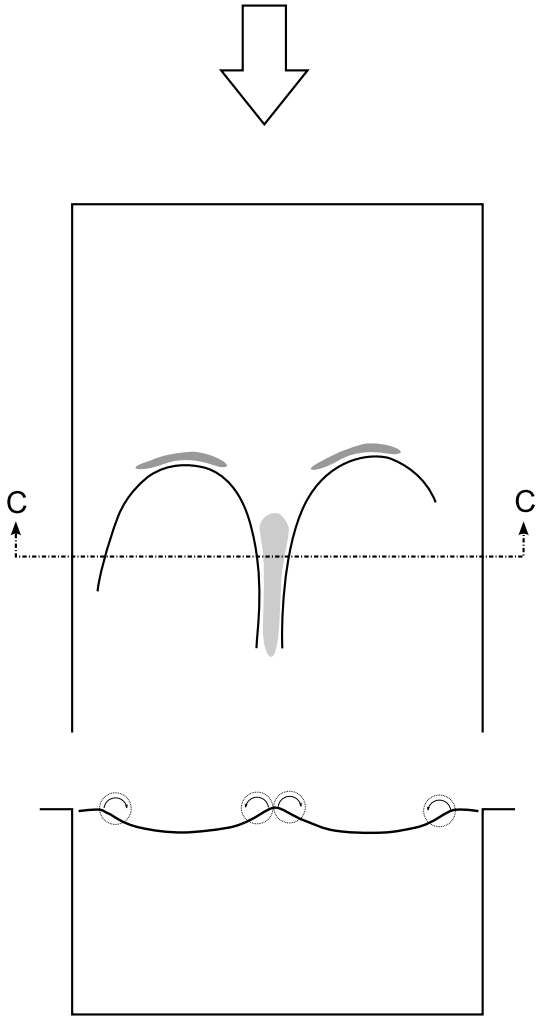

Figure 6.14: Sketch showing a cross section view through the dye sheet, indicating the locations of the streamwise vortices. Flow from top to bottom.

6.3 Mixing layer structure at the sides of the cavity

The thickness of the shear layer is considerable compared to the width (and depth) of the cavity within the present Reynolds number range of $Re_D = 2,700-11,900$. Thus a three-dimensional shear region is formed as the growing mixing layer interacts with the flat plate adjacent to the cavity. In this region, the streamwise-orientated portion, or 'leg', of the shear layer 'spanwise roller' vortices (see figure 6.7) convects upwards over the cavity sides (this is shown more clearly in figure 6.19).

Figure 6.15 shows dye visualisation of the mixing region about the sides of the cavity. A streakline is released from a dye probe just above the flat plate at the side of the cavity, whilst simultaneously a sheet of dye is released from the dye slot to allow for visualisation of the shear layer vortices. Observing the blue streakline, the figure shows that fluid from the side of the cavity is drawn in and around each shear layer vortex. With the variation of time and position, the streakline is deflected either towards or away from the centreline of the cavity indicating a mixing of fluid between the shear layer over the cavity, and the boundary layer at the sides of the cavity.

A distinctive tornado-like vortex forms at regular intervals adjacent to each spanwise roller. This vortex is indicated by the arrow in figure 6.16 (in order to obtain a clearer photograph, the circulation control flap was adjusted so that the feature was stronger than usual). This vortex appears to lift fluid up from the flat plate surface. The vortex then turns towards the centreline and then down into the cavity.

Figure 6.17 shows the distinctive instantaneous dye pattern formed adjacent to the cavity. In the figure, lighter coloured regions on the flat plate would tend to suggest either more diffusion has occurred or fluid is transported laterally and replaced by undyed fluid. The tornado-like vortex can be seen and is marked by a curved arrow which indicates the direction of circulation of the vortex. Also there is an inner edge visible containing a lighter coloured region. There is additionally an outer edge containing darker fluid. Located downstream, the edge of the previous cycle of this pattern can be seen – this marked region of fluid has continued to grow outwards as it travels downstream.

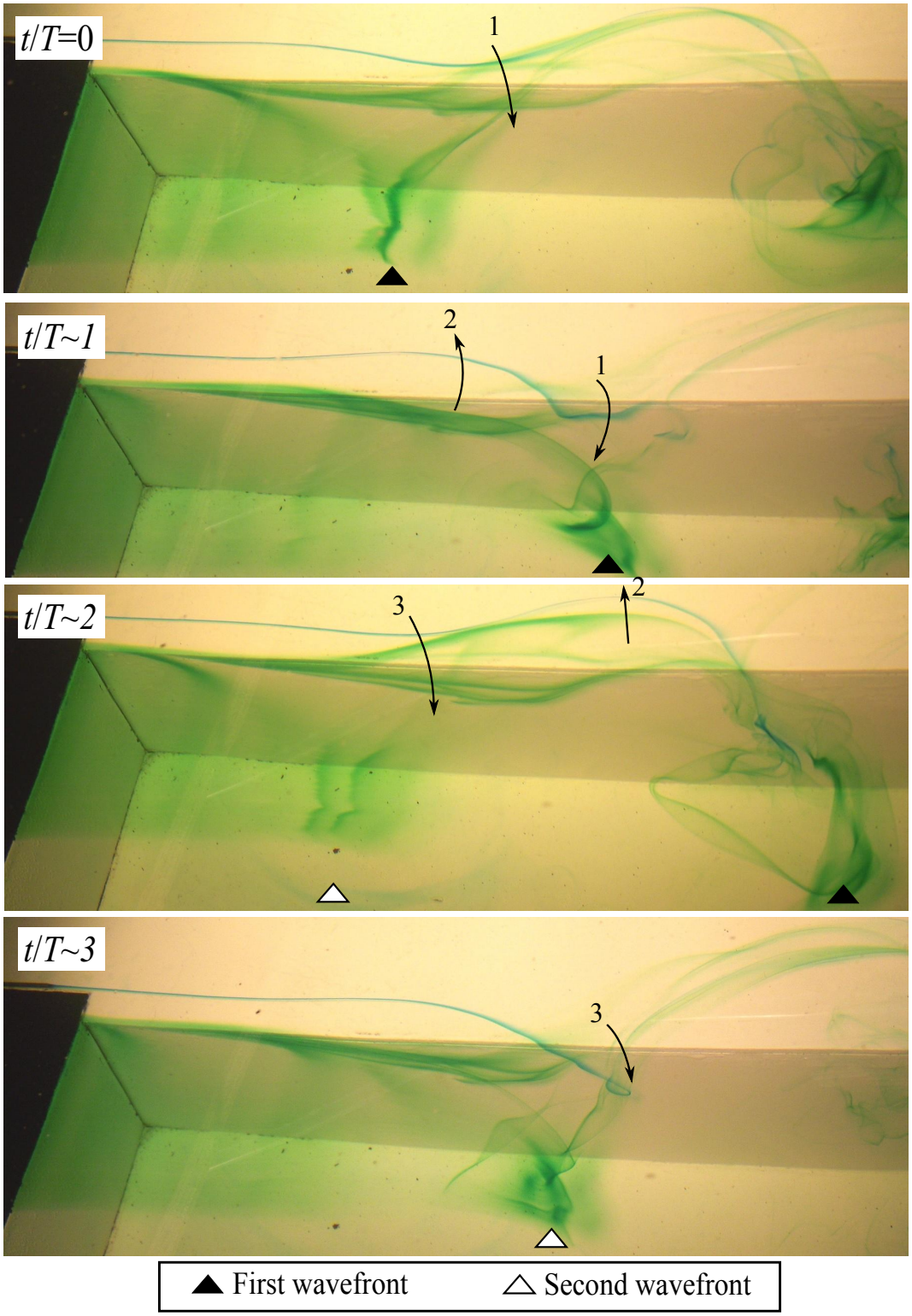

Figure 6.15: Dye visualisation of the mixing region formed at the sides of a three-dimensional, narrow, cavity at $Re_D = 2700$ ($U = 40$ mm/s). Blue dye is released from a probe above the flat plate and adjacent to the side of the cavity. Green dye is released from the dye slot in the flat plate, upstream of the cavity. Note that the numbered arrows represent the direction of the motion of the structure, at the instant of the photograph.

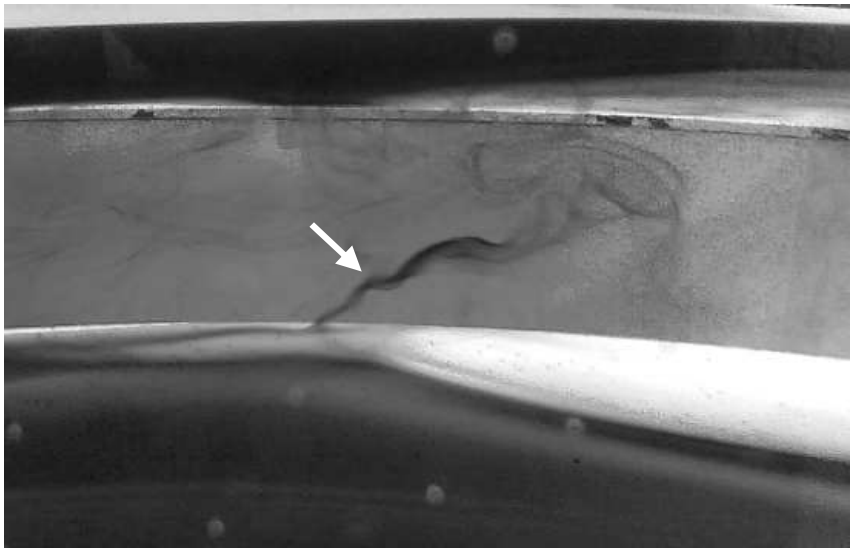

Figure 6.16: A tornado-like vortex formed at the sides of the cavity as indicated by the arrow. Flow is from left to right. The vortex is located on near side (to camera) of flat plate adjacent to cavity. Oblique view covering, approximately, $0.2 \leq x/L \leq 0.7$.

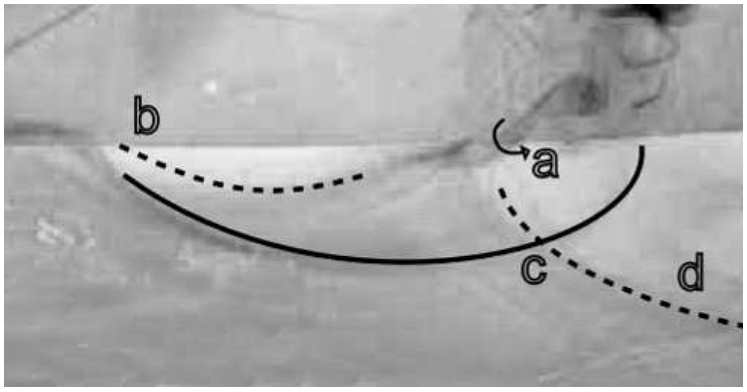

Figure 6.17: Dye pattern formed at the side of the cavity. Flow is from left to right. The field of view is as per 'Detail A' on figure 6.7. (a) Tornado-like vortex. (b) Edge of inner, lighter region. (c) Edge of outer, darker region. (d) Previous cycle of this pattern, having convected downstream.

Figure 6.18: Cut-away sketch of instantaneous dye visualisation pattern, when dye was released from a slot in the plate upstream of the cavity at $Re_D = 2700$ with $L/D = 6$ and $W/D = 2$. Upstream laminar boundary layer with $D/\delta_0 \approx 5.2$ and $D/\theta_0 \approx 39$. The sketch is cut at the vertical centreline plane of the cavity ($z = 0$). The observed pattern was symmetrical about this plane.

Figure 6.18 shows a cut-away sketch of the instantaneous dye visualization pattern of figure 6.7. In the sketch, the main features that have been previously discussed are summarised. These features include the curved shear layer 'spanwise roller' vortices, streamwise vortices within the shear layer, and tornado-like vortices at the sides of the cavity.

Figure 6.19(a)-(c) shows a series of video frames which illustrate the interaction of the stream-wise orientated portions, or 'legs', of the shear layer vortices. The earlier leg (believed to be the 'kinked' region of dye) appears to be drawn under and around the leg of the later shear layer vortex as sketched in figure 6.19. A further series of video frames is shown in figures 6.20 & 6.21. In figure 6.21 the solid lines approximately represent the edges of the vortices. Further to fig. 6.19, in figure 6.21(c)-(e) the earlier leg intertwines with the leg of the later vortex. Later, the tornado vortex is formed, anchored to the flat plate adjacent to the cavity (figure 6.21(f)).

Figure 6.22 shows the same sequence of events, as described previously, in a clearer format. The blue represents the previous primary vortex, the red represents the current primary vortex and the green represents the next primary vortex. In 'a' & 'b', we see the 'leg' of the previous vortex interacting with the current vortex. In 'c', we see the current vortex becoming attached to the side wall of the cavity. In 'd', the remaining vorticity of the previous vortex has become anchored to the flat plate at the side of the cavity, forming the tornado-like vortex.

Supporting the interactions proposed in figure 6.22(c), is the flow visualisation shown in figure 6.23. The dark streakline has been released upstream at approximately $z/D = 1$ and was initially released adjacent to the flat plate surface. It can be observed at the left-hand part of figure 6.23 that the streakline is wrapped around the shear layer vortex (which itself is attached to the side wall of the cavity), as in figure 6.22(c). The streakline then moves outwards, following the mixed fluid which convects up and out over the side edge of the cavity.

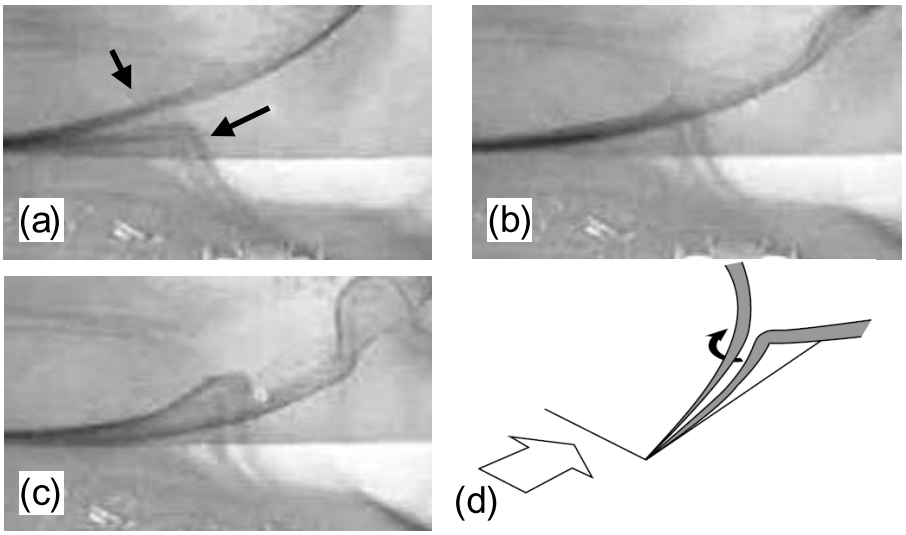

Figure 6.19: Interaction of sequential vortices. From from left to right. Rectangular cavity with $L/D = 6$ & $W/D = 2$ at $Re_D = 2,700$ ($U = 40$ mm/s). (a)-(c) Video frames, view as per 'Detail B' on fig. 6.7. (d) Sketch of interaction.

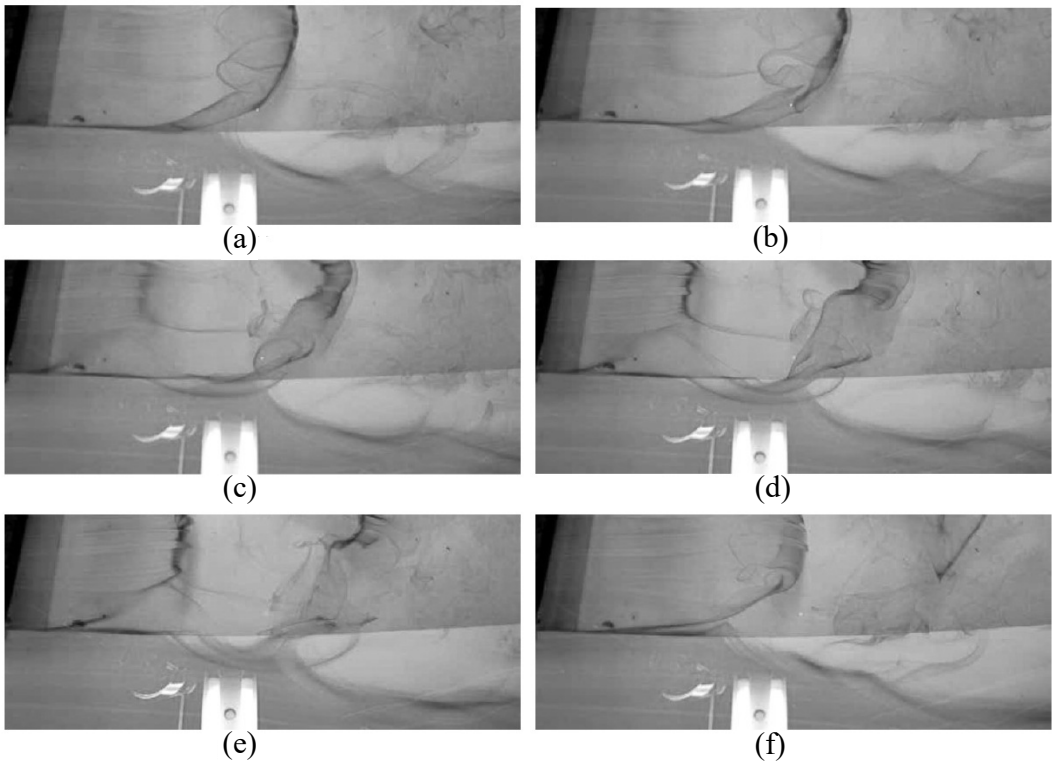

Figure 6.20: Series of video frames that show the interaction of the shear layer vortices. Similar (although expanded) field of view as 'Detail A' on fig. 6.7. Parts (a) to (f) show increasing time. Flow is from left to right. Rectangular cavity with $L/D = 6$ & $W/D = 2$ at $Re_D = 2,700$ ($U = 40$ mm/s). There is a reflection from overhead lighting on the free surface of the water.

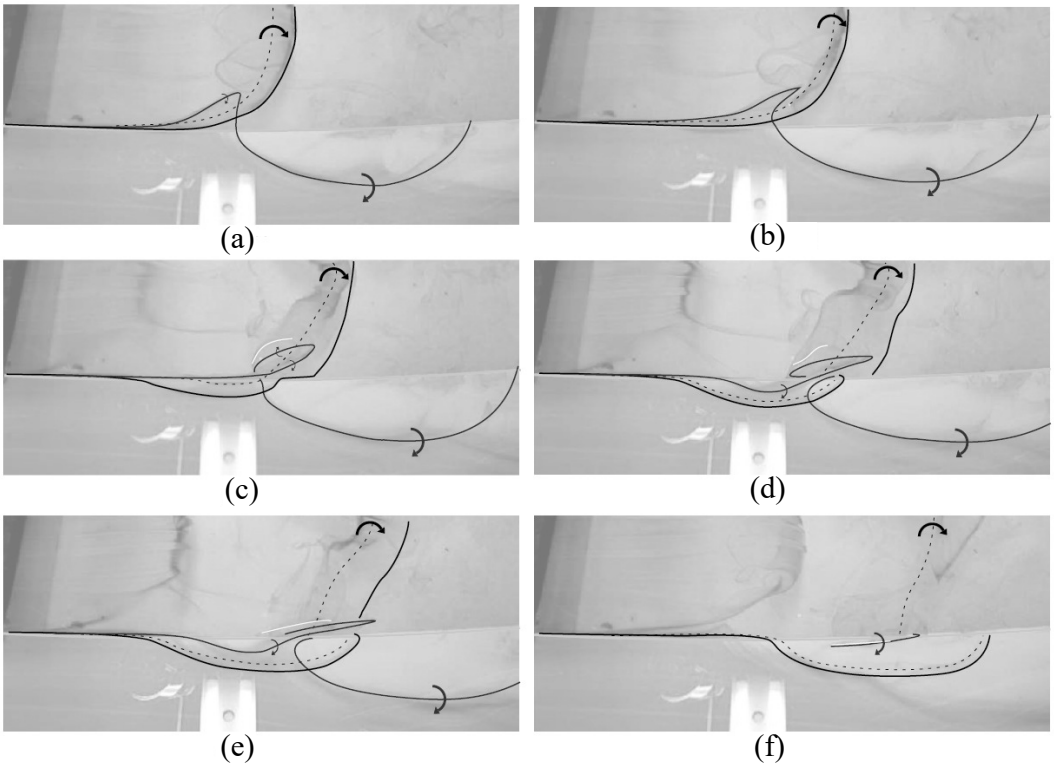

Figure 6.21: Annotated version of figure 6.20.

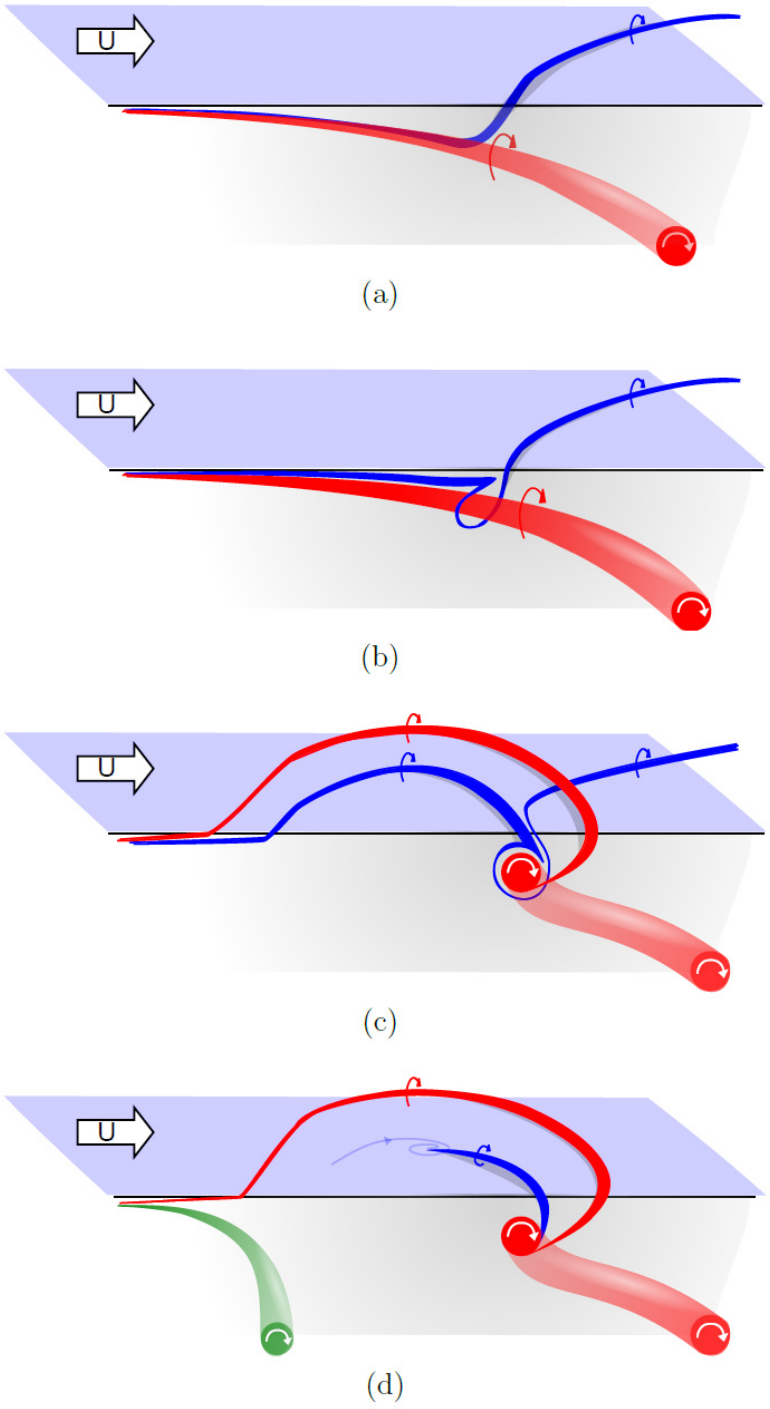

Figure 6.22: Illustration of the interaction of the previous and current vortex in the side region on the cavity. The view is looking at the far side of the cavity, with the side plate above the black line and the side wall of the cavity below the black line. In (d), the leg has become anchored to the flat plate at the side of the cavity to form a tornado-like vortex and the rest of the leg has diffused away, so as to become indiscernible.

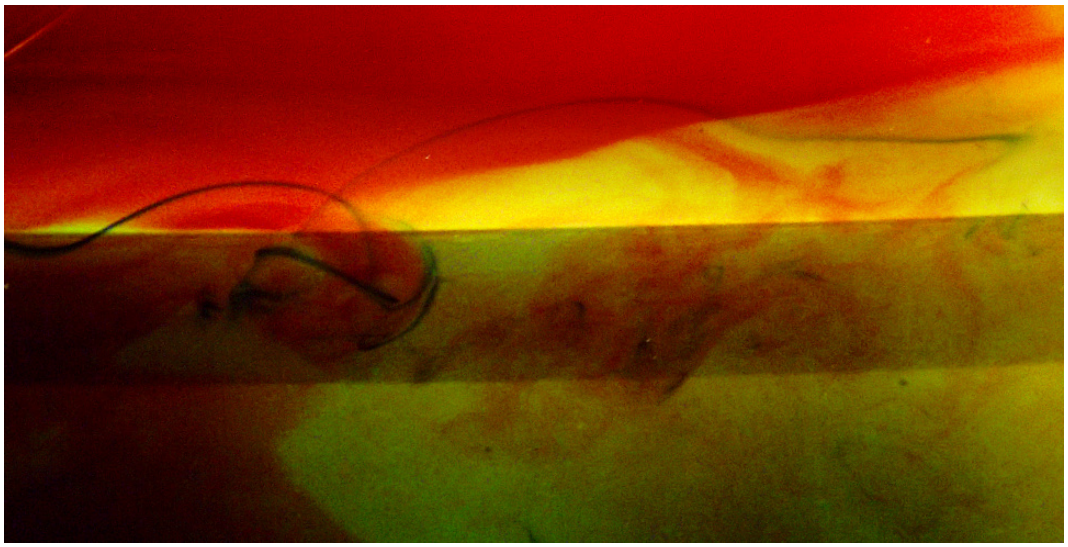

Figure 6.23: Flow visualisation at the side of the $L/D = 6$ cavity. The red dye is released from the upstream spanwise dye slot. The dark streakline was released upstream at approximately $z/D = 1$, and was initially released adjacent to the flat plate surface. View from approximately $L/D \approx 2$ to $L/D \approx 5$. For orientation, the top horizontal portion is the flat plate, the middle is the side wall of the cavity, and the lower portion of the picture is the floor of the cavity. Flow from left to right. Rectangular cavity with $L/D = 6$ & $W/D = 2$ at $Re_D = 2,700$ ($U = 40$ mm/s).

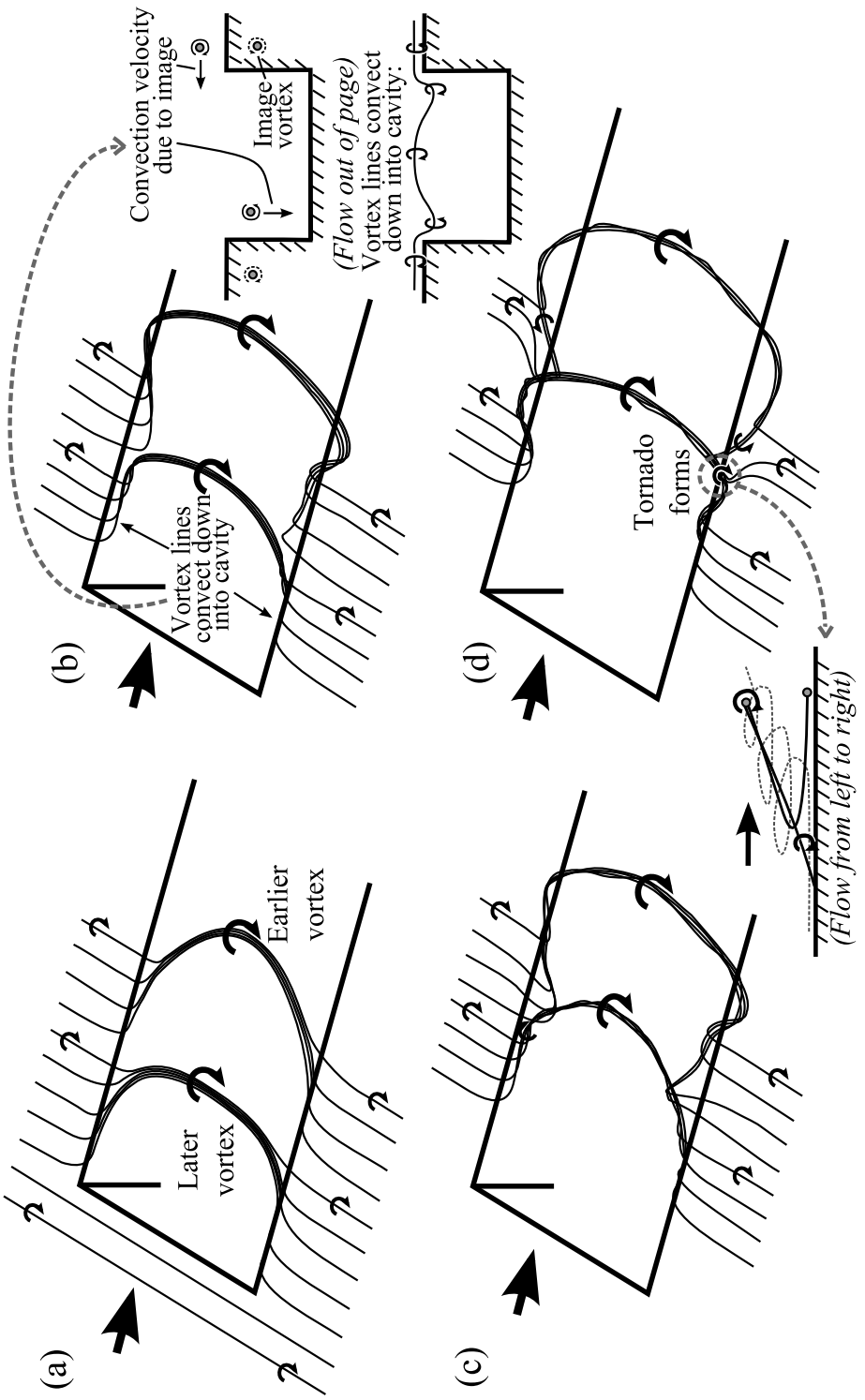

Figure 6.24: Vortex line representation. $Re_D = 2700$ with $L/D = 6$ and $W/D = 2$. Upstream laminar boundary layer with $D/\delta_0 \approx 5.2$ and $D/\theta_0 \approx 39$.

A vortex line representation is given in figure 6.24. Vortex lines approaching the cavity are initially parallel. The velocity within the cavity shear layer is higher than that within the boundary layer, causing the vorticity in the shear layer to travel faster relative to that in the neighbouring boundary layer. As the vortex lines bunch due to the shear layer instability, vortex loops form with streamwise-orientated legs. The initial deformation of the vortex lines causes each leg to then descend laterally down into the cavity due to the vortex induced velocity of their image vortices. These vortices are shown with their image pairs in figure 6.24(b). This behaviour is consistent with the identification of lateral in-flow in the upstream part of the cavity by Crook, Kelso and Drobik (2007).

Figure 6.24(b) shows how the spanwise roller curves and stretches, forming a half-ring which by self-induction will tend to convect higher, out of the cavity, as with the earlier vortex. Subsequently, the 'leg' of the earlier vortex interacts with the 'leg' of the later vortex as shown in figure 6.24(c). Shortly thereafter the vortices emerge over the sides of the cavity, with careful observation confirming that these features did indeed contain vorticity. (An explanation for the emergence is that the sharp corner of the vortex loop causes an increased rate of upward convection.) The side of the earlier vortex is then drawn into the later vortex (see figures 6.20 and 6.21), causing a region of velocity reversal on the floor, stretching and also uplift. This leads to the formation of a tornado vortex as in figure 6.24(d). The tornado vortex is in an unsteady sense anchored to the flat plate, as the anchor point continues to convect downstream with the flow. Note that, at a similar time to these events, the remainder of the shear layer vortex appears to become anchored to the inside side walls of the cavity.

Figure 6.25 shows a proposed instantaneous surface flow pattern at the side of the rectangular cavity. The proposed pattern consists of spiral nodes separated by saddles. There may be a bifurcation line that forms when the outside edge of the vortex attaches down onto the side-plate.

The stable spiral node might form when the trailing part of the *previous* shear layer vortex attaches onto the side plate. This forms the tornado-like vortex. At the tornado-like vortex, fluid is lifted upwards off the side plate and carried downstream. Figure 6.26 shows a cross-section through the flow, indicating the lifting of fluid up from the flat plate surface by the torado-like vortical feature.

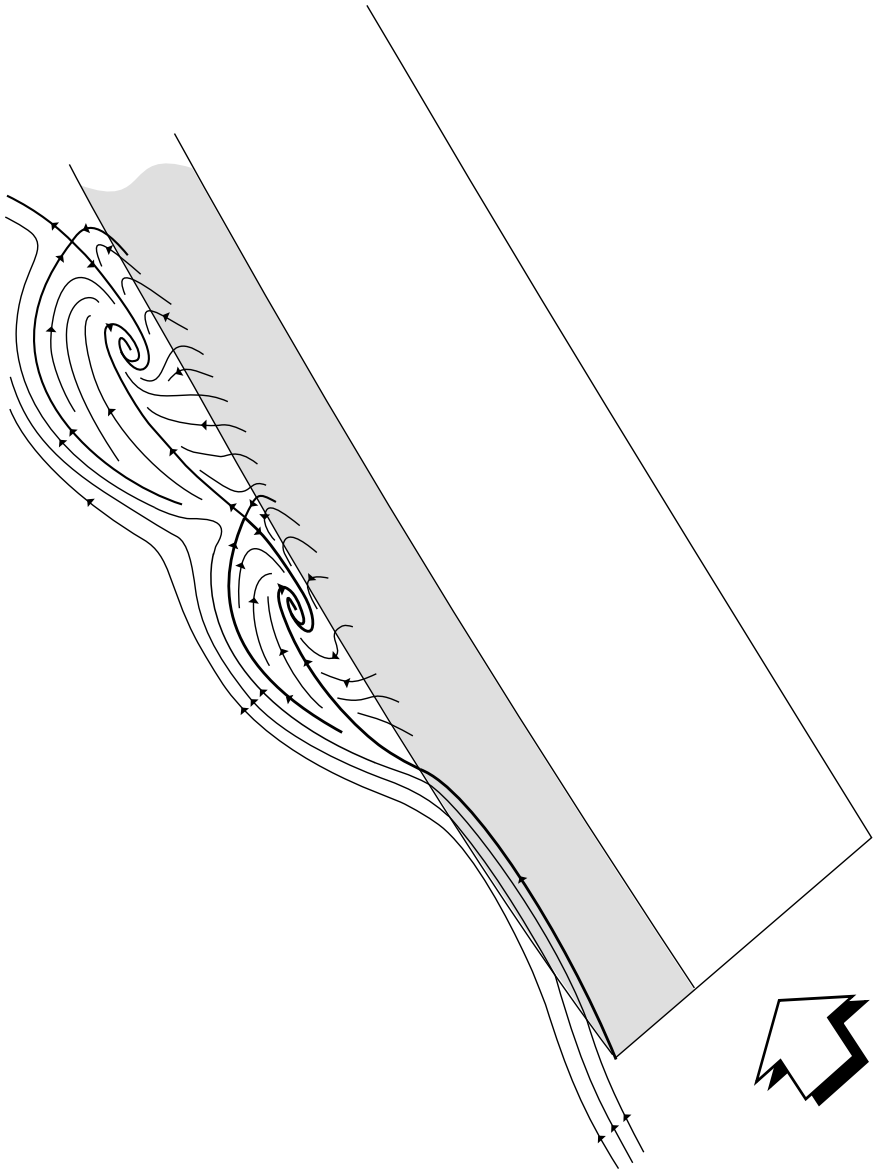

Figure 6.25: Proposed unsteady surface flow pattern found at the sides of narrow cavities. Not to scale. Flow from left to right. Only the pattern at the far side of the cavity is drawn.

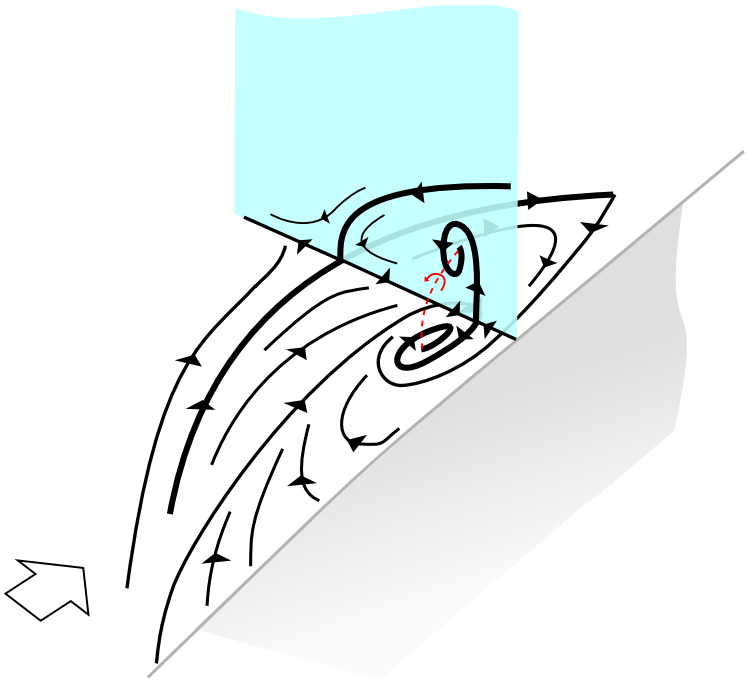

Figure 6.26: Possible surface flow pattern, showing also the pattern in a lateral cross-section through the flow. The diagonal line at the bottom right of the sketch represents the side edge of the cavity. The sketch represents an oblique perspective looking downstream at the side-plate at the far side of the cavity.

Figure 6.27 shows proposed cross-sections through the flow and how they may correspond to the surface flow pattern. The mushroom pattern formed by the 'legs' of the half-rings are shown, indicating the trailing streamwise parts of the primary vortices which convect higher and ultimately out over the side edges of the cavity. It is proposed that these vortical features attach to the flat plate at the side of the cavity, forming the tornado-like vortices.

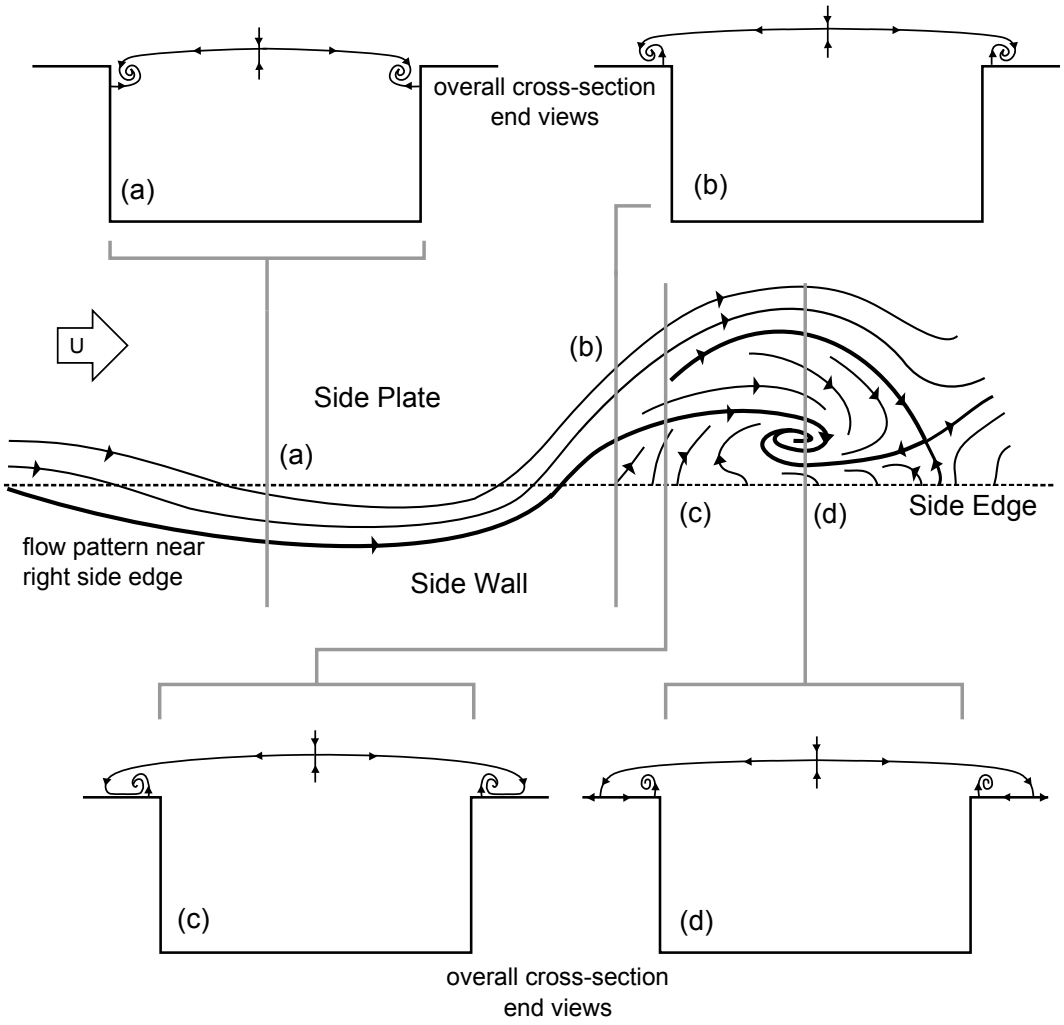

Figure 6.27: Cross-sections through the flow showing possible evolution of the trailing streamwise portions of the primary vortices, corresponding to the surface flow pattern at the side of the cavity. Note that 'side plate' corresponds to the flat plate at the side of the cavity.

6.4 Rear corner vortices

A velocity measurement was conducted which showed the presence of a pair of rear corner vortices adjacent to, and downstream of narrow cavities. These additional measurements were taken in the open jet anechoic wind tunnel using a scale version of the water tunnel three-dimensional model. The free stream velocity was $U = 3$ m/s (turbulence intensity $< 1\%$) with $L = 194$ mm, $D = 32$ mm and $W = 68$ mm, giving a depth-based Reynolds number of 6,400. This is similar to the various water tunnel flow visualisations: the dye visualisation was primarily conducted at $Re_D = 2,700$, while the hydrogen bubble visualisation was primarily conducted at $Re_D = 10,700$.

Boundary layer characterisation

The accumulated contraction boundary layer was redirected under a circular nose profile. That is, the model (or level of the flat plate) was raised up slightly compared to the level of the horizontal part of the jet outlet, and a circular nose was added. There was no circulation control flap. The cavity leading edge boundary layer was measured to be approximately $\delta_0 = 8.0$ mm thick with a shape factor, approximately $H = 2.0$. The momentum thickness was $\theta_0 = 1.0$ mm so that $\theta_0/D = 3.1 \times 10^{-2}$.

Velocity profiles recorded upstream of the cavity using a single-wire hot-wire are shown in figure 6.28. It was found that the flow is very slightly asymmetric across the span of the flat plate but this is not thought to be too significant. The values which were recorded at five positions across the span are tabulated in table 6.2. The shape factor is approximately 2 indicating a transitional boundary layer.

Table 6.2: Boundary layer properties measured upstream of the AWT 3D cavity at $x/D = -0.16$.

Spanwise pos., z/D	-1.1	-0.53	0	0.53	1.1
δ, mm	7.75	7.5	7.5	7.5	8.5
δ*, mm	1.8	1.8	1.9	2.1	2.4
θ, mm	0.95	0.91	0.94	1.0	1.2
Shape factor, H	1.9	2.0	2.0	2.1	2.0
U_e, m/s	2.89	2.93	2.95	2.95	2.93

Profiles

Some specific velocity profiles through the flow are now given. These are given at different x/D. These profiles clearly show the 'dips' that are evident on the velocity maps, which will be discussed later.

Figure 6.29 shows the properties of streamwise velocity above the cavity, at approximately the mid-chord of the cavity. It can be seen that the streamwise velocity and root-mean-square fluctuation velocity are fairly uniform across the span.

Figure 6.30 shows the velocity properties across the cavity span of the three-dimensional cavity just downstream of the cavity trailing edge, at a fixed height. Comparing figure 6.29(a) to figure 6.30(a) shows that two dips have developed in the streamwise velocity either side of the side edges of the cavity. Part (b) shows that there are two peaks in the root-mean-square fluctuation velocity associated with these dips.

Finally, figure 6.31 shows the streamwise velocity properties, one and a half cavity depths downstream of the cavity in the streamwise direction. Effectively this in the 'wake' of the cavity. It can be seen that, by this location, the profile is quite different to that found upstream. As with other wakes, there is a velocity deficit and a high level of turbulence downstream of the cavity itself.

Velocity maps

Figure 6.32 shows a plan view of the velocity magnitude recorded near the flat plate surface and over the cavity, measured in a grid with streamwise spacing of 9 mm and spanwise spacing of 3 mm. The time-averaged flow properties appear to be reasonably symmetrical about the downstream portion of the cavity.

Figure 6.32 shows that regions of lower velocity magnitude and higher velocity fluctuation are found near each of the rear corners of the cavity. A cross-stream (lateral) view of this behaviour measured near the upper rear corner (at positive Z) is shown in figure 6.33. Both profiles show that there is a region of low mean velocity and high velocity fluctuation immediately adjacent to the corner of the cavity. This behaviour may be related to low velocity fluid emerging laterally from the cavity, over the sides, forming a vortical feature (longitudinal vortices).

Flow visualisation of rear corner vortex

Figure 6.34 shows a rear corner vortex found about the $L/D = 3.33$ cavity. The green streakline is released a short distance upstream of the imaged region at $y/D = -0.08$ (above the flat plate) and $z/D = -1.2$.

In figure 6.34, the green streakline appears to rotate around the streamwise vortical structure – evident just downstream of the cavity trailing edge. The inset figure shows the proposed orientation of the vortex. The green streakline

apparently goes over the top and then underneath the vortex. It is unclear whether this is a similar structure to that identified in figure 6.32.

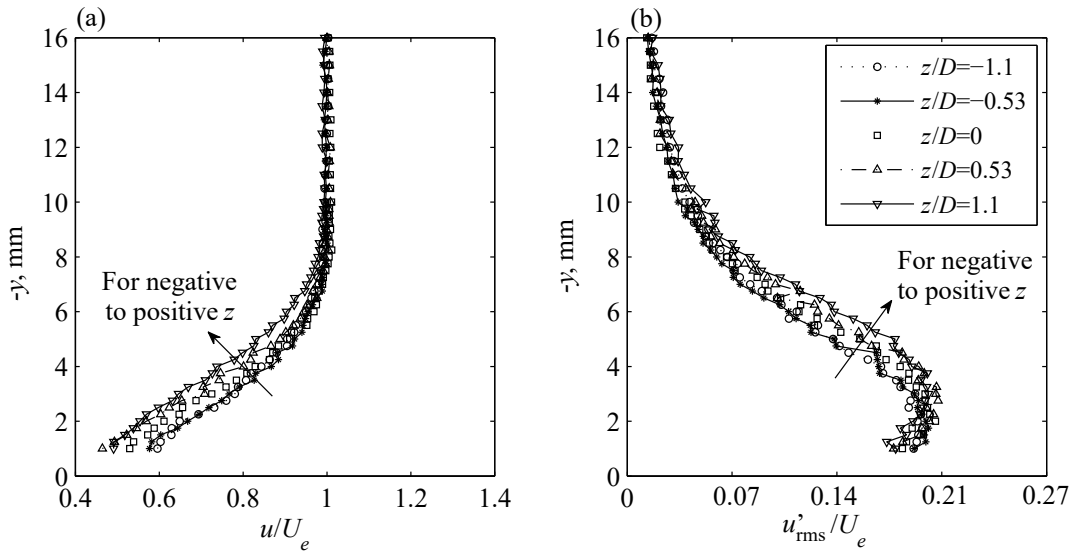

Figure 6.28: Velocity profiles upstream of the three-dimensional AWT cavity recorded at $x/D = -0.16$. (a) Normalised local velocity. (b) Root-mean-square fluctuation velocity.

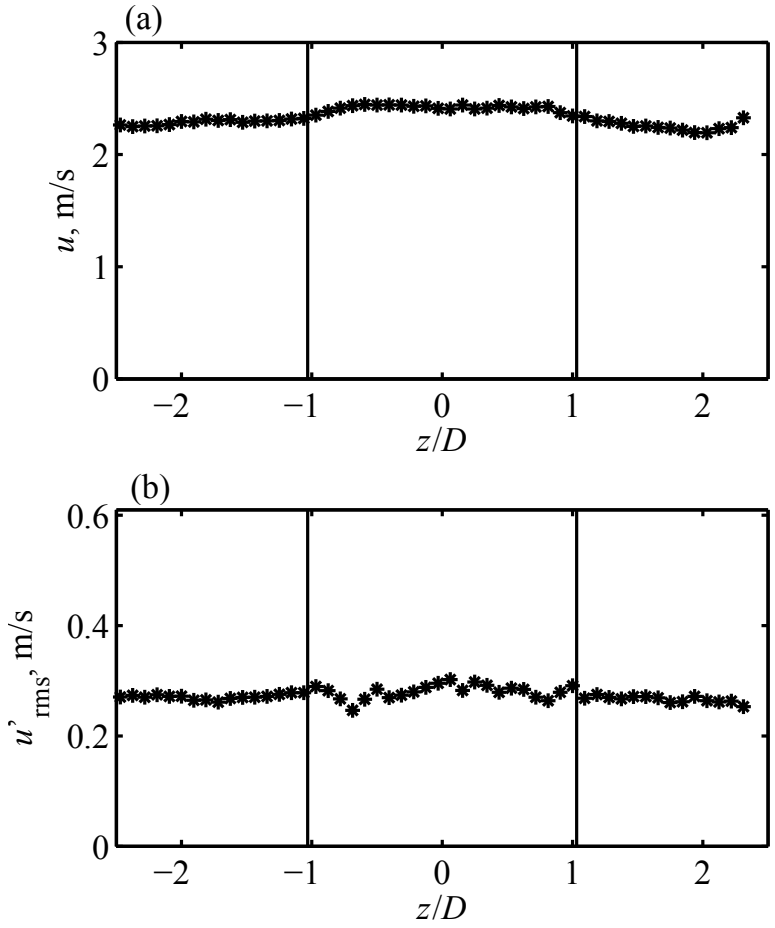

Figure 6.29: Velocity properties across the cavity span at $x/D = 3.0$ (approximately halfway along the cavity). $Re_D = 6,400$, $L/D = 6$ and $W/D = 2.1$. (a) Streamwise velocity. (b) Root-mean-square fluctuation velocity. Measurement height was $y/D = -0.17$. The solid vertical lines indicate the position of the two side edges of the cavity.

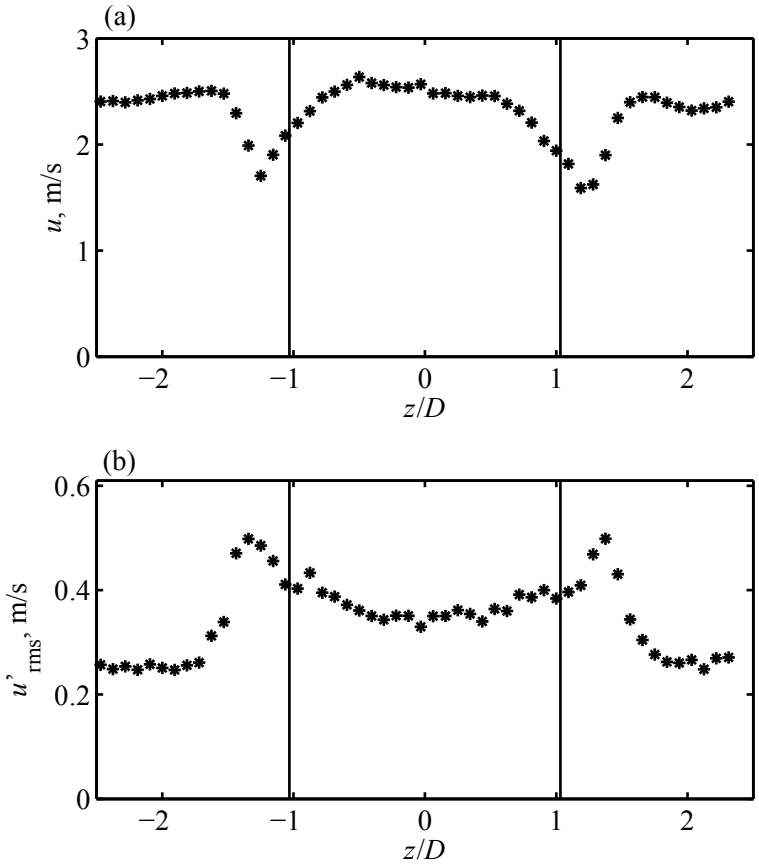

Figure 6.30: Velocity properties across the cavity span at $x/D = 6.1$ (just downstream of the cavity trailing edge). $Re_D = 6,400$, $L/D = 6$ and $W/D = 2.1$. (a) Streamwise velocity. (b) Root-mean-square fluctuation velocity. Measurement height was $y/D = -0.17$. The solid vertical lines indicate the position of the two side edges of the cavity.

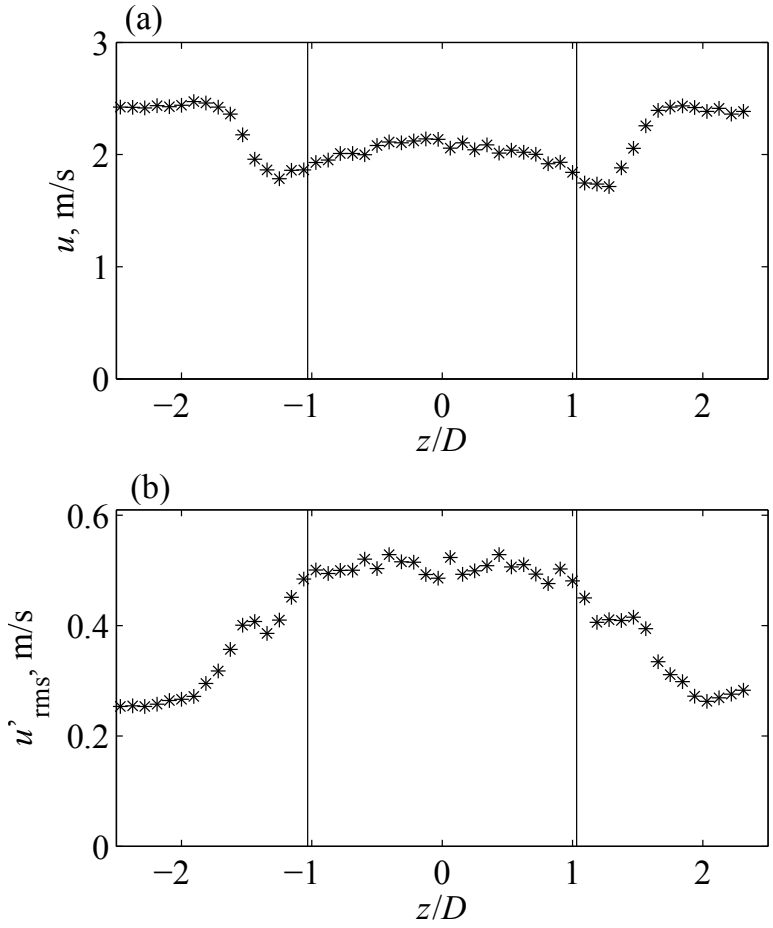

Figure 6.31: Velocity properties across the span at $x/D = 7.5$ (downstream of the cavity). $Re_D = 6,400$, $L/D = 6$ and $W/D = 2.1$. (a) Streamwise velocity. (b) Root-mean-square fluctuation velocity. (Note that the length of the cavity was $6D$.) Measurement height was $y/D = -0.17$. The solid vertical lines indicate the position of the two side edges of the cavity.

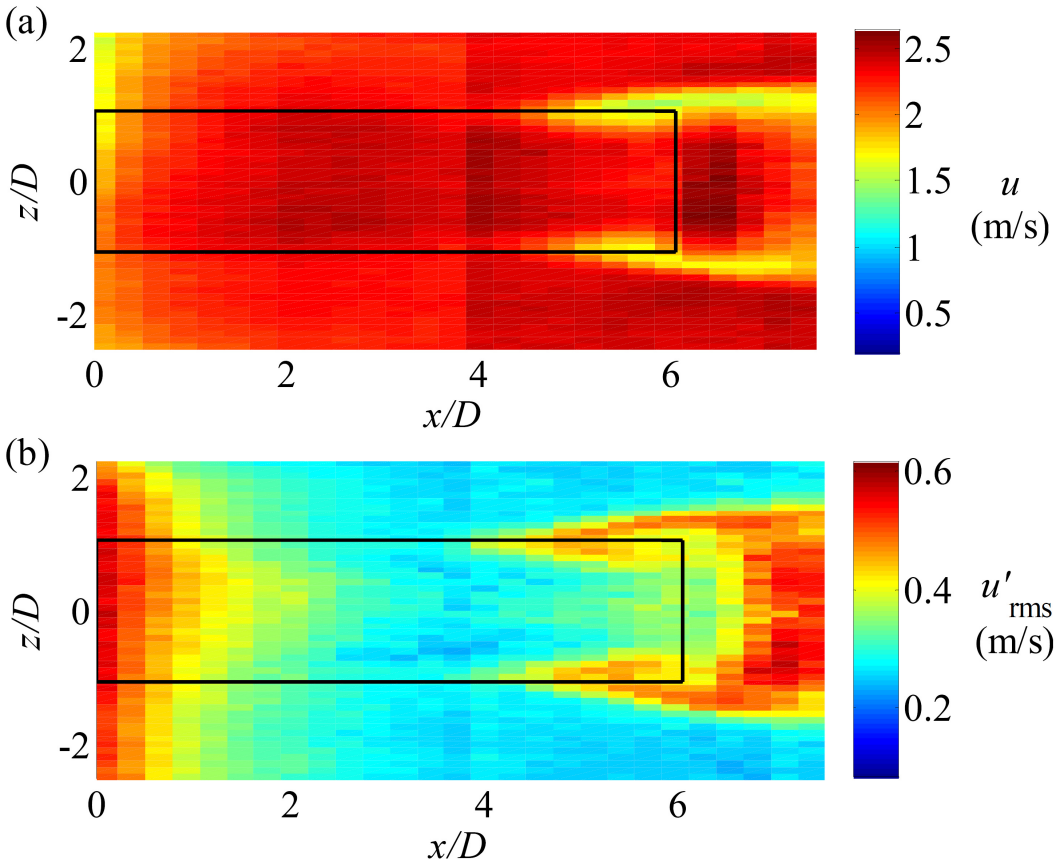

Figure 6.32: Plan view of the cavity (indicated by black lines) with flow from left to right. (a) Local velocity magnitude. (b) Local root-mean-square fluctuation velocity. $Re_D = 6,400$, $L/D = 6$ and $W/D = 2.1$. Measurement taken at a height of $y/D = -0.17$.

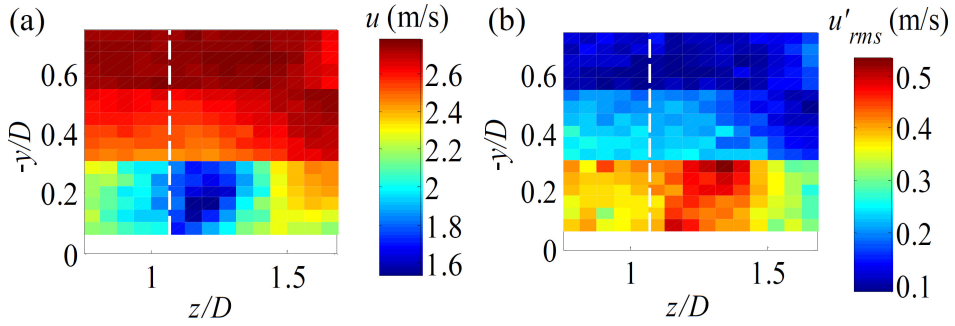

Figure 6.33: Cross stream view of velocity measurements near the rear corner of the cavity at $x/D = 6.07$. The cavity is to the left of the dashed white line. (a) Mean velocity magnitude. (b) RMS fluctuation velocity. $Re_D = 6,400$, $L/D = 6$ and $W/D = 2.1$.

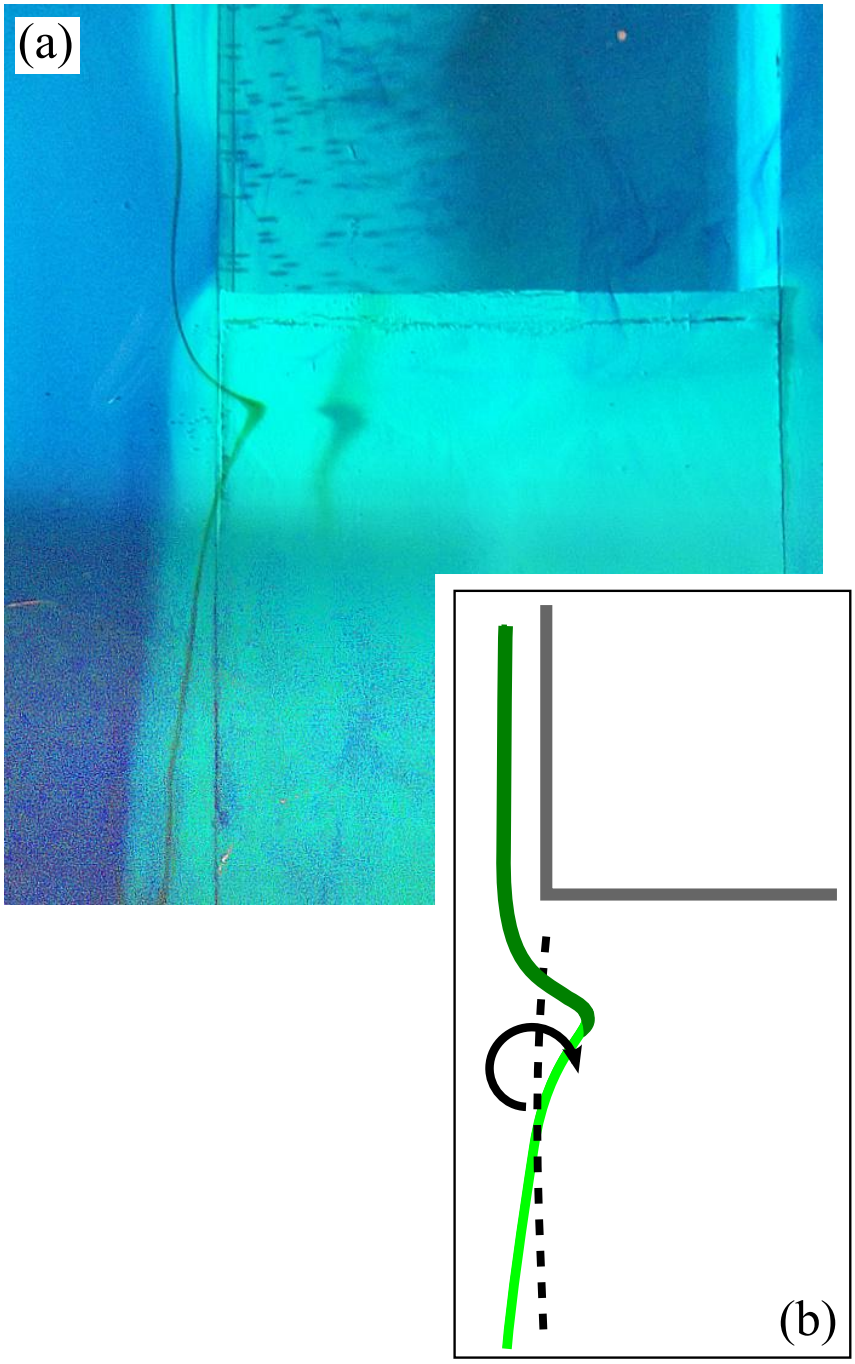

Figure 6.34: Dye visualisation showing rear corner vortex present about rectangular cavity with $L/D = 3.33$ at $Re_D = 2,700$. Flow is from from top to bottom. The blue dye is released from the upstream spanwise dye slot in the flat plate. The green streakline is released from a dye probe at the height $y/D = -0.08$ (above the flat plate) and $z/D = -1.2$. The light source is located to the left of the image, and above the flat plate: this explains the shadow produced by the green dye streak.

6.5 Chevron-shaped cavities

The chevron cavity configuration consists of a chevron-shaped front wall with a double-swept rear wall. This creates a cavity with the same length-to-depth ratio all the way across, but with a sweep of 45° applied to each half. A schematic is shown in figure 6.35.

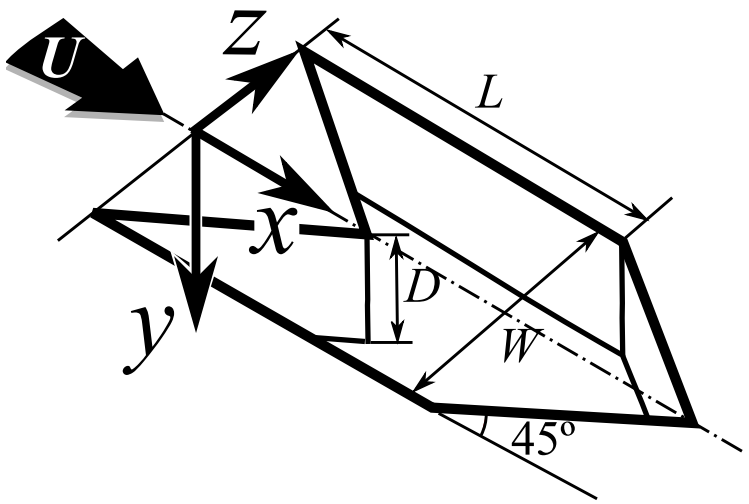

Figure 6.35: Schematic diagram of chevron cavity configuration, with flow from top-left to bottom-right. L represents the effective length of the cavity such that L/D is the effective length-to-depth ratio.

Flow over this chevron-shaped cavity configuration was found, unexpectedly, to produce an asymmetric flow pattern. Figure 6.36 shows an example of this asymmetric pattern. Hence this flow pattern, and the proposed explanation – twisting of the shear layer – is discussed in detail here.

This pattern was found to exist across a range of Reynolds numbers, and with increasing L/D was found to come into existence from a symmetric pattern before losing the asymmetry as L/D was increased further. Depth-based Reynolds numbers between 8,000 and 14,000 were tested (corresponding to the range of velocities where hydrogen bubble visualisation was effective), with no significant effect of Reynolds number found in this range. The most pronounced asymmetric behaviour was identified within an effective L/D range of 2 to 3.84. It is believed the pattern can be attributed to a net in-flow of fluid on one-side of the cavity, balanced by a net out-flow of fluid on the other.

The asymmetry would occasionally have an opposite direction of preference which suggests that it cannot be solely explained by some bias in the water tunnel or experimental model (i.e., it appears the flow could be considered 'bistable'). Figure 6.36 shows one direction of preference, while figure 6.37 shows the other. Unfortunately the changeover itself was not observed; occasionally the flow pattern changed direction of preference upon stopping and restarting the water tunnel flow.

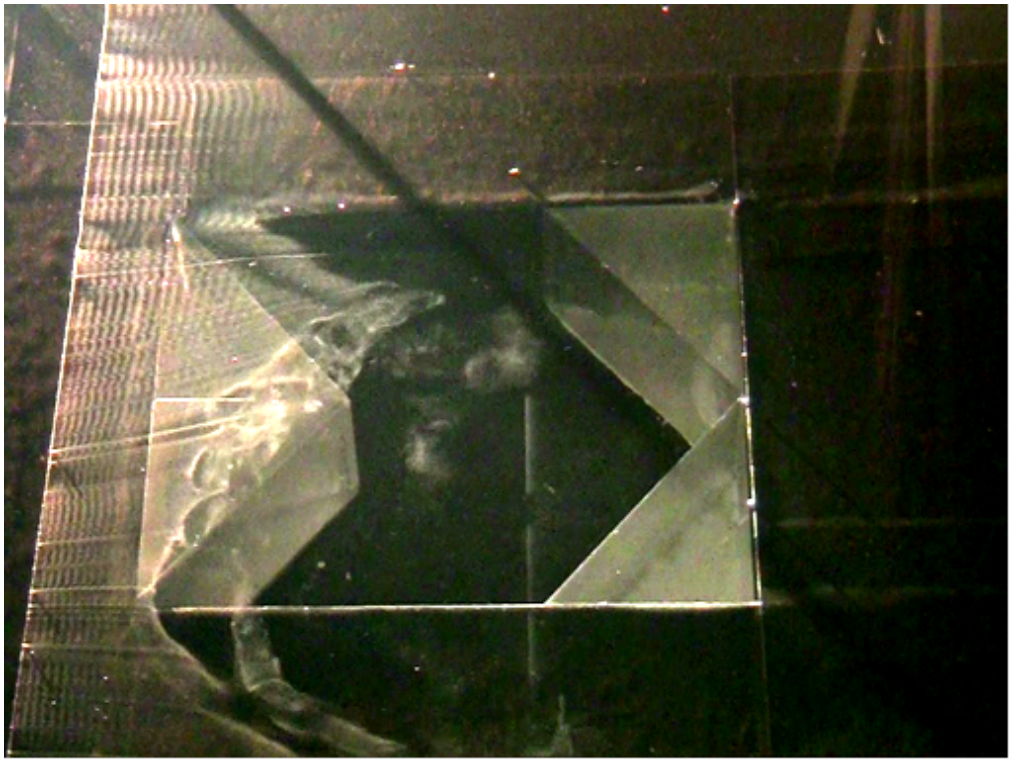

Figure 6.36: Flow pattern produced by chevron-cavity configuration at $U = 111$ mm/s and $Re_D = 8,250$. Effective $L/D = 2$. Flow from left to right.

With regards to the period of the asymmetry, in the present experiment it could not be determined. With regards to the period of a different asymmetry over a shallow, narrow, *rectangular* cavity, Crook, Lau, and Kelso (2013) state "this process, which may be periodic or random, is postulated to occur on time scales which are much larger than the sampling times of the current experiment..." The sampling times of the experiment were of the order of minutes for each imaging region (Crook, 2011, p. 72).

The proposed explanation in the present case is that flow is entering the cavity on one side which is balanced by an outwards flow on the other side. Around the out-flow side of the cavity, there is a standing vortex and other vortices owing to the wake. Conversely on the other side where the fluid preferentially flows into the cavity, the flow is very smooth. Comparing figure 6.38(a) to figure 6.38(b), it can be seen that the flow pattern on the in-flow side of the cavity is dramatically different to that of the out-flow side. On the in-flow side of the cavity, smooth streaklines are observed, which are deflected downwards into the cavity slightly. For an equivalent location of the vertical bubble wire on the out-flow side of the cavity, the streaklines are clearly deflected upwards with the presence of multiple vortices both about the shear layer and over the side plate next to the cavity.

In figure 6.39, the flow upwards from the 'out-flow' side of the cavity can

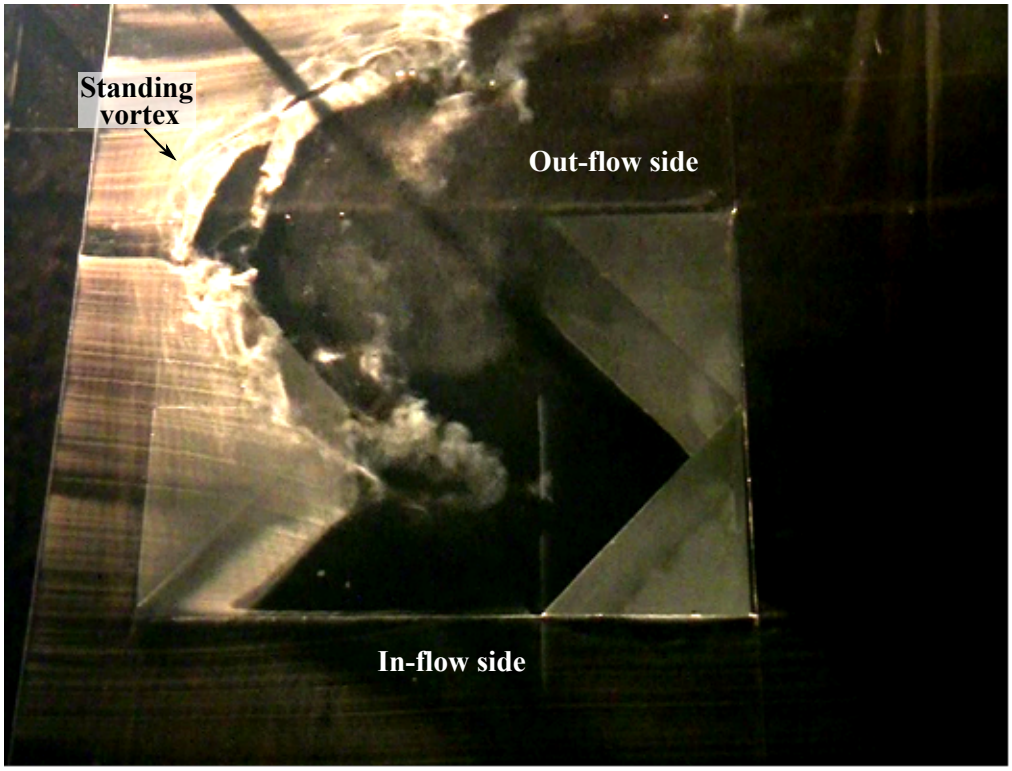

Figure 6.37: The other flow pattern produced by the identical chevron-cavity configuration at $U = 111$ mm/s and $Re_D = 8,250$. Effective $L/D = 2$. Flow from left to right.

be seen. There are multiple vortices clearly visible in the shear layer, which convect downstream with the flow. The spanwise structure of these vortices can be more clearly seen in figures 6.36 and 6.37. Interestingly, these vortices extend beyond the side edge of the cavity, and are also present above the flat plate at the side of the cavity. Around the front of the shed vortices, a standing vortex can be seen. This is most evident in figures 6.36 & 6.37. This vortex is mostly located over the flat plate and above the chevron front wall insert, rather than being located over the cavity itself. From the available visualisations, the sign of the standing vortex is difficult to determine.

By putting these observations together, a sketch of the vortical pattern can be formed. Figure 6.40 shows sketches of the flow patterns about the chevron-shaped cavity. Part (a) shows a proposed vortex line representation. Around the front of the region of out-flow there is a standing vortex. Vortex lines appear to shed from here and form the shear layer vortices. In plan (a), the out-flow side of the cavity is the lower half of the sketch. Part (b) shows streaklines which indicate the shear layer vortices on the out-flow side of the cavity. Part (c) shows streaklines which indicate the smooth movement of fluid into the cavity on the in-flow side of the cavity.

To investigate the effect of L/D on the asymmetry, the (effective) length-to-depth ratio was varied in the range 1 through 5. The depth based Reynolds number was fixed at 10,700.

The asymmetric flow pattern was found to occur over a specific range of length-to-depth ratio ($L/D \sim 2-3.84$), as shown in figure 6.41. These images were chosen to represent the typical behaviour observed for each L/D case. For $L/D = 1$ the pattern was observed to be symmetrical, as illustrated in figure 6.41(a). When the length-to-depth ratio is increased to 2, a strongly asymmetric pattern develops which can be seen in figure 6.41(b). In that instance, the out-flow side appears on the far-side (top) of the picture. When L/D is increased further to $L/D = 2.84$, the asymmetric flow pattern is still found as shown in figure 6.41(c). In this instance the asymmetry has switched to the other side, although this is not related to the L/D ratio itself. As the L/D is increased further to 3.84 [figure 6.41(d)], an asymmetric pattern is still found. However, when L/D is increased to 5 [figure 6.41(e)], no longer is a strongly asymmetric pattern found. As the oblique camera angle in figure 6.41(e) makes the flow pattern difficult to observe, a clearer overhead view of chevron-shaped cavity with $L/D = 5$ is given in figure 6.42. This figure shows that the strongly asymmetric pattern seen in figure 6.36 is no longer evident. Instead, while the pattern is still slightly asymmetric, it is quite a different pattern to that observed in the range $L/D = 2$–3.84. Here, the asymmetry is weakened and vortices are shed across the span of the cavity – i.e., the suppression of vortex shedding due to in-flow on one side of the cavity is no longer found at this L/D.

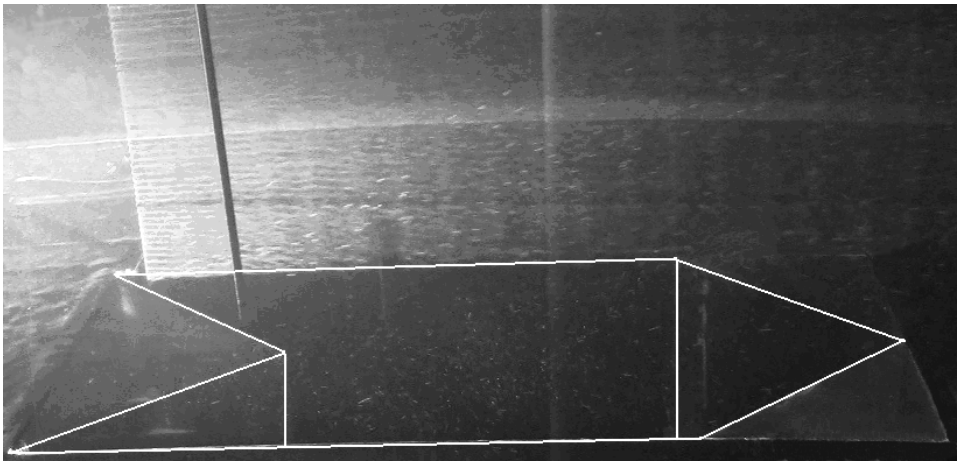

(a) In-flow side. Wire location $z/D = 0.9$ and $x/D = 0.1$.

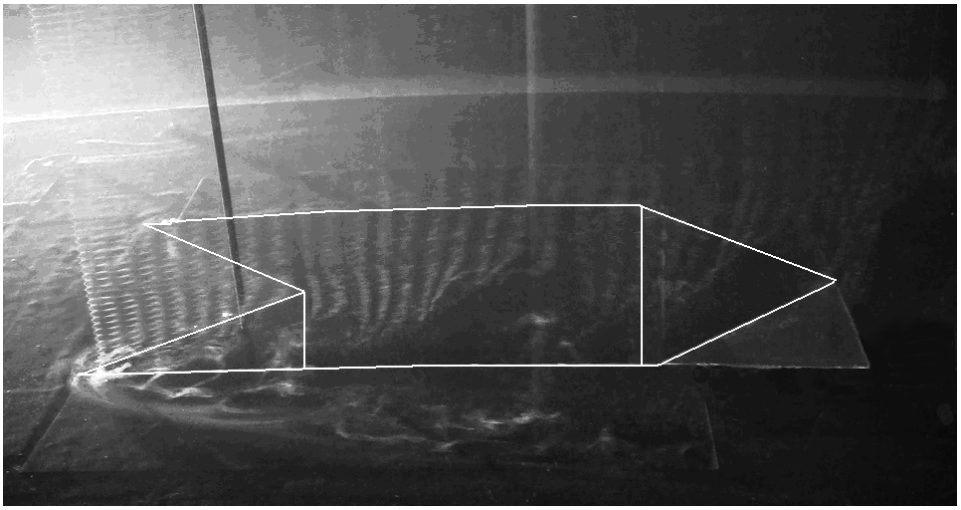

(b) Out-flow side. Wire location z/D =-0.9 and $x/D = 0.1$.

Figure 6.38: Hydrogen bubble patterns produced by vertical wire within chevron-shaped cavity at $L/D = 2.84$ and $Re_D = 10,700$. The white outlines represent the top, and internal, edges of the cavity.

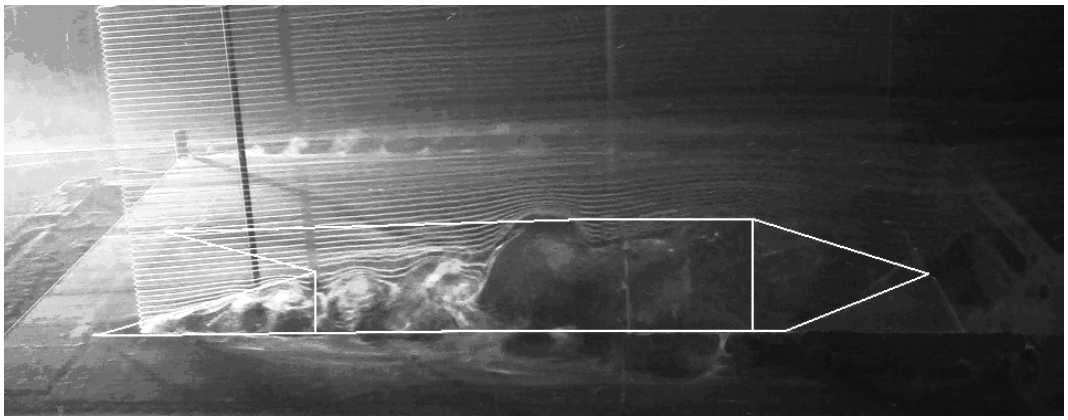

Figure 6.39: Flow pattern produced by both vertical and horizontal bubble wires at effective $L/D = 2.84$ and $Re_D = 10,700$. The vertical wire is located at z/D =-0.9 and $x/D = 0.1$. The white outline shows the edges of the cavity.

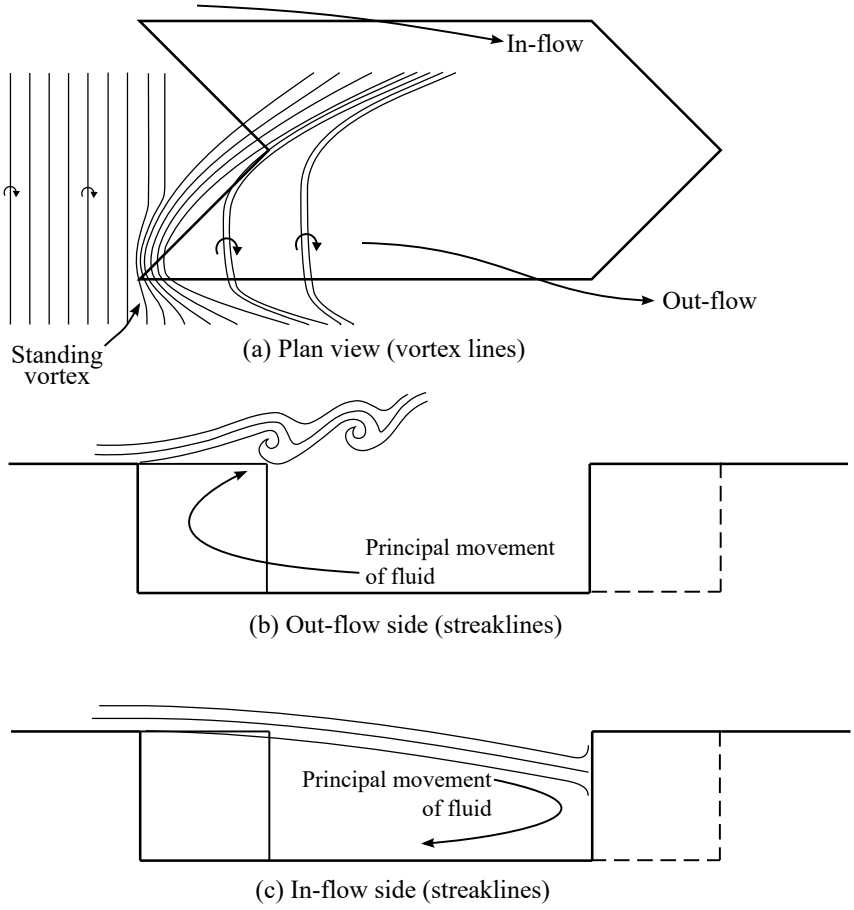

Figure 6.40: Sketch of flow patterns about the chevron-shaped cavity. Flow from left to right.

(a) $L/D = 1$

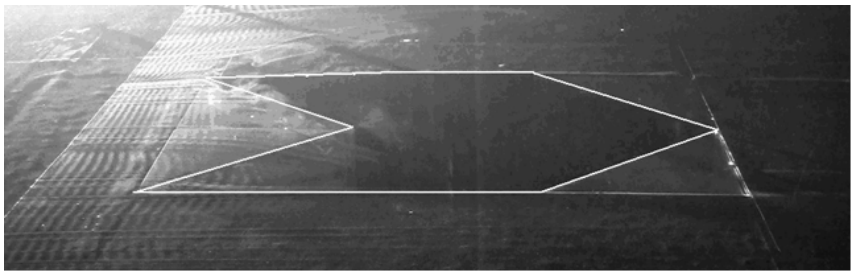

(b) $L/D = 2$

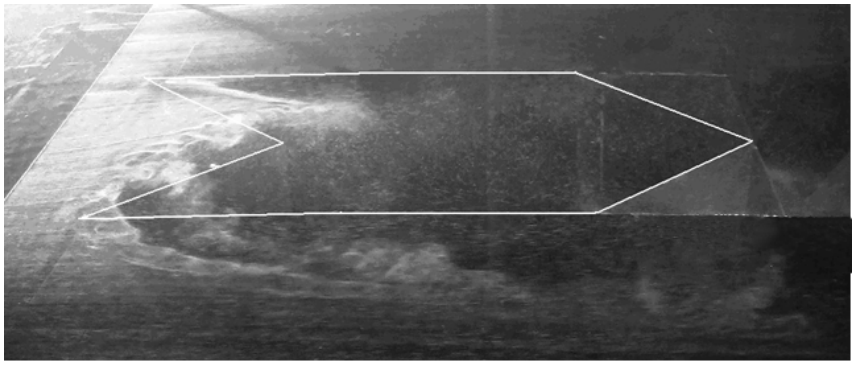

(c) $L/D = 2.84$

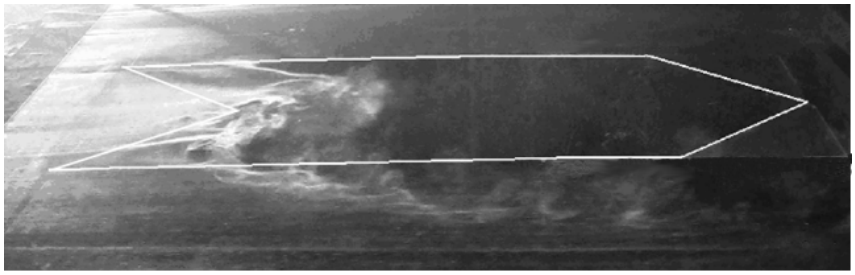

(d) $L/D = 3.84$

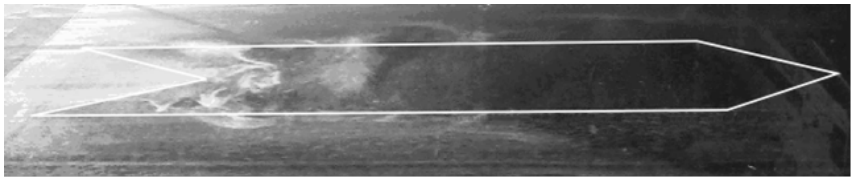

(e) $L/D = 5$

Figure 6.41: Hydrogen bubble flow pattern produced by the chevron-shaped-cavity for different effective L/D ratios. Flow from left to right. Depth-based Reynolds number of 10,700. The white outline represents the top edge of the cavity.

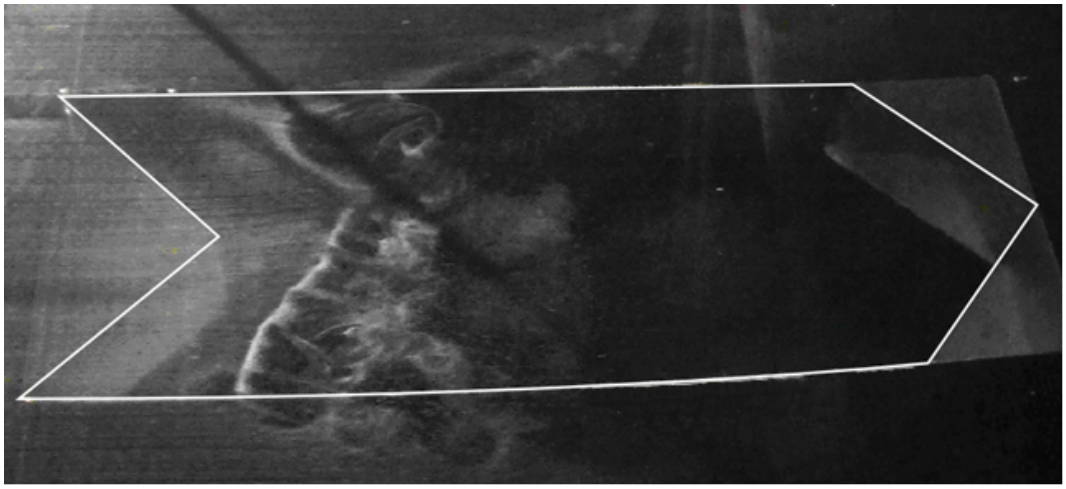

Figure 6.42: Clearer overhead view of hydrogen bubble visualisation of shear layer over chevron-shaped cavity at depth-based Reynolds number of 10,700. Effective length-to-depth ratio, $L/D = 5$. The white outline represents the top edge of the cavity. Flow from left to right.

PIV flow measurements were taken in a plane parallel to the flat plate, over the chevron-shaped cavity. For $z/D < 0$, there is a region where the flow diverges from parallel, downstream of the leading edge of the cavity. The measurement plane is 0.35 cavity depths above the flat plate surface, hence the asymmetric flow structures are found to have a large region of influence beyond the edges of the cavity.

Figure 6.43 shows the streamlines calculated from time-average velocity vectors over the chevron-shaped cavity for $Re_D = 10,700$ ($U = 144$ mm/s) at $y/D \approx -0.35$ (above the flat plate), for a cavity of effective length-to-depth ratio of $L/D = 2$. It can be observed that the flow upstream of the cavity is quite uniform in direction. In the negative Z region of the cavity, the flow pattern indicates the emergence of fluid out-of-the-page from within the cavity. The divergence of the free stream fluid around this feature can be seen clearly.

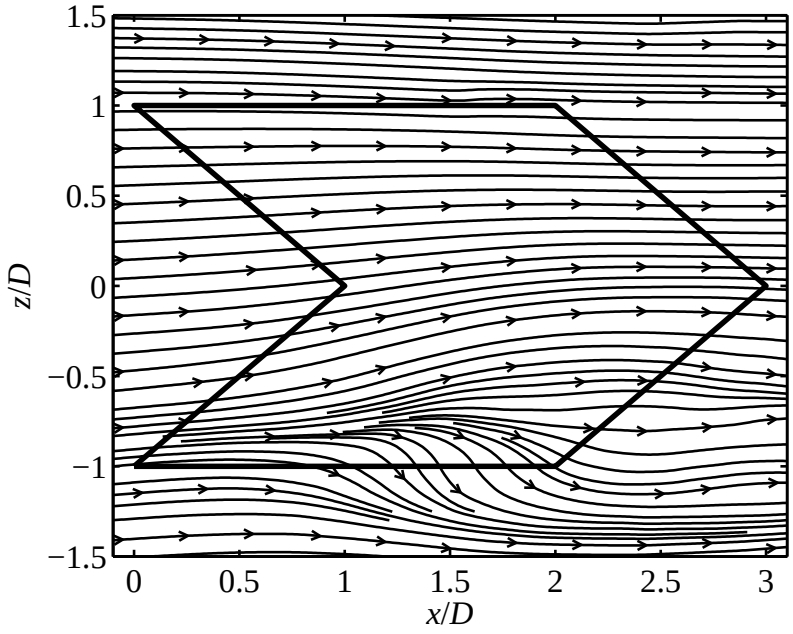

Figure 6.43: Streamlines calculated from time-average velocity vectors over the chevron-shaped cavity with effective $L/D = 2$. The depth-based Reynolds number was 10,700 ($U = 144$ mm/s). Flow from left to right. This is a (top-down) plan view. Measurement at a height of $y/D \approx -0.35$ (i.e., above the flat plate).

Figure 6.44 shows the time-average velocity magnitude over the chevron-shaped cavity. There is a large low velocity region on only one side of the cavity corresponding to the outflow region where vortex shedding occurs.

Figure 6.45 shows the time-average root-mean-square fluctuation velocity. There is a region of high-fluctuation located on the outflow side of the cavity. This is consistent with a region of vortex shedding being located here, as seen

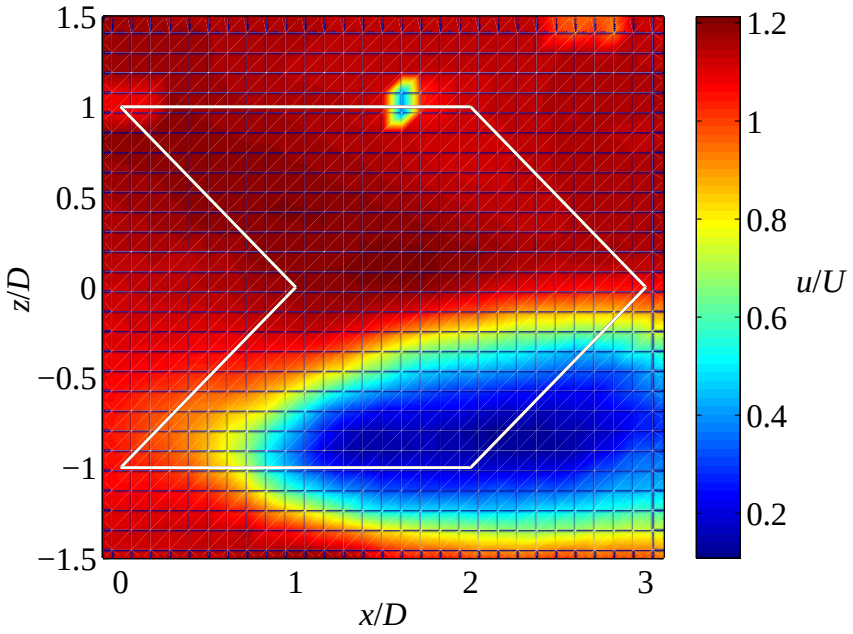

Figure 6.44: Mean velocity magnitude calculated from time-average velocity vectors over the chevron-shaped cavity with effective $L/D = 2$. The depth-based Reynolds number was 10,700 ($U = 144$ mm/s). Flow from left to right. This is a top-down view. The measurement height was $y/D \approx -0.35$ (i.e., above the flat plate). Erroneous velocity values are found near $z/D \sim 1$ and $x/D \sim 2$, which is due to reflection of light from the flat plate, and also a reflection from the edge of the cavity.

in the hydrogen bubble visualisation.

Figure 6.46 shows the time-average vorticity field about the y-axis (out-of-page). From the bottom to the top of the figure, a region of counter-clockwise vorticity is found between z/D=-1.5 and -0.7. Conversely a region of clockwise vorticity is found between z/D=-0.7 and 0. This is consistent with the existence of a wake-like structure that forms due to the interaction between the freestream and the slow-moving fluid on the outflow side of the cavity.

Streamline patterns from individual PIV image pairs are presented in figure 6.47. The figure shows four sequential image pairs. Close examination of the figure shows the convection of low-velocity regions representing vortical structures. These are the non-stationary vortical structures which are associated with the wake-like structure.

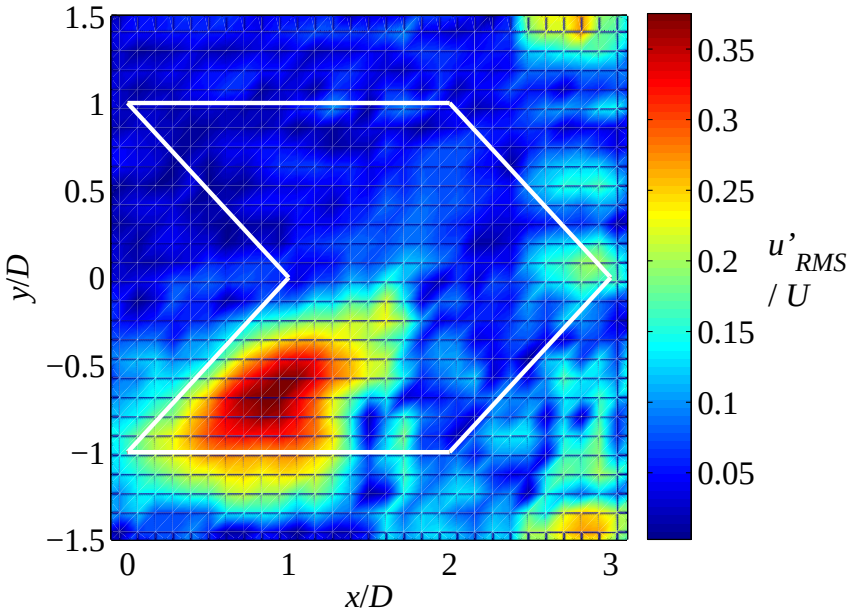

Figure 6.45: Time-average R.M.S. fluctuation velocity over the chevron-shaped cavity with effective $L/D = 2$. The depth-based Reynolds number was 10,700 ($U = 144$ mm/s). Flow from left to right. This is a top-down view. The measurement height was $y/D \approx -0.35$ (i.e., above the flat plate).

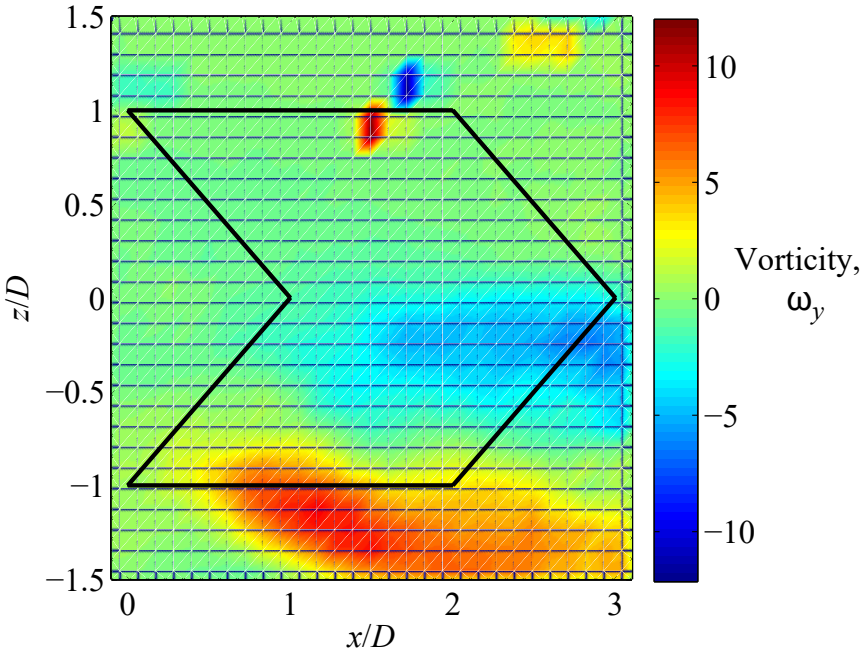

Figure 6.46: Out-of-plane time-average vorticity, ω_y, over the chevron-shaped cavity with effective $L/D = 2$. The depth-based Reynolds number was 10,700 ($U = 144$ mm/s). Flow from left to right. This is a top-down view. The measurement height was $y/D \approx -0.35$ (i.e., above the flat plate). Erroneous vorticity is found near the top of the figure, $z/D > 0.5$, which is due to reflection of light from the flat plate, and also a reflection from the edge of the cavity.

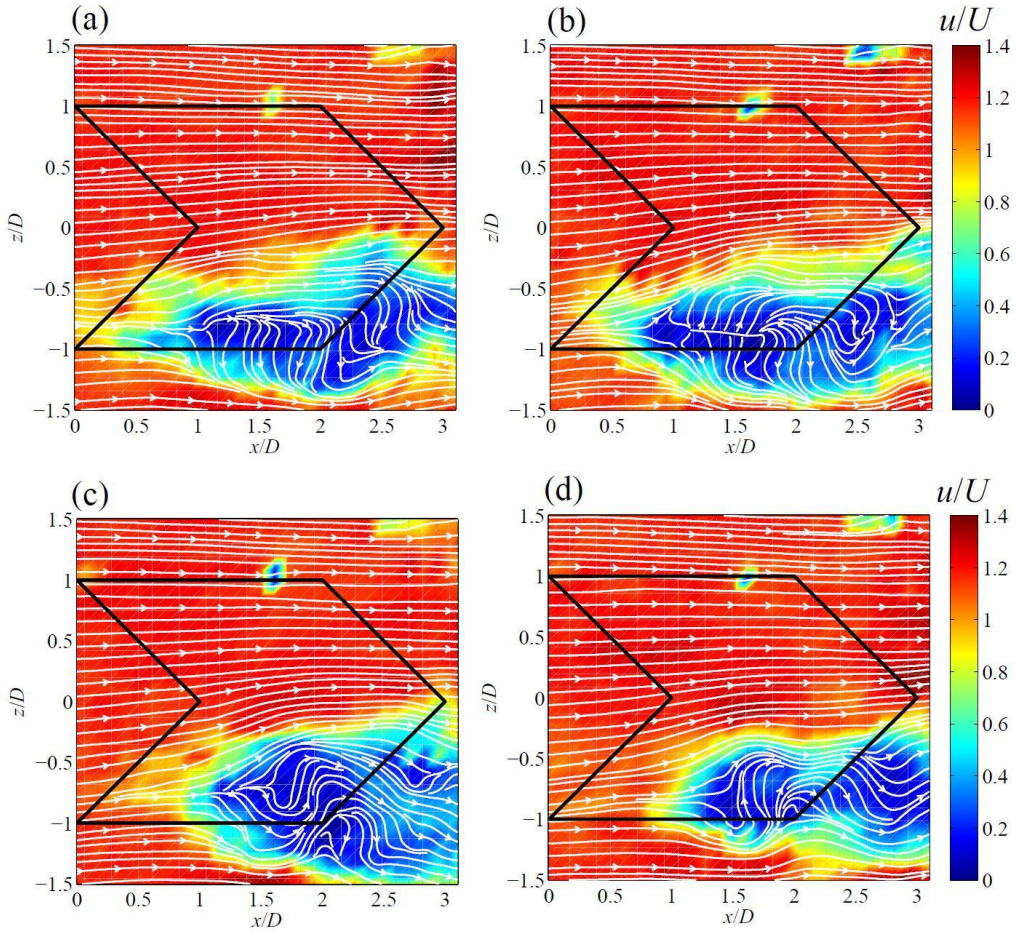

Figure 6.47: Streamlines and velocity magnitude calculated from individual image pairs for flow over the chevron-shaped cavity with effective $L/D = 2$. (a) $t = 0$ s, (b) $t = 0.4$ s, (c) $t = 0.6$ s, and (d) $t = 0.8$ s. The depth-based Reynolds number was 10,700 ($U = 144$ mm/s). Flow from left to right. This is a top-down view. The height of the sheet was $y/D = -0.35$.

6.6 Summary

The structure of the mixing layer within and around shallow, narrow cavities has been investigated. With increasing L/D, increased breakdown of the shear layer vortices was found. Significant end effects due to the finite width of the cavity were found. The 'spanwise roller' shear layer vortices were found to have significant curvature. These vortices were found to form a half-ring, which by self-induction would tend to convect higher out of the cavity.

At the sides of the narrow cavity a periodic structure has been identified, which has not been previously reported in the literature. This structure forms because of the spanwise growth of the mixing layer. The pattern has been explained in terms of an interaction of the 'legs' of the shear layer vortices. Also, a surface flow pattern has been proposed.

Finally, a modified chevron-like cavity geometry was found to create an asymmetric flow structure within the investigated Reynolds number and L/D range. This is attributed to a twisting mode of the shear layer, causing inflow on one (lateral) side of the cavity and balanced by outflow on the other side.

Chapter 7

Conclusion

7.1 Summary of main findings

This study has investigated the noise produced by, and flow about, two- and three-dimensional rectangular and modified cavities in the low-to-moderate Reynolds number range of the order of 10^3 to 10^4 (based on either the cavity depth or the cavity length). Experiments were conducted in anechoic wind tunnel and water tunnel facilities.

An 'airfoil with cavity' model was designed to investigate the noise produced by rectangular and modified two-dimensional cavity flows. The model consisted of a super-elliptic nose profile, a flat plate section with cavity cut-outs, and a linearly tapered trailing edge section. The cavity depth, D, was fixed while the cavity length, L, was varied giving length-to-depth ratios of $L/D = 1.17$, 2.33, 3.5 and 4.67. The Reynolds numbers based on cavity depth were in the range Re_D = 3,800–15,300 while the Reynolds numbers based on the estimated momentum thicknesses were in the range Re_θ = 100–190.

Initially, rectangular cavities were investigated. It was found that the number of cavity oscillation modes increased with increasing L/D while the intensity of each mode tends to decrease. This may be explained by a reduction in the coherence of structures along the cavity as L/D increases (for fixed D and Re_D). The mean convection velocity ratio ($\kappa = U_c/U$) of shear layer vortices for the non-dimensional cavity length range of $L/\delta_0 = 5$ to 48 were estimated from experimental data, extending the data available compared to the literature. The cavity oscillation mode numbers that are expected in the range $L/\delta_0\sqrt{\mathrm{Re}_{\delta_0}} = 350$ to 1800 were plotted.

Later, two-dimensional modified geometries were investigated to examine the effects of sloping the front or rear cavity walls at various L/D ratios. It was found that:

- the sloped rear wall is responsible for a reduced broadband noise component of cavity noise – attributed to reduced impingement of shear layer turbulence on the cavity trailing edge,

- sloping the front wall produces a reduction in tonal levels but no reduction in broadband levels – attributed to a delayed separation that stabilises the shear layer, and

- reducing the effective cavity length, i.e., the length of the cavity exposed to the boundary layer flow over the flat plate, to below the minimum required for the onset of oscillations, will eliminate the cavity tones completely, even if the volume of the cavity is maintained constant.

The production of airfoil tonal noise was unexpectedly found from the 'airfoil with cavity' profile. Thus, an investigation was conducted to determine the mechanism responsible, and the role of the cavity within the mechanism. The general characteristics of the noise were found to be consistent with those of airfoil tonal noise as documented in the literature. For instance, the tones were found to scale with velocity in the manner expected for airfoil tonal noise. This indicated that these tones were indeed produced by an airfoil tonal noise mechanism of some form.

Velocity measurements were taken in the airfoil boundary layer using a hot-wire velocity probe, in order to investigate disturbances in the flow around the airfoil that could contribute to airfoil noise production. The existence of disturbances in the boundary layer at the airfoil tonal frequencies was confirmed. Since these disturbances were only found in the boundary layer downstream of the cavity, this supported the existence of a feedback loop between the airfoil trailing edge and the cavity trailing edge.

Subsequently, the effect of acoustic forcing was investigated and it was found that the airfoil's boundary layer responded most strongly at the airfoil tonal frequencies, rather than other intermediate frequencies within the range of instability. This is due to reinforcement of the naturally occurring feedback loop – i.e., the feedback loop was not 'saturated' before the application of additional acoustic forcing. Additional feedback strengthens the boundary layer disturbances, then as these disturbances pass the airfoil trailing edge, stronger noise is radiated. Finally this stronger self-noise provides for further enhanced feedback (in addition to the 'initial' external forcing) and so on.

To investigate the attachment of the flow, surface flow visualisation was conducted which found the existence of a region of separated flow along the tapered tail section of the airfoil. A stability analysis of the flow over the smooth airfoil (that is, without the cavity), using a code supplied by Dr. Michael J. Kingan (Kingan and Pearse 2009) was conducted. This analysis showed that high levels of amplification were predicted over the region of separation, consistent with the findings of the boundary layer velocity measurements.

In the literature, amplification of boundary layer disturbances over a trailing edge separation bubble has been proposed as the main mechanism for airfoil tonal noise by Nash *et al.* (1999) (with 'some' feedback about the bubble, although not so as to produce multiple discrete tones). Here, although the trailing edge separation bubble does exist and play a role in the amplification

of the disturbances, *in this case* it exists in the context of an overall mechanism where an aeroacoustic feedback loop, of a form similar to that proposed by Arbey & Bataille (1983), is also important.

An overall proposed airfoil tonal noise mechanism for the 'airfoil with cavity' is presented in figure 7.1. The boundary layer upstream of the cavity is essentially stable, since a favourable pressure gradient exists here. Downstream, the shear layer over the cavity itself is unstable at backward-facing-step vortex shedding frequencies, but stable to the lower frequencies of the airfoil tonal noise. The most unstable point of the boundary layer is located near the cavity trailing edge and downstream of the cavity, where inflectional boundary layer profiles are present. Here, the boundary layer is receptive to the aeroacoustic feedback provided by the airfoil tonal noise. Approaching the trailing edge of the airfoil, a region of separated flow is present, over which the boundary layer instabilities are highly amplified. Finally, the airfoil tonal noise is generated as these instabilities pass the trailing edge, thereby closing the feedback loop. These vortices then convect downstream of the airfoil through the wake.

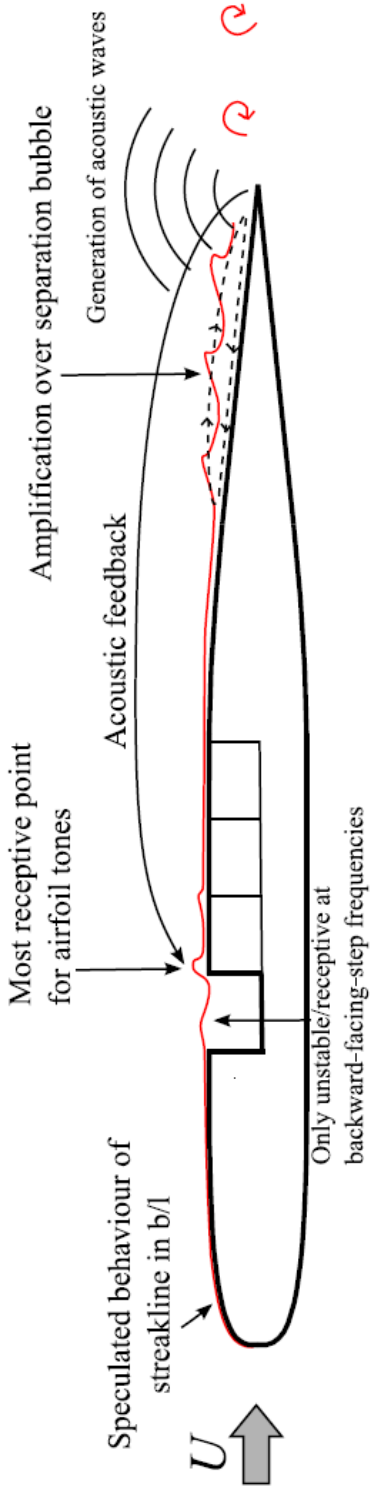

Figure 7.1: Sketch of the proposed overall tonal noise mechanism for the 'airfoil with cavity' model. Note that 'speculated behaviour of streakline in b/l' refers to the behaviour of a streakline released into the boundary layer very near to the stagnation point.

Flows over three-dimensional ('narrow') cavities were investigated in the anechoic wind tunnel using a three-dimensional cavity model, as well as in a recirculating water tunnel using a three-dimensional cavity model previously designed and constructed by Crook (2011). The experimental techniques used were flow visualisation, noise measurement, and velocity measurement by hot-wire probe in air and particle image velocimetry in water.

The broadband noise produced by flow over a three-dimensional cavity with a turbulent upstream boundary layer was measured in the anechoic wind tunnel for $Re_D \sim 10^5$. Broad peaks in the noise spectra were invariant with velocity and were attributed to standing wave modes of the overall flat plate model containing the three-dimensional cavity. Sloping the rear wall of the cavity was found to produce a significant reduction in sound pressure levels, compared to the rectangular cavity.

Results from flow visualisation of the three-dimensional cavity shear layer in water were compared to results from the two-dimensional 'airfoil with cavity' model in air, which had similar flow parameters. Both of these cavity flows had laminar upstream boundary layers and $Re_D \sim 10^3 - 10^4$. Cavity noise spectra and shear layer velocity spectra were highly correlated with shear layer roll-up mode. With increasing L/D (with other parameters fixed), increased breakdown of the shear layer vortices was found.

The shear layer vortical roll-up process was also strongly affected by cavity shape. Sloping the front and rear walls of the cavity, produced a significant change in in the cavity oscillation modes detected. Where the rectangular cavity oscillated in the third cavity oscillation mode, the sloped front and rear wall cavity oscillated in both the third and fourth cavity oscillation modes – even though L/δ_0 was below the value where combined third and fourth mode oscillations would be expected for a rectangular cavity.

The structure of the cavity mixing layer within and around shallow, narrow cavities with $W/D \approx 2$ was investigated. In narrow cavities at low Reynolds number, 'spanwise' shear layer vortices were in fact found to have significant curvature. These vortices were found to form a half-ring, which by self-induction would tend to convect higher out of the cavity. As the vortex lines bunch due to the shear layer instability, streamwise-orientated legs form, following behind the half-rings. The initial deformation of the vortex lines causes each leg to then descend laterally down into the cavity due to the vortex induced velocity with image vortices in the cavity sides. This behaviour was consistent with the identification of lateral in-flow in the upstream part of the cavity by Crook (2011).

Significant end effects due to the finite width of the cavity were found. At the sides of the narrow cavity a periodic structure was identified, which has not been previously reported in the literature. This structure forms because of the spanwise growth of the mixing layer. Specifically, as sequential streamwise-orientated legs interact, a tornado-like feature is formed from this vorticity, which eventually becomes anchored to the flat plate at the side of the cavity,

that is, just beyond the finite span of the cavity. Figure 7.2 shows a cut-away sketch of the main features observed in the instantaneous dye visualisation of the narrow rectangular cavity.

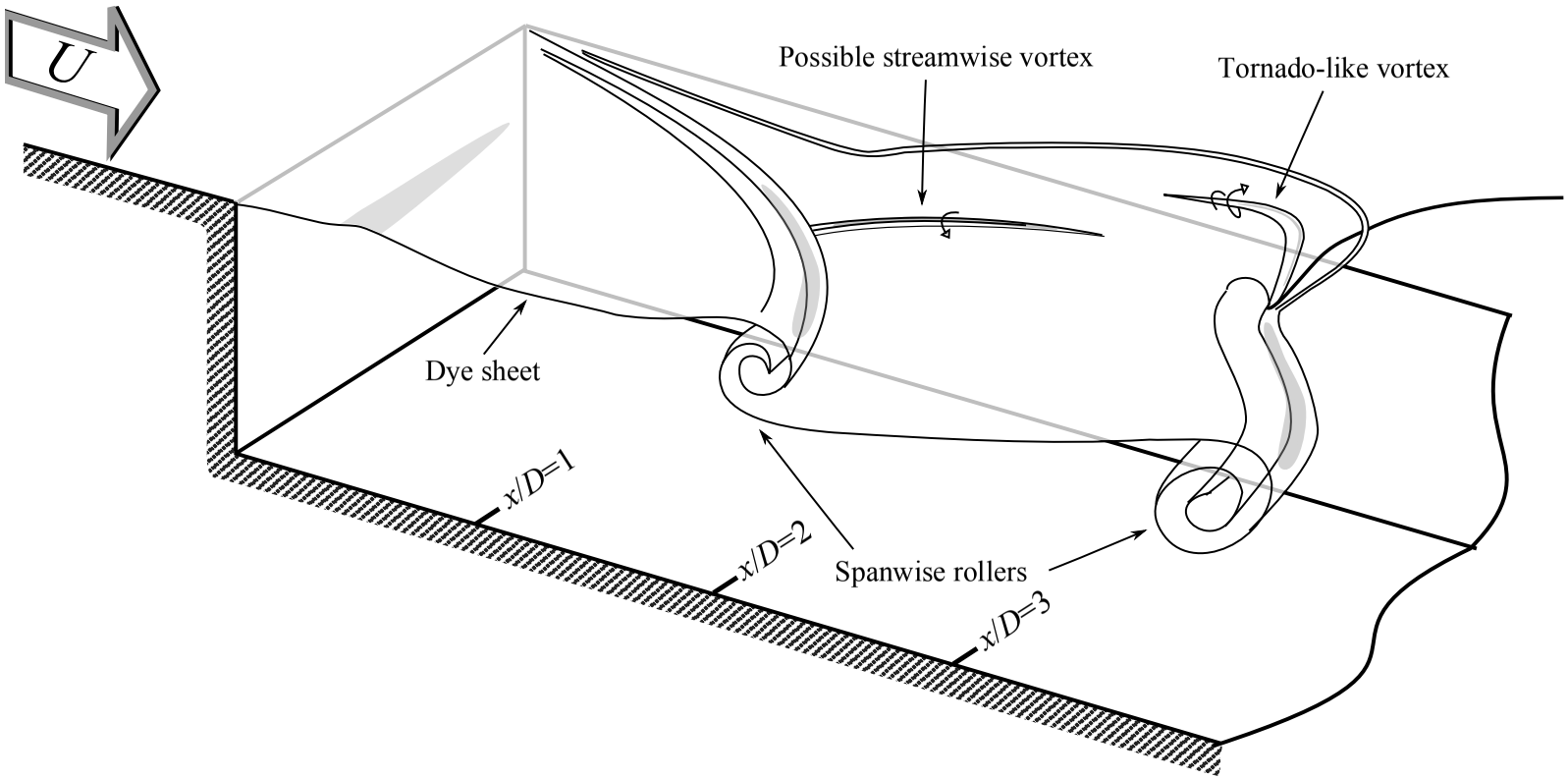

Figure 7.2: Cut-away sketch of instantaneous dye visualisation pattern when dye was released from a slot in the plate upstream of the cavity at $Re_D = 2700$. The narrow, rectangular, three-dimensional cavity has $L/D = 6$ and $W/D = 2$. The sketch is cut at the vertical centreline of the cavity ($z = 0$), as the observed pattern was symmetrical about this plane.

A shallow, narrow cavity with $L/D = 6$ and $W/D = 2.1$ was tested in air, with a transitional upstream boundary layer and $Re_D \sim 10^3$. Using hot-wire velocity measurement, longitudinal rear corner vortices were found, which were also observed in flow visualisation in water.

Finally, a modified chevron-like cavity geometry was unexpectedly found to create an asymmetric flow structure within the tested Reynolds number range ($Re_D = 8{,}250 - 10{,}700$) and L/D range ($L/D = 2 - 3.84$). The chevron-shaped cavity is formed by a cavity with the same length-to-depth ratio all the way across, but with a sweep of 45° applied to each half as per figure 7.3. The direction of preference of the asymmetric flow pattern appeared to be random, as the orientation of the pattern would sometimes reverse upon stopping and restarting the water tunnel flow. A wake-like structure forms about one lateral half of the cavity. This structure contains a standing vortex upstream, and a series of shed vortices that convect downstream and upwards from the surface of the flat plate.

The unexpected flow structure is attributed to a twisting mode of the shear layer, similar to that previously identified by Crook (2011) for a rectangular cavity, such that fluid is entering the cavity on one side which is balanced by an outwards flow on the other side. The flow pattern on the in-flow side of the cavity is dramatically different to that of the out-flow side. Using hydrogen bubble visualisation, smooth streaklines were observed on the in-flow side of the cavity, which were deflected downwards into the cavity slightly. For an equivalent but opposite spanwise location of the vertical bubble wire on the out-flow side of the cavity, it was observed that the streaklines were clearly deflected upwards with the presence of multiple vortices both about the shear layer and over the flat plate next to the cavity. The influx of high momentum fluid on the 'in-flow' side of the cavity appears to suppress the shedding of vortices on that side of the cavity. A representation is shown in figure 7.3.

7.2 Concluding remarks

This thesis described an experimental investigation into low Reynolds number flows over cavities, of both rectangular and modified geometry. Cavity flow noise (including the cavity aeroacoustic feedback loop), and flow structures, were investigated using two- and three-dimensional cavities in an anechoic wind tunnel. Flow structures were investigated further using a three-dimensional cavity model in a water tunnel. Previously undocumented flow structures, which exist at the sides of narrow cavities of finite span, were described. A chevron-shaped cavity was found to produce an asymmetric flow pattern due to a shear layer twisting mode. Furthermore, the two-dimensional cavity model (taking the form of an airfoil with a two-dimensional cavity cut-out) was found to produce airfoil tonal noise, and the role of the cavity in the production of this noise was determined to be due to an aeroacoustic feedback loop between the airfoil trailing edge and the cavity trailing edge.

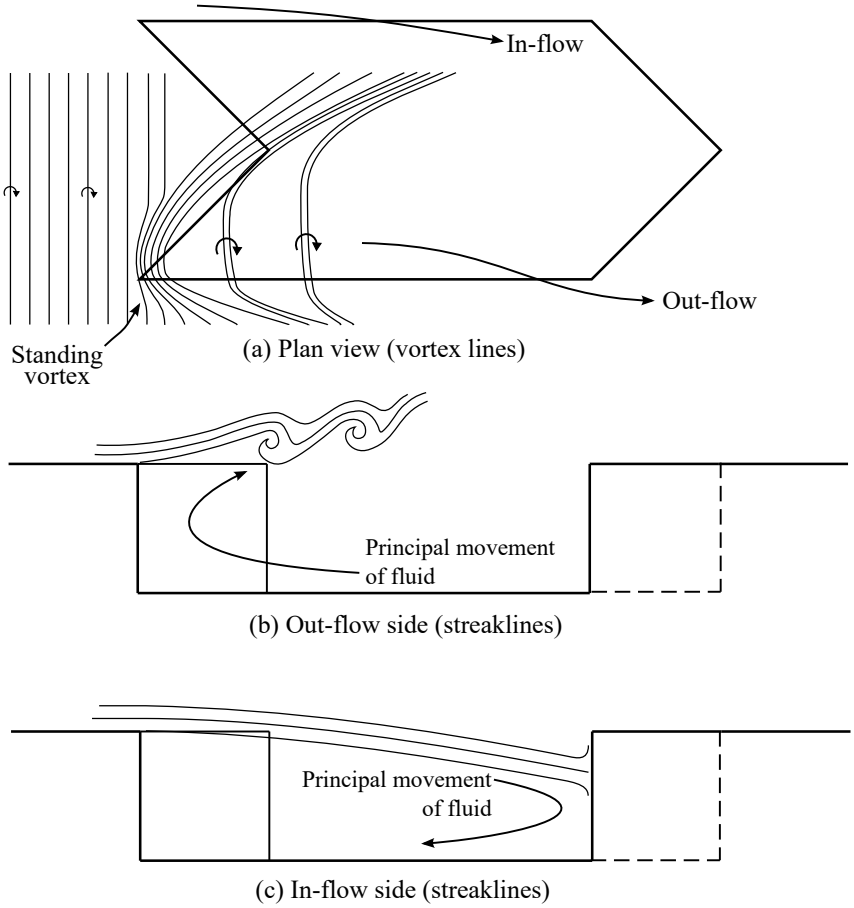

Figure 7.3: Sketch of flow patterns about the chevron-shaped cavity. Flow from left to right.

Suggestions for further research include:

- An investigation of the effect of a cavity cut-out on the tonal noise produced by NACA-series airfoils.

- For an NACA-series airfoil at zero angle of attack, the proper placement of two cavity cutouts at *different* chordwise positions on the top and bottom surfaces might allow for destructive interference of some or all of the airfoil tones. Possibly, this might enable some reduction of the peak, or overall, sound pressure levels produced by the airfoil. For instance, the cavity on the lower surface could be positioned out-of-phase by half a convective wavelength, in chordwise-position, compared to the cavity

on the top surface. [1]

- The 'airfoil with cavity' profile could be simulated using computational fluid dynamics and computational aeroacoustics techniques, using the experimental results for the purposes of validation. This would enable a more detailed quantification and analysis of the this phenomenon than that which is practical using experimental techiques.

- Further characterisation of the flow structures formed at the sides of the cavity due to the finite width of three-dimensional cavities – especially those formed about narrow cavities, where $L/W < 1$ – are warranted.

- The shear layer twisting phenomenon, as found by Crook (2011) and especially as seen in the chevron-shaped cavity in this study, warrants further investigation. The parametrical range where the twisting mode occurs (e.g., in terms of non-dimensional boundary layer thicknesses and cavity aspect ratios), and also the relative 'strength' of the twisting mode over this range of parameters remain to be determined both for rectangular, chevron-shaped, and possibly other cavity geometries.

[1] The frequency range of instabilities ('broadband hump') of the boundary layer may be reasonably similar for both surfaces. While a cavity positioned half-a-wavelength out of phase on the lower surface would cause tones with a slightly different frequency spacing to be produced, the difference could be small and some destructive interference may still be possible. For example, a 5% difference in Δf may exist between the disturbances produced by the two surfaces – assuming a range of 'broadband' boundary layer instabilities peaking at 1000 Hz, a convective velocity of 10 m/s giving a convective wavelength of 10mm, and thus a distance from the cavity to the trailing edge of 0.1 m and 9.5 $\times 10^{-}2$ m respectively on either surface.

References

Ahuja, K K, and Mendoza, J, 1995, *'Effects of Cavity Dimensions, Boundary Layer and Temperature on Cavity Noise with Emphasis on Benchmark Data to Validate Computational Aeroacoustic Codes'*, Technical Report, NASA Contractor Report 4653.

Ali, M S M, Doolan, C J, and Wheatley, V, 2011, 'Low Reynolds number flow over a square cylinder with a splitter plate', *Physics of Fluids*, vol. 23 pp. 033602-1.

Ali, M S M, Doolan, C J, and Wheatley, V, 2011, 'The sound generated by a square cylinder with a splitter plate at low Reynolds number', *Journal of Sound and Vibration*, vol. 330 no. 15 pp. 3620–3635.

Arbey H, and Bataille J, 1983, 'Noise generated by airfoil profiles placed in a uniform laminar flow', *Journal of Fluid Mechanics* vol. 134 pp. 33–47.

Archibald, F S, 1975, 'The laminar boundary layer instability excitation of an acoustic resonance', *Journal of Sound and Vibration* vol. 38 no. 3 pp. 387–402.

Arcondoulis, E, Doolan, C J, Zander, A C, and Brooks, L A, 2010, 'A review of trailing edge noise generated by airfoils at low to moderate Reynolds number', *Acoustics Australia*, vol. 38 no. 3 pp. 129–33.

Arcondoulis, E, Doolan, C J, Zander, A C, Brooks, L A, and Liu, Y, 2019, 'An investigation of airfoil dual acoustic feedback mechanisms at low-to-moderate Reynolds number', *Journal of Sound and Vibration*, vol. 460 pp. 114887-1 – 114887-19.

Ashcroft, G, and Zhang, X, 2005, 'Vortical structures over rectangular cavities at low speed', *Physics of Fluids*, vol. 17 no. 1 pp. 015104–015104-8.

Bari, A, and Chambers, F W, 1993, 'Shear layer resonance over open cavities at angles to the flow direction', *AIAA Paper* no. 93–4397.

Bendat, J S, and Piersol, A G, 2010, '*Random Data: Analysis and Measure-*

ment Procedures', 4th edition, John Wiley & Sons, Inc., Hoboken, New Jersey, United States.

Bergh, H, and Berg, B, 1958, 'On the Visualisation of Laminar Boundary Layer Oscillations and the Transition to Turbulent Flow', *Journal of Applied Mathematics and Physics*, vol. IXb pp. 97–104.

Bliss, D B, and Hayden, R. E, 1976, *'Landing Gear and Cavity Noise Prediction'*, NASA Contractor Report, NASA CR-2714.

Block, P, 1976, *'Noise Response of Cavities at Varying Dimensions at Subsonic Speed'*, Technical Note, NASA TN D-8351.

Borwick, J, 1990, *'Microphones: Technology and Technique'*, Focal Press, London.

Brès, G A,and Colonius, T, 2008, 'Three-dimensional instabilities in compressible flow over open cavities', *Journal of Fluid Mechanics*, vol. 599 pp. 309–339.

Brøns, M, Thompson, M C, and Hourigan, K, 2009, 'Dye visualization near a three-dimensional stagnation point: application to the vortex breakdown bubble', *Journal of Fluid Mechanics*, vol. 62 pp. 177–194.

Brooks T F, Marcolini M A, and Pope D S, 1986, 'Airfoil Trailing Edge Flow Measurements', *AIAA Journal* vol. 24 no. 8 pp. 1245–51.

Brooks, T F, Pope, D S, and Marcolini, M A, 1989, '*Airfoil self-noise and prediction*', Technical Report, NASA Reference Publication 1218.

Cattafesta, L, Song, Q, Williams, D, Rowley, C, and Alvi, F, 2008, 'Active control of flow-induced cavity oscillations', *Progress in Aerospace Sciences*, vol. 44 no. 7–8 pp. 479–502.

Cimballa, J M, Nagib, N M, and Roshko, A, 1988, 'Large structure in the far wakes of two-dimensional bluff bodies', *Journal of Fluid Mechanics*, vol. 190 pp. 265–298.

Covert, E, 1970, 'An Approximate Calculation of the Onset Velocity of Cavity Oscillations', *AIAA Journal*, vol. 8 no. 12 pp. 2189–2194.

Crook, S D, 2011, '*A study of the flow within shallow, narrow cavities at low Reynolds number*', Ph.D. thesis, The University of Adelaide, Adelaide, Australia.

Crook, S D, Lau, T C W, and Kelso, R M, 2013, 'Three-dimensional flow within shallow, narrow cavities', *Journal of Fluid Mechanics*, vol. 735 pp. 587–612.

Crook, S, 2005, *'Aeroacoustics of Aircraft Cavities'*, Progress Report, School of Mechanical Engineering, The University of Adelaide, Australia.

Crook, S, Hassan, E, and Kelso, R, 2008, 'Low Speed Cavity Flows: Principal Flow Features', In: *Proceedings of the Fifth Australian Conference on Laser Diagnostics in Fluid Mechanics and Combustion*, Perth, Western Australia, Australia.

Crook, S, Kelso, R, and Drobik, J, 2007, 'Aeroacoustics of Aircraft Cavities', In: Proceedings of the *16*th *Australasian Fluid Mechanics Conference*, 2-7 December, Gold Coast, Queensland, Australia.

Curle, N, 1955, 'The infludence of solid boundaries upon aerodynamic sound', *Proceedings of the Royal Society A*, vol. 231 no. 1187 pp. 505–514.

Czech, M, Savory, E, Toy, N, and Disimile, P J, 2000, 'Aerodynamic phenomena associated with yawed rectangular cavities', In: Proceedings of the *18th AIAA Applied Aerodynamics Conference*, 14–17 August, Denver, Colorado, United States of America, AIAA Paper no. 2000-3927.

Debiasi, M, Yan, P, Little, J, Özbay, H, Myatt, J, and Samimy, H, 2004, 'An Experimental Study of Subsonic Cavity Flow – Physical Understanding and Control', In: Proceedings of the *2nd AIAA Flow Control Conference*, 28 June – 1 July, Portland, Oregon, United States of America.

Delprat, N, 2000, 'Rossiter's Formula: A Simple Spectral Model for a Complex Amplitude Modulation Process', *Physics of Fluids*, vol. 18 pp. 071703-1–071703-4.

Desquesnes, G, Terracol, M, and Sagaut, P, 2007, 'Numerical investigation of the tone noise mechanism over laminar airfoils', *Journal of Fluid Mechanics* vol. 591 pp. 155–182.

Diwan, S S, and Ramesh, O N, 2009, 'On the origin of the inflectional instability of a laminar separation bubble', *Journal of Fluid Mechanics* vol. 629 pp. 263–298.

Dix, R E, and Butler, C, 1990, *'Cavity Aeroacoustics'*, Technical paper, Arnold Engineering Development Center.

Doolan C J, Tetlow, M R, Moreau, D J, and Brooks, L A, 2012, 'Vortex Shedding and Tonal Noise from a Sharp Bevelled Trailing Edge', In: Proceedings of *50th AIAA Aerospace Sciences Meeting*, Nashville, Tennessee.

Doolan, C J, and Leclercq, D, 2007, 'An Anechoic Wind Tunnel for the Investigation of the Main-Rotor/Tail-Rotor Blade Vortex Interaction', In: Proceedings of *6th Australian Vertiflite Conference on Helicopter Technology*, 19–22 March, Melbourne, Victoria, Australia.

Doolan, C J, 2007, 'Numerical Evaluation of Contemporary Low-Speed Wind Tunnel Contraction Designs', *Journal of Fluids Engineering*, vol. 129 pp. 1241–1244.

Doolan, C, 2008, 'A Review of Airfoil Trailing Edge Noise and its Prediction', *Acoustics Australia*, vol. 36 no. 1 pp. 7–12.

Doran, D, 2006, '*Experimental Investigation of Transonic Cavity Flow Control*', M.Sc. thesis, Cranfield University, Cranfield, United Kingdom.

Dovgal, A V, Kozlov, V V, and Michalke, A, 1994, 'Laminar boundary layer separation: Instability and associated phenomena', *Progress in Aerospace Sciences* vol. 30 pp. 61–94.

Drault, P Gloerfelt, X, and Mervant, T, 2009, 'Aeroacoustic analysis of cavity flows using Quadratic Stochastic Estimation coupled with Proper Orthogonal Decomposition', In: Proceedings of the *30th AIAA Aeroacoustics Conference*, AIAA Paper no. 2009-3358.

East, L, 1966, 'Aerodynamically Induced Resonance in Rectangular Cavities', *Journal of Sound and Vibration*, vol. 3 no. 3 pp. 277–287.

Efe, M, Debiasi, M, Yan, P, Ozbay, H, and Samimy, M, 2005, 'Control of subsonic cavity flows by neural networks – analytical models and experimental validation', *AIAA Paper* no. 2005-0294.

El Hassan, M, Keirsbruck, L, and Labraga, L, 2009a, 'Aero-Acoustic Coupling Inside Large Deep Cavities at Low-Subsonic Speeds', *Journal of Fluids Engineering*, vol. 131 pp. 011204-1–011204-10.

El Hassan, M, Keirsbruck, L, and Labraga, L, 2009b, 'Non-Oscillating/Oscillating Shear Layer over a Large Deep Cavity at Low Subsonic Speeds', *Flow Turbulence & Combustion*, vol. 82 pp. 359-374.

El Hassan, M, Labraga, L, and Keirsbulck, L, 2007, 'Aero-acoustic oscillations

inside large deep cavities', In: Proceedings of the *16th Australasian Fluid Mechanics Conference*, Gold Coast, Queensland, Australia.

ESDU, 2005, *'Aerodynamics and Aero-Acoustics of Rectangular Planform Cavities, Part I: Time-Averaged Flow'*, ESDU Data Sheet no. 02008.

Faure, T M, Adrianos, P, Lusseyran, F, and Pastur, L, 2007, 'Visualisation inside an open cavity at medium range Reynolds numbers', *Experiments in Fluids*, vol. 42 pp. 169–184.

Franke, M E, and Carr, D L, 1975, 'Effect of Geometry on Open Cavity Flow-Induced Pressure Oscillations', *Progress in Astronautics and Aeronautics*, vol. 45 pp. 297–314.

Gharib, M, and Roshko, A, 1987, 'The Effect of Flow Oscillations on Cavity Drag', *Journal of Fluid Mechanics*, vol. 177 pp. 501–530.

Gharib, M, 1983, '*The Effect of Flow Oscillations on Cavity Drag a Technique for their Control*', Ph.D. Thesis, California Institute of Technology.

Gursul, L, Lusseyran, D, and Rockwell, D, 1990, 'On interpretation of flow visualization of unsteady shear flows', *Experiments in Fluids*, vol. 9 pp. 257–266.

Heller, H H and Bliss, D B, 1975, 'Flow-Induced Pressure Fluctuations in Cavities and Concepts for Their Suppression', *Progress in Astronautics and Aeronautics*, vol. 45 pp. 281-296, also *AIAA Paper* no. 75–491.

Heller, H H, and Delfs, J, 1996, 'Cavity Pressure Oscillations: The Generating Mechanism Visualised', *Journal of Sound and Vibration*, vol. 196 no. 2 pp. 248–252.

Heller, H H, Holmes, D G, and Covert, E E, 1971, 'Flow-Induced Pressure Oscillations in Shallow Cavities', *Journal of Sound and Vibration*, vol. 18 no. 4 pp. 545–553.

Howe, M S, 2004, 'Mechanism of sound generation by low Mach number flow over a wall cavity', *Journal of Sound and Vibration*, vol. 273 pp. 103–123.

Hughes, G, Mamo, T, and Dala, L, 2009, 'Use of Active Surface Waviness for Control of Cavity Aeroacoustics in Subsonic Flows', In: Proceedings of *15th AIAA/CEAS Aeroacoustics Conference (30th AIAA Aeroacoustics Conference)*, 11–13 May, Miami, Florida, United States of America.

Ikeda, T, Atobe, T, and Takagi, S, 2012, 'Direct simulations of trailing-edge

noise generation from two-dimensional airfoils at low Reynolds numbers',*Journal of Sound and Vibration* vol. 331 pp. 556–574.

Jones, L E, Sandberg, R D, and Sandham, N D, 2010, 'Stability and receptivity characteristics of a laminar separation bubble on an aerofoil', *Journal of Fluid Mechanics* vol. 648 pp. 257–296.

Kang, W, and Sung, H J, 2009, 'Large-scale structures of turbulent flows over an open cavity', *Journal of Fluids and Structures*, vol. 25 pp. 1318–1333.

Kang, W, Lee, S B, and Sung, H J, 2008, 'Self-sustained oscillations of turbulent flows over an open cavity', *Experiments in Fluids*, vol. 45 pp. 693–702.

Kaufman II, L, and Clark, R, 1980, '*Mach 0.6 to 3.0 flows over rectangular cavities*', Technical Report, AFWAL-TR-82-3112.

Kingan, M J, and Pearse, J R, 2009, 'Laminar boundary layer instability noise produced by an aerofoil', *Journal of Sound and Vibration* vol. 322 pp. 808–28.

Knowles, K, Lawson, N J, and Ritchie, S A2007, 'An Experimental and Computational Investigation of a 3D, l/h=5 Transonic Cavity Flow', In: Proceedings of *3rd International Symposium on Integrating CFD and Experiments in Aerodynamics*, 20–21 June, Colorado, United States.

Koschatzky, V, Delfos, R, Boersma, J, and Westerweel, J, 2009, 'Boundary layer influence on cavity noise generation' in *Advances in Turbulence XII*, ed. Eckhardt B, pp. 847–850.

Krishnamurty, K, 1955, '*Acoustic radiation from two-dimensional rectangular cutouts in aerodynamic surfaces*', Technical Report, NACA TN-3487.

Kuo, C and Huang, S, 2001, 'Influence of flow path modification on oscillation of cavity shear layer', *Experiments in Fluids*, vol. 31 pp. 162–178.

Kurelek, J W, Kotsonis, M, and Yarusevych, S, 2018, 'Transition in a separation bubble under tonal and broadband acoustic excitation', *Journal of Fluid Mechanics*, vol. 853 pp. 1 – 36.

Lai, H, and Luo, K H, 2008, 'A Conceptual Study of Cavity Aeroacoustics Control Using Porous Media Inserts', *Flow Turbulence and Combustion*, vol. 80 pp. 375–391.

Lai, J C S, Yue J, and Platzer, M F, 2002, 'Control of backward-facing step flow using a flapping foil', *Experiments in Fluids* vol. 32 pp. 44–54.

Lasagna, D, Donelli, R, De Gregorio, F, and Luso, G, 2011, 'Effects of a trapped vortex cell on a thick wing airfoil', *Experiments in Fluids*, vol. 51 no. 1369.

Lasheras, J C, and Choi, H, 1988, 'Three-dimensional instability of a plane free shear layer: an experimental study of the formation and evolution of streamwise vortices', *Journal of Fluid Mechanics*, vol. 189 pp. 53–86.

Lawson, S and Barakos, G, 2008, 'Passive Control of Transonic Cavity Flow', *8th World Congress on Computational Mechanics*, June 30 – July 5, Italy.

Lawson, S J, and Barakos, G N, 2009, 'Assessment of Passive Flow Control for Transonic Cavity Flow Using Detached-Eddy Simulation', *Journal of Aircraft*, vol. 46 no. 33 pp. 1009–1029.

Leclercq D, Doolan C, and Reichl J, 2007, 'Development and validation of a small scale anechoic wind tunnel', In: Proceedings of the *14th International Congress on Sound and Vibration*, Cairns, Australia.

Lighthill, M J, 1952, 'On Sound Generated Aerodynamically I. General Theory', *Proceedings of the Royal Society of London. Series A, Mathematical and Physical Sciences*, vol. 211 no. 1107 pp. 564–587.

Lilley, G M, 2001, 'The prediction of airframe noise and comparison with experiment', *Journal of Sound and Vibration*, vol. 239 no. 4 pp. 849–859.

Lin, J C, and Rockwell, D, 2000, '*Organised oscillations of initially turbulent flow past a cavity*', Technical Report, LM-00K80.

Lin, J C, and Rockwell, D, 2001, 'Organized Oscillations of Initially Turbulent Flow past a Cavity', *AIAA Journal*, vol. 36 no. 6.

Loh, C Y, 2004, '*Computation of Low Speed Cavity Noise*', Technical Report, NASA/CR-2004-212892.

Lu, F K, 2010, 'Surface oil flow visualization', *The European Physical Journal: Special Topics*, vol. 152 pp. 51–63.

Ma, R, Slaboch, P E, and Morris, S C, 2009, 'Fluid mechanics of the flow-excited Helmholtz resonator', *Journal of Fluid Mechanics*, vol. 623 pp. 1–26.

MacManus, D, and Doran, D, 2008, 'Passive Control of Transonic Cavity Flow', *Journal of Fluids Engineering*, vol. 130 pp. 064501-1 – 064501-4.

Manovski, P, Giacobello, M and Soria, J, 2007, 'Particle Image Velocimetry over an Aerodynamically Open Two-Dimensional Cavity', In: Proceedings of the *16th Australian Fluid Mechanics Conference*, 2–7 December, Gold Coast, Queensland, Australia.

Manovski, P, Honnery, D R, and Soria, J, 2005, 'Investigation of Flow Past a Cavity using PLIF and MCCDPIV', In: Proceedings of the *4th Australian Conference on Laser Diagnostics in Fluid Mechanics and Combustion*, 7–9 December, Adelaide, South Australia, Australia.

Marquardt, M F, 1975, '*An Experimental Investigation of Pressure Oscillations in Two-Dimensional Open Cavities*', Technical Report, AD–A023 355, M.Sc. Thesis, Air Force Institute of Technology, Ohio, United States of America.

Marsden, A, Wang, M Dennis, J E, and Moin, P, 2007, 'Trailing-edge noise reduction using derivative-free optimization and large-eddy simulation', *Journal of Fluid Mechanics*, vol. 572 pp. 13–36.

Maull, D, and East, L, 1963, 'Three-dimensional flow in cavities', *Journal of Fluid Mechanics*, vol. 16 pp. 620–632.

McAlpine, A, Nash, E C, and Lowson, M V, 1999, 'On the generation of discrete frequency tones by the flow around an aerofoil', *Journal of Sound and Vibration* vol. 222 no. 5 pp. 753–779.

Merzkirch, W, 2007, 'Flow Visualization', chapter in *Springer Handbook of Experimental Fluid Mechanics*, pp. 857–870.

Milbank, J, 2004, '*Investigation of fluid-dynamic cavity oscillations and the effects of flow angle in an automotive context using an open-jet wind tunnel*', Ph.D. thesis, RMIT University, Melbourne, Victoria, Australia.

Milbank, J, Watkins, S and Kelso, R, 2001, 'An Instance of Cavity Resonance Interaction with an Open-Jet Tunnel Free Shear Layer', In: Proceedings of the *14th Australasian Fluid Mechanics Conference*, 10–14 December, Adelaide, South Australia, Australia.

Moreau, D J, Brooks, L A, and Doolan, C J, 2011, 'On the aeroacoustic tonal noise generation mechanism of a sharp-edged plate', *The Journal of the Acoustical Society of America*, vol. 129 no. 4 pp. EL154–160.

Moreau, D J, Geyer, T F, Doolan, C J, and Sarradj, E, 2018, 'Surface curva-

ture effects on the tonal noise of a wall-mounted finite airfoil', *The Journal of the Acoustical Society of America*, vol. 143 pp. 3460 – 3473.

Morris, S C, 2011, 'Shear-Layer Instabilities: Particle Image Velocimetry Measurements and Implications for Acoustics', *Annual Review of Fluid Mechanics*, vol. 43 pp. 529–550.

Murray, N, Sallstrom, E, and Ukeiley, L, 2009, 'Properties of subsonic open cavity flow fields', *Physics of Fluids*, vol. 21 pp. 095103-1–095103-16.

Nakano, T, Fujisawa, N, and Lee, S, 2006, 'Measurement of tonal-noise characteristics and periodic flow structure around NACA0018 airfoil', *Experiments in Fluids*, vol. 40 pp. 482–90.

Narasimha, R, and Prasad, S N, 1994, 'Leading edge shape for flat plate boundary layer studies', *Experiments in Fluids*, vol. 17 pp. 358–360.

Nash, E C, Lowson M V, and McAlpine, A, 1999, 'Boundary-layer instability noise on airfoils', *Journal of Fluid Mechanics*, vol. 382 pp. 27–61.

Neary, M D, and Stephanoff, K D, 1987, 'Shear-layer-driven transition in a rectangular cavity', *Physics of Fluids*, vol. 30 no. 10 pp. 2936–2946.

Olsman W F J, and Colonius T, 2011, 'Numerical simulation of flow over an airfoil with cavity', *AIAA Journal*, vol. 49 pp. 143–149.

Olsman W F J, Willems JFH, Hirschberg A, Colonius T, Trieling RR,, 2011, 'Flow around a NACA0018 airfoil with a cavity and its dynamical response to acoustic forcing', *Experiments in Fluids*, vol. 51 pp. 493–509.

Olsman, W F J, and Colonius, T, 2011, 'Numerical simulation of flow over an airfoil with cavity', *AIAA Journal*, vol. 49 pp. 143–149.

Olsman, W F J, Willems, J F H, Hirschberg, A, Colonius, T, and Trieling, R R, 2011. 'Flow around a NACA0018 airfoil with a cavity and its dynamical response to acoustic forcing', *Experiments in Fluids*, vol. 51 pp. 493–509.

Ozalp, C, Pinarbasi, A, and Sahin, B, 2010, 'Experimental measurement of flow past cavities of different shapes', *Experimental Thermal and Fluid Science*, vol. 34 pp. 505–515.

Özsoy, E, Rambaud, P, Stitou, A, and Riethmuller, M L, 2005, 'Vortex characteristics in laminar cavity flow at very low Mach number', *Experiments in Fluids*, vol. 38 pp. 133–145.

Panton, R L, 1988, 'Excitation of Helmholtz Resonators by Turbulent Boundary Layers; the Effect of Orifice Geometry', *AIAA Paper* no. 1988–181.

Paterson, R W, Vogt, P G, Fink, M R, and Munch, C L, 1973, 'Vortex noise of isolated airfoils', *Journal of Aircraft*, vol. 10 no. 5 pp. 296–302, also *AIAA Paper* no. 72-656.

Pereira, J C F, and Sousa, J M M, 1994, 'Influence of Impingement Edge Geometry on Cavity Flow Oscillations', *AIAA Journal*, vol. 32 no. 8 pp. 1737–1740.

Perry, A E, and Chong, M S, 2000, 'Interpretation of Flow Visualization', in Smits, A J and Lim, T T (eds), *Flow Visualization: Techniques and Examples*, Imperial College Press, London, UK.

Perry, A E, 1982, '*Hot-wire anemometry*', Oxford: Clarendon Press, Oxfordshire, England.

Plogmann, B, Herrig, A, and Würz, W, 2013, 'Experimental investigations of a trailing edge noise feedback mechanism on a NACA 0012 airfoil', *Experiments in Fluids*, vol. 54 no. 1480.

Plumbee, H S, Gibson, J S, and Lassiter, L W, '*A theoretical and experimental investigation of the acoustic response of cavitis in an aerodynamic flow*', Technical Report, Wright Patterson Air Force Base WADDTR-61-75.

Pröbsting, S, Scarano, F, and Morris, S C, 2015, 'Regimes of tonal noise on an airfoil at moderate Reynolds number', *Journal of Fluid Mechanics*, vol. 780 pp. 407 – 438.

Pröbsting, S, and Yarusevych, S, 2015, 'Laminar separation bubble development on an airfoil emitting tonal noise', *Journal of Fluid Mechanics*, vol. 780 pp. 167 – 191.

Raffel, M, Willert, C, and Kompenhans, J, 1998, '*Particle Image Velocimetry: A Practical Guide*', Springer, Berlin, Germany.

Raman, G, Envia, E, and Bencic, T J, 2002, 'Jet-Cavity Interaction Tones', *AIAA Journal*, vol. 40 no. 8 pp. 1503–1511.

Reichl, J, 2007, '*Redesign of the Anechoic Wind Tunnel at the University of Adelaide*', M.Sc. thesis, University of Adelaide, Adelaide, Australia.

Rockwell, D, and Knisely, C, 1980, 'Observations of three-dimensional nature of unstable flow past a cavity', *Physics of Fluids*, vol. 23 no. 3 pp. 425–431.

Rockwell, D, and Naudascher, E, 1978, 'Review – Self-Sustaining Oscillations of Flow Past Cavities', *Journal of Fluids Engineering*, vol. 100 pp. 152–165.

Rockwell, D, and Naudascher, E, 1979, 'Self-Sustained Oscillations of Impinging Free Shear Layers', *Annual Review of Fluid Mechanics*, vol. 11 pp. 67–94.

Rockwell, D, 1983, 'Oscillations of impinging shear layer', *AIAA Journal*, vol. 21 no. 5 pp. 645–664.

Roshko, A, 1955a, 'Some Measurements of Flow in a Rectangular Cutout', *Technical Note*, NACA TN 3488.

Roshko A, 1955b, 'On the wake and drag of bluff bodies', *Journal of Aeronautical Sciences* vol. 22 pp. 124–132.

Rossiter, J E, 1964, '*Wind-Tunnel Experiments on the Flow over Rectangular Cavities at Subsonic and Transonic speeds*', Aeronautical Research Council Reports and Memoranda, Report Number 3438, London, UK. Also RAE Technical Report no. 64037.

Rowley, C, 2002, '*Modelling, Simulation and Control of Cavity Flow Oscillations*', Ph.D. thesis, California Institute of Technology.

Rowley, C, Colonius, T, and Basu, A, 2002, 'On self-sustained oscillations in two-dimensional rectangular flow over cavities', *Journal of Fluid Mechanics*, vol. 455 pp. 315–346.

Rowley, C W, and Williams, D R, 2006, 'Dynamics and Control of High-Reynolds-Number Flow over Open Cavities', *Annual Review of Fluid Mechanics*, vol. 38 pp. 251–276.

Samimy, M, Debiasi, M, Caraballo, E, Serrani, A, Yuan, X, Little, Y, and Myatt, Y H, 2007, 'Feedback control of subsonic cavity flows using reduced-order models', *Journal of Fluid Mechanics*, vol. 579, pp. 315–346.

Sarohia, V, 1975, '*Experimental and Analytical Investigation of Oscillations in Flows over Cavities*', Ph.D. Thesis, California Institute of Technology.

Sarohia, V, 1977, 'Experimental investigation of oscillations in flows over shallow cavities', *AIAA Journal*, vol. 15 no. 7 pp. 984–991.

Shaw L, Clark, R, and Talmadge, D, 1988, 'F-111 Generic Weapons Bay Acoustic Environment', *Journal of Aircraft*, vol. 25 no. 2 pp 147–153.

Sinha, S N, Gupta, A K, and Oberai, M M, 1982, 'Laminar Separating Flow over Backsteps and Cavities Part II: Cavities', *AIAA Journal*, vol. 20 no. 3 pp. 370–375.

Smith, D L, and Shaw, L L, 1975, '*Predictions of the Pressure Oscillations in Cavities Exposed to Aerodynamic Flow*', Technical Report, AFFDL-TR-75-34.

Stallings, R L, and Wilcox, F J, 1987, 'Experimental cavity pressure distributions at supersonic speeds', *Technical Paper*, NASA TP-2683.

Stanek, M, Visbal, M, Rizzetta, D, Ruben, S, and Khosla, P, 2007, 'On a mechanism of stabilizing turbulent free shear layers in cavity flows', *Computers & Fluids*, vol. 36 pp. 1621–1637.

Takagi, S, and Konishi, Y, 2010, 'Frequency Selection Mechanism of Airfoil Trailing-Edge Noise', *Journal of Aircraft*, vol. 47 pp. 1111–1116.

Tam, C K W, and Block, P J, 1978, 'On the Tones and Pressure Oscillations Induced by Flow over Rectangular Cavities', *Journal of Fluid Mechanics*, vol. 89 pp. 373–399.

Tam, C K W, 1974, 'Discrete tones of isolated airfoils', *The Journal of Acoustical Society of America*, vol. 55 no. 6 pp. 1173–1177.

Tam, C K W, and Ju, H, 2012, 'Aerofoil tones at moderate Reynolds number', *Journal of Fluid Mechanics*, vol. 690 pp. 536–570.

Thorpe, S A, 1987, 'Transitional Phenomena and the Development of Turbulence in Stratified Fluids: A Review', *Journal of Geophysical Research*, vol. 92 no. C5 pp. 5231–5248.

Tillman, W, 1944, 'Additional Measurements of the Drag of Surface Irregularities in Turbulent Boundary Layers', *Technical Memorandum*, NACA TM 1299.

Tracy, M, and Plentovich, E, 1997, 'Cavity Unsteady-Pressure Measurement at Subsonic and Transonic Speeds', *NASA Technical Paper* 3669.

TSI Incorporated, 2000, *'Model 1127/1128 Air Velocity Calibrator: Instruction Manual'*, Minneapolis, United States of America.

Unalmis, O H, Clemens, N T and Dolling, D S, 2004, 'Cavity Oscillation Mech-

anisms in High-Speed Flows', *AIAA Journal*, vol. 42 no. 10 pp. 2035–2041.

van Osch, M, 2008, '*Dynamics of a 2D aircraft wing with cavity: Test of a new experimental method*', M.Sc. thesis, Eindhoven University of Technology.

Vikramaditya, N S, and Kurian, J, 2009, 'Pressure Oscillations from Cavities with Ramp', *AIAA Journal*, vol. 47 no. 12 pp. 2974–2984.

Watmuff, J H, 1999, 'Evolution of a wave packet into vortex loops in a laminar separation bubble', *Journal of Fluid Mechanics* vol. 397 pp. 119–169.

Watmuff, J, 2009, '*Review of Cavity Aeroacoustic Phenomena and Previous Research Initiatives*', Technical Report, Defence Science and Technology Organisation, Australia.

Werner, M J, Würz, W, and Krämer, E, 2017, 'Experimental investigation of an aeroacoustic feedback mechanism on a two-dimensional side mirror model', *Journal of Sound and Vibration*, vol. 387 pp. 79 – 95.

Wieghardt, K, 1942, '*Erh´ohung des turbulenten Reibungswiderstandes durch Oberflachenstorungen*', ZWB Forschungsbericht 1563, March 19, 1942.

Wernet, M P, and Edwards, R V, 1990, 'New space domain processing for pulsed laser velocimetry', *Applied Optics*, vol. 29 pp. 970–115.

Yamamoto, H, Seki, N, and Fukusako, S, 1979, 'Forced Convection Heat Transfer on Heated Bottom Surface of a Cavity', *Journal of Heat Transfer*, vol. 101 pp. 475–479.

Yao, H, Cooper, R K, and Raghunathan, S, 2004, 'Numerical Simulation of Incompressible Laminar Flow over Three-Dimensional Rectangular Cavities', *Journal of Fluids Engineering*, vol. 126 pp. 919–927.

Zhang, K, and Naguib, A M, 2011, 'Effect of finite cavity width on flow oscillation in a low-Mach-number cavity flow', Exp. Fluids, vol. 51 pp. 1209–1229.

Zhang, X, and Edwards, J A, 1992, 'Experimental investigation of supersonic flow over two cavities in tandem', *AIAA Journal*, vol. 30 no. 5 pp. 1182–1190.

Zhuang, N, 2007, '*Experimental Investigation of Supersonic Cavity Flows and Their Control*', Ph.D. thesis, The Florida State University, Florida, United States of America.

Zhuang, N, Alvi, F S, Alkislar, M B, Shih, C, Sahoo, D, and Annaswamy,

A M, 2003, 'Aeroacoustic Properties of Supersonic Cavity Flows and Their Control', In: Proceedings of the *9th AIAA/CEAS Aeroacoustics Conference*, 12–14 May, South Carolina, United States of America.

Ziada, S, Buhlmann, E T, and Bolleter, U, 1989, 'Flow Impingement as an Excitation Source in Control Valves', *Journal of Fluids and Structures*, vol. 3 pp. 529–549.

Appendix A

Additional airfoil tonal noise literature

A number of relevant studies have been published on the topic of airfoil tonal noise production since research for the relevant chapter (Chapter 5: Airfoil Tonal Noise: Results and Discussion) was principally completed and received for journal publication on 25 January 2013[1] (having been presented at a conference on 3 December 2012[2]). The studies have shown considerable evidence for the existence of a feedback loop between the airfoil trailing edge and an unstable separated shear layer, in the present study at a region with an inflectional velocity profile just downstream of the cavity trailing edge, and in other studies near the location of flow separation at a separation bubble on the pressure side and/or suction side airfoil surface (Plogmann, Herrig, and Würz, 2013; Pröbsting, Scarano, and Morris, 2015; Pröbsting, and Yarusevych, 2015; Moreau *et al.*, 2018; Arcondoulis *et al.*, 2019) or near the location of flow separation near a styling ridge on an automotive wing mirror (Werner, Würz, and Krämer, 2017).

In their paper published on 23 April 2013, Plogmann, Herrig and Würz (2013) stated that 'the existence of the proposed feedback loop could be confirmed'. Plogmann, Herrig and Würz (2013) used surface roughness strips to vary the location of flow separation on a NACA 0012 airfoil. This resulted in proportional changes to the airfoil tonal frequency spacing, consistent with a feedback loop existing between the airfoil trailing edge and the location of flow separation fixed by the roughness strip.

Strong tonal noise was only found for cases where a laminar separation bubble was present on the pressure surface near the trailing edge (Plogmann,

[1]Schumacher, K L, Doolan, C J, and Kelso, R M, 2014, 'The effect of a cavity on airfoil tones', *Journal of Sound and Vibration*, vol. 333 no. 7 pp. 1913 – 1931. Received 25 January 2013, revised 22 November 2013, accepted 30 November 2013, available online 18 December 2013.

[2]Schumacher, K, Doolan, C, and Kelso, R, 2012, 'Aerofoil Tones Produced by a Streamlined Plate with Cavity', In Proceedings of: *18th Australasian Fluid Mechanics Conference*, 3-7 December, Launceston, Tasmania, Australia.

Herrig and Würz, 2013). For a case with weak airfoil tones ($\alpha = 4°$, $Re_C = 1.57 \times 10^6$), a laminar separation bubble near the trailing edge was not detected. By comparison, much stronger tones were found at $\alpha = 6°$ ($Re_C = 1.57 \times 10^6$), where a laminar separation bubble was detected. The primary airfoil tone had 20 dB greater amplitude in the noise spectrum for the latter case.

Plogmann, Herrig and Würz (2013, p. 8)[3] developed their methdology on the following basis: 'for two-dimensional rectangular roughness strips a maximum receptivity is obtained for a streamwise extent of the roughness strip corresponding to approximately half a wavelength of the convective boundary layer instability mode' and for a roughness element with a height less than approximately 5% of the boundary layer displacement thickness, 'the roughness element only fixes the point of maximum acoustic receptivity' and is sufficiently thin to not trip the boundary layer to a turbulent state. Therefore, 'the influence of different receptivity locations on the acoustic feedback mechanism can ... be investigated by fixing the point of acoustic-roughness receptivity with the help of very thin, two-dimensional roughness elements.'

For $\alpha = 6°$ and $Re_C = 1.57 \times 10^6$, the roughness strip was positioned at $x/C = 0.75$ on the airfoil pressure side and boundary layer properties were measured between $x/C = 0.8$ and 1.0025. It was confirmed that the roughness strip did not prematurely cause transition. Weak boundary layer waves at the tonal frequencies were found upstream of $x/C = 0.95$, the location of boundary layer separation. Downstream of $x/C = 0.95$, the boundary layer waves were found to be strongly amplified over the separation zone.

These findings by Plogmann, Herrig and Würz (2013) for a NACA 0012 are very similar to the findings in the present study for the 'airfoil with cavity' profile. In the present study, the location of acoustic receptivity was located near the cavity trailing edge and the boundary layer disturbances were similarly amplified over a separation bubble approaching the airfoil trailing edge. This suggests a very similar mecanism of airfoil tonal noise production is involved for both the NACA 0012 and 'airfoil with cavity' profiles.

For a NACA 0012 at $Re_C = 1.49 \times 10^6$ and $\alpha = 6°$, the roughness element on the airfoil pressure surface was placed at $x/C = 0.5$, 0.6, 0.7, and 0.75 (Plogmann, Herrig and Würz, 2013). A change in the airfoil tonal frequencies (a change in both the frequencies and frequency spacing of secondary tones) was found for each roughness strip position. This is consistent with the findings in the present study where different tonal frequencies were found when the position of the cavity trailing edge was varied.

The T-S wave excited at the roughness strip was regarded as 'a linear complex superposition of the two T-S waves at the front (f) and rear (r) edge of

[3]Reprinted by permission from Springer, *Experiments in Fluids*, 'Experimental investigations of a trailing edge noise feedback mechanism on a NACA 0012 airfoil', Plogmann, B, Herrig, A, and Würz, W, Copyright 2013.

the roughness strip, respectively' (Plogmann, Herrig and Würz, 2013, p. 10)[4]. It was found that the peak frequency of the discrete tones was 'close to the most convectively amplified disturbance mode within the boundary layer on the pressure side (Plogmann, Herrig and Würz, 2013, p. 11) consistent with previous literature (Nash *et al.*, 1999, Desquesnes *et al.*, 2007) as well as the present study.

Plogmann, Herrig and Würz (2013) derived a feedback loop model based on a boundary layer stability analysis and on the appropriate number of convective wavelengths existing between the acoustic receptivity location and the airfoil trailing egde, such that constructive feedback occured. The frequency spacing was calculated based on this model, with exceptional agreement found for the cases with the roughness strip (and hence well-defined receptivity location) and good agreement found for the smooth airfoil case (where receptivity had been assumed to occur at the neutral stability point on the pressure surface). A similar boundary layer stability analysis and estimation of tonal frequencies was conducted in the present study in section 5.11.

Pröbsting, Scarano, and Morris (2015) selectively eliminated tonal noise production by flow over either the pressure or suction surface of a NACA 0012 at small angles of attack by tripping the boundary layer on that surface, in order to isolate the tonal noise produced by flow over the opposite surface, and compared the results to the smooth airfoil. At some Reynolds numbers at non-zero angles of attack, both suction and pressure surfaces contributed to the tonal noise spectra of the smooth NACA 0012 airfoil, however intensities of suction-side tones and pressure-side tones were only comparable near the characterisitic Reynolds number (see next paragraph) and most tonal noise 'regimes' could be classed as either strongly suction-side dominated or strongly pressure-side dominated.

Pröbsting, Scarano, and Morris (2015) identified a characteristic chord-based Reynolds number between 130,000 and 210,000 where the NACA 0012 airfoils at small angles of attack switched from suction-side-dominated tonal noise production (below the characteristic Reynolds number) to pressure-side-dominated tonal noise production (above the characteristic Reynolds number). Probsting found a 'ladder structure', as per Paterson (1973) and Arbey and Bataille (1983), for the higher Reynolds number pressure-side-dominated tones, but not for the lower Reynolds number suction-side-dominated tones.

The 'ladder structure' was also found for the tones produced by the 'airfoil with cavity' in the present study, suggesting that pressure-side-dominated tonal noise production applies in the present case. The range of chord-based Reynolds numbers in the present study were 67,000 to 330,000.

Pröbsting & Yarusevych (2015) and Pröbsting, Scarano, & Morris (2015) detailed changes in flow separation location as angle of attack and Reynolds

[4]Reprinted by permission from Springer, *Experiments in Fluids*, 'Experimental investigations of a trailing edge noise feedback mechanism on a NACA 0012 airfoil', Plogmann, B, Herrig, A, and Würz, W, Copyright 2013.

number were varied. As angle of attack was increased, the separation point moved further upstream on the suction side of the NACA 0012 and further downstream on the pressure side of the NACA 0012. As Reynolds number was increased,

> *'the transition point moves upstream on both sides of the airfoil, leading to coherent vortical structures on the pressure side and initial stages of 3D turbuluent breakdown on the suction side.'*
>
> *(Pröbsting, Scarano, and Morris, 2015, p. 429)*[5]

This phenomenon is responsible for the shift from suction-side-dominated tonal noise production to pressure-side-dominated tonal noise production at the characteristic Reynolds number. Furthermore, the existence of a separated shear layer on either side of the airfoil near the trailing edge was therefore 'confirmed to be a necessary condition for the generation of tonal noise' (Pröbsting, Scarano, and Morris, 2015, p. 429).

Arcondoulis *et al.* (2019) considered a number of possible feedback lengths that could best describe the production of airfoil tonal noise from a NACA 0012 airfoil at chord-based Reynolds numbers of 50,000 – 150,000. L_S was the length from the point of flow separation to the airfoil trailing edge, while L_E was an empirically-derived feedback length based on best fit to experiment and from the best match to the ratio of experimentally-found airfoil secondary tonal frequencies. The lengths L_S and L_E were very similar, which implied:

> *'that the boundary layer separation feedback lengh is the most suitable feedback length of those considered in this study and an excellent fit to the tone frequency data.'*
>
> *(Arcondoulis et al., 2019, p. 16)*[6]

Particularly, for non-zero angle of attack the smallest prediction error was found for $L_{S_{s+p}}$, which was a 'dual acoustic feedback mechanism' with L_{S_s} being the feedback length to the separation location on the suction side and L_{S_p} being the feedback length to the separation location on the pressure side. With suitable (but differing) values of n on each surface, a nearly-identical tonal frequency is produced by each surface, resulting in acoustic superposition and a strong primary tone. The acoustic feedback produced at this frequency simultaneously excited the separated shear layer on both the suction and pressure

[5]Pröbsting, S, Scarano, F, and Morris, S C, 'Regimes of tonal noise on an airfoil at moderate Reynolds number', *Journal of Fluid Mechanics*, vol. 780, pp. 407 – 438, reproduced with permission.

[6]Reprinted from *Journal of Sound and Vibration*, Vol. 460, E. Arcondoulis, C. J. Doolan, L. A. Brooks, Y. Liu,'An investigation of airfoil dual acoustic feedback mechanisms at low-to-moderate Reynolds number', Pages No. 114887-1–114887-19, Copyright (2019), with permission from Elsevier.

surfaces. This did not occur for all flow cases, but where it did occur it resulted in the production of a strong flow tone.

Furthermore, for non-zero angle of attack a greater number of secondary tones were found compared to the zero angle of attack case. These were explained as tones produced by either suction-side disturbances or pressure-side disturbances (owing to the different separation location on each surface at non-zero angle of attack and hence different feedback length and mode nubers on each surface), but which did not match the frequency of disturbances on the opposite surface (Arcondoulis *et al.*, 2019).

Similar to the results of Arcondoulis *et al.* (2019), the results of Pröbsting and Yarusevych (2015, p. 174) suggested 'that vortices originating from the suction and pressure side lock on the same frequency'. This was attributed to 'a likely upstream influence of the tonal noise on the separated shear layer development'. The 'pressure side dominated trailing-edge tone, with contribution from the suction-side feedback loop', was considered responsible for this dual feedback mechanism.

Moreau *et al.* (2018) investigated the effect of airfoil camber on NACA XX12 series tonal noise production, with zero camber, 2%, 4%, and 8% camber at 40% chord. Chord-based Reynolds number was 46,000 – 230,000, with angles of attack from 0° to 8°. The authors found that increasing camber resulted in a shift of airfoil tonal noise production to higher Reynolds number. Changing camber resulted in changes in the location of separation bubbles on the pressure and suction surfaces of the airfoil, thereby changing tonal noise generation.

For Re_C = 230,000, at 0% and 2% camber, the separation bubble on the pressure side was located near the airfoil trailing edge (Moreau *et al.*, 2018), most likely resulting in shedding of coherent vortices responsible for tonal noise production. At 4% and 8% camber (Re_C = 230,000), the separation bubble on the pressure side was instead located near the airfoil leading edge, promoting a transition to turbulence on the pressure side of the airfoil, and hence a lack of tonal noise production from the pressure surface. At these levels of camber, a separation bubble is present near the mid-chord of the suction surface which results in the production of a mutlitude of weaker tones, compared to the strong pressure-side-dominated tones at low levels of camber.

Recent studies have also looked at the effect of external acoustic forcing on separation bubbles on airfoil surfaces. Pröbsting & Yarusevych (2015, p. 188) found that the effect of external acoustic excitation was to reduce the size of the separation bubble, cause the separation bubble to move upstream, and promote transition. Kurelek, Kotsonis, and Yarusevych (2018) also examined the effect of external acoustic excitation and similarly found 'earlier shear layer roll-up and reduction in separation bubble size'.

Appendix B

PIV methodology

Particle image velocimetry (PIV) is a technique whereby the velocity field is determined based on the displacement of randomly-distributed particles within a, most commonly, two-dimensional imaging plane for a known time delay, δt. In principle, the imaging region is divided into numerous 'interrogation windows' within each of which the displacement is calculated statistically via a cross-correlation, thereby obtaining a velocity vector. This is shown in figure A.1. In practice, to improve subpixel precision the raw data is first replaced by three-point Gaussian estimators which represent the particles.

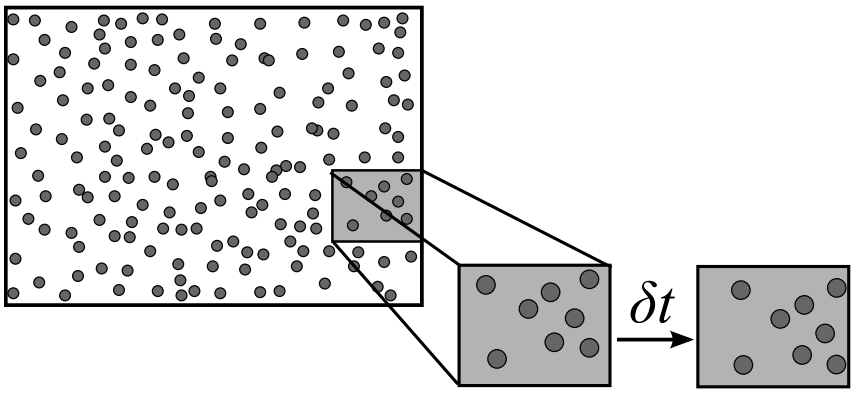

Figure B.1: A diagram of the basic principle of PIV.

In this experiment, a double-oscillator Nd:YAG laser (model 'Quantel Brilliant B Twins') at 10 Hz was used. This laser produces light at a wavelength of approximately $\lambda = 532$ nm (green). A timing box allows control of the time delay (δt) between the two laser pulses. All the imaging has been conducted with the imaging plane approximately parallel to the surface of the flat plate.

The laser beam is formed into a diverging sheet by using a simple optics train, as shown in the schematic drawing of the experimental set-up in figure 3.17. Two 532nm 45°mirrors were used to direct the laser beam to below the water tunnel, where the other optics were located. A pair of irises were used

Table B.1: Parameters used in PIV experiments

Property	Value
Laser type	Nd:YAG
Light frequency	532 nm
Time delay, δt	1.4 ms
Flow velocity, U	90, 144 mm/s
Re_D	6,700, 10,700
Image size	2048 × 2048 px
Dimension of imaging plane	$\sim$ 250 mm × 250 mm
Acquisition rate of pairs	5 Hz
Interrogation window	128 × 128 px
Particle type	Polyamid particles
Average particle diameter	50 μm
Number of pairs	212

to align the beam axially. To form a laser sheet, a convex lens with a focal length of +100 mm was used in series ahead of a concave lens with a focal length of -50 mm which is followed by a cylindrical lens. Finally, a specially-coated mirror placed at 45°is used to direct the diverging laser sheet towards the region of interest.

B.1 Tracer particles

The tracer particles used in PIV are required to effectively scatter the laser light, while also following the flow faithfully. The seeding particles in the present experiment were of the 'Polyamid' type. These particles have a mean diameter of 50 μm and a relative density of 1.03 compared to water at 20°C.

To quantify the ability of the tracer particles to faithfully follow the flow, a Stokes number, Stk, is used. The Stokes number represents a ratio of the settling timescale of the particle, to the timescale of the fluid motions. The Stokes number is given by equation A.1, where ρ_p is the particle density, d_p is the particle diameter, $U_{\text{char.}}$ is the characteristic velocity, μ is the dynamic viscosity ($\sim 10^{-3}$), and $L_{\text{char.}}$ is the characteristic length (Hansen, 2012, p. 115).

$$\mathrm{Stk} = \frac{\rho_p d_p^2 U_{\text{char.}}}{18 \mu L_{\text{char.}}} \tag{B.1}$$

It is required that Stk << 1. In the present instance, the characteristic length is $L_{\text{char.}}$ =0.075 m (the depth of the cavity) and the characteristic velocity is $U_c = 0.147$ m/s. Therefore, the Stokes number is 2.8 $\times 10^{-1}$, which is less than 1 as required.

B.2 Out-of-plane motion

To account for the laser sheet thickness, the following relation should be met with regards to the out-of-plane displacement ($\overrightarrow{v}$). In the present experiments, the sheet thickness (Δy_0) was observed to be approximately 2 mm, therefore $0.25\Delta y_0 \approx 0.5$ mm. For 90 mm/s, $|\overrightarrow{v}|+3v'$ was estimated to be approximately 0.28 mm, while for 147 mm/s, $|\overrightarrow{v}| + 3v'$ was estimated to be approximately 0.45 mm, thus the relation was met.

$$\overrightarrow{v} + 3v' \leq 0.25\Delta y_0 \tag{B.2}$$

B.3 PIV Processing

The PIV processing is divided into two sections: the preprocessing section and the postprocessing section. The displacement in mm effectively represents the velocity provided the known time-step, δt.

B.3.1 Initial outlier tests

Initial outlier removal consisted of two steps: a maximum displacement test, and a maximum difference test. These were adjusted as appropriate for the specific time-step, δt. Outlier replacement is discussed below.

B.3.2 PIV error correction

A process proposed by Hart (2000) was used to improve the calculated vector fields. Hart (2000) summarises that 'out-of-boundary particle motion, correlations occuring between unmatched particle pairs, particle overlap, non-uniform particle distribution, and variations in image intensity' can contribute to errors. In Hart's (2000) method the correlation table for one interrogation region is multiplied by that of an adjacent region that overlaps by 50%. This is said to reduce correlation anomalies and possibly produce a clear correlation peak even when neither individual window possesses one.

B.3.3 Temporal averaging and outlier replacement

Subsequent to the pre-processing, a temporal averaging process was employed to work out the time-average flow properties. The process involved:

1. Omitting outliers.

2. Replacing these outliers with a weighted average of surrounding values.

Outlier replacement involves replacing 'outlier' vectors with a weighted average of surrounding vectors (Hansen, 2012). The vector $\overrightarrow{v}(u_0, v_0)$ is replaced by $\overrightarrow{v}'(u_0', v_0')$, where each of:

$$u_0' = \frac{\sum_{i=1}^{3}\sum_{j=1}^{3} w_{i,j}u(y_i, z_j)}{\sum_{i=1}^{3}\sum_{j=1}^{3} w_{i,j}} \tag{B.3}$$

$$v_0' = \frac{\sum_{i=1}^{3}\sum_{j=1}^{3} w_{i,j}v(y_i, z_j)}{\sum_{i=1}^{3}\sum_{j=1}^{3} w_{i,j}} \tag{B.4}$$

The weighting coefficient, $w_{i,j}$ is determined as follows:

$$w_{i,j} = \Delta \begin{bmatrix} \frac{1}{\sqrt{2}} & 1 & \frac{1}{\sqrt{2}} \\ 1 & 0 & 1 \\ \frac{1}{\sqrt{2}} & 1 & \frac{1}{\sqrt{2}} \end{bmatrix} \tag{B.5}$$

B.4 PIV error analysis

There are many sources of error in particle image velocimetry experiments. According to Hansen (2012, p. 131), a typical PIV system is 'complicated ... with a large number of inter-dependent variables'. The typical sources of uncertainties are summarised as follows:

- Ruler error,
- Timing error,
- Particle image diameter,
- Particle image displacement,
- Particle image density,
- Particle image quantisation,
- Background noise,
- Velocity gradient, and
- Perspective error.

To determine the contribution of different types of errors to PIV, Raffel, Willert and Kompenhaus (1998) performed Monte Carlo simulations. The authors categorise the error into two components: $\epsilon_{U_{\text{bias}}}$ & $\epsilon_{U_{\text{rms}}}$, with the former due to the calculation technique of PIV and the latter due to the flow itself. The total error is given by the sum of these errors, as in equation A.6.

$$\epsilon_{\text{tot}} = \epsilon_{U_{\text{bias}}} + \epsilon_{U_{\text{rms}}} \tag{B.6}$$

Wernet and Edwards (1990) state that the uncertainty is the square root of the sum of the squares of the constituent uncertainties. In the case of PIV conducted here, the error is dominated by the uncertainty in the particle displacement (Crook 2011). Here, N is the number of pairs used to compute the mean. The relevant uncertainties in the mean velocity are given by:

$$\epsilon_{U_{\text{bias}}} = \sqrt{\frac{1}{N}\left[\left(\frac{\sigma_r}{r_0}\right)^2 + \left(\frac{\sigma_t}{\delta t}\right)^2 + \sum\left(\frac{\sigma_s}{\delta s}\right)^2\right]} \tag{B.7}$$

where the errors in the mean particle displacement are,

$$\sum\left(\frac{\sigma_s}{\delta s}\right)^2 = \left(\frac{\sigma_d}{\delta s}\right)^2 + \left(\frac{\sigma_D}{\delta s}\right)^2 + \left(\frac{\sigma_\rho}{\delta \rho}\right)^2 + \left(\frac{\sigma_q}{\delta s}\right)^2 + \left(\frac{\sigma_n}{\delta s}\right)^2 + \left(\frac{\sigma_{\Delta V}}{\delta s}\right)^2 + P_e^2 \tag{B.8}$$

also,

$$\epsilon_{U_{\text{rms}}} = \sqrt{\frac{1}{N}\left[\frac{\overline{|<u>'|}}{\overline{|<\vec{U}>|}}\right]^2} \tag{B.9}$$

In the following calculations, representative time-step is $\delta t = 1.4$ ms, representative displacement is $\delta s = 1.44$ px, and representative particle image diameter is 4 px.

Ruler error, $\frac{\sigma_r}{r_0}$ The system was calibrated by imaging a ruler (two-dimensional grid), which was then used to determine the pitch of the pixel array in the imaged plane. The purpose being to convert the scale in pixels to a scale in millimetres, with the typical resolution being approximately 1 mm to 7 pixels.

The length calibration was conducted using a ruler of at least $\Delta L = 160$mm length. The length, ΔL, was measured over at least 1120 pixels. This gave a conversion factor $r_0 = 160 \pm 0.25\text{mm}/1120 \pm 0.5\text{px} = 0.1429 \pm 0.0003$ mm/px, when considering an uncertainty of 0.25 mm on the ruler and an uncertainty of 0.5 pixels in determining the scale's length in pixels. I.e., the uncertainty $\sigma_r = 0.0003$ mm/px, giving a ruler error of $\sigma_r r_0 = 0.0003/0.1429 = 2.1 \times 10^{-4}$.

Timing error, $\frac{\sigma_t}{\delta t}$ Although the timing is controlled by a timing box, there is a certain, very small 'jitter' associated with each laser pulse. Standard r.m.s. jitter is considered to be $\sigma_t = 250\ ns$ (Crook, 2011). This is then compared to the smallest time-step used between the frames (δt) to give the worst case timing error. Consulting table A.1, the time step is 1.4 ms. Therefore, this error equates to $\sigma_t/(\delta t) = 1.79 \times 10^{-4}$.

Particle image diameter, $\frac{\sigma_d}{\delta s}$ This relates to the uncertainty in calculated displacement due to the particle image diameter. A trend given by Raffel *et al.* (1998, p. 139, Fig. 5.23a) shows that the uncertainty, due to particle image diameter, decreases with increasing window size. Therefore the value for a window size of 64 × 64 pixels can be used as a conservative estimate here, although 128 × 128 pixels was the window size used. The RMS-uncertainty given by Raffel *et al.*(1998, p. 139, figure 5.23a) is 0.013 px, based on a particle image diameter of approximately 4 px obtained in the current experiments, with a typical displacement of $\sim$ 1.5 px between frames.

Particle image displacement, $\frac{\sigma_D}{\delta s}$ Regarding the uncertainty caused by the chosen particle image displacement, in the present case the typical displacement was approximately 1.5 pixels. Raffel *et al.* (1998, p. 139, figure 5.26) gives an estimated RMS-uncertainty of 0.013 pixels, based on a window size of 64 × 64 px and a particle image size of approximately 4 pixels. Note that, since the figure shows a trend of decreasing uncertainty for increasing window size, this is a conservative estimate (a window size of 128 × 128 px was used in the present experiment). This equates to an uncertainty of $\frac{\sigma_D}{\delta s} = 0.013/1.44 = 9.0 \times 10^{-3}$.

Particle image density, $\frac{\sigma_\rho}{\delta \rho}$ The quantity $N_I F_i F_o$ represents the particle image density (the number of particles in an interrogation window), N_I, multiplied by the proportion of pairs lost in-plane, F_i, multiplied by the proportion of pairs lost out-of-plane, F_o (Raffel *et al.*, 1998, p. 141). Effectively, it is the number of matching particle pairs found in an interrogation window between two corresponding frames. By conservatively extrapolating from the data of Raffel *et al.* (1998, p. 142, figure 5.29) for a particle image shift of $\approx$ 1.4 px and a particle image density of $N_I \approx 20$, then the RMS uncertainty due to particle image density is $\sigma_\rho \approx 0.03$ px. Based on a typical displacement, $\delta s = 1.44$ px, this gives an uncertainty $\sigma_\rho/\delta\rho = 2.1 \times 10^{-2}$.

Particle image quantisation, $\frac{\sigma_q}{\delta s}$ The uncertainty of particle image quantization relates to the uncertainty due to digitization of the image. The fewer the number of bits, the higher the relevant uncertainty. Raffel *et al.* (1998, p. 143) state that provided 4 bits per pixel or more are used, then there is 'practically no influence [of image quantisation] on the measurement uncertainty or displacement bias error'.

In the present experiment, images were stored at 16 bits per pixel, but reduced to 8 bits per pixel for processing (i.e., a less refined scale of grayscale intensities). Extrapolating from Raffel *et al.* (1998, p. 143, Fig. 5.30), for a particle image shift of approximately 1.44 pixels, this gives an RMS-uncertainty of 0.025 px. Thus for a typical displacement $\delta s = 1.44$ px, the uncertainty is $\sigma_q/\delta s = 0.025/1.44 = 1.7 \times 10^{-2}$.

Background noise, $\frac{\sigma_n}{\delta s}$ In the present experiments, background noise was quite significant in many instances. Assuming a worst-case 50% background noise level, extrapolating from Raffel *et al.* (1998, p. 145, Fig. 5.33) gives a worst-case RMS-uncertainty of approximately ~ 0.1 pixels. Thus with a typical displacement $\delta s = 1.44$ px, the uncertainty is approximately $\frac{\sigma_n}{\delta s} = 0.10/1.44 = 6.9 \times 10^{-2}$.

Velocity gradient, $\frac{\sigma_{\Delta V}}{\delta s}$ The velocity gradient is the rate of change of displacement (i.e., velocity) with position. It is assumed that the maximum gradient occurs with a complete 180° reversal of the flow between adjacent interrogation windows which, given the typical displacement of 1.44 px, means a change in displacement of 2.88 px.

For the 128 × 128 px windows there is a 50% overlap, which means the change in displacement occurs over a distance of 64 pixels between each vector position. Thus, the representative velocity gradient is 2.88 px / 64 px = 0.045 px/px.

Extrapolating from Raffel *et al.* (1995, p. 145, figure 5.33) gives an estimated RMS-uncertainty of 0.6 px, for interrogation windows of 128 × 128 px with average seeding density of $N_I \approx 20$. This gives a displacement uncertainty of $\frac{\sigma_n}{\delta s} = 0.6/1.44 = 4.2 \times 10^{-1}$, using a representative displacement $\delta s = 1.44$ px.

Perspective error, P_e The perspective error, P_e, occurs due to the physical depth, Δy_0, of the laser sheet. Figure A.2 shows how the maximum perspective error occurs for an actual displacement of δs_{rear} at the rear of the laser sheet, which appears as an apparent displacement of $\delta s_{\text{apparent}}$ at the front of the laser sheet. This error is less significant in the case where the principal flow direction is in-plane, rather than the case where the principal flow direction is out-of-plane (i.e., imaging cross-sections perpendicular to the main flow). The former is the case here. Following the notation in figure A.2, simple geometry gives:

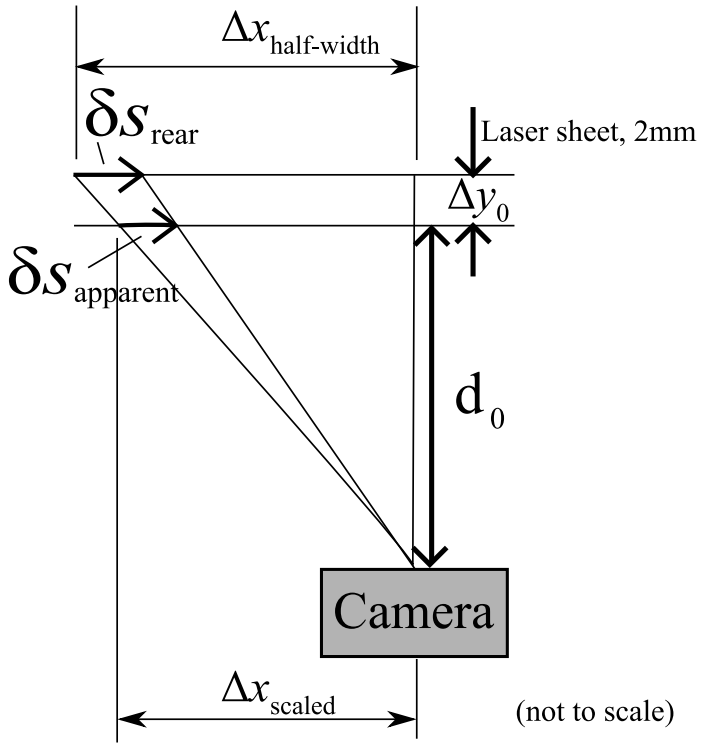

Figure B.2: PIV perspective error sketch, showing the apparent displacement, $\delta s_{\text{apparent}}$, that is measured for an actual displacement of δs_{rear} at the rear of the laser sheet.

$$
\begin{aligned}
\frac{d_0 + \Delta y_0}{\Delta x_{\text{half-width}}} &= \frac{d_0}{\Delta x_{\text{scaled}}} \\
\therefore \Delta x_{\text{scaled}} &= \frac{d_0 \Delta x_{\text{half-width}}}{d_0 + \Delta y_0} \\
\delta s_{\text{apparent}} &= \delta s_{\text{rear}} \times \frac{\Delta x_{\text{scaled}}}{\Delta x_{\text{half-width}}} \\
\therefore \delta s_{\text{apparent}} &= \delta s_{\text{rear}} \times \frac{1}{\Delta x_{\text{half-width}}} \frac{d_0 \Delta x_{\text{half-width}}}{d_0 + \Delta y_0} \\
\therefore \frac{\delta s_{\text{apparent}}}{\delta s_{\text{rear}}} &= \frac{d_0}{d_0 + \Delta y_0} \\
\therefore 1 - \frac{\delta s_{\text{apparent}}}{\delta s_{\text{rear}}} &= 1 - \frac{d_0}{d_0 + \Delta y_0} = P_e
\end{aligned}
\tag{B.10}
$$

Here, the laser sheet thickness was $\Delta y_0 \approx 2mm$ and the distance to the camera was $d_0 = 600$ mm. Therefore equation A.10 gives the maximum perspective error as $P_e = 3.3 \times 10^{-3}$.

Table B.2: Summary of uncertainties in PIV

(a) Error per image pair

Uncertainty	Value
Ruler error, $\frac{\sigma_r}{r_0}$	2.1×10^{-4}
Timing error, $\frac{\sigma_t}{\delta t}$	1.79×10^{-4}
Particle image diameter, $\frac{\sigma_d}{\delta s}$	9.0×10^{-3}
Particle image displacement, $\frac{\sigma_D}{\delta s}$	9.0×10^{-3}
Particle image density, $\frac{\sigma_\rho}{\delta \rho}$	2.1×10^{-2}
Particle image quantization, $\frac{\sigma_q}{\delta s}$	1.7×10^{-2}
Background noise, $\frac{\sigma_q}{\delta s}$	6.9×10^{-2}
Velocity gradient, $\frac{\sigma_n}{\delta s}$	4.2×10^{-1}
Perspective error, P_e	3.3×10^{-3}

(b) Combined error per set of 212 pairs

Error	Value
Combined bias error, ϵ_{bias}	2.9 %
Combined R.M.S. error, $\epsilon_{\text{r.m.s.}}$	6.9 %
Total error, ϵ_{total}	9.8%

Total bias error Using equation A.7 (and the prior discussed constituent uncertainties in table A.2a), the total bias error was computed. To compute the mean properties, a total of $N = 212$ samples were used. The total bias error was found to be $\epsilon_{U_{\text{bias}}} = 0.029$, i.e., 2.9 %.

Measurement (RMS) error Using equation A.9, the measurement (RMS) error was found. The mean fluctuation velocity magnitude was conservatively estimated as being comparable to the mean freestream velocity, i.e., $\overline{|< u >'|} = 144$ mm/s. Also, $N = 212$ and the typical freestream velocity was $|< \vec{U} >| = 144$ mm/s. Therefore, equation A.9 gave that $\epsilon_{\text{r.m.s}} = 0.069$, i.e., 6.9 %.

Total error Following equation A.6, the total error is given as $\epsilon_{\text{total}} = \epsilon_{U_{\text{bias}}} + \epsilon_{\text{r.m.s}} = 0.029 + 0.069 = 0.098$, or 9.8 %.

B.5 Background subtraction

It was found that preliminary PIV results were effectively 'contaminated' around the edges of the cavity, due to a reflection of the nearby laser sheet by the edges of the cavity (as the laser sheet was parallel to and close to the surface of the plate). It was thought this could be corrected by subtracting a background image from each of the PIV images. Unfortunately illuminated 'background' images, with unseeded flow, were not captured for all geometries.

It was considered that by taking an average of the raw PIV images, the particles would approximately behave as random noise (and 'cancel') so that the signal from the background reflections would remain. This was repeated for each of the lasers, i.e., odd images and even images respectively. This mean image would then be considered an approximation of an illuminated but unseeded flow. These means were subtracted from the odd and even frames respectively, before the PIV images were processed in the manner as previously discussed.

Figure A.3 shows a comparison of a section of an arbitrary raw PIV image before and after the subtraction of the mean respectively. In the upper image there is a diagonal band visible, where reflected luminosity from the laser sheet was scattered from the cavity wall (perpendicular to the flow). In this instance there is a double-swept rear wall, with the upper (positive Z) swept half visible due to perspective effects. In the lower image, after subtraction, the visibility of this cavity wall is reduced whilst the relative signal-to-noise ratio of the particles is enhanced. Note that the scale, from black to white, is adapted to fit the range of grayscale values present in the image.

Furthermore, figure A.4 shows the mean velocity magnitude calculated from the set of PIV images, before and after the mean images (for each laser) were subtracted. Figure A.4(b) shows reduced 'contamination' around the edge

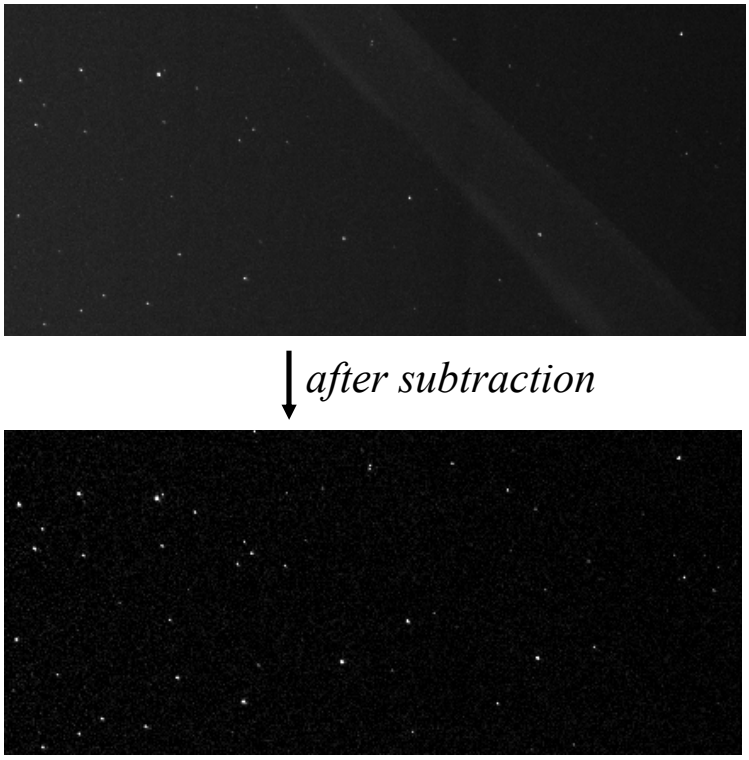

Figure B.3: Comparison of an identical section of an arbitrary PIV frame, both before and after subtraction of the mean image for that laser (i.e., either odd or even) from the set.

of the cavity compared to figure A.4(a). On the other hand, the values of velocity magnitude in the rest of the imaging area do not appear to be effected appreciably. This suggests that subtracting the mean (for each laser) is a reasonable approximation for subtracting the true background reflections of unseeded flow. Therefore, this technique was applied for all processed PIV data.

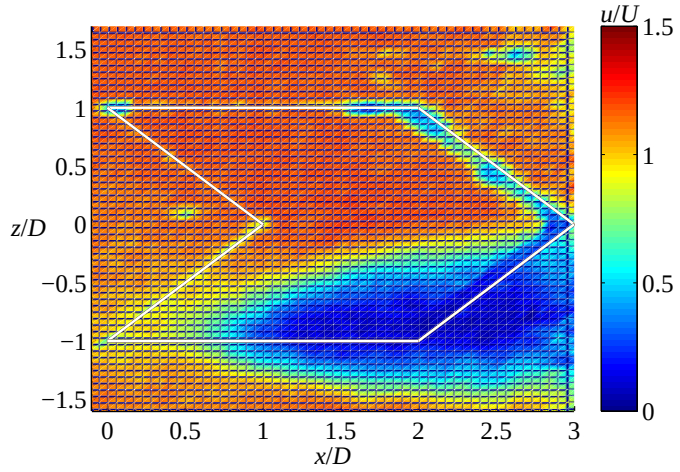

(a) Before subtraction of background reflections

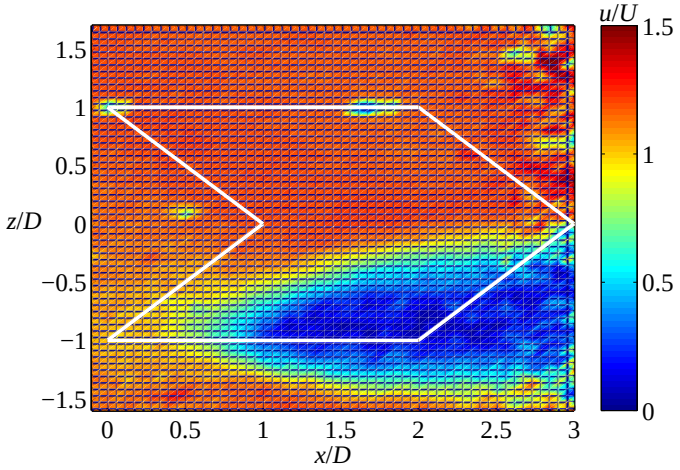

(b) After subtraction of background reflections

Figure B.4: Mean velocity magnitude calculated from the PIV vectors, before and after the mean of the raw PIV images (for each laser, i.e., odd or even frames) were subtracted. $Re_D = 10,900$ (U=147 mm/s), $y/D = -0.35$ (i.e., above the flat plate), for an effective L/D of 2.